APPLICATIONS OF IN SITU MAGNETIC RESONANCE SPECTROSCOPY FOR STRUCTURAL ANALYSIS OF OXIDE-SUPPORTED CATALYSTS

By

NICHOLAS RYAN JAEGERS

A dissertation submitted in partial fulfillment of
the requirements for the degree of

DOCTOR OF PHILOSOPHY

WASHINGTON STATE UNIVERSITY
The Gene and Linda Voiland School of Chemical Engineering and Bioengineering

DECEMBER 2019

To the Faculty of Washington State University:

The members of the Committee appointed to examine the dissertation of NICHOLAS RYAN JAEGERS find it satisfactory and recommend that it be accepted.

_____

Yong Wang, Ph.D., Chair

_____

Norbert Kruse, Ph.D.

_____

Jean-Sabin McEwen, Ph.D.

_____

Junming Sun, Ph.D.

ACKNOWLEDGMENT

I would first like to extend my sincerest gratitude to Professor Yong Wang for accepting me into his research group and providing me his constant support throughout my PhD studies. It has been a truly rewarding experience comprised of more opportunities than I could have hoped to encounter. His tenacity for fundamental insight and student development is a true asset to his group and his talents in directing research are admirable, providing sufficient direction to promote success as well as the freedom to explore new concepts. I truly appreciate his critical lessons, support, and feedback throughout this process. Thank you very much!

Dr. Jian Zhi Hu has also been an integral part of my development as a chemical engineering scientist. I am grateful to him for allowing me to conduct my PhD studies under his guidance and the extensive opportunities afforded by the arrangement. His instruction and innovative approach to NMR have broadened my perspective and allowed me to explore numerous areas of chemical science. I have greatly enjoyed my time with him and the process of developing and applying key characterization technology as well as our deep discussion about science, career-development, and life.

I thank my PhD committee members, Norbert Kruse, Jean-Sabin McEwen, and Junming Sun for their time, assessment, and advice on my work. A special thanks to Professor Israel Wachs for his collaborations and discussions on metal-oxide catalysis. Thanks to the Voiland School of Chemical Engineering and Bioengineering and the Graduate School for admittance into the program, James Petersen for taking the time to introduce me to the school and discuss the department's research and faculty, Steven Saunders for his guidance during my teaching

assistant appointment, and Dr. Wang's research group members (past and present) for the innumerable discussions and support throughout the process. Additionally, I appreciate the support of the administrators who have helped ensure the processes run smoothly, especially Samantha Baily, Christina Stevenson, and Donna Sturdevant. The talent and character of the machinists at PNNL, especially Mark Townsend and James Ewing, have enabled these studies and vastly simplified experiments. I am also grateful to numerous scientists and post docs at PNNL for their collaborations and discussions: Libor Kovarik, Janos Szanyi, Bojana Ginovska, Nancy Washton, Andy Lipton, Jesse Sears, Sarah Burton, Robert Dagle, Vanessa Dagle, Huamin Wang, Feng Gao, Zdenek Dohnalek, Chongmin Wang, Oliver Guitierez, Don Camaioni, Vijayakumar Murugesan, Johannes Lercher, Lu Zhang, Fan Lin, Yiqing Wu, Meng Wang, Manish Shetty, Nick Nelson, Feng Chen, Ying Chen, and Yang He. From my undergraduate university, those who made graduate studies a possibility: Jacqueline Shanks, Stephanie Loveland, Lona Davenport, and Brent Shanks. From secondary school, who fostered an interest in chemistry, mathematics, and engineering: Kevin McGinity, Brook Fischels, Sue Happel, Miriam Kenning, Richard Wortmann, and Mark Anderson. I wish to also thank the Columbia Valley Section of AIChE for the experience and opportunities afforded as a member.

I must also thank my friends and family, both departed and incarnate, for their support throughout this process. I appreciate their encouragement and tolerance for my absence during gatherings and events. My parents especially have been a constant source of inspiration; my mother, Tina, who shows great strength and determination in the face difficult circumstances, and my father, David, who exhibits hard work and dedication to the goals at hand. My sister, Cassie, is a source of joy and is always willing to supply humor when needed most. My wife, Sarah, is a strong supporter, best friend, and caring companion. I thank her for her love, patience,

and tolerance, especially while we lived apart for our respective graduate studies. I appreciate my friends, spatially distant, who have stayed in touch and maintained our close connection. I also wish to thank the new friends made during this journey, especially Xavier, Berlin, James, Gasim, Austin, Sarai, and Cameron who have provided new perspective and much-needed respite from academic endeavors, with a special thanks to my friend Konstantin Khivantsev for the extensive scientific discussions and companionship. I also offer a thanks to my special little buddy, Kit Kat, who has been with me through the whole process. Further, I am grateful to the Heavenly Father, whose laws I seek to understand herein.

Finally, I must thank the co-authors from my published and upcoming work, without whose support this work would not have been completed: Alexandr B. Aleksandrov, Hristiyan A. Aleksandrov, Lawrence M. Anovitz, Markus Bleuel, Mark E. Bowden, Sarah D. Burton, Donald M. Camaioni, Feng Chen, Ying Chen, Yingwen Chen, Zhong Chen, Aurora E. Clark, Sue B. Clark, Wenwen Cui, Vanessa Dagle, Calvin H. Delegard, Mateusz Dembowski, Xuchu Deng, Miroslaw A. Derewinski, David A. Dixon, Mark Engelhard, Andrew R. Felmy, Feng Gao, Vassiliki-Alexandra Glezakou, Trent R. Graham, Miroslaw S. Gruszkiewicz, Oliver Y. Gutiérrez, Kee Sung Han, Jonathan C. Hanson, Yang He, David W. Hoyt, Jian Zhi Hu, Mary Y. Hu, Patricia L. Huestis, Jason Toyoda, Sebastien Kerisit, Konstantin Khivantsev, Greg A. Kimmel, Dan Klaus, Iskra Z. Koleva, Libor Kovarik, Jay A. La Verne, Jun-Kun Lai, Mal-Soon Lee, Johannes A. Lercher, Ping Li, Fan Lin, Andrew S. Lipton, Jue Liu, Jun Liu, Ernesto Martinez-Baez, Donghai Mei, David F. R. Mildner, Joshua Monk, Karl Todd Mueller, Vijayakumar Murugesan, Alpha T. N'Diaye, Thomas M. Orlando, Katharine Page, Carolyn I. Pearce, Kristin A. Persson, Micah P. Prange, Sebastian Prodinger, Zhaohai Qin, Zhaohai Qind, Nav Nidhi Rajput, Kevin M. Rosso, Roger Rousseau, Gregory K. Schenter, Yuyan Shao, Manish

Shetty, Dachuan Shi, Hui Shi, Yongwoo Shin, Andrew G. Stack, János Szanyi, Yu Tang, Franklin Tao, Monica Vasiliu, Georgi N. Vayssilov, Israel E. Wachs, Eric Walter, Chuan Wan, Chongmin Wang, Hsiu-Wen Wang, Huamin Wang, Hui Wang, Meng Wang, Yong Wang, Zheming Wang, Austin Winkelman, Dongmin Yun, Hailin Zhang, Lu Zhang, Xiaoyan Zhang, Xin Zhang, and Meirong Zong.

The research involving vanadium oxide catalysts and a portion of the capability development was supported by the U.S. Department of Energy, Office of Science, Office of Basic Energy Sciences, Division of Chemical Sciences, Biosciences, and Geosciences. The review of biomedical applications and a portion of the capability development was supported by the National Institute of Health, National Institute of Environmental Health Sciences Grant R21ES029778. Research pertaining to energy storage applications was supported by the Joint Center for Energy Storage Research, an Energy Innovation Hub funded by the U.S. Department of Energy, Office of Science, Office of Basic Energy Sciences. The research described in Appendix H is part of the Quickstarter Initiative, through the Laboratory Directed Research and Development Program at Pacific Northwest National Laboratory (PNNL). A portion of the research was performed using EMSL, a national scientific user facility sponsored by the Department of Energy's Office of Biological and Environmental Research and located at Pacific Northwest National Laboratory. ^{51}V NMR experiments were conducted in part using a Bruker 600 MHz NMR spectrometer acquired with support from the US Department of Energy, Office of Science, Office of Basic Energy Sciences (Project Number 66628). EMSL's supercomputers were utilized as a resource for computational modeling. Pacific Northwest National Laboratory is a multi-program national laboratory operated by Battelle for the US Department of Energy under Contract DE-AC05-76RL0 1830.

APPLICATIONS OF IN SITU MAGNETIC RESONANCE SPECTROSCOPY FOR STRUCTURAL ANALYSIS OF OXIDE-SUPPORTED CATALYSTS

Abstract

by Nicholas Ryan Jaegers, Ph.D.
Washington State University
December 2019

Chair: Yong Wang

Nuclear Magnetic Resonance (NMR) stands as an invaluable non-destructive technique to probe catalytic materials. The rise of *in situ* NMR has enabled detailed structural analysis of materials under tightly controlled conditions that are relevant for the chemistry of interest. Herein, the utilization of such technology has been described as it pertains to supported oxide catalysts—in particular, supported vanadium oxide materials. Metal oxides are notoriously challenging to characterize due to the distribution of species (monomer, dimer, polymer, and bulk oxides) they possess, often under the same conditions, as well as their sensitivity to the chemical environment surrounding the active center. ^{51}V NMR is extensively used to understand the structure of vanadia-based catalysts under different environmental conditions. Dehydrated structures are analyzed for silica, titania, and titania/silica supports where the active structures for emissions controls applications are proposed. Vanadia materials under hydrated conditions are also considered where dramatic changes in the surface species towards both less support-coordinated structures and oligomers are present. Dry materials which have previously experienced harsh hydrothermal treatment or have undergone reaction cycles are shown to redisperse on the

surface, including dispersion of the bulk V_2O_5 oxide phase after a single redox cycle of ethanol oxidative dehydrogenation. Finally, the interactions of water and other small molecules with the acid sites of MFI zeolite under strictly controlled environments are explored by monitoring both the interacting chemical constituent and the active site of the oxide. In each case, a firm control over the environment of the materials has enabled the observation of the catalysts under relevant conditions to better understand the nature of the active species. These studies represent a foundation for the wealth of information *in situ* NMR is capable of providing to the understanding of catalytic systems.

TABLE OF CONTENTS

Page

ACKNOWLEDGMENT iii

ABSTRACT vii

LIST OF TABLES xii

LIST OF FIGURES xv

CHAPTER ONE: INTRODUCTION 1

1.1 Foundations of MAS NMR 2

1.2 Development of *in situ* NMR: A Brief Review 11

1.3 Fundamentals of NMR for Vanadium Oxide Catalysts 22

CHAPTER TWO: STRUCTURE OF DEHYDRATED, SUPPORTED VANADIUM OXIDE CATALYSTS 32

2.1 Silica-supported V_2O_5 32

2.2 Promoted Titania-Supported V_2O_5 Catalysts for SCR 44

2.3 Structure of V_2O_5/TiO_2 on Preferentially-Exposed Facets 68

2.4 Structure of Vanadia on bi-layered TiO_2/SiO_2 Supports 83

CHAPTER THREE: STRUCTURE OF WATER-PERTURBED VANADIUM OXIDE CATALYSTS 91

3.1 Water-Mediated Structural Transformation of Silica-Supported V_2O_5 Catalysts 91

3.2 Hydrated Titania-Supported V_2O_5 Catalysts 102

3.3 Impact of Hydrothermal Aging on Titania-Supported V_2O_5 Catalysts 106

3.4 Reaction-Mediated Structural Changes in V_2O_5/TiO_2 Materials 114

CHAPTER FOUR: SOLID-ACID CATALYSTS IN HYDRATED ENVIRONMENTS 122

4.1 Thermally-Perturbed Behavior of Water & Other Small Molecules 123

4.2 Genesis of Hydronium Ions in Zeolites 134

4.3 Other Small-Molecular Interactions with Zeolite Active Centers 154

CHAPTER FIVE: CONCLUDING REMARKS 158

5.1 Summary 158

5.2 Future Direction 160

REFERENCES 167

APPENDIX 216

Appendix A: Equipment Schematics 217

Appendix B: Experimental Methods 237

Appendix C: Additional Supporting Data 254

Appendix D: *In situ* EPR Studies of Methanol oxidation on MoO_3/MOx catalysts 282

Appendix E: Additional Data for Other Oxide Systems 296

Appendix F: The Mechanisms of Ethanol to Butenes over $Ag/ZrO_2/SiO_2$ by *In situ* ^{1}H MAS NMR 316

Appendix G: Second-Order Quadrupolar Energy Perturbations 358

Appendix H: Publication – Adsorption and Thermal Decomposition of Electrolytes on Nanometer Magnesium Oxide:An *in situ* ^{13}C MAS NMR Study 361

Appendix I: Publication – Catalytic activation of ethylene C-H bonds on uniform d^8 Ir(I) and Ni(II) cations in zeolites: toward molecular level understanding of ethylene polymerization on heterogeneous catalysts 383

Appendix J: Publication – Variable Temperature, Pressure Operando MAS NMR for Catalysis Science 425

Appendix K: Publication – *In situ* and Ex Situ NMR for Battery Research 445

LIST OF TABLES

Page

Table 1. First-order quadrupolar energy perturbation coefficients for quadrupolar half-integer spins. The energy is the product of the coefficient and hXq*(3cos2θ-1) 27

Table 2. Second-order quadrupolar energy perturbation coefficients for quadrupolar half-integer spins under MAS. The energy is the product of the coefficient and $(hX_q)^2$ 27

Table 4. Reported species identification of ^{51}V NMR signals of titania-supported vanadia catalysts. 31

Table 5. Quantitative characteristics of V_2O_5/SiO_2 hydrated catalysts 35

Table 6. Integrated area of Gaussian/Lorentzian model fits with a side band simulation of ^{51}V NMR spectra 37

Table 7. Comparison of experimental and calculated vanadium chemical shifts of model compounds. All values are reported as ppm relative to $VOCl_3$. 38

Table 8. Calculated ^{51}V chemical shifts in ppm with reference to $VOCl_3$ based on the TiO_2-supported calculations 39

Table 9. Calculated ^{51}V NMR chemical shifts of vanadium clusters relative to $VOCl_3$ 40

Table 10. Rate and abundance calculation for vanadia-based SCR 66

Table 11. Surface properties of synthesized titania nanoparticles. 71

Table 12. Vanadia contents of facet-dominant supported catalysts. 72

Table 13. Summarized approximate species contributions to the ^{51}V MAS NMR signals of dominant facet titania nanoparticle-supported catalysts. 77

Table 14. Integrated peak fractions for each modeled species of the ^{51}V NMR spectra 94

Table 15. DFT-optimized structures of hydrated vicinal silica models. 94

Table 16. Calculated ^{51}V NMR chemical shifts of vanadium clusters relative to $VOCl_3$ 95

Table 17. Calculated ^{51}V NMR chemical shifts for hydrated cluster models of altered surface morphologies due to the hydrolysis of anchoring sites..... 97
Table 18. Calculated ^{51}V chemical shift values of decavanadate at different levels of protonation (P), resulting in different charges (-4, -5, -6), and using COSMO for solvation effects (w). ZORA results are found in the brackets [ZORA] 102
Table 19. Vanadia content of hydrothermally aged samples determined by ICP. 110
Table 20. Relative abundance of different vanadia species in thermally and hydrothermally treated SCR catalysts. 111
Table 21. Quantification of reduced vanadia species in thermally and hydrothermally treated catalysts. 113
Table 22. Calcination temperature of TiN and the corresponding degree of oxidation. 115
Table 23. Small cluster model calculations of the ^{1}H chemical shift in water as a function of cluster size. 130
Table 24. Liquid and gas ^{1}H chemical shifts at 206°C and 17.67 bar water vapor at different gas to liquid fractions tuned by modulating the water content in a 294 µl rotor. 131
Table 25. Spin-spin relaxation time of different H species in the H-ZSM5 zeolites. 142
Table 26. DFT ^{1}H NMR calculations of selected hydrated clusters 146
Table 27. Extracted parameters from DFT-optimized models of ZSM-5 acid sites with different water loadings. 149
Table 28. Catalyst formulations for metal-oxide promoted SCR. 162
Table 29. Representative chemical shift ranges and times scales for nuclei at two magnetic fields. 457

Table 30. Summary of in situ ^{7}Li NMR Observations. Reprinted with permissions from J. Am. Chem. Soc. 137, 7, 2600-2607. Copyright 2015 American Chemical Society. 476

LIST OF FIGURES

Page

CHAPTER ONE: INTRODUCTION

Figure 1.1. Representative scheme of the Zeeman Effect. 4

Figure 1.2. Representative NMR pulse sequences..... 7

Figure 1.3. Sketch of the time scales available for probing via NMR..... 10

Figure 1.4. High-pressure, high-temperature rotors developed for in situ NMR. The first generation (A) is shown constructed, with an internal view of the fit and matched components and the valve. The modified version of the first generation (B) is portrayed constructed, exploded, and with an internal view of the matched/fit components. The second generation (C) includes an assembled external view, an exploded interpretation, and an internal depiction. The third generation (D) is shown with a constructed depiction, exploded perspective, and an internal view of the fit components..... 13

Figure 1.5. Development of in situ MAS NMR rotors and the associated operating limits and drawbacks. 14

Figure 1.6. Anticipated flow profile within the designed NMR cell, where blue and red coloration represent slower and faster velocity, respectively. Top and bottom flow channels are offset by 30°..... 21

Figure 1.7. Representative static NMR spectra of ethanol dehydration on ZSM-5..... 22

Figure 1.8. Energy level diagram of spin 7/2 nuclei..... 24

Figure 1.9. Spinning sideband patterns of V_2O_5 at different spinning rates and magnetic fields where * represents the center band. 30

Figure 1.10. Representative tetrahedral and square pyramidal monomeric vanadia species..... 31

CHAPTER TWO: STRUCTURE OF DEHYDRATED, SUPPORTED VANADIUM OXIDE CATALYSTS

Figure 2.1. Centerband determination of ^{51}V MAS NMR spectra of dehydrated V_2O_5/SiO_2 catalysts of varying loading, 8% and 3%, at different spinning rates. 36

Figure 2.2. Optimized structures from Table 8 where A is a monomer, B is a dimer, C is a linear trimer, and D is a cyclic trimer. 41

Figure 2.3. Representative mechanistic interpretation of the one-site SCR of NO by NH_3 with vanadia-based catalysts where the proton is transferred to the vanadyl bond (top) or a V-O-Ti bridging bond (bottom). 47

Figure 2.4. Representative mechanistic interpretation of the two-site SCR of NO by NH_3 with vanadia-based catalysts involving both an acid site and a redox site. 48

Figure 2.5. Log [reaction rate] vs log [vanadium oxide loading] for the SCR reaction. Data were recorded at 200°C. 50

Figure 2.6. Turn-over-frequency plot (per vanadia per second) of the SCR reaction of NO_X by NH_3 as a function of surface vanadia loading. Data were recorded at 200°C. 51

Figure 2.7. X-ray diffraction (XRD) patterns of 5% V_2O_5/TiO_2 prepared by incipient wetness impregnation demonstrating the observance of only the anatase and rutile phases of TiO_2 from the P25 support material. 52

Figure 2.8. Raman spectra of dehydrated supported vanadium and tungsten oxides on titania. .. 54

Figure 2.9. ^{51}V MAS NMR results of dehydrated, supported V_2O_5/TiO_2 catalysts prepared by impregnation. Spectral deconvolution summation is presented by the red line and compared to the collected data (blue). Sidebands displayed are indicated by (*). 56

Figure 2.10. DFT clusters used to model monomeric structures on TiO_2, including distorted VO_4 (a), distorted VO_4 with bridge bond protonation (b), distorted VO_4 using two oxygen from TiO_2 (c), distorted square pyramidal (d), and distorted square pyramidal with bridge bond protonation (e). Atoms represented include vanadium (orange), titanium (grey), oxygen (red), and hydrogen (white). 58

Figure 2.11. Turn-over-frequency plot (per vanadia per second) of the SCR reaction of NO_X by NH_3 as a function of surface tungsta loading at a constant 1% V_2O_5 coverage. Reactions were conducted at 200°C. 61

Figure 2.12. The log [reaction rate] vs log [tungsten oxide loading] (bottom) shows a strong correlation between tungsten oxide content and catalytic performance. Reactions were conducted at 200°C. 62

Figure 2.13. Solid state ^{51}V MAS NMR spectra of dehydrated, impregnated 1% V_2O_5-(3-5)% WO_3/TiO_2 catalysts. Spectral deconvolution summation is presented by the red line and compared to the collected data (blue). All spectra were externally referenced to V_2O_5 at -614 ppm. Sidebands displayed are indicated by *. 65

Figure 2.14. Reaction rate vs polymeric vanadium species. 67

Figure 2.15. XRD patterns of synthesized TiO_2 nanoparticles confirming the presence of anatase TiO_2. 70

Figure 2.16. TEM micrographs of TiO_2-101 (left) and TiO_2-001 (right) nanoparticles synthesized to exhibit dominant facets. 71

Figure 2.17. TEM micrographs of TiO_2-001 as a function of tilting angle illustrating the stepped nature of the relatively flat edge. 71

Figure 2.18. EELS mapping of P25 and TiO_2-101-supported vanadia catalysts. 73

Figure 2.19. Raman spectra of the titnia-supported nanoparticles for facet-dominant samples... 74

Figure 2.20. ^{51}V MAS NMR spectra of vanadia supported on titnia nanoshapes exhibiting dominant facets. 76

Figure 2.21. Methanol ODH reactivity of facet-dominant supported vanadia catalysts. 79

Figure 2.22 STEM images and election diffraction pattern of TiO2-(001) [top] and –(101) [bottom] after methanol ODH reaction for 2 hours. 80

Figure 2.23. XPS results of supported vanadia catalysts indicating the presence of potassium on the (001)-supported vanadium oxide catalyst. 81

Figure 2.24. Impact of potassium doping on 1V-001. 81

Figure 2.25. SCR activity of dominant facet titania catalysts..... 83

Figure 2.26. ^{51}V MAS NMR of V_2O_5/x% TiO_2/SBA-15 catalysts. 90

CHAPTER THREE: STRUCTURE OF WATER-PERTURBED VANADIUM OXIDE CATALYSTS

Figure 3.1. Solid-state ^{51}V MAS NMR of supported 8% and 3% VO_x/SiO_2 under hydrated (36 kHz) and dehydrated (38 kHz) conditions. 93

Figure 3.2. Optimized DFT structures of V_2O_5/SiO_2 where a is the monomer, b is a di-hydrated monomer, c is a dimer, d is a tetra-hydrated dimer, e is a linear trimer, f is a tetra-hydrated linear trimer, g is a cyclic trimer, and h is a di-hydrated cyclic trimer. 96

Figure 3.3. Optimized Geometries from Table 16. Calculated ^{51}V NMR chemical shifts for hydrated cluster models of altered surface morphologies due to the hydrolysis of anchoring sites. Where a is a di-grafted monomer, b is a tri-hydrated di-grafted monomer, c is a tetra-hydrated di-grafted monomer, d is a mono-grafted monomer, e is a hydrated mono-grafted monomer, f is a non-grafted monomer, g is a hydrated non-grafted monomer, h is a non-grafted dimer, i is a

hydrated non-grafted dimer, j is a di-grafted dimer, k is a hydrated di-grafted dimer, l is a V-$(OH)_2$-V bridge di-grafted dimer, and m is a hydrated V-$(OH)_2$-V bridge di-grafted dimer 98

Figure 3.4. Optimized geometry of di-protonated decavanadate structure with vanadium reference numbers. COSMO was used for hydration with a radius of 1.9 Å and dielectric of 78.39..... 101

Figure 3.5. ^{51}V MAS NMR results of hydrated V_2O_5(-WO_3)/TiO_2 catalysts prepared by impregnation (I) and co-precipitation (C). Spectral deconvolution summation is presented by the red line. All spectra were externally referenced to V_2O_5 at -613.8 ppm. 105

Figure 3.6. DFT optimized cluster models of hydrated vanadium structures on TiO_2, including distorted tetrahedral (a), distorted tetrahedral with bridge bond protonation (b), di-bridged dimers (c), dehydrated tetrahedral with a hydrolyzed bridge bond (d), and tetrahedral with a hydrolyzed bridge bond. Atoms represented include vanadium (orange), titanium (grey), oxygen (red), and hydrogen (white). 106

Figure 3.7. SCR performance of thermally and hydrothermally aged promoted vanadia catalysts. 108

Figure 3.8. In situ Raman spectra of dehydrated initial (calcined at 650 C for 4 hrs in flowing air) and hydrothermally treated (650 °C for 50 hrs in flowing 10% O_2, 8% H_2O, 7% CO_2, 75% N_2) supported 1% V_2O_5-1to8% WO_3/TiO_2 catalysts. 109

Figure 3.9. ^{51}V MAS NMR data of thermally (left) and hydrothermally (right) treated catalysts. 111

Figure 3.10. EPR spectra of thermally and hydrothermally treated catalyts. 113

Figure 3.11. In situ NMR centerband spectra (top) and spinning sideband pattern (bottom) of dehydrated a) $V/TiO_{0.04}N_{0.98,}$ b)$V/TiO_{0.12}N_{0.94}$, c)$V/TiO_{0.26}N_{0.87}$, d)$V/TiO_{0.8}N_{0.6}$, e) $V/TiO_{1.3}N_{0.35}$, and f) V_2O_5 measured after dehydration at 300ºC for 1h in dry air..... 117

Figure 3.12. TOF values at zero residence time as a function of the degree of oxidation of supports (%). 118

Figure 3.13. In situ NMR centerband spectra of the dehydrated oxidized $V/TiO_{0.04}N_{0.98}$ (bottom), the sample reduced in a stream of ethanol at 200ºC for 1 hour (middle), and then reoxidized in 10% O_2/N_2 at 200ºC for one hour (top). 120

Figure 3.14. In situ NMR centerband spectra of dehydrated a)$V/TiO_{0.04}N_{0.98,}$ b)$V/TiO_{0.12}N_{0.94}$, and c) $V/TiO_{0.26}N_{0.87}$, measured after dehydration at 300ºC for 1h in dry air (left) and then after reduction in ethanol at 200ºC followed by reoxidation at 200ºC for one hour (right). 121

Figure 3.15. In situ ^{51}V MAS NMR spectra of 1% and 5% V_2O_5/TiO_2 catalysts after one hour of SCR reaction conditions. 121

CHAPTER FOUR: SOLID-ACID CATALYSTS IN HYDRATED ENVIRONMENTS

Figure 4.1. Proton (right) and oxygen (left) data collected for chemical shift and full-width at the half-maximum (top) and spin-lattice relaxation time (bottom). 200 µl of 2% $H_2{}^{17}O$ was loaded into the rotor to maintain primarily condensed phase water throughout the experiments. [a]Data extracted from Gottlieb et al. J Org Chem **1997**, 62, 7512-7515..... 126

Figure 4.2. Representative scheme of tetrahedrally-coordinated water..... 127

Figure 4.3. Representative inversion recovery result showing the spectral intensity as a function of delay time for ^{17}O in water at 170°C. 127

Figure 4.4. Transition from ice to liquid water where the liquid component (top) is observed to increase and the broad solid feature (bottom) diminishes as the phase transition occurs..... 128

Figure 4.5. Representative NMR spectra of vaporized water at 260°C for ^{1}H and ^{17}O NMR.... 130
Figure 4.6. Gas:liquid exchange depicted by ^{1}H NMR with differing degrees of gas fraction.. 131
Figure 4.7. ^{1}H NMR chemical shift data for TMS, cyclohexane, ethanol, and isopropanol in the liquid and gas phase a function of temperature. Approximately 15 µl of liquid was added to the rotor during the runs to allow for the clear observation of gas phase constituents..... 133
Figure 4.8. ^{1}H one-pulse and ^{1}H-^{29}Si Cross Polarization (CP) MAS solid-state NMR spectra; and dependencies of CP signal relative intensities of zeolites on water loading of dehydrated zeolites. (a, b) The deconvolution of the first ^{1}H NMR and CP ^{29}Si spectrum is shown at the bottom of b, and the dependencies of these relative intensities are shown in c and f. 137
Figure 4.9. Representation of BAS environment for a) bare acid site, b) low water concentrations with hydronium ion formation, and c) high water concentrations with extended phase. Dotted arrows suggest relative H-Si distances where solid lines indicate chemical exchange between protons..... 139
Figure 4.10. DFT-optimized structures of BAS hydration in the H-ZSM5 zeolite channel with increasing numbers of water molecules optimized by DFT cluster calculations. From a to d, the number of water molecules increases from 1–4 with the shortest O-H distance labeled in each cluster..... 140
Figure 4.11. (a - j) Comparison of ^{1}H spin-echo MAS NMR spectra of different water loading on the zeolites acquired with varying echo times. Spinning rate was 9.5 kHz and the echo time varied from 0.1 to 40 ms. The recycle delay was 10 s and 16–1024 scans were acquired depending on the signal/noise. The shaded areas indicate the range of H_2O/BAS ratios when the signal at 9 ppm appeared..... 141

Figure 4.12. ^{1}H (a) and ^{27}Al (b) NMR spectra of $Al(NO_3)_3 \cdot 9H_2O$ at 20 kHz MAS. The proton spectrum shows signals relating to water surrounding Al ions (9.3 ppm), system background as determined by pulse width calibration (6.6 ppm), and water in an outer shell that link octahedral within the same layer and nitrate anions (4.3). Two ^{27}Al signals are present (0.1 and -1.4 ppm) which relate to the two similar, but distinct, Al octahedral in the crystal structure..... 145

Figure 4.13. Geometry optimized structures of $Al(H_2O)_6^{3+}$ (one water shell) and $Al(H_2O)_6^{3+} \cdot 12H_2O$ (two water shells). 145

Figure 4.14. ^{1}H one-pulse NMR spectra of perchloric acid with different concentrations (left), dependences of ^{1}H chemical shift on molar fraction of the acid (upper right) or the ratio between H^+ and H_2O (lower right). 147

Figure 4.15. ^{1}H one-pulse NMR spectra of dehydrated H-ZSM5-15 with different amounts of perchloric acid solution in two different concentrations..... 148

Figure 4.16. Comparison of ^{1}H one-pulse NMR spectra of H-ZSM5-15 loaded with different amounts of water at different temperatures. All thermal effects were reversible. The numbers of water molecules (and uncertainties) determined by spin counting, are listed on the left of each spectrum. 150

Figure 4.17. In-situ ^{1}H one-pulse NMR spectra of H-ZSM5-15 at different temperatures with different water loadings. From a to d, 0.5, 1.0, 2.3 and 15 water molecules per acid site were obtained from the samples respectively, and the insert figure in d shows the comparison between the sample and water in a narrow range. Asterisks denote spinning sidebands. 152

Figure 4.18. ^{13}C NMR of ethanol adsorbed to the acid site of ZSM-5 as a function of temperature. 156

Figure 4.19. ^{13}C spectra of neat ethanol as a function of temperature. 157

CHAPTER FIVE: CONCLUDING REMARKS

Figure 5.1. ^{51}V MAS NMR results of V_2O_5(-WO_3)/TiO_2 catalysts treated with NH_3 and NO, prepared by impregnation. Spectral deconvolution summation is presented by the red line. All spectra were externally referenced to V_2O_5 at -613.8 ppm..... 166

Dedication

To my parents

with much love.

CHAPTER ONE: INTRODUCTION

For nearly 300 years, catalysts have been a vital component of industrial operations. It is estimated that a catalyst is involved at some stage in the manufacturing of nearly 90% of all commercial products and chemicals. The market size for the catalyst materials alone was approximately $25 billion in 2018 and projected to expand by 4.5% annually.[1] The combined value and growth are a clear indication of the importance of these materials for a variety of applications. With such extensive societal value, there exists a strong desire to understand the fundamental principles behind these catalytic materials to rationally guide the development of new materials for improved energy and atom efficiencies with mitigated environmental impact.

Extensive efforts to understand these systems have relied upon a variety of methods to characterize materials and probe reaction mechanisms. Spectroscopic techniques are of great interest due to their potential ability to detect surface structures or reaction intermediates and direct observation of the interactions between substrates and catalysts. Combining a variety of techniques is often essential to gain a complete view of the catalyst system. One powerful technique which will be a central focus of this work is Nuclear Magnetic Resonance (NMR). NMR probes the nuclei of molecules exposed to the magnetic field in a non-destructive and quantitative fashion. By noting the chemical environments of these nuclei, one can gather useful structural information to aid in addressing related scientific questions. Furthermore, NMR's ability to quantitatively detect many of the nuclei commonly present within organic molecules (^{1}H, ^{2}H, ^{13}C, ^{14}N, ^{15}N, ^{17}O, ^{19}F, ^{31}P) makes it an attractive option to supplement other spectroscopy techniques when *in situ* detection is desired. Thus, NMR can help elucidate the structure-function relationships involved in catalyst systems via providing the information on structural aspects and reactive properties of catalyst materials, reaction pathways involved, or, in

some cases, kinetics analyses. Advancement to truly *in situ* conditions comes with its own set of challenges, however. Herein, the foundations of this spectroscopic technique will be laid out and advances in technology for *in situ* NMR will be described in Chapter 1. In subsequent chapters, efforts to study materials under controlled environments for a deeper understanding of oxide systems will be described. The studies are centered on understanding to the structure of active sites under controlled environments, in particular as they pertain to vanadium oxide catalysts, an important class of materials for industrial catalysis science applications including emission abatement, selective oxidation of hydrocarbons, and sulfur dioxide oxidation. Chapter 2 will explore the dry structure of vanadium oxide materials, including published work on silica-supported vanadium oxide and promoted vanadium oxide materials for selective catalytic reduction (SCR) to identify the active surface structures. Efforts to understand how the surface anchoring sites may play a role in the structure of vanadia are described as they pertain to dominant-facet titania and bi-layered, TiO_2-SiO_2 supports. In Chapter 3, the effects of moisture are briefly explored for silica- and titania-supported catalyst, including the evolution of surface species with hydrothermal treatment. Chapter 4 extends the application of *in situ* NMR to explore the evolution of solid-acid active site structures under controlled environments. The results herein represent advances in both the understanding of these catalyst systems as well as methodology in the characterization of catalyst materials.

1.1 Foundations of MAS NMR

Nuclear magnetic resonance spectroscopy (NMR) serves as a non-destructive tool in characterizing samples across an array of applications. This spectroscopic technique operates by the detection of emitted electromagnetic radiation, typically in the range of 10 MHz to 1GHz (radio waves). This interaction stems from two properties of atoms, nuclear magnetism and

nuclear spin. Nuclear magnetism is a weak property that dictates a nuclei's interaction with magnetic fields. The nuclear spin state is a vector quantity that refers to the relative direction of the magnetism induced by the motion of a charged particle (a spinning nucleus). These two properties can be exploited to better understand the environment around the nucleus of interest for nuclei of non-zero spin. In the absence of a magnetic field, the nuclear spins are randomly oriented and degenerate to each other. Upon exposure to a magnetic field, spin states are either in alignment with or against the applied external magnetic field, causing an energy separation known as the Zeeman Effect (Figure 1.1). High energy spin states oppose the magnetic field and low energy spin states match alignment. The distribution of these species is a thermodynamic equilibrium which can be described by a Boltzmann distribution (Eq. 1).

$$\frac{N_u}{N_l} = e^{-\Delta E/kT} \qquad \text{Eq. 1}$$

Where N is the population of the spin states in the upper and lower energy levels, ΔE is the energy difference between the two states and k is the Boltzmann constant. NMR takes advantage of this equilibrium by exciting a nucleus and recording the response.

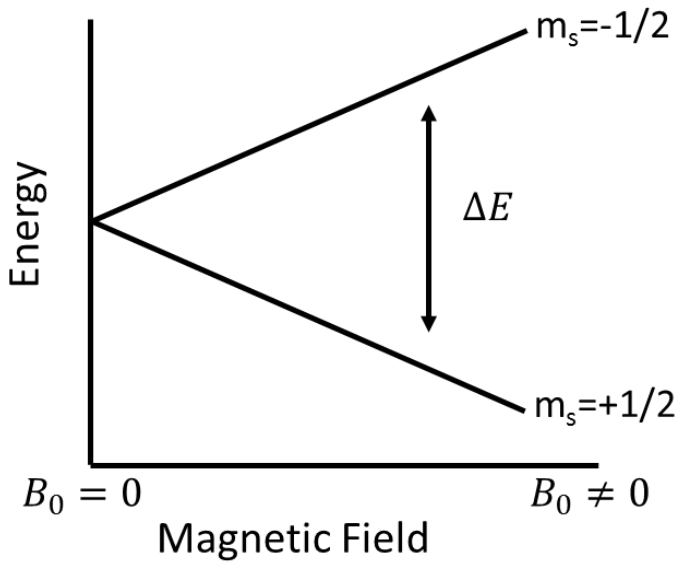

Figure 1.1. Representative scheme of the Zeeman Effect.

To understand the excitation-relaxation process, it must be understood that the spins have an angular frequency of precession around the external magnetic field.[2] This frequency is known as the Larmor frequency, and it is characteristic of the nucleus via the gyromagnetic ratio (γ) and proportional to the external magnetic field (B^0) as shown in Eq. 2. This same angular frequency relates to the energy difference between the spin states as shown in Eq. 3.

$$\omega^0 = \gamma B^0 \qquad \text{Eq. 2}$$

$$\omega = 2\pi v = \frac{\Delta E}{2\pi h} \qquad \text{Eq. 3}$$

This difference in energy between the two states dictates the ratio of population states through a Boltzman distribution (Eq. 1). By applying a radio field pulse near the frequency

corresponding to this energy difference, low-energy spins can be flipped to a high energy state, generating a precessing transverse magnetization. The rotating magnetic movement creates a magnetic field that is also rotating and generating an electric field. This field modulates the electrons in the NMR detection coil and this oscillation is recorded as the free-induction decay (FID) of the NMR spectrum, which can be further processed to generate an NMR spectrum. Small changes to the local structure around the nucleus will slightly alter the energy of the precession, resulting in contrasting chemical shifts of different species and enabling detection of different species in the spectrum. Due to the low abundance of the excited, low-energy spin population, the resulting signal is quite small. This insensitivity may be compounded by low gyromagnetic ratios and a small natural abundance of the NMR-active isotope. The relatively low sensitivity of NMR compared to other spectroscopic techniques is one of the greatest challenges to the wide utilization of MAS NMR, in addition to the high resource needs.

The signal generated by the excited spins eventually subsides, necessitating repeated scans for improved signal distinction above the noise generated by thermal motions of electrons in the receiver coil. The two relation mechanisms are described by spin-lattice (T_1) and spin-spin (T_2) relaxation. Spin-lattice relaxation refers to the tendency for the parallel component of excited spins to relax back to thermodynamic equilibrium as energy is dissipated. Spin-spin relaxation accounts for longitudinal relaxation due to dephasing of spin states as they interact with each other. In practical terms, it takes approximately five spin-lattice relaxation time constants (T_1) for the system to reach thermodynamic equilibrium and become ready for another radio frequency (RF) pulse.

Two typical pulse sequences are shown in Figure 1.2. A single pulse experiment, such as the depicted ^{13}C SP sequence, will consist of a recycle delay to ensure all nuclei are relaxed, an RF pulse to excite the nuclei, and a detection period where decoupling may be present on another probe channel to minimize the effects of J-coupling. This pulse will provide information on all carbon species present, provided the abundance is sufficient for detection (given that the natural abundance of ^{13}C is 1.11%). A second pulse sequence commonly employed is that of cross-polarization (CP). In this sequence, an abundant and sensitive nucleus is excited, and the energy is transferred to a less abundant nucleus to enhance the detected signal. In the depiction, protons (99.985% ^{1}H naturally) are excited with an RF pulse. A contact pulse is then applied to both the ^{1}H and ^{13}C channels to match their respective frequencies according to the Hartman-Hahn condition (spin-locking). This contact pulse enables polarization transfer from ^{1}H to nearby ^{13}C nuclei typically resulting in increased signal strength and faster repetition since the high γ ^{1}H nucleus relaxes faster.

Due to the necessity of spins to be adjacent and locked, the cross-polarization pulse sequence only detects those species which are fairly rigid and in close proximity to the excited nuclei. A species in free motion will not efficiently transfer the energy, thereby resulting in no observed signal. As such, the CP pulse sequence is employed to detect and enhance the signal of surface-immobilized species, a feature useful in heterogeneous catalysis where the interactions of interest take place on the surface.

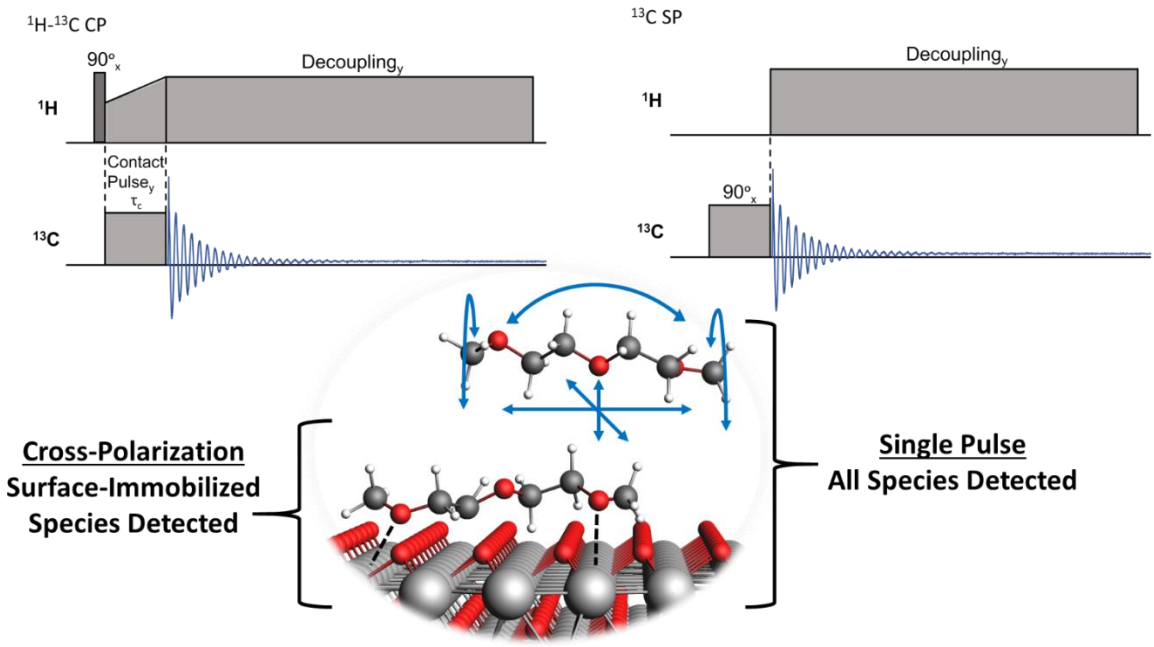

Figure 1.2. Representative NMR pulse sequences.

To conduct detailed studies on solid samples with an enhanced quantity of spectral resolution, a technique known as magic angle spinning (MAS) is required.[3-4] MAS addresses the orientation-dependent (anisotropic) interactions of NMR by spinning the sample about the magic angle—54.7356° with respect to the magnetic field—which dramatically narrows the lines observed in solids and introduces side bands to the spectra from spin echos.[5] The line narrowing arises from the mathematical formulation of the Hamiltonian, which represents the energy of the interaction between the spin and magnetic field. Further details are available elsewhere[6-7], but representative Hamiltonians which make up the operator for NMR are shown in Eq. 4 (chemical shift, scalar coupling, J-coupling, quadrupolar of the nth order, knight shift, paramagnetic, etc.).[1]

[1] J-coupling results from through-bond interactions in which the spin state of a nearby nucleus perturbs the spin of the reference, giving rise to peak splitting; knight shift arises in conducting solids where the presence of a magnetic field splits the energy of conduction electron spins states and induces a magnetic moment on the nucleus; paramagnetic coupling refers to additional magnetic fields generated at the nucleus by localized unpaired electrons.

Under this condition, the directionally dependent interactions can be reduced to simulate the Brownian motion realized by liquids. This results in an averaging of the chemical shift to reveal an isotropic chemical shift, and dipolar interactions arising from the two magnetic dipoles in close proximity are reduced to zero. Similarly, quadrupolar interactions can be reduced, but only those of odd order (Q^1, Q^3, etc.) .

Though quadrupolar interactions are not eliminated entirely, the broadening induced by quadrupolar interactions is dramatically reduced by MAS. This principle and value are derived from the fundamental quantum mechanics-based mathematical description of these interactions, which have an angular dependency with respect to the magnetic field of $3\cos^2\theta$-1. At the magic angle, this term is reduced to zero, canceling out the interactions.

$$\hat{H} = \hat{H}_{Zeeman} + \hat{H}_{CS} + \hat{H}_{DD} + \hat{H}_J + \hat{H}_Q^n + \hat{H}_K + \hat{H}_P \cdots \quad \text{Eq. 4}$$

Though the primary concern herein lies with changes in chemical shift as samples are modulated, in some cases the species change over time and this change can be monitored by NMR. Typically, the temporal resolution is highly dependent upon the sensitivity of the nucleus and its abundance in the system. For time-resolved ^{1}H spectra, for example, spectra can often be generated on the order of seconds. This will provide snapshots of the average chemical environments of molecules during the experiment. For a less sensitive nucleus such as ^{13}C, repeated scans may take several minutes or days in the case of supported vanadia catalysts. NMR is also capable of probing shorter time domains as depicted in Figure 1.3. In addition to the chemical shift value describing length-based information about the chemical environment over

time, the linewidth of a given signal provides the dynamic properties of a molecule, such as the rotational and translational behaviors. This motion is partially related to the interchanging of species environment, termed chemical exchange. A given nucleus may sample a range of magnetic environments over the course of an NMR pulse, such as a ligand exchange. The resulting NMR spectrum can provide kinetic information regarding the rate of this exchange. The concept is analogous to the uncertainty principle whereby the uncertainty in the resonance frequency is inversely proportional to the lifetime in a given state. A high rate of exchange means that the lifetime in a given state is low and the resonant frequency is apparent. The limits of detecting the chemical exchange rate are determined by the difference in frequency between environments, and thus the nucleus and magnetic field according to Eq. 5.

$$\tau_{coalescense} = \left(\sqrt{2}\pi\Delta v\right)^{-1} = k^{-1} \qquad \text{Eq. 5}$$

Δν difference in frequency between the environments. For a slowly exchanging process, each resonance will be well-resolved. Higher exchange rates will broaden the lines of each species and stimulate the migration of them towards the weighted average signal location. When the exchange rate reaches an order of magnitude higher than the frequency difference between the species, the resonances are averaged to a single broad line, which progressively narrows to a sharp resonance as the exchange rate reaches three orders of magnitude higher than the difference in the frequencies. Random molecular motions related to translation, rotation, and vibration can also be measured by the T_1 and T_2. This can be extracted by relating the measured relaxation time constants to the correlation time τ_c (Eq. 6 and Eq. 7). Scalar coupling (dipole-

dipole coupling) can provide the threshold for the molecular motion to different environments; for example, if the lifetime of the species in a given environment is short compared to the inverse of the coupling constant, no coupling will be observed in favor of a single resonance. Chemical exchange rates can be measured by assessing the frequency differences between two species that are exchanging. Further details on the determination of these rates are available in a related work by Hu, Jaegers, Hu, and Mueller[8] or in Appendix K: Publication – *In situ* and Ex Situ NMR for Battery Research.

$$\frac{1}{T_1} = \frac{3}{160}\frac{\mu_0 \gamma^4 \hbar^2}{r^6}\left[\frac{\tau_C}{1+\omega^2\tau_C^2} + \frac{4\tau_C}{1+4\omega^2\tau_C^2}\right] \quad \text{Eq. 6}$$

$$\frac{1}{T_2} = \frac{3}{320}\frac{\mu_0 \gamma^4 \hbar^2}{r^6}\left[3\tau_C + \frac{5\tau_C}{1+\omega^2\tau_C^2} + \frac{2\tau_C}{1+4\omega^2\tau_C^2}\right] \quad \text{Eq. 7}$$

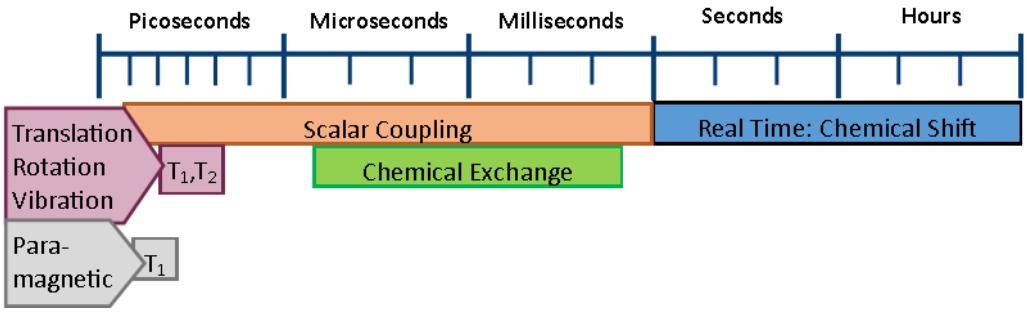

Figure 1.3. Sketch of the time scales available for probing via NMR.

From Hu, Jaegers, Hu, and Mueller, *Journal of Physics Condensed Matter 2018* 30, with permission from IOP Science.

1.2 Development of *in situ* NMR: A Brief Review

Based on Nicholas R. Jaegers, Mary Y. Hu, David W. Hoyt, Yong Wang, and Jian Zhi Hu; "Development and application of in-situ high-temperature, high-pressure magic angle spinning NMR" In: G. Webb *Modern Magnetic Resonance, 2nd edition*, Springer, Cham DOI: 10.1007/978-3-319-28388-3_93

To provide fundamental insights on catalytic systems, spectroscopic methods are extensively utilized to provide thorough insight on the species or properties present in that system. There exists a strong desire to measure these systems under the conditions at which the reactive transformations take place for observation of the chemical species under relevant conditions. Since chemical species are often highly dependent on their chemical environment, observation of detailed structural information under realistic reaction conditions has prompted improvements to NMR technology that enable measurements under harsher conditions than those possible with commercial NMR technology. The quality of spectra acquired, and thus the information acquired from solid samples, has been substantially enhanced by magic angle spinning (MAS) NMR; however, methods that permitted high-pressure environments were not reported for decades after the development of MAS.[3-4] Without such technologies, systems that are strongly impacted by the chemical environment, such as trace water leaking into the rotor from purge gas or a temperature- or pressure-dependent structure, are hindered. The critical need to develop *in situ* MAS NMR techniques was clearly identified to provide relevant spectroscopic information to mirror the relatively harsh conditions of catalytic chemistry.

Early advancement of *in situ* NMR technology was mired by an array of technical challenges. In particular, the NMR rotor has to withstand the conditions present within its walls as it performs several thousand rotations per second. Metallic sample cells may be an attractive option to withstand high pressures, but they are unusable due to the generation of powerful eddy currents from spinning metal in a magnetic field. This limits the construction to materials such as glasses, ceramics, and plastics. Work from the 1990s and early 2000s utilized flame- or epoxy-sealed Pyrex tubes inserted into commercial rotors to probe the chemistry of polymers plasticized by dense gases.[9-11] Due to the fragility of the glass insert, this format experienced challenges in exceeding 70 bar of internal pressure. It was further impossible to reuse or open the glass cell to charge additional material, limiting the ease of use and applications to a variety of chemical systems and encouraging advancement of technologies based on other materials and designs.

Polymer-based PEEK™ and Delrin™ inserts were also employed to enhance the operational range of NMR. These capsules were fitted inside a regular ceramic rotor sleeve and could retain 70 bar of pressure, but dramatic chemical penetration of CO_2, N_2O, and CH_3F into the polymer material was evident, which decreased the pressure over time and contributed to background signals.[12-13] Further pressure limitations (40 bar) were also encountered when MAS rates reached several kilohertz due to the difficulties in fabricating a high-pressure sealing mechanism on small rotors. This method was hindered by severe carbon and proton background signals that convoluted analysis of the NMR samples. The prevailing limitations of polymer- and glass-based NMR rotors led researchers to employ ceramic materials for high-temperature, high-pressure (HTHP) applications of MAS NMR.

The initial design of high-pressure, high-temperature, MAS-capable ceramic rotors utilized commercial NMR zirconia rotors fit with custom components.[14] As shown in Figure 1.4a and the development outlined in Figure 1.5, standard ceramic zirconia sleeves (1) and commercial drive tips (e.g., Kel-F or Vespel) (2) were joined. The internal sleeve walls above and below the sample space were roughened and an epoxy was applied to tightly bind the PEEK bushings (4, 5) to the interior surface of the sleeve. A removable TORLON plug (7) and valve adapter (6) were threaded into the bushings on each side and sealed with O-rings. The sample cell could then be sealed by inserting the TORLON valve (8) and threading it into place, a reversible process that allowed for relatively simple recharging or modulation of the cell environment.

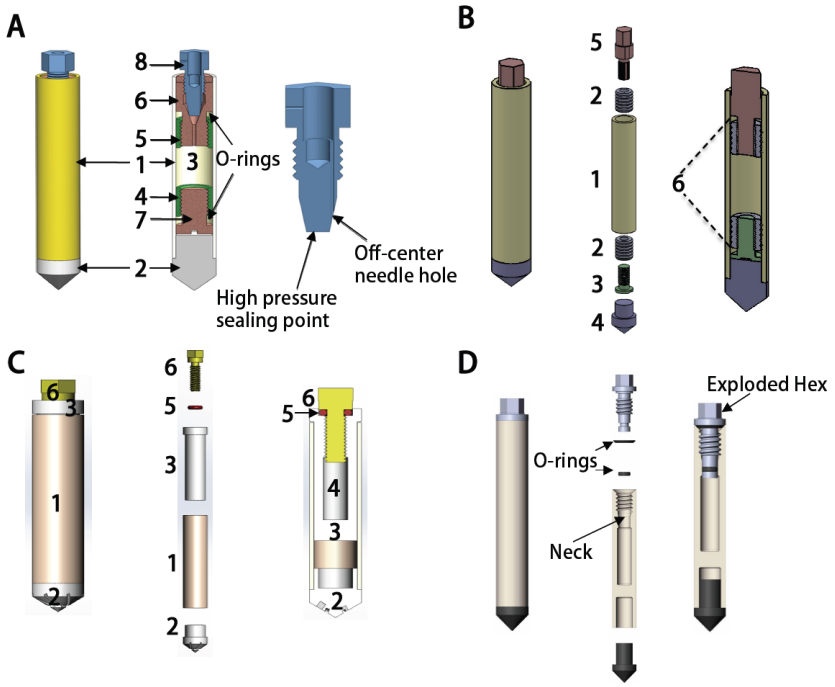

Figure 1.4. High-pressure, high-temperature rotors developed for in situ NMR. The first generation (A) is shown constructed, with an internal view of the fit and matched components and the valve. The modified version of the first generation (B) is portrayed constructed, exploded, and with an internal view of the matched/fit components. The second generation (C) includes an assembled external view, an exploded interpretation, and an internal depiction. The third generation (D) is shown with a constructed depiction, exploded perspective, and an internal view of the fit components.

These and the below images are adapted from the *Journal of Magnetic Resonance*, vol. 212, D. W. Hoyt et al., "High-pressure magic angle spinning nuclear magnetic resonance," pp. 378–385, 2011 and *Journal of Magnetic Resonance*, vol. 226, R. V. F. Turcu et al., "Rotor design for high pressure magic angle spinning nuclear magnetic resonance," pp. 64–69, 2013 with permission from Elsevier, *Angewandte Chemie International Edition*, vol. 53, A. Vjunov et al., "Following Solid-Acid-Catalyzed Reactions by MAS NMR Spectroscopy in Liquid Phase—Zeolite-Catalyzed Conversion of Cyclohexanol in Water," pp. 479–482, 2014 with permission from John Wiley & Sons, *Chemical Communications*, vol. 51, J. Z. Hu et al., "Sealed rotors for *in situ* high temperature high pressure MAS NMR," pp. 13458–13461, 2015 with permission from The Royal Society of Chemistry, and *Modern Magnetic Resonance*, Jaegers et al. "Development and Application of *in situ* MAS NMR" with permission from Springer.

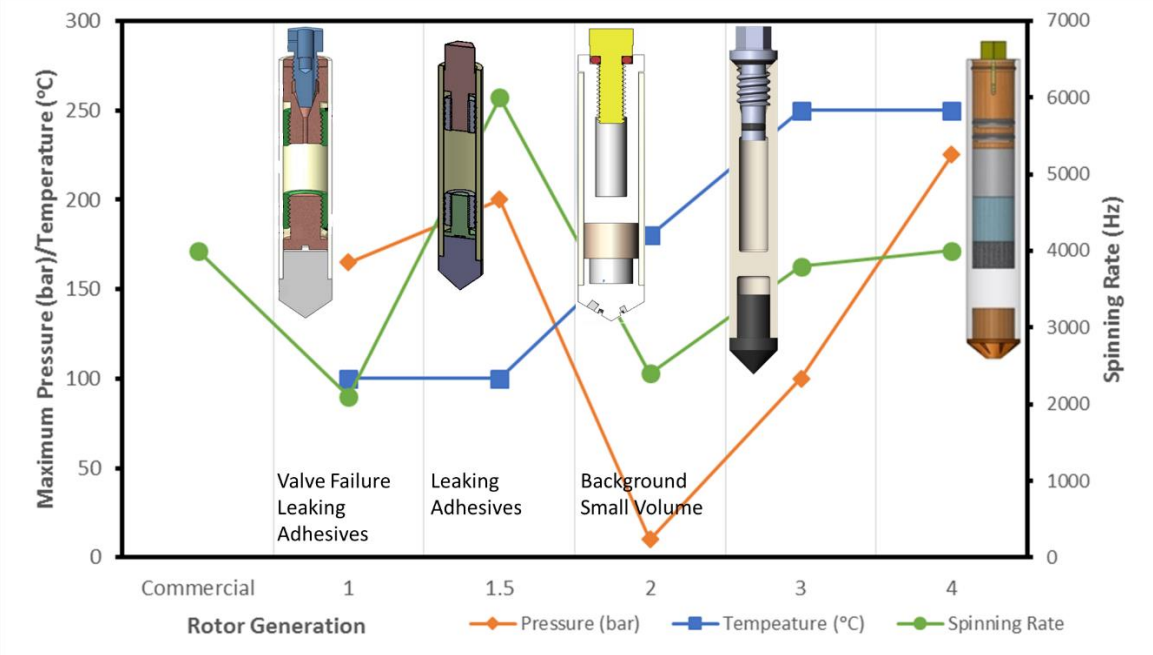

Figure 1.5. Development of in situ MAS NMR rotors and the associated operating limits and drawbacks.

The sealing valve for this original model also contained an off-center needle hole to allow for the injection of high-pressure liquids and quick sealing by turning the valve less than one quarter turn without altering the pressure inside the cell. A high-pressure loading chamber accompanied the design to allow for the loading of fluids and subsequent sealing under a high-pressure, controlled environment.[14] An improved version of this loading chamber designed to work with the current generation of *in situ* NMR rotors will be described below. Enhanced spectral signals were realized by this design owing to the large sample volume allowed by its configuration. For example, the original 9.5 mm OD rotor featured a sample volume of 350 μl. To estimate the limits of pressure for structural integrity, the two contributions to the effective pressure inside the rotor—centrifugal force (F_C) and sample pressure (P_S)—must be accounted for. These contributions are estimated by Eq. 8, where R_1 and R_2 are the inner and outer rotor radii, respectively, and ω is the rotational frequency in radians per second.

$$P_T = P_C + P_S = \frac{F_C}{A} + P_S = \frac{(R_2^2 - R_1^2) * \rho * \omega^2 * R_2}{2 * R_1} + P_S \qquad \text{Eq. 8}$$

Given the tradeoff between spinning rate and sample pressure, this design allowed for 360 bar of internal pressure spinning at 3.5 kHz before the rotor sleeve would fracture. The TORLON valve adapter is the least pressure-resistant component, experiencing a breaking pressure of 344 bar with test helium charging. It demonstrated stable operation at 165 bar and 2.1 kHz with only a 19% loss of internal pressure over 72 hours.

Though the TORLON valve design highlighted improvements to the state of the art, two design challenges required improvement for widespread application in the research community:

the failure point of the valve adapter at high operating pressures and the spinning limitations due to the relationship between spinning rate and sample pressure. Operating at high pressure conditions severely limits the rotation rate and causes detrimental peak broadening or sideband overlap in the NMR spectra. A second iteration of the first design (Figure 1.4b) addressed the former challenge by incorporating sealing plugs (3, 5) that thread directly into the bushings (2) and compress an O-ring as the sealing surface rather than a valve adapter.[15] Standard 7.5 mm zirconia MAS rotors (1) and spin tips (4), which could operate at pressures of up to 200 bar while spinning at 6 kHz, were employed for this design, drastically improving the quality of the acquired spectra as associated signal due to the slightly larger sample volume of 446 μl. The break point for this design remained the plastic sealing mechanism, but it still made improvements over previous iterations where only a 12.5% reduction in spectral intensity was realized after 90 hours of operation.

A revised rotor design was created to further improve the operational range of the system. Previous designs were limited to temperatures of 100°C due to degradation of the adhesives at elevated temperatures. This new cell design, depicted in Figure 1.4c, utilized a commercial 9.5 mm ceramic sleeve (1) and spin tip (2) as before. In contrast to valve adapters, a custom ceramic insert (3) was fitted into the rotor sleeve to form the sample cell.[16] This insert was threaded at the top to allow sealing with a plastic screw (6) pressing down on an O-ring (5) exhibiting high thermal resistance. High-temperature glue extended this rotor's operational range to 180°C and could withstand pressures of 10 bar at 2.4 kHz. While this design improved upon the operational flexibility through enhanced thermal resistance and mechanical strength, the adhesive and the end of the plastic screw fell within the detection area of the RF coil, contributing to background signals in the ^{13}C and ^{1}H channels. Additionally, the sample volume was limited to just 220 μl,

increasing experimental time by a multiple of four over previous generations of high-pressure rotors to achieve the same sensitivity. The crucial necessity to improve this serious issue led to further developments.

A third major improvement to rotor technology was formulated to address the drawback of sensitivity and continue propelling the technology to withstand harsher sample conditions. The modern design features maximum mechanical strength, chemical resistance, and temperature independence by fully utilizing ceramics.[17] In this design (Figure 1.4d and draft document example in Appendix A: Equipment Schematics), all components save the sealing O-ring and spin tip are fabricated high-mechanical strength ceramics. The main body rotor sleeve is a cavern-style rotor with a ceramic cylinder cut out on the bottom to accommodate a commercial spin tip. The top end also contains a cavity partially bored into the rotor to allow a solid, ceramic barrier between the sample and spin tip spaces. No additional spacer is required to maintain sample location as in standard rotors. The top is threaded to allow for a ceramic cap to be securely screwed into the rotor sleeve with a hexagonal head where it seals the vessel by pressing either one or two O-rings. Reverse threading is employed to ensure MAS does not loosen the cap. This simple design is suitable for a wide range of rotor sizes and has been demonstrated for 9.5 mm, 7.5 mm, 5.0 mm, 4.0 mm, and 3.2 mm. These rotors house large sample spaces of approximately 430 μl, 350 μl, 75 μl, 40 μl, and 20 μl, respectively. All sizes are suitable for operation up to at least 100 bar and 250°C, a notable increase in operational potential. The current operational restrictions primarily stem from probe technology limitations in sample heating.

A complimentary technology was recently developed that substantially reduces production resources through the use of snap-in features that fit directly within a commercial rotor sleeve.[18] This WHiMS MAS rotor (named after the primary inventors) avoids the need for specialized loading equipment through the use of a check valve for gas loading in a simple chamber, such as a capped stainless steel tube. This rotor can withstand 275 bar of pressure and 325°C. Both contemporary designs are quite similar in operational viability, having a scalable size (rotor sizes from 4 mm to 9 mm) and sample volumes of ~400 μl for the 7.5 mm OD iterations. The preparation of solids and liquids in the rotors is nearly identical and sealing for both is dependent on a force applied to an O-ring through either direct threading compression (all-zirconia) or radial compression (WHiMS). The largest difference in these rotors comes from the required resources and the flexibility of sample preparation, where the all-zirconia rotors necessitate additional resources to produce and operate, but offer enhanced flexibility of sample preparation over the WHiMS configuration.

In short, the WHiMS rotor takes advantage of a check valve to maintain the pressurized atmosphere within the vessel and charges gas by exposing the rotor exterior to a high-pressure environment. Gases can be sequentially added to the desired makeup, including adding more gas after a measurement to save time and maintain consistency in solid sample preparation. The external gas pressure must simply exceed both the internal pressure and the pressure required to open the check valve (~10 bar). A specially designed rotor loading chamber is required to charge the all-zirconia rotors with a gas atmosphere. The gas atmosphere can be customized with varying pressures (from vacuum up to >2,000 psi), temperatures (ca. <0 to >100°C), and compositions. When the conditions are satisfactory, an externally-magnetically coupled cap screwdriver opens the threaded rotor cap fixed within the chamber to allow the rotor to take in

the prepared environment. The magnetic coupling enables a tight seal without the need for rotating surfaces to hold the internal pressure. Though such a dedicated system is resource intensive, the modular nature of the interior enables rotors from 9.5 mm to 2.5 mm to be used in the same system while requiring fewer additional resources. Further, simplified versions of the loading chamber (such as the example depicted in Appendix A: Equipment Schematics) can be more easily produced. As such, the complementary technologies of all-zirconia and WHiMS designs offer options either for preparation convenience with fewer resource requirements or for fine control of the internal environment of the rotor with additional required equipment. More complete details regarding the loading chamber can be found in Appendix A: Equipment Schematics.

Though batch-like NMR systems have agreed with batch reactor systems well in terms of reactivity, energetics, and product distribution[19], matching the flow characteristics of a fixed-bed reactor remains in a state of infancy. Challenges exist in maintaining a seal for metered gas flow while spinning to improve spectral quality. To take advantage of the spinning, some rotor designs have been utilized that allow for flow during sample rotation.[20-26] Substantial challenges regarding the utilization of these rotors for *operando* measurement exist. The absence of a gas-tight seal between the injection line and the rotor allows product and reactant gases to escape the system without coming into contact with the catalyst bed and/or analysis in some cases, and channeling becomes a concern due to the high spinning frequencies employed which push even well packed beds to the rotor walls away from the axial tubes. The application of vacuum to the downstream side of the catalyst bed has also been implemented to promote better flow,[27] but much gas still escapes; resultantly, residence times are high and the flow profile poorly resembles plug flow conditions. Alternative designs have used ceramic bearings to help reduce

the effect of the drive and bearing gas interfering with the flow design, but these still demonstrate backflow.[28] Furthermore, channeling due to the fast rotation leads to some gases passing through with minimized exposure to the catalyst bed, further complicating comparisons to a plug flow reactor.

Another attempt to rectify the differences between a flowing and spinning reactor led to the development of the magic angle hopping technique.[29] Flexible tubing was employed to provide a gas-tight seal and allow the rotor to spin at discrete, fractional rotations at the magic angle. This technique allowed for the production of 2D spectra that represent the isotropic and anisotropic dimensions without a gap in the transfer lines[30]; however, due to the complexity of the pulse sequence and strict timing required for the mechanical rotation, concerns regarding sensitivity and extended measurement time have hindered its application.

In recognition of the importance of reproducing fixed-bed reactor conditions inside the magnet for direct comparison to reactor studies, attempts to replicate plug-flow conditions during NMR measurement were made. Herein, the design and implementation of static, flow-through NMR measurements to attempt to quantify surface species observed during the reaction is described. To accomplish this goal, a drop-in, flow-through NMR cell has been designed to meet the standards of a typical plug-flow reactor and conform to the existing probe setup. The cell incorporates internal components that rest just outside the magnetic detection coil. As can be seen from the simulated velocity profile in Figure 1.6, gaseous reactants travel down a central tube of 0.8 mm in diameter before traveling though the conical section at the bottom, which directs the flow through the gas dispersion channels spaced around the central axis. From there, gas enters an annular catalyst bed, then travels through the upper gas channels (offset 30^{o} from

the lower ones) and out of the magnet for analysis by gas chromatography. Flow through the catalyst bed was modeled with the Brinkman equation (Eq. 9),[31] an extension to Darcy's law; the permeability was approximated with the Blake-Kozeny equation, which estimates permeability for uniform, spherical particles at low Reynold's numbers (Eq. 10.)[32] Further drawings and simulation results can be found in Appendix A: Equipment Schematics.

$$\mu\nabla^2 u - \nabla p - \mu a^2 u = 0 \qquad \text{Eq. 9}$$

$$\kappa = \frac{d_p \cdot \varepsilon^3}{150 \cdot (1-\varepsilon)^3} \qquad \text{Eq. 10}$$

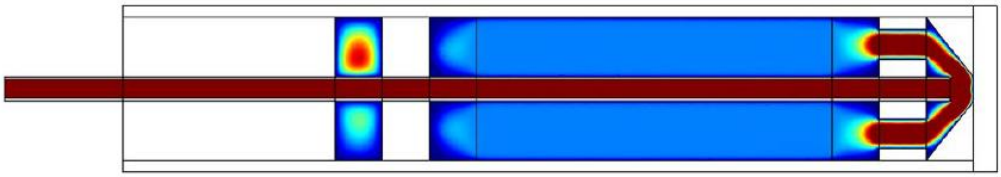

Figure 1.6. Anticipated flow profile within the designed NMR cell, where blue and red coloration represent slower and faster velocity, respectively. Top and bottom flow channels are offset by 30°.

The velocity profile within the annular catalyst bed approximates plug flow with a boundary layer of approximately δ = 0.1D. In theory, the cell and accompanying tubing should demonstrate a limited pressure drop of less than 0.16 kPa/cm at a fluid velocity of 15 m/s, allowing for reasonable replication of microreactor conditions. In practice, the pressure drop experienced was nearly two orders of magnitude higher than computed, which sometimes caused the upper portion of the cell to eject during reaction if the flow rate was too high. Design alterations to correct this issue were considered, such as implementing larger channels, opening

up impingement points, and threading the top instead of using an O-ring seal, but the static NMR spectral quality did not warrant such efforts (Figure 1.7). The systems of interest suffered from indeterminate observations due to dramatic line broadening. For example, when investigating the dehydration of ethanol on HZSM-5, only the CH_3 groups of ethanol adsorbed on the zeolite were well-resolved enough to accurately assign. This clearly illustrates that static, flow-through NMR may only be useful to particular systems where resonances lie far apart.[33-37]

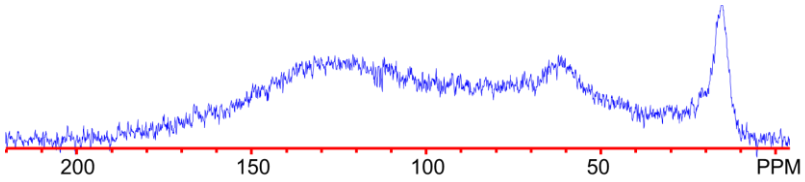

Figure 1.7. Representative static NMR spectra of ethanol dehydration on ZSM-5.

1.3 Fundamentals of NMR for Vanadium Oxide Catalysts

Discovered in 1801 by Andrés Manuel del Río as a component of vanadinite, vanadium has been a material of interest for a wide array of applications, most abundantly as an additive for steel.[38] Vanadium is readily oxidizable/reducible both as a solid and in solution, where it exhibits electronic states with contrasting optical properties, e.g. $[V(H_2O)_6]^{2+}$ (violet), $[V(H_2O)_6]^{3+}$ (green), VO^{2+} (blue), and VO_2^{+} (yellow). The most commercially important compound is the V(V) oxide V_2O_5, produced either from metallic vanadium burning with oxygen or from the decomposition of ammonium metavanadate (as is often employed in catalyst preparation). Vanadium pentoxide is an important material for sulfuric acid production by way of the oxidation of sulfur dioxide to sulfur trioxide in the contact process.[39] Vanadium oxide catalysts have been identified as suitable materials for promoting a large number of important chemical processes. Notable applications

span a diverse collection of reactions, including the selective oxidation of paraffins, olefins, and alcohols,[40] non-oxidative dehydrogenation of alkanes,[41] selective catalytic reduction of NO_x,[42] oxidation of a wide variety of organic molecules,[43] and the aforementioned oxidation of sulfur dioxide.[44] These catalysts have taken on homogeneous configurations, such as those for alkane, alkene, aldehyde, and ketone oxidation reactions, and have also supported heterogeneous sites.[45] When it comes to revealing active sites, in general, metal oxide catalysts can be more complex than conventional metal catalysts due to the multiple geometrical structures (i.e. monomer, dimer, oligomer, polymer, and bulk) in varying oxidation states which develop once incorporated onto the support. As such, careful and detailed characterization of these materials on the various is essential and a challenging problem.

Heterogeneous materials have employed an assortment of oxide support materials, such as zeolites, molecular sieves, bi-layered and co-precipitated mixed oxides, and pure metal oxides, which are shown to impact the functionality of the catalyst and demonstrate improvements relative to the bulk V_2O_5 phase.[40] On these supported vanadium oxide materials, the most relevant active species are V^{5+} sites, which can be reduced to V^{4+} and reoxidized during a catalytic cycle. This V^{5+} oxidation state is diamagnetic, meaning all electrons are paired and it is well-suited for NMR spectroscopy. Conveniently, the most abundant vanadium nucleus (^{51}V: 99.75%) is an NMR-active nucleus with spin 7/2 and short relaxation times. Despite these advantages, ^{51}V is often present as a minority species in catalyst samples (~1%), making detection of broad features more challenging. Note that ^{50}V is also NMR-active, with a natural abundance 0.24% and spin 6, but suffers from even poorer sensitivity and very broad lines compared to ^{51}V.[46] Further, nuclei with spin greater than ½ have a non-spherical electric charge distribution, giving rise to the quadrupole interaction. In contrast to spin ½ nuclei, the less

symmetric charge distribution around the nucleus splits the spins into more than two energy levels under an applied magnetic field (2n+1 levels). For ^{51}V, a spin 7/2 nucleus, this manifests as eight energy levels that arise from the Zeeman splitting as shown in Figure 1.8. These energy levels are further perturbed by first- and second-order quadrupolar interactions, as described below. Note that the magnitude of the quadrupolar perturbations is not to scale, but the direction is representative.

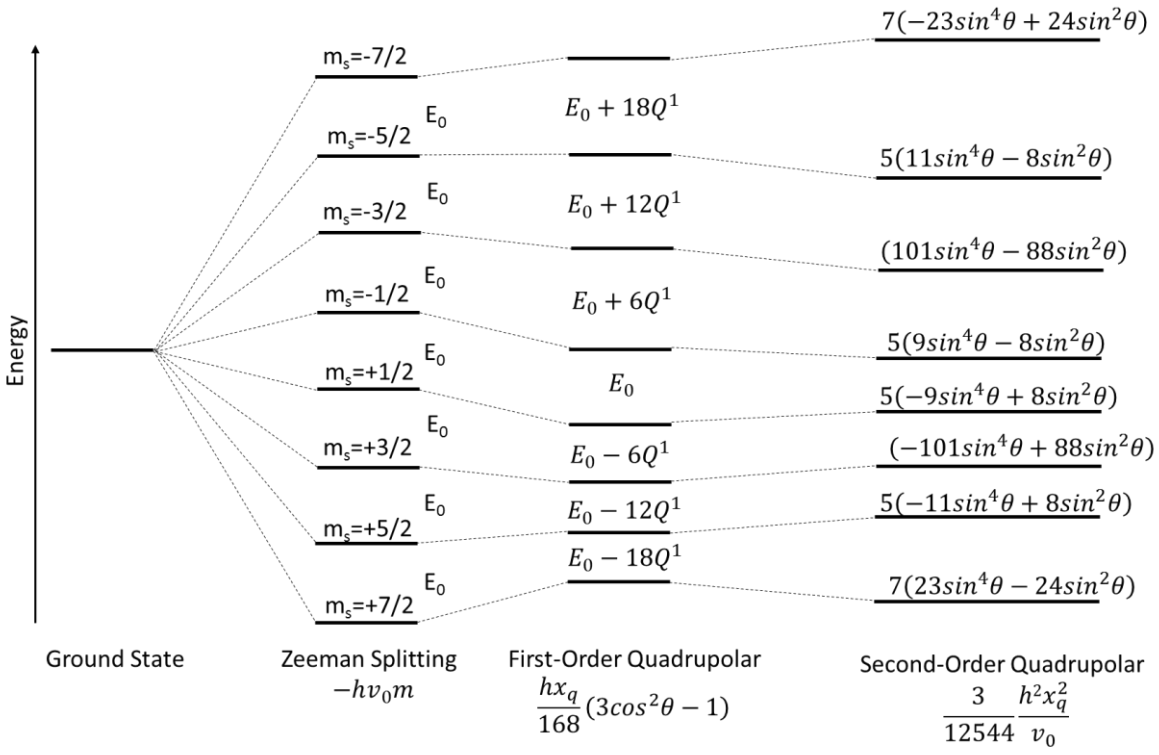

Figure 1.8. Energy level diagram of spin 7/2 nuclei.

The energy difference between these spin states can be calculated and translated based on perturbations from the first- and second-order quadrupolar interactions. In the high field limit where the quadrupole interaction acts as a perturbation to the Zeeman states in the laboratory frame, Eq. 11 and Eq. 12 quantify this energy where θ and φ are the Euler angles, m is the magnetic quantum number associated with the Zeeman levels, I is the nuclear spin, η is the

asymmetry parameter, h is Plank's constant, X_Q is the quadrupole coupling constant, e is the fundamental charge, Q is the nuclear quadrupole moment, and q is the greatest component of the electric field gradient q-tensor.[47-48] The sum of the Zeeman splitting energy with the first and second order quadrupolar energies ($E^{(1)}$ and $E^{(2)}$) give the energy of each level, where the energy difference is expressed between the energy levels in the diagram for first-order terms and the second-order energy perturbation is directly shown. It should be noted that such equations, in particular the ($3m^2$-I(I+1)) term in $E^{(1)}$ or appropriate expression of multiplication in $E^{(2)}$, are occasionally incorrectly articulated, resulting in the incorrect calculation of the energy terms. Care should be taken to select an appropriate source prior to applying these equations.[49-50]

$$E^{(1)} = \frac{X_Q h}{8I(2I-1)}[3cos^2\theta - 1 + \eta sin^2\theta cos2\varphi]\left(3m^2 - I(I+1)\right) \quad \text{Eq. 11}$$

$$E^{(2)} = -\left(\frac{e^2qQ}{4I(2I-1)}\right)^2 \frac{m}{v_0}\Big[-\frac{1}{5}(I(I+1)-3m^2)(3+\eta^2) \quad \text{Eq. 12}$$

$$+\frac{1}{28}(8I(I+1)-12m^2-3)\big((\eta^2-3)(3cos^2\theta-1)$$

$$+6\eta^2 sin^2\theta cos2\varphi\big)$$

$$+\frac{1}{8}(18I(I+1)-34m^2$$

$$-5)\left(\frac{1}{140}(18+\eta^2)(35cos^4\theta-30cos^2\theta+3)\right.$$

$$\left.+\frac{3}{7}\eta sin^2\theta(7cos^2\theta-1)cos2\varphi+\frac{1}{4}\eta^2 sin^4\theta cos4\varphi\right)\Big]$$

One may apply the condition of axial symmetry (η=0) to express the energy of the first-order terms as a function of nuclear spin and magnetic quantum number as shown for several quadrupolar half-integer spins in Table 1. The energy of the transition may then be derived from the difference between these two energy states (shown in Figure 1.8). Since the -1/2 and 1/2 first-

order quadrupolar energy perturbation terms are the same, the energy of the central transition is not altered by first-order effects. The magnitude of $E^{(1)}$ is independent of the magnetic field strength, but proportional to the quadrupole coupling constant. From observation, the elimination of first-order quadrupolar becomes obvious under the condition of magic-angle spinning, evidenced by the $3\cos^2\theta$-1 term, whose magnitude is modulated by the listed coefficients in Table 1. When MAS is satisfied, this term is averaged to zero. As shown in Eq. 12, the second-order perturbation has a more complicated relationship with the orientation, I, and m. Due to the square dependence on m, the first-order energy corrections shift in the same direction for +m and –m. In the limit of MAS, the second-order coefficients are listed in Table 2. It follows that even under such conditions, a second-order contribution is retained. The energy shifts for +m and –m are in the opposite direction due to a dependence on m^3, and while the first-order correction increases with X_Q, the second-order term increases with X_Q^2. The second-order correction also contains a term which is independent of orientation, showing that the isotropic chemical shift has contributions from quadrupole coupling. Most notably, the second-order quadrupolar perturbation is inversely proportional to the frequency, and thus field strength. This is why high-field magnets are advantageous for quadrupolar nuclei, since they minimize second-order quadrupolar effects. Under conditions of axial symmetry, the second-order energy perturbation may be simplified in a fashion similar to how it is sometimes expressed for lower spin systems. A step-by-step reduction of this equation to a simple expression, fully dependent upon orientation, is available in Appendix G: Second-Order Quadrupolar Energy Perturbations. This was the form used for the second-order terms in Figure 1.8.

Table 1. First-order quadrupolar energy perturbation coefficients for quadrupolar half-integer spins. The energy is the product of the coefficient and hXq(3cos2θ-1)*

m\I	**3/2**	**5/2**	**7/2**	**9/2**
-9/2				1/8
-7/2			1/8	1/24
-5/2		1/8	1/56	-1/48
-3/2	1/8	-1/40	-3/56	-1/16
-1/2	-1/8	-1/10	-5/56	-1/12
1/2	-1/8	-1/10	-5/56	-1/12
3/2	1/8	-1/40	-3/56	-1/16
5/2		1/8	1/56	-1/48
7/2			1/8	1/24
9/2				1/8

Table 2. Second-order quadrupolar energy perturbation coefficients for quadrupolar half-integer spins under MAS. The energy is the product of the coefficient and $(hX_q)^2$

m\I	**3/2**	**5/2**	**7/2**	**9/2**
-9/2				17/2304
-7/2			13/1344	7/6912
-5/2		9/640	-5/9408	-25/13824
-3/2	5/192	-3/640	-31/9408	-29/13824
-1/2	-1/64	-3/800	-5/3136	-1/1152
1/2	1/64	3/800	5/3136	1/1152
3/2	-5/192	3/640	31/9408	29/13824
5/2		-9/640	5/9408	25/13824
7/2			-13/1344	-7/6912
9/2				-17/2304

Another consequence of the quadrupolar interaction is the fluctuation of electric field gradient, which typically results in quick relaxation of the spins, thus decreasing the signal intensity while broadening the spectral features. This dramatically decreases the spectral signal, challenging the characterization of vanadium species by NMR. Each nucleus and the environment in which it finds residence will have different asymmetry, giving rise to properties that describe the quadrupolar nature of the species. The asymmetry parameter, η_Q, describes the

anisotropic lineshape and can be derived from the electrostatic potential of the electron field gradient in a given direction, V(r) (Eq. 13), and determined by a fit of the spinning sideband or wide-line powder pattern. The quadrupole moment, eQ, can be prolate (>0) or oblate (<0) and contributes to the electron field gradient Q tensor and quadrupole coupling constant, C_Q (Eq. 14).

$$\eta_Q = \frac{V_{XX} - V_{YY}}{V_{ZZ}} \qquad \text{Eq. 13}$$

$$X_Q = C_Q = \frac{eQ}{h} V_{ZZ} = \frac{e^2 qQ}{h} \qquad \text{Eq. 14}$$

One consequence of these parameters is that contrasting X_Q and η between species can give rise to selective excitation. If X_Q is large, the separation between adjacent levels varies more dramatically, giving rise to contrasting pulse responses that render quantification challenging. Such an issue can be mitigated by maintaining small pulse angles where selective excitation is effectively minimized. These parameters can also be used to describe and simulate the quadrupolar lineshape of such a nucleus. At sufficiently high magnetic fields under MAS conditions, however, second-order quadrupolar effects are reduced due to the inverse proportionality of quadrupolar broadening and magnetic field strength.[51] At such conditions, spectral resolution is improved and the features may be fit with a simple Gaussian/Lorentzian simulated line. It was previously mentioned that first-order quadrupolar effects could be eliminated by spinning at the magic angle. Second-order effects could likewise be eliminated, but the angle required for such an averaging is dissimilar to 54.7°. As such, these effects are only partially averaged by MAS.[52] When the sample spinning rate is less than the width of the static sample, spinning sidebands for which the overall profile exhibits a similar shape to the powder patter (a projection of the spectrum of all orientations of the single crystal transitions) appear.[53]

This is illustrated in Figure 1.9, where at fast spinning rates (up to 35 kHz), few sidebands of bulk V_2O_5 are present alongside the centerband (-613.8 ppm). At lower spinning rates, the sideband pattern becomes more intense and takes on a more complex profile. This profile is consistent with the wide-line spectrum. As the spinning rate becomes even lower, the sidebands begin to overlap with one another and with the centerband, which would hinder site identification if multiple environments were present. The red spectra were acquired at half the field, necessitating a doubling of the listed spin rate for comparison to the blue spectra and explaining the difference in the wide-line profile stemming from second-order quadrupolar interactions.

On the surface of the catalyst, vanadium oxide is known to reside in many structural conformations, ranging from isolated VO_4 units to bulk-like V_2O_5 crystallites. These structures has been extensively described to evolve from monomeric, distorted tetrahedral with one V=O and three V-O-Support bonds at low loadings through oligomeric species at moderate loadings to the bulk-like V_2O_5 above a monolayer. NMR has been shown to be a tool that can provide some of the most specific insights into the types of structures present in a sample. ^{51}V NMR assignments of these various vanadium species supported on titania materials have been reported and evolved with time as these systems have been better described. Since titania-supported vanadium oxides are a critical focus of the research reported herein, reports which have propelled the understanding of these chemical environments are summarized in Table 3 and representative sketches are shown in Figure 1.10. The assignments used herein are based on this historical evolution of the assignments and match those described in *Angewandte Chemie* 2019.

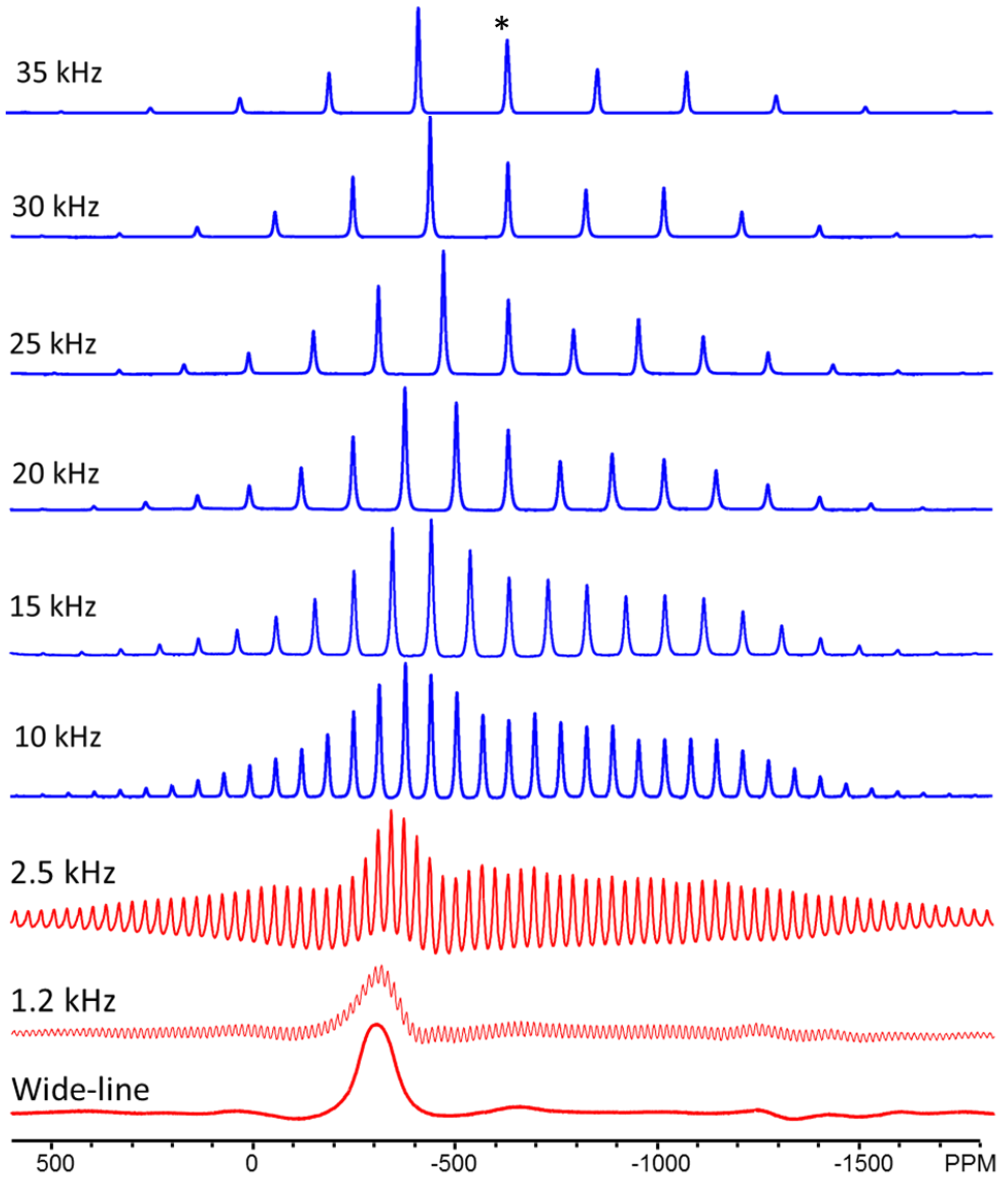

*Figure 1.9. Spinning sideband patterns of V_2O_5 at different spinning rates and magnetic fields where * represents the center band.*

Table 3. Reported species identification of ^{51}V NMR signals of titania-supported vanadia catalysts.

Ref.	-502	-510	-530	-555	-587	-610	-630	-650	
54		Dist. Octa.	Dist. Octa.	Tetra. Poly.		V_2O_5			Poly. Octa.
55		Octa.	Tetra.						
56						V_2O_5		Dist. Octa.l	Poly. Octa.
57		Trigonal Pyramid		Dist. Tetra.		Dist. Octa. (Trigonal Bipyramid)			
19	Tetra. Monomer		Monomer?	Double-Bridge Dimer	Dimer/ Poly.	V_2O_5	Single Bridge Dimer & Poly.	Poly.	
58	Tetra. Monomer		Octa. Monomer	Dimer	Dimer/ Poly.	V_2O_5-like	Poly.		

Dist. – distorted, Octa. – octahedral, Tetra. – tetrahedral, Poly. – polymer

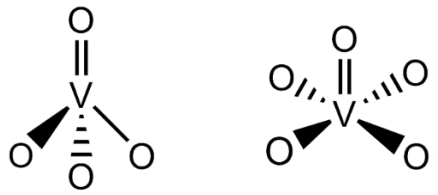

Figure 1.10. Representative tetrahedral and square pyramidal monomeric vanadia species.

CHAPTER TWO: STRUCTURE OF DEHYDRATED, SUPPORTED VANADIUM OXIDE CATALYSTS

The relevance of vanadium-based catalysts on both an industrial and fundamental level makes them materials of interest to characterize. Extensive efforts focus on reactivity and Raman spectroscopy, but the challenges and resources required for MAS NMR experiments have hindered such widespread utilization. In this chapter, recent results both published and unpublished are described which pertain to the dry state of these materials.

2.1 Silica-supported V_2O_5

Based on Nicholas R. Jaegers, Chuan Wan, Mary Y. Hu, Monica Vasiliu, David A. Dixon, Eric Walter, Israel E. Wachs, Yong Wang, and Jian Zhi Hu; "Investigation of Silica-Supported Vanadium Oxide Catalysts by High-Field ^{51}V Magic-Angle Spinning NMR" *The Journal of Physical Chemistry C* 2017 121 (11), 6246–6254 DOI: 10.1021/acs.jpcc.7b01658

Vanadium oxide materials have been investigated on a variety of supporting materials such as CeO_2, Al_2O_3, TiO_2, SiO_2, and zeolites. The support can play a strong role in the catalytic function of these materials. For example, activity for the oxidative dehydrogenation of methanol was found to proceed as $SiO_2 \ll Al_2O_3 \ll Nb_2O_5/Ta_2O_5 < TiO_2 < ZrO_2 < CeO_2$. Between ceria-supported vanadium oxide and silica-supported vanadia, the turnover frequency (TOF) spans a factor of 10^3.[59] Despite the low TOF values on the silica support, it remains a material of interest for catalysis due to the high surface area relative to other oxide supports. As such, understanding the nature of the surface vanadia species for silica-supported catalysts can provide insights into the interactions between the catalyst and reactants, which are necessary to reveal the roles of the

chemical constituents, comprehend how side products such as water might alter the chemistry of the reaction, and rationally engineer better materials with enhanced performance. The specific nature of vanadium oxide structures on supported V_2O_5/SiO_2 catalysts had long remained despite extensive investigation.[40]

Raman spectroscopy is of major significance for the study of supported metal oxide catalysts, especially compared to methods such as X-Ray diffraction (XRD), which requires relatively long-range crystallographic order for detection.[60] *In situ* Extended X-ray Absorption Fine Structure (EXAFS), *in situ* infrared spectroscopy, and Raman spectroscopies were used in conjunction with reference compounds to propose the presence of isolated $O=V(-O-Si)_3$ surface units up to monolayer coverage and the additional presence of crystalline V_2O_5 nanoparticles above this threshold.[61-64] Unlike vanadia supported on other oxide supports, which show clear oligomerization at higher loadings, contrasting conclusions exist for the silica support's propensity to aid in the formation of vanadia oligomers, as evidenced by Raman (absence of V-O-V vibrations at 200–300 cm^{-1}) and UV-Vis Diffuse Reflectance Spectroscopy (DRS) (high E_g values) studies.[8,65] Most oxides will support up to ~8 V/nm^2 prior to monolayer formation, but this was not observed for silica-supported vanadium oxides, where the saturation limit is estimated at 2.7 V/nm^2.[66] Indeed, monolayer coverage of vanadia on silica is widely regarded as 2.7 V/nm^2 and that on other supports is defined as 8 V/nm^2. UV-vis has been proposed as an alternative to Raman spectroscopy and shows that differences in the degree of oligomerization may well be observable.[67] Two recent EXAFS studies have indeed refuted that silica only supported mono-dispersed vanadia and that higher surface vanadium oxide loading on silica leads to a greater degree of oligomerization up to the monolayer limit, but additional demonstration with model compounds is still required to confirm this claim.[68-69]

Previously, solid state NMR was employed to detail the speciation of VO_x/SiO_2 at a 79 MHz field and 8 kHz MAS rate.[70] Faster spinning rates and higher magnetic field strengths that improve the resolution of the collected NMR spectra are readily available. More advanced pulse sequences have also enabled identification of vanadia species for sites which overlap spectroscopically.[71] Silica-supported vanadium prepared by methods such as flame spray pyrolysis[72] and sodium promotion[73] demonstrate a higher monolayer capacity (3.3 and 8.9 V/nm^2) than traditional impregnation onto silica (2.7 V/nm^2), and higher specific activity can be attained with surface organometallic synthesis approaches.[74] Structurally, these studies all suggest the exclusive presence of isolated VO_4 units, consistent with previous speculation. In this section, the structure of dehydrated, silica-supported vanadia is investigated with high-field (20T) MAS NMR at spinning rates above 30 kHz to elucidate the structure of vanadia.

Solid-state ^{51}V MAS NMR spectroscopy was conducted on two silica-supported vanadium oxide catalysts over a range of sub-monolayer coverages, containing 3% and 8% V_2O_5/SiO_2. Specific surface area (SSA) and inductively coupled plasma-determined (ICP) loadings are shown in Table 4 and confirm that only dispersed vanadium oxide species should be present since the surface density is maintained below 2.7 V/nm^2 (the monolayer limit). The coverages correspond to 0.22 and 0.63θ. Furthermore, due to concerns over potential reduction of the surface vanadium oxide species by the catalyst drying procedure, Electron Paramagnetic Resonance (EPR) spectra were collected on the treated samples, which revealed the presence of reduced vanadium V^{+4} species (EPR spectra available in Appendix C: Additional Supporting Data). These measurements revealed that only up to 3.1% of the vanadium was present as V^{4+} in all silica-supported samples analyzed. Paramagnetic V^{4+} species are well known to impact the visibility of diamagnetic vanadium in NMR spectra.[75] An estimated 70% of the vanadium within

10 Å of a V^{3+} center could not be detected. This effect is less dramatic for V^{4+} paramagnetic centers. It is likely such a dramatic signal suppression was amplified by the presence of direct V^{3+}-O-V^{5+} bonds, suggesting that mono-dispersed vanadium should be relatively less impacted by paramagnetic species.[76] The average distances between vanadium atoms in these 3% and 8% samples are 14.6 Å and 8.7 Å, respectively. As such, the 3% V_2O_5/SiO_2 sample should be minimally affected and the 8% sample contains species, on average, near the outer boundary of paramagnetic effects. Considering our average vanadium surface density and V^{4+} concentration (Table 4) as well as the reduced impact of V^{4+}, it is likely that more than 96% of the vanadium environments are detected by solid state ^{51}V MAS NMR spectroscopy and potential reduction of the samples has had little impact on the observations by NMR.

Table 4. Quantitative characteristics of V_2O_5/SiO_2 hydrated catalysts

Sample Name	**ICP Loading**	**SSA (m^2/g)**	**Loading (V/nm^2)**	**% V as V^{4+}**
3% V_2O_5/SiO_2	2.9%	285	0.6	2.5
8% V_2O_5/SiO_2	7.4%	240	1.7	3.1

The identification of the central band in the NMR spectra for each dehydrated catalyst is shown in Figure 2.1. By collecting the spectrum at two spinning rates (38 and 32 kHz), the center band can be identified as any peak which is not repositioned upon changes to the rotation frequency. Chemical shifts are listed for the central band of each spectrum. At the higher spinning rates, rotation was sufficient to distinguish the central band peak from the spinning side bands. In both samples, a single broad feature is present at -675 ppm and all other features arise as the spinning side band pattern.

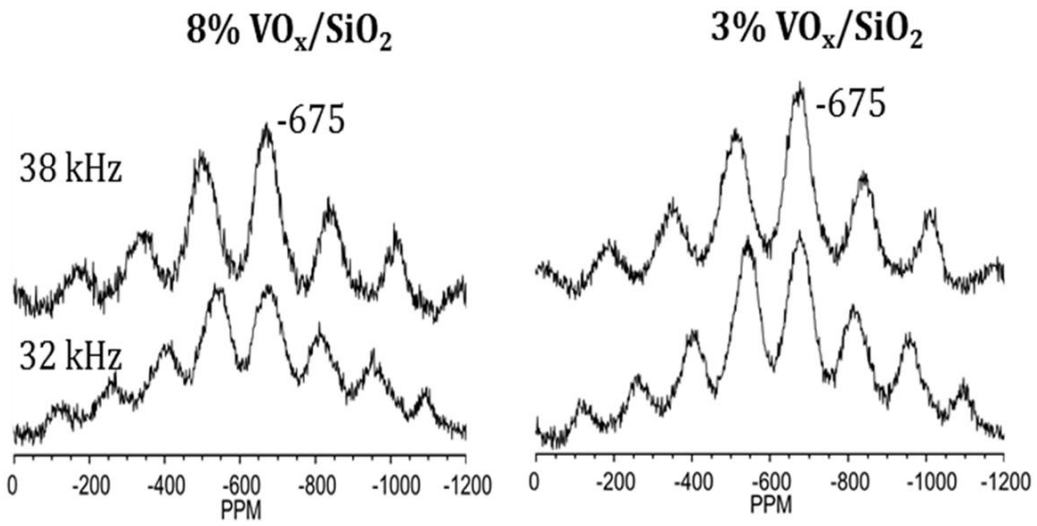

Figure 2.1. Centerband determination of ^{51}V MAS NMR spectra of dehydrated V_2O_5/SiO_2 catalysts of varying loading, 8% and 3%, at different spinning rates.

Reprinted with permission from Jaegers et al. *J. Phys. Chem. C*, 2017, 121, 11. Copyright 2017 American Chemical Society.

These ^{51}V MAS NMR spectra were fit with a Gaussian/Lorenzian lineshape model with a side band simulation. The use of a quadrupolar model was not required to match the spectra due to the reduction in second-order quadrupolar interactions at the high magnetic field. The fitted models overlaid on each NMR spectrum can be viewed in Appendix C: Additional Supporting Data. The integrated area was normalized to the number of scans and the mass of the sample, which resulted in 28 and 46 a.u. As expected, the normalized area was smallest for the supported 3% V_2O_5/SiO_2 sample. Instead of the expected factor of 2.7, this sample contained 1.6 times as many V^{5+} nuclei as the 3% V_2O_5/SiO_2 catalyst (Table 5). This suggests a possible slight overrepresentation in the 3% or an underrepresentation in the 8% sample. Since this trend was retained in untreated materials, a change in oxidation state during pretreatment is not likely the cause. The ratios of the central band areas to total area (central band to side band) are similar within each set.

Table 5. Integrated area of Gaussian/Lorentzian model fits with a side band simulation of ^{51}V NMR spectra

Condition	**Sample**	**Mass (mg)**	**Scans**	**Normalized Area**
Dehydrated	3%	4.9	480k	28
Dehydrated	8%	4.7	120k	46

To interpret the observed chemical shifts, density functional theory-based calculations were performed on small cluster models to simulate the chemical shifts of vanadia structures. The BLYP exchange-correlation functional with dispersion correction that was previously employed to predict the chemical shifts of supported vanadium oxide materials is used again here.[77] To benchmark this approach, the chemical shifts of a set of model compounds were simulated and compared to experimental data (Table 6). A model cluster of V_2O_5 containing eight vanadate atoms with a total charge of -5 was extracted from the crystal structure from the American Mineralogist Crystal Structure Database.[78] Terminal oxygen atoms were charge-balanced and optimized to provide an estimate of the chemical shift of bulk V_2O_5. The experimental ^{51}V NMR spectra of bulk vanadium pentoxide compare well with the quantum chemical calculation, with a predicted shielding just 11 ppm upfield of the experimental value at the BLYP-D level. The calculated chemical shifts on the vanadium-containing silsesquioxane agree with the reported experimental value[70] within 25 ppm at both levels. The predicted chemical shift for tris(triphenylsilyl) vanadate shows a larger discrepancy with the experiment,[70] with deshielding differences up to 80 ppm. This may be due to enhanced vanadyl (V=O) interactions with hydrogen molecules in the triphenylsilyl ligands in our model as compared to the powder samples. These benchmark calculations demonstrate that this approach can be

reasonably utilized to provide insight on our experimental results given the very large linewidth of silica-supported vanadia signals in the ^{51}V MAS NMR spectra.

Table 6. Comparison of experimental and calculated vanadium chemical shifts of model compounds. All values are reported as ppm relative to $VOCl_3$.

Compound	Exp.	BLYP-D	BLYP/ZORA
V_2O_5	-610	-633 (ave) -622 (center)	-636 (ave) -624 (center)
$(Ph_3SiO)_3V{=}O$	-736[a]	-672	-656
$[(c\text{-}C_6H_{11})_7(Si_7O_{12})V{=}O]_2$	-714[a]	-700, -715	-690, -703

[a]Results from Das *et al*.[70]

The predicted chemical shift of a simple, neutral tetrahedral vanadium center ($VO(OH)_3$) of -574 ppm at the BLYP/ZORA level (Appendix C: Additional Supporting Data) is predicted to be near the experimental result of -573 ppm. A tetrahedral positively charged $V(OH)_4^+$ structure is too shielded (-704 ppm, BLYP/ZORA) and a negatively charged tetrahedral V site ($VO_2(OH)_2^-$ [1]) is too deshielded (-498 ppm (BLYP/ZORA)). Other charged structures are even less consistent with the observed chemical shifts; thus, larger explored structures with neutral tetrahedral vanadium sites likely represent the appropriate structures for the models. Geometries from a previous theoretical effort for titanium-supported vanadium oxide[77] were modified with silica substituting titania and used as an initiation point since they exhibited largely tetrahedral structures. These structural models deviated substantially from the experimentally observed chemical shifts (Table 7). The dehydrated, isolated VO_4 unit was predicted to have a chemical shift of -459 ppm (BLYP-D) or -452 ppm (BLYP/ZORA), and the dimers are predicted to have chemical shifts between -580 ppm and -590 ppm. As such, utilizing vicinal silanols as the anchoring sites for vanadium is not appropriate for modeling the surface structures, and likely

not the anchored configuration in the experimental material due to strain exhibited by small silica rings.

Table 7. Calculated ^{51}V chemical shifts in ppm with reference to $VOCl_3$ based on the TiO_2-supported calculations

Cluster V Si O H	**Cluster Formula**	**BLYP-D**	**BLYP/ZORA**
	$OVO_3(SiO(OH))_3$	-459	-452
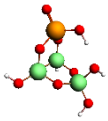	$OVO_2(Si_3O_3(OH)_3)OH$	-499	-505
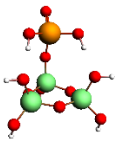	$OV(OH)_2O(Si_3O_3(OH)_5)$	-527	-534
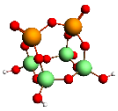	$V_2O_7(SiO(OH))_4$	-590	-581
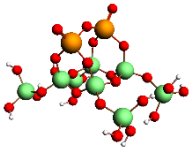	$V_2O_7(SiO((OSi(OH_3))_4$	-594	-583
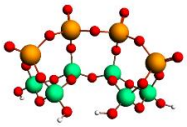	$V_4O_{13}O(SiO_3(SiOH)_2)_2$	-600	-575, -654, -659, -581
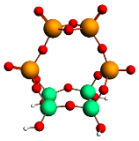	$V_4O_{12}(SiO(OH))_4$	-591	-643, -570, -567, -653
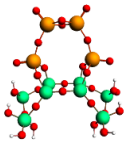	$V_4O_{12}(SiO((OSiOH)_3))_4$	-590	-650, -569, -566, -645

Larger clusters with at least O-Si-O bridges between silicon bonding sites were also considered and modeled. Table 8 shows the calculation results for these monomer, dimer, and trimer species anchored to silicon atoms that possess a hydroxyl group. Figure 2.2 provides a visual representation of these cluster models, where the dehydrated monomer (A), dimer (B), linear trimer (C), and cyclic trimer (D) are depicted. Models where anchoring silica atoms contain a full coordination sphere of siloxane can be found in Appendix C: Additional Supporting Data.

Table 8. Calculated ^{51}V NMR chemical shifts of vanadium clusters relative to $VOCl_3$

Cluster	**BLYP-D**	**BLYP/ZORA**
Monomer	-676	-680
Dimer	-670 -672	-675 -678
Linear Trimer	-515 -614 -619	-537 -632 -636
Cyclic Trimer	-661 -661 -706	-661 -679 -703

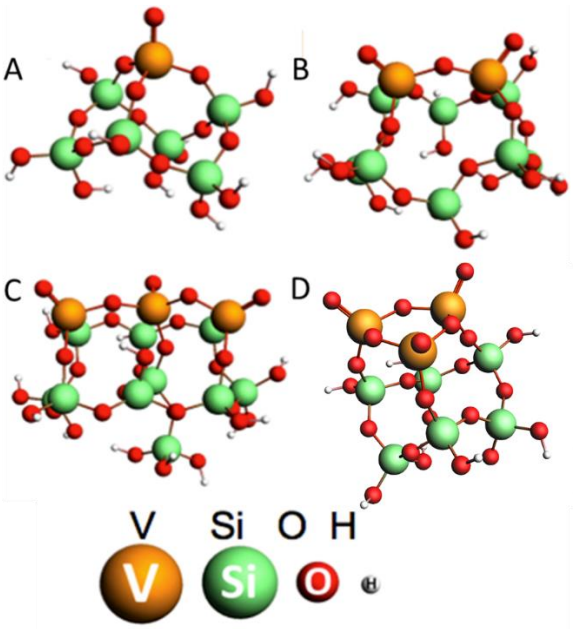

Figure 2.2. Optimized structures from Table 8 where A is a monomer, B is a dimer, C is a linear trimer, and D is a cyclic trimer.

Reprinted with permission from Jaegers et al. *J. Phys. Chem. C*, 2017, 121, 11. Copyright 2017 American Chemical Society.

The monomeric species has a predicted chemical shift of -675 ppm in the hydroxyl case with both theoretical approaches. In the large model case, the siloxane $Si(OH)_3$ ligands fold upwards leading to interaction with the vanadium, deshielding the nucleus by ~30 ppm. Since the coordination environment around the surface silicon restricts the hydroxyl ligand interactions with vanadium, the smaller model provides a less distorted depiction of the true chemical environment in the sample. For this reason, the hydroxyl cases are considered most closely. Chemical shift values centered on -671 ppm were calculated for the dimeric vanadia species. In the linear trimer model, the central vanadium atom exhibited a chemical shift deshielded by nearly 100 ppm (BLYP-D), or 80 ppm (BLYP/ZORA) relative to the outer two vanadium atoms

(-515 vs. -615). The cyclic trimer model presented a chemical shift similar to the monomer and dimer values.

The results of the solid state ^{51}V MAS NMR spectra clearly show that dehydrated supported V_2O_5/SiO_2 catalysts exhibit primarily one resonance feature at -675 ppm, similar to what was reported by Das,[70] Grant[73], and Love et al.[79] (-694 ppm). This contrasts the results of the flame-made and SOMC catalysts, which show peaks at -715 ppm and -615 ppm, respectively.[72, 74] Each of these works ascribes the observed chemical shift to isolated VO_4 monomers exclusively. The elemental analysis evaluated by ICP confirms the expected vanadium loadings of 3% and 8% in the samples, but no significant changes were observed between the NMR spectra of these two catalysts, suggesting that the structures are quite similar despite the difference in surface densities. When comparing these solid state ^{51}V NMR spectra to the chemical shifts predicted by DFT, the dehydrated state chemical shift closely resembles that of the monomer (VO_4) hydroxyl cluster, which was calculated at -676 ppm (BLYP-D) and at -680 ppm (BLYP/ZORA). Interestingly, the dehydrated dimer might also be present, with a calculated chemical shift of -671 ppm (BLYP-D) and -676 ppm (BLYP/ZORA). This is similar to both the monomer calculation and the ^{51}V MAS NMR spectra. The dehydrated linear trimer model is unlikely since the central vanadium atom is predicted to have a substantially deshielded nucleus. This would translate to an additional downfield peak, corresponding to the central vanadium, of half the intensity of the signal for the other two nuclei, which is not present in the spectra. The cyclic trimer, however, may be present since its average signal is between -681 and -685 ppm; Raman spectra of dehydrated supported VO_x/SiO_2 catalysts also do not exhibit the obvious presence of bridging V-O-V bonds, bending modes at ~200-300 cm^{-1}, indicating that the isolated surface VO_4 sites on the SiO_2 support may indeed be the dominant surface vanadia

species.[61] Tielens and colleagues noted the relative stability of tri-grafted (isolated VO_4) units compared to mono- or di-grafted species upon full dehydration, supporting our confirmation of isolated, fully anchored VO_4 units dominating the surface in the absence of water.[63]

The necessity of the nuclei anchoring to the silica support in larger rings that provide an O-Si-O bridge between anchoring sites should be reiterated. This result is well aligned with the findings by Tielens et al. in their investigation of model silica surfaces for supported vanadium oxide catalyst calculations. They conclude that three-ring silica species tend to break open upon hydration in agreement with earlier conclusions from Raman spectroscopy showing the elimination of the three-ring silica sites (~605 cm^{-1}) upon impregnation of vanadia on silica.[8,80] This is in agreement with our prediction of vanadia anchoring to larger silica rings with at least an O-Si-O linkage between bonding support atoms.

This investigation employed solid-state ^{51}V MAS NMR as a spectroscopic technique to probe the molecular structure of silica-supported vanadium oxide catalysts under dehydrated conditions. Faster spinning rates at a higher field confirmed that dehydrated samples have a single resonance located at -675 ppm. The results were the same for loadings of 3% and 8%, indicating no significant structural change with more than double the surface vanadium oxide coverage. Electronic structure calculations of the NMR chemical shifts for different models of potential vanadium oxide structures suggest the presence of isolated VO_4 units and potentially dimers and cyclic trimers, which cannot be distinguished by chemical shift for the dehydrated system. It was found that the presence of linear trimers is unlikely on the basis of the single observed resonance. Vanadia anchored to strained, three-member silica rings was also refuted by the combined ^{51}V MAS NMR and computational results.

Efforts to further understand this class of materials were recently published, whereby two deposition approaches were compared on mesoporous MCM-41: grafting and co-condensation.[81] Unlike the results here and in previous works, [70, 73, 79 52] more than one peak was observed in the MCM-41 sample. Instead, co-condensation reveals two lines at -682 and -718 ppm. Grating revealed only -718 ppm, similar to flame-made materials.[50] Using the DFT results described in this section in conjunction with quadrupolar line analysis of the spinning sideband patter, this new work has ascribed these two peaks to distinct monomeric and oligomeric species that are visible on MCM-41 due to the structure of the support material.

2.2 Promoted Titania-Supported V_2O_5 Catalysts for SCR

Based on Nicholas R. Jaegers, Jun-Kun Lai, Yang He, Eric Walter, David A. Dixon, Ying Chen, Chongmin Wang, Mary Y. Hu, Karl T. Mueller, Israel E. Wachs, Yong Wang, and Jian Zhi Hu; "Mechanism by which Tungsten Oxide Promotes the Activity of Supported V_2O_5/TiO_2 Catalysts for NOx Abatement: Structural Effects Revealed by ^{51}V MAS NMR Spectroscopy" *Angewandte Chemie International Edition* 2019 131, 12739–12746 DOI: 10.1002/anie.201904503 [Inside Back Cover]

Among the numerous vanadia-catalyzed reactions, SCR stands as an important contributor to emissions control chemistry. Combustion-generated air contaminants such as sulfur oxides, carbon oxides, residual hydrocarbons, and particulate matter remain strong environmental trepidations, and nitrogen oxides (N_2O, NO, N_2O_3, NO_2, N_2O_4, and N_2O_5) are of particular concern due to their negative impact on the environment, including their roles in smog

formation, acid rain creation, ozone depletion, and the generation of greenhouse gases associated with climate change.[82] Concern for the state of the environment and human health prompted stricter NO_X emissions standards, resulting in a concomitant implementation of abatement technologies such as passive adsorption.[83] The selective catalytic reduction (SCR) of nitrogen oxides by ammonia is widely practiced to mitigate NO_x emissions (see Eq. 15 and Eq. 16). Although zeolite-supported Cu and Fe catalysts have recently found use in mobile applications, titania-supported vanadium oxide catalysts have been widely employed at stationary industrial facilities and large boilers for many decades due to their relatively high activity, selectivity in the range of 300–400°C, and low cost.[84] Of the more than 107 million tons of NO_x emitted each year, ~40% come from such operations.[85] Given the magnitude of its utilization, a fundamental understanding of the reaction mechanism is imperative to improving the performance of SCR catalysts. To understand the mechanism, however, a molecular-level depiction of the active centers is required. Such a description can be provided by thorough characterization of the materials.

$$4NO + 4NH_3 + O_2 \rightarrow 4N_2 + 6H_2O \qquad \text{Eq. 15}$$

$$2NO_2 + 4NH_3 + O_2 \rightarrow 3N_2 + 6H_2O \qquad \text{Eq. 16}$$

Despite its extensive use and high value, much remains unknown in vanadia-based SCR. In addition to the mechanism of this transformation,[86] the contributions of surface Brønsted and Lewis acid sites are contested.[87-88] Mechanistically, a one-site scheme invoking an Eley-Rideal (E-R)-type mechanism was proposed involving a reaction between gas phase NO and adsorbed ammonia on Lewis acid sites, leading to the formation of nitrosamide (NH_2NO) (Figure 2.3).[89]

An alternate description consisting of two sites has been proposed, involving NH_3NO formation via a Langmuir-Hinshelwood (L-H)-type scheme where the adsorbed ammonia interacts with weakly or briefly adsorbed NO (Figure 2.4).[86, 89-92] Isotopic $^{18}O_2$ labeling experiments have provided strong support that a Mars-van Krevelen (MvK) mechanism is also occurring, with surface vanadia sites providing the oxygen participating in the SCR mechanism and the catalytic cycle is completed by reoxidation of the reduced surface vanadia species by gas phase molecular O_2.[92-96] However, the MvK mechanisms does not distinguish between the participation of one or two catalytic active sites in the SCR reaction.

A mechanistic description is complementary to identification of the catalytic active sites themselves. This descriptor holds great importance for rationally designing catalysts with improved performance. Many factors have been shown to impact SCR performance, such as the selection of promoter, surface vanadium oxide and promoter loading, method of preparation, and even the chemical environment.[84, 97-104] Of the promoters explored, tungsten oxide is one that has achieved wide industrial utilization on V_2O_5/TiO_2 catalysts due to its enhancement of measured Brønsted acidity, SCR activity, broadening of the operational temperature range, improvements to the product selectivity, reduction of active site poisoning, and stabilization of the catalyst against thermal sintering.[86, 105-106] These effects demonstrate the significance of catalyst formulation on the interactions between the catalyst and reacting substrates, and have given rise to multiple explanations for the improvements in performance caused by the addition of tungsten oxide. One such scientific debate is centered on whether the promotion of SCR reactivity with tungsten oxide proceeds via a structural effect or purely an electronic effect where the redox properties of vanadia are modified through induction, conjugation, and/or electronic spin state.[86]

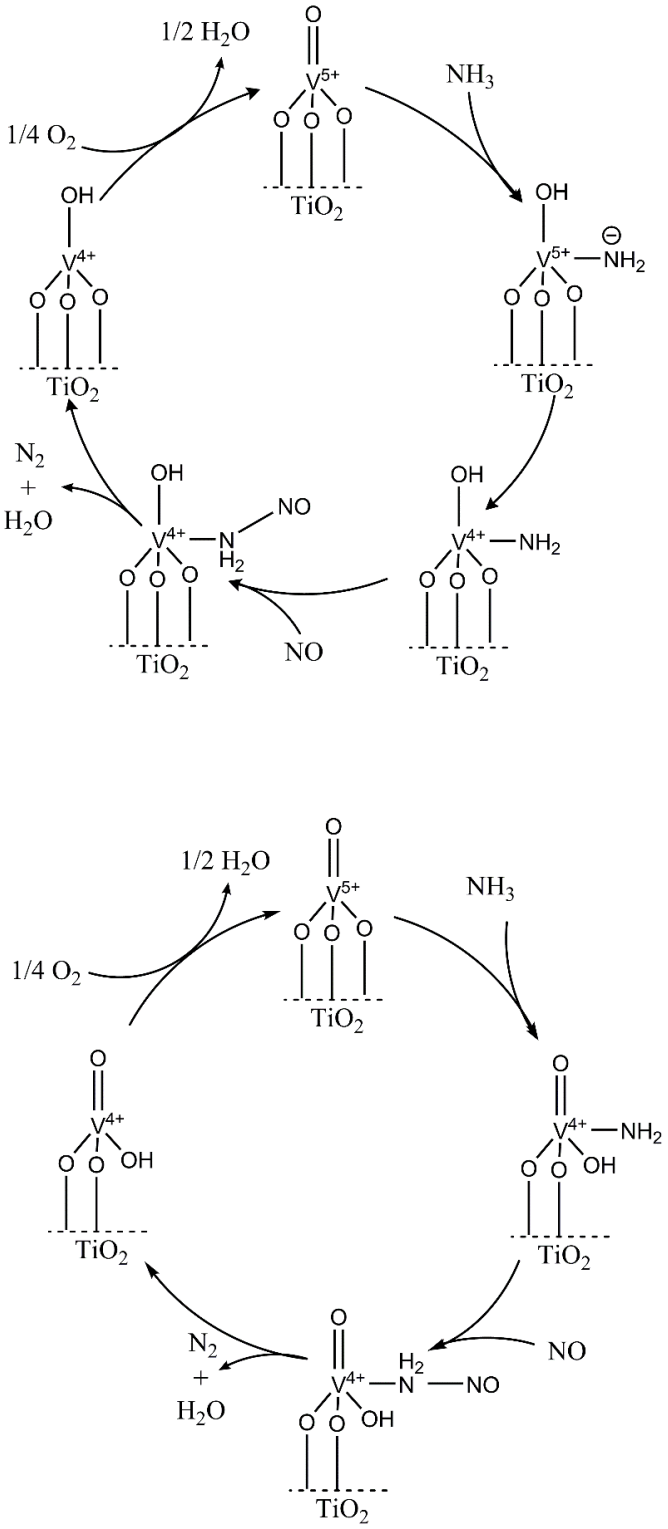

Figure 2.3. Representative mechanistic interpretation of the one-site SCR of NO by NH_3 with vanadia-based catalysts where the proton is transferred to the vanadyl bond (top) or a V-O-Ti bridging bond (bottom).

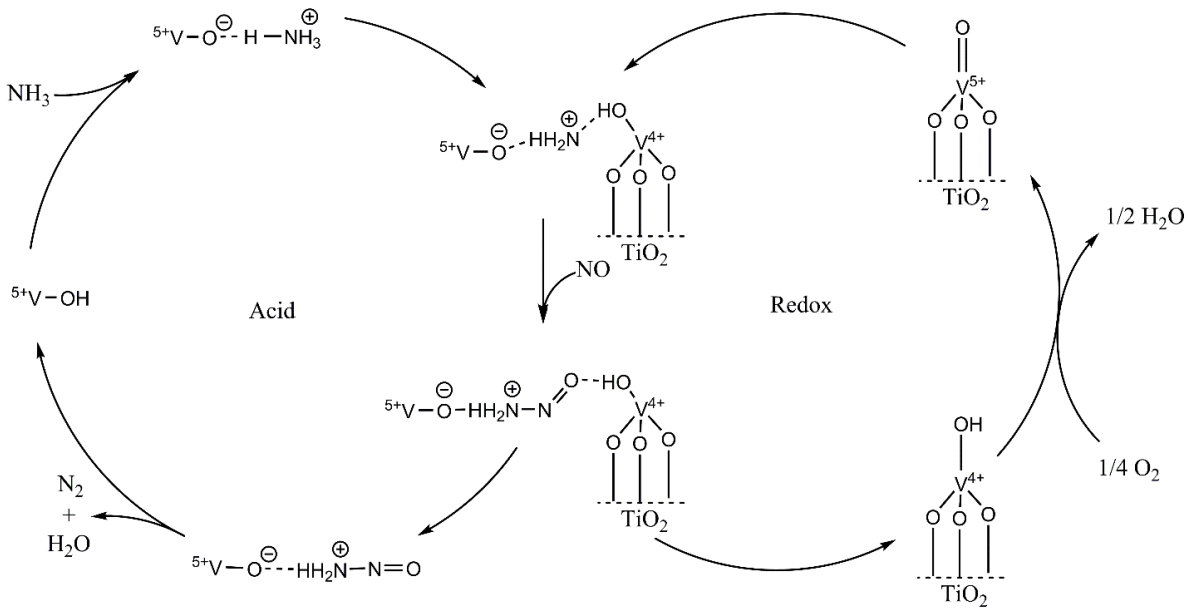

Figure 2.4. Representative mechanistic interpretation of the two-site SCR of NO by NH_3 with vanadia-based catalysts involving both an acid site and a redox site.

To identify the nature of the active surface vanadia sites on TiO_2 supports in order to promote a detailed description of the structure-function relationships between the catalytic active centers and SCR activity and selectivity, many spectroscopic techniques (including IR,[89] Raman,[42, 44, 107-108] and UV-vis[65]) have been deployed; however, difficulties exist in providing a quantitative illustration of the distribution of the surface vanadia sites. Spectral assignments of vanadia sites on promoted oxide supports are challenging to make due to signal overlap with the other oxides present in the system. To overcome the shortfalls of other spectroscopic techniques, high-field ^{51}V solid state MASNMR can be used to probe catalytic materials and reveal the structure of vanadia on the catalyst, with no overlap from other oxides due to the nuclear specificity.[77, 109] Previous limitations in the magnetic field, sample spinning rate, and spectral interpretation have hindered the identification of the surface vanadia structures present on oxide supports.[110-113]

In this section, *in situ* spectroscopic measurements (MAS NMR, Raman, EPR), DFT-based models structures, and catalytic kinetic studies are combined to clearly demonstrate that incorporation of tungsten oxide as a promoter improves the SCR catalytic activity by altering the molecular structure of the surface vanadia sites to configurations favorable to SCR of NO_x by NH_3. This observation provides direct evidence of molecular structural changes that occur on the surface vanadium oxide active centers in the presence of metal oxide promoters, indicating that the promotion mechanism of tungsten oxide proceeds by modifying the structure of the vanadia species to configurations conducive to a two-site transformation.

The bare TiO_2 support has exhibited negligible activity for the SCR reaction at relevant reaction conditions; however, it is important for activation of the surface vanadia sites through a support effect.[89, 114] In contrast, supported V_2O_5/TiO_2 materials exhibit notable activity for NO_X abatement via SCR. The changes in SCR reactivity upon progressive addition of vanadia onto a TiO_2 support are illustrated in Figure 2.5 where the conversion was maintained below 6%. The reaction rate (mol/g cat-s) steadily increases with the addition of vanadia onto the TiO_2 support up to 5% V_2O_5/TiO_2 (monolayer coverage). A more than 30-fold increase in the reaction rate is observed over the analyzed loadings from 1% to 5% V_2O_5 on the TiO_2 support, indicating a strong relation between the quantity of surface vanadia sites and the SCR reaction rate. This observation is preserved when considering the specific SCR turnover frequency (TOF, molecules of NO converted per vanadia site per second), since a 5.5-fold increase in TOF is observed over a 5-fold enhancement of surface vanadia loading below monolayer coverage, which indicates that each surface vanadia atom is, on average, more catalytically active at higher loadings (Figure 2.6). This is likely due to differences in the structure of these vanadia species at contrasting loadings. At high vanadia loadings approaching the monolayer, side reactions, such

as ammonia oxidation, become relevant, negatively affecting the observed reaction rate as observed previously (>3% V_2O_5, selectivity N_2 ~ 85%; >7% WO_3, selectivity N_2 ~91%).[42, 89] When imposing the measured reactivity into a plot of log [reaction rate] vs. log [VO_x loading], a slope of ~2 is derived, indicating that the SCR reaction rate varies proportionally to the square of the concentration of surface vanadia sites ($[VO_x]^2$) and suggesting that the reaction mechanism involves two surface vanadia sites.

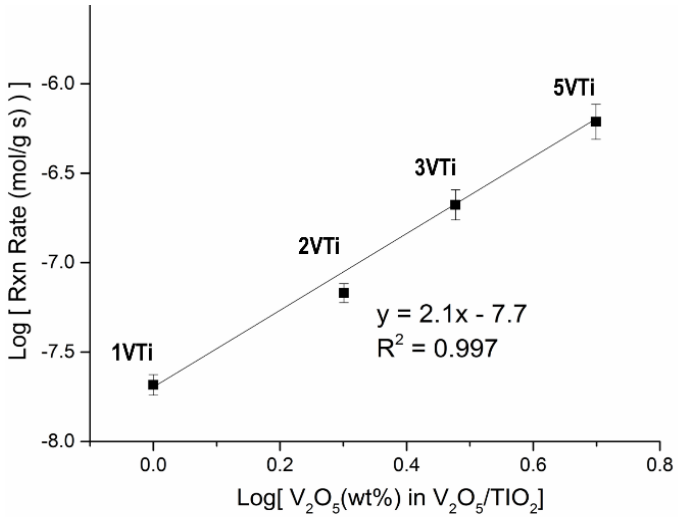

Figure 2.5. Log [reaction rate] vs log [vanadium oxide loading] for the SCR reaction. Data were recorded at 200°C.

Reprinted with permission from Jaegers et al. *Ange. Chem.*, 2019, 58, 12609. Copyright 2019 Wiley-VCH Verlag GmbH & Co.

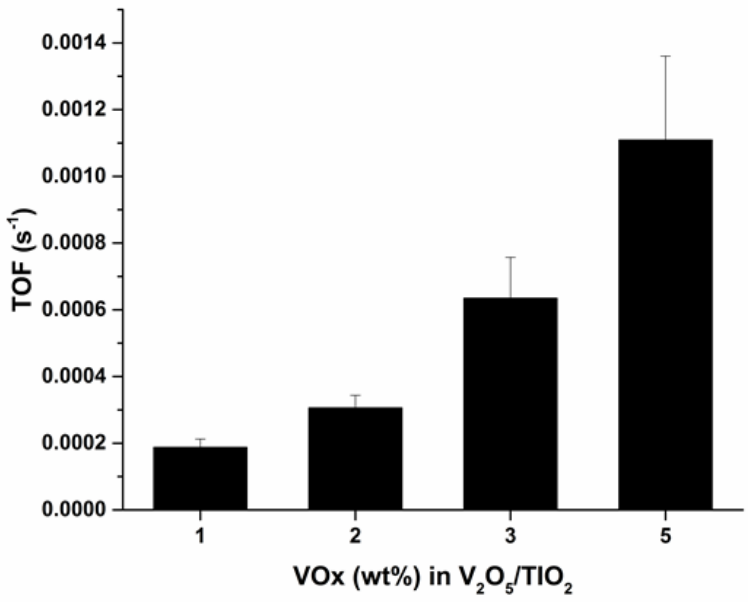

Figure 2.6. Turn-over-frequency plot (per vanadia per second) of the SCR reaction of NO_X by NH_3 as a function of surface vanadia loading. Data were recorded at 200°C.

These vanadia catalysts were characterized to reveal the molecular structure of the surface vanadia active sites on the TiO_2 support. The X-ray diffraction pattern (Figure 2.7) demonstrates the absence of large (>3 nm) V_2O_5 crystallites and only contains the diffraction patterns for the anatase (84%) and rutile (16%) titania as determined by Rietveld refinement. This is confirmed by high-resolution transmission electron microscopy (Appendix C: Additional Supporting Data), where the electron diffraction pattern reveals an abundance of anatase TiO_2 and a minor rutile component that largely overlaps with anatase, except at 3.26 A where the rutile 110 ring is lightly visible. Analysis of the supported 5% V_2O_5/TiO_2 catalyst by high-resolution scanning transmission electron microscopy (STEM) coupled with electron energy loss spectroscopy (EELS) (Appendix C: Additional Supporting Data) confirms that the vanadia is highly dispersed since it was observed along all probed edge positions. Non-edge vanadium

detection is hindered by titania thickness, whereas exterior edge detection is enhanced by both a thinner support layer and a higher abundance of vanadia aligned parallel to the electron beam, enhancing the EELS signal.[115] It should be noted that TiO_2 edges also demonstrate an expansion of the lattice spacing when surface vanadia is detected on the TiO_2 support (from 3.35 to 3.91 Å on $[0\bar{1}1]$). This illustrates the strong VO_X-TiO_2 anchoring interaction resulting in reconstruction of the TiO_2 support surface.

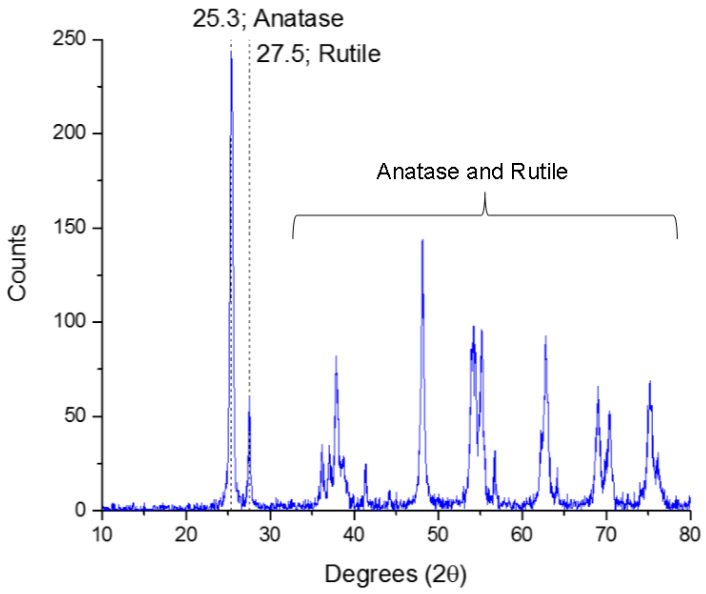

Figure 2.7. X-ray diffraction (XRD) patterns of 5% V_2O_5/TiO_2 prepared by incipient wetness impregnation demonstrating the observance of only the anatase and rutile phases of TiO_2 from the P25 support material.

Raman spectroscopy of unpromoted V_2O_5/TiO_2 catalysts reveals the nature of surface vanadia sites and the structural changes that occur during the dehydration process. This dry condition dominates the surface during the SCR reaction at elevated temperatures due to the rapid desorption of moisture from the catalyst surface.[42, 107, 116] The *in situ* Raman spectra (Figure

2.8) of the bare TiO_2, supported 1% V_2O_5/TiO_2, and supported 5% V_2O_5/TiO_2 exhibit the formation of vanadyl (V=O) vibrations of surface VO_4 sites indicated by a band around 1032 cm^{-1}.[86] This terminal V=O band blue shifts slightly with increasing surface vanadia coverage due to the vibrational coupling of adjacent vanadyl bonds, providing evidence for oligomerization of the surface vanadia sites at higher surface vanadia coverage[107-108, 117-118] and is associated with the concomitant lowering of the apparent activation energy of the SCR reaction.[65, 90, 119] This effect has been extensively noted on different metal oxide supports (ZrO_2, TiO_2, Al_2O_3) and has shown small shifts in the observed wavenumber with increasing polymeric vanadia content. In addition, weak and broad bands at ~930 cm^{-1} and ~799 cm^{-1} are present that that arise from bridging V-O-Ti vibrations of the surface VO_4 sites and TiO_2 anatase overtones, respectively.[62, 86, 120] The 930 cm^{-1} band is a broad and weak feature not easily observed on these samples for low vanadia loadings (1%). This band becomes more apparent at high surface VOx coverage due to the presence of more vanadia on the surface (and thus more V-O-Ti linkages). The presence of additional VOx species at higher loadings directly form additional V-O-Ti bonds that can then be detected by Raman spectroscopy. Numerous experimental and theoretical studies have ascribed this peak to V-O-Ti linkages[62, 86, 120-122]; however, it is noted that some debate remains where this peak is alternatively identified as V-O-V vibrations. Theoretical works predict this bridging V-O-V will arise at ~800 cm^{-1}. [62, 86, 120-122] The absence of a Raman band at 995 cm^{-1} from crystalline V_2O_5 nanoparticles reveals that the vanadia in these catalyst samples are 100% dispersed on the titania support at these monolayer and lower loadings. The addition of more vanadia would stimulate the formation of crystalline V_2O_5 nanoparticles that are less active than the surface vanadia sites.[44]. The peak at 799 cm^{-1} is ascribed to the overtone bands on anatase

TiO_2, evidenced by its presence on the bare TiO_2 sample. Any overlapping V-O stretches in this region would be overshadowed by the relatively intense overtone at the same position.

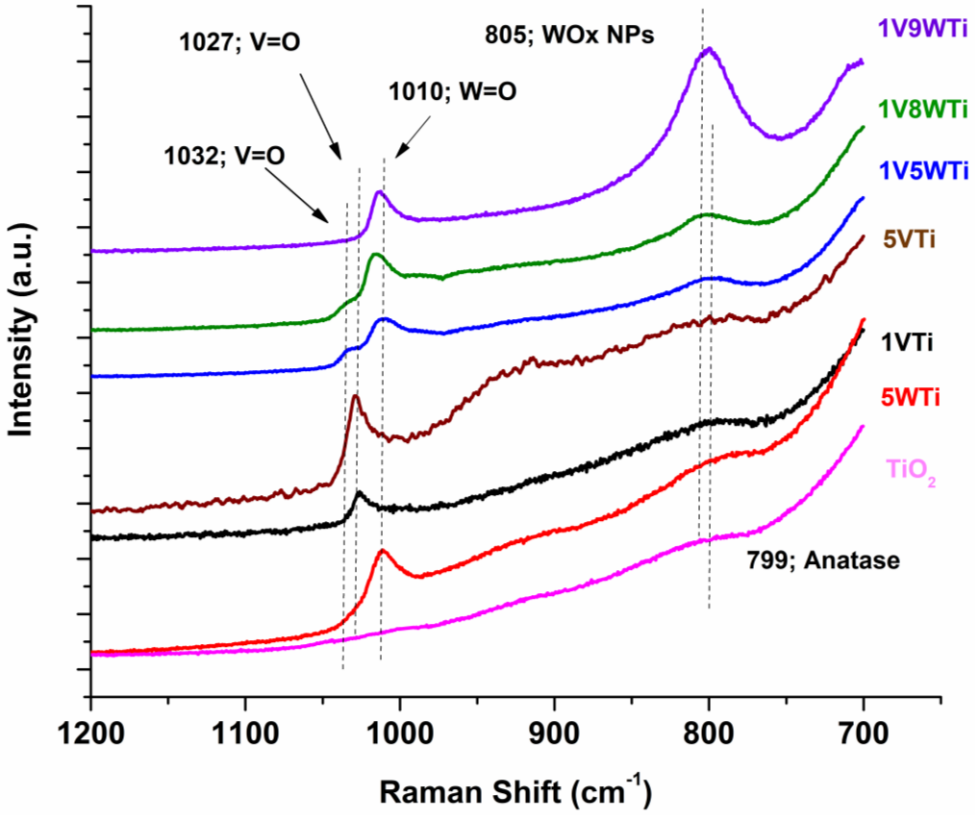

Figure 2.8. Raman spectra of dehydrated supported vanadium and tungsten oxides on titania.

Solid state ^{51}V MAS NMR provides specific information regarding the molecular structures of the surface vanadia sites as a function of vanadia coverage. The *in situ* ^{51}V MAS NMR spectra for the dehydrated supported V_2O_5/TiO_2 catalysts in the center-band region are displayed in Figure 2.9, and demonstrate that the vanadia structure is more complex on titania than on silica (2.1 Silica-supported V_2O_5).[77, 109] Full sideband patterns at 14 and 20T are visible in Appendix C: Additional Supporting Data, where differences in spectral signals are related to spinning rate-induced separation of side bands and slight quadrupolar broadening effects.

Although NMR can only detect V^{5+} species, the contributions from V^{+4} paramagnetic species can be detected with Electron Paramagnetic Resonance (EPR) spectroscopy (Appendix C: Additional Supporting Data). The EPR spectra show that V^{+4} species are minimal and account for no more than 1% of the total vanadium in the catalysts of this study, providing confidence that NMR will detect nearly all vanadium oxide sites on the titania support.

The 1% V_2O_5/TiO_2 (~0.2 monolayer coverage) and 5% V_2O_5/TiO_2 (~1 monolayer coverage) catalysts exhibit distinct structural differences. The supported 5% V_2O_5/TiO_2 catalyst primarily contains features below the ^{51}V NMR -544 ppm peak (93%), similar to those previously reported for such a formulation.[77] A relatively narrow feature at -612 ppm accounts for 13% of the total vanadia species in the supported 5% V_2O_5/TiO_2 catalyst which is the approximate position of V_2O_5 nanoparticles, but may also be related to large, 2D oligomeric surface vanadia structures at these higher loadings. Small quantities of this signal also appear to be present (~6%), even for the supported 1% V_2O_5/TiO_2 catalyst as previously reported,[77] further suggesting that these signals may belong to large oligomers. Raman spectroscopy is highly sensitive to V_2O_5 crystallites that are not observed even in the supported 5% V_2O_5/TiO_2 catalyst, highlighting the complementary nature of the two spectroscopic techniques.

For the dehydrated supported 5% V_2O_5/TiO_2 catalyst (about monolayer coverage), the solid state ^{51}V MAS NMR spectrum exhibits a broad peak at -645 ppm accounting for nearly 26% of the vanadium oxide and was previously assigned to dimeric and linear oligomeric surface vanadia sites.[77] Peaks in this region also display a strong side band pattern. Downfield of -612 ppm, the features between -550 ppm and -590 ppm account for about 54% of the total vanadia and two smaller peaks at -526 ppm and -544 ppm account for the remaining 7%. The solid state

^{51}V MAS NMR spectrum of the dehydrated supported 1% V_2O_5/TiO_2 catalyst (~0.2 monolayer coverage), however, only possesses 4% of the vanadia at -645 ppm corresponding to oligomeric species. This catalyst with lower surface coverage possesses a wider array of low field signals, with a broad line at -480 ppm and two distinct lines at -507 ppm and -533 ppm that account for nearly half of the surface vanadia sites.

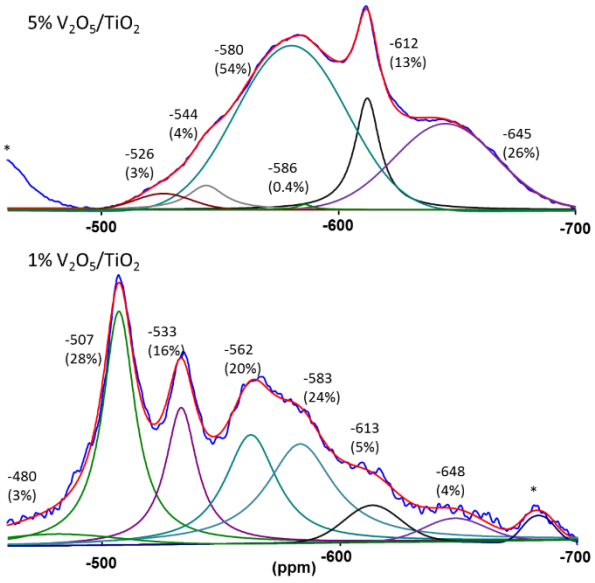

Figure 2.9. ^{51}V MAS NMR results of dehydrated, supported V_2O_5/TiO_2 catalysts prepared by impregnation. Spectral deconvolution summation is presented by the red line and compared to the collected data (blue). Sidebands displayed are indicated by (*).

Prior literature on NMR for titania-supported vanadia was hindered by low magnetic field strengths, slow spinning rates, and wide-line spectra where only a couple of signals were detected. For instance, a line at -555 ppm was originally assigned to a distorted VO_4 structure and a line at -510 ppm was assigned to a distorted VO_6 structure, with the VO_4 coordination also

reported at -530 ppm.[123-125] A recent investigation of the ^{51}V MAS NMR signals for titania-supported vanadia catalysts was supported by DFT calculations on small cluster models of various vanadium oxide species.[77] The results suggested the presence of monomeric surface vanadia sites with lines at -502 ppm and -529 ppm, dimeric surface vanadia sites with lines at -555 ppm and -630 ppm (with the latter arising from dimeric structures with one V-O-V bond as well as linear oligomeric surface vanadium oxide chains), and signals near -610 ppm ascribed to highly-oligomerized vanadia species such as crystalline V_2O_5-like nanoparticles.

These cluster models were consistent with the experimental NMR data, but not all peaks could be assigned based on these models. Additionally, the role of facet-dependent structures is currently being debated and the unconstrained titania models may not account for subtle structural differences present when surface vanadia species are anchored on a low index titania facet.[126-127] Since anatase (101) and (001) were the most abundantly observed facets on these samples, they were used as the basis for DFT modeling to consider the impact of the anchoring facet. These additional models of surface vanadia anchored to anatase (101) and (001) surfaces were constructed (see Figure 2.10) for use in the electronic structure calculations.

Periodic density functional theory (DFT) calculations have suggested that distorted VO_5 environments are relatively more stable on the (001) facet, but distorted VO_4 structures dominate on (101).[128-130] Our monomeric models for the (101) surface reflect distorted VO_4 structures (Figure 2.10a–c) that provide a calculated shift of -506 ppm and -487 ppm for structures with protons placed on nearby titania and on the bridging V-OH-Ti bond, respectively. These protons charge-balance the DFT cluster and are justified by the generation of Brønsted acidity as vanadium oxide atoms titrate surface titanol sites.[88] Indeed, signals at the first two values are

observed for the vanadia-only catalyst impregnated on TiO_2 (-507 ppm and -480 ppm). Structures on the (001) surface optimized to yield five-coordinate vanadium atoms are depicted in Figure 2.10d–e.

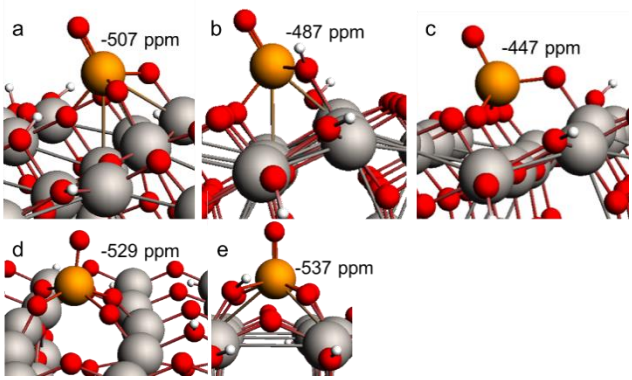

Figure 2.10. DFT clusters used to model monomeric structures on TiO_2, including distorted VO_4 (a), distorted VO_4 with bridge bond protonation (b), distorted VO_4 using two oxygen from TiO_2 (c), distorted square pyramidal (d), and distorted square pyramidal with bridge bond protonation (e). Atoms represented include vanadium (orange), titanium (grey), oxygen (red), and hydrogen (white).

Similarly, two structures with different proton placement align well with the experimental chemical shift and the reported formation energies reported by Du et al.[128] These peaks are predicted at -529 ppm (Figure 2.10d) and -537 ppm (Figure 2.10e, which is the preferred configuration at high surface vanadia coverage[129]) and are likely candidates for the -533 ppm peak observed in the NMR spectra. This peak has been previously ascribed to various surface vanadia structures, including a monomer, but these DFT calculations provide strong support for assignment to a monomeric-type surface vanadia species.[77, 123-124] The low-field broad signal at -480 ppm may be related to surface vanadia sites anchored near oxygen-vacant titania, where modeling predicts nuclear deshielding by about 25 ppm (see Appendix C: Additional Supporting

Data), but the slightly altered tetrahedral monomer configuration from Figure 2.10c also explains this signal. On the basis of the computational and ^{51}V MAS NMR experimental results, we can assign the low-field ^{51}V MAS NMR peaks as an array of monomeric species present on the titania surface: distorted VO_4 with a nearby OH or oxygen vacant VO_4 (-480 ppm), disordered VO_4 (-507 ppm), and distorted VO_5 (-533 ppm). Dimeric surface vanadia structures are predicted to resonate at -639 ppm and -553 ppm for mono- and di-linked structures, respectively.[77] Differences were also noted for oligomeric chains of surface vanadia species, where the small cluster models predicted shifts near -630 ppm. Different chemical shifts are computed for internal and terminating vanadium atoms in polyvanadate chains, with the outer vanadium atoms predicted at -663 ppm and the inner vanadium atoms at -633 ppm. The observed expansion of the lattice spacing of TiO_2 edges when vanadia is anchored (Appendix C: Additional Supporting Data; from 3.35 to 3.91 Å on $[0\bar{1}1]$) is consistent with the DFT predictions of expansion for the four local Ti atoms around monomeric surface vanadia (3.45 to 4.33 Å on [001]). The combination of the computational and spectroscopic work allows for the conclusion that the broad signals in the -640 ppm region retain their assignment to oligomeric surface vanadia structures. As such, surface VO_x monomers account for ~47% (shifts downfield of -540 ppm) of the surface vanadia sites at low coverage (~0.2 monolayer) and only ~3% of the surface vanadia sites at high coverage (monolayer) on the TiO_2 support. In contrast, dimeric and oligomeric surface VO_x sites on TiO_2 support (shifts of -560 ppm to -580 ppm and peaks below bulk V_2O_5) represent 48% of the surface vanadia sites at low coverage and 80% of the surface vanadia sites at monolayer coverage. These trends reflect the oligomerization of surface vanadia sites on the TiO_2 support with increasing surface vanadia coverage, supporting the established notion of

increasing oligomerization of surface vanadia sites at higher surface coverage since these upfield signals are present in the supported 5% V_2O_5/TiO_2 catalyst.

As previously indicated, incorporation of tungsten oxide as a promoter provides a number of benefits, notably improved SCR activity.[89, 131] These improvements also include an increase in the number of Brønsted and Lewis acid sites and their corresponding acid strengths, ammonia adsorption capacity, and enhanced reducibility of surface vanadia sites.[105, 132-133] Supported $V_2O_5/WO_3/TiO_2$ catalysts consist of surface $O=WO_4$ sites on the TiO_2 support below monolayer coverage (4.5 W atoms/nm^2) and exhibit the W=O vibration at ~1010–1015 cm^{-1} that blue shifts with surface coverage from oligomerization of the surface WO_5 sites (see Figure 2.8). When WO_5 coverage exceeds a monolayer on TiO_2 (>4.5 W atoms/nm^2), crystalline WO_3 nanoparticles also form. Further, shifts in the vanadyl vibration are restricted to ~1–3 cm^{-1} and such peak shifts can be challenging both to observe and to assign. Since the quantity of vanadia in 1% VOx-(x%) WOx/TiO_2 samples remains low, no additional V-O-Ti linkages (930 cm^{-1}) are expected compared to 1% V_2O_5/TiO_2. Conceptually, fewer of these linkages will be present with tungsten addition due to oligomerization of surface vanadia and the increase in V-O-V bonds suppressing V-O-Ti bonds. Two VO_4 monomers will have 6 V-O-Ti linkages (3 each). Upon dimer formation, two of these become V-O-V linkages, lowering the abundance of V-O-Ti and hindering spectroscopic observation.

The impact of tungsten oxide promotion on the SCR activity of supported 1% V_2O_5-xWO_3/TiO_2 catalysts (x= 0–8% WO_3, up to monolayer coverage) is presented in Figure 2.11 and Figure 2.12. These show the progressive increase in SCR reaction rate and specific rate with tungsten oxide addition. The observed reaction rate for the supported 1% V_2O_5/TiO_2 catalyst

increases 50-fold with the impregnation of 8% WO_3, a value that mimics the TOF increase since the surface vanadia loading is constant. A plot of log [rate of NOx conversion] vs. log [WO_3 loading] (Figure 2.12) yields a slope of ~1.9 reflecting the strong promoting effect of surface tungsten oxide on the SCR reaction. It is important to note that neither exposed titania sites nor surface WO_3/TiO_2 significantly catalyze SCR of NO with NH_3 at 200ºC.[89, 134]

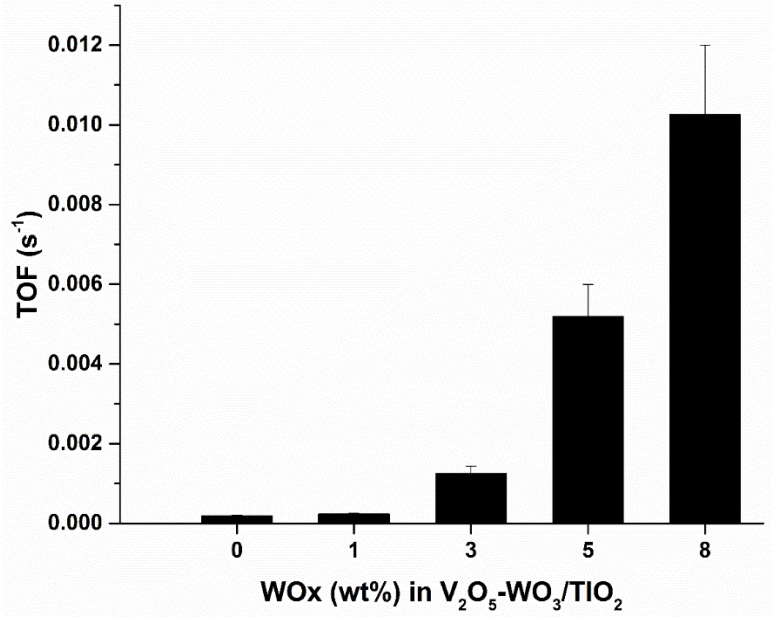

Figure 2.11. Turn-over-frequency plot (per vanadia per second) of the SCR reaction of NO_X by NH_3 as a function of surface tungsta loading at a constant 1% V_2O_5 coverage. Reactions were conducted at 200ºC.

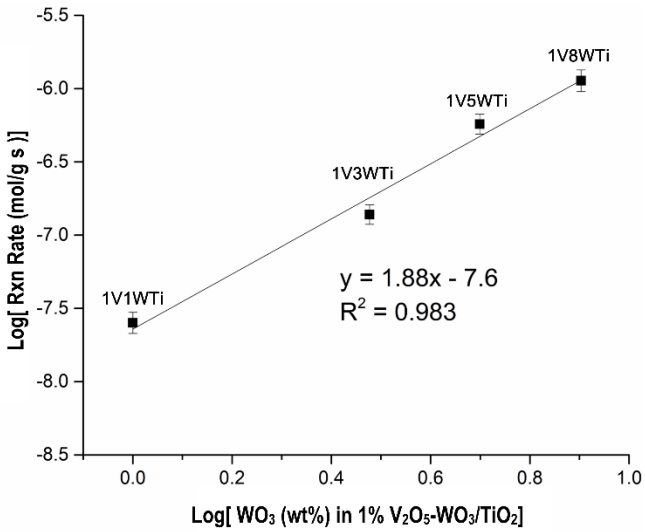

Figure 2.12. The log [reaction rate] vs log [tungsten oxide loading] (bottom) shows a strong correlation between tungsten oxide content and catalytic performance. Reactions were conducted at 200°C.

Reprinted with permission from Jaegers et al. *Ange. Chem.*, 2019, 58, 12609. Copyright 2019 Wiley-VCH Verlag GmbH & Co.

As previously indicated, the origin of the SCR reactivity enhancements by tungsten oxide promotion has been evaluated as either an electronic effect or a structural effect.[97, 132, 135-136] To evaluate the influence of the surface tungsta promoter on the structure of the surface vanadia sites, ^{51}V MAS NMR was employed to compare unpromoted 1% V_2O_5/TiO_2 with promoted 1% V_2O_5-3-5% WO_3/TiO_2 catalysts. Figure 2.13 depicts the MAS NMR of 1% V_2O_5-(3–5)% WO_3/TiO_2 catalysts. Incorporation of surface tungsta sites to the supported 1% V_2O_5/TiO_2 catalyst results in a redistribution of the surface vanadia species in the NMR spectrum. Tungsten oxide addition alters the species present in a spectrum to reveal lines at -517 ppm and -530 ppm (monomeric structures), a broad feature at -568 ppm from dimeric and oligomeric surface sites (due to the expansive chemical shift range, this may represent multiple environments), and a

broad signal at -630 ppm for larger 2D oligomers. There is a clear increase in oligomeric signals with the addition of promoter (~53% oligomeric surface vanadia species for the W-free catalyst vs. 63% and 82% oligomeric surface vanadia species for the 3% and 5% tungsta-promoted catalyst, respectively) based on the spectra presented in Figure 2.13. Though theoretical investigations have suggested the energetic preference of VO_x/TiO_2 domains over mixed, supported VO_x-WO_x/TiO_2 structures in the promoted system,[137] the existence of surface VO_x-WO_x dimers on TiO_2 is not disproved. A number of W^{VI}-O_x-V^V on Ti(IV) cluster models were evaluated to explore the possibility of VO_x-WO_x dimers (Appendix C: Additional Supporting Data).

The small models (O=)(HO)W^{VI}-O-V^V(=O) and (O=)W^{VI}-O-V^V(=O) had predicted chemical shifts of -576 ppm and -603 ppm, respectively. A portion of the observed signals may potentially be represented by such structures on the basis of chemical shift. In additional models (Appendix C: Additional Supporting Data), structures with two V^V bonded to a single W^{VI} were examined. A structure with two O bridge atoms between with the W and each V (VWV) leads to ^{51}V chemical shifts of -600 ppm, which is slightly higher than observed, but similar to (O=)W^{VI}-O-V^V(=O). Asymmetric structures containing one W connected with two bridge bonds to a central V, which is also a single-bridge oxygen linked to an additional V, was predicted at -578 ppm for the central V and -665 ppm for the terminal V. This trimer showed consistence of the observed signal with the -578 ppm prediction, but a rise in experimental -665 ppm features was not observed in these spectra, refuting its presence. A second asymmetric structure with a VVW ($W(=O)_2$) motif was found to be 1.6 kcal/mol higher in energy than the preceding asymmetric structure, but exhibited a calculated shift of -552 ppm for the central V and -529 ppm for the V bonded to only the other V and Ti. These signals are both present in the NMR spectrum and also

result in vanadia occurring in closer proximity to one another, satisfying the two-site requirement. Two slightly altered cluster models—one with a W connected with two bridge bonds to a central V, which is connected to an additional V by a single bridge O, and one with a WO_2 unit single bridge bonded to two V centers were considered. The former is 2.1 kcal/mol in energy higher than the latter and predicted ^{51}V chemical shifts of -578 ppm for the central V and -665 ppm for the terminal V. This is again dissimilar to the observed spectral trend. The latter, lower energy structure has two asymmetric V sites with ^{51}V chemical shifts of -603 ppm and -626 ppm, making it an unlikely candidate due to the -613 ppm feature of the spectra processing the same chemical shift and lineshape as those in the unpromoted catalysts. Energetically, structures with W between the two V atoms are preferred by a small amount of energy independent of whether the W has one or two W=O bonds; however, the chemical shifts are not consistent with experimental data for these structures.

The presence of oligomeric surface vanadia domains on TiO_2 in the presence of surface tungsten oxide sites has been previously proposed on the basis of TPR, Raman, and activity measurements.[138-139] NMR, however, provides a direct observation of oligomerization of surface vanadia sites on TiO_2 in the presence of tungsten oxide sites. Additionally, support for promotion-induced structural effect is found in redox chemical probe reaction studies of SO_2 oxidation. As a reaction which requires one surface vanadia site to proceed, the reactivity of promoted and unpromoted materials were shown to exhibit comparable TOF values.[140-141] This observation supports that the origin of promotion by surface tungsten oxide lies primarily in structural changes induced by tungsta's role in oligomerizing vandia sterically and satisfying the requirement for two catalytic sites and that promotion largely does not stem from electronic effects such as induction, conjugation, and electron spin state. Further benefits of surface

tungsten oxide to supported V_2O_5/TiO_2 catalysts arise from the generation of new Brønsted acidity on the catalyst, which impacts the adsorption mode of ammonia (surface NH_3 on Lewis and surface NH_4^+ on Brønsted acid sites), and a decrease in surface Lewis acid sites from the exposed titania support.[88] The Brønsted acid sites from surface vanadia have been shown to dominate the overall reaction.[88] Although Lewis acid sites are intrinsically more active for SCR under mild conditions, they constitute a minority of species during SCR reaction conditions.

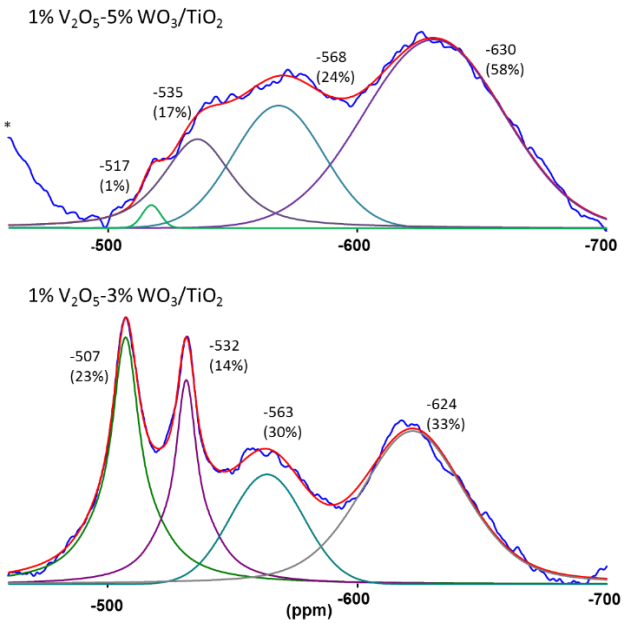

*Figure 2.13. Solid state ^{51}V MAS NMR spectra of dehydrated, impregnated 1% V_2O_5-(3-5)% WO_3/TiO_2 catalysts. Spectral deconvolution summation is presented by the red line and compared to the collected data (blue). All spectra were externally referenced to V_2O_5 at -614 ppm. Sidebands displayed are indicated by *.*

Acknowledging the roles additional effects such as acidity and defect sites as well as the potential inaccuracies in relative abundance from fitting such broad spectral features, correlating

the observed structures of vanadium with the SCR activity remains of great interest to provide evidence for structure-function relationships. Table 9 shows reveals the measured rate and estimated site abundance of monomeric, dimeric, and polymeric species in the series of samples. Estimations for the intrinsic rate of each species were calculated by treating the overall reaction rate as a linear combination of the rates of each species. The measured rates were then compared to the calculated rate derived from the intrinsic species rate and the site abundance. The sum of squared residuals was minimized using a generalized reduced gradient solver method. Several solutions were sought, but the lowest residual was found for when $R_{monomer}$ and R_{dimer} were negligible and the $R_{polymer}$ was $6.82*10^{-7}$. A plot of the reaction rate as a function of polymeric content is shown in Figure 2.14. This reveals an increasing relationship between polymeric vanadia species and the reaction rate.

Table 9. Rate and abundance calculation for vanadia-based SCR.

Sample	**Rate mol/g/s/%V**	**$f_{Monomer}$**	**f_{Dimer}**	**$f_{Polymer}$**	**$Rate_{Calc}$**	**$\Delta Rate^2$**
1VTi	2.03E-08	47	44	9	6.14E-08	1.68E-15
5VTi	1.36E-07	7	54	39	2.66E-07	1.68E-14
1V3WTi	1.38E-07	37	30	33	2.25E-07	7.56E-15
1V5WTi	5.50E-07	18	24	58	3.96E-07	2.37E-14
					SSR	4.98E-14

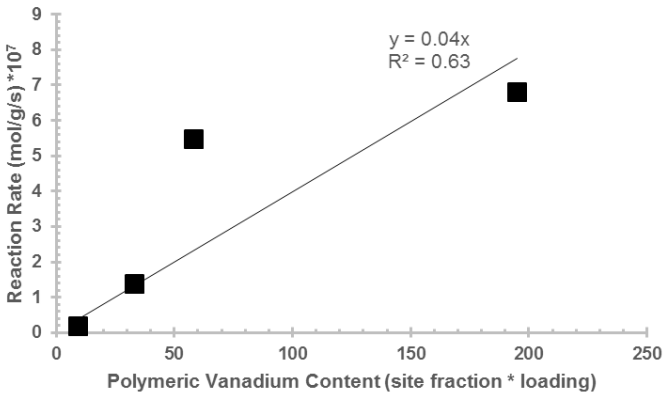

Figure 2.14. Reaction rate vs polymeric vanadium species.

The mechanisms of this oligomerization of vanadia by tungsten oxide remains unknown. An increased surface vanadia abundance has been demonstrated to enhance the prevalence of oligomerized species. Similar effects on the vanadia species are apparently present from tungsten oxide addition. It can be speculated that this effect may arise from tungsten oxide coverage forcing the formation of local surface vanadia islands that result in high local concentrations of oligomeric vanadia, similar to the proposed oligomerization due to a loss of available surface sites for sulfated materials.[104, 142] If this hypothesis is an accurate description of the effect in tungsten-promoted and sulfated materials, surface crowding or displacement leading to oligomerization may also play a role in other industrially relevant promoters (e.g. MoO_3).

In summary, enhanced reaction rates and TOFs are observed with increasing surface vanadia coverage. Surface tungsten oxide addition is well correlated with an increasing quantity of oligomerized vanadia, which possess a greater number of adjacent vanadia active sites. The requirement for two neighboring sites for the SCR reaction is illustrated by the relationship of rate to $[VO_x]^2$ for supported V_2O_5/TiO_2 catalysts with increasing surface vanadia coverage.

Adding tungsten oxide promoter to the supported V_2O_5/TiO_2 catalysts enhances oligomerization of the surface vanadia sites and results in increased SCR reactivity.

2.3 Structure of V_2O_5/TiO_2 on Preferentially-Exposed Facets

It has been well-established the nature of the supporting material plays a critical role in the performance of vanadia-based catalyst materials, ascribed to the necessity of breaking the V-O-Support bonds in oxidative dehydrogenation reactions.[143] This support effect can result in several orders of magnitude difference in catalytic activity across materials; however, many studies rely on supports that contain inhomogeneous surface sites leading to a less specific description of the impact of the support. Indeed, it has been shown for cerium oxide supports that the exposed surface facet (structure) has a pronounced effect on the activity of the material, ascribed to differences in oxygen vacancy formation energy of the preferentially-exposed facet.[144] The potential effect of titania facets to impact the reactivity of vandia was explored by isobutane oxidative dehydrogenation with rods, truncated rhomboids, and spheres exhibiting [(010), (001)], [(101), (010), (001)], and [(101), (001), (010)] facets, respectively[127]. In contrast to the study with cerium oxide, minimal differences were presented in the activity of these three supported materials. The absence of marked differences in performance across the different nanoshapes was attributed to the small difference in oxygen vacancy formation energy across the facets: (101) 4.7 eV > (010) 4.4 eV > (001) 4.38 eV. Further, each of the shapes studied was a mixture of several facets, so decoupling the intrinsic reactivity differences between the facets was further complicated. Across the three samples, Kraemer et al. noted no differences in surface vanadia structure, though characterization was limited to Raman spectroscopy.

A second study has also investigated the potential effects of titania anchoring facet for vanadia-based catalysis. Tetragonal bipyrimids and rod-like materials were used as the support to provide preferentially (101) and (001) facets at ratios of 80:20 and 93:7, respectively.[145] It was suggested that vanadia preferentially anchors on the (001) facet as dispersed V^{4+} species prior to occupying the (101) facet as dispersed and oligomeric species. However, quantification of the vanadia oxidation state was performed using XPS. At such high vacuum conditions, vanadium is known to readily reduce from the V^{5+} state. Further, the facet distribution was quite similar, complicating a decisive determination. Herein, titania supported-vanadia materials which exhibit preferentially the (101) and (001) facets of anatase titania were synthesized and evaluated to better understand the structure and performance of the facets of interest. In addition to other characterization techniques, ^{51}V MAS NMR is employed to provide a detailed view of the vanadium speciation on these dominant-facet materials.

Anatase TiO_2-101 and -001 support materials were synthesized by previously reported hydrothermal methods.[146-148] Briefly, a commercially sourced titania (P25) was dissolved in a basic KOH solution and heated at 200^{o}C for 24 hours to produced potassium titanate nanowires ($K_2Ti_6O_{13}$). The resulting precursor was then suspended as a 3-4 mM solution and the pH was adjusted to <5 for (101) and to > 13 for TiO_2 (001) where urea was employed as a capping agent for TiO_2 (001). After hydrothermal treatment, the materials were washed and calcined to generate (101)- and (001)-dominant anatase TiO_2. The purity of the polymorph was confirmed by X-ray diffraction (Figure 2.15)

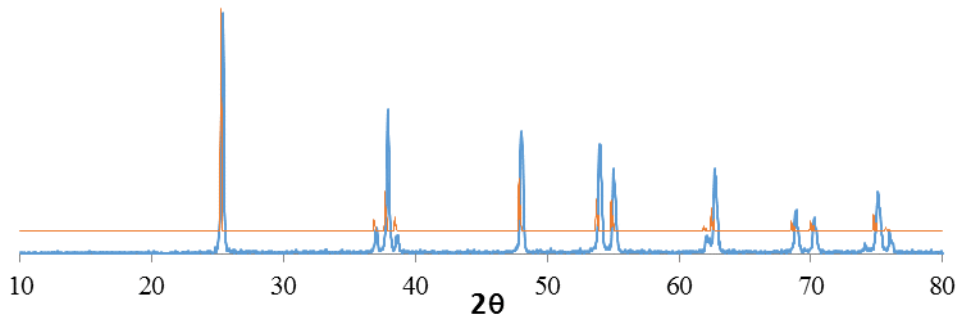

Figure 2.15. XRD patterns of synthesized TiO_2 nanoparticles confirming the presence of anatase TiO_2.

The resulting particles clearly demonstrate contrasting morphologies between the two samples. Figure 2.16 depicts the structure of the materials. The (101) dominant sample is an octahedrally-shaped bipyramid of ~50 nm in size that exhibits primarily the (101) facet. TiO_2-001 exhibits a plate-like structure of ~200 nm in size which exhibits the (001) on the long, flat surface and (101) on the edges. To gain a deeper understanding of the surface structure of the (001) facet-dominant titania sample, tilting experiments were conducted on the particles of titania to reveal the 3D nature of the shape. Figure 2.17 reveals that the large surface of TiO_2-001 is not perfectly flat, but is slightly convex, as a lens. From these steps, the facet distribution along this edge was measured as the flat components (red) being (001) and the stepped components (blue) as (101) based on the TEM results. The estimated surface facet fractions are 98% (101) with 2% (001) and 35% (101) with 65% (001) for TiO_2-101 and TiO_2-001, respectively (Table 10). These materials represent an advance over previous comparisons due to the large differences between the surface facets of each material. Impregnation with ammonia metavanadate was completed on these materials with contrasting precursor solution concentration to yield the resulting supported vanadia catalysts.

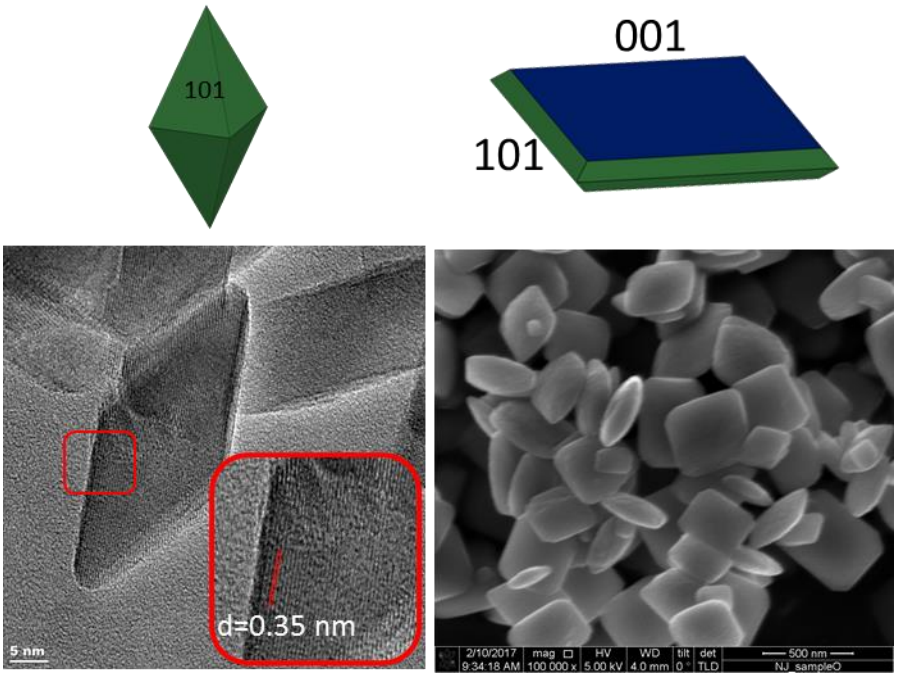

Figure 2.16. TEM micrographs of TiO_2-101 (left) and TiO_2-001 (right) nanoparticles synthesized to exhibit dominant facets.

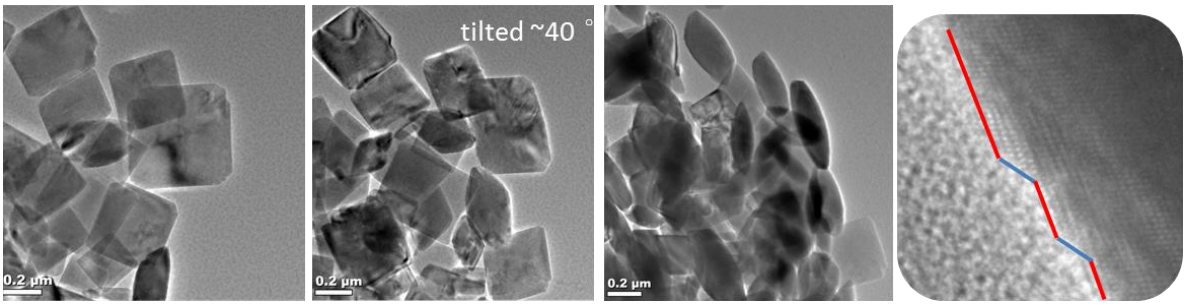

Figure 2.17. TEM micrographs of TiO_2-001 as a function of tilting angle illustrating the stepped nature of the relatively flat edge.

Table 10. Surface properties of synthesized titania nanoparticles.

Catalysts	**Facet (%)**		**Surface Area (m^2/g)**
	(101)	**(001)**	
TiO_2 (101)	**98**	2	42.8
TiO_2 (001)	35	**65**	8.4

Since the two facets had markedly different surface areas, the samples were targeted to match the vanadium density on the surface instead of matching the mass-based loading. For additional comparison, commercial P25 titania (a mixture of anatase and rutile) was also prepared and evaluated. The catalysts, termed xV-yyy where x is the vanadium density in V atoms/nm^2 and y is the support material, were evaluated for weight loading based on masses during impregnation, solid-state NMR, and inductively-coupled plasma. The results depicted in Table 11 show reasonable agreement between the mass, NMR, and ICP-determined loadings, wich some slight over-representation of the NMR signals for the very low loading samples due to their low sensitivity increasing error in spin-counting.

Table 11. Vanadia contents of facet-dominant supported catalysts.

Catalyst V/nm^2	**Wt.%**	**NMR Loading**	**ICP Loading**
1V-P25	1% V_2O_5/TiO_2 (P25)	1.00%	0.83%
2V-P25	2.5% V_2O_5/TiO_2 (P25)	1.92%	1.94%
5.7V-P25	5% V_2O_5/TiO_2 (P25)	2.33%	3.63%
1V-101	0.7% V_2O_5/TiO_2 (101)	0.95%	0.66%
2V-101	1.5% V_2O_5/TiO_2 (101)	1.95%	1.20%
4.7V-101	3% V_2O_5/TiO_2 (101)	1.64%	2.60%
1V-001	0.15% V_2O_5/TiO_2 (001)	0.44%	0.11%
2V-001	0.25% V_2O_5/TiO_2 (001)	0.36%	0.22%
7.9V-001	1% V_2O_5/TiO_2 (001)	1.01%	0.92%

Electron energy loss spectroscopy was used to map the location of vanadia on the various supports. Figure 2.18 illustrates such mapping for 5.7V-P25 and 4.7V-101. As previously described, the signals along the outer edge indicate that vandia is well-dispersed on the catalyst materials. The P25 sample contains additional signal from V that is related to vanadia signal background subtraction. Only the bright spots should be considered for this sample. The 4.7V-101 sample shows a thing trace of vanadium around the outer edge of each particle. The apparent inter-particle intense signals are due to the alignment of vanadia at the edge of multiple particles. Similar mapping for 7.9V-001 was attempted, but due to the thickness of the titania particle, the successful observation of vanadia was not achieved. Since EELS mapping provided only a macroscopic description of the materials, characterization of the vanadia species was conducted using Raman spectroscopy to provide molecular-level insights.

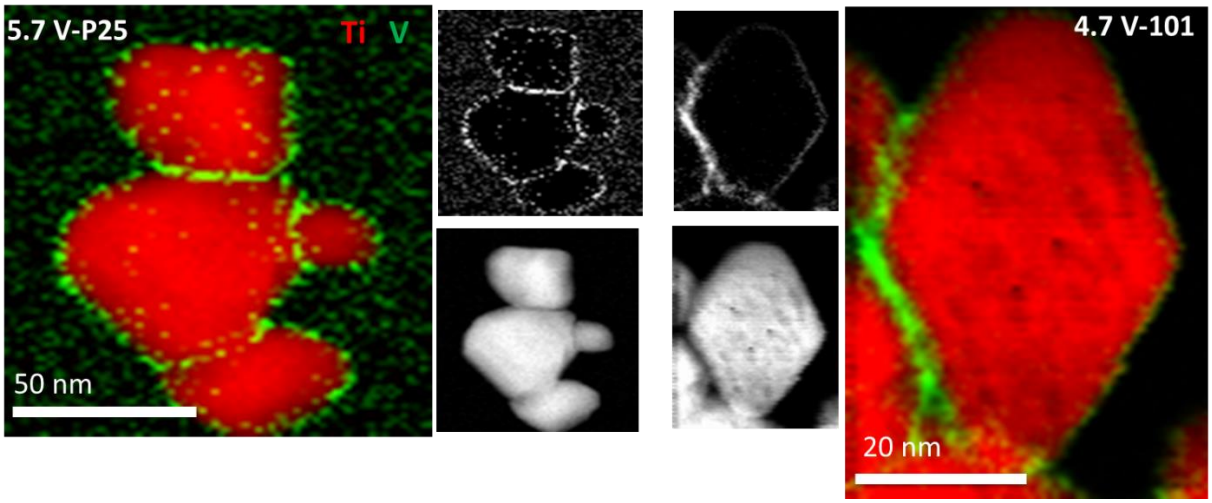

Figure 2.18. EELS mapping of P25 and TiO_2-101-supported vanadia catalysts.

Figure 2.19 displays the Raman spectra for this series of catalysts. In all samples, the anatase overtone band is present at 790 cm^{-1}. With the addition of vanadia, the vanadyl virbration (V=O) becomes apparent at ~1030 cm^{-1}. At the higher loadings, this vanadyl vibration blue shifts due to vibrational coupling and the band at 925 cm^{-1} becomes visible, which is indicative of V-O-Ti bonds. No traces related to V_2O_5 are visible in any of these samples. It should be noted that the bands associated with vandia are difficult to observe in the Raman spectra for TiO_2-001 due to the low abundance of vanadium oxide impregnated onto this sample. This does not appear to be due to fluorescence-induced impurities from urea due to the favorable baseline across the entire spectrum. Overall, the Raman spectra indicate good dispersion and suggested the expected trend of increasing vanadia oligomerization at higher vanadium oxide loadings.

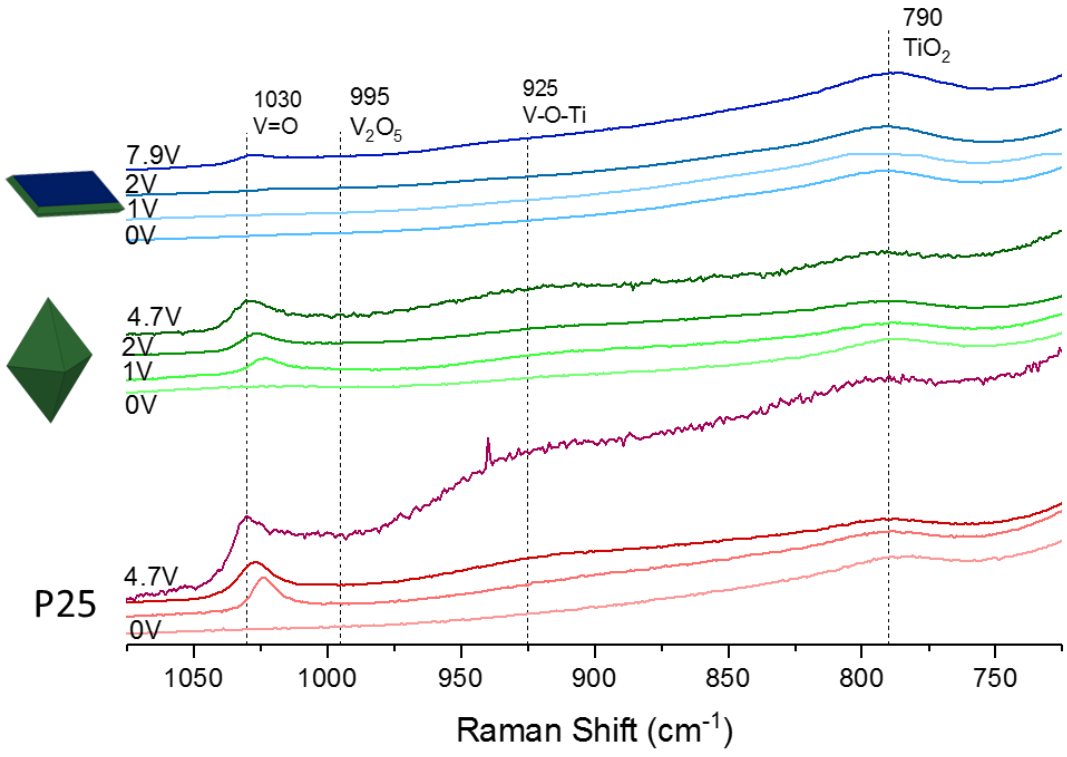

Figure 2.19. Raman spectra of the titnia-supported nanoparticles for facet-dominant samples.

Since ^{51}V MAS NMR has been shown to provide specific molecular structural information, it was employed as a tool to better understand how the structures of the vanadia species differ on each support. The results of these NMR experiments are shown in Figure 2.20 and summarized in Table 12. The P25-supported vanadia catalysts show an evolution of species that is typical of titania. At low coverages, the 1V-P25 catalyst exhibits about 50% of the species as isolated VO_4 units (-515 ppm). The 2V-P25 sample apparently contains as similar distribution of species, but the maximum density of vanadium loaded on this support exhibits extensive oligomerization, forming a species distribution similar to those presented previously.[58, 149] The V-101 materials exhibit a similar distribution and evolution of species to that of the P25-supported materials. The 1V-101 sample contained a majority of species as monomeric vanadia with approximately 10% larger 2D polymers present at -635 ppm. At higher loadings, the quantity of dimeric species at -570 ppm was dramatically increased at the expense of monomers. At 4.7 V/nm^2, the TiO_2-101 sample contains an extensive quantity of dimeric and polymeric species with only 25% of all vanadia remaining as monomers. In contrast to the P25 and TiO_2-101 supports, the TiO_2-001 supported vanadia catalyst exhibits a striking difference in vanadia species distribution. Even from the very low vanadium density, a large quantity of the vanadia are in oligomeric configurations. Only 17% are monomeric in the 1V-001 sample. As the vanadium oxide loading increases, the concentration of oligomeric vanadia also increased where the distribution revealed about 65% as 2D polymeric species. Another striking differences Is the large abundance of square pyramidal-type monomers at -530 ppm on the (001) facetted material. This is consistent with theoretical predictions for the relatively high stability of this species on TiO_2-001.[128-130] Overall, these NMR spectra confirm that at higher vanadia contents,

oligomerization of surface species is present. The P25 and (101)-dominant samples exhibit similar species contributions to each other across the loadings. The (001) samples give rise to an enhanced quantity of oligomeric species, even under very low vanadium densities (1V/nm^2). In most cases, the relative population of dimeric species is maximized at the 2V/nm^2 surface vanadia density.

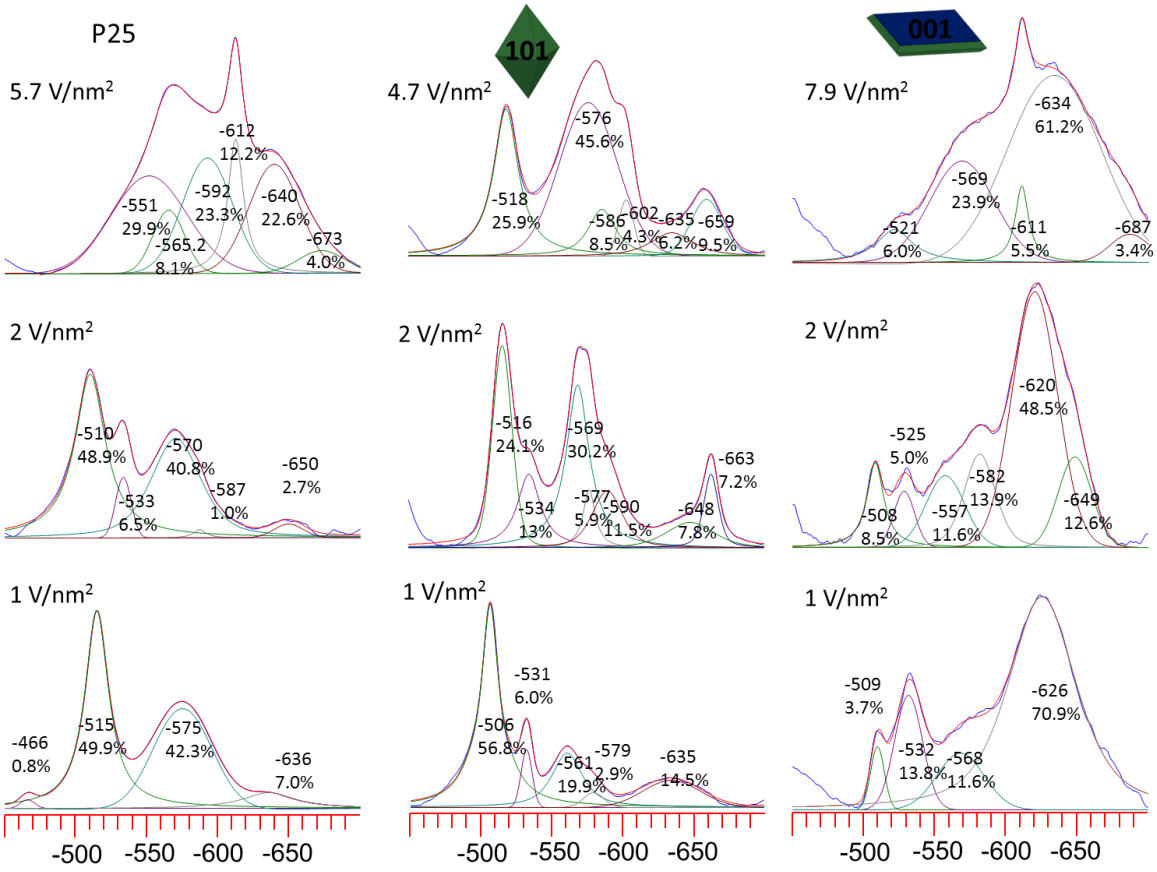

Figure 2.20. ^{51}V MAS NMR spectra of vanadia supported on titnia nanoshapes exhibiting dominant facets.

Table 12. Summarized approximate species contributions to the ^{51}V MAS NMR signals of dominant facet titania nanoparticle-supported catalysts.

	P25		101		001	
1V/nm^2	Monomer:	50.7%	Monomer:	62.8%	Monomer:	17.5%
	Dimer:	42.3%	Dimer:	22.8%	Dimer:	11.6%
	Polymer:	7%	Poly:	14.5%	Poly:	70.9%
	Bulk:	0%	Bulk:	0%	Bulk:	0%
2 V/nm^2	Monomer:	55.4%	Monomer:	37.1%	Monomer:	13.5%
	Dimer:	40.8%	Dimer:	36.1%	Dimer:	11.6%
	Polymer:	2.7%	Poly:	26.5%	Poly:	61-75%
	Bulk:	0%	Bulk:	0%	Bulk:	0%
5-8 V/nm^2	Monomer:	0%	Monomer:	25.9%	Monomer:	6%
	Dimer:	38.1%	Dimer:	45.6%	Dimer:	23.90%
	Polymer:	26.6-49.9%	Poly:	15.7-24.2%	Poly:	64.60%
	Bulk:	12.2%	Bulk:	4.3%	Bulk:	5.5%

To better characterize the differences between these materials. The oxidative dehydrogenation (ODH) of methanol to formaldehyde was used as a probe reaction to gauge the performance of these species. The resulting reactivity data is presented in Figure 2.21. In all cases, conversion was maintained below 10% and selectivity to formaldehyde was greater than 95%. Each support material is presented in a unique color [P25 – red, (101) – orange, and (001) –blue] and each vanadium density uses a different marker shape [1V – circle, 2V – diamond, and maximum V – square]. The results indicate that for the P25-supported material, the maximum activity is achieved at 2V/nm^2, exhibited by a higher catalytic turnover frequency (per V atom) and lower apparent activation barrier (63 kJ/mol). The 1V-P25 and 5.7V-P25 both exhibited

lower activities and higher apparent barriers 99 and 76 kJ/mol, respectively. The trends were similar for the (101) dominant titania facet support. The activity was maximized at 2V/nm^2 and the apparent barrier minimized (54 kJ/mol). In contrast, the 1V-101 material exhibited the lower turn-over frequency, but maintained the highest barrier (96 kJ/mol), consistent with the 1V-P25 catalyst. The 4.7V-101 material exhibited a similar barrier to the analogous P25 sample (78 kJ/mol). The TiO_2-001 support presented the most dramatic trend. The 1V-001 sample was relatively inactive, orders of magnitude lower than that reported for any other material (right vertical axis and blue dashed line). However, the 2V-001 sample was the most active, exhibiting an apparent barrier of 63 kJ/mol. The 7.9V-001 sample also exhibited similar reactivity and barriers to the P25 and TiO_2-101 supports (77 kJ/mol). Across all samples, the 1V/nm2 vanadia catalysts presented the highest apparent activation energy, which was reduced to about 63 kJ/mol at 2V/nm^2. Higher vanadium loadings decreased the turn-over frequency. Such a non-linear variation in ODH reactivity has been previously reported for supported vandaia catalysts and other substrates.[44, 118, 150] The effect was attributed to the relative activity of oligomers over polymeric species and the possible presence of bulk V_2O_5 at higher loadings. This contrasts reports which suggest that monomeric and dimeric species may be most active for methanol ODH.[149] Given the data presented herein, there may be a correlation with the dimeric species present with higher activity, but the relationship is not as clear. In particular, the low activity of the 1V-001 sample is not explained on the basis of vanadia speciation. It should be noted that the nanoparticles exhibited no obvious restructuring after 2 hours of testing in the reactor (Figure 2.22).

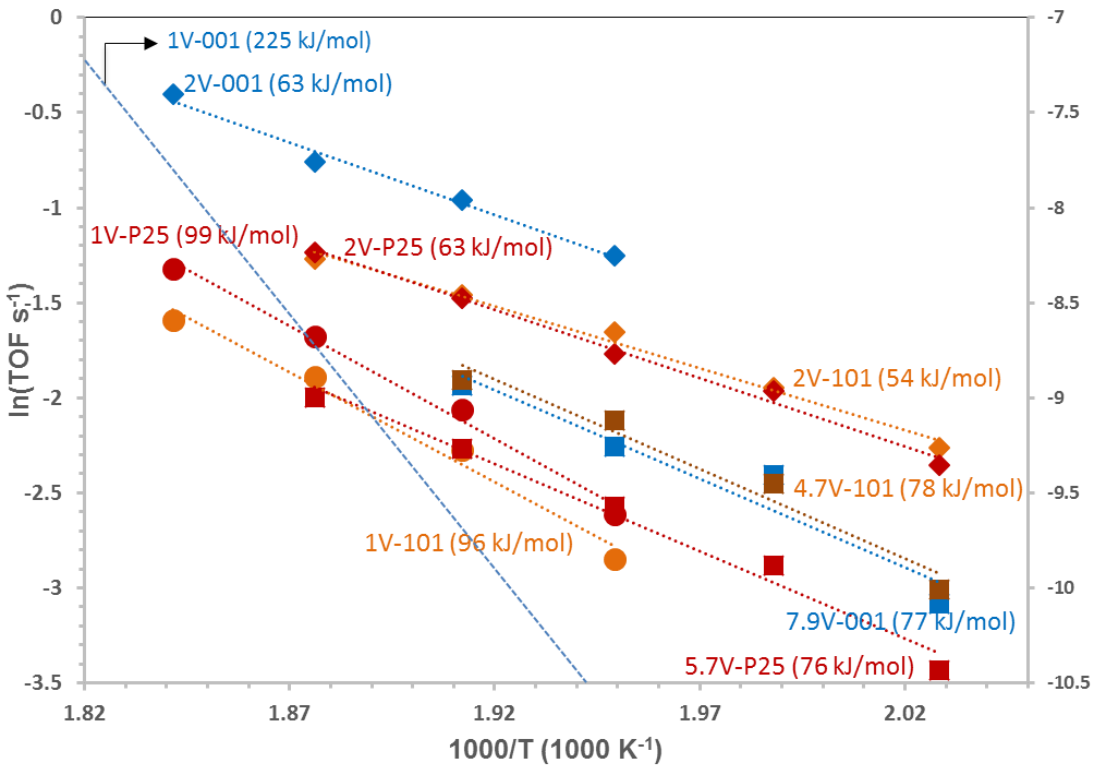

Figure 2.21. Methanol ODH reactivity of facet-dominant supported vanadia catalysts.

In an effort to understand the repeatable low activity of the 1V-001 sample, additional characterization was performed. Though ICP indicated the absence of potassium, the X-ray Photoelectron Spectroscopy (XPS) results identified the clear presence of trace quantities of potassium on the catalyst (Figure 2.23). This potassium is likely residual from the synthesis procedure since the preparation of TiO_2-001 requires the addition of KOH, which may not be effectively removed even after an abundance of washing stages. Such alkali species are well-known to inhibit methanol ODH reactivity.[151-153] Since the K 2p signal was detected in the baseline of the XPS spectra, its abundance could be estimated to be between 0.01 and 0.02%. These conditions would provide enough potassium species to impact reactivity, which is first observed at alkali-vanadium ratios of 0.25. At higher vanadium loadings, the effect of trace quantities of potassium presence is apparently lessened. To evaluate the effect of further

potassium loading, an additional 0.02% of potassium was doped on the 1V-001 sample. The resulting reactivity (Figure 2.24) was consistent with the parent sample, indicating that further potassium addition was not impacting the observed reactivity. The 2V-001 sample experienced moderate reactivity inhibition of ~30% and the 7.9V-001 sample was less affected.

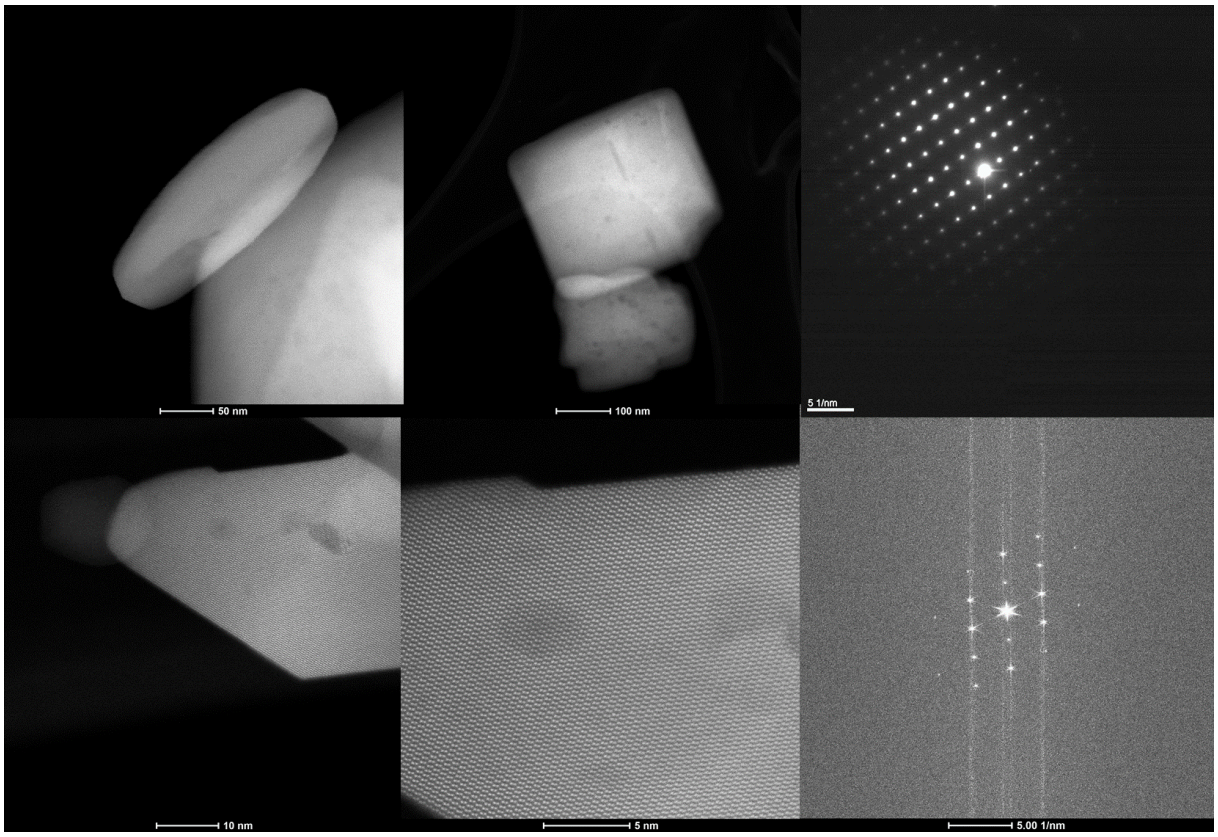

Figure 2.22 STEM images and election diffraction pattern of TiO2-(001) [top] and –(101) [bottom] after methanol ODH reaction for 2 hours.

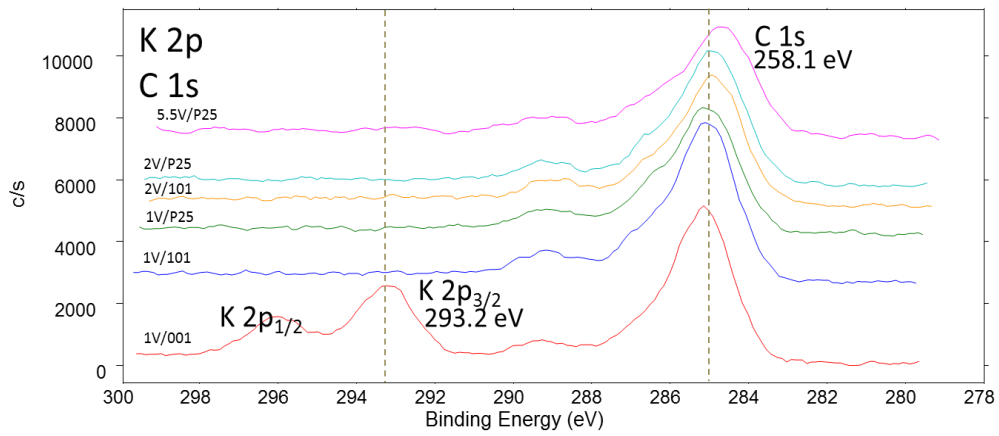

Figure 2.23. XPS results of supported vanadia catalysts indicating the presence of potassium on the (001)-supported vanadium oxide catalyst.

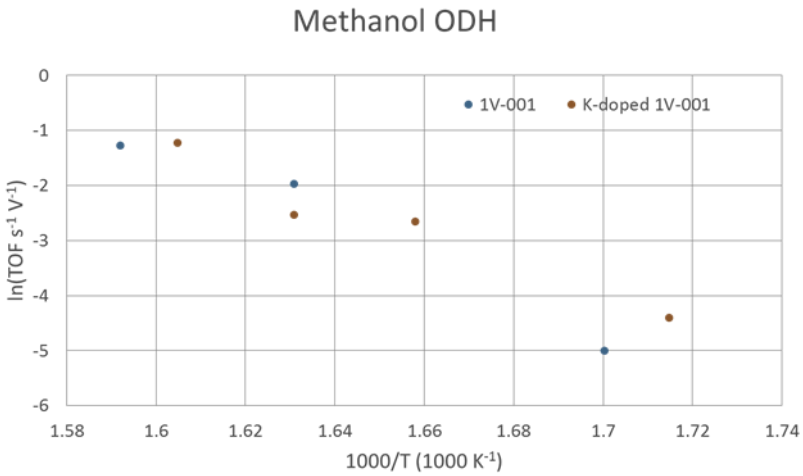

Figure 2.24. Impact of potassium doping on 1V-001.

Given the challenges of decoupling the facet effect and the vanadia structure effect on the reactivity, it is at present difficult to draw definitive conclusions about the properties of the support which alter the chemical reactivity. There appears to be a maximum activity on each sample when 2V/nm^2 were anchored to the support, with TiO_2-001 showing the highest activity

among the three supports compared. This is potentially be due to the high abundance of dimeric vanadia which may exhibit higher intrinsic reactivity than other sites, but this correlation is not well-illustrated. It is, however, clear that agglomeration is favored on (001)-supported samples. This may be due to the preferential deposition of vanadia on TiO_2-001 as previously reported,[145] or perhaps crowding of vanadia occurs on the minority facet of (101) due to the higher surface energy of TiO_2-101. Given the dominating presence of the -530 ppm peak on these TiO_2-001 samples, it seems likely that at least some monomeric vanadia are anchored to the (001) facet or the step sites along the plate-like particle planes. It can also be speculated that residual urea species or potassium atoms leftover on the (001) are directing vanadia to be anchored on the (101) facet. If such a crowing on the minority (101) facet was the dominating explanation for the observed vanadia speciation, it could be approximated that the local vanadia density for 1V-001 was up to $3V/nm^2$ on the (101) facet of 1V-001. A comparison of the species observed for 2V-101 and 4.7V-101 to those on 1V-001 illustrates that such local surface densities on the (101) facet would not generate oligomerization to the extent exhibited on 1V-001. As such, it is hypothesized that the vanadia are anchoring to the (001) facet as well, but may have a preference for the relatively defective step sites which are minimal in quantity. Indeed, it has been shown that the (112) facet can serve as part of a transition between (101) and (001) and it exhibits an even higher surface free energy than (101) (0.44 vs 0.65 eV).[154] This facet was described for titania nanoparticles with curved surfaces, similar to some portions of the long edge of the TiO_2-001 support. As such, these species are tentatively ascribed to vanadia agglomerated along these step sites. Given this property for TiO_2-001 to promote oligomerization, however, it is feasible to assume based on the previous section that V-001 materials would make good catalysts for the SCR reaction. To apply this finding, SCR was conducted on the series of samples and presented

in Figure 2.25. As predicted, the TiO_2-001 supported samples demonstrate higher SCR TOF (per V atom per s) than the other materials. Interestingly, the 2V-001 sample exhibited the highest performance for SCR of NO by NH_3. These observations illustrate how the properties of the exposed facet can be examined and exploited for enhanced operational performance. In this study, it was shown that the (001)-dominant titania nanoshape preferentially anchored vanadia in the form of dimeric and oligomeric surface species for reasons speculated above. As such, the 2-site requirement for the SCR reaction could be satisfied more readily on the (001) catalyst.

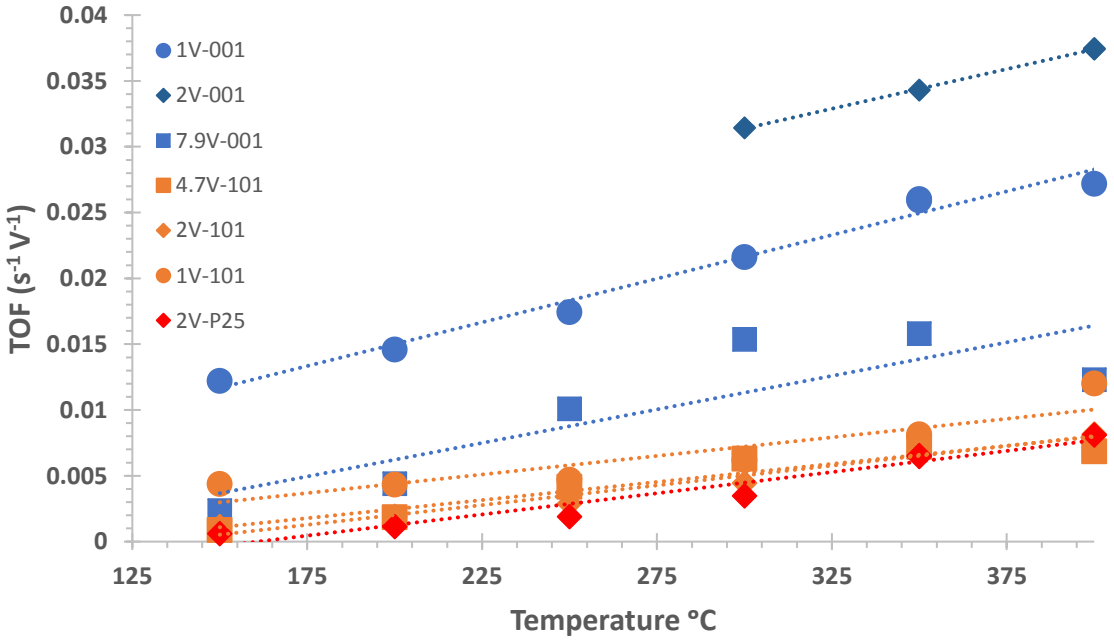

Figure 2.25. SCR activity of dominant facet titania catalysts.

2.4 Structure of Vanadia on bi-layered TiO_2/SiO_2 Supports

Maximizing both the vanadia dispersion and loading the maximum quantity on a surface is a challenging balance for materials such as silica, which exhibits fairly high surface area, but

experiences limitations in the quantity of vandia that can be dispersed. Mesoporous silica has become an attractive option due to the relatively high surface area (>800 m^2/g) and ordered channels with tunable pore sizes. MCM-41 was shown to be highly active and selective with increased amounts of vanadium [155]. The SBA-15 was selected for this study has a typical surface area between 600 and 1200 m^2/g on the hexagonal channels with tunable diameters in the range of 5-30 nm. The large surface area suggests that higher amounts of vanadia that can be dispersed within the mesoporous channels.[156] Thermal and hydrothermal stability is also enhanced by the thicker walls (31-64 Å) of this support, making it a highly suitable support for vanadia catalyst applications. When compared to conventional silica, improved reactivity was observed for the propane ODH reaction.[157] [158] SBA-15 synthesis has also been the specific target of some literature [159-161]. An advantage of SBA is the tunable support size, which can alter surface use efficiency and mass transport limitations, but also makes consistent synthesis more challenging.[162]

Efforts to characterize the structure of these supported vanadia materials have resulted in contrasting observations, which likely originate from small differences in the synthesis conditions and available anchoring sites on the mesoporous silica.[163-164] Structurally, no crystalline V_2O_5 was observed until a loading of 4% vanadia was achieved on SBA-15 (0.81 V/nm^2); [165] however, the structural similarity across loadings has also been noted for vanadia catalysts on SBA up to 3.1 V/nm^2 which comprised of primarily dispersed and some oligomeric vanadia up to this loading, with the ratio depending on the quantity of vanadia present.[158] Raman studies have shown the absence of bulk V_2O_5 up to both 1.45 V/nm^2 and 0.69 V/nm^2.[157, 166]

The desire to improve catalytic performance and take advantage of the high surface area of silica has led to the demonstration of augmenting the support with a layer of a second supporting material (bi-layered catalysts) to improve the catalytic reactivity by 2-3 orders of magnitude.[143, 167-168] Methanol-TPSR was also used as a chemical probe to distinguish the surface acidic (dimethyl ether), redox (formaldehyde), and basic (carbon oxides) sites of the bi-layered catalysts on silica since dissociative chemisorption forms CH_3O.[143] When vanadia was placed on the titania layer, the reaction rate constant was relatively high for all three reactions probed compared to vandia on silica alone. The selectivity with the modified surface layer was largely the same as with only VO_x/SiO_2 except for the case of alumina modification. The main effect across all modifying layers was enhanced activity.[143] The surface structure did not appear to change with the addition of the titania layer, suggesting that differences in activity are not attributed to structural, but chemical changes through a ligand effect.[169 170-171]. It was proposed that the enhanced redox activity is related to the lower electronegativity of the substrate (Si>Al>Ti~Zr), which is inversely related to the electron density at the V-O-S bridge commonly assigned as the active site. Nevertheless, detailed investigations into the structure of these bi-layered supported oxides were conducted to provide a detailed description of the surface.

The anchoring positions of vanadia on layered alumina on silica, for example, were explored and found that the Al-OH hydroxyls were consumed first during V deposition due to the more basic properties of Al-OH relative to Si-OH (Al(III) is less electronegative than Si(IV) and has the higher pH at PZC). [172] This preference in support coordination is believed to be responsible for the redox activity enhancement, Dehydration reactivity (acid sites) was not found to change with the application of vanadia, possibly because the Si-OH-Al proton is the active site for such reactions. A similar study for $V_2O_5/ZrO_2/SiO_2$ demonstrated a preference for vandia

deposition on zirconia and increased methanol oxidation TOF as well. The surface is less basic than pure zirconia and the electron density on the V-O-Zr bridge increases relative to silica due to the lower electronegativity.[173] This study has confirmed that catalyst enhancement is possible with bi-layered supports. Supports with low electronegativity have a lower tendency to withdraw electrons from the V-O-S bond, allowing for better electron exchange with the reactants of oxidation reactions.[174-175]

To take advantage of what has been learned from silica-supported and titania-supported vanadia characterization to help better understand how the reactivity enhancement occurs, the $V_2O_5/TiO_2/SiO_2$ class of materials was selected as the system of choice to elucidate the structure of vanadia on the surface. It was shown before with Raman, UV-vis DIR DRS, XANES, and XPS that, similar to the silica-supported materials, vanadia was predominantly isolated VO4 units under dry conditions and apparently polymerized upon hydration.[176] In this case, the vanadium preferentially binds to the titanium over the silica, but not exclusively as the ratio of $O=V(O\text{-}Si/Ti)_3$ varies with vanadia and titania loading as suggested by TPR and other investigation [164, 177]. This is supported by the higher surface free-energy observed for exposed TiO_2 sites relative to SiO_2 [178]. The ligand ratio greatly impacts the chemical properties of the VO_4. As previously described, the TOF for methanol oxidation is much higher with the bilayer support relative to silica alone, but the reducibility is still lower than that for titania support, so silica still influences the catalytic properties. The synergy between the high surface area of mesoporous silica and a titania overlayer was demonstrate by Herrera who highlighted enhanced vanadia dispersion on the bilayer due to the relative inactivity of silica towards vanadia deposition.[179] Titania was added to achieve ~1.33 TiO_2/nm^2 (~10 wt% on MCM-41 with SA = 689 m^2/g).[180] When vanadia was included, only isolated VO_4 sites are present up to monolayer

coverage (~12% or 2.6V/nm^2) with terminal titanol sites observed. Vanadia was shown to preferentially interact with Ti on surface due to the more basic character relative to Si, evidenced by Raman bands corresponding to V-O-Ti bonds. Methanol oxidation increased by an order of magnitude when a layered support included on silica. Both polymeric and isolated vanadia sites were speculated.[181]

On silica, about 4 Ti/nm^2 equates to monolayer coverage and 2.6 V/nm^2 does as well.[61, 66] The results suggest that the surface structure of the titanium layered onto silica may be similar to crystalline anatase, but depends strongly on the environmental conditions.[66] At 1% loading on dehydrated silica, isolated TiO_4 units are observed. Polymerized, one-dimensional TiO_5 species observed at 5% loading. When monolayer coverage is approached, two-dimensional polymerized Ti is the dominant species. XANES demonstrated an increase in coordination upon hydration. Two types of TiO_2/SBA-15 supports differing in their microporosity were tested for crystal structure of the titanium. Crystallization in the highly microporous sample began at 150°C, while the other did not see significant crystallization until 350°C, suggesting that nanocrystalline titania in the micropores initiates nucleation to form the anatase phase observed. As a result, vanadia is anticipated to adsorb to the microporous structure selectively to interact with titania.[182] This was later confirmed by Raman spectroscopy.[183]

NMR has also been employed to provide a detailed view of the surface of SBA-15-supported vanadia. The results indicate the dominance of isolated tetrahedral V^{5+} with the potential presence of minimally polymerized sites. A weak signal appeared for the dehydrated 4.5% sample, suggesting a more highly coordinated phase more commonly seen in hydrated samples.[157, 184] Isolated V^{5+} species are proposed to be of the $O=V(-O-S)_3$ configuration as

previously reported and after hydration, take on an octahedral morphology and coordinate with two water molecules.[155] While no direct studies using NMR were noted for vanadium on bi-layered titania and SBA-15, useful information can be extracted from previous studies with bi-layer supports of other silicas. Early reports of titania supports demonstrated bulk-like vanadia environments, but limited sample information is presented to accompany the claim.[185] However, a well-documented vapor deposition procedure demonstrated varying surface morphologies based on the loading and dispersion of the vanadia.[186] Other reports of mixed oxide supports with silica have suggested more similarities to the other metal component than with a pure silica support.[187] ^{51}V NMR for $V_2O_5/ZrO_2/SiO_2$ catalyst also demonstrated isolated tetrahedral morphology of the vanadia.[188]

To confirm enhanced dispersion with bi-layered supports, ^{51}V NMR was used to probe V_2O_5/TiO_2/MCM-41, another mesoporous silica-based bi-layered catalyst. In this work, the spectra of bulk V_2O_5 were compared to that of V_2O_5/MCM-41 and V_2O_5/TiO_2/MCM-41.[189] The results showed that loading vandia directly on the mesoporous silica generated bulk-like V_2O_5 due to poor interactions with the support during synthesis. When titania was applied, however, the dispersion was greatly enhanced. Dehydrated vanadia on titania on silica produced two peaks at -280 and -460 ppm.[190] Lapina reports deconvolution of the spectra and confirmed the presence of tetrahedral and octahedral sites for hydrated and dehydrated sites. However, there were concerns of poor TiO_2 dispersion resulting from the synthesis technique (incipient wetness). Another NMR study reported only a small peak for vanadium coordinated to O-Ti, suggesting poor Ti coverage.[191] A broad spectrum of three peaks was present which represent tetrahedral (-515 ppm), octahedral (-320 ppm), and a peak in between at lower intensity for five-coordinated species which may be bonded to titania (-420 ppm).

Such detailed insight is of great interest for these systems to better describe how the vanadia sites evolve with catalyst formulation to better understand their reactivity. The ^{51}V MAS NMR data for a series of V_2O_5/x% TiO_2/SBA-15 is presented in Figure 2.26. The results for vanadia directly loaded onto SBA-15 reveal two features; one at -590 and one at -688 ppm. The previously presented results on the dry silica catalyst suggest that the -688 ppm peak corresponds to isolated VO_4 units on the silica surface and may potentially also represent dimers or cyclic trimer species. The smaller peak at -590 ppm may be related to vanadia accumulation in the micropores, evidenced by its relatively narrow linewidth suggesting a more uniform structure.[182] With the progressive addition of titania to the SBA-15 support, the line at -688 ppm is shown to gradually migrate downfield to -678 ppm and broaden. This may be a consequence of V-O-Si linkages exchanging for V-O-Ti linkages at the interface modulating the chemical shift and decreasing the homogeneity of sites. However, due to the amorphous surface structure of mesoporous silica, the same limitations in speciation identification with ^{51}V NMR are apparently present for bi-layered systems where silica is first supporting layer as they were with silica-supported vandaia. At the maximum titania loading, 13%, the monolayer of vanadia on SBA-15 (4%) was exceeded to probe if the titania enabled a higher capacity for vandia as the bulk oxide does. The NMR spectrum revealed the presence of a sharp peak at -613 ppm, indicating that bulk V_2O_5 had formed at this higher vandaia coverage.

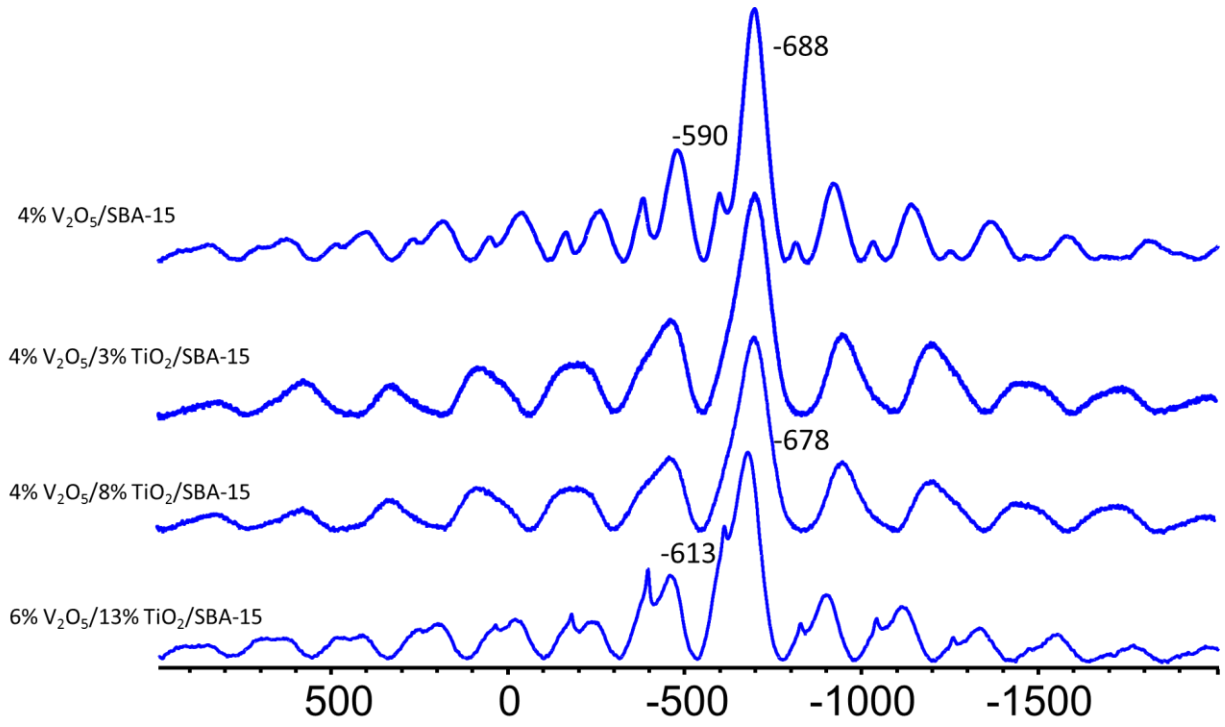

Figure 2.26. ^{51}V MAS NMR of V_2O_5/x% TiO_2/SBA-15 catalysts.

In summary, bi-layered supports offer an attractive option to tune the reactive of vanadia-based catalysts by depositing another metal oxide on the high surface area of silica. Characterization by ^{51}V MAS NMR to provide specific information regarding the speciation of vanadia on the surface suffers from the same limitations as the pure silica support even when the second oxide layer is present; however, a gradual shift in the main resonance feature and its broadening may indicate V-O-Ti linkages are forming at higher titania surface densities in place of some of the V-O-Si support bonds (noting that titania-supported resonances typically appear downfield of those from silica-supported vanadia).

CHAPTER THREE: STRUCTURE OF WATER-PERTURBED VANADIUM OXIDE CATALYSTS

Water is a common constituent to many chemical systems and has been noted to have an effect on the structures of catalytic materials such as vanadium oxide. At high-temperature reaction conditions, the surface is described as retaining a dry state due to the limited interaction of water with the catalyst material; however, during low-temperature applications or extended operational times, water may well induce structural changes to the catalyst. In this chapter, the effects of water on the active sites of vanadia catalysts will be explored, highlighting the importance of ensuring spectroscopic measurements under relevant conditions due to the vast changes that present themselves.

3.1 Water-Mediated Structural Transformation of Silica-Supported V_2O_5 Catalysts

Based on Nicholas R. Jaegers, Chuan Wan, Mary Y. Hu, Monica Vasiliu, David A. Dixon, Eric Walter, Israel E. Wachs, Yong Wang, and Jian Zhi Hu; "Investigation of Silica-Supported Vanadium Oxide Catalysts by High-Field ^{51}V Magic-Angle Spinning NMR" *The Journal of Physical Chemistry C* 2017 121 (11), 6246-6254 DOI: 10.1021/acs.jpcc.7b01658

Prior investigations of the molecular structure of supported vanadium oxide catalysts noted significant structural changes between a dehydrated sample and one that was exposed to ambient conditions. This was demonstrated conclusively by *in situ* Raman spectroscopy of vanadium oxide supported on titania and alumina[192] as well as X-ray Absorption Near Edge Spectroscopy (XANES) and another Raman study ascribed the change to V_2O_5-like structures under hydrated conditions.[61, 193] Multiwavelength Raman has even successfully identified a

second monomeric surface VO_x species on silica at submonolayer coverages that was ascribed to a partially hydroxylated vanadium oxide center.[194] One hypothesis suggested that the changes arise from water coordination which generated a five-coordinated tetrahedral structure.[72] Another relates the system to a phase diagram which demonstrates that the nature of surface vanadium oxide under hydrated conditions depends on the pH of the solution and concentration of vanadium oxide, and that those structures in solution are expected on the oxide surface.[195] With this, increasing vanadia content would cause the pH of the wet surface to decrease, facilitating oligomerization through decavanadate clusters until bulk-like vanadium oxide is formed. The presence of these decavanadate structures have been previously proposed based on Raman spectroscopy.[196] Support bridge bond hydrolysis has been proposed in the presence of sufficient ambient moisture, which may hydrolyze the bridging V-O-Si bonds giving rise to polymeric vanadium oxide species through an olation process, where V-OH-V bridges form and oligomerize until $V_2O_5*(H_2O)_n$ gels form.[61] Further Raman analysis demonstrated the partial reversibility of this hydration process and has asserted that this can occur without large amounts of water.[197] To help elucidate the specific molecular structures of such hydrated samples, high-field NMR measurements were conducted on 3% and 8% V_2O_5/SiO_2. The results of these measurements are presented in contrast to the dehydrated counterparts in Figure 3.1.

Both dehydrated, silica-supported materials exhibit a single broad feature at -675 ppm that may be ascribed to monomeric, dimeric, or cyclic trimeric vanadia structures. In contrast, the low- and high-loading hydrated state samples each split into two resonances, which exhibited major peak at -566 ppm, an upfield shoulder at ca. -610 ppm, and a similar spinning sideband pattern (*). The small peak at -610 ppm is well matched with the signals from bulk V_2O_5, so this signal is likely associated with crystalline V_2O_5 nanoparticles from hydration-induced

agglomeration of the surface vanadium oxide species. Relatively little difference is observed between the two samples in the hydrated state. ^{1}H NMR spectra can be found in the supporting information and demonstrates a broad peak associated with water under ambient conditions, confirming the contrast between the two hydration states.

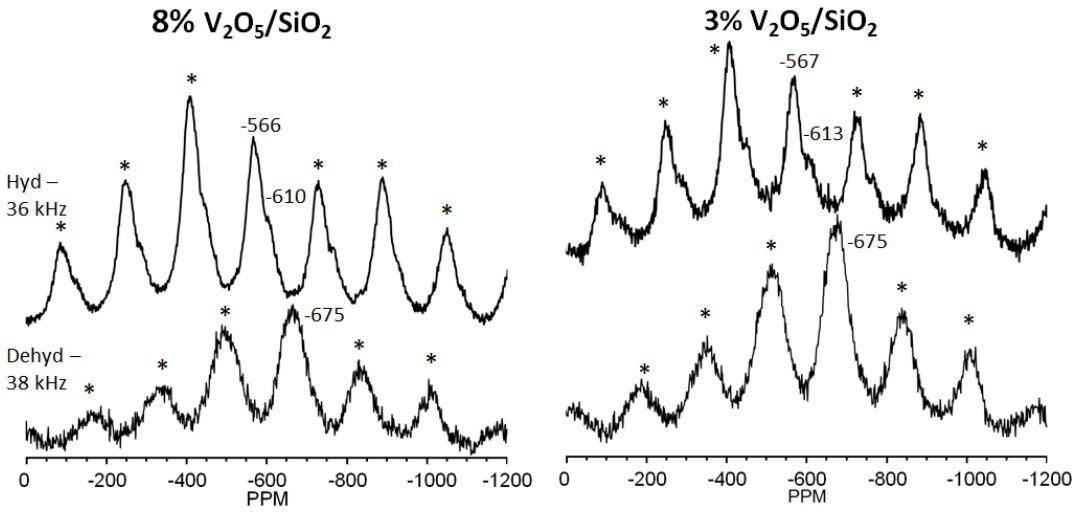

Figure 3.1. Solid-state ^{51}V MAS NMR of supported 8% and 3% VO_x/SiO_2 under hydrated (36 kHz) and dehydrated (38 kHz) conditions.

The fractional comparison of all detected vanadium species for each sample are given in Table 13. These hydrated vanadium oxide catalysts consistently provide more than 84% as the -567 ppm species with the balance identified as the -610 ppm species. To aid in the interpretation of such peaks, models similar to the dehydrated models in 2.1 Silica-supported V2O5 were adapted from those employed in titania-supported materials deviated substantially from the observed chemical shifts (Table 14). Water-coordination to these model surfaces can modulate the calculated shielding by 20 ppm, but the results remain inconsistent. As such, utilizing vicinal silanols as the anchoring sites for hydrated vanadium species is likewise inappropriate.

Table 13. Integrated peak fractions for each modeled species of the ^{51}V NMR spectra

Sample	**-566**	**-610**	**-675**
Hydrated 3%	0.842	0.158	-
Hydrated 8%	0.876	0.124	-

Table 14. DFT-optimized structures of hydrated vicinal silica models.

Cluster V Si O H 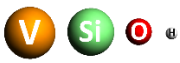	**Cluster Formula**	**BLYP-D Hydrated**	**BLYP/ ZORA Hydrated**
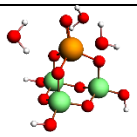	$OVO_3(SiO(OH))_3$	-408	-401
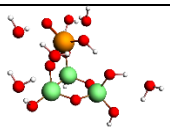	$OVO_2(Si_3O_3(OH)_3)OH$	-493	-500
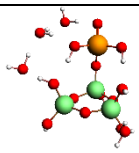	$OV(OH)_2O(Si_3O_3(OH)_5)$	-534	-541
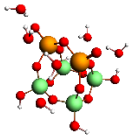	$V_2O_7(SiO(OH))_4$	-570	-593, -558
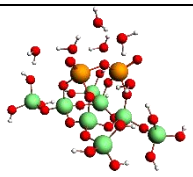	$V_2O_7(SiO((OSi(OH_3))_4$	-569	-576
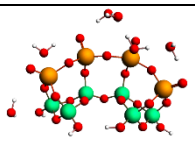	$V_4O_{13}O(SiO_3(SiOH)_2)_2$	-584	-572, -626, -643, -567
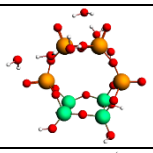	$V_4O_{12}(SiO(OH))_4$	-579	-583, -602, -601, -600
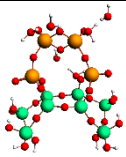	$V_4O_{12}(SiO((OSiOH)_3))_4$	-591	-627, -589, -598, -620

Water was also added to those dehydrated models which exhibited good agreement with the experimental observations. In these, two water molecules were added to the system and coordinated with the VO_4 unit (quantified in Table 15 and depicted in Figure 3.2). This addition resulted in a downfield shift of the monomer by about 7 ppm with both theoretical approaches. Chemical shift values centered on -671 ppm were calculated for the dehydrated dimer, but when hydrated, two vanadium atoms in the dimer exhibit a difference of about 20 ppm from each other (centered at -621 for BLYP-D and -626 ppm for the BLYP/ZORA). In the linear trimer model, the central vanadium atom exhibited a chemical shift deshielded by nearly 100 ppm (BLYP-D) or 80 ppm (BLYP/ZORA) relative to the outer two vanadium atoms. Hydration changed the predicted chemical shifts to -572 and -653 ppm (BLYP-D) and to -579 and -658 ppm (BLYP/ZORA). The cyclic trimer model exhibited a modest change in chemical shift with hydration. Generally, the chemical shifts predicted in the presence of water are deshielded relative to their dry components. Apart from the hydrated dimer structure at -620 ppm, further addition of water did not permit the shifts near the observed -610 ppm peak. When six water molecules were added to the dimer instead of four, the chemical shift decreased to -630 ppm.

Table 15. Calculated ^{51}V NMR chemical shifts of vanadium clusters relative to $VOCl_3$

Cluster	**Number of H_2O**	**BLYP-D**	**BLYP-D Hydrated**	**BLYP/ ZORA**	**BLYP/ZORA Hydrated**
Monomer	2	-676	-669	-680	-673
Dimer	4	-670 -672	-631 -611	-675 -678	-635 -617
Linear Trimer	4	-515 -614 -619	-572 -656 -649	-537 -632 -636	-579 -661 -654
Cyclic Trimer	2	-661 -661 -706	-663 -682 -687	-661 -679 -703	-658 -675 -680

Vanadium atoms are ordered to match dry with hydrated.

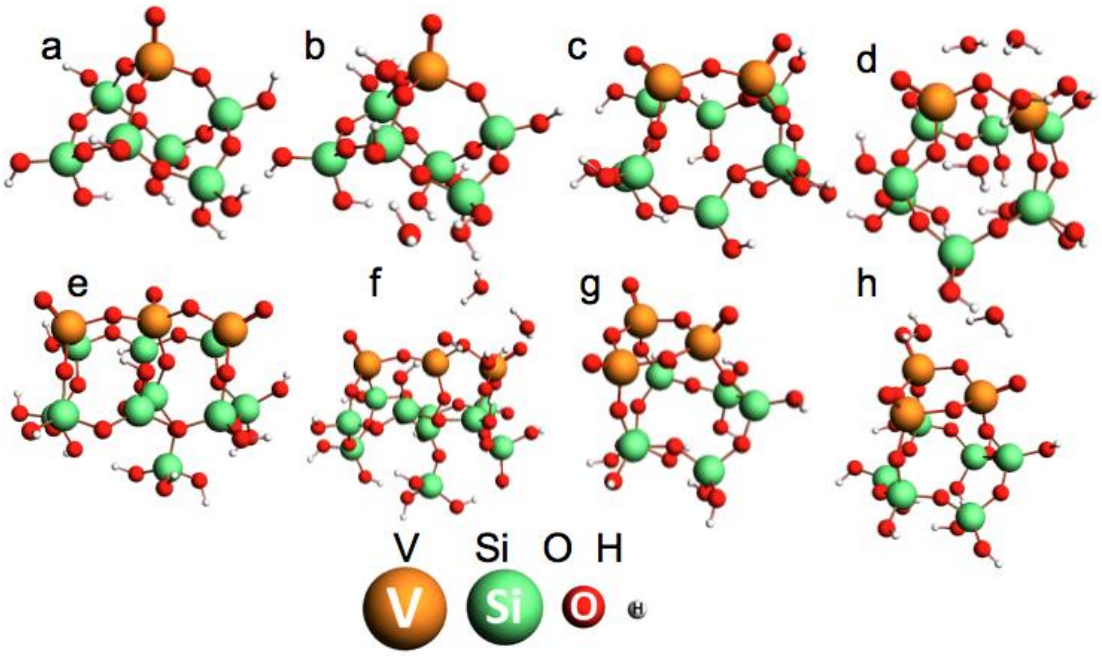

Figure 3.2. Optimized DFT structures of V_2O_5/SiO_2 where a is the monomer, b is a di-hydrated monomer, c is a dimer, d is a tetra-hydrated dimer, e is a linear trimer, f is a tetra-hydrated linear trimer, g is a cyclic trimer, and h is a di-hydrated cyclic trimer.

Models were also generated to gauge the effect of the V-O-Support bridge hydrolysis to test the hypothesis of a hydrolysis mechanism leading to the formation of vanadia gels. A hydrolyzed $VO_2(H_2O)_4^+$ cluster well agrees with the primary feature in the hydrated samples (-575 ppm, BLYP/ZORA). As such, hydrolyzed structures are promising initiation points for the evaluation of hydrated molecular structures on silica. A series of hydrolyzed monomer and dimer clusters was investigated which analyzed the progressive hydrolysis of support bridges and formation of V-O-V bonds. The most relevant results are presented in Table 16 and additional configurations are located in Appendix C: Additional Supporting Data. A visual representation of these structures is available in Figure 3.3. The listed calculated chemical shifts for hydrolysis steps proposed by Gao[61] and Xie[197] generally result in deshielded nuclear resonances relative to

dehydrated, anchored structures. The di-grafted monomer structure with triple water coordination (Figure 3.3b) and di-grafted dimer (Figure 3.3j) (which has two bridge bonds hydrolyzed) both show chemical shifts at the BLYP-D and BLYP/ZORA levels near the -566 ppm experimental value. Additionally, the dry di-grafted monomer (Figure 3.3a) and the structure with four waters (Figure 3.3c) are predicted to have chemical shifts from about -620 to about -630 ppm, similar to the chemical shift calculated for bulk vanadium oxide, the experimental V_2O_5 reference, and the experimental chemical shift observed in the hydrated spectra. Fully-hydrolyzed isolated clusters (Figure 3.3e-i) resulted in chemical shifts near -500 ppm to -520 ppm, as did the V-$(OH)_2$-V cluster (Figure 3.3l-m). Structures with molecular water bridging between a monomer and dimer also were predicted for various separation distances between the two vanadium species. The results (Appendix C: Additional Supporting Data) indicate deshielding relative to isolated monomer structures (-590 ppm), but do not correspond to the observed -566 ppm. The remaining cluster models demonstrate chemical shifts between -460 and -560 ppm.

Table 16. Calculated ^{51}V NMR chemical shifts for hydrated cluster models of altered surface morphologies due to the hydrolysis of anchoring sites

Cluster	**Number H2O**	**BLYP-D dry**	**BLYP-D Hydrated**	**BLYP/ZORA dry**	**BLYP/ZORA Hydrated**
Di-grafted monomer	4	-625	$3H_2O$: -574 $4H_2O$: -619	-631	$3H_2O$: -579 $4H_2O$: -625
Mono-grafted monomer	8	-603	-510	-610	-516
Non-grafted monomer	4	-492	-525	-499	-532
Non-grafted dimer	2	-533 -550	-550 -601	-541 -557	-594 -606
Di-grafted dimer	2	-560 -566	-584 -589	-567 -572	-591 -594
V-$(OH)_2$-V bridge di-grafted	4	-463 -508	-488 -507	-469 -514	-516 -498

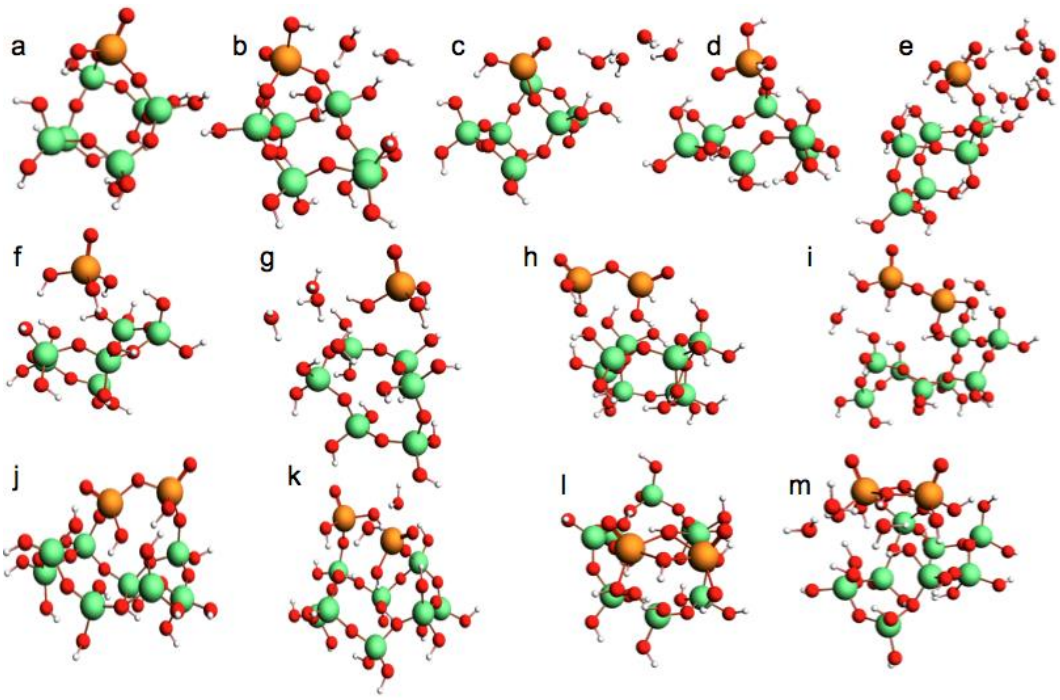

Figure 3.3. Optimized Geometries from Table 16. Calculated ^{51}V NMR chemical shifts for hydrated cluster models of altered surface morphologies due to the hydrolysis of anchoring sites. Where a is a di-grafted monomer, b is a tri-hydrated di-grafted monomer, c is a tetra-hydrated di-grafted monomer, d is a mono-grafted monomer, e is a hydrated mono-grafted monomer, f is a non-grafted monomer, g is a hydrated non-grafted monomer, h is a non-grafted dimer, i is a hydrated non-grafted dimer, j is a di-grafted dimer, k is a hydrated di-grafted dimer, l is a V-$(OH)_2$-V bridge di-grafted dimer, and m is a hydrated V-$(OH)_2$-V bridge di-grafted dimer

The results of the solid state ^{51}V MAS NMR spectra clearly show a change in the chemical environment for the vanadium nuclei for the supported V_2O_5/SiO_2 catalysts depending on the presence or absence of water. With hydration, a major peak at -567 ppm and a shoulder at -613\0 are detected. The NMR spectra clearly confirm the presence of a side peak in the hydrated sample similar to reports by Schimmoeller *et al.*[72] No significant changes were noted between the NMR spectra of the 3% and 8% samples, suggesting that the structures of these two catalysts are similar given the difference in surface densities. Assignments of the two observed peaks for the hydrated phase structure are less straightforward than their dehydrated counterparts, as expected from conflicting literature reports. The proposed hydrolysis of the V-O-support bonds

leads to the observed species present in the hydrated NMR spectra. Structural models with a varying number of linkages were employed to gauge the stability of the various hydrolyzed structures. Tielens *et al*. found that under ambient hydration conditions, the mono-grafted species is the most stable up to 220 K and di-grafted is the most stable species from 220-550 K. These thermodynamic calculations support the preference for a di-grafted over mono-grafted in our system (at about 300 K). The results of this study do indeed suggest the possibility of di-grafted species being present with water coordination resonating at -567 ppm. The hydrated dimer species with two bridge bonds (di-grafted dimer) also has a calculated chemical shift at -586 ppm (BLYP-D) and -592 ppm (BLYP/ZORA), which is somewhat similar to the observed value of -566 ppm. The hydrated non-grafted dimer may also be present. Given the difference between the calculated and observed model compound chemical shifts, the hydrated dimer species with two bridge bonds cannot be eliminated as a possibly observed species. The small -610 ppm peak observed in these hydrated spectra is evidence of a bulk V_2O_5 component being present as crystalline nanoparticles stemming from prolonged exposure of the samples to ambient conditions. The lack of this minor -610 ppm feature in the dehydrated catalysts indicates that the small V_2O_5 nanoparticles have likely dispersed upon the SiO_2 support during the dehydration-evacuation step.

The potential presence of hydrated decavanadate clusters and vanadia gels are also considered. Literature reports of the chemical shift for decavanadate have indicated that a minor peak at -426 ppm and foremost peaks at -512 and -531 ppm should be present for a di-protonated decavanadate structure.[198] Consulting the pH phase diagram proposed by Baes,[195] this should be the form present on the silica support whose isoelectric point is typically recorded to be between 2 and 3 on the pH scale. Model structure calculations for $[V_{10}O_{26}(OH)_2]^{4-}$, $[V_{10}O_{27}(OH)]^{5-}$, and

$[V_{10}O_{28}]^{6-}$ (Figure 3.4 and Vanadia gels are not easily generalized. There are at least two distinct vanadia gel compounds that have been identified on the basis of the degree of hydration.[199-200] A second complication is the uncertainty surrounding layering of the crystal structure. Two competing hypothesis suggest that either water is inserted between the layers of the bulk V_2O_5 or that there are two vanadium oxide layers with terminal oxygen atoms facing a water layer on either side of the bilayer.[201] Furthermore, reports concerning the ^{51}V chemical shift of these vanadia gel materials have varied greatly. Nabavi *et al*. initially reported a resonance at -276 ppm,[202] and later reported the static spectrum at -340 ppm.[203] MAS resolved this material to broad isotropic shift resonating at -559 ppm.[204] Three more recent studies have found four peaks in the vanadia gel samples that resonate near -572, -593, -622, and -663 ppm.[205-207] Though the chemical shifts of these four peaks are near the peaks in the hydrated V_2O_5/SiO_2 spectra, only two of these features match what is observed: -572 ppm is near the observed -566 ppm peak and -622 ppm is reasonably close to the observed -610 ppm peak. The other two features detected in vanadia gel (-593 and -663 ppm) were not observed in the hydrated V_2O_5/SiO_2 spectra. The lack of continuity between vanadia gel spectra and those collected for the hydrated V_2O_5/SiO_2 suggests that the structure is likely to be isolated, di-grafted or di-grafted dimer vanadia species. This would also explain the increase in anisotropy relative to the isolated VO_4 unit observed in the dehydrated sample. The peak at -610 ppm likely correlates strongly with the bulk V_2O_5-like structures, which become dispersed again upon dehydration.

Table 17) show a similar peak distribution across protonation levels to the reported spectra, but with a horizontal shift. None of these peaks are observed in the hydrated ^{51}V NMR spectra, however, indicating that decavanadate is not present.

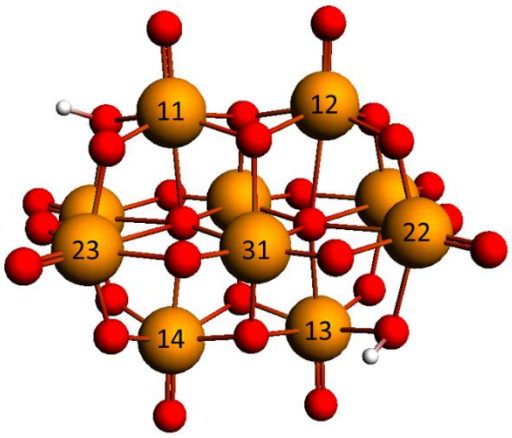

Figure 3.4. Optimized geometry of di-protonated decavanadate structure with vanadium reference numbers. COSMO was used for hydration with a radius of 1.9 Å and dielectric of 78.39.

Vanadia gels are not easily generalized. There are at least two distinct vanadia gel compounds that have been identified on the basis of the degree of hydration.[199-200] A second complication is the uncertainty surrounding layering of the crystal structure. Two competing hypothesis suggest that either water is inserted between the layers of the bulk V_2O_5 or that there are two vanadium oxide layers with terminal oxygen atoms facing a water layer on either side of the bilayer.[201] Furthermore, reports concerning the ^{51}V chemical shift of these vanadia gel materials have varied greatly. Nabavi *et al*. initially reported a resonance at -276 ppm,[202] and later reported the static spectrum at -340 ppm.[203] MAS resolved this material to broad isotropic shift resonating at -559 ppm.[204] Three more recent studies have found four peaks in the vanadia gel samples that resonate near -572, -593, -622, and -663 ppm.[205-207] Though the chemical shifts of these four peaks are near the peaks in the hydrated V_2O_5/SiO_2 spectra, only two of these features match what is observed: -572 ppm is near the observed -566 ppm peak and -622 ppm is reasonably close to the observed -610 ppm peak. The other two features detected in vanadia gel (-593 and -663 ppm) were not observed in the hydrated V_2O_5/SiO_2 spectra. The lack of

continuity between vanadia gel spectra and those collected for the hydrated V_2O_5/SiO_2 suggests that the structure is likely to be isolated, di-grafted or di-grafted dimer vanadia species. This would also explain the increase in anisotropy relative to the isolated VO_4 unit observed in the dehydrated sample. The peak at -610 ppm likely correlates strongly with the bulk V_2O_5-like structures, which become dispersed again upon dehydration.

Table 17. Calculated ^{51}V chemical shift values of decavanadate at different levels of protonation (P), resulting in different charges (-4, -5, -6), and using COSMO for solvation effects (w). ZORA results are found in the brackets [ZORA]

Protons – charge - water	V(11)	V(12)	V(13)	V(14)	V(21)	V(22)	V(23)	V(24)	V(31)	V(32)
0P -6	-410 [-421]	-419 [-430]	-411 [-427]	-416 [-422]	-384 [-396]	-383 [-394]	-384 [-395]	-382 [-396]	-282 [-290]	-278 [-294]
1P -5	-412 [-422]	-465 [-475]	-461 [-441]	-431 [-471]	-412 [-393]	-388 [-425]	-381 [-400]	-413 [-424]	309 [-316]	-303 [321]
2P -4	-470 [-479]	-478 [-487]	-484 [-485]	-477 [-492]	-432 [-437]	-436 [-452]	-426 [-448]	-440 [-443]	-303 [-329]	-318 [-315]
0P -6 w	-473	-468	-474	-468	-443	-447	-443	-446	-342	-342
1P -5 w	-467	-497	-495	-474	-461	-440	-442	-462	-353	-344
2P -4 w	-497	-497	-504	-498	-465	-470	-460	-468	-339	-346

3.2 Hydrated Titania-Supported V_2O_5 Catalysts

The effect of moisture exposure of the catalyst is also of interest in light of the dramatic structural changes that occur to vanadium under these environments.[121, 208-209] Further, such

conditions have recently been shown to be relevant for the photocatalytic oxidation of methanol since at low temperatures, moisture can remain at the surface and impact the structure of vanadia.[210] These changes were probed with ^{51}V MAS NMR of the silica-supported vanadia catalysts in the preceding section, but a change in speciation is expected for tiania-supported catalysts as well.

Titania-supported samples exposed to an ambient environment were probed by ^{51}V MAS NMR and are presented in Figure 3.5. In a striking change over the dehydrated spectrum (Figure 2.9), the 5% V_2O_5/TiO_2 catalyst's distribution narrowed to only two distinct spectral features. The majority signal, -614 ppm, exhibits a strong sideband pattern and is ascribed to bulk V_2O_5 particles, which form surface formate species in the photocatalytic oxidation of methanol. The minority signal at -628 ppm, consisting of just 19% of the total signal, is narrow and produces no obvious sideband pattern, indicative of a relatively mobile phase, potentially forming a solution-like layer of dissolved vanadia. This 5% V_2O_5/TiO_2 catalyst clearly demonstrates a dramatic modulation of surface species when hydrated.

The 1% V_2O_5/TiO_2 sample under a hydrated environment no longer contains the signal ascribed in the dehydrated spectra to tetrahedral monomers with a protonated oxygen bridge (-480 ppm). A small shift and reduction in quantity of tetrahedral monomers was also observed. This signal near -513 ppm is also consistent with DFT predictions of the vanadium chemical shift of monomeric vanadia interacting with water molecules (Figure 3.6). The peak ascribed to square pyramidal vanadia around -533 ppm increases slightly (2–3%), but this may also be a result of tetrahedral monomers interacting with water (Figure 3.6). A peak at -540 is generated upon interaction with water. This feature may be related to double-bridged dimers interacting

with water (-540, -550 ppm), though the dehydrated (-562 ppm) species' concertation in the sample is roughly the same for both dry and hydration conditions, indicating that agglomeration of monomers would be taking place if this identification were correct. A reduction (~8%) in the species around -580 and a slight downfield shift (2–8 ppm) is also apparent relative to dehydrated materials. Initial calculations of the water-free model suggested this peak in the spectra of hydrated vanadia on silica could be related to monomeric tetrahedra with a bridge bond hydrolyzed, the presence of which was predicted theoretically, but interaction with water would result in an upfield shift to -600 ppm (Figure 3.6), which is not observed.[121] The assignment of this species is thus retained as oligomerized vanadium, but diminished in intensity and shifted due to interactions with water and surface restructuring. High-field signals show a dramatic increase in contribution to the total signal in both samples, which suggest more polymeric vandia species. A broad signal at -630 ppm dominates the spectrum at 40%. This species likely includes the bulk V_2O_5 signal noted in small quantities in the dehydrated case and accounts for a wide distribution of similar signals. The center of the peak shifts to a lower field, which may indicate longer polyvanadate chains since internal vanadia resonate nearer this value.

Specific changes to the tungsten-promoted sample are less clear due to the broader nature of the vanadium signals and relatively minimal changes to the spectra, which may be indicative of the promotional effect of the element and the relative stability of vanadium over tungsten on titania.[211] The impregnated sample suggests the near elimination of monomeric species and the development of a broad peak at -560 ppm that appears to be partially comprised of the transformed monomers and the broad -590 ppm peak from the dehydrated condition. The species assigned to bulk V_2O_5 may again be contained within the broad peak at -626 ppm, but this time

the feature contains an obvious shoulder at -660 ppm, indicating the formation of polymeric vanadia.

The overall effects of water can be summarized as having a dramatic impact under conditions of relatively high vanadium loading where the majority of the species are observed as bulk-like V_2O_5 crystallites. At low loading, some monomeric species are retained with water coordination apparent. A slight decrease in dimeric species between -560 and -580 ppm is noted in favor of higher-order polymeric species upfield of V_2O_5, as evidenced by signal increases and the downfield shift associated with internal vanadium atoms within a chain. Tungsten-containing catalysts are relatively stable, but also exhibit a reduction in monomeric species in preference of oligomers.

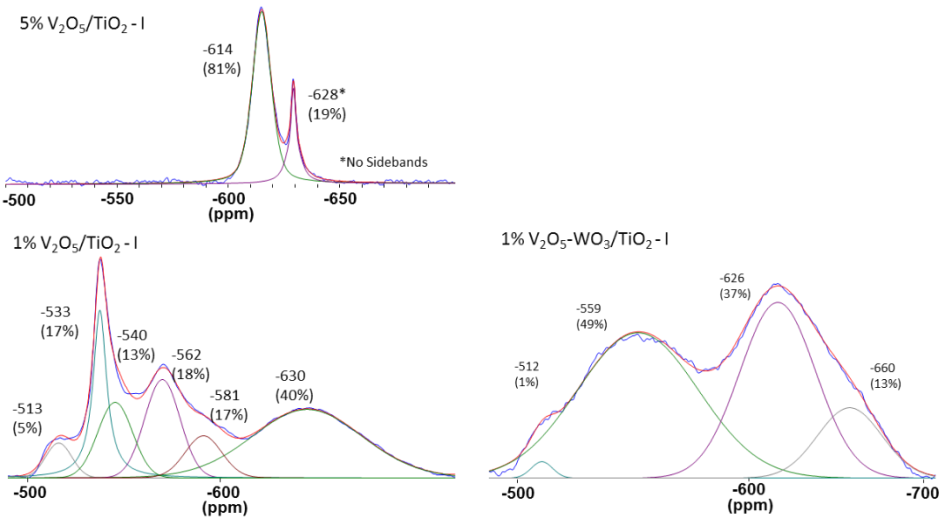

Figure 3.5. ^{51}V MAS NMR results of hydrated V_2O_5(-WO_3)/TiO_2 catalysts prepared by impregnation (I) and co-precipitation (C). Spectral deconvolution summation is presented by the red line. All spectra were externally referenced to V_2O_5 at -613.8 ppm.

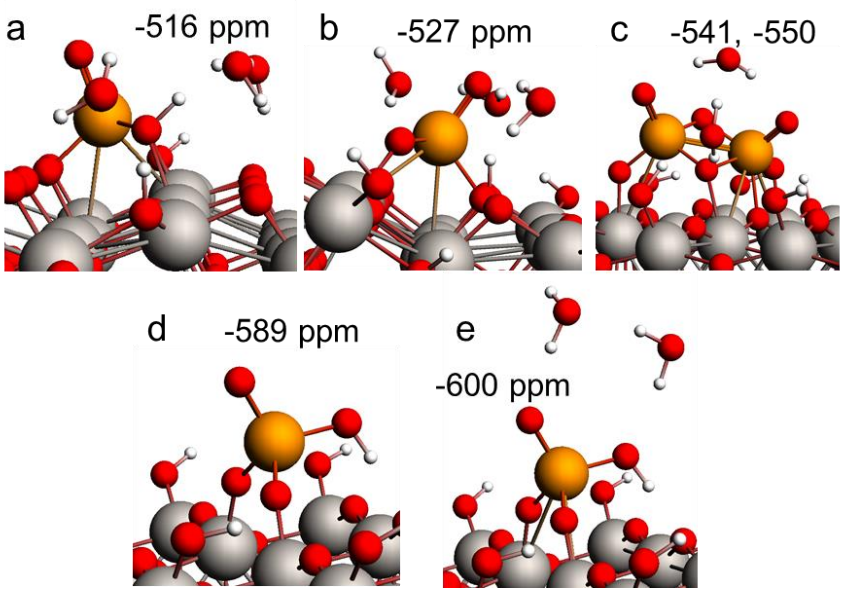

Figure 3.6. DFT optimized cluster models of hydrated vanadium structures on TiO_2, including distorted tetrahedral (a), distorted tetrahedral with bridge bond protonation (b), di-bridged dimers (c), dehydrated tetrahedral with a hydrolyzed bridge bond (d), and tetrahedral with a hydrolyzed bridge bond. Atoms represented include vanadium (orange), titanium (grey), oxygen (red), and hydrogen (white).

3.3 Impact of Hydrothermal Aging on Titania-Supported V_2O_5 Catalysts

Combustion of fossil fuels generates not only harmful nitrogen oxides, but a significant quantity of water. Such species have been shown to inhibit low-temperature SCR and enhance selectivity at high temperatures.[212-214] At very high temperatures (above 600°C), the catalyst begins to deactivate.[215] Low loading samples were shown to increase activity under mild hydrothermal aging conditions, which was proposed to potentially result from the formation of polymeric species which may be more active. Higher loadings were shown to deactivate. One mechanism for deactivation is the volatility of vanadium.[216] The oxide forms of vanadium are carcinogenic species and potential environmental hazards. This stands as another reason the application of vanadia in transportation operations is limited.

Though roles of tungsten oxide and its promotion mechanism are being revealed, they are still not fully understood. Tungsten oxide has been shown to stabilize the TiO_2 support by

minimizing the anatase to rutile titania transformation at higher temperatures.[93, 217] Tungsten operates as a stabilizing agent for the less thermally-stable supported V_2O_5/TiO_2 catalysts at elevated temperatures and hydrated environments, as suggested in the previous section.[87, 89] To better elucidate the roles of tungsten oxide in stabilizing the performance of SCR after extended use, hydrothermal aging was conducted on a series of samples with varying quantities of tungsten oxide to simulate extended operation of the catalyst material. The materials were treated at 650°C for 50 hours both in the presence and absence of water (10% O_2, 8% H_2O, 7% CO_2, 75% N_2). Their catalytic and spectroscopic properties were then evaluated to explain the differences in performance.

The results of the catalytic SCR testing are presented in Figure 3.7. As the quantity of tungsten increases, the activity of the material is shown to increase. At low tungsten loadings, the 50-hour hydrothermally aged material performs poorer than the thermally aged material. The 1% tungsten oxide loaded sample exhibits about half the activity of the thermally treated sample. The difference between the two conditions gradually diminishes up to monolayer tungsta coverage where the difference between the two treatment conditions is indistinguishable.

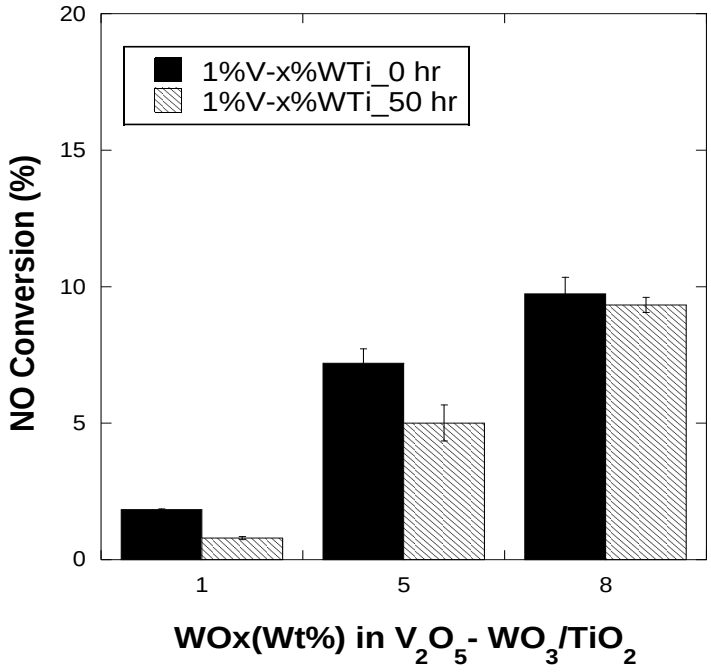

Figure 3.7. SCR performance of thermally and hydrothermally aged promoted vanadia catalysts.

To help understand the surface transformations that lead to these reactivity trends, the Raman spectra of the thermally and hydrothermally treated catalysts are presented in Figure 3.8. The results indicate that a severe phase transformation of the titania support occurs at low tungsten oxide concentrations. Raman features associated with rutile titania appear at the expense of those associated with anatase titania. This contrasts the higher tungsten oxide contents where the surface of titnaia is relatively stabilized, as previously described. The vanadia and tungsta vibrational region suggests that 1V1WTi catalyst does not possess Raman bands from surface VO_4 and WO_5 sites. Several possible explanations may account for this observation: (i) the weaker Raman scattering from the TiO_2(rutile) phase diminishes the intensity of Raman scattering from the surface metal oxide species, (ii) surface $V^{+5}O_4$ is reduced to $V^{+4}O_4$ that is soluble in the TiO_2(rutile) lattice,[218] or (iii) volatilization of metastable crystalline V_2O_5/WO_3 nanoparticles induced by the harsh hydrothermal treatment. The relatively stable

1V5WTi and 1V8WTi catalysts, however, still exhibit the characteristic Raman bands of anatase titania as well as the dehydrated surface VO_4 and WO_5 sites on the TiO_2(anatase) support. Though these spectra suggest the same type of sites for the two samples, high-field ^{51}V MAS NMR is required for a detailed look at the species present. First, the potential contribution of volatilization of vanadia was considered.

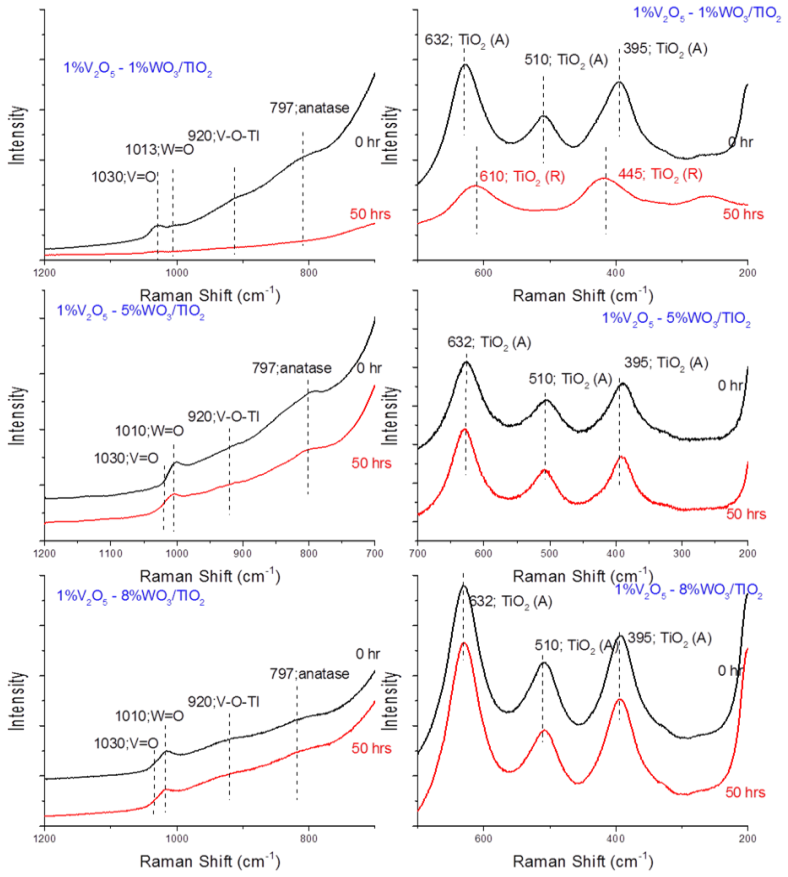

Figure 3.8. In situ Raman spectra of dehydrated initial (calcined at 650 C for 4 hrs in flowing air) and hydrothermally treated (650 °C for 50 hrs in flowing 10% O_2, 8% H_2O, 7% CO_2, 75% N_2) supported 1% V_2O_5-1to8% WO_3/TiO_2 catalysts.

It should be noted that a small quantity of vanadia was lost from the catalyst material during hydrothermal treatment, evidenced by ICP analysis. Table 18 shows that the 1% tungsten oxide promoted material exhibits the smallest loss in vanadia content, which gradually increases

with tungsten oxide addition. This is counter to reports of tungsten oxide stabilizing vanadia on the surface, but the speciation of vanadium oxide or the tungsten oxide surface may still be more stable at these higher loadings, explaining the relatively similar activity. Due to the opposite trend in vanadia loss compared to reactivity, it is obvious that loss of vanadia is not the origin of catalyst deactivation in this sample set. Further, it is not the origin of the low surface oxide signals exhibited in Raman by the 1V1WTi sample.

Table 18. Vanadia content of hydrothermally aged samples determined by ICP.

Sample	**Vanadia Content**
1% V_2O_5-1%WO_3/TiO_2	0.94% V_2O_5
1% V_2O_5-5%WO_3/TiO_2	0.78% V_2O_5
1% V_2O_5-8%WO_3/TiO_2	0.76% V_2O_5

To gain a deeper understanding of the surface vanadia species present, ^{51}V MAS NMR was used to characterize these samples. The spectra of thermally and hydrothermally aged materials are presented in Figure 3.9 and summarized in Table 19. Relative to the non-aged samples from the previous chapter (Figure 2.13), there appear to be slightly more monomeric and dimeric species when hydrothermally aged. Overall across the thermally aged samples, the 1V1WTi and 1V5WTi sample show consistency with previous measurements in that at higher tungsten oxide loadings, agglomeration of vanadia is more prevalent. These two samples after hydrothermal aging seem to retain this trend as well. This is not the case for hydrothermally aged vanadia catalysts, which exhibit a sizable quantity of monomeric species (>24%). The trends across the samples from thermal to hydrothermal aging indicate that hydrothermal aging results in agglomeration of the surface species, but the effects are not too dramatic. Indeed, these differences do not appear to coincide with the changes in reactivity observed since the

hydrothermally aged samples are less active at 1% and 5% tungsta loadings, but these also contain more oligomers than the thermally aged materials. As such, it is critical to evaluate the potential generation of reduced V^{4+} species during the harsh treatment.

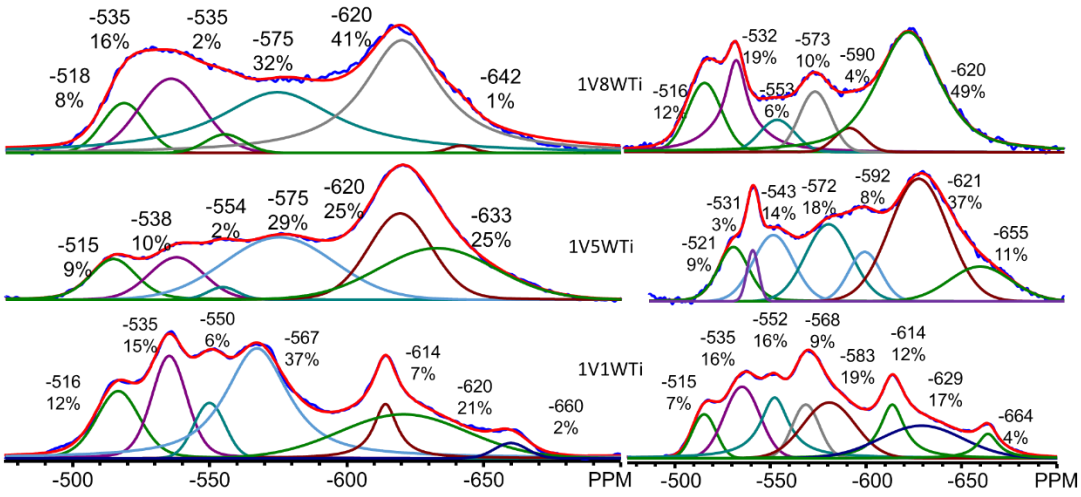

Figure 3.9. ^{51}V MAS NMR data of thermally (left) and hydrothermally (right) treated catalysts.

Table 19. Relative abundance of different vanadia species in thermally and hydrothermally treated SCR catalysts.

	Monomer	Dimer	V_2O_5	Polymer
1V1W	27	43	7	23
1V1WHTA	23	44	12	21
1V5W	19	31	25	25
1V5WHTA	12	40	37	11
1V8W	24	34		42
1v8WHTA	31	20		49

The results of the EPR measurements are presented in Figure 3.10 and quantified in Table 20. Across all samples, an order of magnitude more reduced species is present than in the

non-aged samples from the previous chapter. As the quantity of tungsten oxide on the surface increased, reduction of vanadia centers became more substantial. Hydrothermal treatment seems to impact the vanadia enters less severely than did the thermally aged samples alone. It is important to note that the inconsistency in vanadia species distribution for the 1V8WTi samples may stem from the presence of these reduced vanadia. The apparent enhancement of monomeric species may arise from the tendency for reduced vanadium centers to make nearby nuclei invisible. Since an oligomeric species would contain nearby vanadia species inherently, a reduced center on a polymer would result in a disproportionate suppression of oligomeric vanadia signals. Indeed the high reduced species contents (~10%) likely render the observation of a significant fraction of vanadia species by NMR impossible. Interestingly, the sample which exhibited the greatest extent of rutile conversion (1V1WTi-HTA) also contained the smallest quantity of reduced vanadia, which may suggest that these reduced species arise from more than just the titania phase transformation and that the extent of reduction may be related to the redox properties of the more highly oligomeric samples. From the EPR spectra, it is clear that the 1V5WTi and 1V8WTi samples contain two types of reduced vanadia, which may be indicative of surface and sub-surface vanadia.[219]

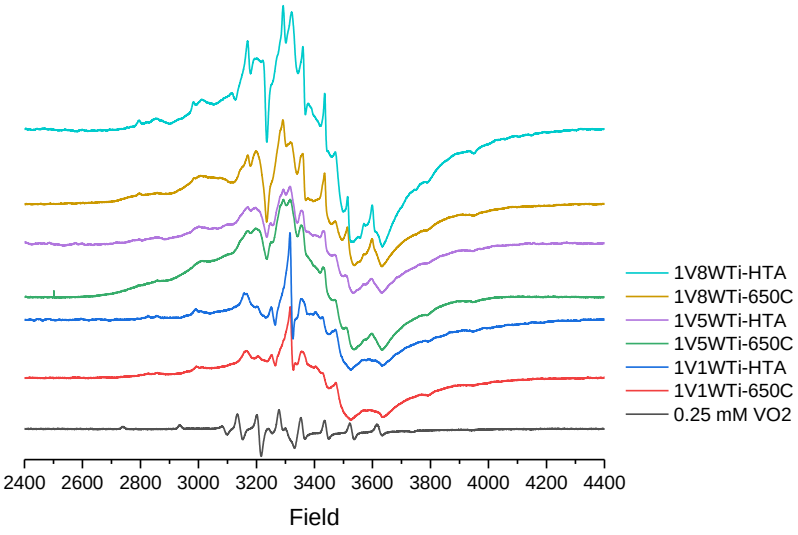

Figure 3.10. EPR spectra of thermally and hydrothermally treated catalyts.

Table 20. Quantification of reduced vanadia species in thermally and hydrothermally treated catalysts.

	%V as V^{4+}
1V1WTi-650C	8.5
1V1WTi-HTA	6.7
1V5WTi-650C	14.6
1V5WTi-HTA	7.3
1V8WTi-650C	15.8
1V8WTi-HTA	12.6

Overall, the reactivity of thermally and hydrothermally aged catalysts was shown to improve with tungsten loading. Tungsten also stabilizes the activity under conditions of hydrothermal aging and helps to resist the support transition from anatase to rutile. The characterization indicates that vanadia does more extensively agglomerate at higher tungsten oxide loadings and that a suppression in oligomeric signals is likely due to the presence of reduced vanadia. Hydrothermal aging both results in fewer reduced vanadia species and few monomeric vanadia species which are relatively less active for SCR. The combined results may

suggest that the hydrothermal treatment is modulating the acidity and/or redox properties of the catalyst, hindering one or both cycles in the 2-site SCR mechanism. Indeed, it has been suggested that hydrothermal aging treatment severely reduces the acidity of vanadia-based catalyst materials, which may partially explain these observations.[220]

3.4 Reaction-Mediated Structural Changes in V_2O_5/TiO_2 Materials

Based on Dongmin Yun, Nicholas R. Jaegers, Jian Zhi Hu, José E. Herrera, and Yong Wang; "Catalytic Consequences of surface oxidation degree and vanadia coverage for the oxidative dehydrogenation of ethanol: V/TiO_xN_y catalyst" [Final Editing]

As shown previously, the identification and quantification of the active species at the atomic level in mixed metal oxide catalysts remains a challenge. The problem is further complicated when substantial reconstructions take place on the surface of the reducible metal oxides during oxygen atom exchange with the surrounding atmosphere.[115] Recent work suggests that not all vanadia species equally participate in the catalytic redox cycle and that the more highly dispersed vanadia moieties (particularly monomeric and dimeric) are the most active species for the oxidative dehydrogenation of light alcohols.[149, 221-222] To control the speciation to well-dispersed vanadia, a synthesis method involving the use of TiN as the support was employed to tune the anchoring sites available for vanadia deposition. The vanadia catalysts were impregnated onto an oxygen-unsaturated titanium oxynitride surface ($TiO_{2x}N_{1-x}$) and characterized by the activity for ethanol ODH as well as for a structural understanding of the materials, including the evolution of the species with the reaction.

As previously stated, vanadia species are anchored to the surface by the consumption of hydroxyl groups present on the support surface.[223-224] The complex nature of the titania surface by way of non-uniformly coordinated surface hydroxyls, various facets orientations, and polymorphs generates uncertainty in the grafting consumed upon incorporation of vanadia. To minimize the inherent complexities from the titania surface, control over the degree of surface oxidation of titanium nitride was exercised. Though stable at ambient temperatures, TiN can form a surface oxide layer with abundant oxygen vacancies upon it exposure to oxidizing atmospheres at temperatures exceeding 300ºC.[225-226] During oxidation, the insertion of O into TiN leads to formation of a $TiO_{2x}N_{1-x}$ type structure with different degrees of surface oxygen functionalities which serve as anchoring sites for vanadia. To determine a stoichiometry of the $TiO_{2x}N_{1-x}$ materials synthesized at different temperatures, the change in mass was monitored by thermogravimetic analysis (TGA), enabling the calculation of the degree of oxygen exchange in the support (the x value in $TiN+xO_2 \rightarrow TiO_{2x}N_{1-x} + 0.5xN_2$). The calculated weight gain from the TGA profile is displayed in Table 21 along with the support chemical formula.

Table 21. Calcination temperature of TiN and the corresponding degree of oxidation.

Calcination temperature (ºC)	Chemical formula
350	$TiO_{0.04}N_{0.98}$
400	$TiO_{0.12}N_{0.94}$
450	$TiO_{0.26}N_{0.87}$
500	$TiO_{0.80}N_{0.60}$
550	$TiO_{1.28}N_{0.36}$
600	$TiO_{1.30}N_{0.35}$

A monolayer of vanadia (7.2 wt% V_2O_5) was impregnated onto the resulting supports, denoted as V/TiO_xN_y. These materials were characterized by ^{51}V MAS NMR (Figure 3.11). The dehydrated samples prepared on $TiO_{2x}N_{1-x}$ supports calcined at low temperature ($V/TiO_{0.04}N_{0.98,}$

and $V/TiO_{0.12}N_{0.94}$) demonstrate the typical features of well-dispersed vanadia species. Both show signals indicative of monomeric structures at approximately -515 and -530 ppm (tetrahedral and square pyramidal type). Additionally, dimeric and oligomeric species are observed between -560 and -700 ppm. What is particularly interesting for the cases where vanadia is supported on the low-temperature formed titania oxynitride (<450^{o}C) is extensive presence of dispersed vanadia species even at near nominal monolayer levels. This result is remarkable since it is well stablished that crystalline V_2O_5 nanoparticles form on titania at near monolayer vanadia coverages. As higher support oxidation temperatures (>450^{o}C), the $V/TiO_{0.26}N_{0.87}$, $V/TiO_{0.8}N_{0.6}$, and $V/TiO_{1.30}N_{0.35}$ materials exhibit the formation of primarily a single species around -614 ppm. This species comprised between 63% and 83% of the observed vanadia signals. While often attributed to bulk V_2O_5, it may also arise from the formation of highly oligomerized vanadia prior to V_2O_5 nanocrystal formation. The spinning sideband pattern of these supported samples is compared to that of the bulk V_2O_5 reference and suggests the chemical environment around these vanadium nuclei is well-aligned with that of the bulk V_2O_5 nanoparticles. Evidence of less oligomerized features is still present, including a small quantity (~2%) of monomeric vanadia on $V/TiO_{0.26}N_{0.87}$. This typical heterogeneous coexistence of VOx clusters (dispersed, oligomeric, polymerized, and nanocrystalline vanadia) with different sizes is ordinarily observed at high vanadia coverages. This observed trend of more highly dispersed vanadia for less-oxidized TiN supports is ascribed to the predominant presence of strongly bound –OH groups (terminal), or potentially defect sites, under conditions of relatively mild oxidation of the surface TiN layers. However, surface density effects may also play a small role in some of this trend since the surface area of the titanium oxynitride slightly decreased at higher oxidation temperatures.

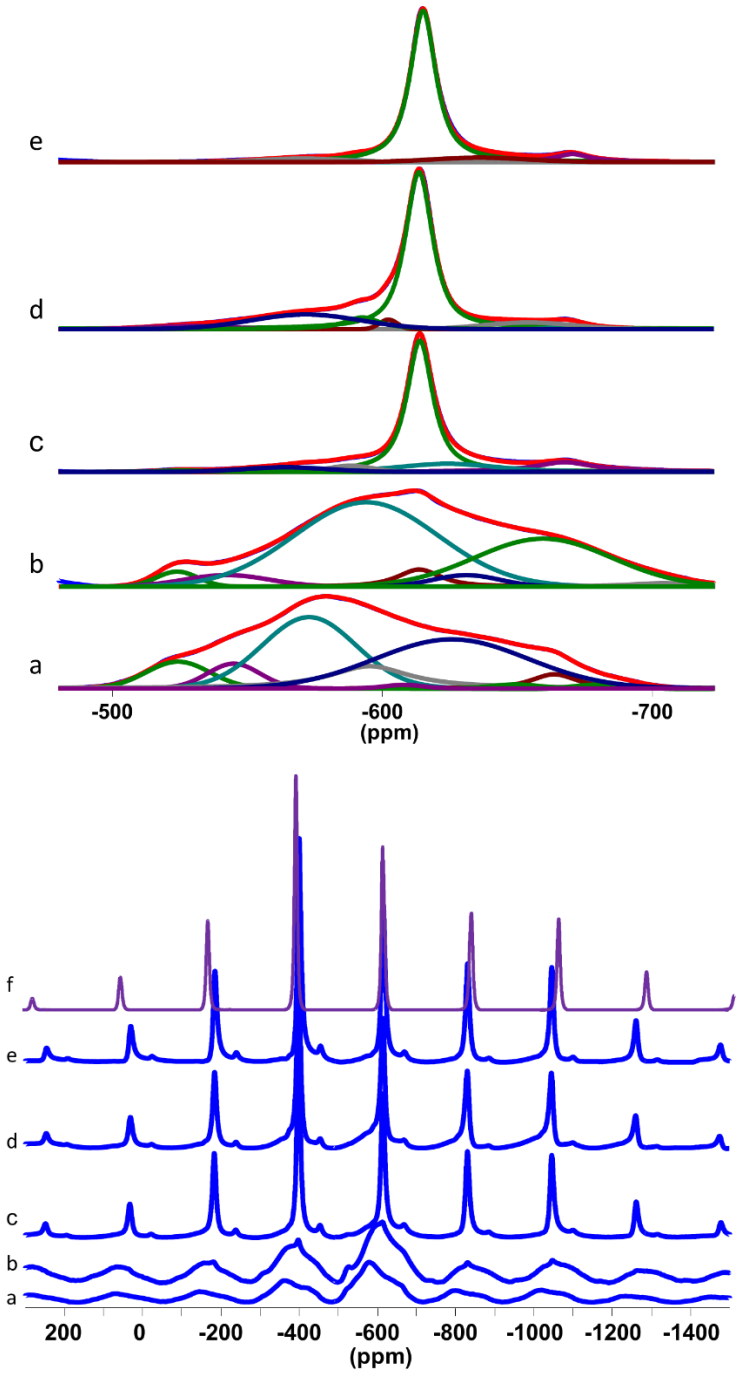

Figure 3.11. In situ NMR centerband spectra (top) and spinning sideband pattern (bottom) of dehydrated a) $V/TiO_{0.04}N_{0.98,}$ b)$V/TiO_{0.12}N_{0.94}$, c)$V/TiO_{0.26}N_{0.87}$, d)$V/TiO_{0.8}N_{0.6}$, e) $V/TiO_{1.3}N_{0.35}$, and f) V_2O_5 measured after dehydration at 300°C for 1h in dry air.

The oxidative dehydrogenation of CH_3CH_2OH to CH_3CHO was used as probe reaction to evaluate sample catalytic activity. Under the experimental conditions (WHSV > 26,000 mL/g cat.-h, 438 - 468K), acetaldehyde selectivity was maintained above 98%. Regardless of the partial pressure of O_2 used in this study, combustion products such as CO and CO_2 were not detected. The activity of these materials is communicated in Figure 3.12. Plotted as a function of the degree of support oxidation, a higher activity is exhibited at the lower degrees of oxidation due to the better dispersion of vanadia particles. Interestingly, the 10% oxidized sample (450°C, $TiO_{0.26}N_{0.87}$) exhibited comparable TOFs to $TiO_{0.04}N_{0.98}$ despite being primarily comprised of bulk V_2O_5 nanoparticles. This is surprising since such surface nanoparticles are widely considered less active than the dispersed counterparts.

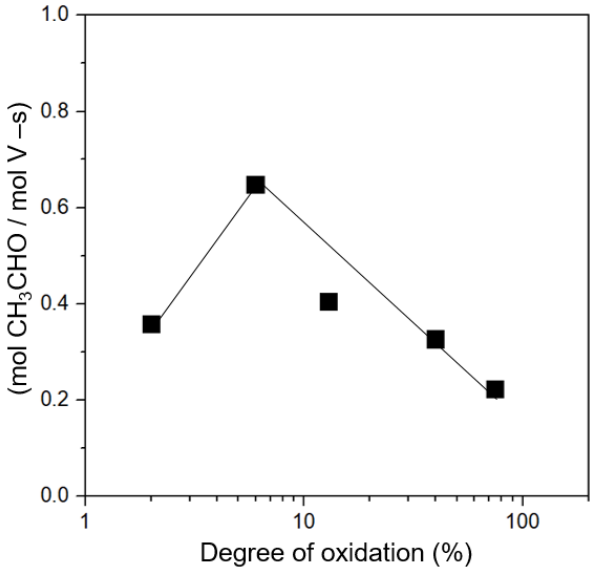

Figure 3.12. TOF values at zero residence time as a function of the degree of oxidation of supports (%).

Due to the discrepancy between the apparent activity of the $V/TiO_{0.26}N_{0.87}$ sample and the detected surface species, ^{51}V MAS NMR was also conducted on samples reduced in ethanol and then reoxidized in 10% O_2/N_2 at 200°C. Figure 3.13 shows this progression for the $V/TiO_{0.04}N_{0.98}$ material. After initial dehydration, the range of species indicating well-dispersed vanadia are observed. Subsequent reduction in an ethanol/N_2 environment for one hour resulted in the elimination of nearly all ^{51}V NMR signals due to the reduction of V^{+5} centers to paramagnetic species which cannot be observed and impair observation of nearby nuclear spins. A very small signal around -515 ppm remains, which can be ascribed to monomeric vanadia in a tetrahedral-like configuration. Additionally, small quantities of oligomeric vanadia are also still visible. This severe minority of species was neither reduced nor located near a reduced center after reaction treatment. After reoxidation at the reaction temperature, the vanadia signals are restored with a slight redistribution of detected species favoring monomeric and dimeric vanadia downfield of -600 ppm, suggesting an enhancement of the vanadia dispersion. The initial and post-reoxidation states of the catalysts for $V/TiO_{0.04}N_{0.98,}$ $V/TiO_{0.12}N_{0.94}$, and $V/TiO_{0.26}N_{0.87}$ can be observed in Figure 3.14. It is interesting to note that in the case of the support oxidized at 450°C ($V/TiO_{0.26}V_{0.87}$), the relative intensity of the primarily bulk-like feature at -614 ppm dramatically decreases in favor of dimeric and oligomeric species after a reaction cycle, which is indicative of a redistribution of species at this position to active species that are well dispersed, such as monomeric and dimeric vanadia moieties. This redistribution explains the expectantly high activity for ethanol ODH for this sample. Further redistribution may be present after several reaction cycles which would more fully disperse the vanadia on the surface. For each of the three samples, the dispersion of vanadia apparently increased after a redox cycle. This result clearly demonstrates the dynamic nature of the vanadia species under reaction conditions and the

potential for the reaction to reconfigure vanadia to structures more favorable for catalytic turnover.

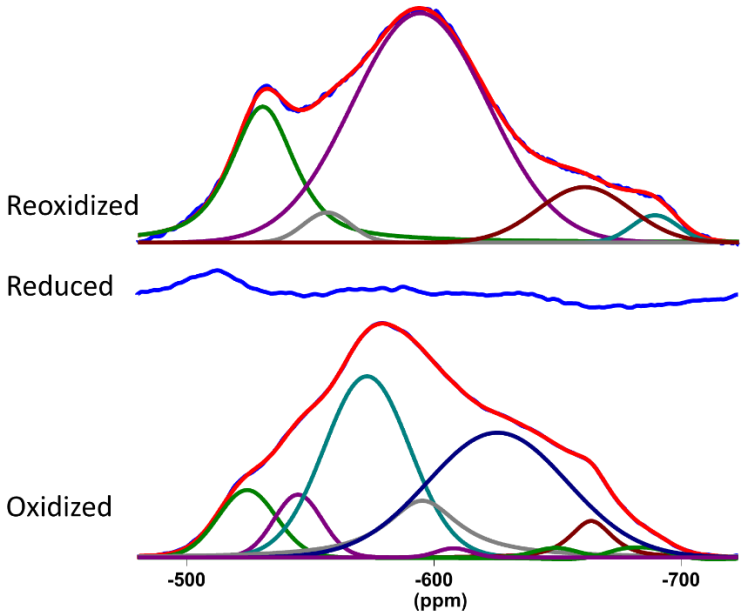

Figure 3.13. In situ NMR centerband spectra of the dehydrated oxidized $V/TiO_{0.04}N_{0.98}$ (bottom), the sample reduced in a stream of ethanol at 200°C for 1 hour (middle), and then reoxidized in 10% O_2/N_2 at 200°C for one hour (top).

The findings of the ethanol ODH reaction impacting the dispersion of vanadia species is truly an interesting observation. It is known that the reactive environment plays a role on the species of supported metal oxide catalysts, but the specific structural alterations are not well understood. This finding lays the foundation for studying such transitions in vandia catalysts under other reaction conditions. Below in Figure 3.15, the spectra of SCR catalysts at low and high vanadia contents are shown after one hour of SCR reaction, followed by purging of the reaction gases. The preliminary results suggest minimal changes in surface site speciation for low-loaded vanadia catalysts after SCR treatment. The 5% vanadia catalyst exhibited the formation of more of the larger, bulk-like V_2O_5 species, which may be an indication of surface oligomerization under reaction conditions. Clearly, more is required to fully grasp the trends in these changes and the mechanism by which they occur, but *in situ* NMR appears to offer a

unique window into the configurational changes under reaction conditions. Such detailed information will be essential to equate vanadia structures with catalytic function and understand the deactivation of vanadia species over time and with different reaction conditions.

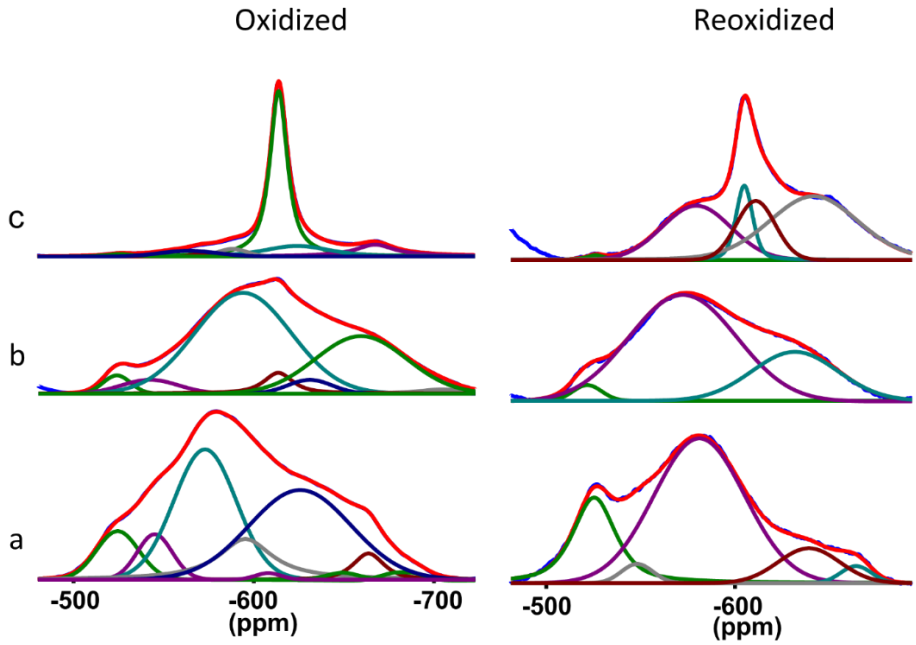

Figure 3.14. In situ NMR centerband spectra of dehydrated a)$V/TiO_{0.04}N_{0.98,}$ b)$V/TiO_{0.12}N_{0.94}$, and c) $V/TiO_{0.26}N_{0.87}$, measured after dehydration at 300°C for 1h in dry air (left) and then after reduction in ethanol at 200°C followed by reoxidation at 200°C for one hour (right).

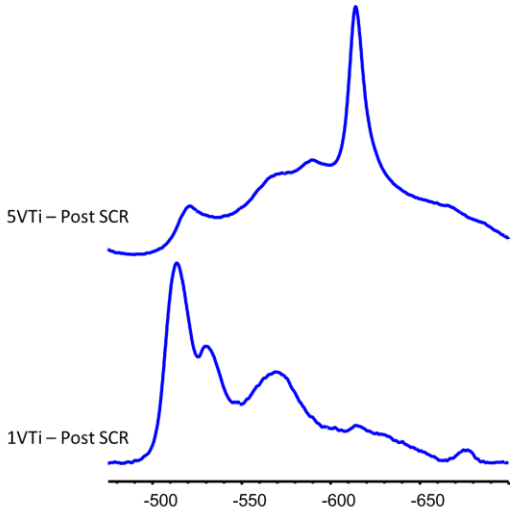

Figure 3.15. In situ ^{51}V MAS NMR spectra of 1% and 5% V_2O_5/TiO_2 catalysts after one hour of SCR reaction conditions.

CHAPTER FOUR: SOLID-ACID CATALYSTS IN HYDRATED ENVIRONMENTS

As shown in the previous chapter, water is a ubiquitous chemical constituent in many systems that may impact materials surfaces. This small molecule is vital to biological life and societal development. Despite this, water's chemical properties are being discovered on an ongoing basis, highlighting the vast uncertainties this molecule offers.[227] Its presence in multi-component systems sometimes obfuscates the simplicity of the chemistry, such as how water has been shown to both improve and retard the rates of C-H activation in zeolites or enhance Fischer-Tropsch synthesis rates on ruthenium.[228-229] Identifying the specific interactions of water with material surfaces is complicated by the challenging interpretation of spectroscopic data. *In situ* solid-state nuclear magnetic resonance (NMR) spectroscopy is no exception and is becoming an increasingly prevalent spectroscopic technique owing to the presence of high sensitivity protons in most chemical systems, offering enhanced temporal resolution over what is typically possible with other nuclei. Challenges from water arise due to mobility and affinity for hydrogen bonding interactions that result in a dramatic temperature-dependent chemical shielding. The ability to understand and interpret the signatures of water and other solvent molecules under reactive environments has become increasingly important as *in situ* and operando NMR studies become more prominent. The non-destructive insights provided reveal much about the chemical systems, where the structure of water in porous materials and on surfaces plays an important role in reactivity and modifying the active centers.[58, 230-233] In protonated MFI zeolite, for instance, it will be shown in 4.2 Genesis of Hydronium Ions in Zeolites that water interacts with Brønsted acid sites to form hydrated hydronium ions under specific hydration conditions.[230] To understand and interpret the signatures of water and other solvents in more complex systems at elevated temperatures, it is necessary to lay the foundation for these constituents alone. Previous efforts

have investigated such a domain for water;[234] however, the previously described developments in solid-state NMR technology have allowed for *in situ* detection at elevated temperatures and pressures.[235] In this chapter, the behavior of water and other small molecules alone will be clearly outlined and then applied to a heterogeneous solid-acid catalysts to provide detailed molecular insights on the catalyst's interactions with the molecules.

4.1 Thermally-Perturbed Behavior of Water & Other Small Molecules

Based on Nicholas R. Jaegers, Yong Wang, and Jian Zhi Hu; "Thermal perturbation of NMR properties in small polar and non-polar molecules" *Scientific Reports* [Under Review]

Since analysis of catalyst systems containing water or other small molecules may require harsh conditions, an extension of the scientific understanding for the spectroscopic behaviors of neat water will aid in the understanding of complex *in situ* experimentation. Herein, the NMR-observable properties of small molecules such as water are presented on the basis of physical phenomena to clarify the spectral changes which occur in more complex systems.

The chemical shift, linewidth, and spin-lattice relaxation time of ^{1}H and ^{17}O species in condensed-phase 18.2 MΩ water as a function of temperature are presented in Figure 4.1. Magic-angle spinning was employed to aid spectroscopy during the freezing process since solid water results in anisotropies in nuclear interactions, and it is not expected to impact the liquid signals.[19] From the presented data, higher temperatures result in a continual decrease of the ^{1}H chemical shift of water. The following relationship was derived across the presented temperature range:

$\Delta(T) = 1.17042 * 10^{-5} * T^2 - 0.01088 * T + 5.1093$. The observed increase in chemical shielding can be explained by fluctuations in the hydrogen bonding network of liquid water. With increasing temperature, hydrogen bonding interactions are suppressed, resulting in stronger O-H covalent bonds. This robust interaction increases the electronic shielding of the proton nuclei since they are drawn closer to the electronic environment of the covalently-bound oxygen atom. The measured trend is consistent with previous reports for liquid water, plotted as blue triangles.[234] Observation of the ^{1}H chemical shift at super-cooled temperatures was possible due to the enhanced pressure inside the fluid as the rotor spins as well as the premelting phenomenon.[236] The trends for ^{17}O chemical shifts also show a steady decrease over the wide temperature range, with greatly enhanced thermal resolution over what was previously reported.[237] This decrease is a direct consequence of an increase in diamagnetic shielding as hydrogen bonding is debilitated at higher temperatures.

The ^{1}H spectral linewidth is reported across the same temperature range, where a non-trivial profile is presented. Fairly narrow lines are present at high temperatures, induced by the enhanced molecular mobility of water. Molecular mobility reduces the variation in observed electronic environments due to signal averaging from quicker random molecular motion. At lower temperatures, this effect is reduced and the subsequent linewidth increases. Around 50^{o}C, the linewidth reaches a maximum where smaller linewidths are present below this temperature. This may indicate an increase in ordering of liquid water at lower temperatures. Indeed, it has been noted that the onset of tetrahedrally-coordinated domains in water occurs near 50^{o}C.[238] This ordered structure is depicted in Figure 4.2 and may explain the decreased linewidth observed. As temperatures decrease in this regime, the bonding network becomes less distorted and takes on more tetrahedral character which increases the linewidth. At temperature above this tetrahedral

regime, the observed linewidth is driven by mobility. The balance between high temperature mobility and low-temperature tetrahedral ordering results in a volcano-shaped linewidth profile. This is the first-known correlation between the structure and dynamics of water molecules and a volcano-type linewidth profile. It should be noted that the absolute values for linewidth will depend on the instrument setup, magnet shimming, chemical environment, and operating parameters, however the expressed trends are representative. In contrast, the linewidth for ^{17}O is about an order of magnitude larger than the ^{1}H linewidth (quadrupolar spin 5/2 nucleus) and continually decreases up to 100°C as the mobility of the water molecules increases. The larger nucleus and linewidth of ^{17}O atoms is less impacted by the ordering of water molecules in tetrahedral patches under these conditions.

Spin-lattice relaxation times were also measured for each nucleus using an inversion-recovery pulse sequence (π-τ-$\pi/2$). An example of the resulting spectral intensity as a function of pulse delay time is available in Figure 4.3. As proton mobility increased, the measured T_1 also increased, which can be explained by a reduction in correlation time as ordering is suppressed and mobility is enhanced. Above 100°C, the ^{1}H T_1 measurement leveled off at about 4.5 s. The increased error in this high-temperature regime is a consequence of the longer measured relaxation times and insufficient repetition delays, ideally $5T_1$. Likely, this value continues to increase at a slower rate, evidenced by the continually decreasing slope. T_1 measurements for the ^{17}O nuclei show a continual increase over the reported temperature range due to a decreased correlation time. The absolute values for T_1 are dependent on the magnetic field, but the trends presented herein are representative.

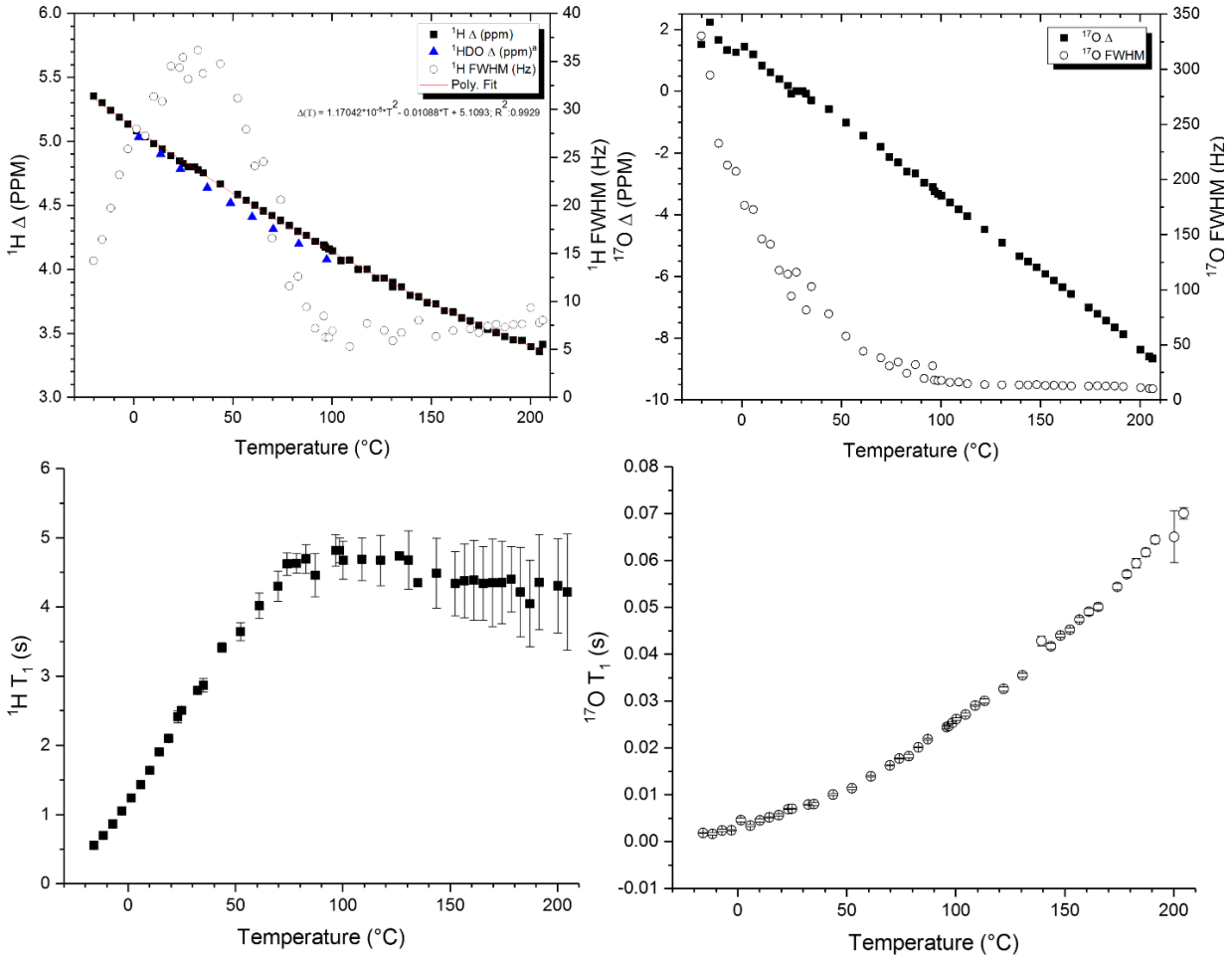

*Figure 4.1. Proton (right) and oxygen (left) data collected for chemical shift and full-width at the half-maximum (top) and spin-lattice relaxation time (bottom). 200 μl of 2% $H_2{}^{17}O$ was loaded into the rotor to maintain primarily condensed phase water throughout the experiments. [a]Data extracted from Gottlieb et al. J Org Chem **1997**, 62, 7512-7515.*

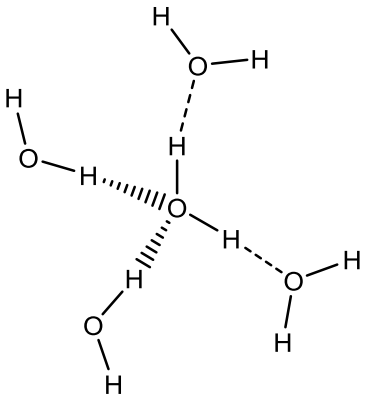

Figure 4.2. Representative scheme of tetrahedrally-coordinated water.

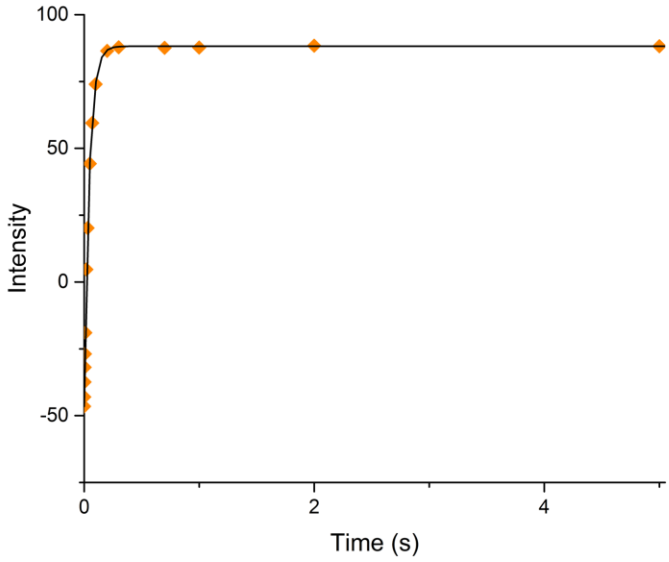

Figure 4.3. Representative inversion recovery result showing the spectral intensity as a function of delay time for ^{17}O in water at 170°C.

The water would freeze at low temperatures which would dramatically reduce the spectral intensity of liquid water in favor of a very broad (~30 kHz) solid-state feature centered at ~7 ppm under MAS conditions of ~4 kHz. The linewidth of ice is expected to be broad and the chemical shift has been shown to depend on the phase of ice.[239-240] MAS NMR narrows the linewidths of the solid features and enables the observation of the phase transition between solid and liquid water. Figure 4.4 illustrates the thawing process spectroscopically. The top series of

spectra illustrate the increase in liquid signal as the ice melts. This liquid feature is enhanced over the course of the experiment at the expense of the solid ice signal (bottom series). The solid signal is shown to initially narrow as the thawing processes initiates and the intensity of the solid feature decreases over time concomitant with the liquid signal enhancement.

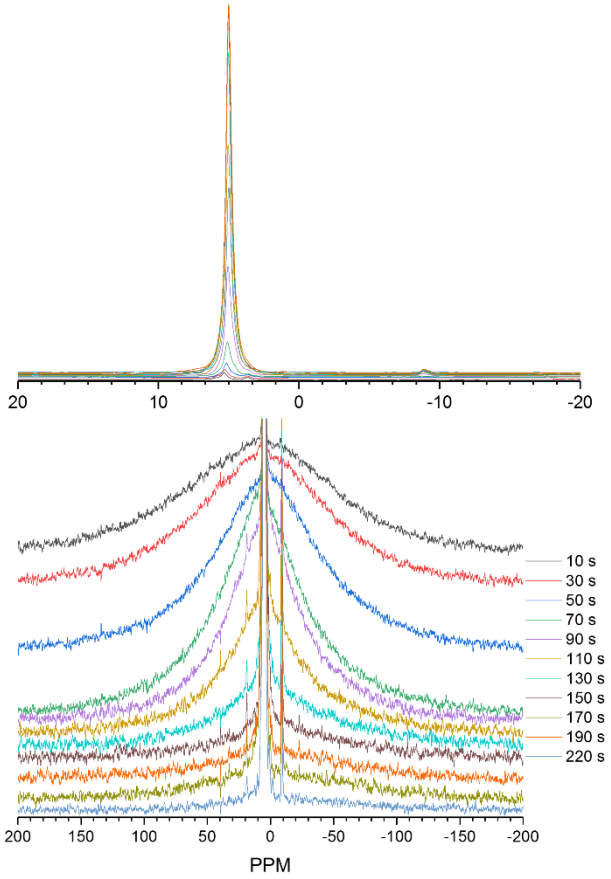

Figure 4.4. Transition from ice to liquid water where the liquid component (top) is observed to increase and the broad solid feature (bottom) diminishes as the phase transition occurs.

The vapor pressure of water is enhanced at elevated temperatures [Antoine's Equation: $P(T)_{vap}\ (torr) = 10^{C_0 - \frac{C_1}{T - C_2}}$ with c_0: 8.14019, c_1: 1810.91, and c_2: 244.485], enabling the

observation of the gas phase water signal.[241] Clear upfield movements in chemical shift are observed for the gas phase species, indicating reduced interactions with neighboring water molecules and substantially stronger covalent character. As shown in Figure 4.5, gaseous proton species resonate at ca. 0.5 ppm and gaseous oxygen nuclei resonate at -37.9 ppm. The gas phase water ^{1}H resonance can be modeled using simplified smaller DFT clusters (Table 22). Small water clusters (< 4 molecules) have reduced interactions with neighboring molecules resulting in predicted chemical shifts (~0.1-0.6 ppm) within the observed range for gas phase water. The addition of more water molecules to the cluster establishes a hydrogen bonding network which moves the signals downfield (~4.9 ppm). Water clusters have been thoroughly modeled by DFT, statistical mechanics, and other computations to reflect enhanced accuracy and detail, where entropic terms are expected to have an effect on chemical shielding.[242-245] ^{1}H-^{17}O spin-spin coupling (~80 Hz) is also observed for gaseous oxygen in water, indicating that a higher degree of charge transfer is present when the molecule is relatively isolated compared to the liquid state where hydrogen bonding dominates. This coupling constant is consistent with previous measurements.[246-247]

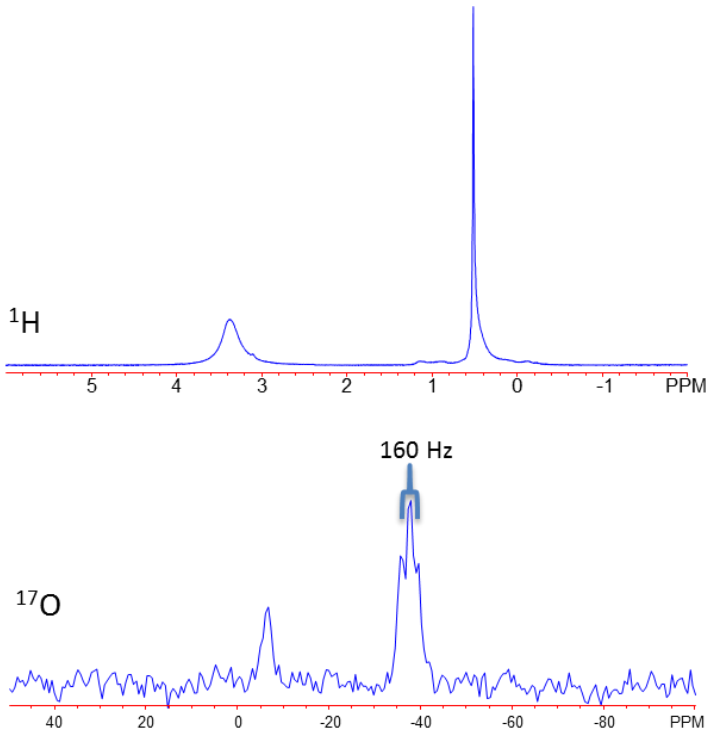

Figure 4.5. Representative NMR spectra of vaporized water at 260°C for ^{1}H and ^{17}O NMR.

Table 22. Small cluster model calculations of the ^{1}H chemical shift in water as a function of cluster size.

Model	**Δppm ^{1}H**
TMS	0
$1H_2O$	0.06
$2H_2O$	0.40
$3H_2O$	0.58
$4H_2O$	4.39
$5H_2O$	4.3
$6H_2O$	4.2
$7H_2O$	4.9
$8H_2O$	4.3
$9H_2O$	5.1
$10H_2O$	5.0
$12H_2O$	4.9

The gas phase chemical shifts of water are relatively independent of temperature. However, small differences are observed for varying gas:liquid fractions (Table 23 and Figure 4.6). With an increasing fraction of gas phase species, the gaseous ^{1}H peaks shift downfield

while the liquid phase shifts upfield. This observation suggests that enhanced chemical exchange between the two phases is present as the surface area of the liquid phase increases under MAS conditions. This chemical exchange effect was minimized in Figure 4.1 by reducing the head space in the rotor to maintain an overwhelming majority of liquid state species. In systems with sufficient vapor fraction and gas-liquid interface however, this exchange effect may dramatically perturb the observed proton species and should be considered during spectral interpretation.

Table 23. Liquid and gas ^{1}H chemical shifts at 206°C and 17.67 bar water vapor at different gas to liquid fractions tuned by modulating the water content in a 294 µl rotor.

Water Content (uL)	^{1}H PPM_{Gas}	^{1}H PPM_{Liquid}	Theoretical Gas Fraction	Experimental Gas Fraction
1.9	0.47	3.54	1	0.96
3.4	0.50	3.42	0.69	0.67
5.8	0.51	3.40	0.40	0.26
10.4	0.52	3.40	0.22	0.15

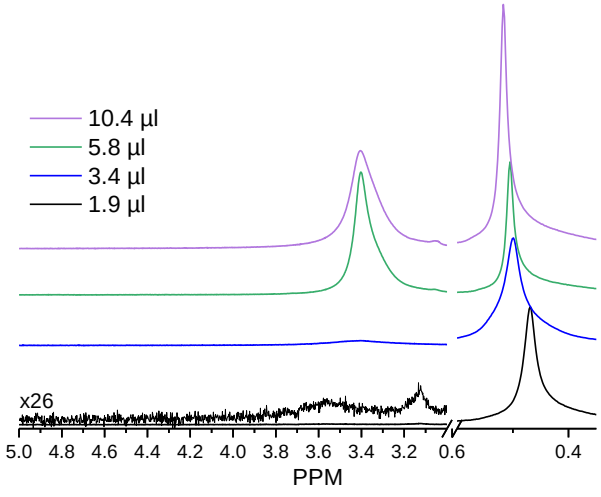

Figure 4.6. Gas:liquid exchange depicted by ^{1}H NMR with differing degrees of gas fraction.

In addition to water, the thermal behavior of the NMR properties of other small molecules is important for chemical systems which contain them. While the relationships

between temperature and methanol or ethylene glycol are well-documented[248], comparison of this behavior to that of other representative molecules can outline a framework which may assist in understanding chemical shielding behavior in an array of complex systems. Figure 4.7 reports such chemical shift data for each ^{1}H environment in tetra methyl silane, cyclohexane, ethanol, and isopropanol. Clear trends are observed among the species present, most notably the relatively small changes in chemical shift with temperature of non-polar compounds TMS and cyclohexane. This is a direct consequence of their decreased interactions with neighboring molecules compared to water, methanol, or ethylene glycol which exhibit hydrogen bonding behavior. Only modest decreases in the chemical shift of the liquid phase protons are observed for these two compounds, which may be indicative of chemical exchange with gas-phase molecules present at higher temperatures. C_2 and C_3 alcohols, similar to methanol, show a temperature-dependent chemical shift. While the CH_3 groups were relatively invariant with temperature due to their limited perturbation by bonding environment changes, protons on the primary carbon exhibited a slight enhancement in shielding at elevated temperatures. This likely arises from their proximity to the alcohol functional group. The –OH group in these two alcohols is dramatically influenced by temperature, showing an increase in chemical shielding as the hydrogen bonding network is weakened. This effect is more pronounced in propanol, possibly due to weaker hydrogen bonding interactions which are more easily perturbed by thermal energy.

For each molecule, the gas phase signals were shielded relative to their liquid phase counterparts (Figure 4.7). This effect was small in non-polar compounds as well as the methyl and methylene groups of alcohols. Small but detectable deshielding of all gas-phase species was observed at higher temperatures due to exchange with liquid-state species. This was most dramatic for –OH protons in alcohol molecules. For comparison, the isopropanol gas peaks at

~225°C were collected in the absence of liquid phase propanol and revealed lower chemical shift values than the high-temperature gas-liquid mixtures. This confirmed the presence of chemical exchange between the two phases when both are present.

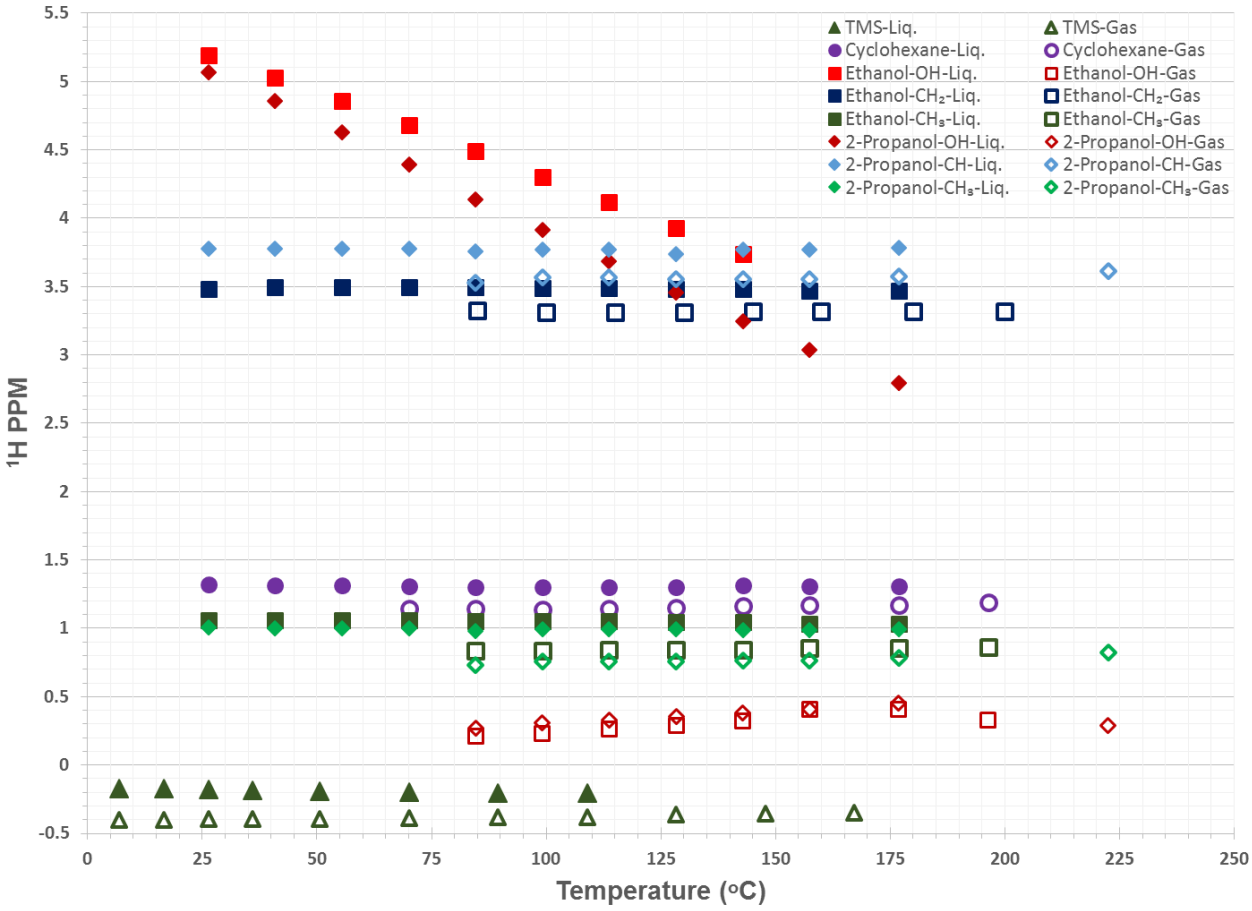

Figure 4.7. ^{1}H NMR chemical shift data for TMS, cyclohexane, ethanol, and isopropanol in the liquid and gas phase a function of temperature. Approximately 15 µl of liquid was added to the rotor during the runs to allow for the clear observation of gas phase constituents.

These data provide an extension of the known thermal perturbation of the properties of water and other small molecules of interest by *in situ* MAS NMR. The ^{1}H and ^{17}O chemical shifts, linewidths, and spin-lattice relaxation times of water are described over a wide range of temperatures with detailed thermal resolution and highlight the reduction of hydrogen bond strength at elevated temperatures. This physical phenomenon results in a decrease in the

chemical shift, narrowing of the linewidth, and decrease in correlation time. The ^{1}H spectra of water highlight the formation of tetrahedral water patches at lower temperatures and a distortion of this ordering up to 50°C where it subsides. The phase transitions of water between solid, liquid, and gas have been documented. The ^{1}H chemical shift properties in other small molecules have also been described over a range of temperatures, showing the limited effect of temperature on non-polar molecules, but dramatic effect on –OH groups involved in hydrogen bonding. Gas phase species are shielded relative to their liquid counterparts due to stronger covalent bonding in the absence of nearest-neighbor interactions, but can undergo chemical exchange with the liquid phase which impacts the observed chemical shifts. The results disclosed herein provide the foundation for understanding small molecules in complex environments such as on a material surface or confined within a pore which enables a more confident understanding of *in situ* NMR results.

4.2 Genesis of Hydronium Ions in Zeolites

Based on Meng Wang, Nicholas R. Jaegers, Mal Soon Lee, Chuan Wan, Jian Zhi Hu, Hui Shi, Donghai Mei, Sarah D. Burton, Donald M. Camaioni, Oliver Y. Gutierrez, Vassiliki-Alexandra Glezakou, Roger Rousseau, Yong Wang, and Johannes A. Lercher; "Genesis and Stability of Hydronium Ion in Zeolite Channels" *Journal of the American Chemical Society* 2019 141 (8), 3444-3455 DOI: 10.1021/jacs.8b07969

Brønsted acid protons from bridging hydroxyl groups that serve to charge balance trivalent cation substitution into the zeolite framework[249-252] are extensively used for myriad

chemical reactions such as dehydration, cracking, dehydrogenation, isomerization, and alkylation.[253-256] These acid sites readily donate protons to substrate and solvent molecules, such as alkenes, aromatics, alcohols, and water.[257-260] Mechanistically, these acid-catalyzed transformations have been extensively explored by kinetic studies and spectroscopic observations of intermediate species.[249-252, 258] However, the presence of solvents or co-reactant species are less understood. As was previously indicated, water is present in an abundance of feedstocks, employed as a solvent, and is also generated as a co-product during some acid-catalyzed reactions. [228, 261-264] As such, elucidating the impact of water on the reactive center is of interest for a full description of the chemical system.

Determination of water's role on reactivity is straightforward to establish. For instance, at low pressures the dehydration rate of alcohols is negatively impacted by water due to stabilization of the adsorbed alcohol,[264] however for alkane C−H bond activation, reaction rates were shown to be enhanced by an order of magnitude at low water contents (≤1 water molecule per BAS) but retarded at high water loadings (>2–3 water molecules per BAS).[228] It has also been reported that the mechanism for dehydration reactions can change as the active site is converted from Brønsted acids to hydrated hydronium ions in the presence of condensed phase water.[258] Other effects of the presence of water include elevated olefin protonation barriers[265] and limiting substrate adsorption.[266] As these are important effects, precise characterization of water's interaction with bridging –OH groups is of great importance for a quantitative molecular description of zeolite systems.

It is well established that a number of species co-exist in the zeolite when water is present. These include Brønsted acid sites, Lewis acid sites with strongly bound water, water

hydrogen-bonded to BAS, hydronium ion clusters, and physically-adsorbed water. [267-289] However, the specific conditions under which these species are present were not precisely quantified. As such, NMR is combined with computational work to provide such detailed insight, enabling the identification of the specific conditions under which hydrated hydronium ions form.

Figure 4.8a and Figure 4.8d display the ^{1}H one-pulse MAS NMR spectra of dehydrated H-ZSM5-15 and H-ZSM5-40 with varying quantities of water adsorbed (0.25 to 13 H_2O/BAS). An array of peaks are featured in the dehydrated samples (bottom of Figure 4.8a and d): a narrow line at 1.7 ppm (silanol groups with a shoulder from nested silanols), a small 2.5 ppm peak on HZSM5-15 (extraframework Al hydroxyls), 3.9 ppm (Brønsted acid sites), and a broad peak at 5 ppm (hydrogen bonded to framework oxygen or water). [290-292] The 5 ppm peak indicates that trace moisture is present in the system due to the N_2 used during pretreatment. By equilibrating the zeolite in a desiccator over a saturated $Ca(NO_3)_2$ solution, water loadings of up to 12-13 water molecules per BAS were obtained, enabling the observation of a series of ^{1}H NMR spectra for zeolite samples of different hydration levels (Figure 4.8a and d).

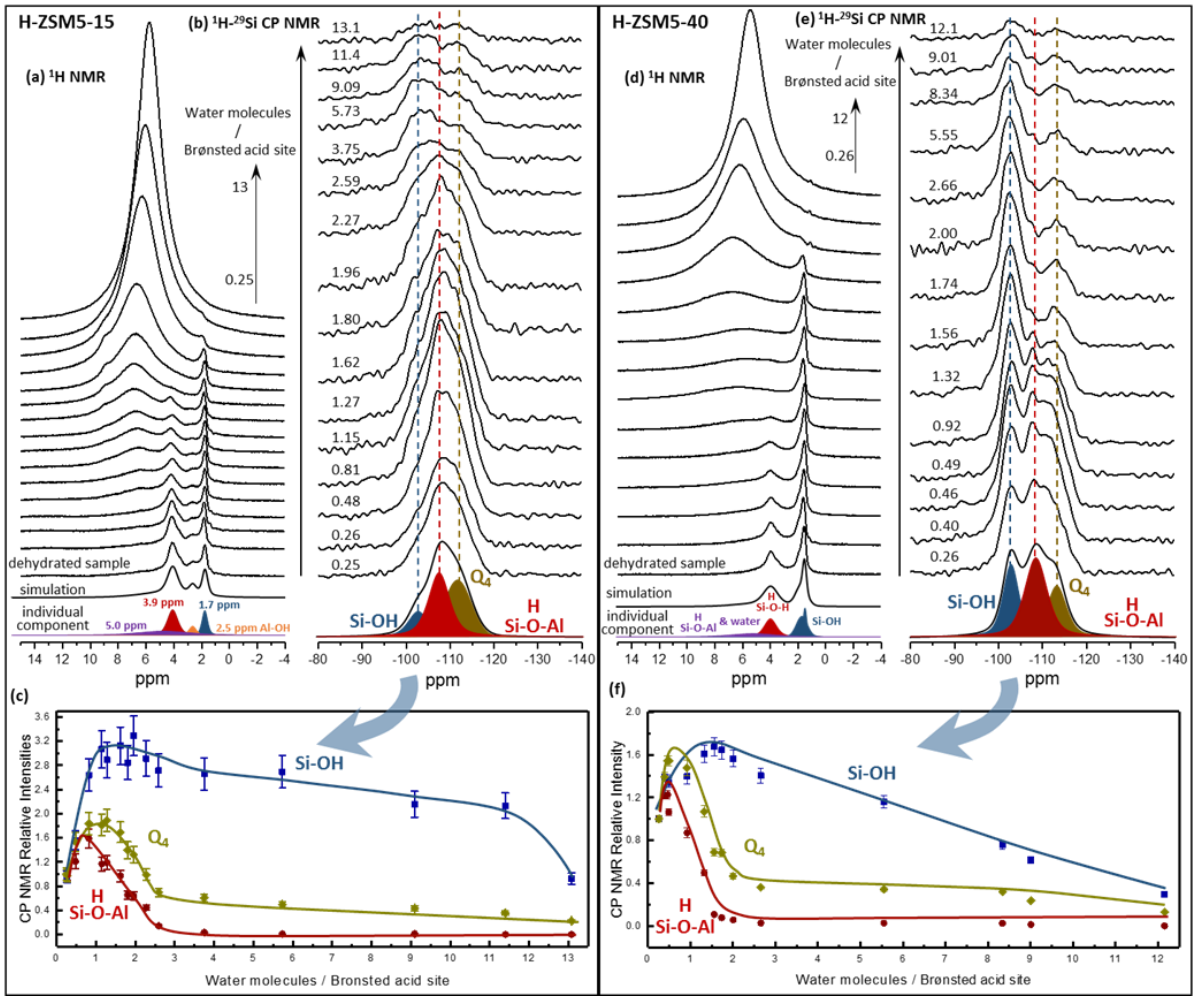

Figure 4.8. [1]H one-pulse and [1]H-[29]Si Cross Polarization (CP) MAS solid-state NMR spectra; and dependencies of CP signal relative intensities of zeolites on water loading of dehydrated zeolites. (a, b) The deconvolution of the first [1]H NMR and CP [29]Si spectrum is shown at the bottom of b, and the dependencies of these relative intensities are shown in c and f.

Interactions between water and SiOHAl sites during hydration can be monitored using ^{1}H-^{29}Si cross polarization (CP) NMR. The relatively broad feature from -110 to -120 ppm is attributed to [$(Si(OSi)_4$] sites.[52, 293-294] Two additional peaks, -102 ppm and -106 to -108 ppm, for terminal Si-OH ([$Si(OSi)_3OH$]) or SiOHAl ([$Si(OSi)_3OHAl$]) species were also detected in the

CP experiments. The ^{29}Si resonance is expected to have a greater downfield shift upon interaction with a proton leading which diminishes shielding.[294] As such, the -102 feature is assigned to a Si bonded to a terminal silanol OH group [$Si(OSi)_3OH$], and the peak at -106 to -108 ppm to Si in a T site bridge bonded to one framework Al atom [$Si(OSi)_3OHAl$]. This is supported by a semi-quantitative analysis of the peak areas. When the concentration of framework Al (Al_F) is comparable to that of SiOH groups, as in H-ZSM5-40, these peaks display similar intensity to that shown in the dehydrated sample (bottom spectrum in Figure 4.8e). The signal for SiOHAl ([$Si(OSi)_3OHAl$]) is shown to decrease in the presence of water (upper spectra in Figure 4.8e) due to the donation of the bridging hydroxyl group proton to water as water is adsorbed.

The abundance of the three Si species, [$(Si(OSi)_4$], SiOHAl ([$Si(OSi)_3OHAl$]), Si-OH ([$Si(OSi)_3OH$]), are deconvoluted for each zeolite and shown in the bottom in Figure 4.8b and e. The evolution of the intensities of these signals as a function of water loading was similar between the two zeolites (Figure 4.8c and f). With the concentration of water approaching one molecule per BAS, the intensities of all signals increased due to the close proximity of additional, relatively immobile protons at framework sites. This is illustrated by the dashed arrow in Figure 4.9a which depicts the H^+ from the Brønsted acid relatively near to the Si. A single water molecule would adsorb nearby and increase the available protons used to polarize the Si atom without dramatically increasing the H-Si distance or enhancing the proton mobility. These ^1H-^{29}Si CP NMR results prove that the distance between the ^{29}Si and the ^1H in the T site remains relatively small and invariant up to 1 water molecule per BAS.

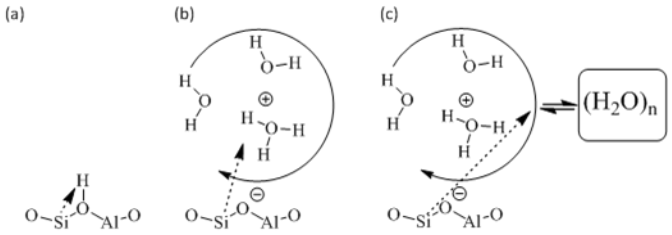

Figure 4.9. Representation of BAS environment for a) bare acid site, b) low water concentrations with hydronium ion formation, and c) high water concentrations with extended phase. Dotted arrows suggest relative H-Si distances where solid lines indicate chemical exchange between protons.

Reprinted with permission from *J. Am. Chem. Soc.* 2019 141 3444-3455. Copyright 2019 American Chemical Society.

As the water loading further increased, the CP signal from SiOHAl ($[Si(OSi)_3OHAl]$) decreased, almost disappearing at two water molecules per BAS. This strongly implies a decrease in the dipolar interaction due to the elongation of the distance between the ^{1}H and ^{29}Si nuclei from the formation of H_3O^+ and an enhanced mobility of the acid proton in the presence of two water molecules. This is depicted by the dashed line in Figure 4.9b showing both an increased H-Si distance (dotted arrow) and enhanced mobility (solid arrow). The CP signal associated with $(Si(OSi)_4$ entities followed a similar trend as with the SiOHAl species, likely due to the main signal of the $(Si(OSi)_4$ coming from the ^{1}H on bridging hydroxyl through the cross polarization. At three water molecules, the signal from SiOHAl was eliminated. This signal remained negligible with the inclusion of additional water and the signal from silanol groups gradually dropped due to enhanced proton mobility. This is further depicted in Figure 4.9c showing molecular exchange with water not directly associated with the hydronium ion cluster. The appearance of a different species, the generation of a hydronium ion, leads to the complete disappearance of the proton signal of the SiOHAl group (11^{th} spectrum, Figure 4.8). The ^{1}H

NMR signal for the bridging hydroxyl group and the CP signal from the corresponding Si both disappeared at ~2 water molecules per BAS. At higher water loadings, the ^{1}H NMR signal of silanol decreased along with the corresponding ^{1}H-^{29}Si CP signal (shown in Figure 4.8c and f).

To help illustrate the framework oxygen-acid proton distance as a function of water loading, DFT calculations were employed. The dry BAS exhibited an O-H distance of 0.977 Å. This distance is predicted to increase to 1.041 Å when one water molecule was adsorbed on BAS. This difference (0.064 Å) is small compared to the variations observed with larger water cluster sizes, such as 1.426 Å with 2 water molecules (Figure 4.10, Table 26).

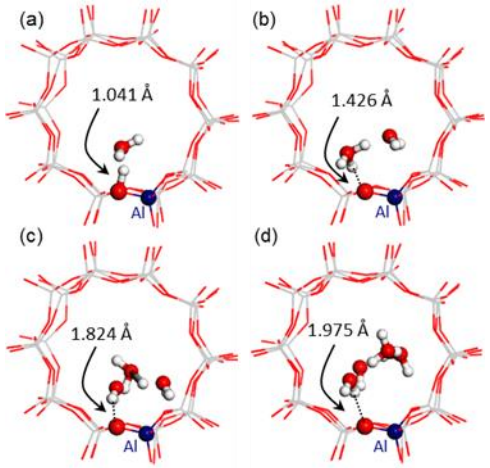

Figure 4.10. DFT-optimized structures of BAS hydration in the H-ZSM5 zeolite channel with increasing numbers of water molecules optimized by DFT cluster calculations. From a to d, the number of water molecules increases from 1–4 with the shortest O-H distance labeled in each cluster.

Each ^{1}H NMR peak exhibited significantly different line widths which did not further narrow at higher spinning rates since the hydrogen spins are dilute.[295] These differences in line

widths likely arise from the distribution of chemical shifts due to inhomogeneous environments and different spin-spin relaxation times (T_2) ($\nu_{1/2}=1/\pi T_2$).[278, 296-297] Spin-echo experiments were conducted with pulse parameters to better characterize the species (Figure 4.11). With this technique, hydrogen species in different chemical environments could be selectively suppressed to isolate individual peaks and provide more detail on their chemical environment.[278, 297] These species are summarized in Table 24.

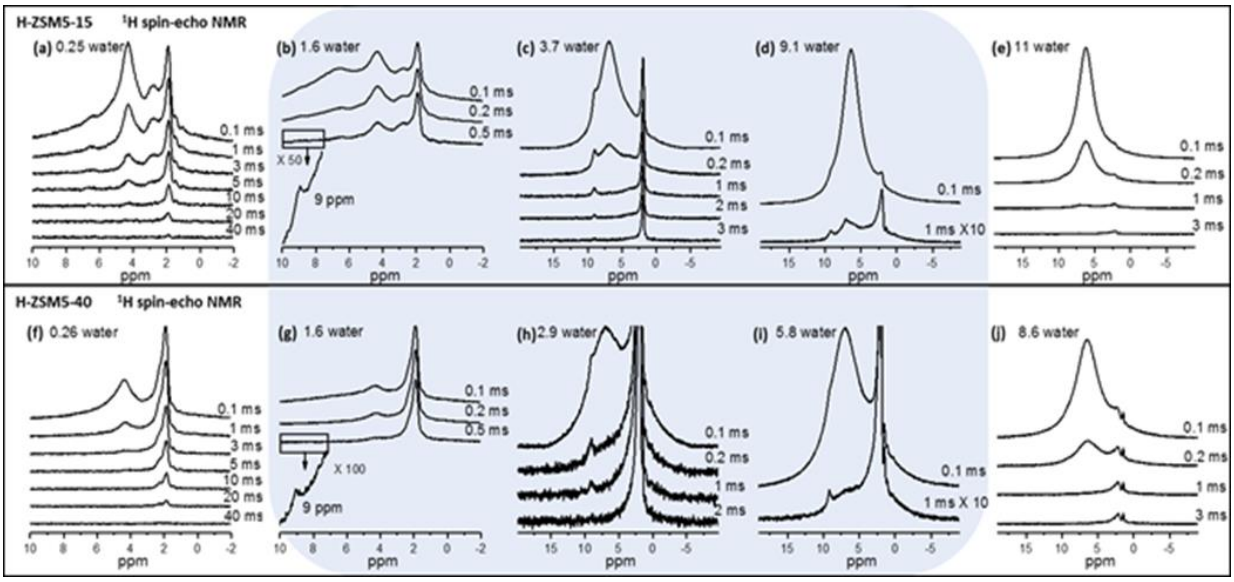

Figure 4.11. (a - j) Comparison of ^1H spin-echo MAS NMR spectra of different water loading on the zeolites acquired with varying echo times. Spinning rate was 9.5 kHz and the echo time varied from 0.1 to 40 ms. The recycle delay was 10 s and 16–1024 scans were acquired depending on the signal/noise. The shaded areas indicate the range of H_2O/BAS ratios when the signal at 9 ppm appeared.

Table 24. Spin-spin relaxation time of different H species in the H-ZSM5 zeolites.

Species	Chemical shift, ppm	T_2, ms [a]	H_2O/BAS Observed
Silanol	1.7	10	< 10
Brønsted acid	4	3	< 2
Water & H-bonded BAS	5‑8	< 0.5	> 0
Hydronium ion	9	~ 1	1.6 – 9.1
			1.3 ‑ 5.5

The dehydrated zeolite spectra in Figure 4.11a (H-ZSM5-15) and Figure 4.11f (H-ZSM5-40) revealed two distinguishable signals, SiOH and SiOHAl groups, with T_2 measured as 10 and 3 ms, respectively. The adsorption of 2 H_2O/BAS lead to the domination of a broad peak at 5 to 8 ppm which exhibited a short T_2 of < 0.5 ms. This species is tentatively assigned to a combination of adsorbed water and hydrogen-bonded BAS sites. When a short echo delay time of 1 ms was used to suppress the broad signal, a small narrow peak at 9 ppm was observed at H_2O/BAS ratios of 1.6–9.1 for H-ZSM5-15 (1.3–5.5 for H-ZSM5-40). This species possessed a longer T_2 of 1 ms. The shaded area in Figure 4.11 highlights the range of H_2O/BAS ratios where this 9-ppm peak can be clearly identified. At H_2O/BAS ratios higher than 9, this 9 ppm feature was masked by a strong broad peak. Careful inspection of the ^{1}H NMR data from Figure 4.8 shows that such features are visible even without selective suppression.

The observed stoichiometries for water interacting with Si and hydroxyl OH groups are consistent with reported water adsorption at room temperature.[298-300] At water loadings below 4 H_2O/BAS, water preferentially interacts with SiOHAl groups.[300] With increasing partial pressure, water interacts with Si-OH and with hydrated hydronium ions.[298-301] Under near saturation conditions, the adsorption capacity in the micropore of the zeolite is limited by the

concentration of SiOHAl and Si-OH species,[298-299] while additional water adsorption likely occurs at the external crystal surface and mesopores.[298, 302-303] At water loadings of approximately 10 H_2O/BAS, water molecules associate with both the SiOHAl and Si-OH in the micropore as well as on the external surface, but these sites are indistinguishable in the NMR spectra.

The narrow peak at about 9 ppm has been observed before on, hydrated H-Y zeolite with a Si/Al ratio of 2.6. This species was attributed to $Al(H_2O)_6^{3+}$ formed via hydration of extra-framework Al.[274-278] However, the concentrations of extra-framework Al in these two H-ZSM5 zeolites are quite low, which reduces the likelihood of $Al(H_2O)_6^{3+}$ observation by ^{1}H NMR. The Al-OH species in H-ZSM5-15 is shown to remain unchanged despite the onset of the 9 ppm feature with increasing water concentrations. Moreover, the signal of $Al(H_2O)_6^{3+}$ in HY zeolite was observed to continuously shift downfield from 7 ppm and continuously narrow (until reaching 9.1 ppm) with increasing water content to 26 water molecules per unit cell.[274] In contrast, the chemical shift and half line-width of the peak at 9 ppm in this study did not change with increasing concentrations of adsorbed water (Figure 4.11a–4j).

Further support for this negation arise from experimental solid state NMR characterization of $Al(NO_3)_3 \cdot 9H_2O$ (configured as $Al(H_2O)_6(NO_3)_3 \cdot 3H_2O$) coupled with theoretical models which show that the peak at 9 ppm cannot, in this case, be attributed to $Al(H_2O)_6^{3+}$. This combination of spectroscopic and theoretical methods was used to better understand the nature of the aluminum hexahydrate complex. As a reference point for comparison, solid $Al(NO_3)_3 \cdot 9H_2O$ was investigated with ^{1}H NMR since it is comprised of $Al(H_2O)_6^{3+}$ octahedra[304] as the first coordination shell structure while the second coordination

shell consists of 3 H_2O and 3 NO_3^- molecules. Two peaks are present (Figure 4.12) at 9.3 and 4.3 ppm, which relate to protons from H_2O surrounding the Al in the first and second coordination shells, respectively. This assignment is validated by DFT cluster calculations of the chemical shift (Table 25), where the proton species in the first coordination shell of Al^{3+} is predicted to resonate at 9.4 ppm. Analogous cluster calculations show that given sufficient neighboring water molecules, or in water clusters without Al^{3+}, the average shift accurately converges to 4.8-4.9 ppm, in excellent agreement with the experimental value of pure bulk water. The results in Table 25 demonstrate the necessity of a second solvation shell for the aluminum hexahydrate, $Al(H_2O)_6^{3+}$ to present ^1H signals at the observed value (~9.5 ppm) since an isolated aluminum hexahydrate complex, $Al(H_2O)_6^{3+}$, without second shell is predicted to have a ^1H chemical shift of 5.7 ppm (Table 25). This second solvation shell contains 12 additional water molecules to total 18 H_2O in the water-abundant Al^{3+} complex. The water in the second hydration shell of the $Al(H_2O)_6^{3+}\cdot 12H_2O$ cluster greatly influences the geometries of the first shell water molecules, i.e., the Al-O distances and the H-O-H bond angles (Figure 4.13). The net result is a deshielding of the first shell water protons, causing the NMR resonance to be shifted downfield relative to the protons in a bare $Al(H_2O)_6^{3+}$ cluster in vacuum. Even though the protons in the first shell of this $Al(H_2O)_6^{3+}\cdot 12H_2O$ cluster have chemical shifts approximately 9.3 ppm, fast exchange with the protons in the second shell would result in an average chemical shift of about 6 ppm. Considering this evidence, we conclude that the 9-ppm peak observed in this study cannot be attributed to $Al(H_2O)_6^{3+}\cdot 12H_2O$. The assignment of 9.2 ppm to hexaquo complexes[278] was based on the report by Akitt, et al. For the aluminum hexahydrate complex in a mixture at 10.2 ppm,[305,277] Akitt et al. intentionally created a condition where exchange is slow so that the different protons could be seen.

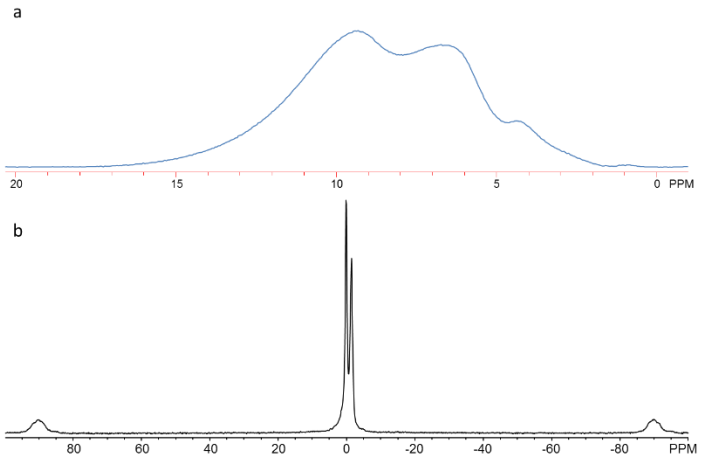

Figure 4.12. ^{1}H (a) and ^{27}Al (b) NMR spectra of $Al(NO_3)_3 \cdot 9H_2O$ at 20 kHz MAS. The proton spectrum shows signals relating to water surrounding Al ions (9.3 ppm), system background as determined by pulse width calibration (6.6 ppm), and water in an outer shell that link octahedral within the same layer and nitrate anions (4.3). Two ^{27}Al signals are present (0.1 and -1.4 ppm) which relate to the two similar, but distinct, Al octahedral in the crystal structure.

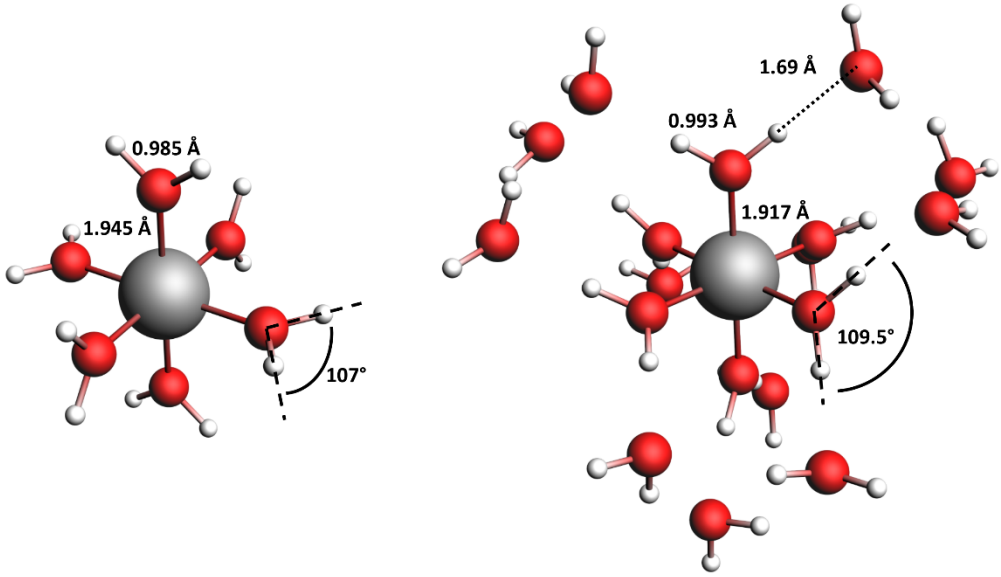

Figure 4.13. Geometry optimized structures of $Al(H_2O)_6^{3+}$ (one water shell) and $Al(H_2O)_6^{3+} \cdot 12H_2O$ (two water shells).

Table 25. DFT ^{1}H NMR calculations of selected hydrated clusters

Model	**Δ ppm ^{1}H**
TMS	0
$Al(H_2O)_6^{3+}$	5.65
$Al(H_2O)_6^{3+}\cdot 12H_2O$	1st Shell: 9.5 2nd Shell: 3.6 Avg.: 5.6
$Al(H_2O)_6^{3+}\cdot 12H_2O$ COSMO	1st Shell: 9.5 2nd Shell: 4.6 Avg.: 6.2
$Al(NO_3)_3\cdot 9H_2O$	1st Shell: 9.4 2nd Shell: 3.7
$1H_2O$	0.06
$2H_2O$	0.40
$3H_2O$	0.58
$4H_2O$	4.39
$5H_2O$	4.3
$6H_2O$	4.2
$7H_2O$	4.9
$8H_2O$	4.3
$9H_2O$	5.1
$10H_2O$	5.0
$12H_2O$	4.9
10 Water on Site 2	7.0*

A free hydronium ion in aqueous phase is expected to have a chemical shift in the range of 7–12 ppm.[276, 278] To assess the assignment of the 9 ppm peak to a hydrated hydronium ion, the ^{1}H NMR spectra of perchloric acid in a wide range of concentrations in water were investigated (Figure 4.14). In agreement with previous reports,[306] the chemical shift moved downfield as the ratio of H_2O/H^+ increased. At H_2O/H^+ ratios of 2.4 and 8, the ^{1}H chemical shifts fell between 8.8 and 6.6 ppm, respectively. To understand the chemical species corresponding to the 9 ppm peak in the zeolite environment, acid solutions were injected into the zeolite with a micro syringe in a glovebox and sealed in the rotor. After the rotor was heated to 140°C and cooled to room

temperature, the ^{1}H NMR spectra (Figure 4.15) showed a narrow peak at 9 ppm with a higher intensity than the sample which had only adsorbed water (Figure 4.9), suggesting that by introducing more hydronium ions into this mixture, the signal at 9 ppm increased, and confirming the attribution of the 9 ppm peak to hydronium ions that do not rapidly exchange protons with water outside their hydration sphere, similar to the depiction in Figure 4.9b. This assignment was further corroborated by theoretical simulations.

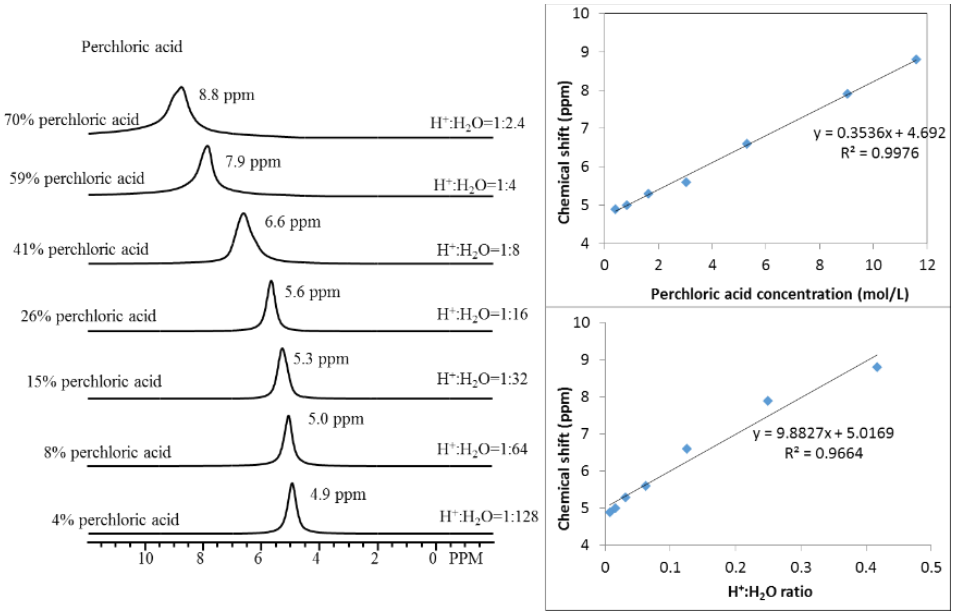

Figure 4.14. ^{1}H one-pulse NMR spectra of perchloric acid with different concentrations (left), dependences of ^{1}H chemical shift on molar fraction of the acid (upper right) or the ratio between H^+ and H_2O (lower right).

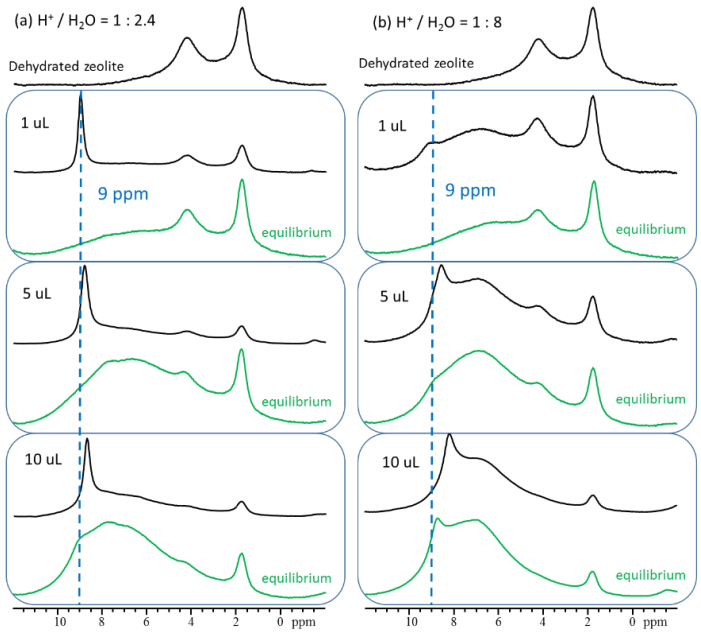

Figure 4.15. ^{1}H one-pulse NMR spectra of dehydrated H-ZSM5-15 with different amounts of perchloric acid solution in two different concentrations.

Theoretical calculations of the ^{1}H NMR chemical shift of the proton species were performed by adding a specified number of water molecules into H-ZSM5 zeolite cluster models. The representation consisted of two different T sites with 0–4 water molecules per BAS (Table 26). The results reveal that with one water molecule adsorbed the bridging O-H bond length is slightly elongated to give chemical shifts of approximately 7 ppm. However, at three water molecules, the proton is completely transferred to the cluster (Figure 4.10 and Table 26). With two or more water molecules, the average chemical shifts of all protons in the cluster are approximately 9 ppm, assuming fast exchange between the acid proton and protons from water in these clusters (Figure 4.9b). The inclusion of more than 4 H_2O/BAS (Appendix C: Additional Supporting Data) shows that with exchange amongst the water molecules, the chemical shift decreases to ~6–7 ppm. Average chemical shifts similar to those listed in Table 26 are expected

when there is a quick exchange among all H species. For instance, Hunger et al. reported that the fast proton exchange among the water molecules in the hydronium ion cluster gives rise to an observable signal at 5–8 ppm in zeolite H-Y.[278] In contrast, we can differentiate several H species in ZSM5 with water loadings below 2 H_2O/BAS because water molecules are heterogeneously distributed among all acid sites. Enhanced exchange with an extended water phase (as illustrated by the solid arrows in Figure 4.9c) is indeed predicted to decrease the observed chemical shift.

Table 26. Extracted parameters from DFT-optimized models of ZSM-5 acid sites with different water loadings.

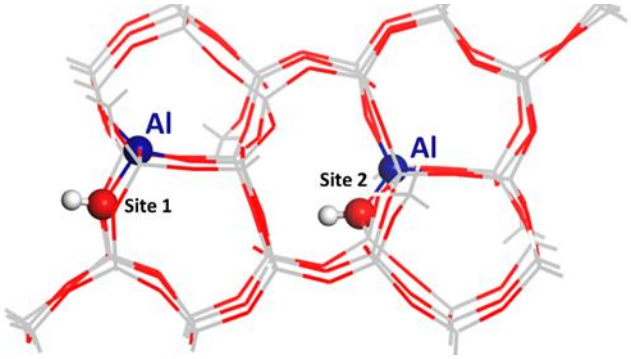

	Site 1		Site 2	
H_2O /BAS	$R_{O–H}$, Å	Average chemical shift, ppm	R_{O-H}, Å	Average chemical shift, ppm
0	0.977	3.7	0.982	4.5
1	1.041	6.9	1.049	7.5
2	1.426	10.2	1.139	8.5
3	1.824	7.5	1.452	8.8
4	1.975	8.1	1.773	8.8

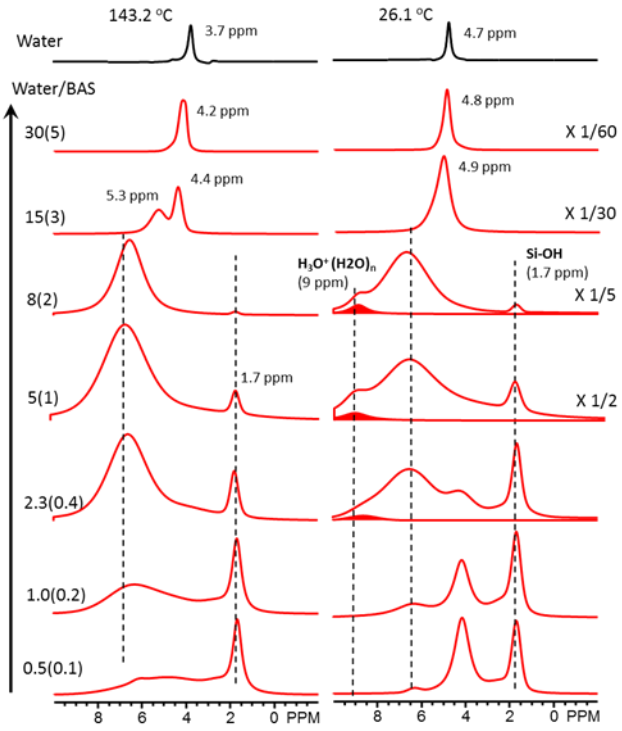

Figure 4.16. Comparison of ^{1}H one-pulse NMR spectra of H-ZSM5-15 loaded with different amounts of water at different temperatures. All thermal effects were reversible. The numbers of water molecules (and uncertainties) determined by spin counting, are listed on the left of each spectrum.

The spectra in Figure 4.16 show that low-temperature *in situ* experiments follow the observations described previously for such water loadings. With the addition of more than 15 water molecules per BAS, all signals merged together and could not be differentiated at room temperature. Spectra recorded at 143°C (left panel) displayed peaks of silanol groups (1.7 ppm) at the same chemical shift and with the same widths at half height as those observed at room temperature, suggesting a limited effect of temperature on the mobility of this relatively non-acidic OH group. The peaks related to the BAS (4–8 ppm) were significantly broadened

compared to their room temperature counterparts. Even the Brønsted acid site at relatively dry conditions was dramatically impacted and the 9-ppm peak never appeared across the broad range of water loadings investigated. Likely, the signals for hydronium ion, water, and Brønsted acid site merged due to fast proton exchange among these species at the elevated temperature. Indeed, molecular dynamics studies have indicated that water clusters which are relatively stable at room temperature and low loading and become highly disordered and mobile at elevated temperatures.[307] This mobility induces exchange between species over a range of chemical environments. Though not explicitly observed, the center of the broad peak shifted downfield with increasing water content from 0.5 to 5 at 143°C. This indicates more weight (fractional identity) to species at higher chemical shifts, such as the 9 ppm peak. It should be mentioned that due to the sealed nature of the NMR rotor, the pressure inside the cavity was elevated at higher temperatures. The expected pressure range for these experiments is 1.4–5.3 atm (total pressure, water and balance N_2), depending on the amount of water added to the rotor and the fraction adsorbed by the zeolite.

Analysis of the sideband patterns (Figure 4.17) revealed that at low water concentrations the sidebands from Brønsted acid signals were relatively strong compared to that of the terminal silanol groups at room temperature. This can be attributed to the dipolar interaction between the hydrogen in the bridging hydroxyl group and the neighboring aluminum.[308] The sidebands from the BAS were significantly suppressed at temperatures higher than 83°C, where the signal at 4 ppm was also absent due to broadening that decreased the intensities of this feature. The line width of the broad peak at about 6.2 ppm narrowed at elevated temperatures where no change was observed in the silanol peak or its sidebands. From this, it is concluded elevated

temperatures induce the quick proton exchange among water molecules and acid-sites in the framework even at low water loadings and at temperatures as low as 53°C.

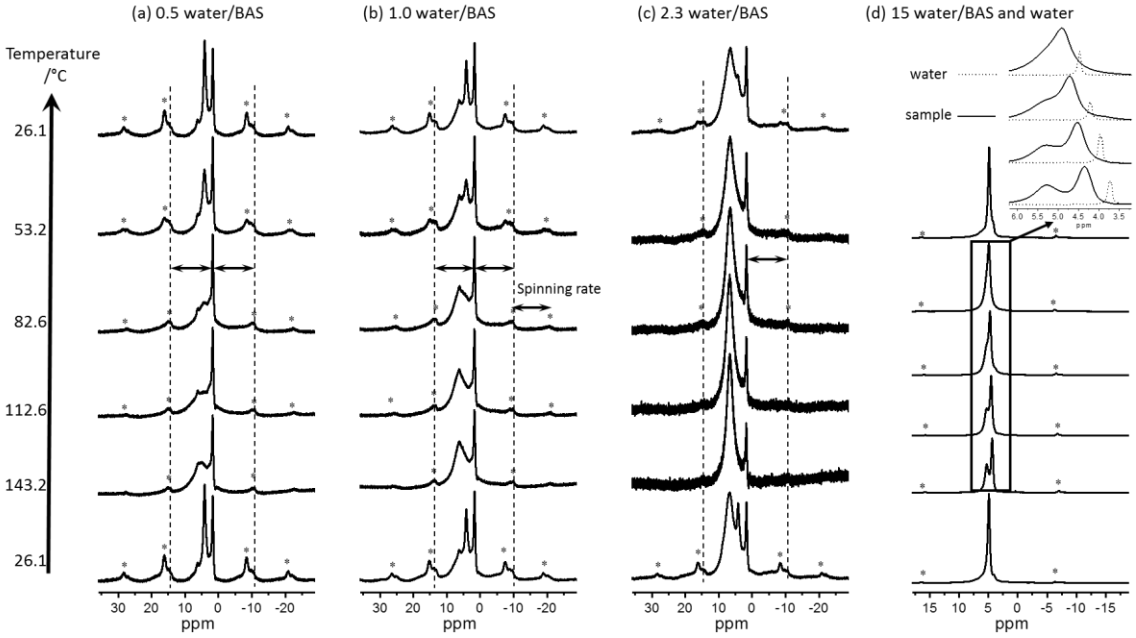

Figure 4.17. In-situ ^{1}H one-pulse NMR spectra of H-ZSM5-15 at different temperatures with different water loadings. From a to d, 0.5, 1.0, 2.3 and 15 water molecules per acid site were obtained from the samples respectively, and the insert figure in d shows the comparison between the sample and water in a narrow range. Asterisks denote spinning sidebands.

Reprinted with permission from *J. Am. Chem. Soc.* 2019 141 3444-3455. Copyright 2019 American Chemical Society.

When fifteen water molecules per acid site were included and the temperature was elevated to 143°C, the signal at 4.9 ppm at room temperature divided into two peaks. These resonance changes indicate the presence of at least two environments of water, such as intraporous and extraporous species, which do not quickly exchange between each other at this temperature and hydration condition. The upfield signal behaved similar to the resonance of pure water (the dashed lines in the inset of Figure 4.17 and 4.1 Thermally-Perturbed Behavior of

Water & Other Small Molecules), shifting upfield at higher temperatures. The chemical shift of the low-field signal (5.3 ppm) remained invariant, while narrowing slightly at higher temperatures. This behavior is consistent that of the broad peak at lower water loadings, leading to the assignment of free water (outside the micropores at high field) and water strongly associated with the hydronium ion (low field) that are distinguished at this water loading.

In this work, the interaction between water and Brønsted acid sites was monitored by *in situ* ^{1}H and ^{1}H-^{29}Si CP MAS NMR. Quantitative spectral analysis revealed the boundary conditions for the initiation of hydronium ions in HZSM-5 pores. Bridging hydroxyl groups are stable at a water loading of one H_2O/BAS. At this conditions, the O-H bond is lengthened by hydrogen bonding with the water molecule, but the proton remains bound to the AlO T-site in the framework. When a second water molecule interacts with the acid site, the hydronium ion is formed with the concomitant proton transfer away from the framework. This phenomenon gives rise to a signal at 9 ppm in the ^{1}H NMR spectra, which has been clearly observed and identified. The 9-ppm signal is visible at room temperature from1.6 to 9.1 waters per BAS for H-ZSM5-15 and 1.3 to 5.5 waters per BAS for H-ZSM5-40, and subsequently disappears at higher water loadings where proton exchange becomes fast compared to the NMR time scale. This leads to the observation of a single peak resembling the bulk water signal.

At water loadings up to 7–8 H_2O/BAS, H_2O forms strong hydrogen bonds with H_3O^+ forming protonated water clusters. These low loadings show that Si-OH groups have weaker interactions with water and thus are visible in the ^{1}H NMR spectra. However, at loadings greater than 8 H_2O/BAS, the excess water interacts with these Si-OH groups causing them to disappear due to fast exchange of water protons with the Si-OH proton. At elevated temperatures, the

signals of all species related to the BAS (bridging hydroxyl group, hydrogen bonded acid site, strongly adsorbed water, and hydronium ion) merged into one broad signal due to chemical exchange, even under conditions of low water content, indicating that even at such temperatures, water is strongly interacting with the acid site. This study lays the foundation for an understanding of the impact of water on reaction mechanisms in catalyst systems. The findings suggest that confined protons readily take on new structural configurations in the presence of water, which will impact the overall catalytic activity of the acid site.

4.3 Other Small-Molecular Interactions with Zeolite Active Centers

The interaction of water with HZSM-5 was shown to have an effect on the structure of the acid site by way of protonating the polar species. Such changes to the availability of the acid proton–from fully available on the framework as the Brønsted acid site, to crowded under conditions of moisture as the fully-hydrated hydronium ion–give rise to the reactivity modulation previously described. To better understand the reactive structures of other molecules, a similar understanding of the bonding configuration at the acid site is highly desirable.

A recent study took a theoretical approach to understand the reactive structures involved in ethanol dehydration to fully describe the mechanism. Efforts to spectroscopically and computationally determine the interactions of alcohols with ZSM-5 have been abundantly reported.[309-316] Indeed, this has even been comprehensively studied with ^{13}C NMR.[317] However, even the adsorption of ethanol onto the Brønsted acid site exhibits behavior that has been speculated, but not proven spectroscopically. Herein, the adsorption of ethanol onto the acid site

of MFI is shown to modify the active structure and, similar to water, form protonated ethanol species which initiates the dehydration of the alcohol.

Ab initio molecular dynamics with support from infrared spectroscopy have been used to support the presence of two types of ethanol structures adsorbed on Brønsted acid sites.[318] In this, an adsorbed monomer was anticipated to conform to a Zundle-type configuration where the acid proton is shared equally between the adsorbed ethanol molecule and the framework oxygen [$CH_3CH_2HO—H_{BA}$--O_F]. At higher temperatures, an Eigen-like structure is computed to dominate where the ethanol is fully protonated by the acid proton [$CH_3CH_2HOH_{BA}$---O_F]. In the case of high ethanol pressures, a dimeric, protonated ethanol species was predicted to be present across all temperatures.

The ^{13}C NMR spectrum in Figure 4.18 conveys the interaction of ethanol with HZSM-5 as a function of temperatures. The ethanol pressure was controlled such that the average ethanol to BAS ratio was less than 1 to isolate the effects of monomeric structures. Indeed, the symmetric lineshape, fairly narrow linewidth, and absence of additional peaks indicates the uniformity of carbon species in the zeolite, where 60.9 ppm may be ascribed to monomeric ethanol adsorbed to acid sites in a Zundel-like configuration. The single peak is shown to deshield as the temperature increases, indicating that the carbon atom gains more positive character relative to its previous state. Likely, the predicted protonation of ethanol at higher temperatures is occurring and the acid proton is interacting much more strongly with oxygen in ethanol, which weaken the covalent interaction between oxygen and carbon as it becomes protonated.

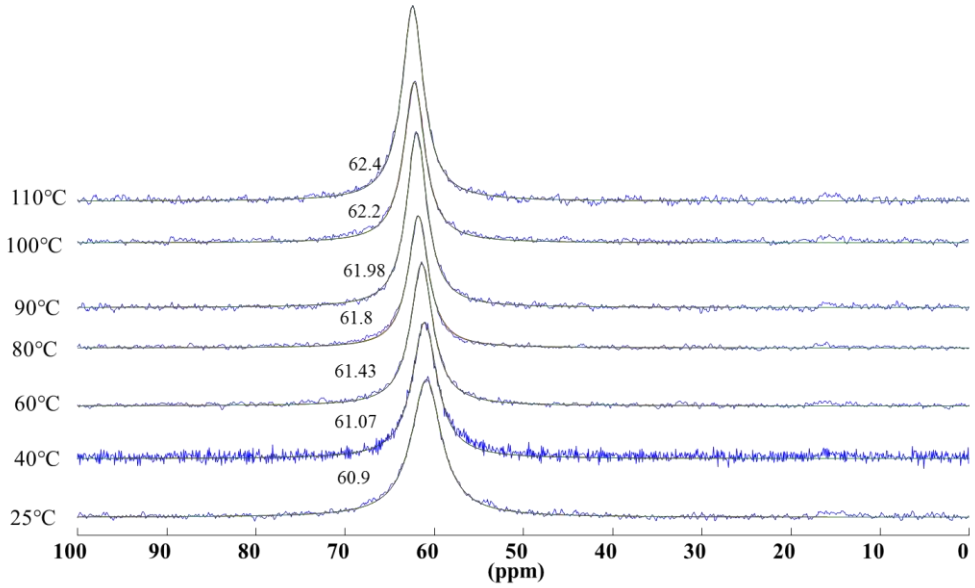

Figure 4.18. ^{13}C NMR of ethanol adsorbed to the acid site of ZSM-5 as a function of temperature.

In previous sections, it was noted that polar molecules may exhibit thermally driven chemical shifts due to changes in hydrogen bonding. As outlined in 4.1 Thermally-Perturbed Behavior of Water & Other Small Molecules, proton shifts in polar molecules tend to decrease at elevated temperatures due to weakened interactions with the extended hydrogen bonding network. In this case, the only hydrogen bonds present are those between ethanol and the zeolite, indicating that this bond must be the only one perturbed by thermal perturbations. Further support for the interpretation of the ^{13}C NMR spectra can be found in Figure 4.19, where the thermally-driven behavior of neat ethanol is relatively invariant across the temperature range of interest. This indicates that whatever changes are observed in the adsorbed ethanol are indicative of structural changes in the adsorption state.

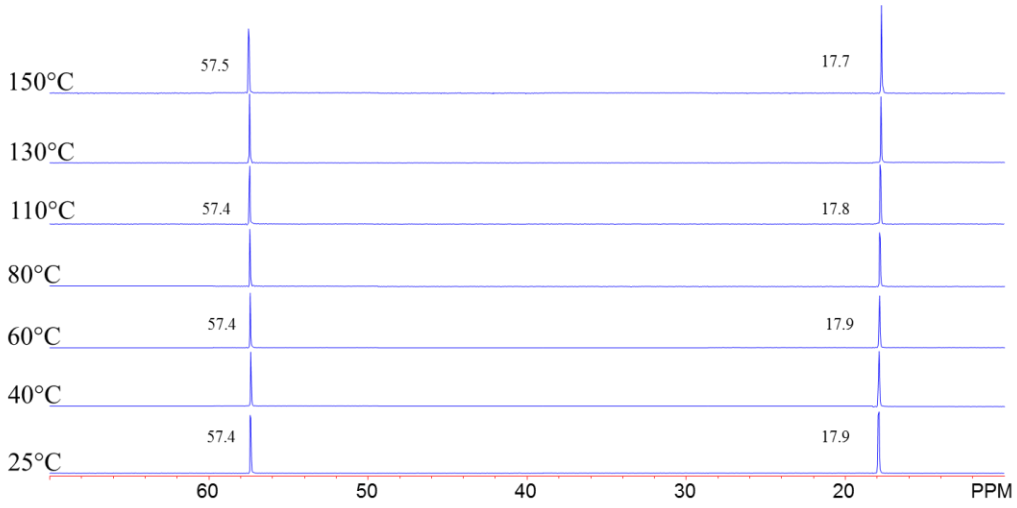

Figure 4.19. ^{13}C spectra of neat ethanol as a function of temperature.

Though a relatively simple observation, this highlights the power of NMR to detect minute changes in the electronic environment of a nucleus. In this, case another polar molecule was shown to interact with acid protons in MFI and readily protonate. The degree of protonation can be observed as a function of temperature, evidenced by the shift in NMR signals at different temperatures. This clearly highlights the genesis of the dehydration of ethanol as the ethanol becomes increasingly protonated, which enables the chemical transformation to take place. Such observations by *in situ* NMR will continue to aid in a detailed understanding of the reactive structures and mechanisms for chemical transformations.

CHAPTER FIVE: CONCLUDING REMARKS

5.1 Summary

Herein, recent representative applications of *in situ* MAS NMR to better understand supported-oxide catalysts have been described. In Chapter 1, the foundations of modern *in situ* NMR technology were outlined where it was shown that all-zirconia NMR rotors enable the study of materials under controlled reaction conditions. The high-strength sealing mechanism enables the environment of interest to be maintained throughout the course of an experiment. Further, specialized loading chambers enable such environments to be prepared from vacuum to elevated pressure conditions. Such advancements open a wide window of systems for which MAS NMR can provide mechanistic insight.

Chapter 2 extensively focuses on the state of dehydrated vanadia catalysts, maintaining a dry environment throughout the course of the NMR experiment. Silica-supported vanadia has historically been challenging to characterize due to ambiguity in spectroscopic results. Analysis by ^{51}V MAS NMR coupled with theoretical calculations revealed the likelihood of monomeric species dominating the surface with dimeric and cyclic trimers as additional possibilities. Dehydrated titania-supported vanadia display distinct signals for monomers, dimers, and polymers which enable unambiguous characterization by ^{51}V NMR. As a consequence, it was shown that oligomeric vanadia promote the SCR of NO by NH_3 via a two-site mechanism. The addition of tungsten oxide to the vanadia catalyst promotes the formation of oligomeric vanadia, which in turn increases SCR reactivity. NMR was also employed to help better understand the role of the supporting facets of catalytic materials. This complex challenge was addressed by

better isolating exposed surface facets of titania and testing each facet with different quantities of loaded vanadium oxide. The (001)-dominant material facilitated the formation of oligomeric vanadia, which led to increased SCR TOFs. Correlations to the methanol ODH reactivity were less well-defined. Finally, bi-layered TiO_2/SiO_2-supported vanadia were characterized by ^{51}V MAS NMR. Mixing the properties of the two supports has been shown to increase the catalytic performance of the material, but characterization by NMR suffers from similar challenges to the silica-supported material with respect to identifying unique vanadia species on the surface.

Chapter 3 then investigates the structure of supported vanadia materials either in the presence of water, or after exposure to hydrated conditions such as hydrothermal aging or genuine reaction conditions. Silica-supported vanadia catalysts under conditions of hydration were found to agglomerate via hydrolysis of V-O-Si bonds followed by surface migration and also be present as stable species that were not fully anchored to the support. Titania-supported hydrated catalysts showed similar tendencies to agglomerate under hydrated conditions, especially at high loadings where both bulk V_2O_5 and a solvated-like vanadia species were observed. Hydrothermal aging of the materials induced dramatic changes to the catalyst, characterized by a reduction in SCR activity and a slight decrease in monomeric species. Thermal treatment alone resulted in the reduction of a significant portion of vanadium centers, which was somewhat inhibited under hydrothermal treatment. The loss in activity was speculated to originate from a reduction in the acid site abundance. Further investigations on aged materials demonstrated the redistribution of vanadia species to more dispersed structures after just one cycle of oxidative dehydrogenation. This includes bulk V_2O_5, which could be redispersed on the surface and exhibited notable catalytic activity.

Chapter 4 extends the application of *in situ* NMR beyond the detection of vanadium species to understand how molecules interact with the surface of the catalyst at a fundamental level. The thermally-perturbed behavior of representative molecules was thoroughly explored and then applied to solid-acid zeolites, which revealed the transition from Brønsted acid species to hydrated hydronium ions in the presence of water, highlighting the changes in the active site for catalysis under environmental conditions of moisture and providing a quantitative description of when the active site is transformed. This phenomenon helps explain previously observed trends in the activity of zeolite materials under hydrated conditions. Further, the progressive protonation of adsorbed ethanol molecules at higher temperatures on such sites confirms the dynamic nature of Brønsted acids in zeolites and provides insights on the early stages of reactivity for chemical transformations.

The results obtained from *in situ* NMR clearly highlight the unique advantages this spectroscopic technique retains in characterizing the state of supported oxide materials. The ability to precisely control the environment of the sample opens up a wide range of applications for which detailed molecular information may be obtained at conditions relevant to reacting systems. Additional works that take advantage of these capabilities are highlighted in the appendices, including *in situ* redox chemistry for molybdenum oxide, dehydration reactions over solid acid catalysts, and other select publications.

5.2 Future Direction

The development of *in situ* NMR has truly enabled a wide array of systems to be analyzed across many different fields. With such tight control over the chemical environment in

the rotor and the ability to form a gas-tight seal, *in situ* NMR has opened up to a new realm of chemical reaction studies that were previously not possible. As it pertains to metal oxide catalysis, NMR must continue to be coupled with other characterization methods and reactivity measurements to accurately understand which species are both present and involved during reaction steps and how the active sites evolve with changing conditions. While the effects of dehydration and moisture are becoming increasingly understood on vanadia-based metal oxide catalysts, the roles of other environments, specifically those which contain reactive substrates are much less explored.

One area of interest for future investigation is that of the impact of other SCR promoters on the structure of vanadia. Molybdenum oxide, for example, has been shown to increase the reaction rate in a similar fashion to tungsten oxide. A number of such promoted catalysts are listed in Table 27. To provide deeper insight into the mechanisms of promotion by these additives, it would be advantageous to further compare the reactivity and vanadia surface structures for contrasting promoter loadings. In a similar fashion to what was explored herein for tungsten oxide promoted SCR, the reactivity of vanadia could be compared to different promoter loadings for the other oxides listed. The speciation of vanadia could then be extracted from Raman and NMR to reveal any structural effects these promoters might exhibit. A comparison of vanadia-only to the promoter-vandia system at similar total metal oxide surface coverages would also help distinguish the mechanism of oligomer promotion (such as surface crowding) if such an effect is present. Indeed, such an investigation could propel the understanding of decades of research by further correlating the catalyst structure with the catalytic function.

Table 27. Catalyst formulations for metal-oxide promoted SCR.

Catalyst	**R_{int} (umol/g s)**
V_2O_5-MoO_3/TiO_2	11.1
V_2O_5-WO_3/TiO_2	8.7
V_2O_5-Nb_2O_5/TiO_2	5.0
V_2O_5-GeO_2/TiO_2	4.6
V_2O_5-Fe_2O_3/TiO_2	4.5
V_2O_5/TiO_2	4.2
V_2O_5-CeO_2/TiO_2	3.2
V_2O_5-MnO_2/TiO_2	2.5
V_2O_5-Ga_2O_3/TiO_2	2.5
V_2O_5-La_2O_3/TiO_2	2.3
V_2O_5-SnO_2/TiO_2	1.8
V_2O_5-ZnO/TiO_2	0.7

In this work, supported vanadium oxide was extensively studied by ^{51}V MAS NMR to describe the surface structures present under different conditions and after various treatments; however, other nuclei can offer key insights into the structures present under controlled conditions. Stable intermediates of the chemical constituents may aid in the discernment of the transformations occurring during a reaction, both to the substrate and the catalyst material itself. In the case of vanadia, it was shown that hydrolyzing a bond with water altered its chemical shift, but observing such changes to other nuclei such as ^{1}H or ^{17}O was not possible due to rapid exchange, a dominating, uncontrolled H_2O signal, high background for ^{1}H, and exceptionally poor sensitivity in the case of ^{17}O. Yet, the observation of other nuclei would dramatically enhance the level of detail of the molecular structures present. Mechanistically, capturing such

V–O-C_xH_y species generated during a reaction or the potential protonation of the vanadyl bond during proton abstraction might offer key insights into reaction mechanisms at play for an array of chemical transformations. Both the substrate and metal oxide nucleus could be probed in such instances, providing a multinuclear description of the system. As Chapter 4 described, beginning with the adsorption of the substrate and studying its properties as a function of chemical coverage and temperature can provide hints on the structural transitions that occur. Such investigations would drive forward the knowledge of metal oxide systems, enabling better prediction of material properties.

A controlled, low-temperature exposure of methanol into a vandia catalyst, for example, could help to reveal adsorption modes on vanadia. The convenience of ^{1}H and ^{13}C would enable the combination of three nuclei to describe the NMR system and provide a multinuclear description of the adsorption modes. Once adsorption was established, the temperature of the system could be slowly modulated to stimulate a transition. During the catalytic step which induces reduction, likely several species would become invisible due to the paramagnetic center generated, but this could help solidify the adsorption modes of the substrate prior to reduction. Such investigations should be coupled with *in situ* EPR to provide a description of the reduced vanadia species geometries and abundance. In situ Raman and IR would also compliment the observations made by NMR and would provide further guidance in directing the DFT models used to interpret the NMR data. Such efforts are already underway.

An often-overlooked nucleus is that of ^{17}O. Since it directly interacts with these metal oxide structures, it can also provide detailed information on the configurational changes that occur under different environments or under reaction conditions. With a relatively short

relaxation time, the shortfalls primarily arise from low natural abundance of 0.038% and the relatively broad lines it exhibits in solid materials. This should, however, be regarded as an important future tool when efficient isotopic labeling methods are realized and as NMR technology continues to improve. Such a technique would enable the observation of not only ^{17}O in the solid catalyst, but in substrates as well to provide further reaction intermediate structures.

As the implementation of smaller HTHP rotor designs becomes more commonplace, employing them at higher fields can help reduce the quadrupolar interaction that many metal oxide nuclei (^{25}Mg, ^{27}Al, ^{47}Ti, ^{49}Ti, ^{51}V, ^{55}Mn, ^{67}Zn, ^{91}Zr, ^{183}W, etc.) suffer from while providing sufficient sideband separation. This comes with its own challenges, such as nuclei sensitivity, resource intensity, and relatively exploratory research, but could offer a unique tool to characterize such systems. Already, these smaller *in situ* rotor designs are being used to monitor the degradation of zeolites under hydrothermal conditions with the ^{27}Al nucleus and will continue to represent a powerful tool in future investigations. When coupled with the specially-designed loading chamber, various gaseous atmospheres at a range of pressures and temperatures can be used to understand the coordination of quadrupolar nuclei under additional environments. Combining such features offers limitless possibilities to explore chemical interactions in a way not previously possible.

To overcome some of the challenges associated with the sensitivity of these species and potentially drive research towards time-resolved studies with insensitive or time-consuming nuclei such as vanadia, a relatively new magnetic resonance technique, dynamic nuclear polarization (DNP), can be considered as an important emerging technique for solid state NMR. Signal enhancements of 20 to 400 times are typical and achieved by adding a polarizing agent or

exploiting a radical species already present on the material to transfer polarization from the radical species to the nucleus of interest by microwave irradiation at the EPR frequency. This technique may open the door for challenging 2D experiments not feasible for standard MAS NMR or even time-resolved studies to monitor the restructuring of vanadia during a reaction. Already, this method has been applied to catalytic materials to gain insight that would have not been possible without the dramatic signal enhancement.[319-320] In fact, a mixed oxide material of V-Mo-W was recently investigated by DNP NMR to enhance the vanadium signal by a factor of 50 (note that the experiment time varies with the square of the signal to noise ratio, equating to a time savings of 250 times).[321] This technology could potentially render 2D and time-resolved detection of even vanadium relatively easy compared to the contemporary challenges such an endeavor would pose. It should be stressed that severe complications do exist in materials preparation for DNP NMR where the necessity of a radical species may require the addition of a constituent which alters the structure of the oxide material of interest, but such technical challenges may hold less importance for some specific applications and are more likely to be resolved as DNP NMR becomes a routine characterization technique. The ability to combine the *in situ* NMR technology with advancements afforded by DNP will open up the periodic table for advanced catalyst characterization.

As a demonstrative step towards investigating materials under reactive environments, vanadia SCR catalysts were analyzed after conditions of NH_3 and NO exposure to better understand how SCR gases interact with vanadia species. The first step of the SCR mechanism on vanadium-based catalysts is currently contested, where both ammonia adsorption on Lewis acids or as NH_4^+ on Brønsted acids are observed.[87, 130, 217] The spectra in Figure 5.1 display the ^{51}V NMR spectra for titania-supported vanadia catalysts, which have been exposed to NH_3 and

NO environments. Generally speaking, these impregnated catalyst samples exhibit signal enhancement in the high field region (-607 to -657 ppm) at the expense of signals in the dimeric region, which might indicate preferential adsorption of the gaseous probing molecules to these dimeric sites. In particular, signals in the -580 to -590 ppm region are substantially diminished, and in the case of the tungsten-containing catalyst, appear to shift downfield. Such changes may offer insights into the dynamics of the structural changes that occur to vanadia as the reaction proceeds or even to the bonding modes of these species. If ^{1}H, ^{15}N, and ^{17}O NMR were used to compliment the observation of the metal oxide nucleus, the provided multinuclear illustration of the bonding interactions would provide unprecedented detail into the molecular structures present within the rotor system. Further, as the HTHP rotor technology matures, holding NH_3, NO, O_2, and a mixture thereof in the rotor during analysis and slowly modulating the temperature as described above would provide further details on the structures and mechanisms involved in SCR. This class of investigation by *in situ* NMR may well propel a detailed molecular understanding of oxide systems for a myriad of chemical transformations.

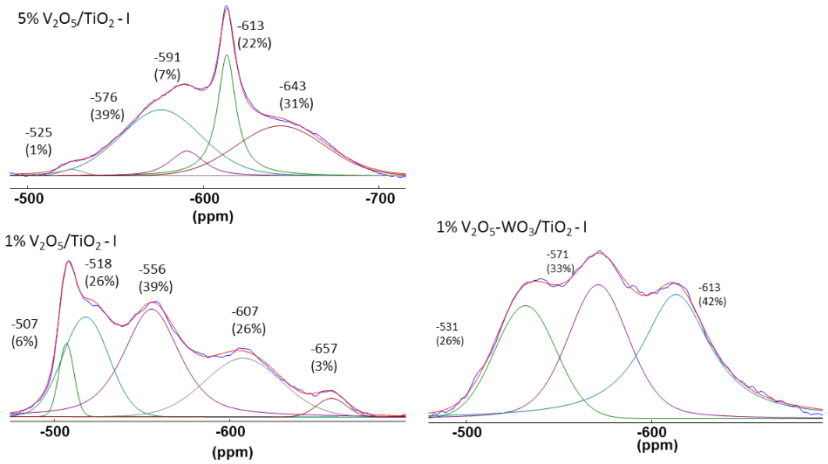

Figure 5.1. ^{51}V MAS NMR results of V_2O_5(-WO_3)/TiO_2 catalysts treated with NH_3 and NO, prepared by impregnation. Spectral deconvolution summation is presented by the red line. All spectra were externally referenced to V_2O_5 at -613.8 ppm.

REFERENCES

1. Research, G. V. *Catalyst Market Size, Share & Trends Analysis Report By Product (Heterogeneous, Homogeneous), By Raw Material (Zeolite, Metals), By Application (Chemical Synthesis, Environmental), And Segment Forecasts, 2019 - 2025*; Grand View Research: 2019; p 250.

2. Levitt, M., *Spin Dynamics: Basics of Nuclear Magnetic Resonance*. John Wiley & Sons: New York, 2001; p 686.

3. Andrew, E. R.; Bradbury, A.; Eades, R. G., *Nature* **1958,** *182* (4650), 1659-1659.

4. Lowe, I. J., *Physical Review Letters* **1959,** *2* (7), 285-287.

5. Maricq, M. M.; Waugh, J. S., *J Chem Phys* **1979,** *70* (7), 3300-3316.

6. Keeler, J., *Understanding NMR Spectroscopy*. 2nd ed.; John Wiley & Sons: 2010.

7. Smith, S. A.; Palke, W. E.; Gerig, J. T., *Concepts in Magnetic Resonance* **1992,** *4* (2), 107-144.

8. Hu, J. Z.; Jaegers, N. R.; Hu, M. Y.; Mueller, K. T., *J Phys-Condens Mat* **2018,** *30* (46).

9. Miyoshi, T.; Takegoshi, K.; Terao, T., *Macromolecules* **1997,** *30* (21), 6582-6585.

10. Miyoshi, T.; Takegoshi, K.; Terao, T., *Polymer* **1997,** *38* (21), 5475-5480.

11. Miyoshi, T.; Takegoshi, K.; Terao, T., *Macromolecules* **2002,** *35* (1), 151-154.

12. Yonker, C. R.; Linehan, J. C., *Progress in Nuclear Magnetic Resonance Spectroscopy* **2005,** *47* (1), 95-109.

13. Deuchande, T.; Breton, O.; Haedelt, J.; Hughes, E., *Journal of Magnetic Resonance* **2006,** *183* (2), 178-182.

14. Hoyt, D. W.; Turcu, R. V. F.; Sears, J. A.; Rosso, K. M.; Burton, S. D.; Felmy, A. R.; Hu, J. Z., *Journal of Magnetic Resonance* **2011,** *212* (2), 378-385.

15. Turcu, R. V. F.; Hoyt, D. W.; Rosso, K. M.; Sears, J. A.; Loring, J. S.; Felmy, A. R.; Hu, J. Z., *J Magn Reson* **2013,** *226*, 64-69.

16. Vjunov, A.; Hu, M. Y.; Feng, J.; Camaioni, D. M.; Mei, D.; Hu, J. Z.; Zhao, C.; Lercher, J. A., *Angewandte Chemie International Edition* **2014,** *53* (2), 479-482.

17. Hu, J. Z.; Hu, M. Y.; Zhao, Z.; Xu, S.; Vjunov, A.; Shi, H.; Camaioni, D. M.; Peden, C. H. F.; Lercher, J. A., *Chemical Communications* **2015,** *51* (70), 13458-13461.

18. Chamas, A.; Qi, L.; Mehta, H. S.; Sears, J. A.; Scott, S. L.; Walter, E. D.; Hoyt, D. W., *Magn Reson Imaging* **2019,** *56*, 37-44.

19. Hu, J. Z.; Hu, M. Y.; Zhao, Z. C.; Xu, S. C.; Vjunov, A.; Shi, H.; Camaioni, D. M.; Peden, C. H. F.; Lercher, J. A., *Chemical Communications* **2015,** *51* (70), 13458-13461.

20. Hunger, M., *Progress in Nuclear Magnetic Resonance Spectroscopy* **2008,** *53* (3), 105-127.

21. Hunger, M., *Catalysis Today* **2004,** *97* (1), 3-12.

22. Hunger, M.; Horvath, T., *J Chem Soc Chem Comm* **1995,** (14), 1423-1424.

23. Hunger, M.; Horvath, T., *J Catal* **1997,** *167* (1), 187-197.

24. Hunger, M.; Horvath, T.; Weitkamp, J., *Micropor Mesopor Mat* **1998,** *22* (1-3), 357-367.

25. Hunger, M.; Seiler, M.; Buchholz, A., *Catal Lett* **2001,** *74* (1-2), 61-68.

26. Jiang, Y. J.; Huang, J.; Marthala, V. R. R.; Ooi, Y. S.; Weitkamp, J.; Hunger, M., *Micropor Mesopor Mat* **2007,** *105* (1-2), 132-139.

27. Hu, J. Z.; Sears, J. A.; Mehta, H. S.; Ford, J. J.; Kwak, J. H.; Zhu, K.; Wang, Y.; Liu, J.; Hoyt, D. W.; Peden, C. H. F., *Physical Chemistry Chemical Physics* **2012,** *14* (7), 2137-2143.

28. Isbester, P. K.; Zalusky, A.; Lewis, D. H.; Douskey, M. C.; Pomije, M. J.; Mann, K. R.; Munson, E. J., *Catalysis Today* **1999,** *49* (4), 363-375.

29. Derouane, E. G.; He, H.; Derouane-Abd Hamid, S. B.; Lambert, D.; Ivanova, I., *Journal of Molecular Catalysis A: Chemical* **2000,** *158* (1), 5-17.

30. Hu, J. Z.; Sears, J. A.; Kwak, J. H.; Hoyt, D. W.; Wang, Y.; Peden, C. H. F., *Journal of Magnetic Resonance* **2009,** *198* (1), 105-110.

31. Durlofsky, L.; Brady, J. F., *Phys Fluids* **1987,** *30* (11), 3329-3341.

32. Macdonald, M. J.; Chu, C. F.; Guilloit, P. P.; Ng, K. M., *Aiche J* **1991,** *37* (10), 1583-1588.

33. Haddix, G. W.; Reimer, J. A.; Bell, A. T., *J Catal* **1987,** *108* (1), 50-54.

34. Haddix, G. W.; Reimer, J. A.; Bell, A. T., *J Catal* **1987,** *106* (1), 111-115.

35. Haddix, G. W.; Bell, A. T.; Reimer, J. A., *Catal Lett* **1988,** *1* (6), 207-212.

36. Haddix, G. W.; Jones, D. H.; Reimer, J. A.; Bell, A. T., *J Catal* **1988,** *112* (2), 556-564.

37. Haddix, G. W.; Bell, A. T.; Reimer, J. A., *The Journal of Physical Chemistry* **1989,** *93* (15), 5859-5865.

38. Weeks, M. E., *Journal of Chemical Education* **1932,** *9* (5), 863.

39. Cook, E., *Nature* **1926,** *117*, 419-421.

40. Wachs, I. E., *Applied Catalysis A: General* **2011,** *391* (1–2), 36-42.

41. Sattler, J. J. H. B.; Ruiz-Martinez, J.; Santillan-Jimenez, E.; Weckhuysen, B. M., *Chem Rev* **2014,** *114* (20), 10613-10653.

42. Wachs, I. E.; Deo, G.; Weckhuysen, B. M.; Andreini, A.; Vuurman, M. A.; Boer, M. d.; Amiridis, M. D., *J Catal* **1996,** *161* (1), 211-221.

43. Wachs, I. E.; Jehng, J.-M.; Deo, G.; Weckhuysen, B. M.; Guliants, V. V.; Benziger, J. B.; Sundaresan, S., *J Catal* **1997,** *170* (1), 75-88.

44. Wachs, I. E., *Dalton Transactions* **2013,** *42* (33), 11762-11769.

45. Langeslay, R. R.; Kaphan, D. M.; Marshall, C. L.; Stair, P. C.; Sattelberger, A. P.; Delferro, M., *Chem Rev* **2019,** *119* (4), 2128-2191.

46. Bleaney, B.; Gregg, J. F.; Wells, M. R., *J Phys C Solid State* **1982,** *15* (11), L349-L352.

47. Duer, M. J.; Farnan, I., *Solid-State NMR Spectroscopy Principles and Applications* **2001**, 179-215.

48. Duer, M. J., *Introduction to Solid-State NMR Spectroscopy*. Wiley-Blackwell: 2005; p 368.

49. Haeberlen, U., *High Resolution NMR in Solids Selective Averaging*. Elsevier Inc.: 1976; p 204.

50. Gerstein, B. C.; Dybowski, C. R., *Transient techniques in NMR of solids: An introduction to theory and practice*. Academic Press Inc.: Orlando, FL, 1983; p 320.

51. Schmidt-Rohr, K.; Spiess, H. W., *Multidimensional Solid-State NMR and Polymers*. London, 1996.

52. Mackenzie, K. J. D.; Smith, M. E., *Multinuclear Solid-State NMR of Inorganic Materials*. Pergamon: New York, 2002; Vol. 6.

53. Man, P. P., Quadrupole Couplins in Nuclear Magnetic Resonance, General. In *Encyclopedia of Analytical Chemistry*, John Wiley & Sons: Chichester, 2002; pp 12224-12265.

54. Eckert, H.; Wachs, I. E., *J. Phys. Chem.* **1989,** *93*, 6796.

55. Luca, V.; Thomson, S.; Howe, R. F., *J Chem Soc Faraday T* **1997,** *93* (12), 2195-2202.

56. Kalinkin, P.; Kovalenko, O.; Lapina, O.; Khabibulin, D.; Kundo, N., *J Mol Catal a-Chem* **2002,** *178* (1-2), 173-180.

57. Borovkov, V. Y.; Mikheeva, E. P.; Zhidomirov, G. M.; Lapina, O. B., *Kinet Catal+* **2003,** *44* (5), 710-717.

58. Jaegers, N. R.; Lai, J. K.; He, Y.; Walter, E.; Dixon, D. A.; Vasiliu, M.; Chen, Y.; Wang, C. M.; Hu, M. Y.; Mueller, K. T.; Wachs, I. E.; Wang, Y.; Hu, J. Z., *Angew Chem Int Edit* **2019,** *131*, 12739-12746.

59. Wachs, I. E., *Catalysis Today* **2005,** *100* (1–2), 79-94.

60. Roozeboom, F.; Mittelmeijer-Hazeleger, M. C.; Moulijn, J. A.; Medema, J.; De Beer, V. H. J.; Gellings, P. J., *The Journal of Physical Chemistry* **1980,** *84* (21), 2783-2791.

61. Gao, X.; Bare, S. R.; Weckhuysen, B. M.; Wachs, I. E., *The Journal of Physical Chemistry B* **1998,** *102* (52), 10842-10852.

62. Magg, N.; Immaraporn, B.; Giorgi, J. B.; Schroeder, T.; Bäumer, M.; Döbler, J.; Wu, Z.; Kondratenko, E.; Cherian, M.; Baerns, M.; Stair, P. C.; Sauer, J.; Freund, H.-J., *J Catal* **2004,** *226* (1), 88-100.

63. Islam, M. M.; Costa, D.; Calatayud, M.; Tielens, F., *The Journal of Physical Chemistry C* **2009,** *113* (24), 10740-10746.

64. Keller, D. E.; Visser, T.; Soulimani, F.; Koningsberger, D. C.; Weckhuysen, B. M., *Vibrational Spectroscopy* **2007,** *43* (1), 140-151.

65. Tian, H.; Ross, E. I.; Wachs, I. E., *The Journal of Physical Chemistry B* **2006,** *110* (19), 9593-9600.

66. Gao, X.; Bare, S. R.; Fierro, J. L. G.; Banares, M. A.; Wachs, I. E., *The Journal of Physical Chemistry B* **1998,** *102* (29), 5653-5666.

67. Bulánek, R.; Čičmanec, P.; Setnička, M., *Physics Procedia* **2013,** *44*, 195-205.

68. Cavalleri, M.; Hermann, K.; Knop-Gericke, A.; Hävecker, M.; Herbert, R.; Hess, C.; Oestereich, A.; Döbler, J.; Schlögl, R., *J Catal* **2009,** *262* (2), 215-223.

69. Zhu, H.; Ould-Chikh, S.; Dong, H.; Llorens, I.; Saih, Y.; Anjum, D. H.; Hazemann, J.-L.; Basset, J.-M., *ChemCatChem* **2015,** *7* (20), 3332-3339.

70. Das, N.; Eckert, H.; Hu, H.; Wachs, I. E.; Walzer, J. F.; Feher, F. J., *The Journal of Physical Chemistry* **1993,** *97* (31), 8240-8243.

71. Lapina, O. B.; Shubin, A. A.; Khabibulin, D. F.; Terskikh, V. V.; Bodart, P. R.; Amoureux, J. P., *Catalysis Today* **2003,** *78* (1–4), 91-104.

72. Schimmoeller, B.; Jiang, Y.; Pratsinis, S. E.; Baiker, A., *J Catal* **2010,** *274* (1), 64-75.

73. Grant, J. T.; Carrero, C. A.; Love, A. M.; Verel, R.; Hermans, I., *ACS Catalysis* **2015,** *5* (10), 5787-5793.

74. Barman, S.; Maity, N.; Bhatte, K.; Ould-Chikh, S.; Dachwald, O.; Haeßner, C.; Saih, Y.; Abou-Hamad, E.; Llorens, I.; Hazemann, J.-L.; Köhler, K.; D' Elia, V.; Basset, J.-M., *ACS Catalysis* **2016,** *6* (9), 5908-5921.

75. Shubin, A. A.; Lapina, O. B.; Bosch, E.; Spengler, J.; Knözinger, H., *The Journal of Physical Chemistry B* **1999,** *103* (16), 3138-3144.

76. Lapina, O. B.; Shubin, A. A.; Nosov, A. V.; Bosch, E.; Spengler, J.; Knözinger, H., *The Journal of Physical Chemistry B* **1999,** *103* (36), 7599-7606.

77. Hu, J. Z.; Xu, S.; Li, W.-Z.; Hu, M. Y.; Deng, X.; Dixon, D. A.; Vasiliu, M.; Craciun, R.; Wang, Y.; Bao, X.; Peden, C. H. F., *ACS Catalysis* **2015,** *5* (7), 3945-3952.

78. Downs, R. T.; Hall-Wallace, M., *American Mineralogist* **2003,** *88* (1), 247-250.

79. Love, A. M.; Carrero, C. A.; Chieregato, A.; Grant, J. T.; Conrad, S.; Verel, R.; Hermans, I., *Chemistry of Materials* **2016,** *28* (15), 5495-5504.

80. Tielens, F.; Gervais, C.; Lambert, J. F.; Mauri, F.; Costa, D., *Chem Mater* **2008,** *20* (10), 3336-3344.

81. de Oliveira Jr, M.; Seeburg, D.; Weiss, J.; Wohlrab, S.; Buntkowsky, G.; Bentrup, U.; Gutmann, T., *Catalysis Science & Technology* **2019**.

82. Skalska, K.; Miller, J. S.; Ledakowicz, S., *Science of The Total Environment* **2010,** *408* (19), 3976-3989.

83. Khivantsev, K.; Jaegers, N. R.; Kovarik, L.; Hanson, J. C.; Tao, F.; Tang, Y.; Zhang, X. Y.; Koleva, I. Z.; Aleksandrov, H. A.; Vayssilov, G. N.; Wang, Y.; Gao, F.; Szanyi, J., *Angew Chem Int Edit* **2018,** *57* (51), 16672-16677.

84. Tao, P.; Sun, M. H.; Qu, S. C.; Song, C. W.; Li, C.; Yin, Y. Y.; Cheng, M. R., *Global NEST Journal* **2017,** *19* (1), 160-166.

85. Agency, I. E. *Energy and Air Pollution: World Energy Outlook Special Reoprt*; International Energy Agency: Paris, 2016, 2016; p 266.

86. Lai, J.-K.; Wachs, I. E., *ACS Catalysis* **2018,** *8* (7), 6537-6551.

87. Marberger, A.; Ferri, D.; Elsener, M.; Krocher, O., *Angew Chem Int Edit* **2016,** *55* (39), 11989-11994.

88. Zhu, M. H.; Lai, J. K.; Tumuluri, U.; Wu, Z. L.; Wachs, I. E., *Journal of the American Chemical Society* **2017,** *139* (44), 15624-15627.

89. Busca, G.; Lietti, L.; Ramis, G.; Berti, F., *Applied Catalysis B: Environmental* **1998,** *18* (1), 1-36.

90. Amiridis, M. D.; Solar, J. P., *Industrial & Engineering Chemistry Research* **1996,** *35* (3), 978-981.

91. Topsoe, N. Y.; Dumesic, J. A.; Topsoe, H., *J Catal* **1995,** *151* (1), 241-252.

92. Ozkan, U. S.; Cai, Y. P.; Kumthekar, M. W., *J Catal* **1994,** *149* (2), 390-403.

93. Zhu, M.; Lai, J.-K.; Tumuluri, U.; Ford, M. E.; Wu, Z.; Wachs, I. E., *ACS Catalysis* **2017,** *7* (12), 8358-8361.

94. Janssen, F. J. J. G.; Van den Kerkhof, F. M. G.; Bosch, H.; Ross, J. R. H., *The Journal of Physical Chemistry* **1987,** *91* (27), 6633-6638.

95. Ozkan, U. S.; Cai, Y.; Kumthekar, M. W., *The Journal of Physical Chemistry* **1995,** *99* (8), 2363-2371.

96. Ozkan, U. S.; Cai, Y. P.; Kumthekar, M. W., *J Catal* **1994,** *149* (2), 375-389.

97. He, Y.; Ford, M. E.; Zhu, M.; Liu, Q.; Tumuluri, U.; Wu, Z.; Wachs, I. E., *Applied Catalysis B: Environmental* **2016,** *193*, 141-150.

98. Yu, W.; Wu, X.; Si, Z.; Weng, D., *Applied Surface Science* **2013,** *283* (Supplement C), 209-214.

99. Marberger, A.; Elsener, M.; Ferri, D.; Kröcher, O., *Catalysts* **2015,** *5* (4).

100. Lee, B. W.; Cho, H.; Shin, D. W., *Journal of Ceramic Processing Research* **2007,** *8* (3), 203-207.

101. Lietti, L.; Forzatti, P.; Bregani, F., *Industrial & Engineering Chemistry Research* **1996,** *35* (11), 3884-3892.

102. Chen, C.; Cao, Y.; Liu, S.; Chen, J.; Jia, W., *Chinese Journal of Catalysis* **2018,** *39* (8), 1347-1365.

103. Lietti, L.; Nova, I.; Forzatti, P., *Topics in Catalysis* **2000,** *11* (1), 111-122.

104. He, G. Z.; Lian, Z. H.; Yu, Y. B.; Yang, Y.; Liu, K.; Shi, X. Y.; Yan, Z. D.; Shan, W. P.; He, H., *Sci Adv* **2018,** *4* (11).

105. Xiao, X.; Xiong, S.; Li, B.; Geng, Y.; Yang, S., *Catal Lett* **2016,** *146* (11), 2242-2251.

106. Chen, J. P.; Yang, R. T., *Applied Catalysis A: General* **1992,** *80* (1), 135-148.

107. Vuurman, M. A.; Wachs, I. E.; Hirt, A. M., *The Journal of Physical Chemistry* **1991,** *95* (24), 9928-9937.

108. Deo, G.; Wachs, I. E., *J Catal* **1994,** *146* (2), 323-334.

109. Jaegers, N. R.; Wan, C.; Hu, M. Y.; Vasiliu, M.; Dixon, D. A.; Walter, E.; Wachs, I. E.; Wang, Y.; Hu, J. Z., *J Phys Chem C* **2017,** *121* (11), 6246-6254.

110. Burkardt, A.; Weisweiler, W.; van den Tillaart, J. A. A.; Schäfer-Sindlinger, A.; Lox, E. S., *Topics in Catalysis* **2001,** *16-17* (1-4), 369-375.

111. Shubin, A. A.; Lapina, O. B.; Courcot, D., *Catalysis Today* **2000,** *56* (4), 379-387.

112. Nielsen, U. G.; Topsøe, N.-Y.; Brorson, M.; Skibsted, J.; Jakobsen, H. J., *J Am Chem Soc* **2004,** *126* (15), 4926-4933.

113. Gheorghe, C.; Gee, B., *Chem Mater* **2000,** *12* (3), 682-685.

114. Ettireddy, P. R.; Ettireddy, N.; Mamedov, S.; Boolchand, P.; Smirniotis, P. G., *Applied Catalysis B: Environmental* **2007,** *76* (1), 123-134.

115. Ek, M.; Ramasse, Q. M.; Arnarson, L.; Georg Moses, P.; Helveg, S., *Nature Communications* **2017,** *8* (1), 305.

116. Jehng, J. M.; Deo, G.; Weckhuysen, B. M.; Wachs, I. E., *J Mol Catal a-Chem* **1996,** *110* (1), 41-54.

117. Kim, D. S.; Ostromecki, M.; Wachs, I. E., *Journal of Molecular Catalysis A: Chemical* **1996,** *106* (1), 93-102.

118. Tian, H.; Ross, E. I.; Wachs, I. E., *J Phys Chem B* **2006,** *110* (19), 9593-9600.

119. Guerrero-Pérez, M. O., *Supported, bulk and bulk-supported vanadium oxide catalysts: A short review with an historical perspective*. 2017.

120. Guimond, S.; Abu Haija, M.; Kaya, S.; Lu, J.; Weissenrieder, J.; Shaikhutdinov, S.; Kuhlenbeck, H.; Freund, H. J.; Döbler, J.; Sauer, J., *Topics in Catalysis* **2006,** *38* (1), 117-125.

121. Lewandowska, A. E.; Calatayud, M.; Tielens, F.; Banares, M. A., *J Phys Chem C* **2011,** *115* (49), 24133-24142.

122. Brazdova, V.; Ganduglia-Pirovano, M. V.; Sauer, J., *J Phys Chem B* **2005,** *109* (49), 23532-23542.

123. Eckert, H.; Wachs, I. E., *The Journal of Physical Chemistry* **1989,** *93* (18), 6796-6805.

124. Luca, V.; Thomson, S.; F. Howe, R., *Journal of the Chemical Society, Faraday Transactions* **1997,** *93* (12), 2195-2202.

125. Borovkov, V. Y.; Mikheeva, E. P.; Zhidomirov, G. M.; Lapina, O. B., *Kinetics and Catalysis* **2003,** *44* (5), 710-717.

126. Li, W.-Z.; Gao, F.; Li, Y.; Walter, E. D.; Liu, J.; Peden, C. H. F.; Wang, Y., *The Journal of Physical Chemistry C* **2015,** *119* (27), 15094-15102.

127. Kraemer, S.; Rondinone, A. J.; Tsai, Y.-T.; Schwartz, V.; Overbury, S. H.; Idrobo, J.-C.; Wu, Z., *Catalysis Today* **2016,** *263*, 84-90.

128. Du, Y.-J.; Li, Z. H.; Fan, K.-N., *Surface Science* **2012,** *606* (11), 956-964.

129. Arnarson, L.; Rasmussen, S. B.; Falsig, H.; Lauritsen, J. V.; Moses, P. G., *The Journal of Physical Chemistry C* **2015,** *119* (41), 23445-23452.

130. Arnarson, L.; Falsig, H.; Rasmussen, S. B.; Lauritsen, J. V.; Moses, P. G., *Physical Chemistry Chemical Physics* **2016,** *18* (25), 17071-17080.

131. Dunn, J. P.; Stenger, H. G.; Wachs, I. E., *Catalysis Today* **1999,** *53* (4), 543-556.

132. He, Y.; Ford, M. E.; Zhu, M.; Liu, Q.; Wu, Z.; Wachs, I. E., *Applied Catalysis B: Environmental* **2016,** *188*, 123-133.

133. Zhang, S.; Zhong, Q., *Journal of Solid State Chemistry* **2015,** *221* (Supplement C), 49-56.

134. Ettireddy, P. R.; Ettireddy, N.; Mamedov, S.; Boolchand, P.; Smirniotis, P. G., *Appl Catal B-Environ* **2007,** *76* (1-2), 123-134.

135. Alemany, L. J.; Lietti, L.; Ferlazzo, N.; Forzatti, P.; Busca, G.; Giamello, E.; Bregani, F., *J Catal* **1995,** *155* (1), 117-130.

136. Ramis, G.; Busca, G.; Cristiani, C.; Lietti, L.; Forzatti, P.; Bregani, F., *Langmuir* **1992,** *8* (7), 1744-1749.

137. Suarez Negreira, A.; Wilcox, J., *The Journal of Physical Chemistry C* **2013,** *117* (46), 24397-24406.

138. Kompio, P. G. W. A.; Brückner, A.; Hipler, F.; Auer, G.; Löffler, E.; Grünert, W., *J Catal* **2012,** *286* (Supplement C), 237-247.

139. Wang, C.; Yang, S.; Chang, H.; Peng, Y.; Li, J., *Chemical Engineering Journal* **2013,** *225* (Supplement C), 520-527.

140. Li, J. H.; Peng, Y.; Chang, H. Z.; Li, X.; Crittenden, J.; Hao, J. M., *Front Env Sci Eng* **2016,** *10* (3), 413-427.

141. Dunn, J. P.; Stenger, H. G.; Wachs, I. E., *J Catal* **1999,** *181* (2), 233-243.

142. Choo, S. T.; Lee, Y. G.; Nam, I. S.; Ham, S. W.; Lee, J. B., *Appl Catal a-Gen* **2000,** *200* (1-2), 177-188.

143. Lee, E. L.; Wachs, I. E., *J Catal* **2008,** *258* (1), 103-110.

144. Wu, Z. L.; Schwartz, V.; Li, M. J.; Rondinone, A. J.; Overbury, S. H., *J Phys Chem Lett* **2012,** *3* (11), 1517-1522.

145. Li, W.-Z.; Gao, F.; Li, Y.; Walter, E. D.; Liu, J.; Peden, C. H. F.; Wang, Y., *J Phys Chem C* **2015,** *119* (27), 15094-15102.

146. Han, X. G.; Wang, X.; Xie, S. F.; Kuang, Q.; Ouyang, J. J.; Xie, Z. X.; Zheng, L. S., *Rsc Adv* **2012,** *2* (8), 3251-3253.

147. Ong, W. J.; Tan, L. L.; Chai, S. P.; Yong, S. T.; Mohamed, A. R., *Nanoscale* **2014,** *6* (4), 1946-2008.

148. Liu, G.; Yang, H. G.; Pan, J.; Yang, Y. Q.; Lu, G. Q.; Cheng, H. M., *Chem Rev* **2014,** *114* (19), 9559-9612.

149. Hu, J. Z.; Xu, S. C.; Li, W. Z.; Hu, M. Y.; Deng, X. C.; Dixon, D. A.; Vasiliu, M.; Craciun, R.; Wang, Y.; Bao, X. H.; Peden, C. H. F., *Acs Catal* **2015,** *5* (7), 3945-3952.

150. Carrero, C. A.; Schloegl, R.; Wachs, I. E.; Schomaecker, R., *Acs Catalysis* **2014,** *4* (10), 3357-3380.

151. Li, Y.; Wei, Z. H.; Sun, J. M.; Gao, F.; Peden, C. H. F.; Wang, Y., *J Phys Chem C* **2013,** *117* (11), 5722-5729.

152. Peng, Y.; Li, J. H.; Huang, X.; Li, X.; Su, W. K.; Sun, X. X.; Wang, D. Z.; Hao, J. M., *Environ Sci Technol* **2014,** *48* (8), 4515-4520.

153. Deo, G.; Wachs, I. E., *J Catal* **1994,** *146* (2), 335-345.

154. Yang, S.; Yang, B. X.; Wu, L.; Li, Y. H.; Liu, P. R.; Zhao, H. J.; Yu, Y. Y.; Gong, X. Q.; Yang, H. G., *Nature Communications* **2014,** *5*.

155. Solsona, B.; Blasco, T.; López Nieto, J. M.; Peña, M. L.; Rey, F.; Vidal-Moya, A., *J Catal* **2001,** *203* (2), 443-452.

156. Liu, Y.-M.; Cao, Y.; Zhu, K.-K.; Yan, S.-R.; Dai, W.-L.; He, H.-Y.; Fan, K.-N., *Chemical Communications* **2002,** (23), 2832-2833.

157. Liu, Y.-M.; Cao, Y.; Yi, N.; Feng, W.-L.; Dai, W.-L.; Yan, S.-R.; He, H.-Y.; Fan, K.-N., *J Catal* **2004,** *224* (2), 417-428.

158. Gruene, P.; Wolfram, T.; Pelzer, K.; Schlögl, R.; Trunschke, A., *Catalysis Today* **2010,** *157* (1–4), 137-142.

159. Phanikrishna Sharma, M. V.; Durga Kumari, V.; Subrahmanyam, M., *Chemosphere* **2008,** *73* (9), 1562-1569.

160. Yang, H.-C.; Lin, H.-Y.; Chien, Y.-S.; Wu, J.-S.; Wu, H.-H., *Catal Lett* **2009,** *131* (3-4), 381-387.

161. Tomer, V. K.; Jangra, S.; Malik, R.; Duhan, S., *Colloids and Surfaces A: Physicochemical and Engineering Aspects* **2015,** *466*, 160-165.

162. Li, Y.; Li, N.; Tu, J.; Li, X.; Wang, B.; Chi, Y.; Liu, D.; Yang, D., *Materials Research Bulletin* **2011,** *46* (12), 2317-2322.

163. Dinse, A.; Wolfram, T.; Carrero, C.; Schlögl, R.; Schomäcker, R.; Dinse, K. P., *The Journal of Physical Chemistry C* **2013,** *117* (33), 16921-16932.

164. Monaci, R.; Rombi, E.; Solinas, V.; Sorrentino, A.; Santacesaria, E.; Colon, G., *Applied Catalysis A: General* **2001,** *214* (2), 203-212.

165. Karakoulia, S. A.; Triantafyllidis, K. S.; Tsilomelekis, G.; Boghosian, S.; Lemonidou, A. A., *Catalysis Today* **2009,** *141* (3–4), 245-253.

166. Karakoulia, S. A.; Triantafyllidis, K. S.; Lemonidou, A. A., *Micropor Mesopor Mat* **2008,** *110* (1), 157-166.

167. Gao, X.; Wachs, I. E., *J Catal* **2000,** *192* (1), 18-28.

168. Sato, S.; Toita, M.; Sodesawa, T.; Nozaki, F., *Applied Catalysis* **1990,** *62* (1), 73-84.

169. 2 - Chemical Periodicity and the Periodic Table. In *Chemistry of the Elements (Second Edition)*, Greenwood, N. N.; Earnshaw, A., Eds. Butterworth-Heinemann: Oxford, 1997; pp 20-31.

170. Lee, E. L.; Wachs, I. E., *The Journal of Physical Chemistry C* **2007,** *111* (39), 14410-14425.

171. Lee, E. L.; Wachs, I. E., *The Journal of Physical Chemistry C* **2008,** *112* (16), 6487-6498.

172. Turek, A. M.; Wachs, I. E.; DeCanio, E., *The Journal of Physical Chemistry* **1992,** *96* (12), 5000-5007.

173. Gao, X.; Fierro, J. L. G.; Wachs, I. E., *Langmuir* **1999,** *15* (9), 3169-3178.

174. Beck, B.; Harth, M.; Hamilton, N. G.; Carrero, C.; Uhlrich, J. J.; Trunschke, A.; Shaikhutdinov, S.; Schubert, H.; Freund, H.-J.; Schlögl, R.; Sauer, J.; Schomäcker, R., *J Catal* **2012,** *296*, 120-131.

175. Kim, H. Y.; Lee, H. M.; Pala, R. G. S.; Shapovalov, V.; Metiu, H., *The Journal of Physical Chemistry C* **2008,** *112* (32), 12398-12408.

176. Gao, X.; Bare, S. R.; Fierro, J. L. G.; Wachs, I. E., *The Journal of Physical Chemistry B* **1999,** *103* (4), 618-629.

177. Comite, A.; Sorrentino, A.; Capannelli, G.; Di Serio, M.; Tesser, R.; Santacesaria, E., *Journal of Molecular Catalysis A: Chemical* **2003,** *198* (1–2), 151-165.

178. Knozinger, H.; Taglauer, E., Toward supported odxide catalysts via solid-solid wetting. In *Catalysis: Volume 10*, Spivey, J. J.; Agarwal, S. K., Eds. The Royal Society of Chemistry: 1993; Vol. 10, pp 1-40.

179. Herrera, J.; Kwak, J.; Hu, J.; Wang, Y.; Peden, C. F., *Topics in Catalysis* **2006,** *39* (3-4), 245-255.

180. Van Hengstum, A. J.; Van Ommen, J. G.; Bosch, H.; Gellings, P. J., *Applied Catalysis* **1983,** *5* (2), 207-217.

181. Gao, X.; Wachs, I., *Topics in Catalysis* **2002,** *18* (3-4), 243-250.

182. Zukerman, R.; Vradman, L.; Titelman, L.; Weidenthaler, C.; Landau, M. V.; Herskowitz, M., *Micropor Mesopor Mat* **2008,** *116* (1–3), 237-245.

183. Zukerman, R.; Vradman, L.; Titelman, L.; Zeiri, L.; Perkas, N.; Gedanken, A.; Landau, M. V.; Herskowitz, M., *Materials Chemistry and Physics* **2010,** *122* (1), 53-59.

184. Lapina, O. B.; Mastikhin, V. M.; Shubin, A. A.; Krasilnikov, V. N.; Zamaraev, K. I., *Progress in Nuclear Magnetic Resonance Spectroscopy* **1992,** *24* (6), 457-525.

185. Eckert, H.; Wacjs, I. E., *MRS Online Proceedings Library Archive* **1987,** *111*, null-null.

186. Nickl, J.; Dutoit, D.; Baiker, A.; Scharf, U.; Wokaun, A., *Applied Catalysis A: General* **1993,** *98* (2), 173-193.

187. Miller, J. M.; Lakshmi, L. J., *Applied Catalysis A: General* **2000,** *190* (1–2), 197-206.

188. Vining, W. C.; Strunk, J.; Bell, A. T., *J Catal* **2011,** *281* (2), 222-230.

189. Kwak, J. H.; Herrera, J. E.; Hu, J. Z.; Wang, Y.; Peden, C. H. F., *Applied Catalysis A: General* **2006,** *300* (2), 109-119.

190. Lapina, O. B.; Nosov, A. V.; Mastikhin, V. M.; Dubkov, K. A.; Mokrinski, V. V., *Journal of Molecular Catalysis* **1994,** *87* (1), 57-66.

191. Mastikhin, V. M.; Terskikh, V. V.; Lapina, O. B.; Filimonova, S. V.; Seidl, M.; Knözinger, H., *Solid State Nuclear Magnetic Resonance* **1995,** *4* (6), 369-379.

192. Chan, S. S.; Wachs, I. E.; Murrell, L. L.; Wang, L.; Hall, W. K., *The Journal of Physical Chemistry* **1984,** *88* (24), 5831-5835.

193. Yoshida, S.; Tanaka, T.; Hanada, T.; Hiraiwa, T.; Kanai, H.; Funabiki, T., *Catal Lett* **1992,** *12* (1-3), 277-285.

194. Wu, Z.; Dai, S.; Overbury, S. H., *The Journal of Physical Chemistry C* **2010,** *114* (1), 412-422.

195. Baes, C. F.; Messmer, R. E., *The Hydrolysis of Cations*. John Wiley & Sons Inc: 1976.

196. Deo, G.; Wachs, I. E., *The Journal of Physical Chemistry* **1991,** *95* (15), 5889-5895.

197. Xie, S.; Iglesia, E.; Bell, A. T., *Langmuir* **2000,** *16* (18), 7162-7167.

198. Pozarnsky, G. A.; McCormick, A. V., *Chem Mater* **1994,** *6* (4), 380-385.

199. Repelin, Y.; Husson, E.; Abello, L.; Lucazeau, G., *Spectrochimica Acta Part A: Molecular Spectroscopy* **1985,** *41* (8), 993-1003.

200. Abello, L.; Husson, E.; Repelin, Y.; Lucazeau, G., *Journal of Solid State Chemistry* **1985,** *56* (3), 379-389.

201. Kristoffersen, H. H.; Metiu, H., *The Journal of Physical Chemistry C* **2016,** *120* (7), 3986-3992.

202. Nabavi, M.; Taulelle, F.; Sanchez, C.; Verdaguer, M., *Journal of Physics and Chemistry of Solids* **1990,** *51* (12), 1375-1382.

203. Nabavi, M.; Sanchez, C.; Livage, J., *Philosophical Magazine Part B* **1991,** *63* (4), 941-953.

204. Luca, V.; Hook, J. M., *Chem Mater* **1997,** *9* (12), 2731-2744.

205. Fontenot, C. J.; Wiench, J. W.; Pruski, M.; Schrader, G. L., *The Journal of Physical Chemistry B* **2001,** *105* (43), 10496-10504.

206. Fontenot, C. J.; Wiench, J. W.; Schrader, G. L.; Pruski, M., *J Am Chem Soc* **2002,** *124* (28), 8435-8444.

207. Durupthy, O.; Steunou, N.; Coradin, T.; Maquet, J.; Bonhomme, C.; Livage, J., *Journal of Materials Chemistry* **2005,** *15* (10), 1090-1098.

208. Lewandowska, A. E.; Calatayud, M.; Tielens, F.; Banares, M. A., *J Phys Chem C* **2013,** *117* (48), 25535-25544.

209. Avdeev, V. I.; Tapilin, V. M., *J Phys Chem C* **2010,** *114* (8), 3609-3613.

210. Kortewille, B.; Wachs, I. E.; Cibura, N.; Pfingsten, O.; Bacher, G.; Muhler, M.; Strunk, J., *Eur J Inorg Chem* **2018,** (33), 3725-3735.

211. Chapman, D. M., *Applied Catalysis A: General* **2011,** *392* (1), 143-150.

212. Busca, G.; Lietti, L.; Ramis, G.; Berti, F., *Appl Catal B-Environ* **1998,** *18* (1-2), 1-36.

213. Madia, G.; Elsener, M.; Koebel, M.; Raimondi, F.; Wokaun, A., *Appl Catal B-Environ* **2002,** *39* (2), 181-190.

214. Turco, M.; Lisi, L.; Pirone, R.; Ciambelli, P., *Appl Catal B-Environ* **1994,** *3* (2-3), 133-149.

215. Nova, I.; Acqua, L. D.; Lietti, L.; Giamello, E.; Forzatti, P., *Appl Catal B-Environ* **2001,** *35* (1), 31-42.

216. Barceloux, D. G., *J Toxicol-Clin Toxic* **1999,** *37* (2), 265-278.

217. Zhu, M.; Lai, J.-K.; Tumuluri, U.; Wu, Z.; Wachs, I. E., *J Am Chem Soc* **2017,** *139* (44), 15624-15627.

218. Gallay, R.; Van der Klink, J. J.; Moser, J. EPR study of vanadium (4+) in the anatase and rutile phases of TiO2, p. 3060-3068-3060-3068. http://infoscience.epfl.ch/record/164391/files/PhysRevB.34.3060.pdf (accessed 1986).

219. Luca, V.; MacLachlan, D. J.; Bramley, R., *Physical Chemistry Chemical Physics* **1999,** *1* (10), 2597-2606.

220. Marberger, A. Adances in Vanadium-Based Catalyst Research for the Selective Catalytic Redcution of NOx by NH3. Ecole Polytechnique Federale De Lausanne, 2017.

221. Yun, D. M.; Song, Y.; Herrera, J., *Chemcatchem* **2017,** *9* (19), 3655-3669.

222. Yun, D. M.; Herrera, J. E., *J Catal* **2017,** *350*, 72-85.

223. Schramlmarth, M.; Wokaun, A.; Baiker, A., *J Catal* **1990,** *124* (1), 86-96.

224. Vittadini, A.; Selloni, A., *J Phys Chem B* **2004,** *108* (22), 7337-7343.

225. Saha, N. C.; Tompkins, H. G., *J Appl Phys* **1992,** *72* (7), 3072-3079.

226. Asahi, R.; Morikawa, T.; Irie, H.; Ohwaki, T., *Chem Rev* **2014,** *114* (19), 9824-9852.

227. Lee, J. K.; Walker, K. L.; Han, H. S.; Kang, J.; Prinz, F. B.; Waymouth, R. M.; Nam, H. G.; Zare, R. N., *Proceedings of the National Academy of Sciences* **2019**, 201911883.

228. Chen, K.; Damron, J.; Pearson, C.; Resasco, D.; Zhang, L.; White, J. L., *ACS Catalysis* **2014,** *4* (9), 3039-3044.

229. Hibbitts, D. D.; Loveless, B. T.; Neurock, M.; Iglesia, E., *Angewandte Chemie International Edition* **2013,** *52* (47), 12273-12278.

230. Wang, M.; Jaegers, N. R.; Lee, M. S.; Wan, C.; Hu, J. Z.; Shi, H.; Mei, D. H.; Burton, S. D.; Camaioni, D. M.; Gutierrez, O. Y.; Glezakou, V. A.; Rousseau, R.; Wang, Y.; Lercher, J. A., *J Am Chem Soc* **2019,** *141* (8), 3444-3455.

231. Sattig, M.; Reutter, S.; Fujara, F.; Werner, M.; Buntkowsky, G.; Vogel, M., *Physical Chemistry Chemical Physics* **2014,** *16* (36), 19229-19240.

232. Jaegers, N. R.; Wan, C.; Hu, M. Y.; Vasiliu, M.; Dixon, D. A.; Walter, E.; Wachs, I. E.; Wang, Y.; Hu, J. Z., *J Phys Chem C* **2017,** *121* (11), 6246-6254.

233. Khivantsev, K.; Jaegers, N. R.; Kovarik, L.; Prodinger, S.; Derewinski, M. A.; Wang, Y.; Gao, F.; Szanyi, J., *Appl Catal a-Gen* **2019,** *569*, 141-148.

234. Gottlieb, H. E.; Kotlyar, V.; Nudelman, A., *J Org Chem* **1997,** *62* (21), 7512-7515.

235. Jaegers, N. R.; Hu, M. Y.; Hoyt, D. W.; Wang, Y.; Hu, J. Z., Development and Application of In Situ High-Temperature, High-Pressure Magic Angle Spinning NMR. In *Modern Magnetic Resonance*, Webb, G. A., Ed. Springer International Publishing: Cham, 2017; pp 1-19.

236. Bluhm, H.; Ogletree, D. F.; Fadley, C. S.; Hussain, Z.; Salmeron, N., *J Phys-Condens Mat* **2002,** *14* (8), L227-L233.

237. Florin, A. E.; Alei, M., *J Chem Phys* **1967,** *47* (10), 4268-&.

238. Mallamace, F.; Corsaro, C.; Stanley, H. E., *Scientific Reports* **2012,** *2*, 993.

239. Pfrommer, B. G.; Mauri, F.; Louie, S. G., *J Am Chem Soc* **2000,** *122* (1), 123-129.

240. Hansen, E. W.; Stocker, M.; Schmidt, R., *J Phys Chem-Us* **1996,** *100* (6), 2195-2200.

241. Perry, R. H.; Green, D. W.; Maloney, J. O., *Perry's Chemical Engineers' Handbook*. McGraw-Hill: 1999.

242. Siskos, M. G.; Choudhary, M. I.; Gerothanassis, I. P., *Molecules* **2017,** *22* (3).

243. Klein, R. A.; Mennuci, B.; Tomasi, J., *J Phys Chem A* **2004,** *108* (27), 5851-5863.

244. Feyereisen, M. W.; Feller, D.; Dixon, D. A., *J Phys Chem-Us* **1996,** *100* (8), 2993-2997.

245. Balevicius, V.; Aidas, K., *Appl Magn Reson* **2007,** *32* (3), 363-376.

246. Sergeyev, N. M.; Sergeyeva, N. D.; Strelenko, Y. A.; Raynes, W. T., *Chem Phys Lett* **1997,** *277* (1-3), 142-146.

247. Sergeyev, N. M.; Sergeyeva, N. D.; Raynes, W. T., *Journal of Magnetic Resonance* **1999,** *137* (2), 311-315.

248. Ammann, C.; Meier, P.; Merbach, A. E., *Journal of Magnetic Resonance* **1982,** *46* (2), 319-321.

249. Corma, A., *Chem. Rev.* **1995,** *95* (3), 559-614.

250. Jentoft, F. C.; Gates, B. C., *Top. Catal.* **1997,** *4* (1), 1-13.

251. de Klerk, A.; Nel, R. J. J., *Ind. Eng. Chem. Res.* **2007,** *46* (22), 7066-7072.

252. Zhang, M.; Yu, Y., *Ind. Eng. Chem. Res.* **2013,** *52* (28), 9505-9514.

253. Kramer, G. J.; van Santen, R. A.; Emeis, C. A.; Nowak, A. K., *Nature* **1993,** *363* (6429), 529-531.

254. Vermeiren, W.; Gilson, J.-P., *Top. Catal.* **2009,** *52* (9), 1131-1161.

255. Martínez, C.; Corma, A., *Coord. Chem. Rev.* **2011,** *255* (13–14), 1558-1580.

256. Primo, A.; Garcia, H., *Chem. Soc. Rev.* **2014,** *43* (22), 7548-7561.

257. Okuhara, T., *Chem. Rev.* **2002,** *102* (10), 3641-3666.

258. Liu, Y.; Vjunov, A.; Shi, H.; Eckstein, S.; Camaioni, D. M.; Mei, D.; Baráth, E.; Lercher, J. A., *Nat. Commun.* **2017,** *8*, 14113.

259. Haw, J. F.; Xu, T.; Nicholas, J. B.; Goguen, P. W., *Nature* **1997,** *389* (6653), 832-835.

260. Dai, W.; Wang, C.; Yi, X.; Zheng, A.; Li, L.; Wu, G.; Guan, N.; Xie, Z.; Dyballa, M.; Hunger, M., *Angewandte Chemie* **2015,** *54* (30), 8783-6.

261. Wang, Q.; Fan, H.; Wu, S.; Zhang, Z.; Zhang, P.; Han, B., *Green Chemistry* **2012,** *14* (4), 1152-1158.

262. Shi, D.; Faria, J.; Pham, T. N.; Resasco, D. E., *ACS Catalysis* **2014,** *4* (6), 1944-1952.

263. Chen, K. Z.; Kelsey, J.; White, J. L.; Zhang, L.; Resasco, D., *Acs Catalysis* **2015,** *5* (12), 7480-7487.

264. Zhi, Y.; Shi, H.; Mu, L.; Liu, Y.; Mei, D.; Camaioni, D. M.; Lercher, J. A., *J Am Chem Soc* **2015,** *137* (50), 15781-15794.

265. Liu, Y.; Baráth, E.; Shi, H.; Hu, J.; Camaioni, D. M.; Lercher, J. A., *Nature Catalysis* **2018,** *1* (2), 141-147.

266. Eckstein, S.; Hintermeier, P. H.; Olarte, M. V.; Liu, Y.; Baráth, E.; Lercher, J. A., *J Catal* **2017,** *352*, 329-336.

267. van Bokhoven, J. A.; Koningsberger, D. C.; Kunkeler, P.; van Bekkum, H., *J. Catal.* **2002,** *211* (2), 540-547.

268. Bugaev, L. A.; van Bokhoven, J. A.; Sokolenko, A. P.; Latokha, Y. V.; Avakyan, L. A., *J. Phys. Chem. B* **2005,** *109* (21), 10771-10778.

269. Drake, I. J.; Zhang, Y.; Gilles, M. K.; Teris Liu, C. N.; Nachimuthu, P.; Perera, R. C. C.; Wakita, H.; Bell, A. T., *J. Phys. Chem. B* **2006,** *110* (24), 11665-11676.

270. Jentys, A.; Warecka, G.; Derewinski, M.; Lercher, J. A., *J. Phys. Chem.* **1989,** *93* (12), 4837-4843.

271. Zecchina, A.; Geobaldo, F.; Spoto, G.; Bordiga, S.; Ricchiardi, G.; Buzzoni, R.; Petrini, G., *J. Phys. Chem.* **1996,** *100* (41), 16584-16599.

272. Mihaleva, V. V.; van Santen, R. A.; Jansen, A. P. J., *J. Chem. Phys.* **2004,** *120* (19), 9212-9221.

273. Cailliez, F.; Stirnemann, G.; Boutin, A.; Demachy, I.; Fuchs, A. H., *J. Phys. Chem. C* **2008,** *112* (28), 10435-10445.

274. Luz, Z.; Vega, A. J., *J. Phys. Chem.* **1987,** *91* (2), 374-382.

275. Vega, A. J.; Luz, Z., *J. Phys. Chem.* **1987,** *91* (2), 365-373.

276. Sauer, J., *J. Mol. Catal.* **1989,** *54* (3), 312-323.

277. Batamack, P.; Doremieux-Morin, C.; Fraissard, J.; Freude, D., *J. Phys. Chem.* **1991,** *95* (9), 3790-3796.

278. Hunger, M.; Freude, D.; Pfeifer, H., *J. Chem. Soc., Faraday Trans.* **1991,** *87* (4), 657-662.

279. Batamack, P.; Doremieux-Morin, C.; Vincent, R.; Fraissard, J., *J. Phys. Chem.* **1993,** *97* (38), 9779-9783.

280. Heeribout, L.; Batamack, P.; Dorémieux-Morin, C.; Vincent, R.; Fraissard, J., *Colloids Surf., A* **1996,** *115*, 229-237.

281. Hunger, M.; Horvath, T., *J. Am. Chem. Soc.* **1996,** *118* (49), 12302-12308.

282. Heeribout, L.; Dorémieux-Morin, C.; Nogier, J. P.; Vincent, R.; Fraissard, J., *Microporous Mesoporous Mater.* **1998,** *24* (1–3), 101-112.

283. Kanellopoulos, J.; Unger, A.; Schwieger, W.; Freude, D., *J. Catal.* **2006,** *237* (2), 416-425.

284. Song, W.; Liu, Y.; Baráth, E.; Zhao, C.; Lercher, J. A., *Green Chem.* **2015,** *17* (2), 1204-1218.

285. Zheng, A.; Li, S.; Liu, S.-B.; Deng, F., *Acc. Chem. Res.* **2016,** *49* (4), 655-663.

286. Jiao, J.; Altwasser, S.; Wang, W.; Weitkamp, J.; Hunger, M., *J. Phys. Chem. B* **2004,** *108* (38), 14305-14310.

287. Semmer-Herlédan, V.; Heeribout, L.; Batamack, P.; Dorémieux-Morin, C.; Fraissard, J.; Gola, A.; Benazzi, E., *Microporous Mesoporous Mater.* **2000,** *34* (2), 157-169.

288. Chen, K. Z.; Abdolrhamani, M.; Sheets, E.; Freeman, J.; Ward, G.; White, J. L., *J Am Chem Soc* **2017,** *139* (51), 18698-18704.

289. Vjunov, A.; Wang, M.; Govind, N.; Huthwelker, T.; Shi, H.; Mei, D. H.; Fulton, J. L.; Lercher, J. A., *Chem Mater* **2017,** *29* (21), 9030-9042.

290. Beck, L. W.; White, J. L.; Haw, J. F., *J. Am. Chem. Soc.* **1994,** *116* (21), 9657-9661.

291. Hunger, M., *Cat. Rev. - Sci. Eng.* **1997,** *39* (4), 345-393.

292. Huo, H.; Peng, L.; Grey, C. P., *J. Phys. Chem. C* **2009,** *113* (19), 8211-8219.

293. Fyfe, C. A.; Feng, Y.; Grondey, H.; Kokotailo, G. T.; Gies, H., *Chem. Rev.* **1991,** *91* (7), 1525-1543.

294. Zhou, Y.; Jin, Y.; Wang, M.; Zhang, W.; Xie, J.; Gu, J.; Wen, H.; Wang, J.; Peng, L., *Chem. Eur. J.* **2015,** *21* (43), 15412-15420.

295. Dec, S. F.; Bronnimann, C. E.; Wind, R. A.; Maciel, G. E., *J. Magn. Reson. (1969-1992)* **1989,** *82* (3), 454-466.

296. Pfeifer, H.; Freude, D.; Hunger, M., *Zeolites* **1985,** *5* (5), 274-286.

297. Price, W. S., *Concepts Magn. Reson., Part A* **2009,** *34A* (1), 60-61.

298. Humplik, T.; Raj, R.; Maroo, S. C.; Laoui, T.; Wang, E. N., *Micropor Mesopor Mat* **2014,** *190*, 84-91.

299. Humplik, T.; Raj, R.; Maroo, S. C.; Laoui, T.; Wang, E. N., *Langmuir* **2014,** *30* (22), 6446-6453.

300. Olson, D. H.; Haag, W. O.; Borghard, W. S., *Micropor Mesopor Mat* **2000,** *35-36*, 435-446.

301. Trzpit, M.; Soulard, M.; Patarin, J.; Desbiens, N.; Cailliez, F.; Boutin, A.; Demachy, I.; Fuchs, A. H., *Langmuir* **2007,** *23* (20), 10131-10139.

302. Chen, H.; Wang, Y., *Ceramics International* **2002,** *28* (5), 541-547.

303. Seredych, M.; Lison, J.; Jans, U.; Bandosz, T. J., *Carbon* **2009,** *47* (10), 2491-2500.

304. Hermansson, K., *Acta Crystallogr., Sect. C: Struct. Chem.* **1983,** *39* (AUG), 925-930.

305. Akitt, J. W.; Elders, J. M.; Fontaine, X. L. R., *J. Chem. Soc., Chem. Commun.* **1986,** (13), 1047-1049.

306. Maemets, V.; Koppel, I., *J. Chem. Soc., Faraday Trans.* **1996,** *92* (19), 3533-3538.

307. Arı, M. U.; Ahunbay, M. G.; Yurtsever, M.; Erdem-Şenatalar, A., *J Phys Chem B* **2009,** *113* (23), 8073-8079.

308. Sarv, P.; Tuherm, T.; Lippmaa, E.; Keskinen, K.; Root, A., *J. Phys. Chem.* **1995,** *99* (38), 13763-13768.

309. Aronson, M. T.; Gorte, R. J.; Farneth, W. E.; White, D., *J Am Chem Soc* **1989,** *111* (3), 840-846.

310. Bucko, T.; Hafner, J., *J Catal* **2015,** *329*, 32-48.

311. Garcia, C. L.; Lercher, J. A., *J Phys Chem-Us* **1991,** *95* (26), 10729-10736.

312. Haase, F.; Sauer, J., *J Am Chem Soc* **1995,** *117* (13), 3780-3789.

313. Krishna, R.; van Baten, J. M., *Langmuir* **2010,** *26* (13), 10854-10867.

314. Nguyen, C. M.; Reyniers, M. F.; Marin, G. B., *Physical Chemistry Chemical Physics* **2010,** *12* (32), 9481-9493.

315. Takahara, I.; Saito, M.; Inaba, M.; Murata, K., *Catal Lett* **2005,** *105* (3-4), 249-252.

316. Van der Mynsbrugge, J.; Hemelsoet, K.; Vandichel, M.; Waroquier, M.; Van Speybroeck, V., *J Phys Chem C* **2012,** *116* (9), 5499-5508.

317. Zhou, X.; Wang, C.; Chu, Y. Y.; Xu, J.; Wang, Q.; Qi, G. D.; Zhao, X. L.; Feng, N. D.; Deng, F., *Nature Communications* **2019,** *10*.

318. Alexopoulos, K.; Lee, M. S.; Liu, Y.; Zhi, Y. C.; Liu, Y. S.; Reyniers, M. F.; Marin, G. B.; Glezakou, V. A.; Rousseau, R.; Lercher, J. A., *J Phys Chem C* **2016,** *120* (13), 7172-7182.

319. Lelli, M.; Gajan, D.; Lesage, A.; Caporini, M. A.; Vitzthum, V.; Mieville, P.; Heroguel, F.; Rascon, F.; Roussey, A.; Thieuleux, C.; Boualleg, M.; Veyre, L.; Bodenhausen, G.; Coperet, C.; Emsley, L., *J Am Chem Soc* **2011,** *133* (7), 2104-2107.

320. Lesage, A.; Lelli, M.; Gajan, D.; Caporini, M. A.; Vitzthum, V.; Mieville, P.; Alauzun, J.; Roussey, A.; Thieuleux, C.; Mehdi, A.; Bodenhausen, G.; Coperet, C.; Emsley, L., *J Am Chem Soc* **2010,** *132* (44), 15459-15461.

321. Thankamony, A. S. L.; Knoche, S.; Bothe, S.; Drochner, A.; Jagtap, A. P.; Sigurdsson, S. T.; Vogel, H.; Etzold, B. J. M.; Gutmann, T.; Buntkowsky, G., *J Phys Chem C* **2017,** *121* (38), 20857-20864.

322. Haber, J., *Catalysis Today* **2009,** *142* (3–4), 100-113.

323. Lutterotti, L.; Vasin, R.; Wenk, H. R., *Powder Diffr* **2014,** *29* (1), 76-84.

324. te Velde, G.; Bickelhaupt, F. M.; Baerends, E. J.; Fonseca Guerra, C.; van Gisbergen, S. J. A.; Snijders, J. G.; Ziegler, T., *Journal of Computational Chemistry* **2001,** *22* (9), 931-967.

325. Fonseca Guerra, C.; Snijders, G. J.; te Velde, G.; Baerends, J. E., *Theoretical Chemistry Accounts 99* (6), 391-403.

326. ADF2014 *SCM*, Vrije Universiteit, Amsterdam, The Netherlands, http://www.scm.com.

327. Lee, C.; Yang, W.; Parr, R. G., *Physical Review B* **1988,** *37* (2), 785-789.

328. Becke, A. D., *Physical Review A* **1988,** *38* (6), 3098-3100.

329. Grimme, S.; Antony, J.; Schwabe, T.; Muck-Lichtenfeld, C., *Organic & Biomolecular Chemistry* **2007,** *5* (5), 741-758.

330. Van Lenthe, E.; Baerends, E. J., *Journal of Computational Chemistry* **2003,** *24* (9), 1142-1156.

331. Wolinski, K.; Hinton, J. F.; Pulay, P., *J Am Chem Soc* **1990,** *112* (23), 8251-8260.

332. Schreckenbach, G.; Ziegler, T., *The Journal of Physical Chemistry* **1995,** *99* (2), 606-611.

333. Schreckenbach, G.; Ziegler, T., *International Journal of Quantum Chemistry* **1997,** *61* (6), 899-918.

334. Wolff, S. K.; Ziegler, T.; van Lenthe, E.; Baerends, E. J., *J Chem Phys* **1999,** *110*, 7689-7698.

335. Wolff, S. K.; Ziegler, T.; van Lenthe, E.; Baerends, E. J., *The Journal of Chemical Physics* **1999,** *110* (16), 7689-7698.

336. Lenthe, E. v.; Baerends, E. J.; Snijders, J. G., *The Journal of Chemical Physics* **1993,** *99* (6), 4597-4610.

337. Autschbach, J.; Ziegler, T., In Calculation of NMR and EPR Parameters: Teory and Applications. Wiley-VCH & Co.: 2004; pp 249-264.

338. Bjornsson, R.; Fruchtl, H.; Buhl, M., *Physical Chemistry Chemical Physics* **2011,** *13* (2), 619-627.

339. Justino, L. L. G.; Ramos, M. L.; Kaupp, M.; Burrows, H. D.; Fiolhais, C.; Gil, V. M. S., *Dalton Transactions* **2009,** (44), 9735-9745.

340. Frisch, M. J.; Trucks, G. W.; Schlegel, H. B.; Scuseria, G. E.; Robb, M. A.; Cheeseman, J. R.; Scalmani, G.; Barone, V.; Petersson, G. A.; Nakatsuji, H.; Li, X.; Caricato, M.; Marenich, A. V.; Bloino, J.; Janesko, B. G.; Gomperts, R.; Mennucci, B.; Hratchian, H. P.; Ortiz, J. V.; Izmaylov, A. F.; Sonnenberg, J. L.; Williams; Ding, F.; Lipparini, F.; Egidi, F.; Goings, J.; Peng, B.; Petrone, A.; Henderson, T.; Ranasinghe, D.; Zakrzewski, V. G.; Gao, J.; Rega, N.; Zheng, G.; Liang, W.; Hada, M.; Ehara, M.; Toyota, K.; Fukuda, R.; Hasegawa, J.; Ishida, M.; Nakajima, T.; Honda, Y.; Kitao, O.; Nakai, H.; Vreven, T.; Throssell, K.; Montgomery Jr., J. A.; Peralta, J. E.; Ogliaro, F.; Bearpark, M. J.; Heyd, J. J.; Brothers, E. N.; Kudin, K. N.; Staroverov, V. N.; Keith, T. A.; Kobayashi, R.; Normand, J.; Raghavachari, K.; Rendell, A. P.; Burant, J. C.; Iyengar, S. S.; Tomasi, J.; Cossi, M.; Millam, J. M.; Klene, M.; Adamo, C.; Cammi, R.; Ochterski, J. W.; Martin, R. L.; Morokuma, K.; Farkas, O.; Foresman, J. B.; Fox, D. J. *Gaussian 16 Rev. A.03*, Wallingford, CT, 2016.

341. Grimme, S.; Antony, J.; Ehrlich, S.; Krieg, H., *The Journal of Chemical Physics* **2010,** *132* (15), 154104.

342. Howard, C. J.; Sabine, T. M.; Dickson, F., *Acta Crystallographica Section B* **1991,** *47* (4), 462-468.

343. Becke, A. D., *J Chem Phys* **1993,** *98* (7), 5648-5652.

344. Kendall, R. A.; Dunning, T. H.; Harrison, R. J., *J Chem Phys* **1992,** *96* (9), 6796-6806.

345. Li, S. G.; Hennigan, J. M.; Dixon, D. A.; Peterson, K. A., *J Phys Chem A* **2009,** *113* (27), 7861-7877.

346. Figgen, D.; Peterson, K. A.; Dolg, M.; Stoll, H., *J Chem Phys* **2009,** *130* (16).

347. te Velde, G.; Bickelhaupt, F. M.; Baerends, E. J.; Fonseca Guerra, C.; van Gisbergen, S. J. A.; Snijders, J. G.; Ziegler, T., *J. Comput. Chem.* **2001,** *22* (9), 931-967.

348. Grimme, S.; Antony, J.; Schwabe, T.; Muck-Lichtenfeld, C., *Org. Biomol. Chem.* **2007,** *5* (5), 741-758.

349. Van Lenthe, E.; Baerends, E. J., *J. Comput. Chem.* **2003,** *24* (9), 1142-1156.

350. Mei, D. H.; Lercher, J. A., *Aiche J* **2017,** *63* (1), 172-184.

351. Jones, A. J.; Carr, R. T.; Zones, S. I.; Iglesia, E., *J. Catal.* **2014,** *312*, 58-68.

352. Massiot, D.; Fayon, F.; Coapron, M.; King, I.; Le Valvé, S.; Alonso, B.; Durand, J.-O.; Bujoli, B.; Gan, Z.; Hoatson, G., *Magnetic Resonance in Chemistry* **2002,** *40*, 70-76.

353. Vega, A. J., *J. Am. Chem. Soc.* **1988,** *110* (4), 1049-1054.

354. Kolodziejski, W.; Klinowski, J., *Chem. Rev.* **2002,** *102* (3), 613-628.

355. Baba, T.; Komatsu, N.; Ono, Y.; Sugisawa, H., *J. Phys. Chem. B* **1998,** *102* (5), 804-808.

356. Baba, T.; Komatsu, N.; Ono, Y.; Sugisawa, H.; Takahashi, T., *Microporous Mesoporous Mater.* **1998,** *22* (1–3), 203-210.

357. Fenzke, D.; Hunger, M.; Pfeifer, H., *J. Magn. Reson. (1969-1992)* **1991,** *95* (3), 477-483.

358. Hunger, M.; Anderson, M. W.; Ojo, A.; Pfeifer, H., *Microporous Mater.* **1993,** *1* (1), 17-32.

359. Klinowski, J., *Chem. Rev.* **1991,** *91* (7), 1459-1479.

360. Hunger, M., *Solid State Nucl. Magn. Reson.* **1996,** *6* (1), 1-29.

361. Munakata, H.; Koyama, T.-r.; Yashima, T.; Asakawa, N.; O-Nuki, T.; Motokura, K.; Miyaji, A.; Baba, T., *J. Phys. Chem. C* **2012,** *116* (27), 14551-14560.

362. Brandhorst, M.; Cristol, S.; Capron, M.; Dujardin, C.; Vezin, H.; Le bourdon, G.; Payen, E., *Catalysis Today* **2006,** *113* (1-2), 34-39.

363. Hu, H. C.; Wachs, I. E., *J Phys Chem-Us* **1995,** *99* (27), 10911-10922.

364. Briand, L. E.; Farneth, W. E.; Wachs, I. E., *Catalysis Today* **2000,** *62* (2-3), 219-229.

365. Caceres, C. V.; Fierro, J. L. G.; Lazaro, J.; Agudo, A. L.; Soria, J., *J Catal* **1990,** *122* (1), 113-125.

366. Il'ichev, A. N.; Shibanova, M. D.; Korchak, V. N., *Kinet Catal+* **2004,** *45* (1), 114-121.

367. Oliver, S. W.; Smith, T. D.; Pilbrow, J. R.; Pratt, K. C.; Christov, V., *J Catal* **1988,** *111* (1), 88-93.

368. Bhaskar, T.; Reddy, K. R.; Kumar, C. P.; Murthy, M. R. V. S.; Chary, K. V. R., *Appl Catal a-Gen* **2001,** *211* (2), 189-201.

369. Chary, K. V. R.; Bhaskar, T.; Kishan, G.; Vijayakumar, V., *J Phys Chem B* **1998,** *102* (20), 3936-3940.

370. Il Kim, S.; Ihl Woo, S., *J Catal* **1992,** *133* (1), 124-135.

371. Reddy, B. M.; Chary, K. V. R.; Rao, B. R.; Subrahmanyam, V. S.; Sunandana, C. S.; Nag, N. K., *Polyhedron* **1986,** *5* (1-2), 191-194.

372. Mastikhin, V. M.; Mudrakovsky, I. L.; Nosov, A. V., *Progress in Nuclear Magnetic Resonance Spectroscopy* **1991,** *23*, 259-299.

373. Kraus, H.; Prins, R., *J Catal* **1996,** *164* (2), 260-267.

374. Knaeble, W.; Iglesia, E., *J Phys Chem C* **2016,** *120* (6), 3371-3389.

375. Angelici, C.; Weckhuysen, B. M.; Bruijnincx, P. C. A., *Chemsuschem* **2013,** *6* (9), 1595-1614.

376. Dagle, V. L.; Flake, M. D.; Lemmon, T. L.; Lopez, J. S.; Kovarik, L.; Dagle, R. A., *Appl Catal B-Environ* **2018,** *236*, 576-587.

377. Zhao, Z. C.; Shi, H.; Wan, C.; Hu, M. Y.; Liu, Y. S.; Mei, D. H.; Camaioni, D. M.; Hu, J. Z.; Lercher, J. A., *J Am Chem Soc* **2017,** *139* (27), 9178-9185.

378. Liu, Y.; Baráth, E.; Shi, H.; Hu, J.; Camaioni, D. M.; Lercher, J. A., *Nature Catalysis* **2018**, 1-7.

379. Deng, X.; Hu, M. Y.; Wei, X.; Wang, W.; Chen, Z.; Liu, J.; Hu, J. Z., *Journal of Power Sources* **2015,** *285*, 146-155.

380. Lv, D. P.; Shao, Y. Y.; Lozano, T.; Bennett, W. D.; Graff, G. L.; Polzin, B.; Zhang, J. G.; Engelhard, M. H.; Saenz, N. T.; Henderson, W. A.; Bhattacharya, P.; Liu, J.; Xiao, J., *Adv Energy Mater* **2015,** *5* (3).

381. Winter, M.; Brodd, R. J., *Chem Rev* **2004,** *104* (10), 4245-4269.

382. Saha, P.; Datta, M. K.; Velikokhatnyi, O. I.; Manivannan, A.; Alman, D.; Kumta, P. N., *Progress in Materials Science* **2014,** *66*, 1-86.

383. Hu, J. Z.; Rajput, N. N.; Wanad, C.; Shao, Y.; Deng, X.; Jaegers, N. R.; Hua, M.; Chena, Y.; Shin, Y.; Monk, J.; Chenc, Z.; Qind, Z.; Muellera, K. T.; Liua, J.; Persson, K., *Nano Energy* **2018,** *46*, 436-446.

384. Ding, M. S.; Diemant, T.; Behm, R. J.; Passerini, S.; Giffin, G. A., *J Electrochem Soc* **2018,** *165* (10), A1983-A1990.

385. Ma, Z.; MacFarlane, D. R.; Kar, M., *Batteries & Supercaps* **2019,** *2* (2), 115-127.

386. Elvira, G. B.; Francisco, G. C.; Victor, S. M.; Alberto, M. L. R., *J Environ Sci-China* **2017,** *57*, 418-428.

387. Hu, M. Y.; Deng, X.; Thanthiriwatte, K. S.; Jackson, V. E.; Wan, C.; Qafoku, O.; Dixon, D. A.; Felmy, A. R.; Rosso, K. M.; Hu, J. Z., *Environ Sci Technol* **2016,** *50* (22), 12373-12384.

388. Ushikubo, T.; Hattori, H.; Tanabe, K., *Chem Lett* **1984,** *13* (4), 649-652.

389. Parrott, S. L.; Rogers, J. W.; White, J. M., *Applied Surface Science* **1978,** *1* (4), 443-454.

390. Liang, S. H. C.; Gay, I. D., *J Catal* **1986,** *101* (2), 293-300.

391. Foyt, D. C.; White, J. M., *J Catal* **1977,** *47* (2), 260-268.

392. Lowe, J. S.; Siegel, D. J., *J Phys Chem C* **2018,** *122* (20), 10714-10724.

393. Shterenberg, I.; Salama, M.; Gofer, Y.; Levi, E.; Aurbach, D., *MRS Bulletin* **2014,** *39* (05), 453-460.

394. Pals, C. R.; Newman, J., *J Electrochem Soc* **1995,** *142* (10), 3274-3281.

395. Pals, C. R.; Newman, J., *J Electrochem Soc* **1995,** *142* (10), 3282-3288.

396. Mahamud, R.; Park, C., *Journal of Power Sources* **2011,** *196* (13), 5685-5696.

397. Baerends, E. J. A., J.; Berger, J. A.; Be´rces, A.; Bickelhaupt, F. M.; Bo, C.; de Boeij, P. L.; Boerrigter, P. M.; Cavallo, L.; Chong, D. P.; et al., Amsterdam Density Functional. Theoretical Chemistry, Scientific Computing & Modelling (SCM), Theoretical Chemistry, Vrije Universiteit: Amsterdam, The Netherlands. (URL: http://www.scm.com.).

398. Grimme, S.; Ehrlich, S.; Goerigk, L., *Journal of Computational Chemistry* **2011,** *32* (7), 1456-1465.

399. Lee, C.; Yang, W.; Parr, R. G., *Physical Review B* **1988,** *37* (2), 785-789.

400. Van Lenthe, E.; Baerends, E. J., *Journal of Computational Chemistry* **2003,** *24* (9), 1142-1156.

401. Liang, S. H. C.; Gay, I. D., *Langmuir* **1985,** *1* (5), 593-599.

402. Sachtler, W. M. H., *Catalysis Today* **1992,** *15* (3-4), 419-429.

403. Klier, K., *Langmuir* **1988,** *4* (1), 13-25.

404. Lonyi, F.; Kovacs, A.; Szegedi, A.; Valyon, J., *J Phys Chem C* **2009,** *113* (24), 10527-10540.

405. Corma, A.; Garcia, H., *Topics in Catalysis* **2008,** *48* (1-4), 8-31.

406. Haruta, A., *Chem Rec* **2003,** *3* (2), 75-87.

407. Barrer, R., Surface Organometallic Chemistry: Molecular Approaches to Surface Catalysis. In *Zeolite Synthesis: An Overview*, Basset, J.-M.; Gates, B. C.; Candy, J.-P.; Choplin, A.; Leconte, M.; Quignard, F.; Santini, C., Eds. Kluwer Academic Publishers: 1988; pp 221-244.

408. Kwak, J. H.; Tran, D.; Burton, S. D.; Szanyi, J.; Lee, J. H.; Peden, C. H. F., *J Catal* **2012,** *289*, 272-272.

409. Sachtler, W. M. H., *Accounts Chem Res* **1993,** *26* (7), 383-387.

410. Finiels, A.; Fajula, F.; Hulea, V., *Catalysis Science & Technology* **2014,** *4* (8), 2412-2426.

411. Baiale, J., US Patent: US3738977A Polymerization of ethylene with a supported palladium catalyst 1971.

412. Khivantsev, K.; Vityuk, A.; Aleksandrov, H. A.; Vayssilov, G. N.; Blom, D.; Alexeev, O. S.; Amiridis, M. D., *Acs Catalysis* **2017,** *7* (9), 5965-5982.

413. Agirrezabal-Telleria, I.; Iglesia, E., *J Catal* **2017,** *352*, 505-514.

414. Yang, A. C.; Garland, C. W., *J Phys Chem-Us* **1957,** *61* (11), 1504-1512.

415. Knozinger, H.; Thornton, E. W.; Wolf, M., *J Chem Soc Farad T 1* **1979,** *75*, 1888-1899.

416. Serna, P.; Gates, B. C., *Angew Chem Int Edit* **2011,** *50* (24), 5528-5531.

417. Khivantsev, K. Selective Synthesis and Characterization of Single-Site Hy Zeolite-supported Rhodium Complexesand their use as Catalysts for EthyleneHydrogenation and Dimerization. PhD Thesis University of South Carolina, 2015.

418. Khivantsev, K.; Vityuk, A.; Aleksandrov, H. A.; Vayssilov, G. N.; Alexeev, O. S.; Amiridis, M. D., *J Phys Chem C* **2015,** *119* (30), 17166-17181.

419. Joshi, R.; Zhang, G. H.; Miller, J. T.; Gounder, R., *Acs Catalysis* **2018,** *8* (12), 11407-11422.

420. Brogaard, R. Y.; Olsbye, U., *Acs Catalysis* **2016,** *6* (2), 1205-1214.

421. Moussa, S.; Concepcion, P.; Arribas, M. A.; Martinez, A., *Acs Catalysis* **2018,** *8* (5), 3903-3912.

422. Khivantsev, K.; Jaegers, N. R.; Koleva, I. Z.; Aleksandrov, H. A.; Kovarik, L.; Engelhard, M.; Gao, F.; Wang, Y.; Vayssilov, G. N.; Szanyi, J., *Chemirxiv* **2019**.

423. Khivantsev, K.; Gao, F.; Kovarik, L.; Wang, Y.; Szanyi, J., *J Phys Chem C* **2018,** *122* (20), 10820-10827.

424. Petkov, P. S.; Aleksandrov, H. A.; Valtchev, V.; Vayssilov, G. N., *Chem Mater* **2012,** *24* (13), 2509-2518.

425. Pomalaza, G.; Capron, M.; Ordomsky, V.; Dumeignil, F., *Catalysts* **2016,** *6* (12).

426. Sushkevich, V. L.; Ivanova, I. I., *Appl Catal B-Environ* **2017,** *215*, 36-49.

427. Cohen, S. A.; Auburn, P. R.; Bercaw, J. E., *J Am Chem Soc* **1983,** *105* (5), 1136-1143.

428. Gao, Y.; Emge, T. J.; Krogh-Jespersen, K.; Goldman, A. S., *J Am Chem Soc* **2018,** *140* (6), 2260-2264.

429. Tsybulevski, A. M.; Kustov, L. M.; Weston, K. C.; Greish, A. A.; Tkachenko, O. P.; Kucherov, A. V., *Industrial & Engineering Chemistry Research* **2012,** *51* (20), 7073-7080.

430. Szanyi, J.; Paffett, M. T., *Microporous Mater* **1996,** *7* (4), 201-218.

431. Martinez-Macias, C.; Serna, P.; Gates, B. C., *Acs Catalysis* **2015,** *5* (10), 5647-5656.

432. Haddleton, D. M.; Perutz, R. N., *J Chem Soc Chem Comm* **1986,** (23), 1734-1736.

433. Khivantsev, K.; Biancardi, A.; Fathizadeh, M.; Almalki, F.; Grant, J. L.; Tien, H. N.; Shakouri, A.; Blom, D. A.; Makris, T. M.; Regalbuto, J. R.; Caricato, M.; Yu, M., *Chemcatchem* **2018,** *10* (4), 736-742.

434. Hu, B.; Getsoian, A.; Schweitzer, N. M.; Das, U.; Kim, H.; Niklas, J.; Poluektov, O.; Curtiss, L. A.; Stair, P. C.; Miller, J. T.; Hock, A. S., *J Catal* **2015,** *322*, 24-37.

435. Goldman, A. S.; Landis, C. R.; Sen, A., *Angew Chem Int Edit* **2018,** *57* (17), 4460-4460.

436. Morra, E.; Martino, G. A.; Piovano, A.; Barzan, C.; Groppo, E.; Chiesa, M., *J Phys Chem C* **2018,** *122* (37), 21531-21536.

437. Kissin, Y. V.; Brandolini, A. J., *J Polym Sci Pol Chem* **2008,** *46* (16), 5330-5347.

438. Zielinski, P.; Lana, I. G. D., *J Catal* **1992,** *137* (2), 368-376.

439. Chakrabarti, A.; Gierada, M.; Handzlik, J.; Wachs, I. E., *Topics in Catalysis* **2016,** *59* (8-9), 725-739.

440. Toulhoat, H., Heterogeneous Catalysis: Use of Density Functional Theory. In *Encyclopedia of Materials: Science and Technology*, Buschow, K. H. J.; Cahn, R. W.; Flemings, M. C.; Ilschner, B.; Kramer, E. J.; Mahajan, S.; Veyssière, P., Eds. Elsevier: Oxford, 2010; pp 1-7.

441. Primo, A.; Garcia, H., *Chem Soc Rev* **2014,** *43* (22), 7548-7561.

442. *Catalytic Ammonia Synthesis: Fundamentals and Practice*. Springer US: New York, 1991; p 452.

443. Vjunov, A.; Hu, M. Y.; Feng, J.; Camaioni, D. M.; Mei, D. H.; Hu, J. Z.; Zhao, C.; Lercher, J. A., *Angew Chem Int Edit* **2014,** *53* (2), 479-482.

444. Hu, J. Z.; Sears, J. A.; Mehta, H. S.; Ford, J. J.; Kwak, J. H.; Zhu, K. K.; Wang, Y.; Liu, J.; Hoyt, D. W.; Peden, C. H. F., *Phys Chem Chem Phys* **2012,** *14* (7), 2137-2143.

445. Wang, W.; Jiang, Y. J.; Hunger, M., *Catalysis Today* **2006,** *113* (1-2), 102-114.

446. Xu, J.; Wang, Q.; Deng, F., *Accounts Chem Res* **2019,** *52* (8), 2179-2189.

447. Zhao, Z. C.; Xu, S. C.; Hu, M. Y.; Bao, X. H.; Hu, J. Z., *J Phys Chem C* **2016,** *120* (3), 1701-1708.

448. Xu, S.; Zhao, Z.; Hu, M. Y.; Han, X.; Hu, J. Z.; Bao, X., **2016**.

449. Hu, J. Z.; Zhang, X.; Jaegers, N. R.; Wan, C.; Graham, T. R.; Hu, M.; Pearce, C. I.; Felmy, A. R.; Clark, S. B.; Rosso, K. M., *J Phys Chem C* **2017,** *121* (49), 27555-27562.

450. Prodinger, S.; Vjunov, A.; Hu, J. Z.; Fulton, J. L.; Carnaioni, D. M.; Derewinski, M. A.; Lercher, J. A., *Chem Mater* **2018,** *30* (3), 888-897.

451. Radhakrishnan, S.; Goossens, P. J.; Magusin, P. C. M. M.; Sree, S. P.; Detavernier, C.; Breynaert, E.; Martineau, C.; Taulelle, F.; Martens, J. A., *J Am Chem Soc* **2016,** *138* (8), 2802-2808.

452. Dagle, V.; Winkelman, A.; Jaegers, N. R.; Hu, J. Z.; Dagle, R. A., *Under Review* **2020**.

453. Qi, L.; Alamillo, R.; Elliott, W. A.; Andersen, A.; Hoyt, D. W.; Walter, E. D.; Han, K. S.; Washton, N. M.; Rioux, R. M.; Dumesic, J. A.; Scott, S. L., *ACS Catalysis* **2017,** *7* (5), 3489-3500.

454. Jaegers, N. R.; Khivantsev, K.; Kovarik, L.; Klas, D. W.; Hu, J. Z.; Wang, Y.; Szanyi, J., *Catalysis Science & Technology* **2019**.

455. Haw, J. F.; Richardson, B. R.; Oshiro, I. S.; Lazo, N. D.; Speed, J. A., *J Am Chem Soc* **1989,** *111* (6), 2052-2058.

456. Moreno-Gonzalez, M.; Hueso, B.; Boronat, M.; Blasco, T.; Corma, A., *J Phys Chem Lett* **2015,** *6* (6), 1011-1017.

457. Xu, J.; Wang, Q.; Li, S.; Deng, F., In Situ Solid-State NMR Investigation of Catalytic Reactions on Zeolites. In *Solid-State NMR in Zeolite Catalysis*, Xu, J.; Wang, Q.; Li, S.; Deng, F., Eds. Springer Singapore: Singapore, 2019; pp 199-254.

458. Kolyagin, Y. G.; Ordomsky, V. V.; Khimyak, Y. Z.; Rebrov, A. I.; Fajula, F.; Ivanova, I. I., *J Catal* **2006,** *238* (1), 122-133.

459. Ivanova, I. I.; Pomakhina, E. B.; Rebrov, A. I.; Derouane, E. G., *Topics in Catalysis* **1998,** *6* (1-4), 49-59.

460. Ivanova, I. I.; Blom, N.; Derouane, E. G., *Stud Surf Sci Catal* **1995,** *94*, 419-426.

461. Wang, X. M.; Xu, J.; Qi, G. D.; Wang, C.; Wang, W. Y.; Gao, P.; Wang, Q.; Liu, X. L.; Feng, N. D.; Deng, F., *J Catal* **2017,** *345*, 228-235.

462. Ilias, S.; Bhan, A., *J Catal* **2014,** *311*, 6-16.

463. Walter, E. D.; Qi, L.; Chamas, A.; Mehta, H. S.; Sears, J. A.; Scott, S. L.; Hoyt, D. W., *J Phys Chem C* **2018,** *122* (15), 8209-8215.

464. Hu, J. Z.; Jaegers, N. R.; Chen, Y.; Han, K. S.; Wang, H.; Murugesan, V.; Mueller, K. T., *ACS Applied Materials & Interfaces* **2019**.

465. Graham, T. R.; Dembowski, M.; Martinez-Baez, E.; Zhang, X.; Jaegers, N. R.; Hu, J. Z.; Gruszkiewicz, M. S.; Wang, H. W.; Stack, A. G.; Bowden, M. E.; Delegard, C. H.; Schenter, G. K.; Clark, A. E.; Clark, S. B.; Felmy, A. R.; Rosso, K. M.; Pearce, C. I., *Inorg Chem* **2018,** *57* (19), 11864-11873.

466. Zhang, X.; Huestis, P. L.; Pearce, C. I.; Hu, J. Z.; Page, K.; Anovitz, L. M.; Aleksandrov, A. B.; Prange, M. P.; Kerisit, S.; Bowden, M. E.; Cui, W.; Wang, Z.; Jaegers, N. R.; Graham, T. R.; Dembowski, M.; Wang, H.-W.; Liu, J.; N'Diaye, A. T.; Bleuel, M.; Mildner, D. F. R.; Orlando, T. M.; Kimmel, G. A.; La Verne, J. A.; Clark, S. B.; Rosso, K. M., *ACS Applied Nano Materials* **2018,** *1* (12), 7115-7128.

467. Zhang, X.; Cui, W.; Hu, J. Z.; Wang, H.-W.; Prange, M. P.; Wan, C.; Jaegers, N. R.; Zong, M.; Zhang, H.; Pearce, C. I.; Li, P.; Wang, Z.; Clark, S. B.; Rosso, K. M., *Crystal Growth & Design* **2019,** *19* (10), 5557-5567.

468. Tfaily, M.; Hu, J. Z.; Heyman, H.; Toyoda, J.; Jaegers, N. R.; Wilson, R.; Chanton, J. In *Tracking the Fate of new C in Northern Peatlands by a Compound-Specific Stable Isotope-Labeling Approach coupled with multiple analytical techniques and gas fluxes analysis*, AGU Fall Meeting Abstracts, 2017.

469. Guo, J.; Xu, Y.; Wang, C., *Nano Letters* **2011,** *11* (10), 4288-4294.

470. Wei Seh, Z.; Li, W.; Cha, J. J.; Zheng, G.; Yang, Y.; McDowell, M. T.; Hsu, P.-C.; Cui, Y., *Nature Communications* **2013,** *4*, 1331.

471. Cao, Y.; Li, X.; Aksay, I. A.; Lemmon, J.; Nie, Z.; Yang, Z.; Liu, J., *Physical Chemistry Chemical Physics* **2011,** *13* (17), 7660-7665.

472. Suo, L.; Oh, D.; Lin, Y.; Zhuo, Z.; Borodin, O.; Gao, T.; Wang, F.; Kushima, A.; Wang, Z.; Kim, H.-C.; Qi, Y.; Yang, W.; Pan, F.; Li, J.; Xu, K.; Wang, C., *J Am Chem Soc* **2017,** *139* (51), 18670-18680.

473. Kissinger, P. T.; Heineman, W. R., *Journal of Chemical Education* **1983,** *60* (9), 702.

474. Nicholson, R. S., *Analytical Chemistry* **1965,** *37* (11), 1351-1355.

475. Wang, C.-M., *Journal of Materials Research* **2015,** *30* (3), 326-339.

476. Wang, C.-M.; Liao, H.-G.; Ross, F. M., *MRS Bulletin* **2015,** *40* (1), 46-52.

477. Haider, M.; Uhlemann, S.; Schwan, E.; Rose, H.; Kabius, B.; Urban, K., *Nature* **1998,** *392*, 768.

478. Krivanek, O. L.; Nellist, P. D.; Dellby, N.; Murfitt, M. F.; Szilagyi, Z., *Ultramicroscopy* **2003,** *96* (3), 229-237.

479. Müller, H.; Uhlemann, S.; Hartel, P.; Haider, M., *Microscopy and Microanalysis* **2006,** *12* (6), 442-455.

480. Batson, P. E.; Dellby, N.; Krivanek, O. L., *Nature* **2002,** *418*, 617.

481. Kisielowski, C.; Freitag, B.; Bischoff, M.; van Lin, H.; Lazar, S.; Knippels, G.; Tiemeijer, P.; van der Stam, M.; von Harrach, S.; Stekelenburg, M.; Haider, M.; Uhlemann, S.; Müller, H.; Hartel, P.; Kabius, B.; Miller, D.; Petrov, I.; Olson, E. A.; Donchev, T.; Kenik, E. A.; Lupini, A. R.; Bentley, J.; Pennycook, S. J.; Anderson, I. M.; Minor, A. M.; Schmid, A. K.; Duden, T.; Radmilovic, V.; Ramasse, Q. M.; Watanabe, M.; Erni, R.; Stach, E. A.; Denes, P.; Dahmen, U., *Microscopy and Microanalysis* **2008,** *14* (5), 469-477.

482. Muller, D. A., *Nature Materials* **2009,** *8*, 263.

483. Retoux, R.; Brousse, T.; Schleich, D. M., *J Electrochem Soc* **1999,** *146* (7), 2472-2476.

484. Laffont, L.; Delacourt, C.; Gibot, P.; Wu, M. Y.; Kooyman, P.; Masquelier, C.; Tarascon, J. M., *Chem Mater* **2006,** *18* (23), 5520-5529.

485. McDowell, M. T.; Cui, Y., *Adv Energy Mater* **2011,** *1* (5), 894-900.

486. Wang, C. M.; Xu, W.; Liu, J.; Choi, D. W.; Arey, B.; Saraf, L. V.; Zhang, J. G.; Yang, Z. G.; Thevuthasan, S.; Baer, D. R.; Salmon, N., *Journal of Materials Research* **2010,** *25* (8), 1541-1547.

487. Huang, J. Y.; Zhong, L.; Wang, C. M.; Sullivan, J. P.; Xu, W.; Zhang, L. Q.; Mao, S. X.; Hudak, N. S.; Liu, X. H.; Subramanian, A.; Fan, H.; Qi, L.; Kushima, A.; Li, J., *Science* **2010,** *330* (6010), 1515.

488. Liu, X. H.; Zhong, L.; Huang, S.; Mao, S. X.; Zhu, T.; Huang, J. Y., *ACS Nano* **2012,** *6* (2), 1522-1531.

489. Liu, X. H.; Huang, S.; Picraux, S. T.; Li, J.; Zhu, T.; Huang, J. Y., *Nano Letters* **2011,** *11* (9), 3991-3997.

490. Liu, Y.; Hudak, N. S.; Huber, D. L.; Limmer, S. J.; Sullivan, J. P.; Huang, J. Y., *Nano Letters* **2011,** *11* (10), 4188-4194.

491. Zhang, L. Q.; Liu, X. H.; Perng, Y.-C.; Cho, J.; Chang, J. P.; Mao, S. X.; Ye, Z. Z.; Huang, J. Y., *Micron* **2012,** *43* (11), 1127-1133.

492. Kushima, A.; Liu, X. H.; Zhu, G.; Wang, Z. L.; Huang, J. Y.; Li, J., *Nano Letters* **2011,** *11* (11), 4535-4541.

493. Liu, X. H.; Wang, J. W.; Liu, Y.; Zheng, H.; Kushima, A.; Huang, S.; Zhu, T.; Mao, S. X.; Li, J.; Zhang, S.; Lu, W.; Tour, J. M.; Huang, J. Y., *Carbon* **2012,** *50* (10), 3836-3844.

494. Li, Q.; Wang, P.; Feng, Q.; Mao, M.; Liu, J.; Mao, S. X.; Wang, H., *Chem Mater* **2014,** *26* (14), 4102-4108.

495. Wang, F.; Yu, H.-C.; Chen, M.-H.; Wu, L.; Pereira, N.; Thornton, K.; Van der Ven, A.; Zhu, Y.; Amatucci, G. G.; Graetz, J., *Nature Communications* **2012,** *3*, 1201.

496. Liu, X. H.; Zheng, H.; Zhong, L.; Huang, S.; Karki, K.; Zhang, L. Q.; Liu, Y.; Kushima, A.; Liang, W. T.; Wang, J. W.; Cho, J.-H.; Epstein, E.; Dayeh, S. A.; Picraux, S. T.; Zhu, T.; Li, J.; Sullivan, J. P.; Cumings, J.; Wang, C.; Mao, S. X.; Ye, Z. Z.; Zhang, S.; Huang, J. Y., *Nano Letters* **2011,** *11* (8), 3312-3318.

497. Liu, X. H.; Zhang, L. Q.; Zhong, L.; Liu, Y.; Zheng, H.; Wang, J. W.; Cho, J.-H.; Dayeh, S. A.; Picraux, S. T.; Sullivan, J. P.; Mao, S. X.; Ye, Z. Z.; Huang, J. Y., *Nano Letters* **2011,** *11* (6), 2251-2258.

498. Williamson, M. J.; Tromp, R. M.; Vereecken, P. M.; Hull, R.; Ross, F. M., *Nature Materials* **2003,** *2*, 532.

499. Woehl, T. J.; Park, C.; Evans, J. E.; Arslan, I.; Ristenpart, W. D.; Browning, N. D., *Nano Letters* **2014,** *14* (1), 373-378.

500. Gu, M.; Parent, L. R.; Mehdi, B. L.; Unocic, R. R.; McDowell, M. T.; Sacci, R. L.; Xu, W.; Connell, J. G.; Xu, P.; Abellan, P.; Chen, X.; Zhang, Y.; Perea, D. E.; Evans, J. E.; Lauhon, L. J.; Zhang, J.-G.; Liu, J.; Browning, N. D.; Cui, Y.; Arslan, I.; Wang, C.-M., *Nano Letters* **2013,** *13* (12), 6106-6112.

501. Holtz, M. E.; Yu, Y.; Gunceler, D.; Gao, J.; Sundararaman, R.; Schwarz, K. A.; Arias, T. A.; Abruña, H. D.; Muller, D. A., *Nano Letters* **2014,** *14* (3), 1453-1459.

502. Sacci, R. L.; Dudney, N. J.; More, K. L.; Parent, L. R.; Arslan, I.; Browning, N. D.; Unocic, R. R., *Chemical Communications* **2014,** *50* (17), 2104-2107.

503. Unocic, R. R.; Sacci, R. L.; Brown, G. M.; Veith, G. M.; Dudney, N. J.; More, K. L.; Walden, F. S.; Gardiner, D. S.; Damiano, J.; Nackashi, D. P., *Microscopy and Microanalysis* **2014,** *20* (2), 452-461.

504. Kong, F.; Kostecki, R.; Nadeau, G.; Song, X.; Zaghib, K.; Kinoshita, K.; McLarnon, F., *Journal of Power Sources* **2001,** *97-8*, 58-66.

505. Inaba, M.; Iriyama, Y.; Ogumi, Z.; Todzuka, Y.; Tasaka, A., *Journal of Raman Spectroscopy* **1997,** *28* (8), 613-617.

506. Hardwick, L. J.; Hahn, M.; Ruch, P.; Holzapfel, M.; Scheifele, W.; Buqa, H.; Krumeich, F.; Novák, P.; Kötz, R., *Electrochimica Acta* **2006,** *52* (2), 675-680.

507. Hardwick, L. J.; Ruch, P. W.; Hahn, M.; Scheifele, W.; Kötz, R.; Novák, P., *Journal of Physics and Chemistry of Solids* **2008,** *69* (5), 1232-1237.

508. Dokko, K.; Mohamedi, M.; Anzue, N.; Itoh, T.; Uchida, I., *Journal of Materials Chemistry* **2002,** *12* (12), 3688-3693.

509. Wu, H.-L.; Huff, L. A.; Gewirth, A. A., *ACS Applied Materials & Interfaces* **2015,** *7* (3), 1709-1719.

510. Park, Y.; Kim, Y.; Kim, S. M.; Jin, S.; Han, I. K.; Lee, S. M.; Jung, Y. M., *Bulletin of the Korean Chemical Society* **2017,** *38* (4), 511-513.

511. Nanda, J.; Datta, M. K.; Remillard, J. T.; O'Neill, A.; Kumta, P. N., *Electrochemistry Communications* **2009,** *11* (1), 235-237.

512. Zhang, X.; Frech, R., *J Electrochem Soc* **1998,** *145* (3), 847-851.

513. Yamanaka, T.; Nakagawa, H.; Tsubouchi, S.; Domi, Y.; Doi, T.; Abe, T.; Ogumi, Z., *Electrochemistry Communications* **2017,** *77*, 32-35.

514. Yamanaka, T.; Nakagawa, H.; Tsubouchi, S.; Domi, Y.; Doi, T.; Abe, T.; Ogumi, Z., *Electrochimica Acta* **2017,** *234*, 93-98.

515. Patel, M. U. M.; Demir-Cakan, R.; Morcrette, M.; Tarascon, J.-M.; Gaberscek, M.; Dominko, R., *Chemsuschem* **2013,** *6* (7), 1177-1181.

516. Aurbach, D.; Chusid, O., *Journal of Power Sources* **1997,** *68* (2), 463-470.

517. Song, S.-W.; Baek, S.-W., *Electrochemical and Solid-State Letters* **2009,** *12* (2), A23-A27.

518. Sun, F.; Osenberg, M.; Dong, K.; Zhou, D.; Hilger, A.; Jafta, C. J.; Risse, S.; Lu, Y.; Markötter, H.; Manke, I., *ACS Energy Letters* **2018,** *3* (2), 356-365.

519. Nelson, J.; Misra, S.; Yang, Y.; Jackson, A.; Liu, Y.; Wang, H.; Dai, H.; Andrews, J. C.; Cui, Y.; Toney, M. F., *J Am Chem Soc* **2012,** *134* (14), 6337-6343.

520. Dahn, J. R., *Physical Review B* **1991,** *44* (17), 9170-9177.

521. Walus, S.; Barchasz, C.; Colin, J.-F.; Martin, J.-F.; Elkaim, E.; Lepretre, J.-C.; Alloin, F., *Chemical Communications* **2013,** *49* (72), 7899-7901.

522. Hatchard, T. D.; Dahn, J. R., *J Electrochem Soc* **2004,** *151* (6), A838-A842.

523. Poizot, P.; Laruelle, S.; Grugeon, S.; Dupont, L.; Tarascon, J. M., *Nature* **2000,** *407*, 496.

524. Yao, K. P. C.; Kwabi, D. G.; Quinlan, R. A.; Mansour, A. N.; Grimaud, A.; Lee, Y.-L.; Lu, Y.-C.; Shao-Horn, Y., *J Electrochem Soc* **2013,** *160* (6), A824-A831.

525. Chan, C. K.; Peng, H.; Liu, G.; McIlwrath, K.; Zhang, X. F.; Huggins, R. A.; Cui, Y., *Nature Nanotechnology* **2007,** *3*, 31.

526. Balasubramanian, M.; Sun, X.; Yang, X. Q.; McBreen, J., *Journal of Power Sources* **2001,** *92* (1), 1-8.

527. Yoon, W.-S.; Chung, K. Y.; McBreen, J.; Yang, X.-Q., *Electrochemistry Communications* **2006,** *8* (8), 1257-1262.

528. Guo, J.-Z.; Wang, P.-F.; Wu, X.-L.; Zhang, X.-H.; Yan, Q.; Chen, H.; Zhang, J.-P.; Guo, Y.-G., *Advanced Materials* **2017,** *29* (33), 1701968-n/a.

529. Ou, X.; Li, J.; Zheng, F.; Wu, P.; Pan, Q.; Xiong, X.; Yang, C.; Liu, M., *Journal of Power Sources* **2017,** *343*, 483-491.

530. Cuisinier, M.; Cabelguen, P.-E.; Evers, S.; He, G.; Kolbeck, M.; Garsuch, A.; Bolin, T.; Balasubramanian, M.; Nazar, L. F., *The Journal of Physical Chemistry Letters* **2013,** *4* (19), 3227-3232.

531. Gao, J.; Lowe, M. A.; Kiya, Y.; Abruña, H. D., *The Journal of Physical Chemistry C* **2011,** *115* (50), 25132-25137.

532. Tang, C. Y.; Haasch, R. T.; Dillon, S. J., *Chemical Communications* **2016,** *52* (90), 13257-13260.

533. Bryngelsson, H.; Stjerndahl, M.; Gustafsson, T.; Edström, K., *Journal of Power Sources* **2007,** *174* (2), 970-975.

534. Lu, Y. C.; Crumlin, E. J.; Veith, G. M.; Harding, J. R.; Mutoro, E.; Baggetto, L.; Dudney, N. J.; Liu, Z.; Shao-Horn, Y., *Scientific Reports* **2012,** *2*.

535. Nandasiri, M. I.; Camacho-Forero, L. E.; Schwarz, A. M.; Shutthanandan, V.; Thevuthasan, S.; Balbuena, P. B.; Mueller, K. T.; Murugesan, V., *Chem Mater* **2017,** *29* (11), 4728-4737.

536. Kondekar, N. P.; Boebinger, M. G.; Woods, E. V.; McDowell, M. T., *ACS Applied Materials & Interfaces* **2017,** *9* (37), 32394-32404.

537. Lahiri, A.; Borisenko, N.; Olschewski, M.; Pulletikurthi, G.; Endres, F., *Faraday Discussions* **2018,** *206* (0), 339-351.

538. Andersson, A. M.; Abraham, D. P.; Haasch, R.; MacLaren, S.; Liu, J.; Amine, K., *J Electrochem Soc* **2002,** *149* (10), A1358-A1369.

539. Bhattacharyya, R.; Key, B.; Chen, H.; Best, A. S.; Hollenkamp, A. F.; Grey, C. P., *Nature Materials* **2010,** *9*, 504.

540. Abbrent, S.; Greenbaum, S., *Current Opinion in Colloid & Interface Science* **2013,** *18* (3), 228-244.

541. Trease, N. M.; Köster, T. K. J.; Grey, C. P., *The Electrochemical Society Interface* **2011,** *20* (3), 69-73.

542. Blanc, F.; Leskes, M.; Grey, C. P., *Accounts Chem Res* **2013,** *46* (9), 1952-1963.

543. Harks, P. P. R. M. L.; Mulder, F. M.; Notten, P. H. L., *Journal of Power Sources* **2015,** *288*, 92-105.

544. Wishart, D. S.; Case, D. A., *Method Enzymol* **2001,** *338*, 3-34.

545. Hu, J. Z.; Rajput, N. N.; Wan, C.; Shao, Y. Y.; Deng, X. C.; Jaegers, N. R.; Hu, M.; Chen, Y. W.; Shin, Y.; Monk, J.; Chen, Z.; Qin, Z. H.; Mueller, K. T.; Liu, J.; Persson, K. A., *Nano Energy* **2018,** *46*, 436-446.

546. Clore, G. M.; Iwahara, J., *Chem Rev* **2009,** *109* (9), 4108-4139.

547. Bryant, R. G., *Journal of Chemical Education* **1983,** *60* (11), 933-935.

548. Jeener, J.; Meier, B. H.; Bachmann, P.; Ernst, R. R., *J Chem Phys* **1979,** *71* (11), 4546-4553.

549. Palmer, A. G.; Grey, M. J.; Wang, C. Y., *Nuclear Magnetic Resonance of Biological Macromolecules, Part C* **2005,** *394*, 430-465.

550. Kleckner, I. R.; Foster, M. P., *Bba-Proteins Proteom* **2011,** *1814* (8), 942-968.

551. Lipari, G.; Szabo, A., *J Am Chem Soc* **1982,** *104* (17), 4559-4570.

552. Bloembergen, N.; Purcell, E. M.; Pound, R. V., *Physical Review* **1948,** *73* (7), 679-712.

553. Hallenga, K.; Koenig, S. H., *Biochemistry* **1976,** *15* (19), 4255-4264.

554. Massi, F.; Johnson, E.; Wang, C. Y.; Rance, M.; Palmer, A. G., *J Am Chem Soc* **2004,** *126* (7), 2247-2256.

555. Deverell, C.; Morgan, R. E.; Strange, J. H., *Mol Phys* **1970,** *18* (4), 553-&.

556. Korzhnev, D. M.; Skrynnikov, N. R.; Millet, O.; Torchia, D. A.; Kay, L. E., *J Am Chem Soc* **2002,** *124* (36), 10743-10753.

557. Pecher, O.; Carretero-Gonzalez, J.; Griffith, K. J.; Grey, C. P., *Chem Mater* **2017,** *29* (1), 213-242.

558. Xiao, J.; Hu, J. Z.; Chen, H. H.; Vijayakumar, M.; Zheng, J. M.; Pan, H. L.; Walter, E. D.; Hu, M.; Deng, X. C.; Feng, J.; Liaw, B. Y.; Gu, M.; Deng, Z. D.; Lu, D. P.; Xu, S. C.; Wang, C. M.; Liu, J., *Nano Letters* **2015,** *15* (5), 3309-3316.

559. Tang, W.; Liu, Y. P.; Peng, C. X.; Hu, M. Y.; Deng, X. C.; Lin, M.; Hu, J. Z.; Loh, K. P., *J Am Chem Soc* **2015,** *137* (7), 2600-2607.

560. Rathke, J. W.; Klingler, R. J.; Gerald, R. E.; Kramarz, K. W.; Woelk, K., *Progress in Nuclear Magnetic Resonance Spectroscopy* **1997,** *30* (3), 209-253.

561. Rathke, J. W., *Journal of Magnetic Resonance (1969)* **1989,** *85* (1), 150-155.

562. Rathke, J. W.; Klingler, R. J.; Woelk, K.; Rex, E. G. I. Near-electrode imager. 2000.

563. Gerald, R. E.; Johnson, C. S.; Rathke, J. W.; Klingler, R. J.; Sandí, G.; Scanlon, L. G., *Journal of Power Sources* **2000,** *89* (2), 237-243.

564. R. E. Gerald, I.; Sanchez, J.; Johnson, C. S.; Klingler, R. J.; Rathke, J. W., *Journal of Physics: Condensed Matter* **2001,** *13* (36), 8269.

565. Tarascon, J. M.; Gozdz, A. S.; Schmutz, C.; Shokoohi, F.; Warren, P. C., *Solid State Ionics* **1996,** *86-88*, 49-54.

566. Chevallier, F.; Letellier, M.; Morcrette, M.; Tarascon, J. M.; Frackowiak, E.; Rouzaud, J. N.; Béguin, F., *Electrochemical and Solid-State Letters* **2003,** *6* (11), A225-A228.

567. Letellier, M.; Chevallier, F.; Clinard, C.; Frackowiak, E.; Rouzaud, J.-N.; Béguin, F.; Morcrette, M.; Tarascon, J.-M., *The Journal of Chemical Physics* **2003,** *118* (13), 6038-6045.

568. Pecher, O.; Bayley, P. M.; Liu, H.; Liu, Z. G.; Trease, N. M.; Grey, C. P., *Journal of Magnetic Resonance* **2016,** *265*, 200-209.

569. Letellier, M.; Chevallier, F.; Morcrette, M., *Carbon* **2007,** *45* (5), 1025-1034.

570. Zaghib, K.; Tatsumi, K.; Sawada, Y.; Higuchi, S.; Abe, H.; Ohsaki, T., *J Electrochem Soc* **1999,** *146* (8), 2784-2793.

571. Tatsumi, K.; Akai, T.; Imamura, T.; Zaghib, K.; Iwashita, N.; Higuchi, S.; Sawada, Y., *J Electrochem Soc* **1996,** *143* (6), 1923-1930.

572. Tatsumi, K.; Conard, J.; Nakahara, M.; Menu, S.; Lauginie, P.; Sawada, Y.; Ogumi, Z., *Journal of Power Sources* **1999,** *81-82*, 397-400.

573. Poli, F.; Kshetrimayum, J. S.; Monconduit, L.; Letellier, M., *Electrochemistry Communications* **2011,** *13* (12), 1293-1295.

574. Chen, H.; Cartmell, S.; Wang, Q.; Lozano, T.; Deng, Z. D.; Li, H.; Chen, X.; Yuan, Y.; Gross, M. E.; Carlson, T. J.; Xiao, J., *Scientific Reports* **2014,** *4*, 3790.

575. Xiao, J.; Hu, J. Z.; Chen, H.; Vijayakumar, M.; Zheng, J.; Pan, H.; Walter, E. D.; Hu, M.; Deng, X.; Feng, J.; Liaw, B. Y.; Gu, M.; Deng, Z. D.; Lu, D.; Xu, S.; Wang, C.; Liu, J., *Nano Lett* **2015,** *15* (5), 3309-16.

576. Tang, W.; Liu, Y.; Peng, C.; Hu, M. Y.; Deng, X.; Lin, M.; Hu, J. Z.; Loh, K. P., *J Am Chem Soc* **2015,** *137* (7), 2600-2607.

577. Tang, W.; Goh, B.-M.; Hu, M. Y.; Wan, C.; Tian, B.; Deng, X.; Peng, C.; Lin, M.; Hu, J. Z.; Loh, K. P., *The Journal of Physical Chemistry C* **2016,** *120* (5), 2600-2608.

578. Hu, J. Z.; Zhao, Z.; Hu, M. Y.; Feng, J.; Deng, X.; Chen, X.; Xu, W.; Liu, J.; Zhang, J.-G., *Journal of Power Sources* **2016,** *304*, 51-59.

579. Key, B.; Bhattacharyya, R.; Morcrette, M.; Seznéc, V.; Tarascon, J.-M.; Grey, C. P., *J Am Chem Soc* **2009,** *131* (26), 9239-9249.

580. Kayser, S. A.; Mester, A.; Mertens, A.; Jakes, P.; Eichel, R. A.; Granwehr, J., *Physical Chemistry Chemical Physics* **2018,** *20* (20), 13765-13776.

581. Arai, J.; Gotoh, K.; Sayama, R.; Takeda, K., *J Electrochem Soc* **2017,** *164* (1), A6334-A6340.

582. Trease, N. M.; Zhou, L.; Chang, H. J.; Zhu, B. Y.; Grey, C. P., *Solid State Nuclear Magnetic Resonance* **2012,** *42*, 62-70.

583. Wiemers-Meyer, S.; Winter, M.; Nowak, S., *Physical Chemistry Chemical Physics* **2017,** *19* (7), 4962-4966.

584. Huo, H.; Chamas, M.; Lippens, P.-E.; Ménétrier, M., *The Journal of Physical Chemistry C* **2012,** *116* (3), 2390-2398.

585. Hu, J. Z.; Zhao, Z.; Hu, M. Y.; Feng, J.; Deng, X.; Chen, X.; Xu, W.; Liu, J.; Zhang, J.-G., *Journal of Power Sources* **2016,** *304*, 51-59.

586. Paik, Y.; Osegovic, J. P.; Wang, F.; Bowden, W.; Grey, C. P., *J Am Chem Soc* **2001,** *123* (38), 9367-9377.

587. Allcock, H. R.; Napierala, M. E.; Olmeijer, D. L.; Best, S. A.; Merz, K. M., *Macromolecules* **1999,** *32* (3), 732-741.

588. Bogle, X.; Vazquez, R.; Greenbaum, S.; Cresce, A. v. W.; Xu, K., *The Journal of Physical Chemistry Letters* **2013,** *4* (10), 1664-1668.

589. Lee, J.; Seymour, I. D.; Pell, A. J.; Dutton, S. E.; Grey, C. P., *Physical Chemistry Chemical Physics* **2017,** *19* (1), 613-625.

590. Guo, B.; Shu, J.; Wang, Z.; Yang, H.; Shi, L.; Liu, Y.; Chen, L., *Electrochemistry Communications* **2008,** *10* (12), 1876-1878.

591. Vijayakumar, M.; Li, L.; Graff, G.; Liu, J.; Zhang, H.; Yang, Z.; Hu, J. Z., *Journal of Power Sources* **2011,** *196* (7), 3669-3672.

592. Andrew, E. R.; Bradbury, A.; Eades, R. G., *Nature* **1958,** *182*, 1659.

593. Dupre, N.; Martin, J.-F.; Guyomard, D.; Yamada, A.; Kanno, R., *Journal of Materials Chemistry* **2008,** *18* (36), 4266-4273.

594. Marino, C.; Darwiche, A.; Dupré, N.; Wilhelm, H. A.; Lestriez, B.; Martinez, H.; Dedryvère, R.; Zhang, W.; Ghamouss, F.; Lemordant, D.; Monconduit, L., *The Journal of Physical Chemistry C* **2013,** *117* (38), 19302-19313.

595. Hu, Y.-Y.; Liu, Z.; Nam, K.-W.; Borkiewicz, O. J.; Cheng, J.; Hua, X.; Dunstan, M. T.; Yu, X.; Wiaderek, K. M.; Du, L.-S.; Chapman, K. W.; Chupas, P. J.; Yang, X.-Q.; Grey, C. P., *Nature Materials* **2013,** *12*, 1130.

596. Key, B.; Morcrette, M.; Tarascon, J. M.; Grey, C. P., *J Am Chem Soc* **2011,** *133* (3), 503-512.

597. Grey, C. P.; Dupré, N., *Chem Rev* **2004,** *104* (10), 4493-4512.

598. Rao, K. S.; Sridhar, R.; Susila, S., *Physica Scripta* **1981,** *24* (6), 925.

599. Cheon, I.-T., *Physics Letters B* **1969,** *30* (2), 81-84.

600. Kerisit, S.; Vijayakumar, M.; Han, K. S.; Mueller, K. T., *The Journal of Chemical Physics* **2015,** *142* (22), 224502.

601. Han, K. S.; Rajput, N. N.; Vijayakumar, M.; Wei, X.; Wang, W.; Hu, J.; Persson, K. A.; Mueller, K. T., *The Journal of Physical Chemistry C* **2016,** *120* (49), 27834-27839.

602. Wei, X.; Cosimbescu, L.; Xu, W.; Hu Jian, Z.; Vijayakumar, M.; Feng, J.; Hu Mary, Y.; Deng, X.; Xiao, J.; Liu, J.; Sprenkle, V.; Wang, W., *Adv Energy Mater* **2014,** *5* (1), 1400678.

603. Huang, J.; Yang, Z.; Vijayakumar, M.; Duan, W.; Hollas, A.; Pan, B.; Wang, W.; Wei, X.; Zhang, L., *Advanced Sustainable Systems* **2018,** *2* (3), 1700131.

604. Vijayakumar, M.; Nie, Z.; Walter, E.; Hu, J.; Liu, J.; Sprenkle, V.; Wang, W., *ChemPlusChem* **2014,** *80* (2), 428-437.

605. Vijayakumar, M.; Wang, W.; Nie, Z.; Sprenkle, V.; Hu, J., *Journal of Power Sources* **2013,** *241*, 173-177.

606. Li, L.; Kim, S.; Wang, W.; Vijayakumar, M.; Nie, Z.; Chen, B.; Zhang, J.; Xia, G.; Hu, J.; Graff, G.; Liu, J.; Yang, Z., *Adv Energy Mater* **2011,** *1* (3), 394-400.

607. Kim, S.; Vijayakumar, M.; Wang, W.; Zhang, J.; Chen, B.; Nie, Z.; Chen, F.; Hu, J.; Li, L.; Yang, Z., *Physical Chemistry Chemical Physics* **2011,** *13* (40), 18186-18193.

608. Cosimbescu, L.; Wei, X.; Vijayakumar, M.; Xu, W.; Helm, M. L.; Burton, S. D.; Sorensen, C. M.; Liu, J.; Sprenkle, V.; Wang, W., *Scientific Reports* **2015,** *5*, 14117.

609. Li, B.; Nie, Z.; Vijayakumar, M.; Li, G.; Liu, J.; Sprenkle, V.; Wang, W., *Nature Communications* **2015,** *6*, 6303.

610. Wang, W.; Luo, Q.; Li, B.; Wei, X.; Li, L.; Yang, Z., *Advanced Functional Materials* **2012,** *23* (8), 970-986.

611. Mai, Z.; Zhang, H.; Li, X.; Bi, C.; Dai, H., *Journal of Power Sources* **2011,** *196* (1), 482-487.

612. Parasuraman, A.; Lim, T. M.; Menictas, C.; Skyllas-Kazacos, M., *Electrochimica Acta* **2013,** *101*, 27-40.

613. Mohammadi, T.; Skyllas-Kazacos, M., *Journal of Membrane Science* **1995,** *98* (1), 77-87.

614. Bamine, T.; Boivin, E.; Boucher, F.; Messinger, R. J.; Salager, E.; Deschamps, M.; Masquelier, C.; Croguennec, L.; Ménétrier, M.; Carlier, D., *The Journal of Physical Chemistry C* **2017,** *121* (6), 3219-3227.

615. Gregor, T.; Mauri, F.; Car, R., *The Journal of Chemical Physics* **1999,** *111* (5), 1815-1822.

616. Rauhut, G.; Puyear, S.; Wolinski, K.; Pulay, P., *The Journal of Physical Chemistry* **1996,** *100* (15), 6310-6316.

617. Pickard, C. J.; Mauri, F., *Physical Review B* **2001,** *63* (24).

618. Segall, M. D.; Lindan, P. J. D.; Probert, M. J.; Pickard, C. J.; Hasnip, P. J.; Clark, S. J.; Payne, M. C., *J Phys-Condens Mat* **2002,** *14* (11), 2717-2744.

619. Schreckenbach, G.; Ziegler, T., *International Journal of Quantum Chemistry* **1998,** *60* (3), 753-766.

620. Seymour, I. D.; Middlemiss, D. S.; Halat, D. M.; Trease, N. M.; Pell, A. J.; Grey, C. P., *J Am Chem Soc* **2016,** *138* (30), 9405-9408.

621. Klamt, A.; Schuurmann, G., *Journal of the Chemical Society, Perkin Transactions 2* **1993,** (5), 799-805.

622. Korth, M., *Physical Chemistry Chemical Physics* **2014,** *16* (17), 7919-7926.

623. Muldoon, J.; Bucur, C. B.; Oliver, A. G.; Sugimoto, T.; Matsui, M.; Kim, H. S.; Allred, G. D.; Zajicek, J.; Kotani, Y., *Energy & Environmental Science* **2012,** *5* (3), 5941-5950.

624. Schreckenbach, G.; Ziegler, T., *International Journal of Quantum Chemistry* **1997,** *61* (6), 899-918.

625. Sadhukhan, M.; Tkatchenko, A., *Physical Review Letters* **2017,** *118* (21), 210402.

626. Kühne Thomas, D., *Wiley Interdisciplinary Reviews: Computational Molecular Science* **2014,** *4* (4), 391-406.

627. Tasaki, K.; Kanda, K.; Nakamura, S.; Ue, M., *J Electrochem Soc* **2003,** *150* (12), A1628-A1636.

628. Tasaki, K., *The Journal of Physical Chemistry B* **2005,** *109* (7), 2920-2933.

629. Leung, K.; Budzien, J. L., *Physical Chemistry Chemical Physics* **2010,** *12* (25), 6583-6586.

630. Ganesh, P.; Kent, P. R. C.; Jiang, D.-e., *The Journal of Physical Chemistry C* **2012,** *116* (46), 24476-24481.

631. Bedrov, D.; Smith, G. D.; van Duin, A. C. T., *The Journal of Physical Chemistry A* **2012,** *116* (11), 2978-2985.

632. Ganesh, P.; Jiang, D.-e.; Kent, P. R. C., *The Journal of Physical Chemistry B* **2011,** *115* (12), 3085-3090.

633. Truflandier, L. A.; Autschbach, J., *J Am Chem Soc* **2010,** *132* (10), 3472-3483.

634. Sterzel, M.; Autschbach, J., *Inorg Chem* **2006,** *45* (8), 3316-3324.

635. Truflandier, L. A.; Sutter, K.; Autschbach, J., *Inorg Chem* **2011,** *50* (5), 1723-1732.

636. Idota, Y.; Kubota, T.; Matsufuji, A.; Maekawa, Y.; Miyasaka, T., *Science* **1997,** *276* (5317), 1395-1397.

637. Key, B.; Bhattacharyya, R.; Morcrette, M.; Seznec, V.; Tarascon, J. M.; Grey, C. P., *Journal of the American Chemical Society* **2009,** *131* (26), 9239-9249.

638. Xu, Y.; Liu, Q.; Zhu, Y.; Liu, Y.; Langrock, A.; Zachariah, M. R.; Wang, C., *Nano Letters* **2013,** *13* (2), 470-474.

639. Kennedy, T.; Mullane, E.; Geaney, H.; Osiak, M.; O'Dwyer, C.; Ryan, K. M., *Nano Letters* **2014,** *14* (2), 716-723.

640. Magasinski, A.; Dixon, P.; Hertzberg, B.; Kvit, A.; Ayala, J.; Yushin, G., *Nature Materials* **2010,** *9*, 353.

641. Kim, H.; Son, Y.; Park, C.; Cho, J.; Choi Hee, C., *Angewandte Chemie International Edition* **2013,** *52* (23), 5997-6001.

642. Chan, C. K.; Zhang, X. F.; Cui, Y., *Nano Letters* **2008,** *8* (1), 307-309.

643. Yuan, F.-W.; Yang, H.-J.; Tuan, H.-Y., *ACS Nano* **2012,** *6* (11), 9932-9942.

644. Seo, M.-H.; Park, M.; Lee, K. T.; Kim, K.; Kim, J.; Cho, J., *Energy & Environmental Science* **2011,** *4* (2), 425-428.

645. Baggetto, L.; Notten, P. H. L., *J Electrochem Soc* **2009,** *156* (3), A169-A175.

646. Chang, H. J.; Trease, N. M.; Ilott, A. J.; Zeng, D.; Du, L.-S.; Jerschow, A.; Grey, C. P., *The Journal of Physical Chemistry C* **2015,** *119* (29), 16443-16451.

647. Jung, H.; Allan, P. K.; Hu, Y.-Y.; Borkiewicz, O. J.; Wang, X.-L.; Han, W.-Q.; Du, L.-S.; Pickard, C. J.; Chupas, P. J.; Chapman, K. W.; Morris, A. J.; Grey, C. P., *Chem Mater* **2015,** *27* (3), 1031-1041.

648. Kang, K.; Meng, Y. S.; Bréger, J.; Grey, C. P.; Ceder, G., *Science* **2006,** *311* (5763), 977.

649. Wu, F.; Chen, J.; Chen, R.; Wu, S.; Li, L.; Chen, S.; Zhao, T., *The Journal of Physical Chemistry C* **2011,** *115* (13), 6057-6063.

650. Bruce, P. G.; Freunberger, S. A.; Hardwick, L. J.; Tarascon, J.-M., *Nature Materials* **2011,** *11*, 19.

651. Aurbach, D.; Pollak, E.; Elazari, R.; Salitra, G.; Kelley, C. S.; Affinito, J., *J Electrochem Soc* **2009,** *156* (8), A694-A702.

652. Patel, M. U. M.; Demir-Cakan, R.; Morcrette, M.; Tarascon, J.-M.; Gaberscek, M.; Dominko, R., *Chemsuschem* **2013,** *6* (7), 1177-1181.

653. Xiao, J.; Hu, J. Z.; Chen, H.; Vijayakumar, M.; Zheng, J.; Pan, H.; Walter, E. D.; Hu, M.; Deng, X.; Feng, J.; Liaw, B. Y.; Gu, M.; Deng, Z. D.; Lu, D.; Xu, S.; Wang, C.; Liu, J., *Nano Letters* **2015,** *15* (5), 3309-3316.

654. See, K. A.; Leskes, M.; Griffin, J. M.; Britto, S.; Matthews, P. D.; Emly, A.; Van der Ven, A.; Wright, D. S.; Morris, A. J.; Grey, C. P.; Seshadri, R., *J Am Chem Soc* **2014,** *136* (46), 16368-16377.

655. Kawase, A.; Shirai, S.; Yamoto, Y.; Arakawa, R.; Takata, T., *Physical Chemistry Chemical Physics* **2014,** *16* (20), 9344-9350.

656. Huff, L. A.; Rapp, J. L.; Baughman, J. A.; Rinaldi, P. L.; Gewirth, A. A., *Surface Science* **2015,** *631*, 295-300.

657. Shimoda, K.; Murakami, M.; Takamatsu, D.; Arai, H.; Uchimoto, Y.; Ogumi, Z., *Electrochimica Acta* **2013,** *108*, 343-349.

658. Yoshio, M.; Wang, H.; Fukuda, K.; Hara, Y.; Adachi, Y., *J Electrochem Soc* **2000,** *147* (4), 1245-1250.

659. Hassoun, J.; Bonaccorso, F.; Agostini, M.; Angelucci, M.; Betti, M. G.; Cingolani, R.; Gemmi, M.; Mariani, C.; Panero, S.; Pellegrini, V.; Scrosati, B., *Nano Letters* **2014,** *14* (8), 4901-4906.

660. Mukherjee, R.; Thomas, A. V.; Datta, D.; Singh, E.; Li, J.; Eksik, O.; Shenoy, V. B.; Koratkar, N., *Nature Communications* **2014,** *5*, 3710.

661. Winter, M.; Novák, P.; Monnier, A., *J Electrochem Soc* **1998,** *145* (2), 428-436.

662. Park, K. H.; Lee, D.; Kim, J.; Song, J.; Lee, Y. M.; Kim, H.-T.; Park, J.-K., *Nano Letters* **2014,** *14* (8), 4306-4313.

663. Simon, P.; Gogotsi, Y., *Accounts Chem Res* **2013,** *46* (5), 1094-1103.

664. Kucinskis, G.; Bajars, G.; Kleperis, J., *Journal of Power Sources* **2013,** *240*, 66-79.

665. Ogata, K.; Salager, E.; Kerr, C. J.; Fraser, A. E.; Ducati, C.; Morris, A. J.; Hofmann, S.; Grey, C. P., *Nature Communications* **2014,** *5*, 3217.

666. Hu, J. Z.; Kwak, J. H.; Yang, Z.; Osborn, W.; Markmaitree, T.; Shaw, L. L., *Journal of Power Sources* **2008,** *182* (1), 278-283.

667. Klett, M.; Giesecke, M.; Nyman, A.; Hallberg, F.; Lindström, R. W.; Lindbergh, G.; Furó, I., *J Am Chem Soc* **2012,** *134* (36), 14654-14657.

668. Whittingham, M. S., *Proceedings of the IEEE* **2012,** *100* (Special Centennial Issue), 1518-1534.

669. Aurbach, D.; Daroux, M. L.; Faguy, P. W.; Yeager, E., *J Electrochem Soc* **1987,** *134* (7), 1611-1620.

670. Aurbach, D.; Zinigrad, E.; Cohen, Y.; Teller, H., *Solid State Ionics* **2002,** *148* (3-4), 405-416.

671. Shi, Z.; Liu, M.; Naik, D.; Gole, J. L., *Journal of Power Sources* **2001,** *92* (1), 70-80.

672. Suresh, P.; Shukla, A. K.; Shivashankar, S. A.; Munichandraiah, N., *Journal of Power Sources* **2004,** *132* (1), 166-171.

673. Stark, J. K.; Ding, Y.; Kohl, P. A., *J Electrochem Soc* **2011,** *158* (10), A1100-A1105.

674. Schweikert, N.; Hofmann, A.; Schulz, M.; Scheuermann, M.; Boles, S. T.; Hanemann, T.; Hahn, H.; Indris, S., *Journal of Power Sources* **2013,** *228*, 237-243.

675. Suo, L.; Hu, Y.-S.; Li, H.; Armand, M.; Chen, L., *Nature Communications* **2013,** *4*, 1481.

676. Ding, F.; Xu, W.; Graff, G. L.; Zhang, J.; Sushko, M. L.; Chen, X.; Shao, Y.; Engelhard, M. H.; Nie, Z.; Xiao, J.; Liu, X.; Sushko, P. V.; Liu, J.; Zhang, J.-G., *J Am Chem Soc* **2013,** *135* (11), 4450-4456.

677. Zhang, Y.; Qian, J.; Xu, W.; Russell, S. M.; Chen, X.; Nasybulin, E.; Bhattacharya, P.; Engelhard, M. H.; Mei, D.; Cao, R.; Ding, F.; Cresce, A. V.; Xu, K.; Zhang, J.-G., *Nano Letters* **2014,** *14* (12), 6889-6896.

678. Xu, W.; Wang, J.; Ding, F.; Chen, X.; Nasybulin, E.; Zhang, Y.; Zhang, J.-G., *Energy & Environmental Science* **2014,** *7* (2), 513-537.

679. Aurbach, D.; Weissman, I.; Zaban, A.; Chusid, O., *Electrochimica Acta* **1994,** *39* (1), 51-71.

680. Huo, H.; Chamas, M.; Lippens, P.-E.; Ménétrier, M., *ACS Appl Mater Interfaces* **2017,** *9* (17), 14741-14748.

681. Vijayakumar, M.; Kerisit, S.; Yang, Z.; Graff, G. L.; Liu, J.; Sears, J. A.; Burton, S. D.; Rosso, K. M.; Hu, J., *The Journal of Physical Chemistry C* **2009,** *113* (46), 20108-20116.

682. Bogle, X.; Vazquez, R.; Greenbaum, S.; Cresce, A. V.; Xu, K., *Journal of Physical Chemistry Letters* **2013,** *4* (10), 1664-1668.

683. Deng, X. C.; Hu, M.; Wei, X. L.; Wang, W.; Mueller, K. T.; Chen, Z.; Hu, J. Z., *Journal of Power Sources* **2016,** *308*, 172-179.

684. Deng, X.; Hu, M. Y.; Wei, X.; Wang, W.; Chen, Z.; Liu, J.; Hu, J. Z., *Journal of Power Sources* **2015,** *285*, 146-155.

685. Wan, C.; Hu, M. Y.; Borodin, O.; Qian, J.; Qin, Z.; Zhang, J.-G.; Hu, J. Z., *Journal of Power Sources* **2016,** *307*, 231-243.

686. Hu, J. Z.; Rajput, N. N.; Wan, C.; Shao, Y.; Deng, X.; Jaegers, N. R.; Hu, M.; Chen, Y.; Shin, Y.; Monk, J.; Chen, Z.; Qin, Z.; Mueller, K. T.; Liu, J.; Persson, K. A., *Nano Energy* **2018,** *46*, 436-446.

687. Pour, N.; Gofer, Y.; Major, D. T.; Aurbach, D., *J Am Chem Soc* **2011,** *133* (16), 6270-6278.

688. Muldoon, J.; Bucur, C. B.; Oliver, A. G.; Zajicek, J.; Allred, G. D.; Boggess, W. C., *Energy & Environmental Science* **2013,** *6* (2), 482-487.

689. Aurbach, D.; Weissman, I.; Gofer, Y.; Levi, E., *The Chemical Record* **2003,** *3* (1), 61-73.

690. Aurbach, D.; Gofer, Y.; Schechter, A.; Chusid, O.; Gizbar, H.; Cohen, Y.; Moshkovich, M.; Turgeman, R., *Journal of Power Sources* **2001,** *97-8*, 269-273.

691. Muldoon, J.; Bucur Claudiu, B.; Gregory, T., *Angewandte Chemie International Edition* **2017,** *56* (40), 12064-12084.

692. Wei, X.; Cosimbescu, L.; Xu, W.; Hu, J. Z.; Vijayakumar, M.; Feng, J.; Hu, M. Y.; Deng, X.; Xiao, J.; Liu, J.; Sprenkle, V.; Wang, W., *Adv Energy Mater* **2015,** *5* (1), 1400678.

693. Kalita, M.; Bukat, M.; Ciosek, M.; Siekierski, M.; Chung, S. H.; Rodríguez, T.; Greenbaum, S. G.; Kovarsky, R.; Golodnitsky, D.; Peled, E.; Zane, D.; Scrosati, B.; Wieczorek, W., *Electrochimica Acta* **2005,** *50* (19), 3942-3948.

694. Wieczorek, W.; Zukowska, G.; Borkowska, R.; Chung, S. H.; Greenbaum, S., *Electrochimica Acta* **2001,** *46* (10-11), 1427-1438.

695. Chung, S. H.; Wang, Y.; Persi, L.; Croce, F.; Greenbaum, S. G.; Scrosati, B.; Plichta, E., *Journal of Power Sources* **2001,** *97-8*, 644-648.

696. Wang, Y. Y.; Sun, C. N.; Fan, F.; Sangoro, J. R.; Berman, M. B.; Greenbaum, S. G.; Zawodzinski, T. A.; Sokolov, A. P., *Phys Rev E* **2013,** *87* (4).

697. Vijayakumar, M.; Han, K. S.; Hu, J.; Mueller, K. T., *eMagRes* **2017**.

698. Ilott, A. J.; Mohammadi, M.; Chang, H. J.; Grey, C. P.; Jerschow, A., *Proceedings of the National Academy of Sciences* **2016,** *113* (39), 10779.

699. Chandrashekar, S.; Trease, N. M.; Chang, H. J.; Du, L. S.; Grey, C. P.; Jerschow, A., *Nature Materials* **2012,** *11* (4), 311-315.

700. Li, Z.; Huang, J.; Yann Liaw, B.; Metzler, V.; Zhang, J., *Journal of Power Sources* **2014,** *254*, 168-182.

701. Ilott, A. J.; Mohammadi, M.; Schauerman, C. M.; Ganter, M. J.; Jerschow, A., *Nature Communications* **2018,** *9*.

702. Krachkoyskiy, S. A.; Pauric, A. D.; Halalay, I. C.; Goward, G. R., *J Phys Chem Lett* **2013,** *4* (22), 3940-3944.

703. Klett, M.; Giesecke, M.; Nyman, A.; Hallberg, F.; Lindström, R. W.; Lindbergh, G.; Furó, I., *J Am Chem Soc* **2012,** *134* (36), 14654-14657.

704. Gunther, W. R.; Michaelis, V. K.; Caporini, M. A.; Griffin, R. G.; Román-Leshkov, Y., *J Am Chem Soc* **2014,** *136* (17), 6219-6222.

705. Blanc, F.; Sperrin, L.; Jefferson, D. A.; Pawsey, S.; Rosay, M.; Grey, C. P., *J Am Chem Soc* **2013,** *135* (8), 2975-2978.

706. Prandolini, M. J.; Denysenkov, V. P.; Gafurov, M.; Endeward, B.; Prisner, T. F., *J Am Chem Soc* **2009,** *131* (17), 6090-6092.

APPENDIX

Appendix A: Equipment Schematics

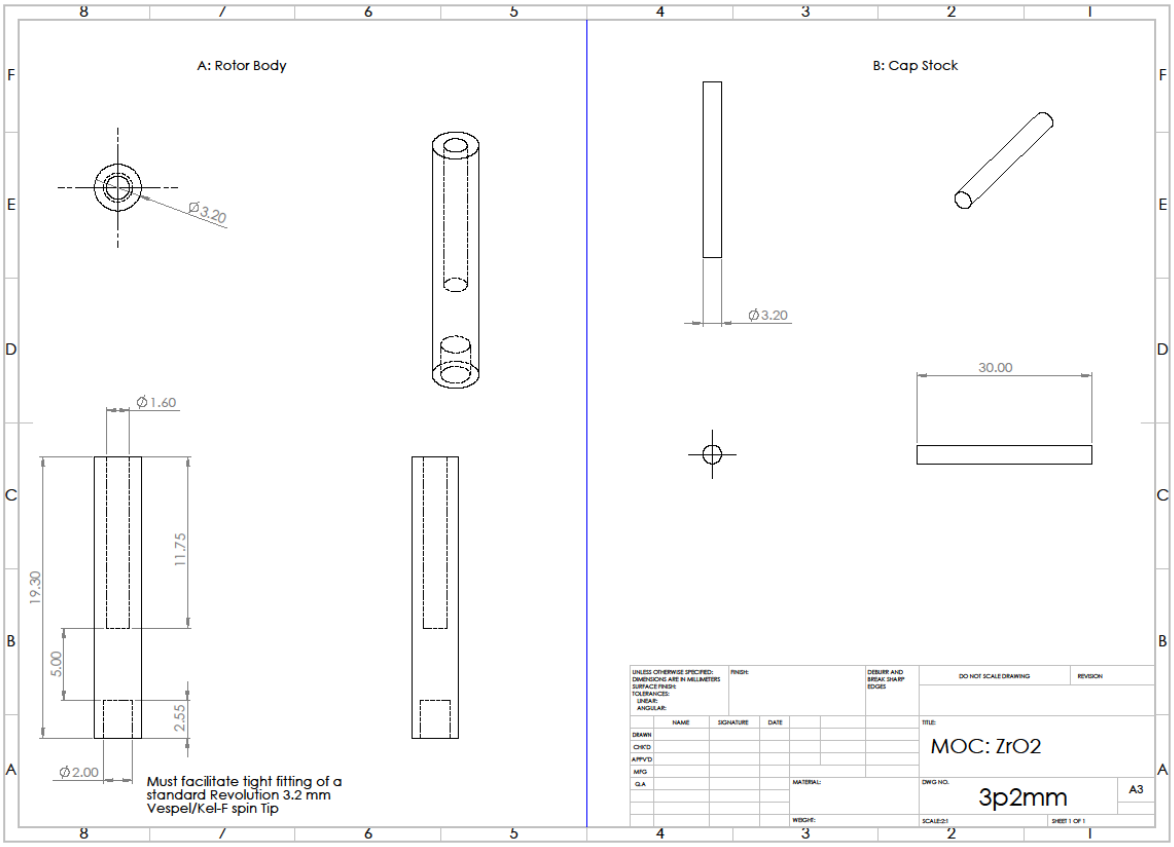

Exhibit A. Drawings for 3.2 mm rotor.

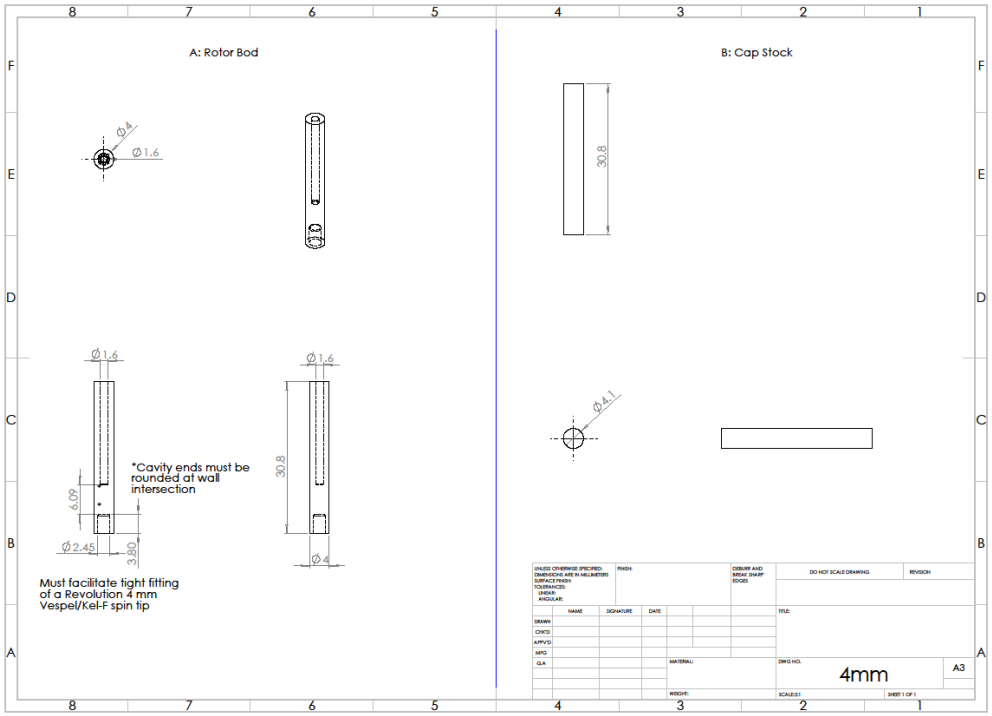

Exhibit B. Drawings for 4.0 mm rotor.

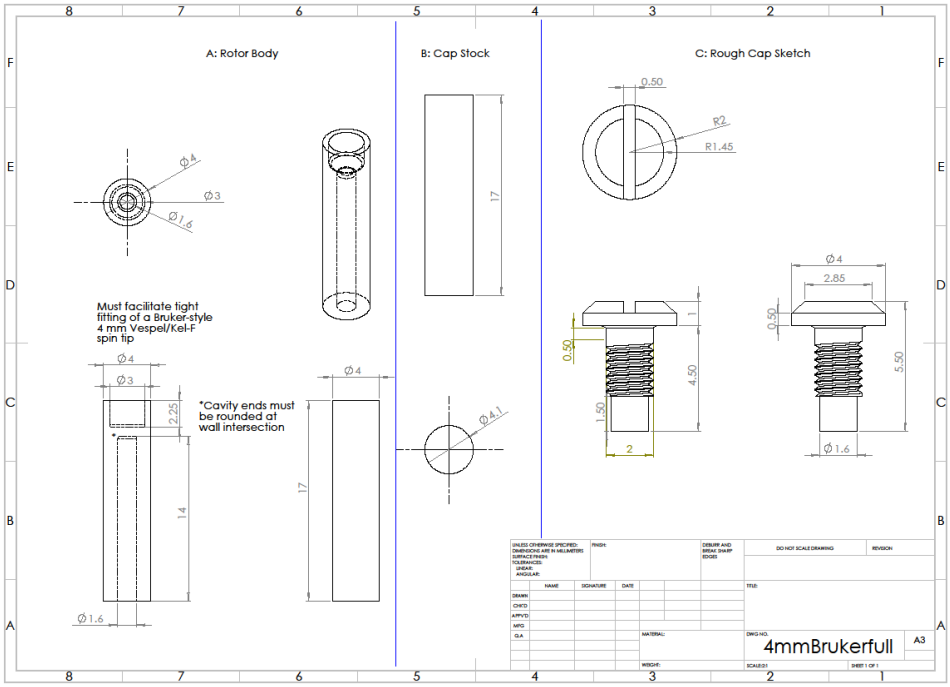

Exhibit C. Drawings for 4.0 mm Bruker-style rotor.

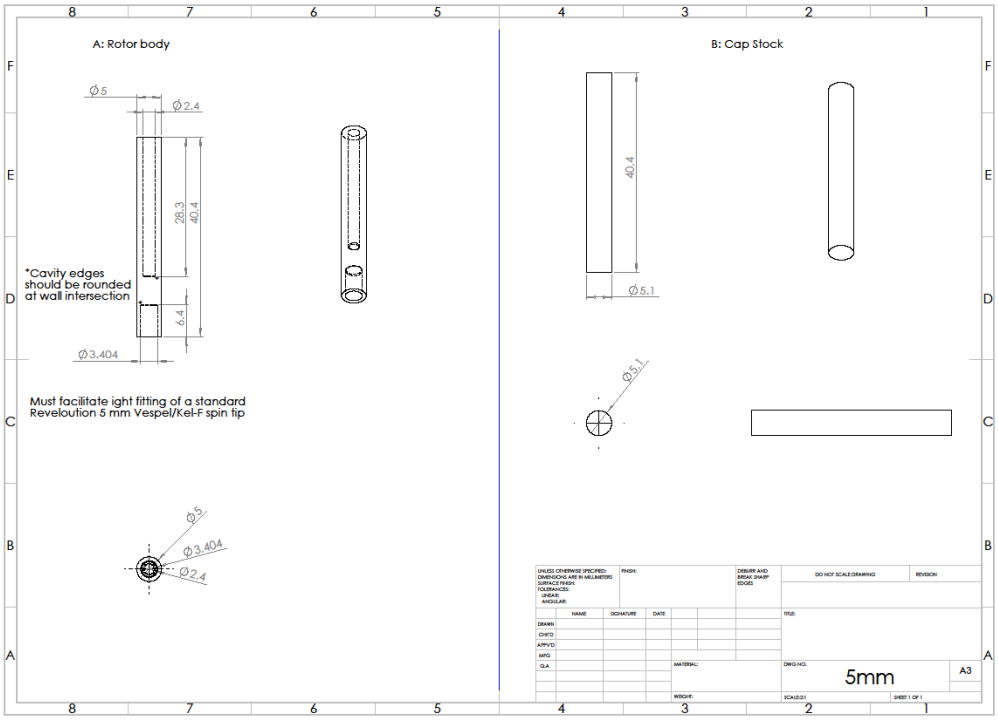

Exhibit D. Drawings for 5.0 mm rotor.

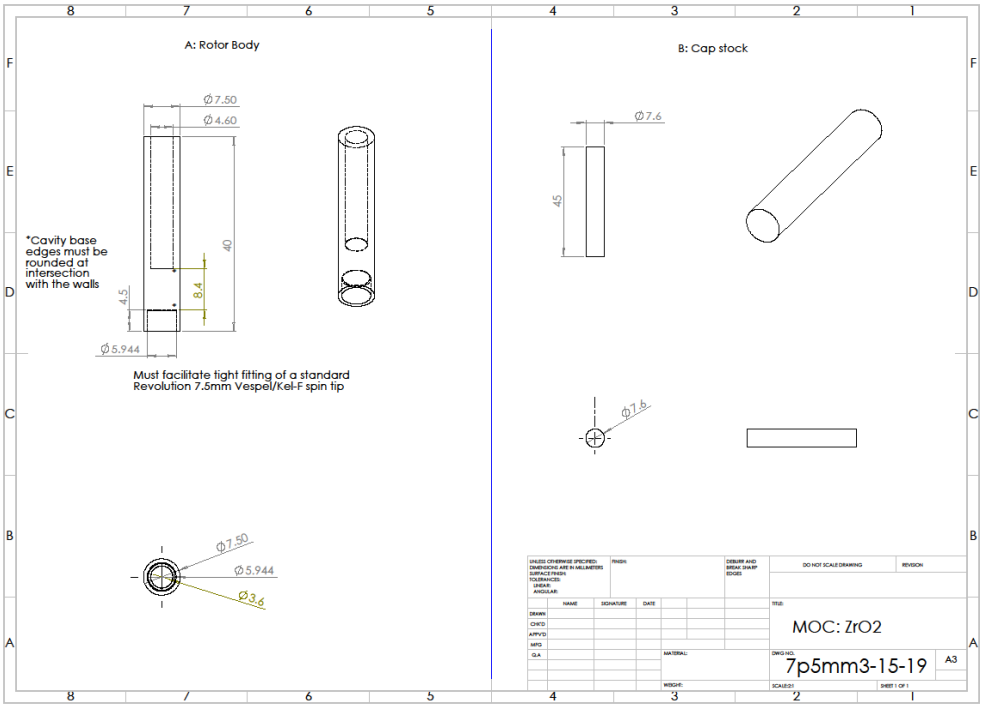

Exhibit E. Drawings for 7.5 mm rotor.

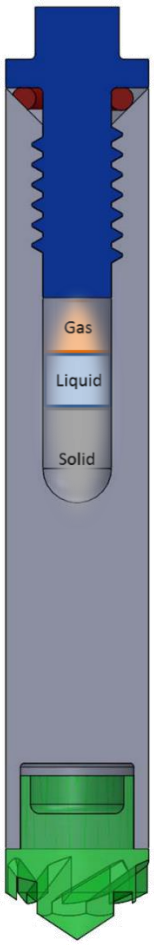

Exhibit F. Diagram of in situ NMR rotor depicting three-phase sample retention.

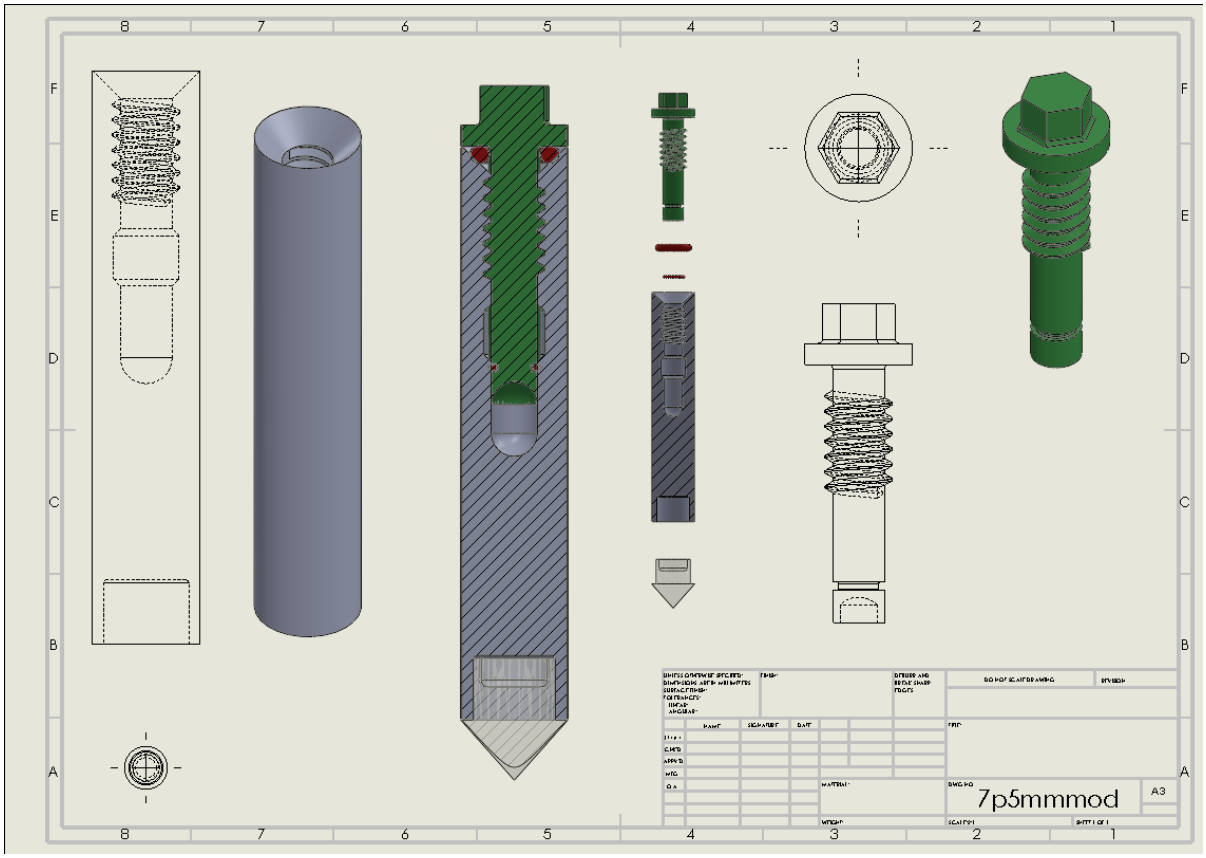

Exhibit G. Representative drawing for in situ rotor design for specialized applications.

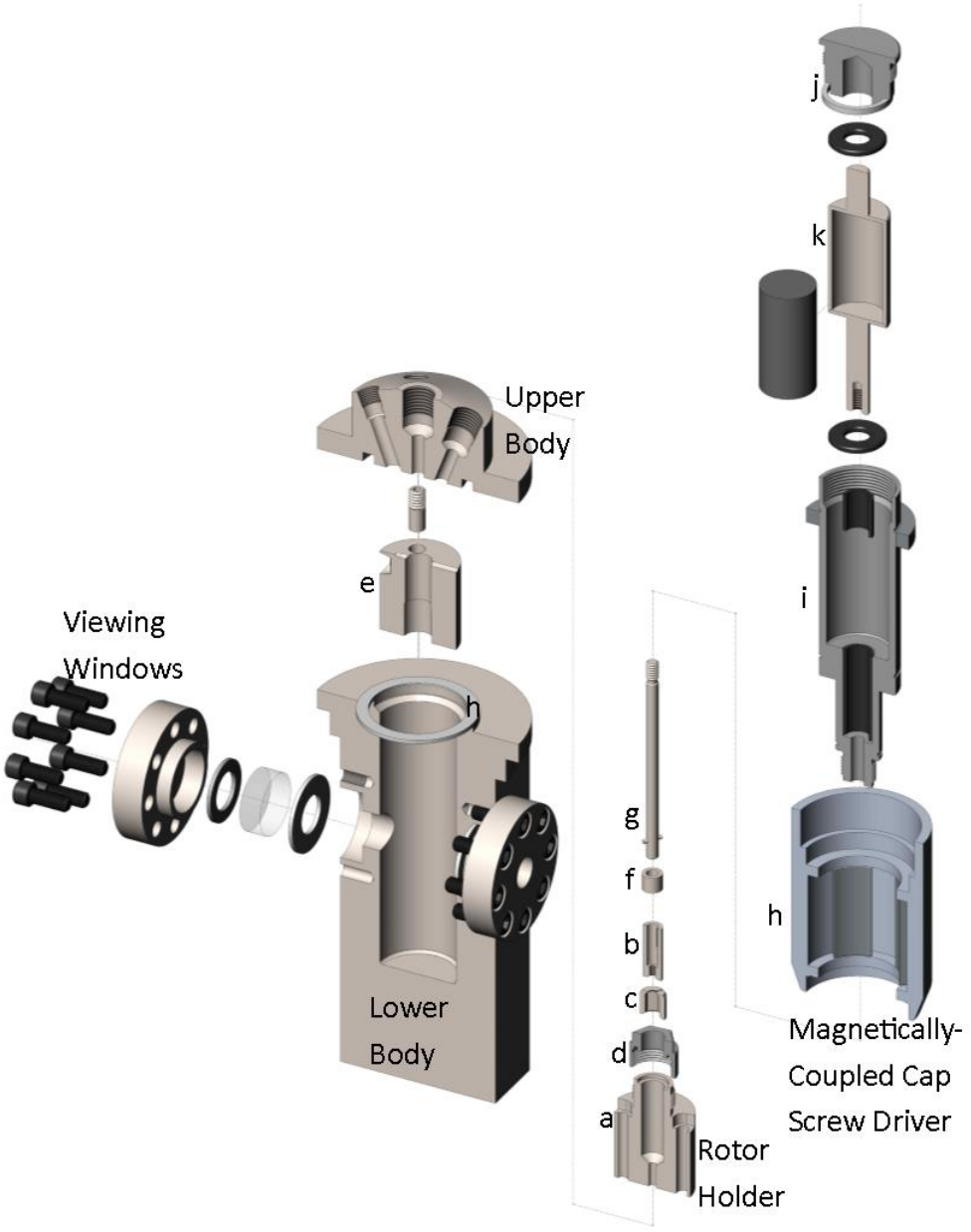

Exhibit H. Schematic of the magnetically-coupled high/low pressure NMR loading vessel.

Component Key: screw holes (a), stainless steel sleeve (b), compression washer (c), threaded nut (d), upper housing (e), bit piece (f), drive shaft (g), magnetically-coupled external cylinder (h), second cylinder (i), high-pressure cap (j), magnetically-coupled internal cylinder (k).

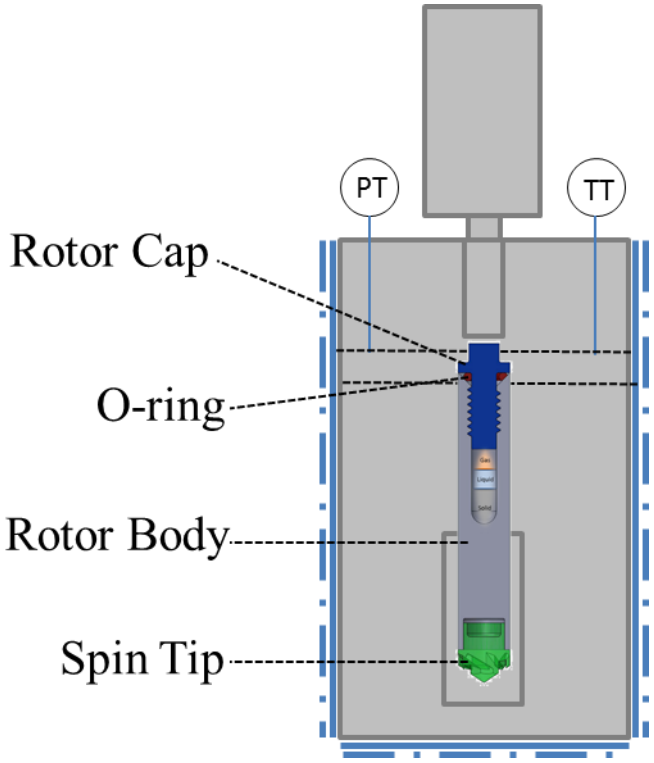

Exhibit I. Schematic of high-temperature, high-pressure operando NMR rotors loaded within the specially-designed loading chamber with magnetic screw coupling and tight control over the chemical environment. The rotor rests with in a modular holder for different rotor sizes and the threaded cap can be rotated to introduce a gas atmosphere.

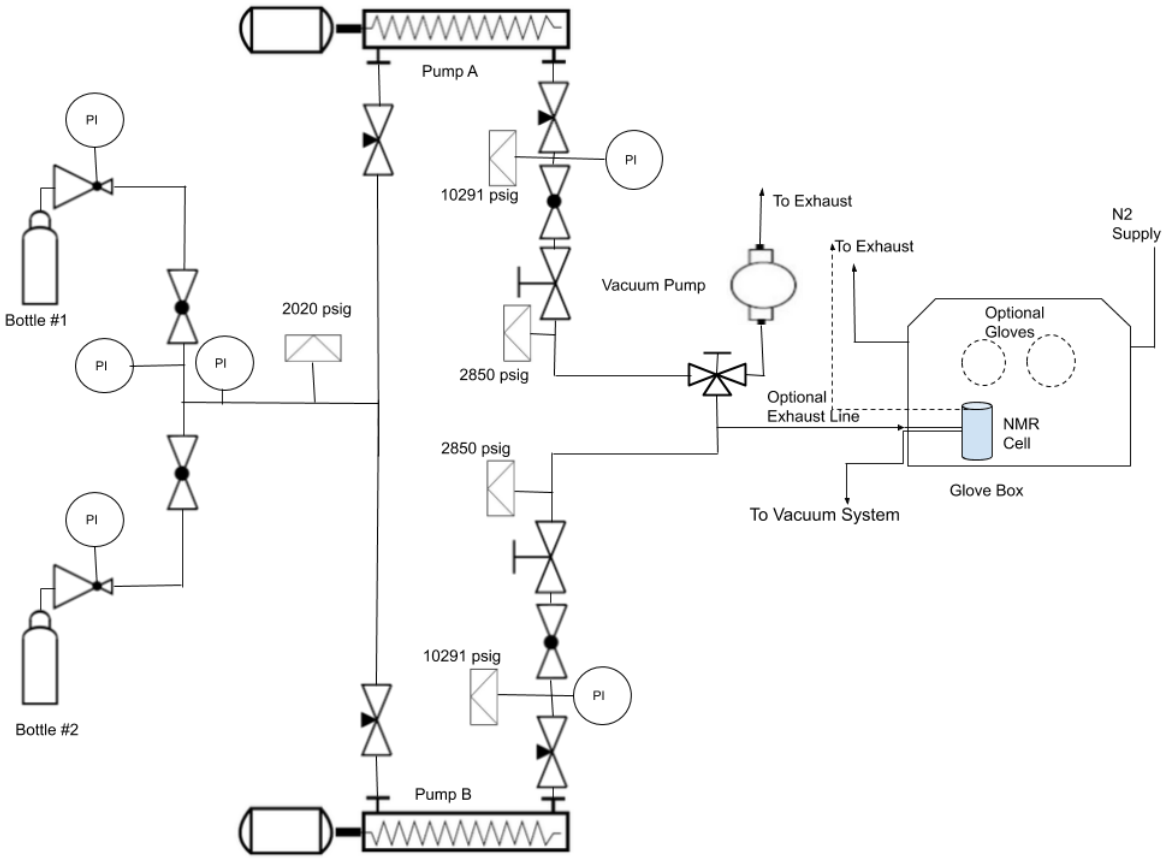

Exhibit J. Schematic of a representative high-pressure delivery aparatus.

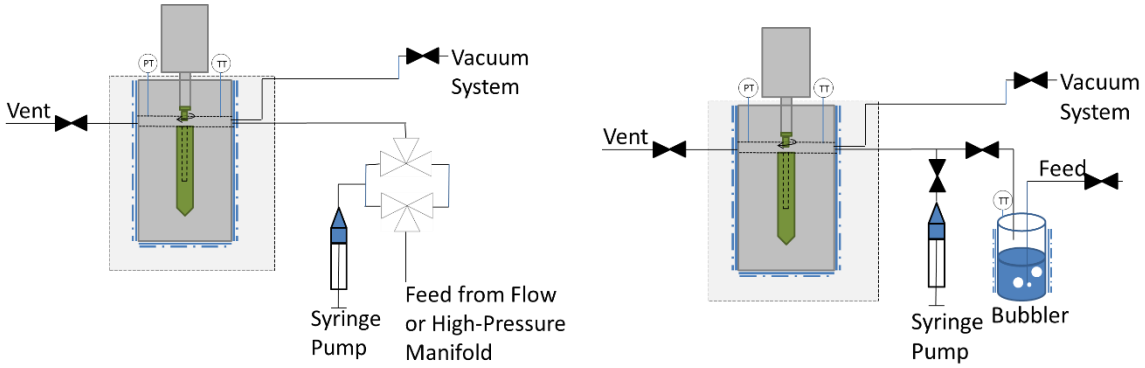

Exhibit K. Representative schematics of gas and vacuum systems coupled with the heated chamber.

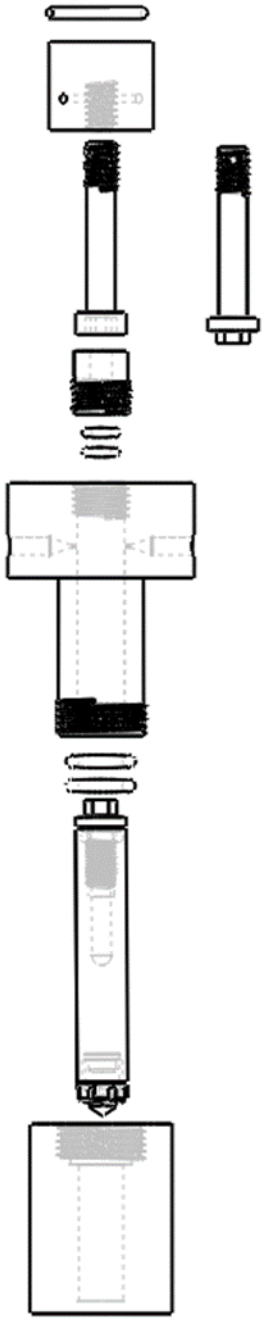

Exhibit L. Exploded view of a simplified, small-volume NMR rotor preparation chamber.

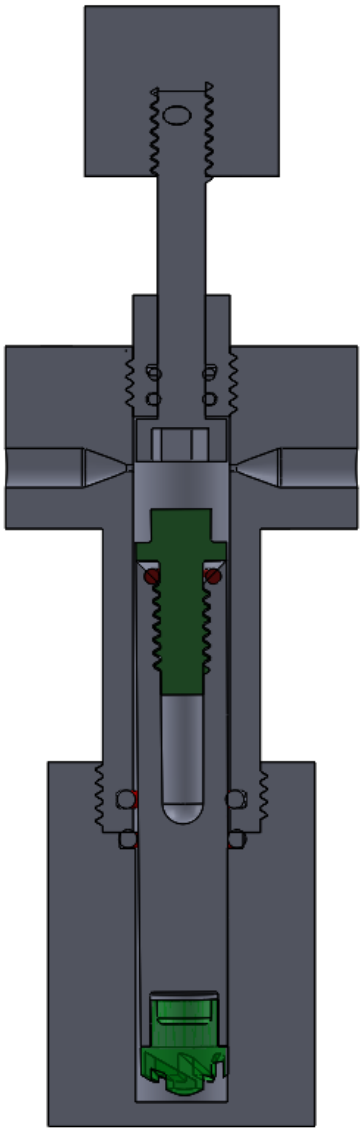

Exhibit M. Section view of a simplified, small-volume NMR rotor preparation chamber.

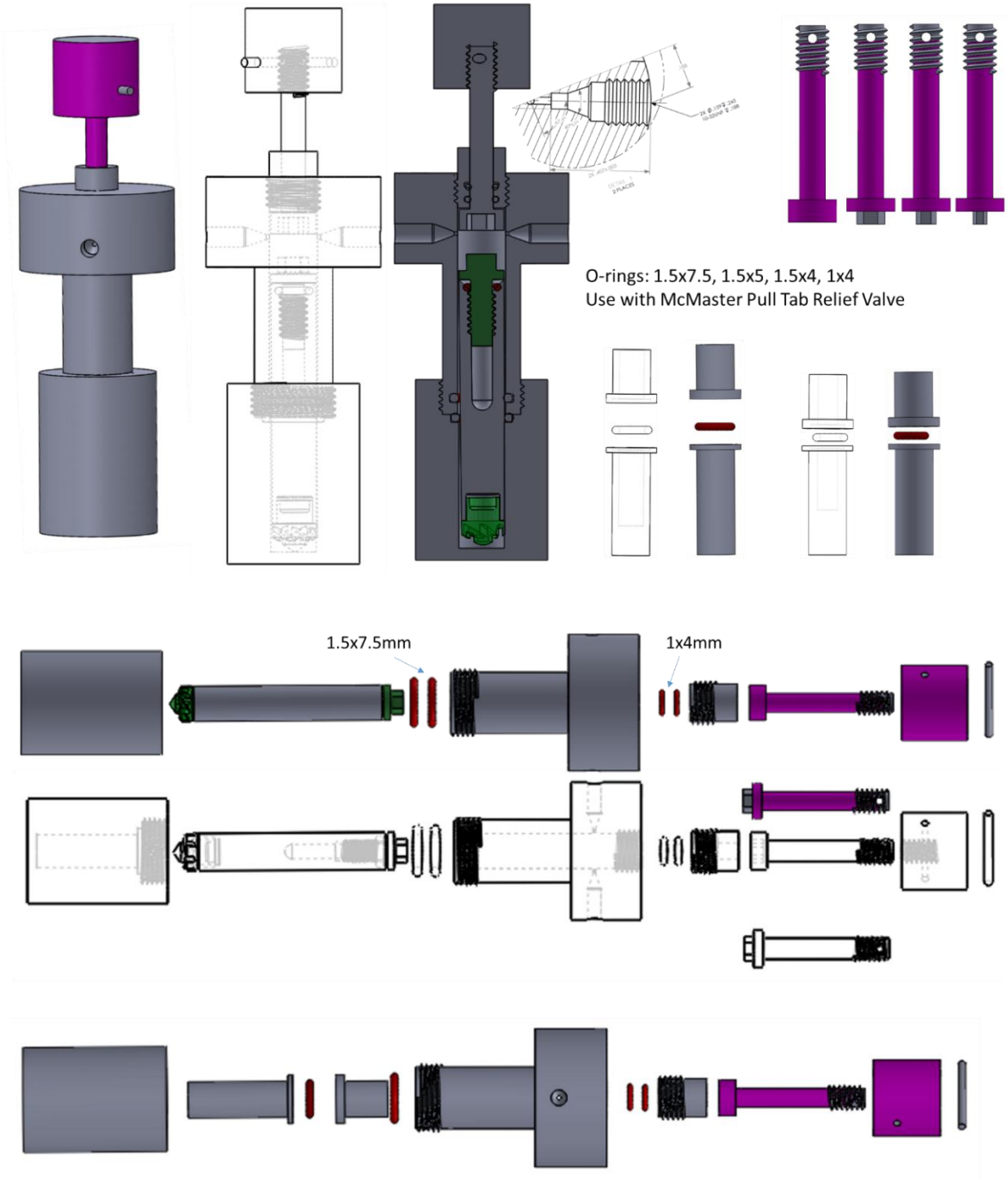

Exhibit N. View of modular components of the simplified, small-volume NMR rotor preparation chamber.

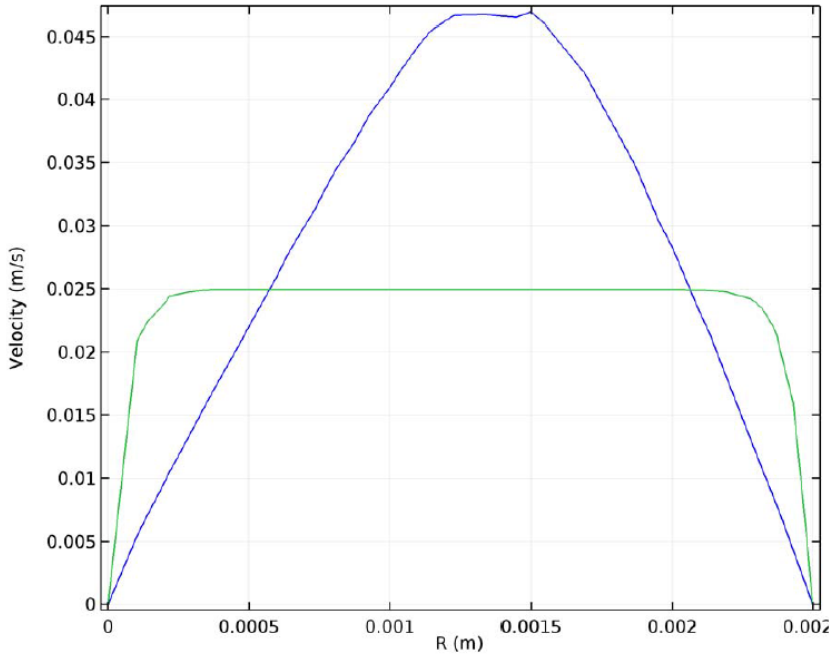

Exhibit O. Representative velocity profile for static flow through NMR cell.

Table S1. Estimated pressure drop for static, flow-through NMR cell.

Characteristic/Inlet Velocity$_{0.8mm}$	**1 m/s**	**5 m/s**	**6.4 m/s**	**10 m/s**	**15 m/s**	**30 m/s**
$\Delta P/L_{0.8}$ (kPa/cm)	0.012	0.054	**0.069**	0.108	0.163	0.35
$\Delta P/L_{1.0}$ (kPa/cm)	0.005	0.026	**0.032**	0.053	0.079	0.16
Flow (ml/g/min) $_{STP}$	140	763	**893**	1527	2290	4580

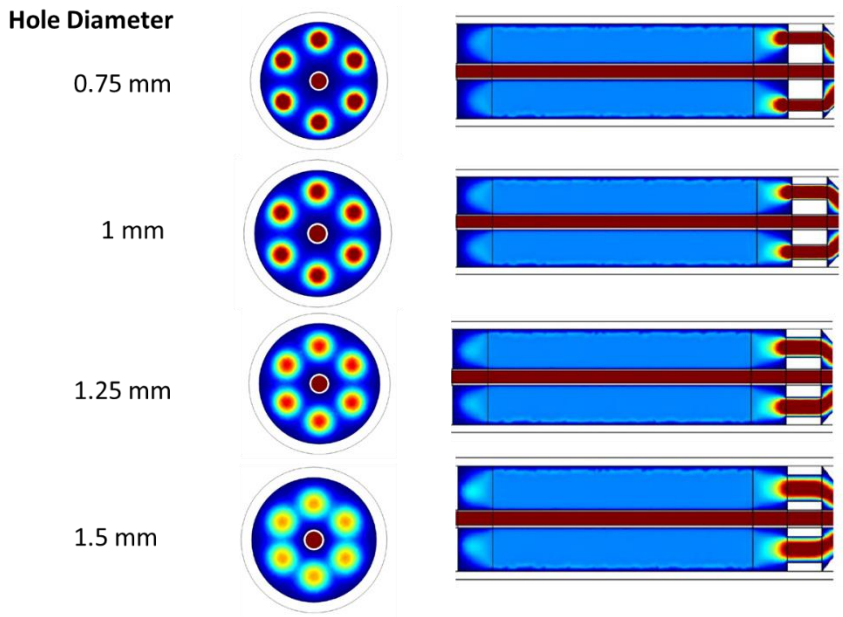

Exhibit P. Flow profiles of contrasting axial channel diameter.

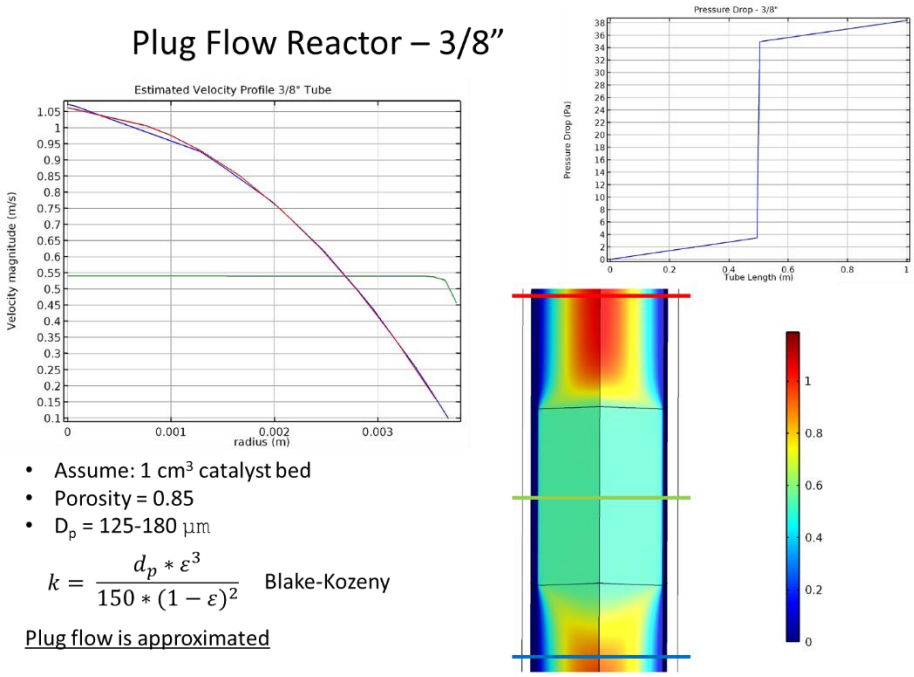

Exhibit Q. Modeled flow profile for a plug-flow tubular reactor.

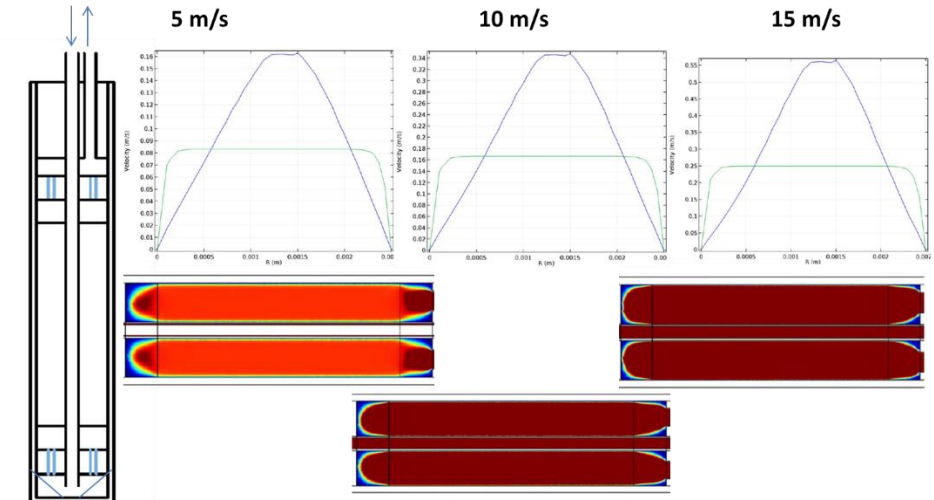

Inlet Tube Size	5 m/s	10 m/s	15 m/s
ΔP/L (kPa/cm)	0.054	0.108	0.163
Flow (ml/g/min) $_{STP}$	763	1527	2290

5% Loading: 237 ml/g/min

10% Loading: 458 ml/g/min

Exhibit R. Flow profiles, velocities, and pressure drops for the static NMR cell.

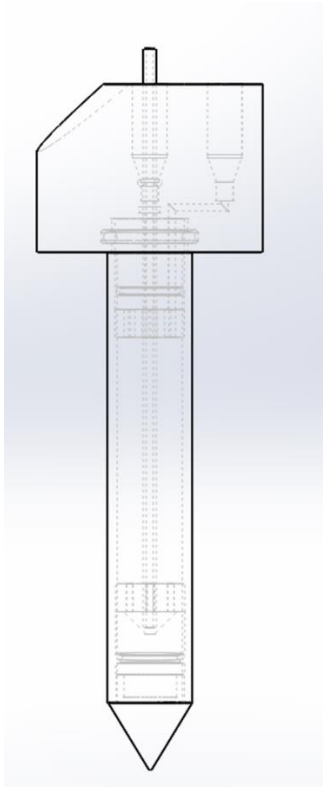

Exhibit S. Schematic of the interior of the static in situ NMR cell.

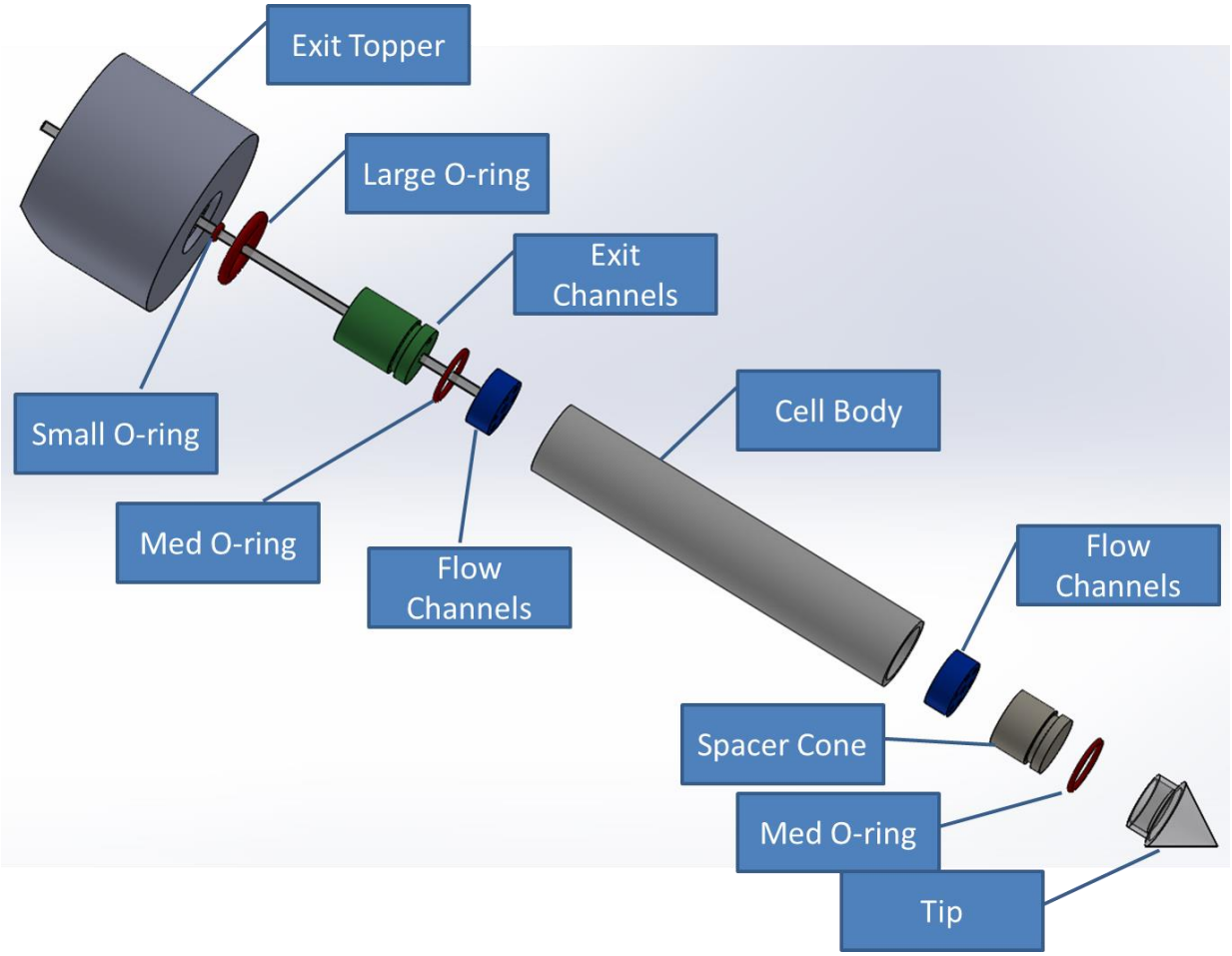

Exhibit T. Exploded view of the static, in situ NMR cell.

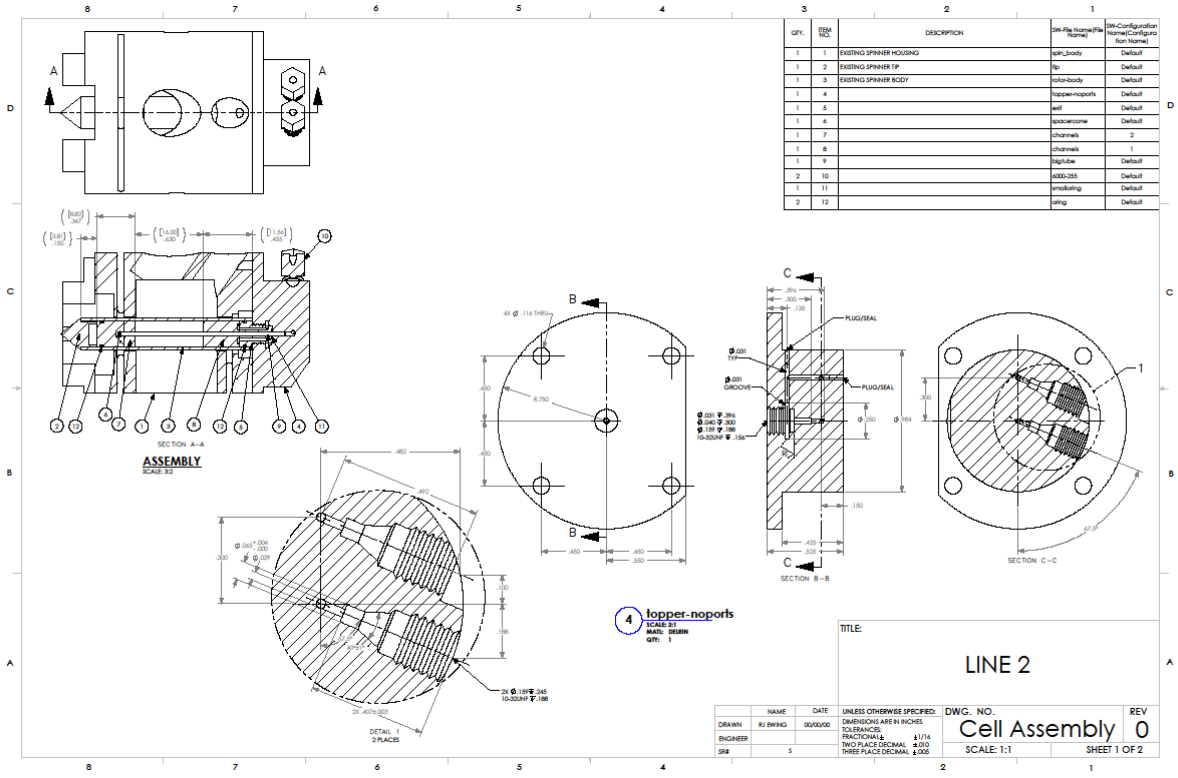

Exhibit U. Drawings for the static, in situ NMR cell assembly.

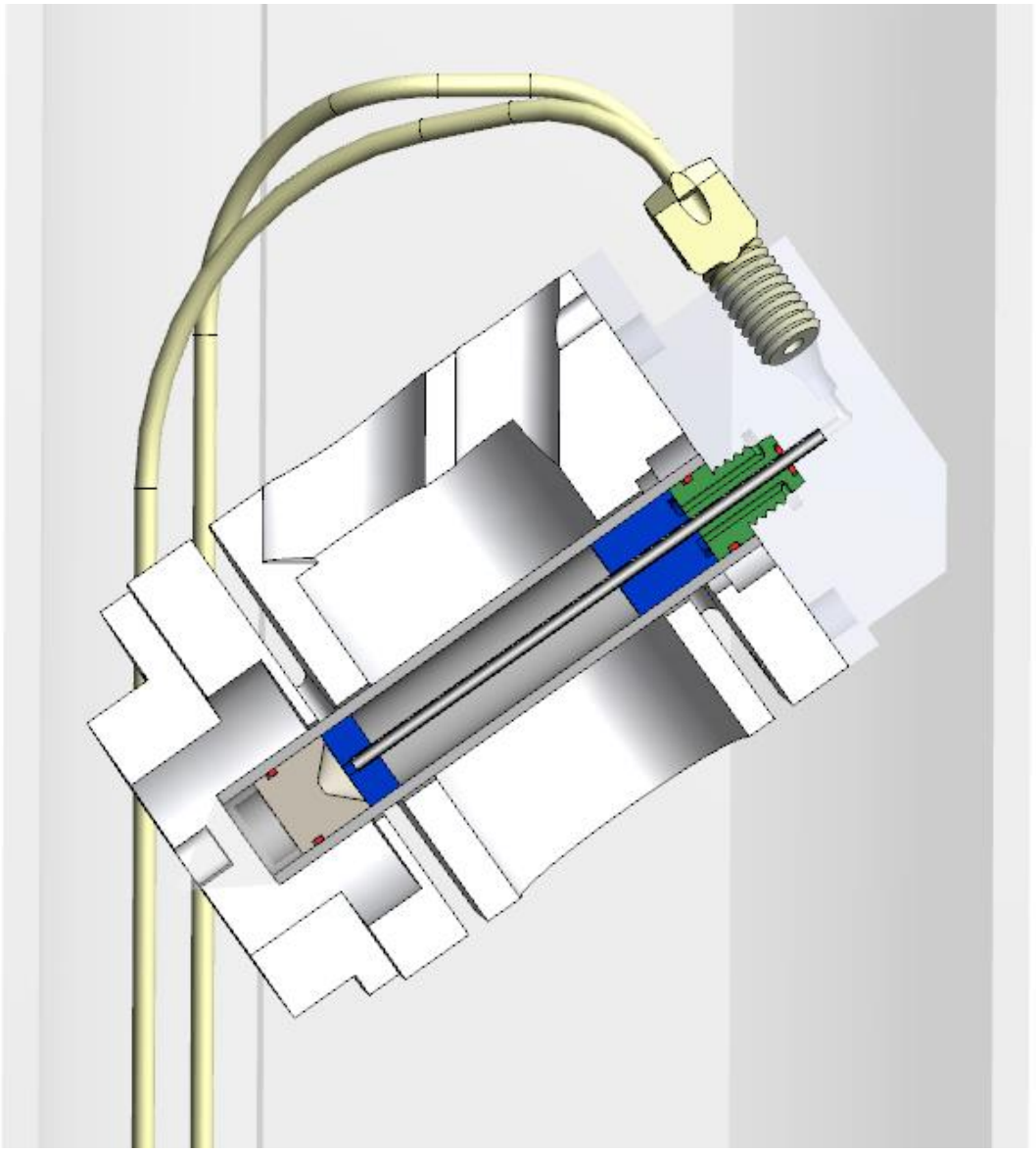

Exhibit V. Cross-section of static, flow-through NMR cell in the NMR probe.

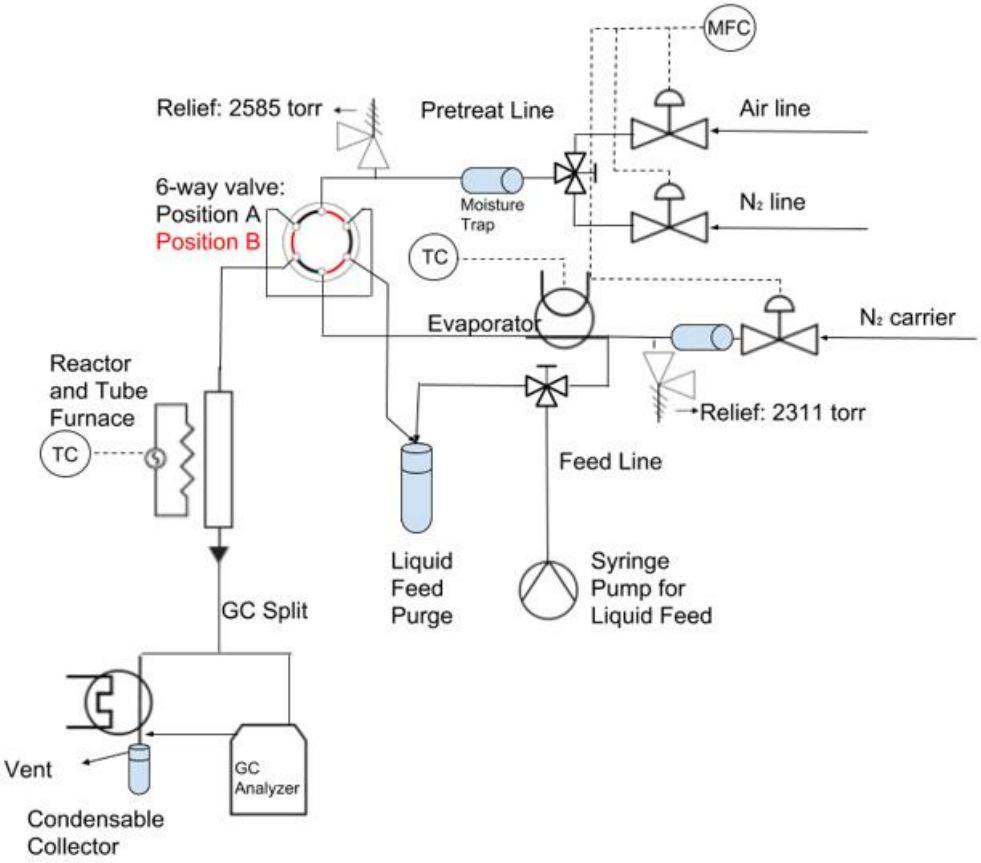

Exhibit W. Schematic for test unit used for dehydration reactions.

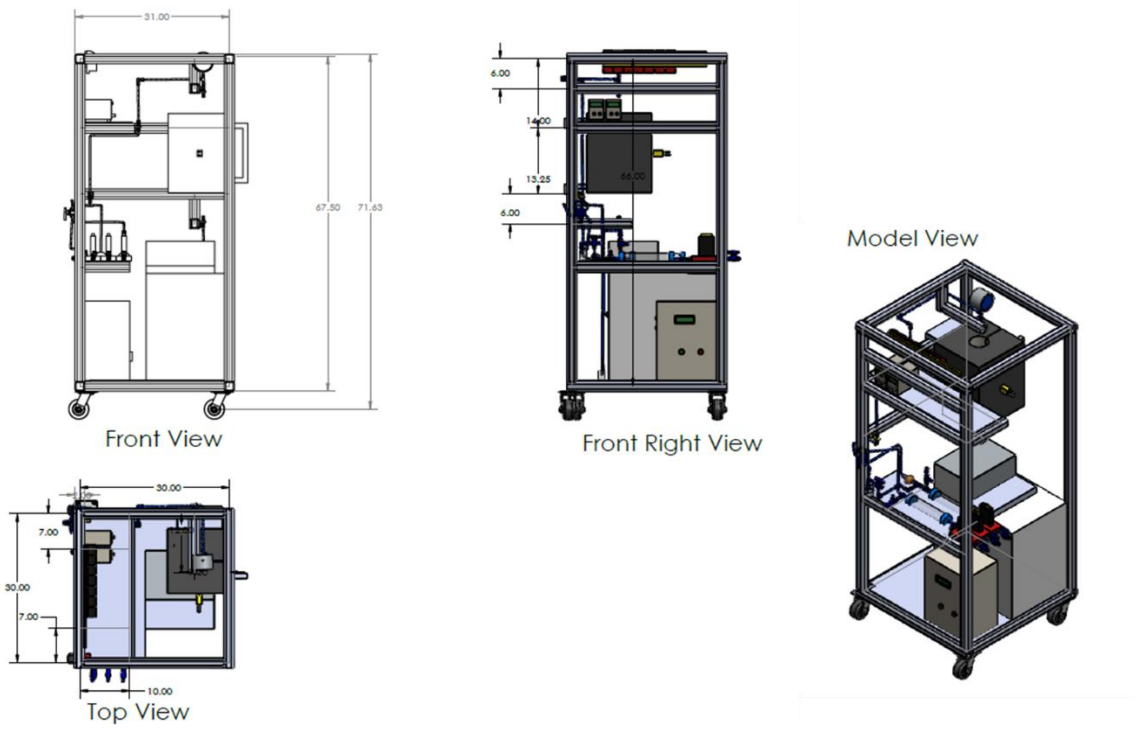

Exhibit X. Reactor test stand.

Appendix B: Experimental Methods

Sample Preparation

The silica support used for the V_2O_5/SiO_2 study was Cabosil EH-5. This fluffy material was pretreated with water in order to condense its volume for easier handling. The wet SiO_2 was dried at 120˚C and subsequently calcined at 500˚C overnight. The supported V_2O_5/SiO_2 catalysts were prepared by the incipient-wetness impregnation of 2-propanol solutions of vanadium isopropoxide ($VO(O\text{-}Pri)_3$, Alfa-Aesar 97% purity). The preparation was performed inside a glovebox with continuously flowing N_2. The SiO_2 support was initially dried at 120°C to remove the physisorbed water before impregnation. After impregnation, the samples were kept inside the glovebox with flowing N_2 overnight. The samples were subsequently dried in flowing N_2 at 120°C for 1 h and 300°C for 1 h. Next, the samples were calcined in flowing air at 300°C for 1 h and 450°C for 2 h. Prepared catalysts were transferred into individual glass tubes and capped with quartz wool for dehydration. The sample tubes were then placed inside a tubular glass vacuum chamber attached to a turbo molecular pump (Agilent TPS Compact) with the application of vacuum controlled by a bellows valve. Vacuum was slowly applied to the sample chamber until a pressure on the order of 10^{-6} Torr was achieved. The temperature of the sample was adjusted with a tube furnace (Thermolyne 21100) and monitored with an Omega MDSSi8 series bench top indicator. The catalysts were heated at 300˚C for three hours. After this time elapsed, the samples were cooled under vacuum and the chamber, sealed closed with a bellows valve, and moved to a N_2 purged glove box for loading into the 1.6 mm pencil-type rotors. The sample color changed from yellow-brown to dark grey-blue upon dehydration, suggesting a change in the coordination environment of vanadium and the possible presence of V^{4+} species.[322]

V_2O_5-WO_3/TiO_2 catalyst samples were prepared by incipient wetness impregnation. An aqueous solution of ammonium metatungstate (0.06 M, Pfaltz & Bauer, 99.5%) or ammonium metavanadate (0.35 M, Aldrich) was added to P25 TiO2 (Degussa, ~55 m2/g) until inceptively wet and the sample was subsequently mixed for 30 minutes. The sample was then dried overnight and subsequent impregnation was repeated with the second metal precursor (if applicable) as previously described[217]. After the second drying step, all samples were dried with flowing air (0.1 L/min) at 120°C for 4 hours. The samples were calcined at 550°C for 4 hours under flowing air and a 1°C/min ramp rate. Prior to magnetic resonance measurements, catalyst samples were dried in flowing dry air (~20 sccm/mg) at 400°C for 3 hours to dehydrate the surface. The samples were sealed under dry air at elevated temperature with isolation valves at each end of the reactor tube and transferred to a dry, N_2 purged glovebox through an antechamber for further processing. The samples were then loaded into 2.5 mm pencil-type Bruker NMR rotors and sealed prior to transfer and analysis in the Bruker 600WB spectrometer (1.6 mm for the 850 MHz measurements). Dehydration of the materials before and after the experiment were confirmed by ^{1}H NMR.

Dominant facet titania nanoparticles were synthesized via a hydrothermal method. $K_2Ti_6O_{13}$ nanowires were first made by dispersing 44.8 g of KOH in 80 ml of water. After ultrasonic treatment for 20 minutes, 2 g of Degussa P25 were added and sonicated until well dispersed. The solution was then placed in 150 ml Teflon autoclave liners inside of autoclaves (50 ml in each) and heated for 24 hours at 200°C. The resulting nanowires were then washed several times with water and ethanol until the washing solution pH was stable. To synthesis

(101) titnia, 0.2 g of nanowires were dispersed in 180 ml water. The pH was adjusted to ~3-5 and then the solution was added to an autoclave for 48 hours at 200°C. TiO_2-(001) was synthesized by dispersing 0.167 g of potassium titanate in 100 ml of water. 30 g of urea was dissolved into the solution as a capping agent. The resulting mixture was brought to pH 13.1 – 13.4 with KOH and well mixed. The solution was then heated in an autoclave at 200°C for 20 hours. The resulting nanoparticles were washed with water. Vanadia was deposited via dry impregnation of ammonia metavandate dissolved in an aqueous solution of dilute oxalic acid.

$V_2O_5/TiO_2/SiO_2$ catalysts were prepared on SBA-15 by impregnating titanium isopropoxide suspended in toluene onto the SiO_2 under an inert environment. The samples were then dried to remove excess solution and calcined at 500°C in dry air to form the supported titanium oxide phase on silica. Vanadium isoporpoxide was then impregnated onto the bi-layered support and calcined for two hours at 500°C.

Titanium nitride nanopowder (TiN, 99.2%, 20m, US Nanomaterials, Inc.) was calcined in an oxidative environment at different temperatures to achieve a differing degree of surface oxidation. The TiN nanopowder was loaded in a vertical quartz tube (250 mm O.D, 180 mm I.D.) and calcined at 350, 400, 450, 550, and 650°C in dry air (UHP, Praxair, 50ml·min^{-1}) for 4 hours. These dry oxidation treatment result in the formation of vacancy-rich TiO_2 with a core-shell structure (TiN core and TiO_2 shell from the oxidation of TiN as denoted to TiO_xN_y hereafter). As synthesized samples are dark blue, light green, yellow, light yellow and white depending on the degree of oxidation. VO_x impregnation over the as-prepared TiO_xN_y supports was carried by incipient wetness impregnation of aqueous vanadium pentoxide (V_2O_5, Sigma Aldrich, ACS grade) dissolved in 1M oxalic acid ($H_2C_2O_4$, Sigma Aldrich, ACS grade) containing the desired

amount of vanadia (7.2 wt% V_2O_5 which corresponds to nominal monolayer coverage). After impregnation, the samples were dried in the oven at 90ºC overnight, and further calcined at 350ºC for 2h in flowing air (Praxair, UHP, 50 ml·min^{-1}). The temperature for the calcination was carefully controlled to avoid the incorporation of additional oxygen in the TiO_xN_y support. Additional catalysts with different loadings of vanadia were prepared using nano-powdered TiO_2 purchased from Sigma-Aldrich (99.7%, 21nm). In order to quantify the amount of oxygen atoms present on the titanium oxynitride support, the mass change experienced by TiN ($TiN + aO_2 \rightarrow TiO_{2a}N_{(1-a)} + aN_2$) was monitored by means of thermal gravimetric analysis (TGA). An inert alumina crucible filled with about 5 mg of TiN nanopowder was placed in a TGA instrument (METTLER TOLEDO). Then temperature was raised from ambient temperature to 900ºC at a ramping rate of 10ºC/min in air flow (UHP, Praxair, 50ml ·min^{-1}).

The zeolites (Si/Al = 15 and 40) were obtained by calcination of the NH_4-form zeolites (CBV3024E and CBV8014 from Zeolyst International) at 450ºC under air flow, and then stored for more than 2 days under ambient temperature and humidity prior to further treatment or measurements. Prior to ^{1}H MAS NMR experiments, the sample was put in a quartz tube, which was later connected to flowing nitrogen (10 ml/min) and heated up to 400°C for 10 hours. The samples were then allowed to cool down to room temperature and packed into NMR rotors in a dry nitrogen glove box as soon as possible. Water was introduced to zeolite samples in the liquid phase for the *in situ* tests. To adsorb water vapor, dehydrated zeolites were first sealed in the glovebox into NMR rotors and then transferred into the NMR probe by a sealed glass vial to avoid exposure to air during transit. After the relocation of the packed rotor, it was exposed to the nitrogen gas used to spin NMR rotor. Even though a grooved Kel-F plunger/plug was used to

seal the rotor, the sample still adsorbed the moisture from nitrogen slowly in some cases. The sample was considered equilibrated when the change of spectra was less than 1 % over several days, after which the rotor was taken out remained capped, but exposed to ambient humidity before returning to the probe for measurements. Alternatively, liquid water was injected into the unsealed rotor[19] using a microliter syringe after which the rotor was sealed. The loadings were calculated gravimetrically, based on the concentration of framework Al site, and were verified with spin counting experiments leading to an error estimation of 10 %. Since the homemade rotor is heavier and thicker than commercial rotors, an ethylene glycol temperature calibration was necessary for accurate temperature set points.

Supported polyoxometalate catalysts were synthesized by incipient wetness impregnation of the crystalline Keggin clusters onto colloidal SiO_2 (Cab-O-sil HS-5; ~300 m^2/g surface area; 1.5 cm^3/g pore volume). The silica was thrice washed with 1M HNO_3 and treated in dry air at 300°C for 5 hours to remove impurities. The polyoxometalate was dissolved in ethanol prior to slow introduction onto the silica support with frequent mixing. The material was then allowed to stand in a sealed container for 24 hours prior to treatment at 150°C in dry air for 24 hours. The weight loading was controlled to 10%, unless otherwise specified, and the use of metal implements was avoided to mitigate potential reduction of the polyoxometalate clusters. $H_5AlW_{12}O_{40}$ was synthesized by dissolving 100 g of $Na_2WO_4 \cdot 2H_2O$ in 400 ml of water. Approximately 23 ml of hydrochloric acid was added to the solution slowly under vigorous stirring to reach a pH of 7.7. The dropwise addition of acid was periodically suspended to allow the tungstic acid precipitate to dissolve. The solution was heated to reflux and 13.32 g of $AlCl_3 \cdot 6H_2O$ dissolved in 80 ml water was added dropwise over the course of two hours under

constant stirring. The solution was prevented from becoming opaque with additional stirring. After all of the aluminum chloride was added, the solution was refluxed for an additional hour, cooled to room temperatures, and filtered. The resulting solution contained $Na_6[Al(AlOH_2)W_{11}O_{39}]$ and exhibited chemical shifts of 73 ppm and 8 ppm. This solution was then acidified to pH 0 with sulfuric acid (~20 ml), then an additional 3 ml sulfuric acid was added prior to heating to reflux. This yellow solution clarified within 16 hours of the reflux and full conversion occurred within 6 days. The solution was then cooled to 0°C and cold sulfuric acid (147 ml) was added to avoid excessive heating. 500 ml of diethyl ether was added and gently shaken in a separatory funnel. Frequent ventilation was required to minimize pressure buildup. The procedure proceeded until evaporation slowed down and shaking could intensify. The three layers were permitted to separate. The middle layer is the aqueous $H_5AlW_{12}O_{40}$ layer and bottom was the etherate layer of $H_5AlW_{12}O_{40}$. The bottom layer was removed and the two remaining layers were repeatedly shaken and extracted further to enhance the extraction efficiency. The total collected etherate layers were concentrated to dryness by rotary evaporation then dissolved in 20 ml of hot water, concentrating by gentle heating followed by cooling to 0°C.

18.2 MΩ water was generated by a Purelab Flex and mixed with $H_2{}^{17}O$ water to formulate 18.2 MΩ 20% $H_2{}^{17}O$.

BET Surface Analysis

Surface analysis was conducted with an ASAP 2020 (Micromeritics). The samples were degassed for four hours at 200°C before measurement. N_2 adsorption and desorption isotherms

were acquired at -195.8°C to determine the BET surface area. Between 0.12 and 0.20 g of material were used for each measurement.

X-ray Diffraction

XRD patterns were collected using a PANalytical X'Pert MPD system with a vertical θ-θ goniometer with a 220 mm radius. The X-ray source is a long-fine-focus ceramic X-ray tube with a CuK- alpha anode (1.54056 Å). The operating power was 45 kV at 40 mA (1.8 kW). The scans were collected over the range of 10° to ~80° (2θ) at a rate of 1.5 deg/min and a step size of 0.04°. Rietveld Refinement was conducted with the aid of the Materials Analysis Using Diffraction software.[323]

Raman Spectroscopy

Raman analysis of the catalysts were determined with a visible (532 nm) laser excitation on a single stage Horiba-Jobin Yvon Laboratory Ram-HR Raman spectrometer with a confocal microscope (Olympus BX-30) and a notch filter (Kaiser Super Notch). The visible excitation was generated by an Nd-YAG double diode pumped laser (Coherent Compass 315M-150, output power of 150 mW with power at the sample of 10 mW). The scattered photons were directed into a single monochromator and focused onto a UV-sensitive liquid N_2 cooled CCD detector (Horiba-Jobin Yvon CCD-3000V) with a spectral resolution of ~1 cm^{-1} for the given parameters. Powder samples were loaded into a Harrick Scientific cell (HVC-DRP4) connected to a gas control system. The

temperature of the reaction chamber was controlled by the Harrick ATC Temperature Controller unit.

Electron Paramagnetic Resonance

Continuous Wave Electron Paramagnetic Resonance (CW-EPR) X-band (9.30 GHz) spectra were collected with a Bruker Elexsys 580 EPR spectrometer. The field was modulated at 100 kHz and a microwave power of 30 dB, with a receiver gain of 80 and 4 repetitions. The sample temperature was maintained at 125 K for all analyses. The weight percent of vanadium in the reduced state was calculated using a 0.5 mM solution of VO_2 dissolved with a small amount of HCl and converted the integral to equivalent mg of vanadium and dividing by the weight of the sample.

Scanning Transmission Electron Microscopy

STEM images were acquired using an FEI Titan 80-300 STEM equipped with a condenser lens spherical aberration corrector. Samples were exposed to ambient atmosphere prior to insertion into the column under ultra-high vacuum.

Density Functional Theory Calculations

To accompany the spectroscopic observations for V_2O_5/SiO_2, NMR chemical shift calculations were conducted to assist in the interpretation of experimental results. Electronic

structure simulations utilized the Amsterdam Density Functional (ADF) package.[324-326] The geometry was optimized utilizing the Generalized Gradient Approximation with the dispersion-corrected Becke-Lee-Yang-Parr functional (GGA-BLYP-D).[327-329] The all electron, triple ζ, two polarization function (TZ2P) was implemented as the basis set with Slater type functionals.[330] Simulated NMR calculations were conducted with density functional theory using the Gauge Independent Atomic Orbital (GIAO) approach based on the findings of the Ziegler group.[331-334] Scalar relativistic effects were included at the two-component zero-order regular approximation (ZORA) level for the NMR calculations with the BLYP functional.[335-337]

^{51}V NMR chemical shifts require a standard reference for direct comparison between the spectra and calculations. $VOCl_3$ has previously been shown to be an acceptable representative molecule for NMR calculations,[338-339] and we have used it as the ^{51}V NMR reference. The resulting calculated electronic shielding for $VOCl_3$ was -1962.8 ppm at the BLYP-D level and -1921 ppm at the BLYP/ZORA level. The resulting calculated shielding for a vanadium atom shift is given as δ_{obs} (ppm) = $\sigma_{ref}(VOCl_3, calc) - \sigma_{calc}$.

The interpretation of the V_2O_5/TiO_2 NMR spectra was aided by NMR chemical shift calculations using density functional theory as implemented in the Amsterdam Density Functional (ADF) software[324-326] and in Gaussian-16.[340] Large model cluster geometries were optimized using the generalized gradient approximation with Grimme's third generation dispersion-corrections applied to the Beck-Lee-Yang-Parr functional (GGA: BLYP-D3).[327-328, 341] Scalar relativistic effects were accounted for using the zero-order regular approximation (ZORA).[336-337] A Slater-type, all-electron, triple- ζ, two-polarization function (TZ2P) was used as the basis set.[330]

Diffraction patterns of both the SCR samples demonstrate anatase as the primary polymorph. As such, cluster models were constructed to mimic the (101) and (001) planes of anatase. Howard et al.'s structural determination of anatase was used as the base model whereby the crystal was cut along the aforementioned faces.[342] The models provided two layers of depth, where the bottom layer was frozen to preserve the crystal structure. Terminal oxygen atoms were charged balanced with protons at a length of 9.7 Å in the direction of the removed Ti atoms. The vanadium structure was placed atop this surface model and optimized as described above. The smaller model cluster calculations were performed with Gaussian 16.[340] The geometries were optimized at the B3LYP[327, 343] level with the aug-cc-pVDZ(-PP)[344-346] pseudopotentials on the V, Ti, and W. The NMR chemical shift calculations were done with ADF using the BLYP functional and the TZ2P basis set with ZORA as described above. To correlate the calculated nuclear shielding from DFT to the observed NMR chemical shifts, vanadium oxytrichloride ($VOCl_3$) was used as the computational standard at 0 ppm.[338-339] The calculated shielding relates to the chemical shift by $\delta(^{51}V) = \sigma_{calc,\ ref} - \sigma_{calc}$. Our model of V_2O_5 predicts peaks at -618 and -607 ppm for the average and center vanadium atoms, respectively, which correlates with the experimental value of -613.8 ppm, providing a validation of our computational approach.

The Amsterdam Density Functional (ADF-2014) package[347] was applied to calculate the electronic structures for the hydronium ion work. The generalized gradient approximation (GGA) based Becke-Lee-Yang-Parr function with dispersion correction (BLYP-D)[348] was used for the geometry optimization. All calculations were performed at the Slater-type TZ2P basis set (triple-ζ, 2-polarization function, all-electron).[349] The geometry-optimized structures at the same level of the theory were applied to calculate the chemical shielding for each atom with the same

basis set. Tetramethylsilane (TMS) was used as the 1H chemical shift reference by converting the calculated shielding to the observed shielding using following equation: $\delta_{iso} = \sigma_{(TMS)} - \sigma_{calc} = 31.4 - \sigma_{calc}$. H-ZSM5 clusters containing 58 T-atoms were extracted from a previous periodic structure optimization[350], cut to the size used in this study, and terminated with H-atoms (Si-H bond lengths fixed at 1.455 Å) to replace terminal O-atoms while maintaining peripheral charge neutrality, as established elsehwere.[351] Except for these charge-balancing protons, atoms exceeding 2 bonds from the Al site were frozen to maintain the integrity of the zeolite structure. Water molecules were added for cluster optimization in a stepwise fashion.

Solid State ^{51}V NMR Spectroscopy

V_2O_5/SiO_2 solid state ^{51}V NMR experiments were performed on a Varian-Inova 850 MHz NMR spectrometer equipped with a commercial 1.6 mm pencil-type MAS probe, operating at a magnetic field of 19.975 T. The corresponding Larmor frequency was 223.367 MHz. The single pulse MAS NMR experiments were acquired with a $\pi/2$ pulse width of 1.85 μs and a spectral width of 5 MHz at a sample spinning rates of 36, 30 and 28 kHz. Rotor-synchronized Hahn echo NMR experiments were performed to collect the ^{51}V MAS NMR spectra. A half echo time equal to one rotor period was used. Depending on the samples, 150,000-330,000 scans were used with a 0.2 s recycle delay. All of the chemical shifts were externally referenced to the center-band of bulk V_2O_5 (-610 ppm relative to $VOCl_3$ based on literature reports). All NMR measurements were carried out at 25°C. Spectral deconvolution was conducted using the DMFIT program,[352] and a spinning side band simulation was incorporated into this analysis.

Other ^{51}V MAS NMR experiments were conducted with a 14.0921 T Bruker 600WB spectrometer utilizing a commercial 2.5 mm pencil-type MAS probe and a Varian-Inova 850 MHz spectrometer equipped with a commercial 1.6 mm pencil-type probe. The corresponding ^{51}V Larmor frequencies are 157.778 and 223.367 MHz. Single pulse NMR experiments were conducted with a $3\pi/16$ pulse width of 1.5 μs, a delay time of 0.2 s, a spectral width of 1 MHz, and an acquisition time of 4.096 ms (1.85 μs, 0.2 s, 5 MHz). Typically, 40,000 scans were collected per ^{51}V MAS NMR spectrum. Chemical shifts were externally referenced to the centerband of bulk V_2O_5 at -613.8 ppm relative to $VOCl_3$. Spinning rates of 32-35 kHz were used for all 600 MHz experiments, which proved a superior option in removing sideband overlap compared to 850 MHz experiments. Comparison of the current results to our previous work will show a chemical shift difference of a few ppm due to our direct utilization of $VOCl_3$ as the standard instead of the secondary reference V_2O_5, which has an isotropic chemical shift of -613.8 ppm relative to $VOCl_3$ and was previously reported as -610 ppm (see Figure S15 and Figure S16).

^{1}H MAS NMR experiments were conducted on a 600WB NMR to verify the dehydrated state of vanadia catalyst materials and collected with a π pulse width of 1.25 μs, a delay time of 2 s, a spectral width of 0.5 MHz, and an acquisition time of 8.192 ms. Typically, 1024 scans were collected per spectrum. Chemical shifts were externally referenced to adamantine at 1.82 ppm. To account for only the signal generated by the sample, rotor and probe background signals were subtracted from each spectra.

In situ NMR spectra collected to characterize the local structure of vanadia species on the catalyst surface. Samples were dehydrated at 300°C (linear heating, 10 °C·min^{-1}) under 10%

O_2/N_2 (0.83 ml·sec^{-1}) for 1 hr. Post-reaction NMR samples were exposed to ethanol (0.1 ml·hr^{-1}) at 200ºC for 1 hr. Oxidized samples were subsequently held at 200ºC in the oxygen stream for 1 hr prior to measurement. The samples were isolated and transferred to an N_2-purged glovebox where they were loaded into the NMR rotors. MAS NMR experiments were conducted with a 600WB Bruker spectrometer employing a commercial 2.5 mm pencil-type MAS probe. ^{51}V NMR spectra were collected with a 3π/16 pulse width of 1.5 μs, a repetition time of 0.2 s, and an acquisition time of 4.096 ms. The corresponding Larmor frequencies are 157.778 MHz.

All NMR spectra for the solvent study were collected with a 300 MHz Varian Inova NMR spectrometer operating at a ^{1}H Larmor frequency of 299.97 MHz and a ^{17}O Larmor frequency of 40.67 MHz. Samples were spun at the magic angle at a spinning rate of 4,000 Hz in a commercial 7.5 mm ceramic probe. A high-temperature, high-pressure NMR rotor was employed to allow for thermal investigations at elevated temperatures and pressures.[19, 235] ^{1}H single pulse experiments were conducted with a pulse width of ~π/140 (0.1 μs), delay time of 200 ms, acquisition time of 1 s, and 32 repetitions. ^{17}O single pulse experiments were conducted with a pulse width of π/2 (8 μs), delay time of 200 ms, acquisition time of 200 ms, and 128 repetitions. Inversion recovery experiments were conducted using a two-pulse sequence of π followed by π/2 (14 and 7 μs for ^{1}H; 16 and 8 μs for ^{17}O) the delay period was varied across 7 to 17 data points to collected the delay-modulated inversion recovery signal. A recycle delay of 10 s was used for ^{1}H measurements and 200 ms for ^{17}O; at least 4 repetitions were used in these measurements with similar acquisition times to the single pulse experiments. All ^{1}H NMR data were externally referenced to adamantane at 1.82 ppm and 17O NMR data were externally referenced to 25ºC water at 0 ppm. The collected inversion data were *fit with* $y(t) =$

$\sum A_i\ (1 - B_i e^{\frac{-t}{T_{1,i}}})$ where y(t) is the normalized spectral intensity as a function of delay time, A is the weighting factor for species i (sum to unity), B is the compensation factor for species i ($1 < B \leq 2$, typically ~2), t is the time used in the pulse delay, and T_1 is the spin-lattice relaxation time of species i. The experimental temperature was controlled using a commercial variable temperature heating stack, externally calibrated with both a methanol and ethylene glycol thermometers. The heating stack flow rate was increased to dramatically reduce thermal gradients across the sample. All free indication decays were processed without line broadening.

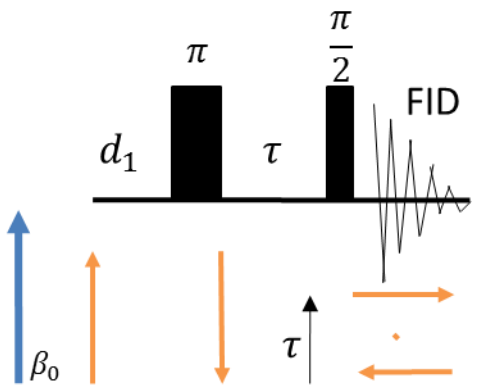

Figure S1. Representative pulse sequence (top) and spin response (bottom) for inversion recover experiments.

^{1}H, and ^{29}Si magic angle spinning (MAS) Solid-state NMR experiments for the hydronium ion work were performed on a Varian-Agilent Inova wide-bore 300 MHz NMR spectrometer and confirmed with a Bruker 600 MHz NMR spectrometer at higher field, ^{27}Al NMR were acquired from an 850 MHz spectrometer. Ex-situ experiments were performed using commercial rotors of different diameters (2.5 mm and 5 mm). Detailed information about each measurement are presented in the figure captions. ^{1}H, ^{27}Al and ^{29}Si spectra were referenced to

tetramethylsilane (TMS at 0 ppm), 0.1 M $Al(NO_3)_3$ in water (0 ppm), and 4,4-dimethyl-4-silapentane-1-sulfonic acid (DSS at 1.534 ppm), respectively. The measurement uncertainty was ±0.1 ppm. After the rotor was loaded into the probe, spin counting techniques were used to estimate the H concentrations. The total hydrogen concentrations were determined via integrating the spectral intensities ranging from 120 to −110 ppm and comparing to an external spin counting standard adamantane. As all spectra were acquired at the same parameters and number of scans, they were normalized to the mass of each sample. The background NMR signals were measured using the same parameters on an empty rotor and subtracted from the spectra. In-situ ^{1}H MAS NMR were carried out using a custom-made 7.5 mm high temperature and high-pressure MAS rotor.[19, 235]

^{1}H-^{29}Si cross polarization (CP) NMR was used to monitor the evolution of the acid site structure during the hydration process. The signal in the ^{1}H–^{29}Si CP MAS NMR spectrum is attributed to the transfer of magnetization from ^{1}H to ^{29}Si mediated by the dipolar interaction, meaning that the CP signals originate only from ^{29}Si in close proximity to ^{1}H nuclei. Thus, CP becomes more efficient as the distance between the ^{29}Si and the ^{1}H nuclei decreases or the adjacent ^{1}H nuclei increase in quantity or localization at a particular position. In absence of ^{1}H nuclei near ^{29}Si atoms or in the case of increased mobility of ^{1}H increases, CP signals disappear.[275, 353-354]

For the in-situ ^{1}H NMR measurements of zeolite, the chemical shift values, spinning sidebands, and line widths observed in dehydrated zeolites have been used to infer the acid strength of bridging hydroxyl groups as well as the distance between hydroxyl protons and the framework aluminum.[355-360] Baba and co-workers showed that the chemical shift value was

independent of the temperature, although the intensity of the spinning sidebands monotonically decreased, and the peak width increased from room temperature to about 100 °C before decreasing.[355, 361]

Catalyst Activity Testing

SCR reactivity of the supported V_2O_5(-WO_3)/TiO_2 catalysts was investigated in a fixed-bed reactor (Altamira AMI-200 temperature programmed system) equipped with an online quadrupole mass spectrometer (Dycor Dymaxion DME200MS) designated for effluent analysis. Typically, 30 mg of catalyst was loaded into a U-type quartz tubes (0.25" OD standard 6.5" AI-2210) and initially treated with 10% O_2/Ar at 400°C for 1 h to activate the catalyst. The reactor system was subsequently flushed with He for 10 min and the SCR reaction mixture was introduced (35 mL/min of NH_3/He (2000 ppm), 35 mL/min of NO/He (2000 ppm), 5 mL/min of 5% O_2/He). The steady-state SCR reaction was performed for 2 h at 200°C. The following m/z ratios were analyzed for the identification of the exiting gas composition: O_2 (m/z = 32), N_2 (m/z = 28), NH_3 (m/z = 17), NO (m/z = 30), NO_2 (m/z = 46) and N_2O (m/z = 44). Activity data was calculated based on NO conversion.

Methanol ODH reactions were carried out in a fixed-bed reactor insulated within a furnace. Catalysts were sieved to 50 um and diluted 50:1 with silicon carbide of the same size (determined to be inert by control experiments). Catalysts were pretreated at 300°C in simulated dry air. Typically, 20 mg of material would be loaded and 100 sccm N_2, 25 sccm of O_2, and 0.43 ml/hr of methanol would be employed to test the materials (~5% methanol). Products were analyzed online with a microGC.

Before catalytic testing for ethanol ODH, all samples were crushed and sieved to a particle size <150 μm. Steady-state partial oxidation of ethanol experiments were conducted in a continuous flow fixed bed quartz glass micro reactor (6.4 mm I.D.) oriented vertically in an electrically heated furnace (VECSTAR, UK) at atmospheric pressure equipped with a digital PID temperature controller (Digi-Sense). Catalyst samples were supported on quartz wool equipped with K-type thermocouples placed at the vertical center of the catalyst bed. The catalyst was pretreated using a 0.16 $^{o}C \cdot sec^{-1}$ at temperature ramp to reaction temperature and held at this temperature for 1 hr under a O_2/He mixture (5% and 0.5%O_2, Praxair, UHP, 2.68 $cm^3 \cdot s^{-1}$ before exposing catalysts to the reactants. After this pretreatment step liquid absolute ethanol (Fisher, HPLC grade) was evaporated into the flowing O_2/He influent stream at 100^{o}C using a liquid syringe pump (New Era Syringe pump) with the flow adjusted to give the desired ethanol partial pressure (0.5 – 11 kPa). All gas transfer lines before and after the liquid injection port were kept above 140^{o}C to prevent condensation of reactants and products. Ethanol conversion rates on V/TiO_xN_y catalysts were measured at 200^{o}C. The flow of 5%O_2/He were adjusted by a mass flow controller (Brooks 5850E) during these experiments. The rates of ethanol partial oxidation are reported either as total V-atom turnover rates (moles of ethanol converted per total V atom ($*_T$) per second). Chemical species in the feed and reactor effluent stream were measured using an online gas chromatograph (Agilent Micro GC 460) with a micro capillary column (CP5) connected to a micro thermal conductivity detector. For the identification of the observed GC peaks, a mixture of acetaldehyde, water, and ethanol was injected to GC confirming the retention time of each chemical.

Appendix C: Additional Supporting Data

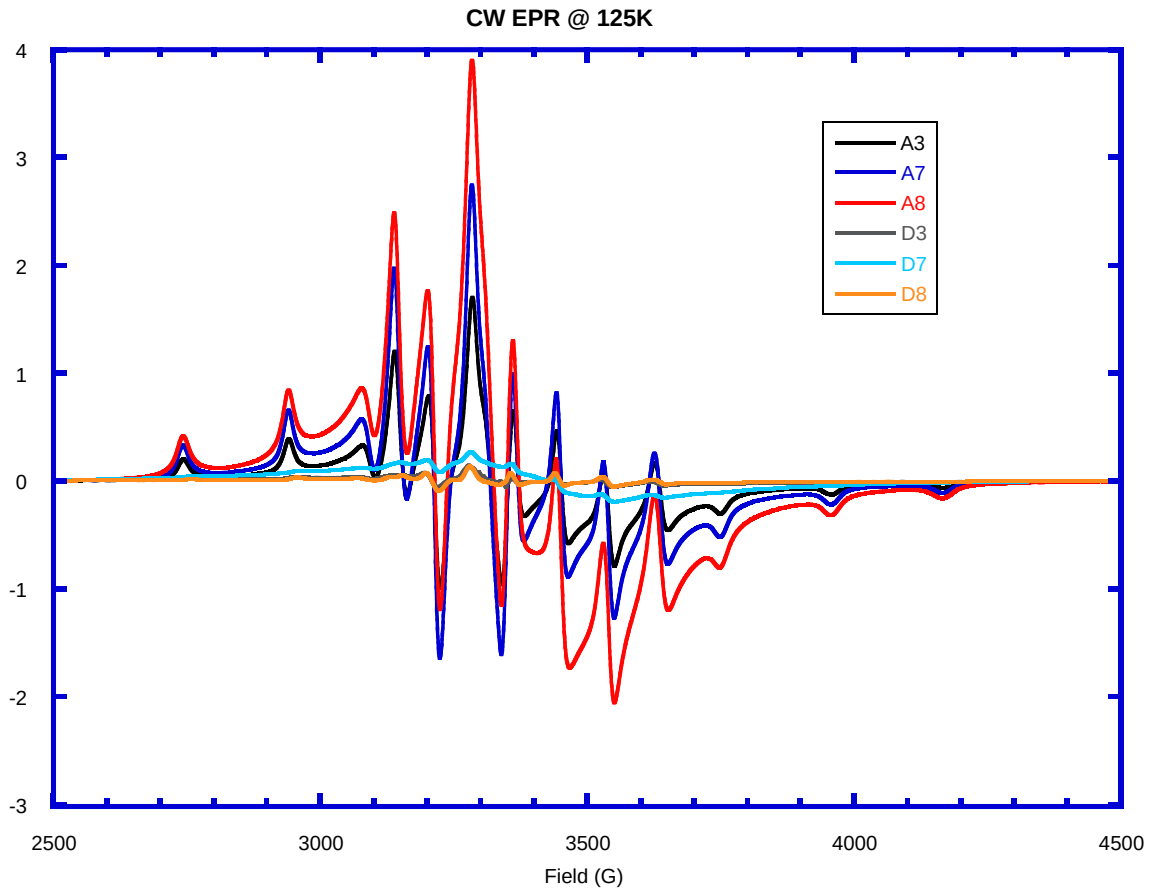

Figure S2: EPR spectra of silica-supported catalysts under ambient (A) and dehydrated (D) conditions.

Table S2 Quantitative EPR Results for vanadium oxide catalyst sunder ambient and dehydrated conditions

Sample	**%V as V^{4+}**
Ambient 3% V_2O_5/SiO_2	2.52
Ambient 8% V_2O_5/SiO_2	3.19
Dehydrated 3% V_2O_5/SiO_2	1.25
Dehydrated 8% V_2O_5/SiO_2	0.31

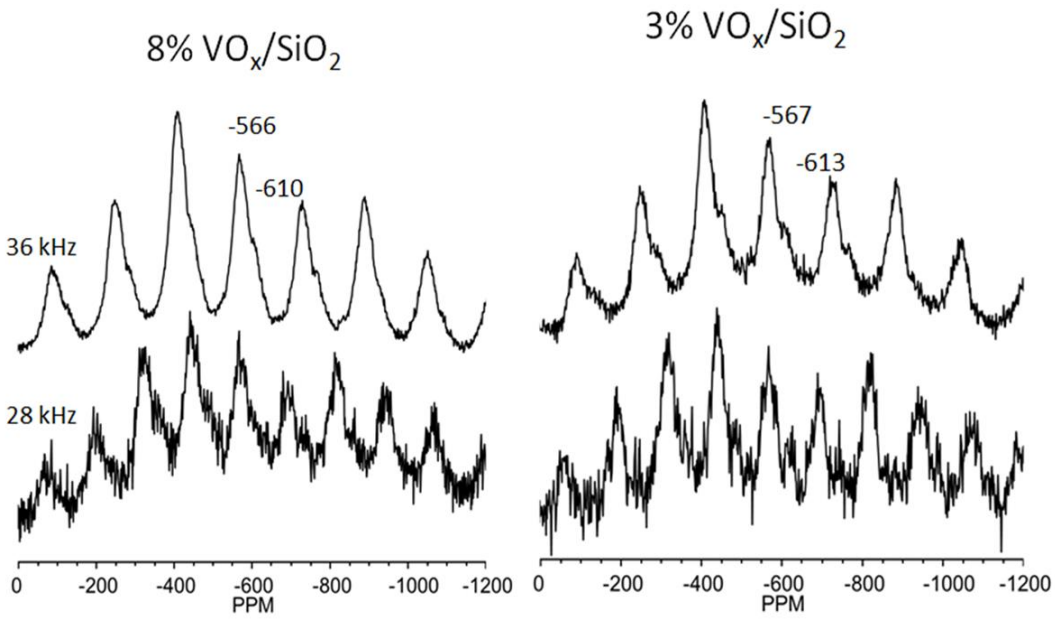

Figure S3. Centerband determination of ^{51}V MAS NMR spectra of V_2O_5/SiO_2 catalysts of varying loading, 8% and 3%, under hydrated conditions at different spinning rates: 8% V_2O_5/SiO_2 at 36 kHz with 210,000 scans; 8% V_2O_5/SiO_2 at 28 kHz with 30,000 scans; 3% V_2O_5/SiO_2 at 36 kHz with 240,000 scans; 3% V_2O_5/SiO_2 at 28 kHz with 60,000 scans. The line broadening used for processing the data was 100 Hz.

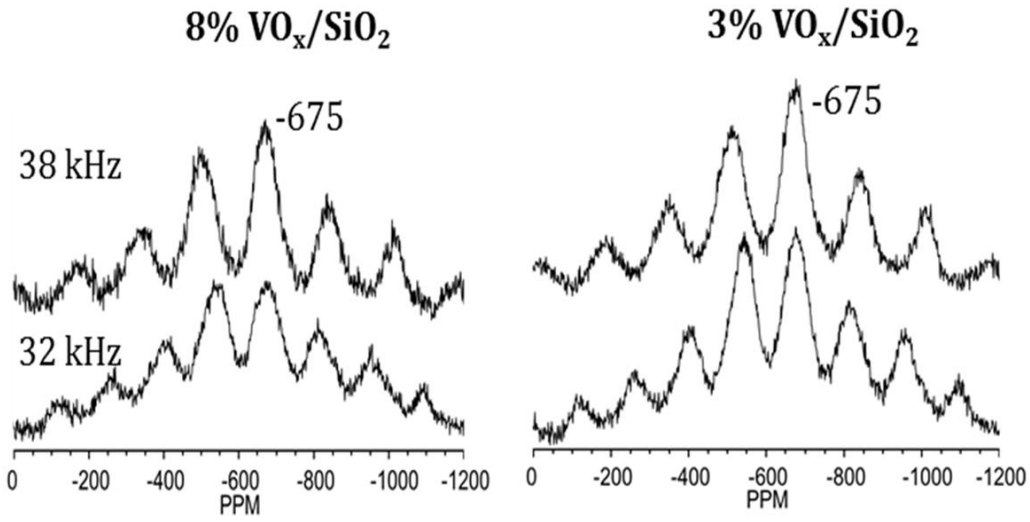

Figure S4. Centerband determination of ^{51}V MAS NMR spectra of V_2O_5/SiO_2 catalysts of varying loading, 8% and 3%, under dehydrated conditions at different spinning rates: 8% V_2O_5/SiO_2 at 38 kHz with 120,000 scans; 8% V_2O_5/SiO_2 at 32 kHz with 150,000 scans; 3% V_2O_5/SiO_2 at 38 kHz with 480,000; 3% V_2O_5/SiO_2 at 32 kHz and 400°C with 630,000 scans. The line broadening used for processing the data was 100 Hz.

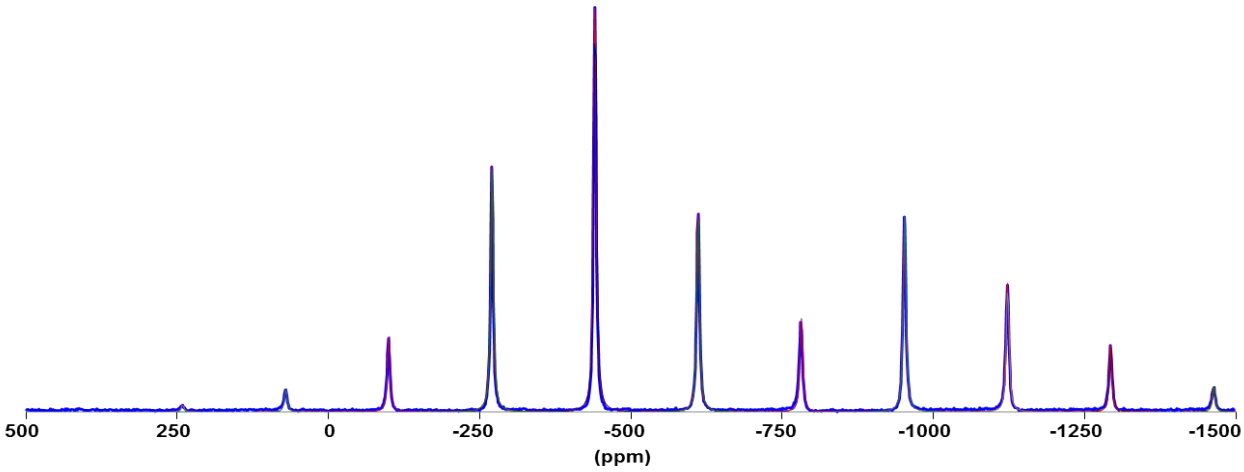

Figure S5. 9.4% V_2O_5 mixed with HBEA ^{51}V MAS NMR reference at 38 kHZ.

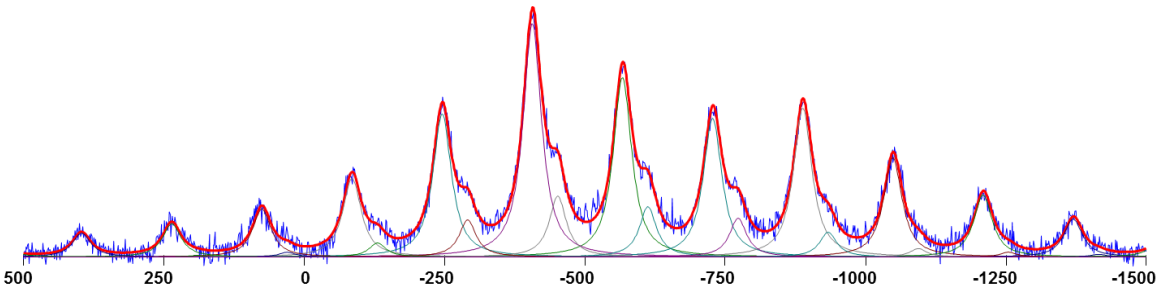

Figure S6. Gaussian/Lorentzian peak fit of hydrated 3% V_2O_5/SiO_2 at 36 kHz with a side band simulation.

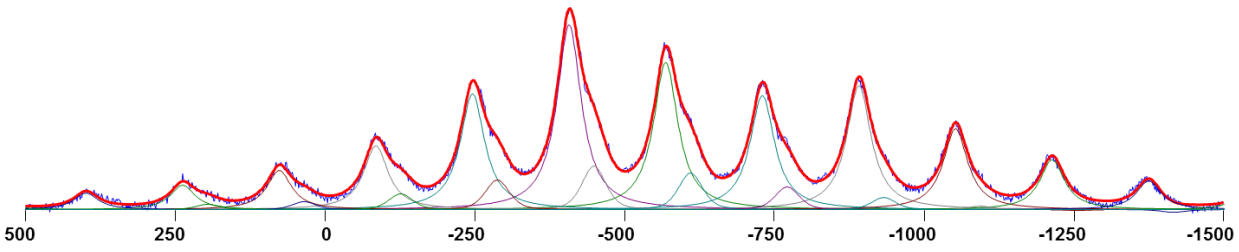

Figure S7. Gaussian/Lorentzian peak fit of hydrated 8% V_2O_5/SiO_2 at 36 kHz with a side band simulation.

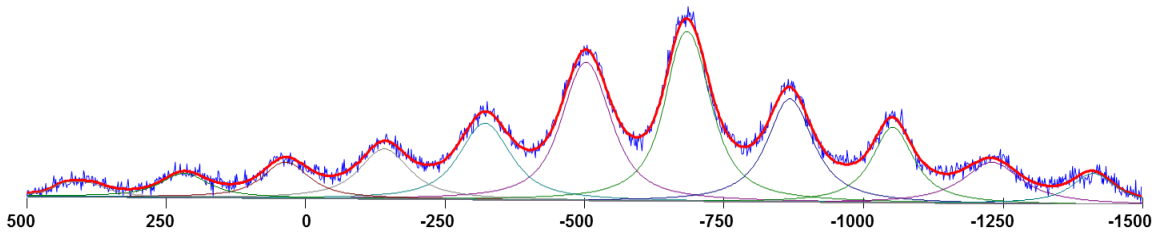

Figure S8. Gaussian/Lorentzian peak fit of dehydrated 3% V_2O_5/SiO_2 at 38 kHz with a side band simulation.

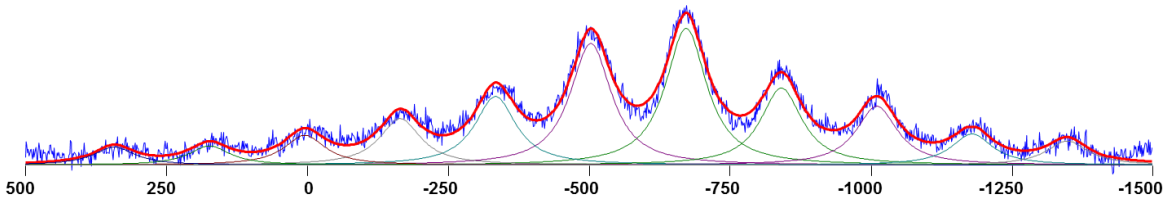

Figure S9. Gaussian/Lorentzian peak fit of dehydrated 8% V_2O_5/SiO_2 at 38 kHz with a side band simulation.

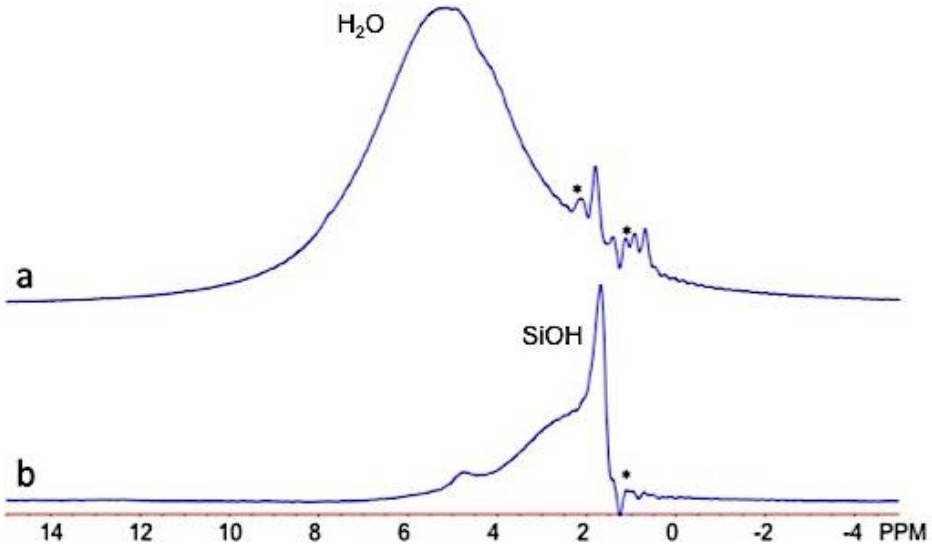

Figure S10. ^{1}H NMR spectra of 8% V_2O_5/SiO_2 under hydrated (a) and dehydrated (b) conditions. Spectra were collected with a Bruker 600 MHz NMR. They hydrated sample shows a broad peak near 5 ppm corresponding to water that is nearly eliminated in the dehydrated sample. The sharp peak at 2 ppm is from silanol protons while the broad peak just downfield is assigned to a small quantity of weakly H-bonded silanols. The '' indicate areas where background subtraction was imperfect due to the very large background signal relative to the sample signal.*

Table S3. Calculated ^{51}V NMR of vanadium siloxane clusters relative to $VOCl_3$

Cluster V Si O H 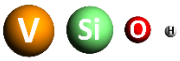	**BLYP-D**	**BLYP-D Hydrated**	**BLYP/ZORA**	**BLYP/ZORA Hydrated**
Monomer 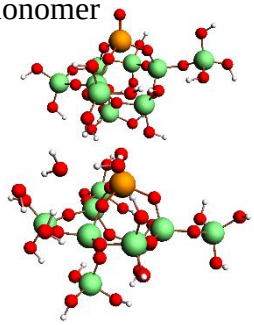	-636	-621	-640	-625
Dimer 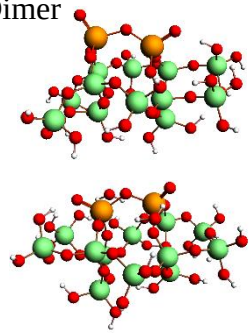	-678 , -681	-640, -644	-682, -686	-649, -646
Trimer 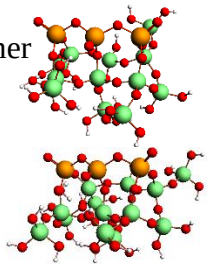	-574, -676, -687	-626, -662, -687	-690, -580, -680	-689, -632, -655

Table S4. Calculated ^{51}V NMR of vanadium clusters at various proposed hydration mechanism configurations relative to $VOCl_3$

Cluster V Si O H	**Description**	**BLYP-D**	**BLYP-D Hydrated**	**BLYP/ ZORA**	**BLYP/ZORA Hydrated**
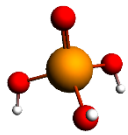	Free VO_4	-517	-497 (COSMO)	-498	-503 (COSMO)
	Free Dimer	-546, -560	-526, -544 (COSMO)	-551, -566	-553, -571 (COSMO)
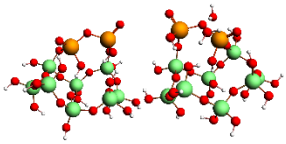	2 bridge bonds hydrolyzed dimer	-560, -566	-584, -589	-572, -567	-594, -591
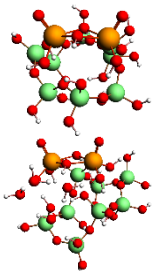	2 V-$(OH)_2$-V bridge 4 hydrolyzed bridges	-463, -508	-498, -508	-469, -514	-516, -498
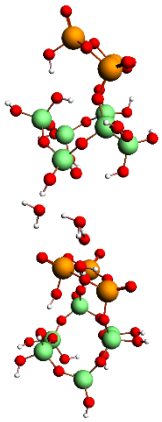	Trimer, 1 hydrolyzed bridge	-539, -560, -606	-609, -663	-603, -536, -590	-639, -603, -674

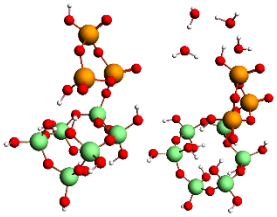	Trimer, 2 hydrolyzed bridges	-617, -619, -648	-577, -599, -601	-613, -642, -614	-594, -576, -596
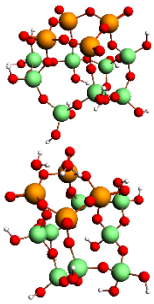	Tetramer	-629, -635, -637, -656	-536, -571, -583, -632	-629, -632, -625, -652	-540, -634, -585, -575

Table S5. Calculated ^{51}V NMR of vanadium monomer-dimer bridge configurations relative to $VOCl_3$

Cluster V Si O H	**Description**	**BLYP-D**	**BLYP-D Hydrated**	**BLYP /ZORA**	**BLYP/ZORA Hydrated**
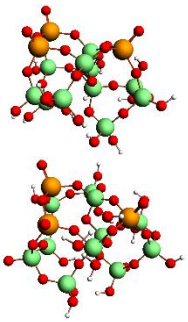	Monomer-dimer bridge, 1 Si separation	-637, -677, -691	-591, -659, -668	-682, -696, -642	-673, -664, -599
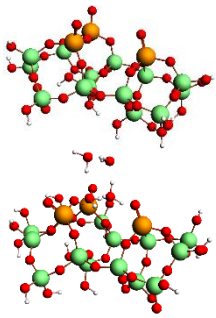	Monomer-dimer bridge, 2 Si separation	-667, -686, -728	-630, -637, -650	-691, -732, -671	-636, -642, -655
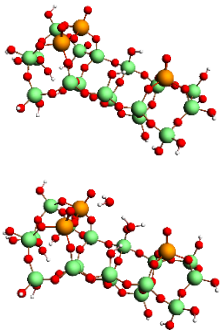	Monomer-dimer bridge, 3 Si separation	-646, -673, -696	-641, -658, -670	-710, -688, -649	-675, -663, -651

Table S6. Additional ^{51}V-NMR model results ($VOCl_3$ as standard) ADF (BLYP/ZORA/TZ2P)

Compound	**^{51}V ppm**
$VO(OH)_3$	-573.9
$VO(OH)_2OSi(OH)_3$	-615.1
$VO(OH)[OSi(OH)_3]_2$	-634.8
$VO[OSi(OH)_3]_3$	-696.5
$VO(OSiH_3)_3$	-682.3
$VO(OH)_2(OSiH_3)$	-610.8
$VO(OH)(OSiH_3)_2$	-646.1
$VO[OSi(OSiH_3)_3]_3$	-712.4
$VO(OH)_2OSi(OSiH_3)_3$	-617.8
$VO(OH)[OSi(OSiH_3)_3]_2$	-662.5
$VO_2(OH)_2^{-1}$	-498.3
$VO_3(OH)^{-2}$	-419.9
VO_4^{-3}	-376.2
$V(OH)_4^{+1}$	-704.4
$VO_2(OH)$	-248.2
$V(OH)_5$	-253.7
VO_2^{+1}	-446.6
$VO_2(H_2O)_4^{+1}$	-575.0
VO_3^{-1}	86.9
$V[OSi(OH)_3]_4^{+1}$	-852.5
$V(OSiH_3)_4^{+1}$	-801.3
$VO_2[OSi(OH)_3]$	-293.1
$VO_2(OSiH_3)$	-298.0
$VO_2[OSi(OH)_3]_2^{-1}$	-577.9

$VO_2(OSiH_3)_2^{-1}$	-599.3
$VO_3[(OSi(OH)_3]^{-2}$	-420.5
$VO_3(OSiH_3)^{-2}$	-446.0
V_2O_5	-307.2 x2
$V_2O_4^{+2}$ (trans)	-533.1 x2
$V_2O_4^{+2}$ (cis)	-531.5 x2
$V_2O_4(OH)_2$ (trans)	-512.2 x2
$V_2O_4(OH)_2$ (cis)	-507.8 x2
$V_2O_4(OH)[OSi(OH)_3]$ (cis)	-554.1, -507.2
$V_2O_4(OH)[OSi(OH)_3]$ (trans)	-568.9, -514.9
$V_2O_4(OH)(OSiH_3)$ (cis)	-540.6, -507.3
$V_2O_4(OH)(OSiH_3)$ (trans)	-550.3, -513.9
$V_2O_4[OSi(OH)_3]_2$(cis)	-550.9, -554.3
$V_2O_4[OSi(OH)_3]_2$(trans)	-566.0, -576.0
$V_2O_4(OSiH_3)_2$ (cis)	-541.5 x2
$V_2O_4(OSiH_3)_2$ (trans)	-552.5, -554.0
$V_2O_3(OH)_4$	-608.1 x2
$V_2O_3(OH)_2[(OSi(OH)_3]_2$	-696.3, -608.2
$V_2O_3[(OSi(OH)_3]_4$	-663.5, -689.9
$VO(OH)[OVO(OH)_2]_2$	-612.3, -606.8(x2)
$VO_2[OVO(OH)_2]_2^{-1}$	-642.5, -566.5 (x2)
$O_2VOVO(OH)_2$	-610.8, -292.7
$O_2VOVO(OH)[OSi(OH)_3]$	-662.0, -291.2
$O_2VOVO[OSi(OH)_3]_2$	-708.1, -301.0

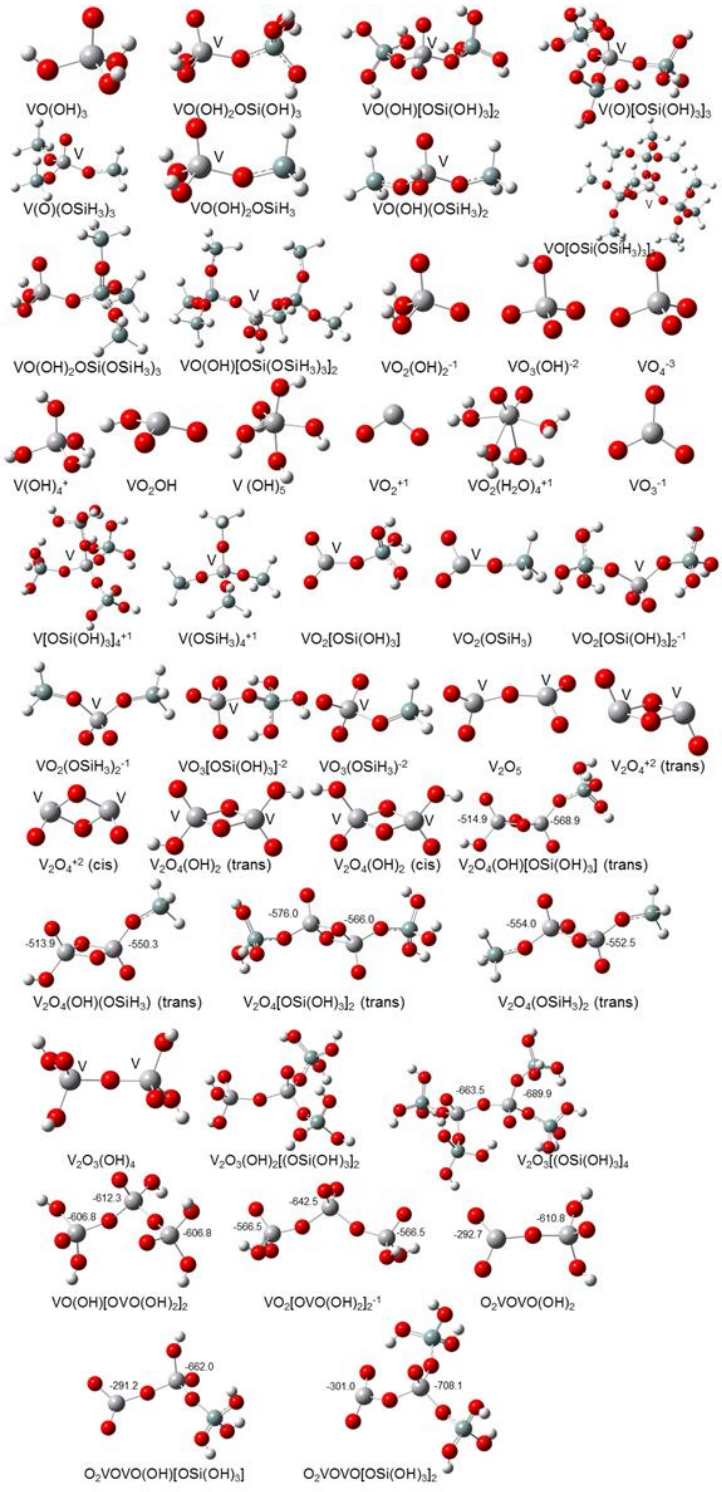

Figure S11. Additional 51V-NMR (VOCl3 as standard) ADF (BLYP/ZORA/TZ2P) structures from Table S6.

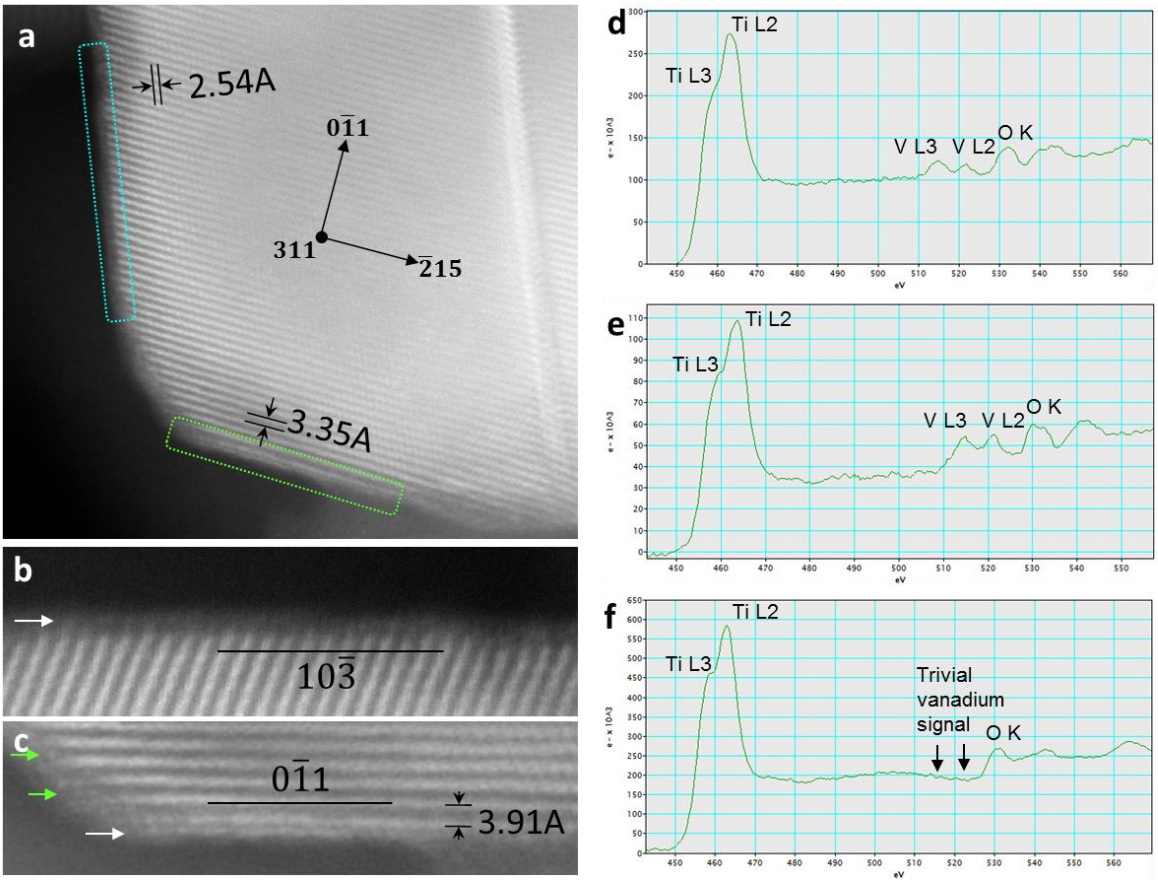

Figure S12. (a) Atomic resolution Z-contrast STEM image of a TiO_2 particle for the supported 5% V_2O_5/TiO_2 catalyst after ambient exposure, but under UHV showing the TiO_2 lattice. (b) Enlarged image of the cyan box region in panel (a) and corresponding EELS spectrum (d) of the thin surface layer (indicated by white arrow in (b)) showing presence of vanadium on the $(10\bar{3})$ *surface of the particle. (c) Enlarged image of the green box region in panel (a) and corresponding EELS spectrum (e) of the thin surface layer (indicated by white arrow in (c)) showing presence of vanadium on the* $(0\bar{1}1)$ *surface of the TiO_2 particle. Vanadium atoms also seems to have widened the spacing of* $(0\bar{1}1)$ *planes near the edge (indicated by green arrows in (c)). The d-spacing of TiO2* $(0\bar{1}1)$ *planes were expanded by the surface vanadia overlayer (as shown in (c)). (f) EELS spectrum collected from inside of the TiO_2 particle showing no discernable peaks from vanadium, which would likely be smeared by the signal form titanium as the electron travels through the thickness direction of the particle.*

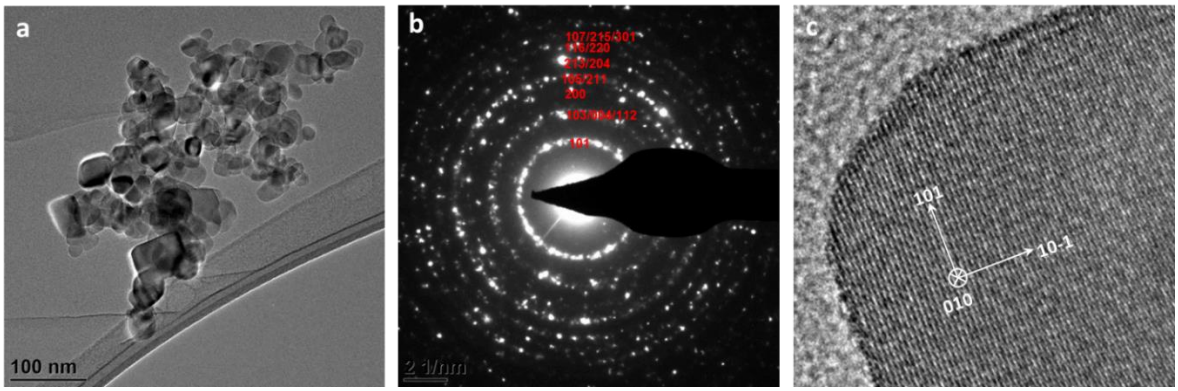

Figure S13. Microstructural characterization of the TiO_2 particles (for supported 5% V_2O_5/TiO_2-I), including (a) Low magnification TEM image of the particles, (b) electron diffraction pattern of the particles in panel (a) which shows a typical pattern of anatase TiO_2, an indication minor rutile presence at 3.26 A and no obvious signal from vanadium oxides, and (c) high resolution TEM image of the edge of a particle demonstrating that each particle is in fact a single crystal. The shape (or surface facet) of the particles are not uniform; but (101) surfaces appears to be the dominant facet.

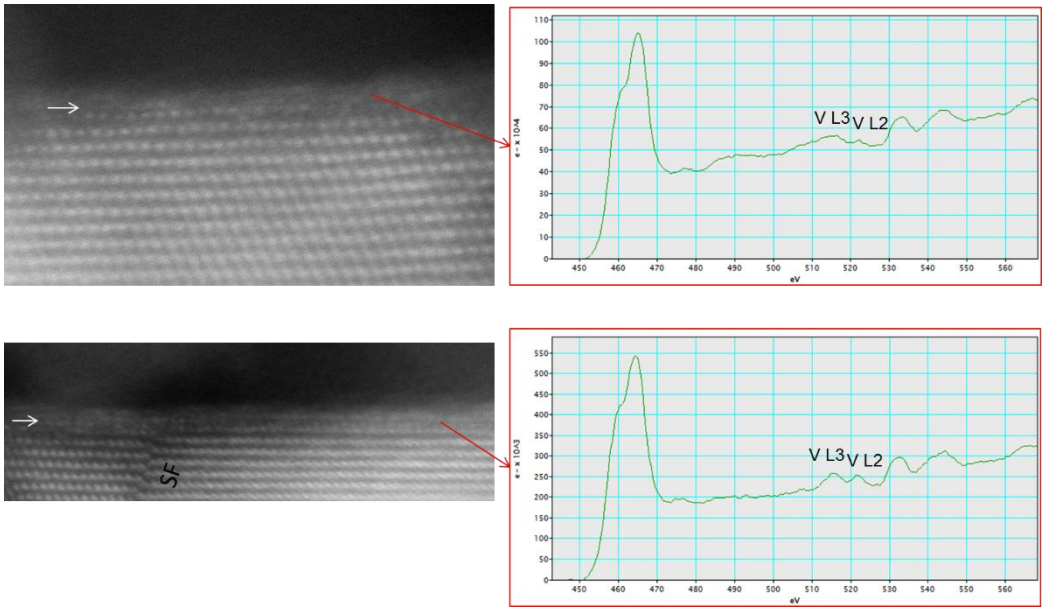

Figure S14. Atomic resolution Z-contrast STEM image of the supported, impregnated 5% V_2O_5/TiO_2 catalyst particle (left) and EEELS spectra (right) providing further evidence of surface vanadium inserted atop titania rows on the particle edges.

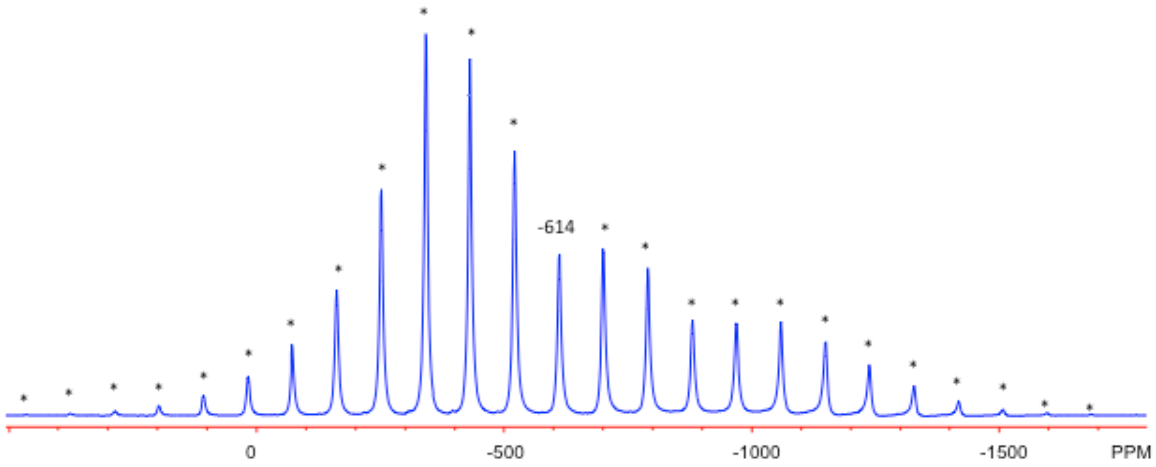

*Figure S15. ^{51}V MAS NMR spectrum of bulk V_2O_5 at high field relative to $VOCl_3$ measured in this study at 0 ppm. The centerband of the bulk V_2O_5 secondary reference is -613.8 ppm. * denotes spinning side band.*

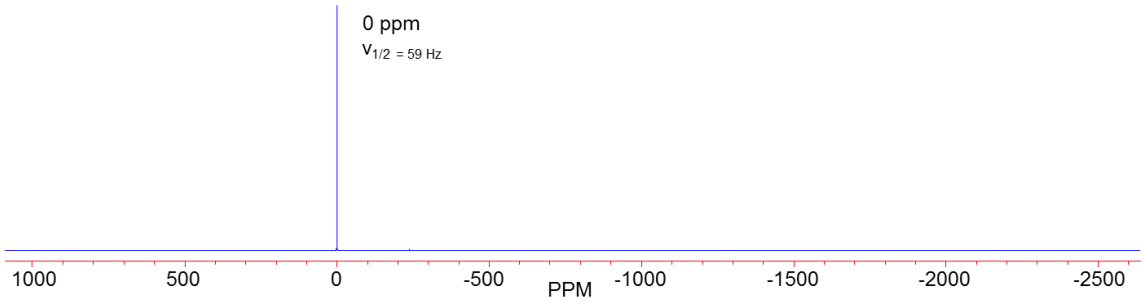

Figure S16. ^{51}V NMR spectrum of $VOCl_3$ referenced to 0 ppm.

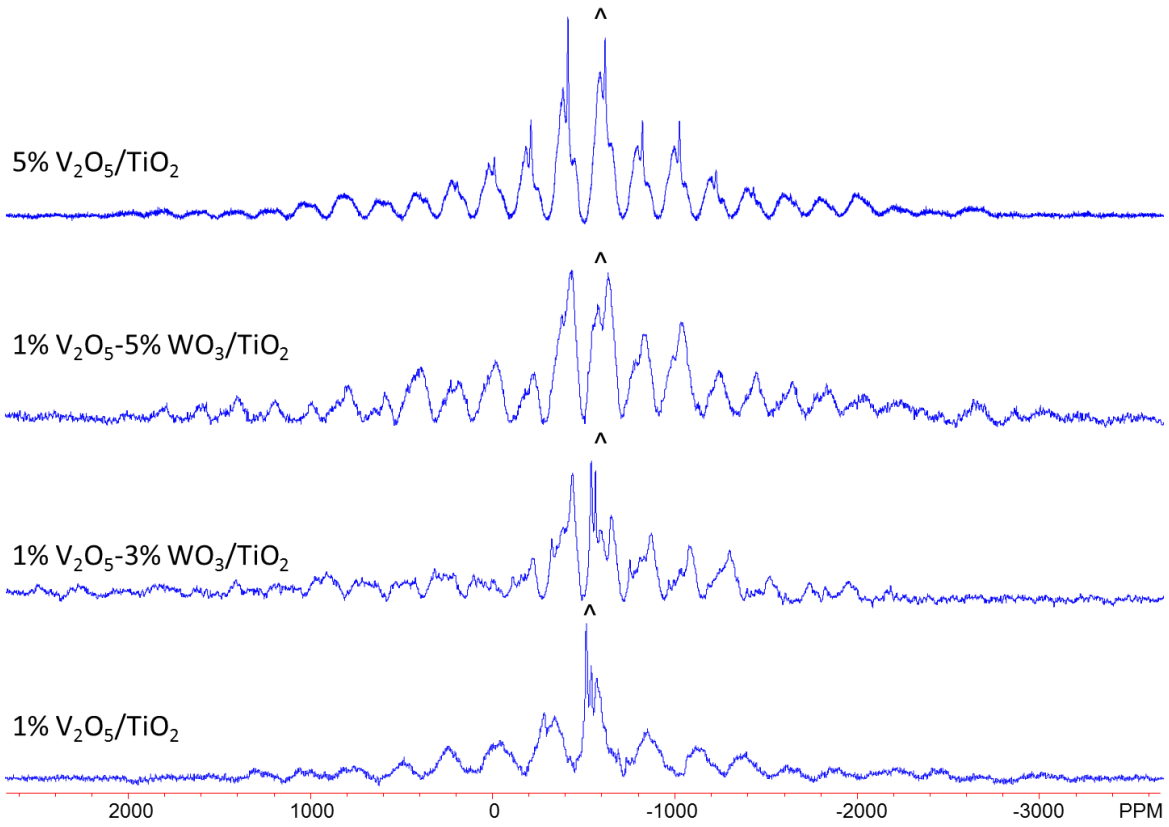

Figure S17. Spinning sideband patterns for the ^{51}V MAS NMR spectra of dehydrated, impregnated V_2O_5/TiO_2 catalysts at 14T and ~35 kHz spinning rate. ^ indicates center band.

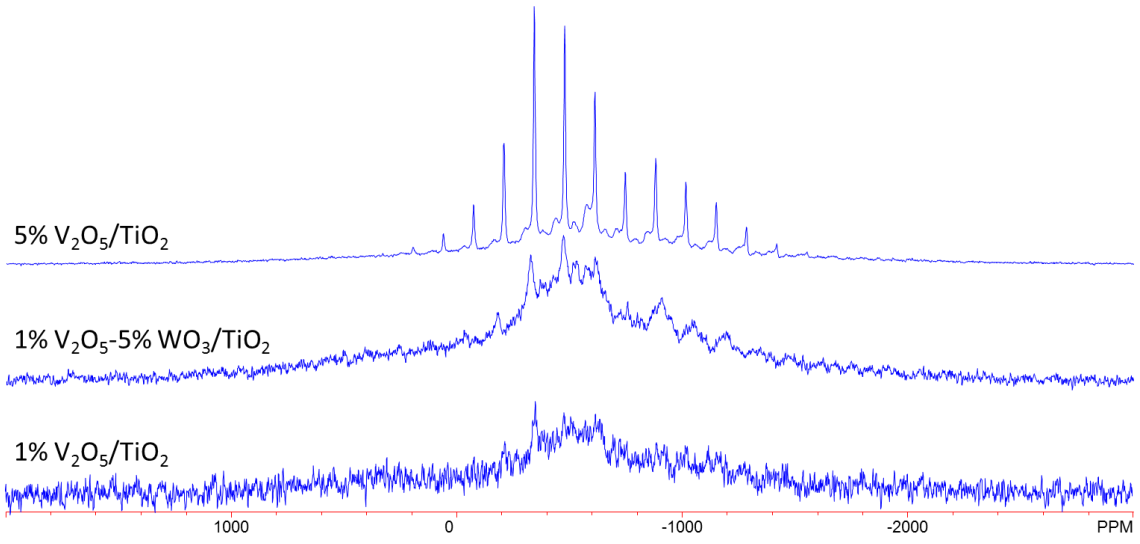

Figure S18. ^{51}V MAS NMR spectra at 21T of dehydrated, supported 1% V_2O_5/TiO_2, 1% V_2O_5-5% WO_3/TiO_2, and 5% V_2O_5/TiO_2 catalysts prepared by impregnation and collected with sample spinning rates of 30, 32.5, and 30 kHz and 38,000, 308,000, and 77,000 repetitions, respectively.

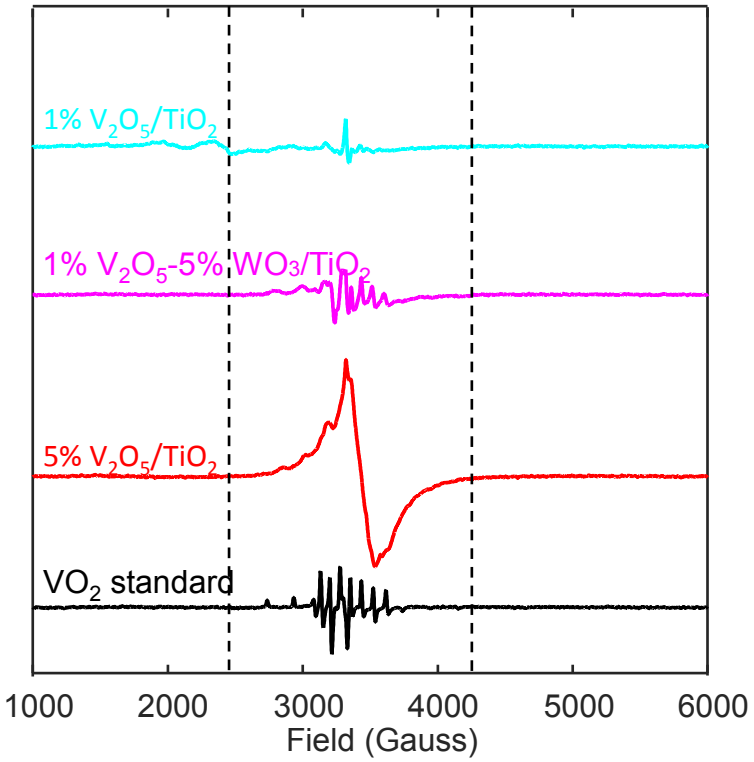

Figure S19. Electron paramagnetic resonance (EPR) spectra of the same dehydrated supported vanadium oxide catalysts probed above by NMR. Small quantities of V^{4+} are present on the samples. G-values are determined as 2.0014 (1% V_2O_5/TiO_2), 1.9829 (1% V_2O_5-5% WO_3/TiO_2), and 1.9376 (5% V_2O_5/TiO_2). The broader lines of the 5% V_2O_5/TiO_2 impregnated catalyst reflect V^{4+} in close proximity to each other.

Table S7. Content of reduced vanadium oxide species determined by EPR line integration, surface vanadium density, average V-V distance, surface tungsten density, and fractional surface coverage of V or W with respect to monolayer coverage.

Sample	%V as V^{4+}	V/nm^2	Avg. V-V dist. Å	W/nm^2	Θ(V/W)
1% V_2O_5/TiO_2	0.25%	1	8.9	-	0.2
5% V_2O_5/TiO_2	1.02%	7	5.2	-	0.6
1% V_2O_5-5% WO_3/TiO_2	0.62%	1	10.3	2.4	0.15/0.53

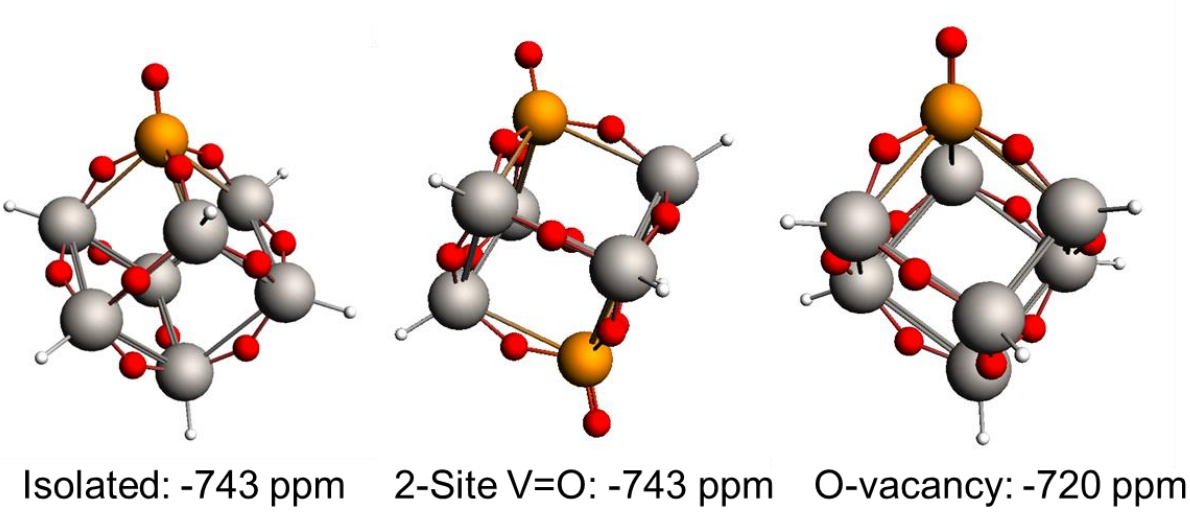

Figure S20. Optimized Goodrow DFT cluster models used to gain an understanding of the impact of oxygen vacancies on the ^{51}V NMR chemical shift. A nearby oxygen vacancy on TiO_2 is predicted to deshield ^{51}V nuclei by approximately 20 ppm.

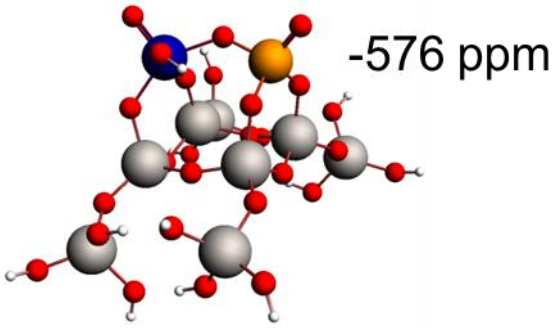

Figure S21. DFT-optimized small cluster model of a VO_X-WO_X dimeric structure. Atoms represented include vanadium (orange), titanium (grey), oxygen (red), tungsten (blue), and hydrogen (white).

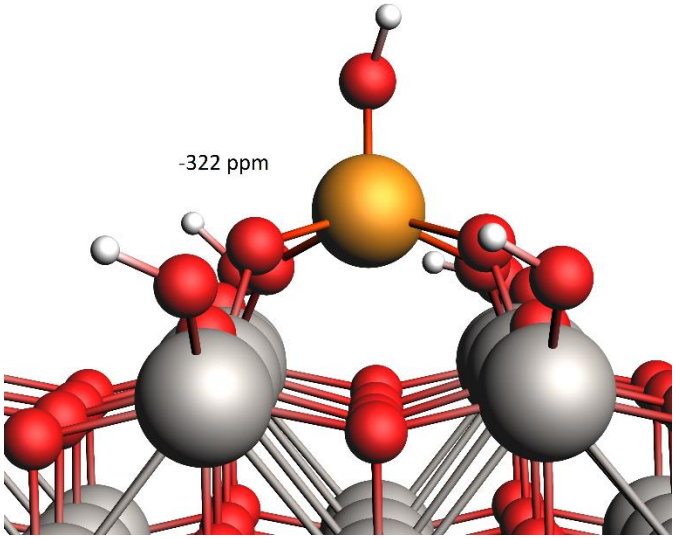

Figure S22. DFT-optimized structure of a vanadia monomer with a protonated vanadyl bond. The predicted chemical shift is far from any resonance observed experimentally.

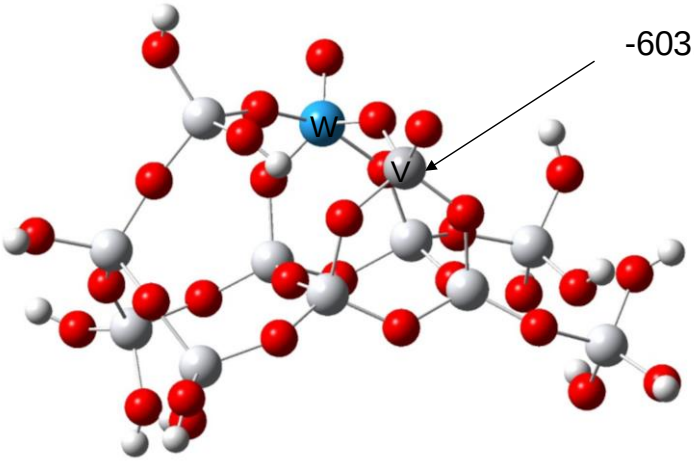

W=O: 1.700 Å, 1036.4 cm^{-1} (21, IR intensity in km/mole)
V=O: 1.575 Å; 1100.2 cm^{-1} (249)

Figure S23. DFT-optimized structure of a VO_X-WO_X dimer on a TiO_2 cluster. The cluster was optimized in Gaussian-16 with B3LYP/aug-cc-pVDZ(H,O)/aug-cc-pVDZ-PP(V,Ti,W). ^{51}V NMR shielding calculations were conducted using ADF with ZORA and BLYP/TZ2P, referenced to $VOCl_3$.

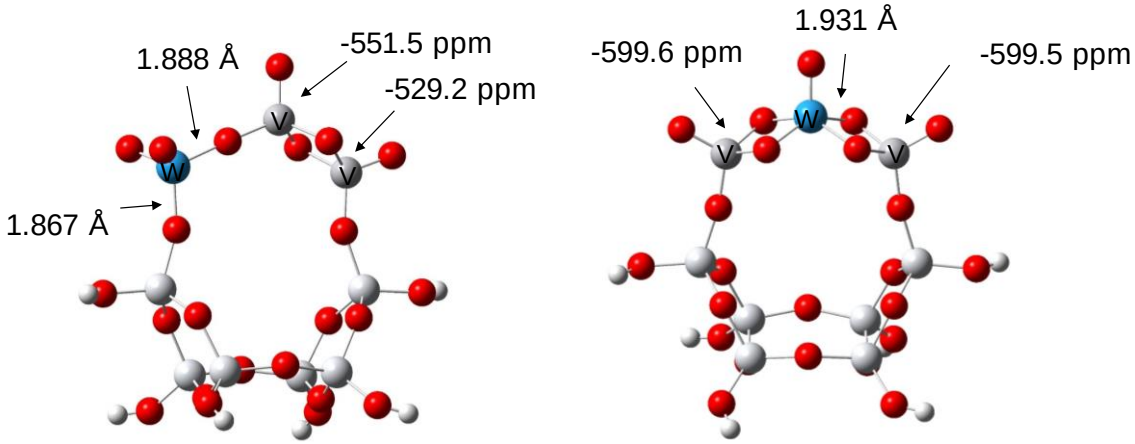

1.6 kcal/mol

W=O: 1.714 Å, 1039.0 (sym) cm^{-1}(3)
977.9 (asym) cm^{-1} (212)
(W)V=O: 1.571 Å;
V=O: 1.575 Å; 1118.2 (sym) cm^{-1} (225)
1094.0 (asym) cm^{-1} (190)

0.0 kcal/mol

W=O: 1.696 Å, 1031.6 cm^{-1} (51)
V=O: 1.575 Å; 1105.4 (sym) cm^{-1} (79)
1098.5 (asym) cm^{-1} (445)

Figure S24. DFT-optimized structure of A) 2VO_X-WO_X trimer (left) and B) VO_X-WO_X-VO_X trimer on TiO_2 cluster 1. The clusters were optimized in Gaussian-16 with B3LYP/aug-cc-pVDZ(H,O)/aug-cc-pVDZ-PP(V,Ti,W). ^{51}V NMR shielding calculations were conducted using ADF with ZORA and BLYP/TZ2P, referenced to $VOCl_3$.

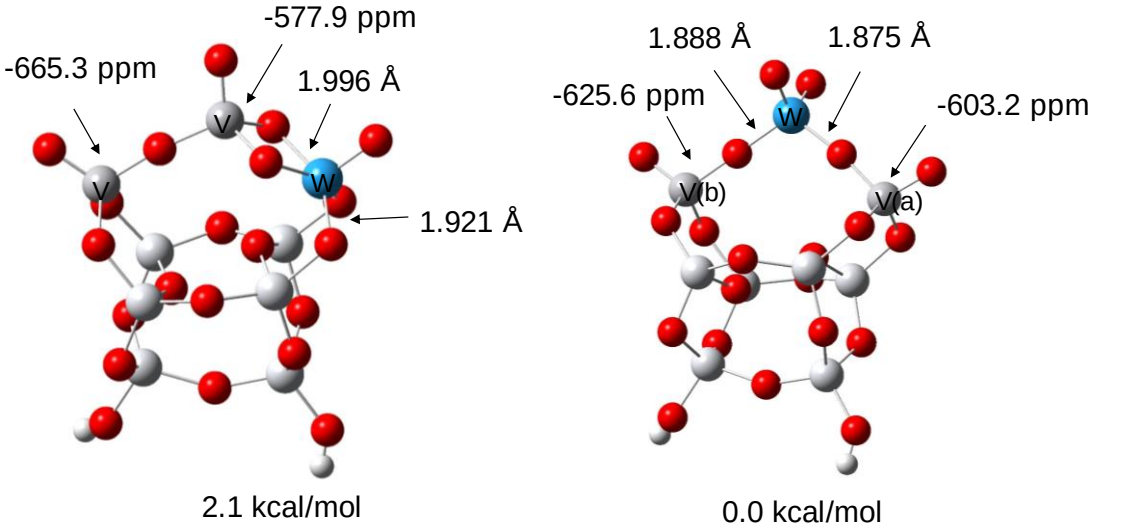

W=O: 1.691 Å, 1037.1 cm^{-1} (125)
(W)V=O: 1.577 Å;
V=O: 1.570 Å; 1109.3 (sym) cm^{-1} (404)
1095.9 (asym) cm^{-1} (149)

W=O: 1.712 Å, 1038.8 (sym) cm^{-1} (1)
980.4 (asym) cm^{-1} (243)
V(a)=O: 1.564 Å;
V(b)=O: 1.567 Å; 1115.0 (sym) cm^{-1} (167)
1112.2 (asym) cm^{-1} (355)

Figure S25. DFT-optimized structure of A) $2VO_X$-WO_X trimer (left) and B) VO_X-WO_X-VO_X trimer on TiO_2 cluster 2. The clusters were optimized in Gaussian-16 with B3LYP/aug-cc-pVDZ(H,O)/aug-cc-pVDZ-PP(V,Ti,W). ^{51}V NMR shielding calculations were conducted using ADF with ZORA and BLYP/TZ2P, referenced to $VOCl_3$.

Table S8. DFT ^{1}H NMR calculations of different water loadings on Site 2 in Table 3.

Water/BAS		**Δ ppm ^{1}H**
0	H(192):	4.5
1	H(192):	14.4
	H(209):	4.3
	H(210):	4.0
2	H(192):	18.6
	H(209):	11.6
	H(210):	5.0
	H(212):	3.0
	H(213):	4.5
3	H(192):	16.1
	H(209):	17.4
	H(210):	6.0
	H(212):	10.8
	H(213):	2.1
	H(218):	1.5
	H(219):	7.6
4	H(192):	6.9
	H(209):	11.6
	H(210):	2.3
	H(212):	17.2
	H(213):	2.3
	H(218):	3.1
	H(219):	11.3
	H(224):	17.9
	H(225):	6.1
5	H(192):	7.7
	H(205):	6.1
	H(207):	10.3
	H(209):	8.5
	H(210):	2.6
	H(212):	15.7
	H(213):	2.3
	H(215):	18.0
	H(216):	3.8
	H(218):	0.6
	H(219):	4.7
6	H(192):	7.6
	H(205):	6.3
	H(207):	9.8
	H(209):	8.7
	H(210):	3.4
	H(212):	16.0
	H(213):	2.1
	H(215):	17.2
	H(216):	5.9
	H(218):	0.2
	H(219):	4.7
	H(220):	6.2
	H(222):	1.3
7	H(192):	9.5
	H(205):	3.7
	H(207):	9.2
	H(209):	17.6
	H(210):	5.6
	H(212):	14.4
	H(213):	12.1
	H(215):	8.1
	H(216):	2.1
	H(218):	5.4
	H(219):	4.7
	H(220):	6.4
	H(222):	4.3
	H(223):	7.0
	H(225):	8.3
	H(58):	9.1
8	H(192):	6.4
	H(205):	9.8
	H(207):	9.2
	H(209):	11.4
	H(210):	11.3
	H(212):	17.5
	H(213):	4.5
	H(215):	13.8
	H(216):	4.2
	H(218):	1.8
	H(219):	4.7
	H(220):	5.5
	H(222):	1.0
	H(223):	2.8
	H(225):	1.5
	H(226):	5.0
	H(228):	6.2
9	H(192):	6.9
	H(205):	9.7
	H(207):	9.1
	H(209):	11.4
	H(210):	10.1
	H(212):	18.0
	H(213):	4.9
	H(215):	13.4
	H(216):	4.3
	H(218):	1.9
	H(219):	4.7
	H(220):	5.2
	H(222):	1.0
	H(223):	2.9
	H(225):	1.2
	H(226):	5.7
	H(228):	6.8
	H(229):	2.1
	H(231):	3.7

Table S9. DFT ^{1}H NMR calculations of different water loadings on Site 1.

Water/BAS		**Δ ppm ^{1}H**
0	H(58):	3.7
1	H(58):	13.6
	H(206):	4.9
	H(207):	2.4
2	H(58):	16.7
	H(206):	5.9
	H(207):	16.9
	H(215):	8.2
	H(216):	3.5
3	H(58):	7.5
	H(206):	4.3
	H(207):	17.2
	H(215):	3.5
	H(216):	0.8
	H(221):	14.8
	H(222):	5.0
4	H(58):	5.2
	H(206):	4.1
	H(207):	11.2
	H(215):	2.0
	H(216):	16.9
	H(221):	12.3
	H(222):	12.6
	H(227):	2.1
	H(228):	7.3

Table S10. DFT ^{1}H NMR calculations of hydrated Al^{3+} clusters.

$Al(H_2O)_6^{3+}$	**Δ ppm**	$Al(H_2O)_6^{3+}\cdot 12H_2O$	**Δ ppm**	$Al(NO_3)_3\cdot 9H_2O$	**Δ ppm**
Average	5.5	Average	5.6		
H(11):	5.53	H(10):	9.41	H(1):	11.12
H(13):	5.52	H(11):	9.41	H(2):	20.18
H(15):	5.53	H(12):	9.41	H(3):	6.93
H(17):	5.52	H(13):	9.41	H(4):	2.42
H(19):	5.52	H(14):	9.41	H(5):	11.77
H(2):	5.53	H(15):	9.41	H(6):	15.91
H(3):	5.53	H(16):	9.41	H(7):	5.99
H(4):	5.52	H(17):	9.41	H(8):	10.04
H(5):	5.52	H(18):	9.41	H(9):	3.22
H(6):	5.52	H(19):	9.41	H(10):	9.99
H(7):	5.53	H(32):	4.38	H(11):	1.33
H(9):	5.53	H(33):	4.38	H(12):	12.33
		H(34):	4.38	H(13):	4.73
		H(35):	4.38	H(14):	5.16
		H(36):	4.38	H(15):	4.22
		H(37):	4.38	H(16):	1.42
		H(38):	4.38	H(17):	3.59
		H(39):	4.38	H(18):	2.42
		H(40):	4.38		
		H(41):	4.38		
		H(42):	4.38		
		H(43):	4.38		
		H(44):	2.6		
		H(45):	2.6		
		H(46):	2.6		
		H(47):	2.6		
		H(48):	2.6		
		H(49):	2.6		
		H(50):	2.6		
		H(51):	2.6		
		H(52):	2.6		
		H(53):	2.6		
		H(54):	2.6		
		H(55):	2.6		
		H(8):	9.41		
		H(9):	9.41		

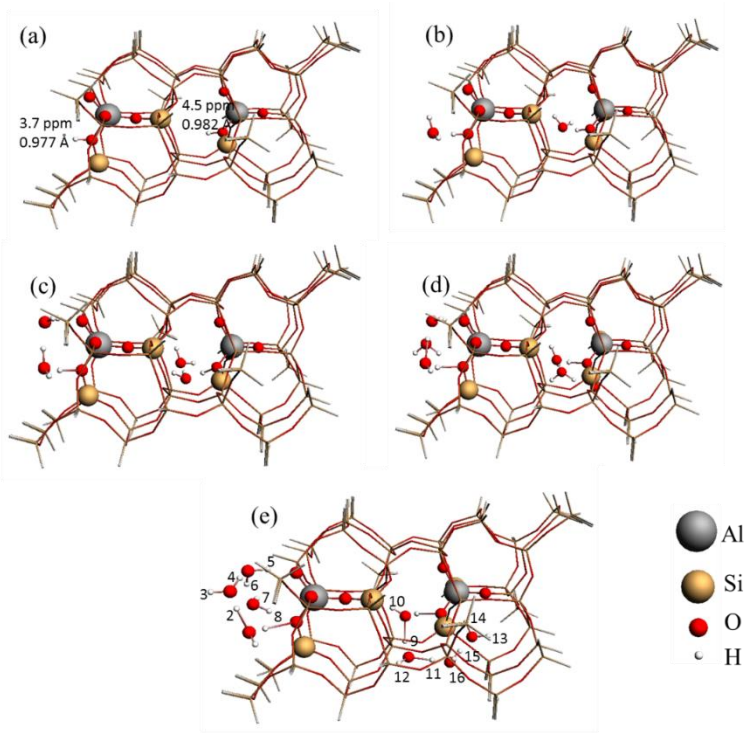
(a)
3.7 ppm
0.977 Å
4.5 ppm
(b)
(c)
(d)
(e)
Al
Si
O
H

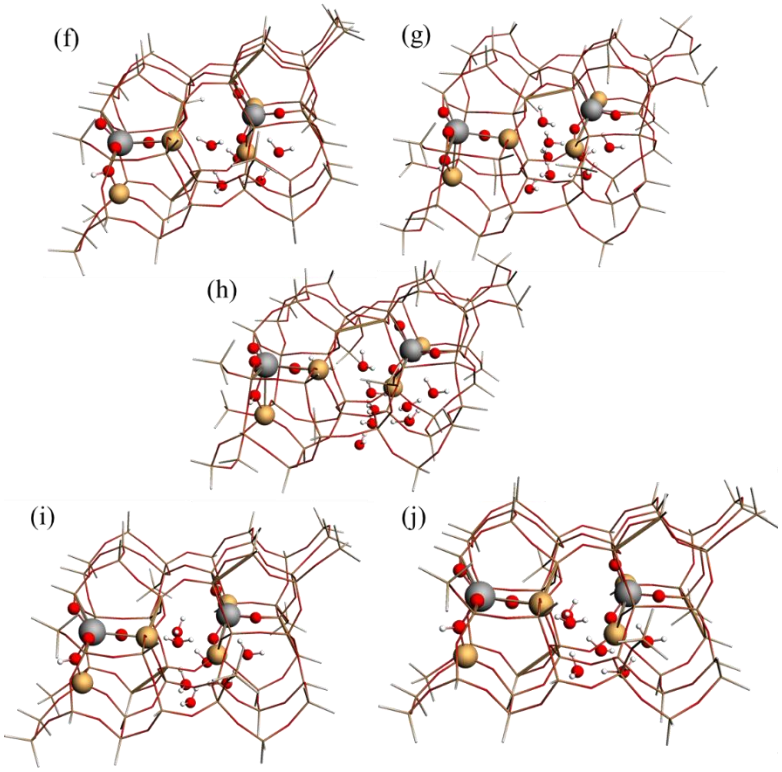

Figure S26. Geometry optimized structures for H_2O molecules bonding with H-ZSM5 clusters. (a) 58T H-ZSM5 cluster, (b) 58T-1H_2O, (c) 58T-2H_2O, (d) 58T-3H_2O, (e) 58T-4H_2O, (f) 58T-5H_2O, (g) 58T-6H_2O, (h) 58T-7H_2O, (i) 58T-8H_2O, (j) 58T-9H_2O.

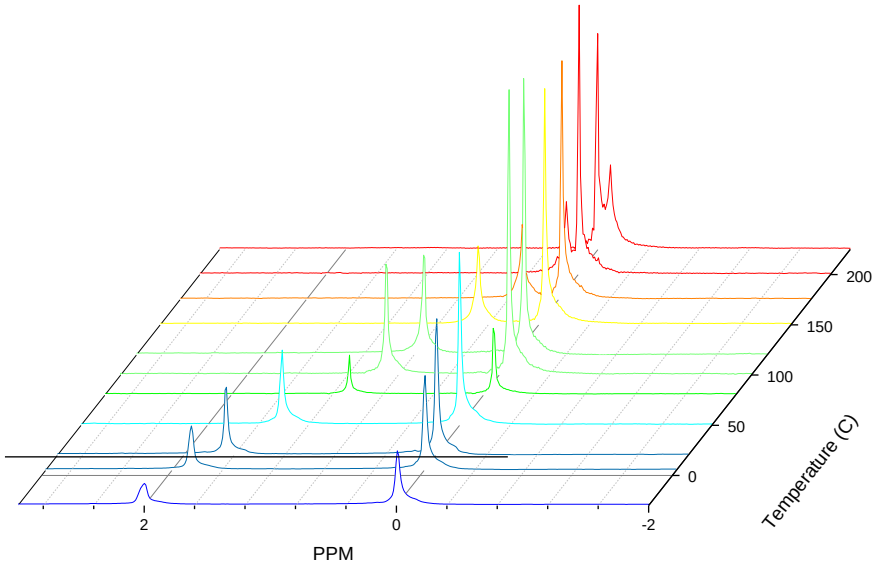

Figure S27.Ethylene glycol temperature calibration results.

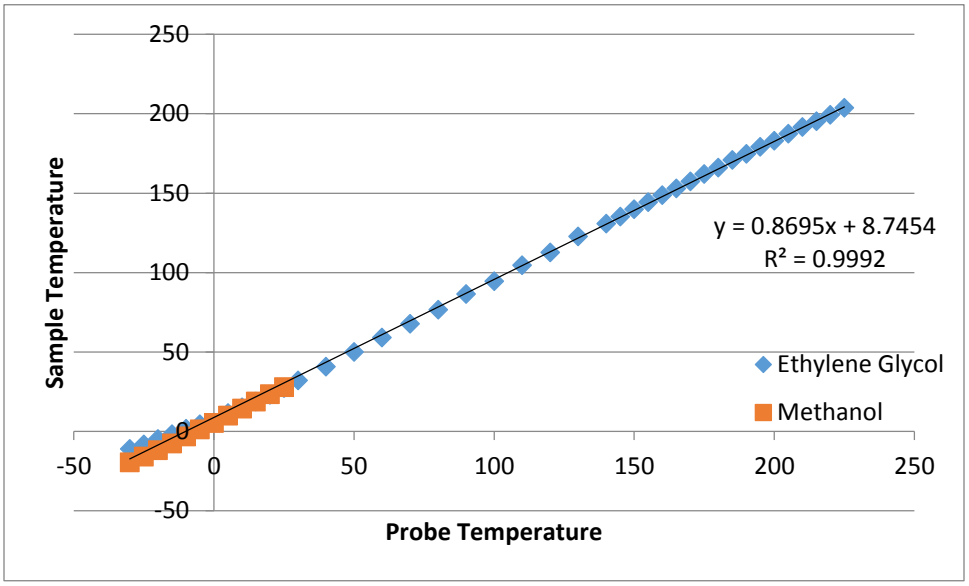

Figure S28. Ethylene glycol temperature calibration results.

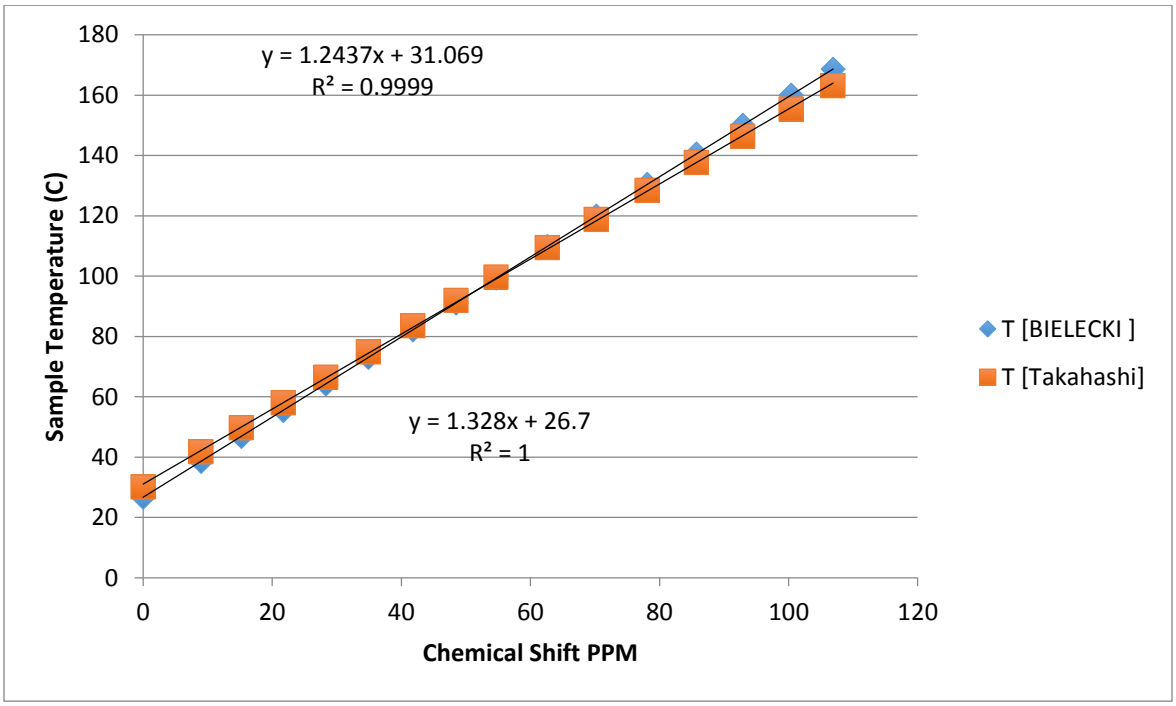

Figure S29. Lead nitrate temperature calibration results.

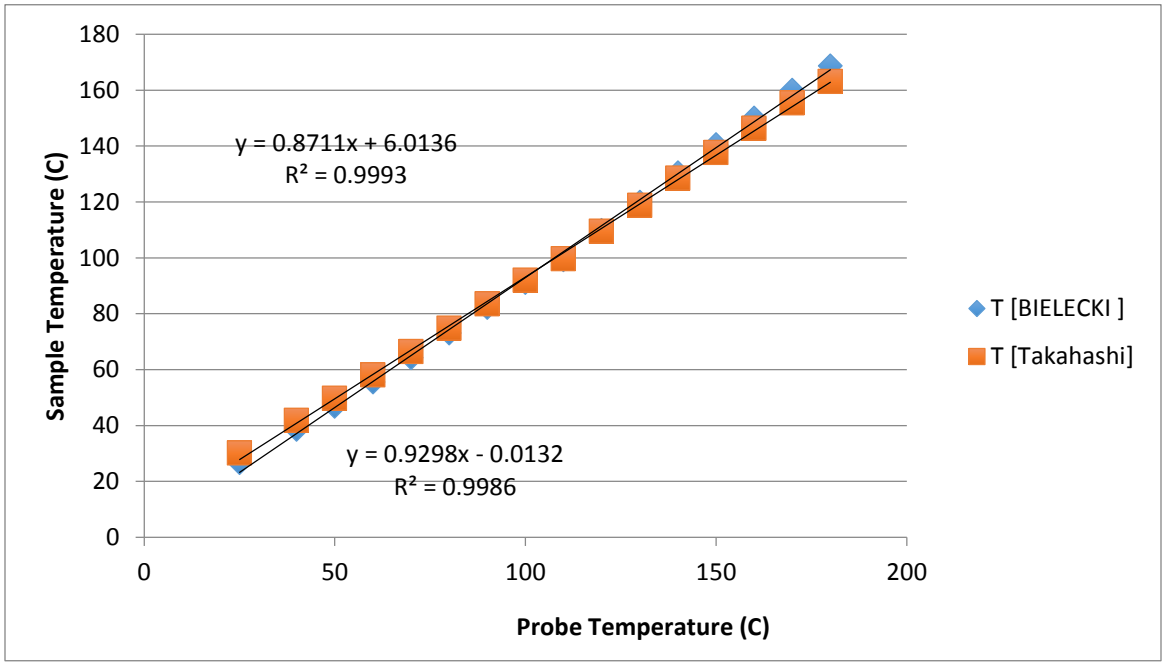

Figure S30. Lead nitrate temperature calibration results.

Appendix D: *In situ* EPR Studies of Methanol oxidation on MoO_3/MOx catalysts

Supported molybdenum catalysts of great use for oxidation chemistry, finding utilization in such applications as hydrodesulphurization, propene selective oxidation, acrolein oxidation, olefin metathesis, epoxidation, propene hydration, and methanol oxidation. Despites its use and the efforts to elucidate uncertainties, there remains a desire to better understand the material during catalytic operation. A body of literature is available that examines the effect of loading and support on the catalytic activity of molybdenum oxide. Namely, enhanced loadings of Mo on the support are shown to increase the TOF and the support impacts the reactivity and selectivity of redox chemistry. This loading observation is supported by EPR which demonstrated the involvement of only one electron per molybdenum where the authors suggested the need for polymolybdenate to complete the redox cycle.[362] Representative reactivity results for methanol oxidative dehydrogenation (ODH) are shown in Table S11, where the last three rows are similar to the materials studied herein. Note that the Al_2O_3-supported catalyst has a three-fold higher Mo loading than the other materials due to the higher monolayer capacity of Mo on Al_2O_3. As shown, the reactivity of supported catalysts follows the order Zr > Ti >> Al.

To gain an understanding of these materials under reaction conditions, we employed *in situ* Electron Paramagnetic Resonance (EPR) spectroscopy to highlight the effect of the support on the reduction of molybdenum centers during methanol ODH and provide information regarding the state of the material.

*Table S11. Reactivity data on molybdenum, supports, and supported molybdenum for methanol oxidative dehydrogenation. As reported previously.[363] *Subsequent investigation suggests ZrO_2-supported Mo shows greater activity than TiO_2-supported.[364]*

Catalyst	**Redox TOF**	**Selectivity**
MoO_3	0.02	FA-0.76, MF-tr, DMM-0.06, DME-0.16, COx-0.02
ZrO_2	-	MF-0.86, DME-tr, COx-0.14
TiO_2	-	DME-.91, COx-.09
Al_2O_3	-	DME-1
5% MoO_3/ZrO_2	0.51*	FA-0.82, MF-0.12, DMM-0.02, DME-0.03, COx-0.01
5% MoO_3/TiO_2	0.58*	FA-0.85, MF-0.03, DMM-0.04, DME-0.06, COx-0.02
18% MoO_3/Al_2O_3	0.094	FA-0.11, MF-tr, DMM-tr, DME-0.89

*FA – Formaldehyde, *MF – Methyl formate, *DMM – Dimethoxymethane, DME – Dimethylether, COx – Carbon oxides, tr-trace. *Considered for Redox TOF except MF on ZrO_2 materials

Continuous Wave Electron Paramagnetic Resonance (CW-EPR) X-band (9.30 GHz) spectra were collected with a Bruker Elexsys 580 EPR spectrometer. The field was modulated at 100 kHz and a microwave power of 19.9 mW. The weight percent of molybdenum in the reduced state will be calculated using a copper standard at room temperature and correlating that to the signal reduction observed at high temperatures (see concluding remarks). The current version of this document uses the integrated intensity normalized by mass and molybdenum loading.

Analyzed materials (5.8% MoO_3/ZrO_2, 17.7% MoO_3/Al_2O_3, and 5.8% MoO_3/TiO_2) were individually placed inside a small tube and held in place by quarts wool. The small tube was

inserted into the flow cell (Figure S31) where a larger tube was fitted concentrically over the smaller one and secured onto the cell block. The lower tubing section was placed held in a continuous flow variable temperature insert in the EPR resonator. The gas flow profile of the *in situ* cell (shown in blue arrows) allows the desired treatment gas to flow in from the left, down the larger tube where it is preheated, and up through the smaller tube in the center where interaction with the catalyst was possible before being discharged to the exhaust. A bubbler was prepared by holding dried methanol in an ice bath and sealing off the flow lines until methanol was utilized.

Approximately 15 mg of material was loaded into the *in situ* cell. The materials were first brought from room temperature to 623 K in 30 K increments under oxidizing environment (10% O_2/Ar, 30-35 ml/min), with an EPR spectra collected at each temperature step. At 623 K, the temperature was held constant for one hour while the spectrometer collected one spectrum ever 83s. At the end of pretreatment, the temperature was reduced to 503 K and the sample signal was allowed to equilibrate. The bubbler was then quickly installed, allowing methanol exposure to the sample. Signal changes were instantaneous and the reaction was monitored until it no further changes were observed over a period of time. The bubbler was then disconnected (temporarily creating a stagnant environment in the cell) before monitoring reoxidation at 503 K.

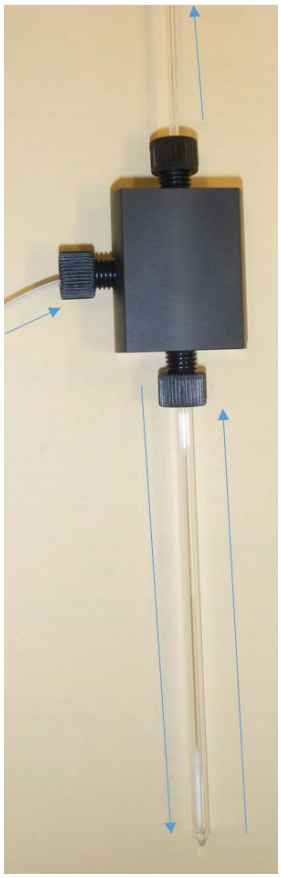

Figure S31. EPR high-temperature flow cell. The gas flow path is depicted by the blue arrows.

EPR spectra of the three as-received samples are shown in Figure S32. At least three unique types of signals are visible in these samples. The first is a tentatively-assigned free radical with a g-value of about 2.05 that is clear on all three samples. This species was observed previously and attributed to O_2^-.[365-366] The second signal is only present on ZrO_2 at a g-value of 2.02. This signal has been reported to be related to reduced molybdenum on ZrO_2-supported catalysts which have not been calcined.[367-368] The third signal type is related to Mo(V) on the surface at a g-value of around 1.98 for all of the three samples with slight differences across the supports (third digit of g-value) and exhibiting an axial powder pattern.[369-370] For the Al_2O_3, at least three overlapping signals are present for the as-received samples. These signals are

characteristic of octahedral or tetrahedral Mo^{5+} oxo-complexes on the surface of metal oxides.[366] Another species in this region was reported at g = 1.975 as a solvated Mo species.[371]

Previous efforts have described Mo substituted into TiO_2 at g-values between 1.79 and 1.944.[365] Signals have also been observed at 1.958, 1.955, and 1.948, depending on the coordination environment (Mo^{5+}_{6c}, Mo^{5+}_{4c}, and Mo^{5+}_{5c}, respectively). For alumina, just one signal at 1.945 was ascribed to Mo^{5+}_{6c}.

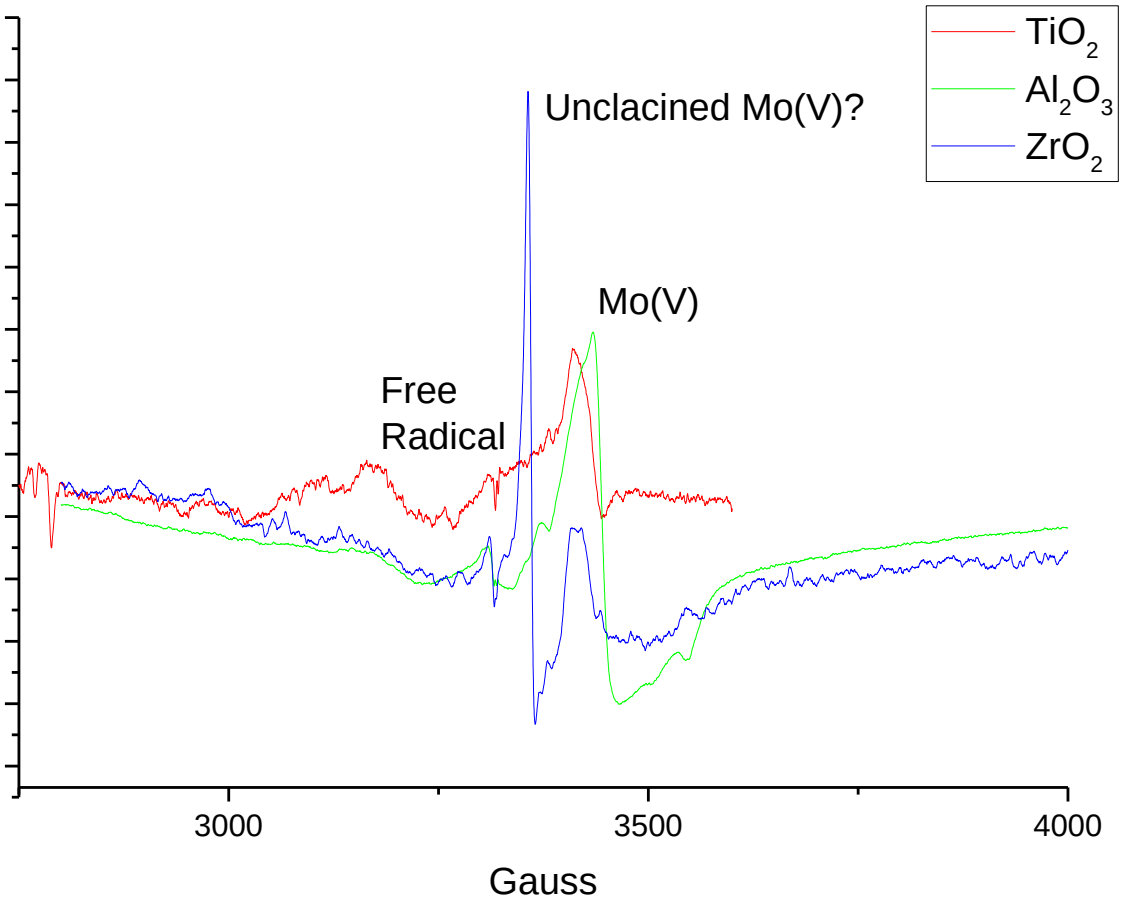

Figure S32. EPR spectra of as-received catalytic materials at 293 K.

After oxidation at 623 K, the samples were cooled to 503 K. Spectra were acquired during this process and prior to methanol introduction. A representative spectrum for each

sample is shown in Figure S33. The radical is still present on each sample in small quantities, as is the uncalcined Mo(V) feature on ZrO_2, though reduced in intensity. The signals for reduced Mo(V) are dramatically decreased after initial oxidation. In particular, the signal from ZrO_2 is nearly absent entirely. The signal from Al_2O_3-supported Mo(V) contains at least two types of signals while that of TiO_2 is broader. Compared to the as-received sample, the break points of the signal for the Al_2O_3-supported Mo(V) after oxidation are blurred/broadened likely due to the distortion of the Mo5+ sites.

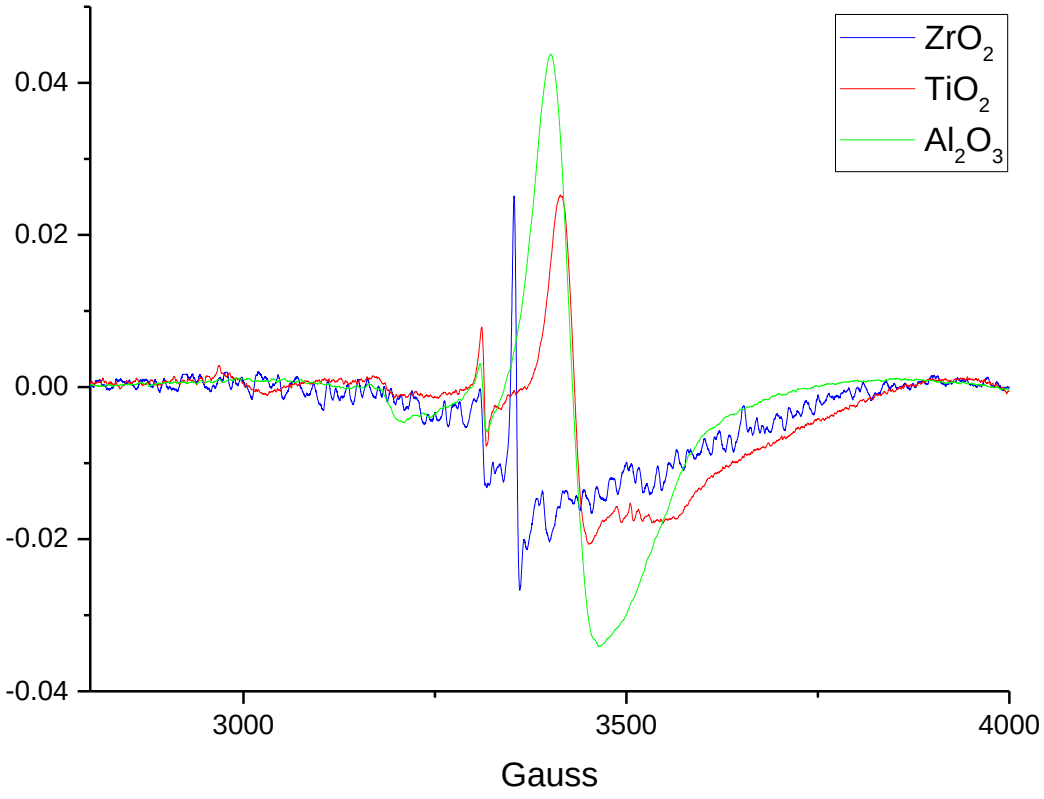

Figure S33. In situ EPR data after initial oxidation, prior to methanol introduction at 503 K.

The introduction of methanol was accompanied by an instantaneous (given our temporal resolution) enhancement of Mo(V) signals for each sample.

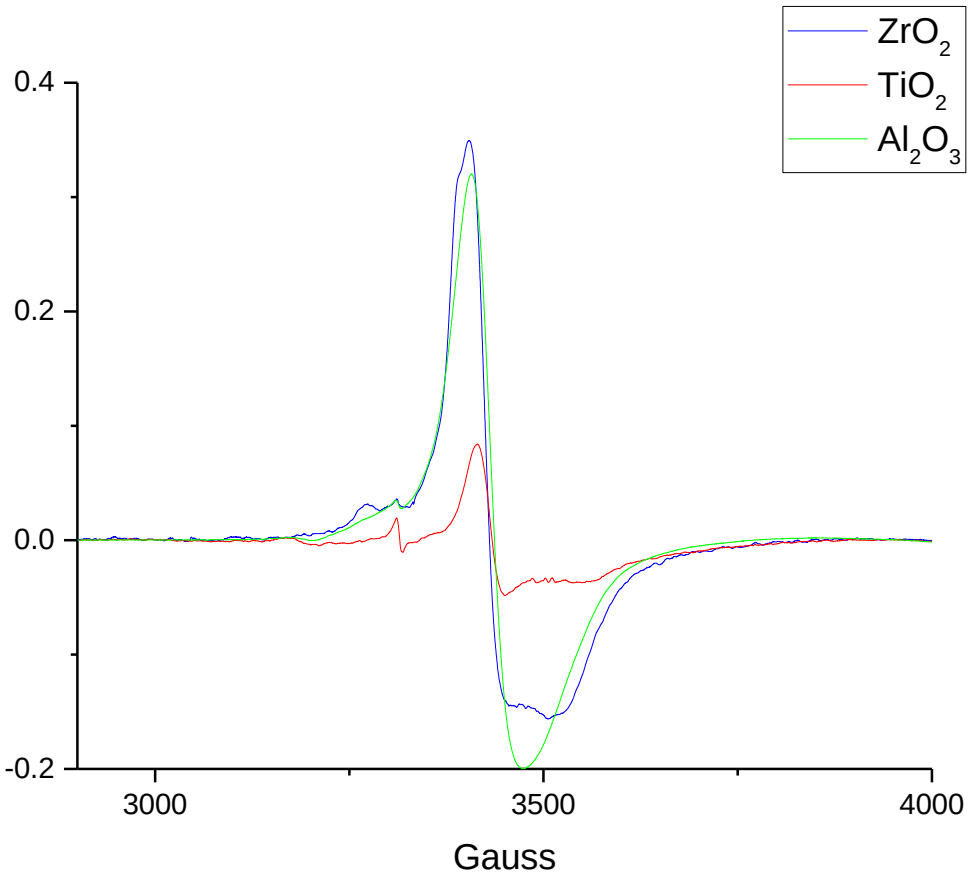

Figure S34 shows the normalized signal from the steady-state methanol ODH reaction occurring during EPR measurements. Titania-supported Mo apparently has the smallest quantity of reduced Mo(V) species present at steady state. Both Al_2O_3 and ZrO_2 supports allow for a comparatively larger quantity of reduced Mo(V) under reaction conditions and may be broadened by spin-spin interactions which is what prevents detection of hyperfine splitting. ZrO_2 has at least two signals overlapping around g = 1.95.

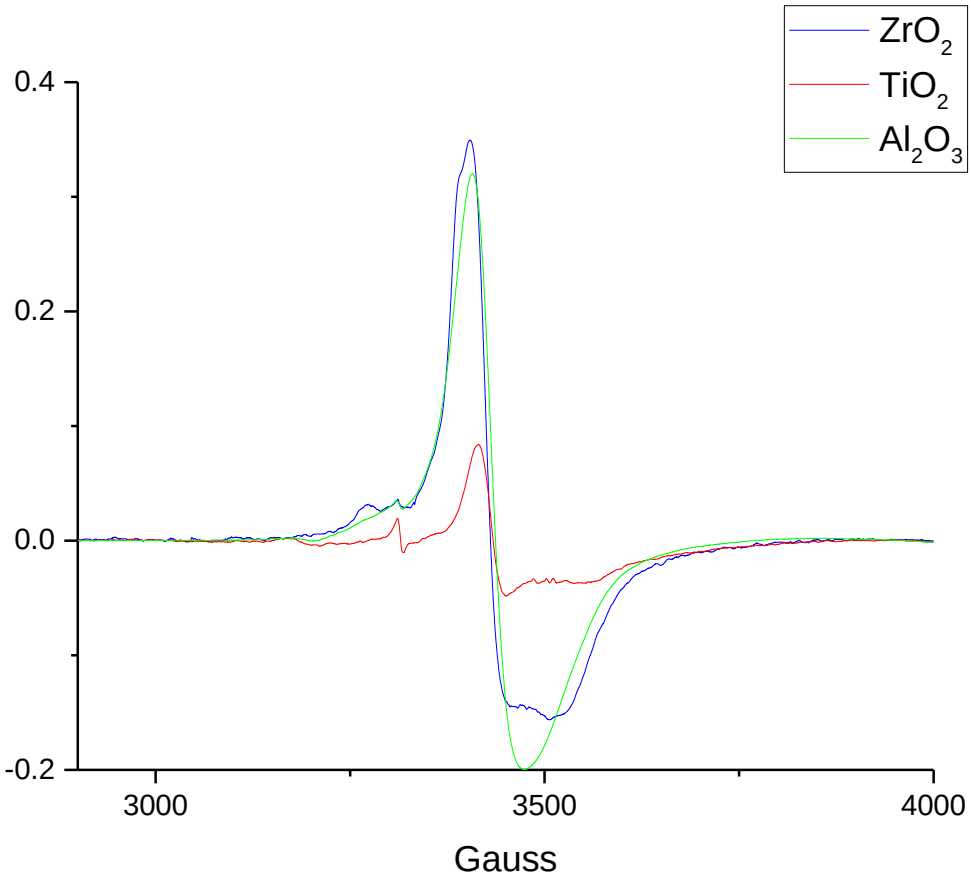

Figure S34. In situ EPR spectra of catalytic materials at steady-state methanol ODH conditions (503 K).

A plot of Al_2O_3-supported Mo at each of the presented conditions is available in Figure S35. Differences in the negative region show the apparent absence of the side peaks after oxidation. Additionally, the positive region appears to shift after oxidative treatment and move slightly back during steady-state methanol ODH, indicating that each treatment affects the environment around the Mo(V) centers. The initial g-value appears to be 1.97 initially and shifts closer to 1.98 upon treatment, which could indicate that Mo(V) was initially solvated under hydrated conditions.

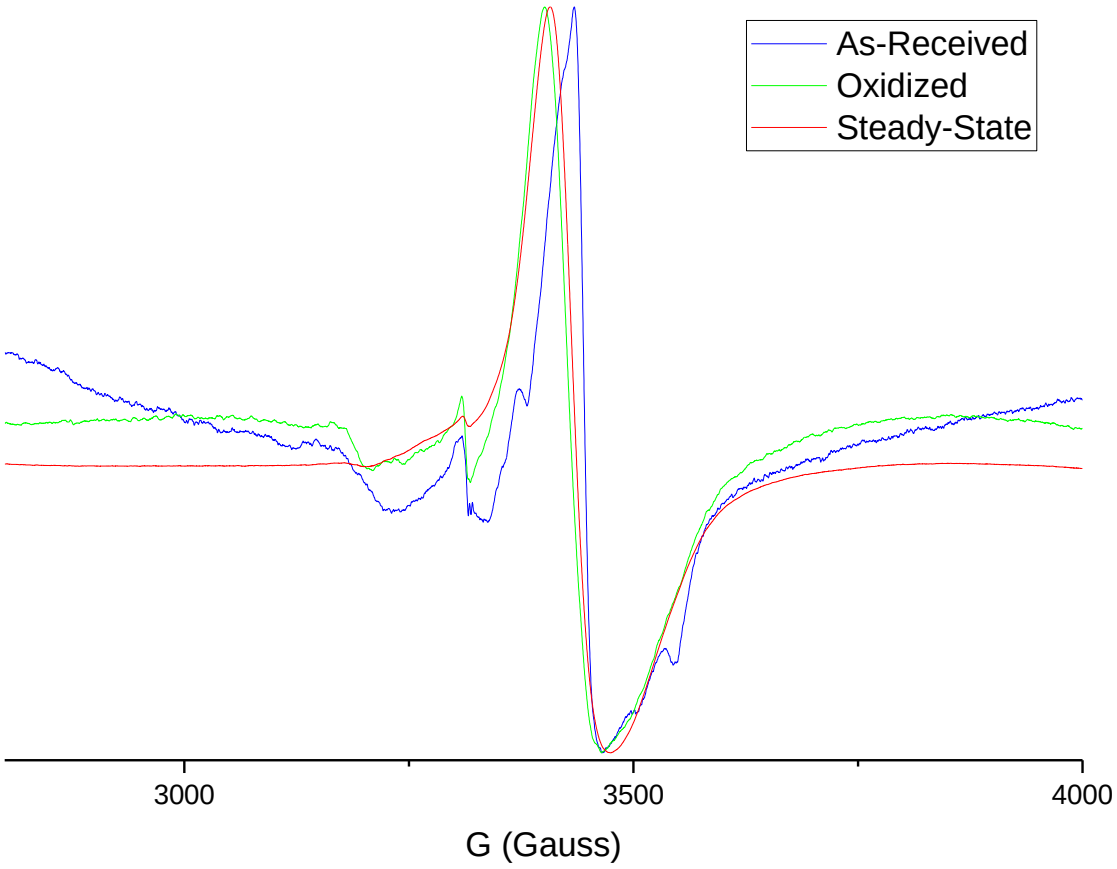

Figure S35. Comparison of alumina-supported Mo at different treatment conditions, normalized to match intensity to highlight differences.

The steady-state spectra were extracted from the time-resolved sample series shown in Figure S36. This stack-plot shows the progression of the catalysts' EPR signal transformation with time. The red lines are the spectra taken prior to methanol introduction. The green lines show spectra acquired after methnol was allowed to pass over the catalyst in the oxidizing atmosphere. Light blue lines after the green are indicative of a stagnant environment created during the disconnection of methanol from the feed line. The dark blue lines were acquired after 10% O_2/Ar was allowed to contact the material (30 sccm) again.

In each of the cases, the quantity of Mo(V) dramatically and instantly increased upon exposure to the substrate. The signals associated with the radical and ZrO_2–based uncalcined Mo(V) likewise increased, but not to the extent of the main reduced Mo(V) feature at g = 1.95. When steady-state was reached, the feed was sealed off, offering a stagnant environment in the catalyst bed while the methanol bubbler was disconnected. During this period, an appreciable quantity of Mo(V) was added to the steady-state intensity presumably due to further conversion to COx in the absence of flow. The instant the oxidizing environment was resumed, the signal from Mo(V) began to decay, indicating reoxidation of the catalyst. The radical species was apparently less impacted by the oxidative treatment (see TiO_2) and persists for an extended time period.

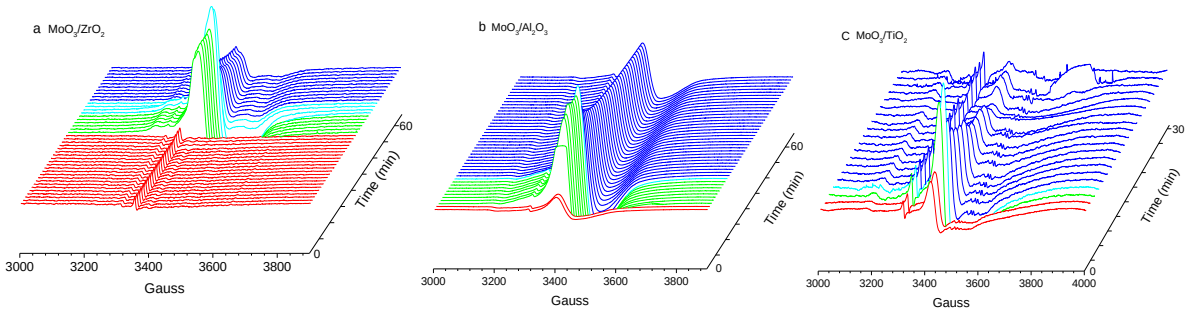

Figure S36. Time-resolved in situ EPR results for methanol ODH on a) ZrO_2, b) Al_2O_3, and c) TiO_2. The red lines indicate the signal prior to methanol introduction. The green lines are during the methanol flow. Light blue lines are during stopped flow. Dark blue lines were collected during reoxidation at 503 K.

To quantitatively compare the materials, the normalized integrated intensity of the Mo(V) signal was plotted as a function of time. The initial period was a flat line at low intensity that instantly increased with methanol introduction. Compared to the pre-reaction condition, Zr showed this largest increase in reduced species (20 fold). Al showed the next largest enhancement by about 9 times the signal intensity. Titania had a relatively small enhancement of

only three-fold and also the lowest normalized intensity, following the trend Zr > Al >> Ti (2632 > 2597 >> 525). After the reaction, the signal decayed, but a single exponential decay function failed to accurately describe the oxidation behavior where Zr showed the smallest time constant of decay (~194 s) and Al showed the longest (~381 s). The time constant was shown to be temperature dependent. Analysis with a double-exponential function will be described based on Figure S38.

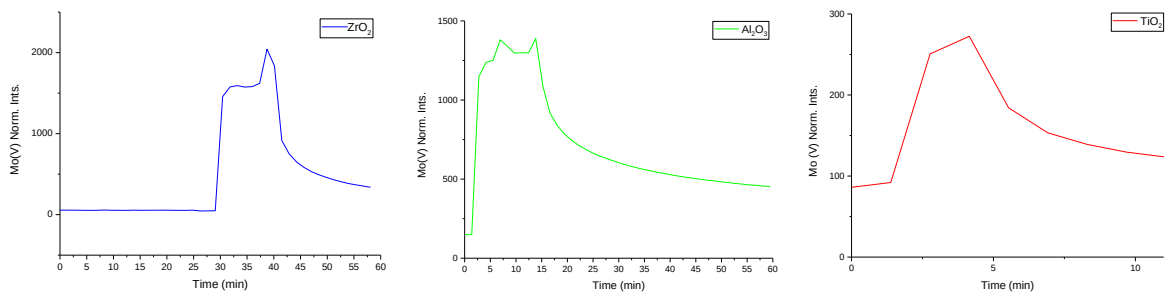

Figure S37. Time-resolved in situ EPR of the integrated, normalized Mo(V) intensity on ZrO_2, $Al2O_3$, and TiO_2.

To illustrate the differences in oxidation behavior, the decay sections of the time-resolved EPR experiments were plotted together showing the fraction of reduced Mo(V) remaining as a function of time. From the results, it is clear that ZrO_2-supported materials have a much faster oxidation rate than the other two materials. Titania is intermediate and Alumina is the slowest of these three samples. Since an exponential decay function failed to accurately represent the oxidation rate, a double exponential function with both a long and short decay constant were employed. The parameters for the fit are shown in Table S12. The time constants were; 1.9 and 17.9 mins for Al_2O_3, 1.0 and 5.2 mins for TiO_2, and only 3.1 mins for ZrO_2. This further supports

the relative ease of oxidation for zirconia-supported Mo at this temperature where Al_2O_3 reoxidizes less readily.

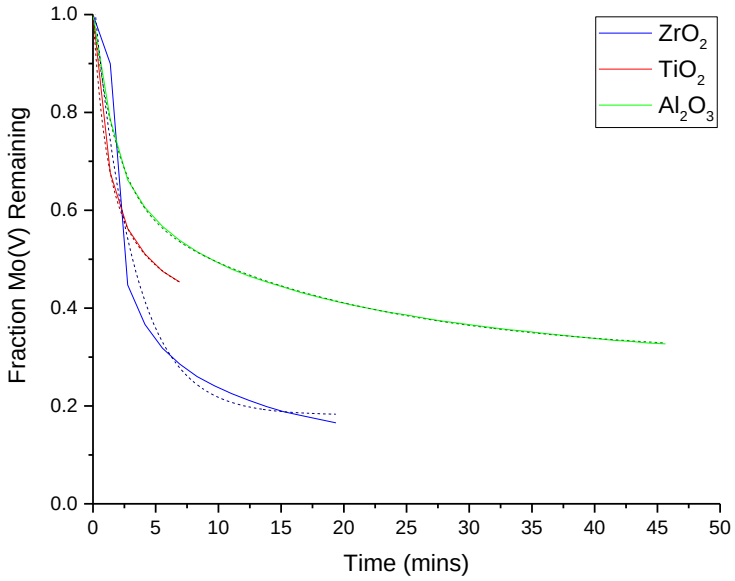

Figure S38. Integrated intensity of Mo(V) during the oxidation after steady-state analysis represented as the fraction of Mo(V) remaining plotted as a function of time. Fitted double exponential functions are shown as dotted lines.

Table S12. Double-exponential decay fitting parameters.

	Al_2O_3	**TiO_2**	**ZrO_2**
R^2	0.99979	0.99995	0.93927
Y0	0.3031	0.37878	0.1813
A1	0.36803	0.3413	0.47179
T1	1.86 min	0.98 min	3.15 min
A2	0.32909	0.27994	0.398
T2	17.9 min	5.19 min	3.15 min

In summary, the quantity of reduced Mo(V) during methanol ODH can be monitored *in situ* during EPR analysis. The as-received samples shown small quantities of reduced Mo(V) which are oxidized during pretreatment. Upon application of methanol feed, a dramatic and

instantaneous enhancement of the Mo(V) signal is observed. TiO_2 shows the smallest quantity of reduced species and Al_2O_3 and ZrO_2 show similar amounts. Zr had the highest fold increase in signal upon reaction initiation. At constant flow, steady-state conditions, Zr had at least two Mo(V) signals and Al may have more than one species or could be broadened by spin-spin interactions. The high performance of Zr-supported Mo may be explained by the relatively high coverage of reduced Mo(V) at steady state (suggesting an easy of reduction) coupled with relatively quick reoxidation (via the time constant), indicating that the energy barrier for these steps may be smaller. The presence of at least two Mo(V) signals may contribute to these favorable attributes.

The next step in data analysis involves the quantification of detected species. According to the Curie law, a Boltzman distribution between spin states is anticipated, barring the existence of detrimental relaxation interference, which can be described by Eq. 17. We can estimate the number of spins detected by correlating the observed signals with a known reference at variable temperature, thereby revealing the specific impact of temperature.

$$\frac{n_{upper}}{n_{lower}} = exp\left(-\frac{E_{upper} - E_{lower}}{kT}\right) \qquad \textit{Eq. 17}$$

To validate the absence of relaxation interference, a demonstration of the impact of temperature on observed signal was conducted on a sample at two different temperatures. Extracted from the test run in Figure S37a, the end of the experiment brought the sample back to 293K. This change in temperature was accompanied by an increase in the signal intensity (representative sketch in Figure S39). At 509 K, the integrated, non-normalized intensity was

77360 while at 293 K, it was 1.33 x 10^5. Comparing this difference (1.72 times the signal at the lower temperature) to our predicted spin population distributions at this energy level and these temperatures (1.74), we can accurately predict the thermal effect of the signal for Mo(V) species. When a reference standard is analyzed at the same spectrometer conditions, the integrated intensities can be converted to an absolute quantity of Mo(V) species.

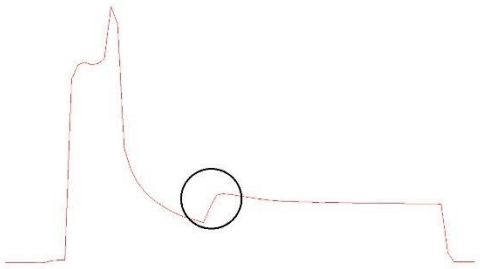

Figure S39. Representative sketch of increasing signal at lower temperatures by Currie's Law.

Appendix E: Additional Data for Other Oxide Systems

Catalytic conversion of liquid phase 2,3, Butanediol on ZSM-5 and $AlPO_4$

The catalytic conversion of 2,3 butanediol to olefins occurs through dehydration steps to isobutyrlaldehyde (IBA), 2-butanone (2BO), and but-3-ene-2-ol (3B2OL). The pathways under different catalytic conditions are not yet understood, driving a desire to investigate the species present, spectroscopically. Such transitions can be monitored *in situ* as dehydration occurs.

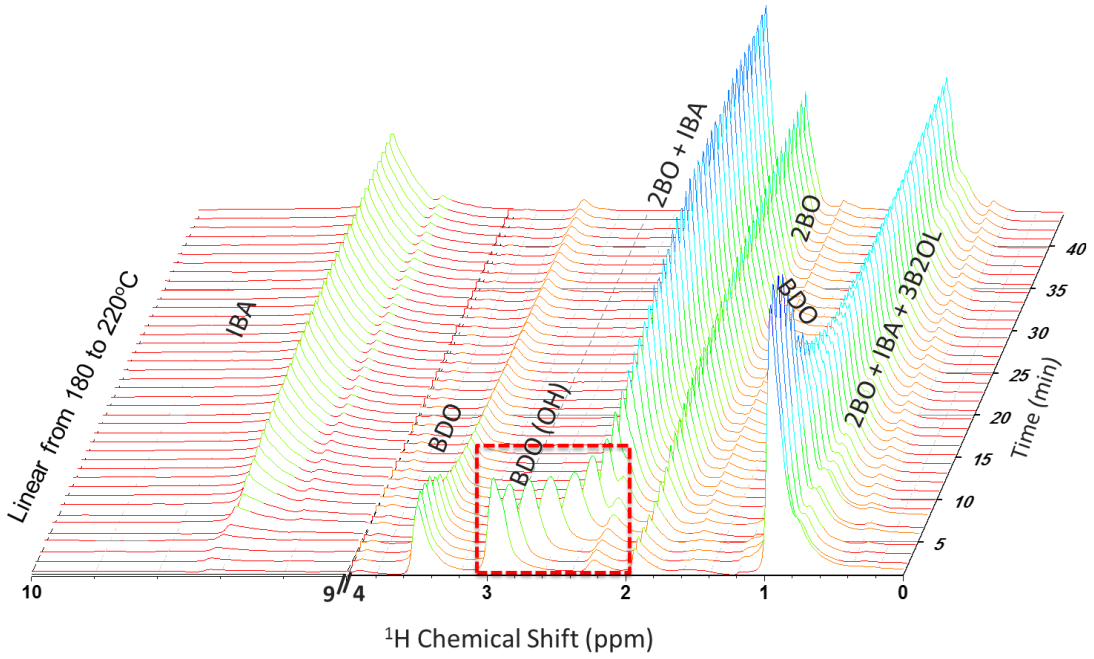

Figure S40. Time-resolved catalytic conversion of 10% 2,3, butanediol, 4% glycerol in D_2O on $AlPO_4$ via in situ ^1H NMR.

A detailed analysis reveals extensive H-D exchange between D_2O and -OH groups in butanediol and glycerol which prevents –OH observation. Isobutryladehyde (IBA) is observed a high temperatures where 2-butanone and butadiene are also formed. It is speculated that heavy

hydration solvates acid site (observed at 3.4 ppm on dry $AlPO_4$), leading to hydronium ion formation. The other species present between 3.5 and 4.5 ppm may be related to glycerol or low-abundance product species.

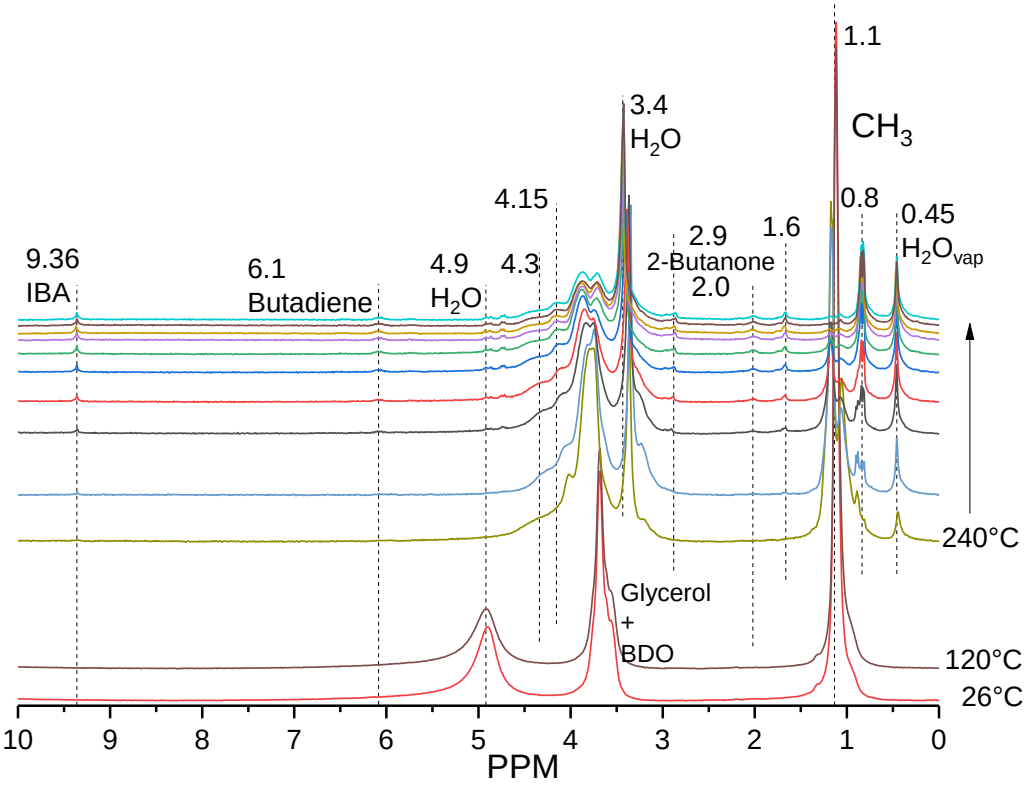

Figure S41. Time- and temperature -resolved catalytic conversion of 10% 2,3, butanediol, 4% glycerol in D_2O on $AlPO_4$ via in situ ^1H NMR.

Under heavily hydrated conditions, the hydrated hydronium ion is extensively mobile. The hydronium ion serves as the active site and due to the accelerated mobility and diffusion, no CP signal is observed since CP NMR detects surface-adsorbed species and these species are heavily mobile. From single-pulse ^{13}C NMR, glycerol and 2-butanone are confirmed in addition to those low-abundance species observed by ^1H NMR.

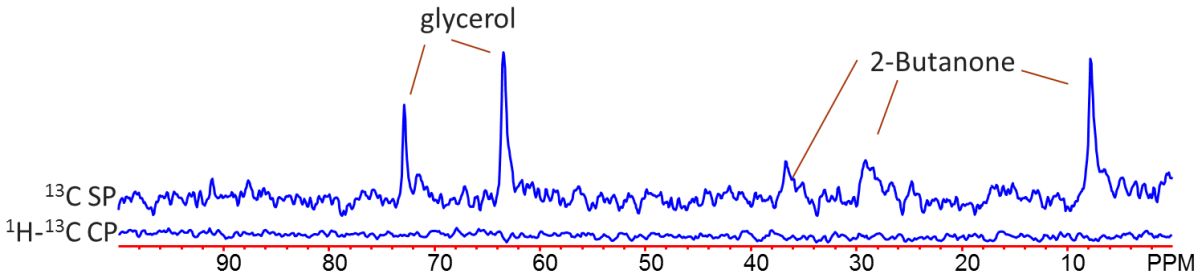

Figure S42. ^{13}C NMR and ^{3}H-^{13}C CP NMR showing mobile glycerol and butanone.

In situ NMR for H_2 activation on Pd/Al_2O_3

All *in situ* MAS NMR spectra were collected on a 300 MHz Varian Inova NMR spectrometer operating at a ^{1}H Larmor frequency of 299.97 MHz. A sample spinning rate of 3,600 Hz was employed at the magic angle for the experimental runs in a commercial 7.5 mm ceramic probe. A single-pulse sequence with a pulse width of 7 μs and a recycle delay time of 5 s were used. Each NMR spectrum was acquired using an accumulation number of 128 to 256. Temperatures were controlled using a commercial variable temperature heating stack externally calibrated with an ethylene glycol thermometer. All free indication decays were processed without line broadening. The 2% Pd/Al2O3 catalyst employed in the NMR studies was first activated at 400°C in a flow reactor for 3 hours. The pretreated material was then sealed and transferred to a dry, N_2-purged glovebox where it was loaded into an all-ceramic, gas-tight, 7.5 mm *in situ* MAS NMR rotor.[19, 235] A specially designed loading chamber was used to introduce hydrogen gas to match the internal rotor pressure to the desired pressure of the experiment without exposure to open atmosphere.

The high field peak at -0.2 ppm has been ascribed to OH groups bound to octahedrally-coordinated Al centers (Al_O-OH).[372] Lower field shifts have been ascribed to more acidic hydroxyl protons. At 2.2 ppm, we observe a broad resonance similar to what has previously been ascribed to a combination of Al_T-OH, Al_T-OH-Al_O, Al_O-OH-Al_O and $3Al_O$-OH.[373] After hydrogen treatment at 0 psig, two relatively sharp OH signals (1.5 and 1.3 ppm) intensify and emerge from the broad feature. These species are retained after removal of H_2 with He purging.

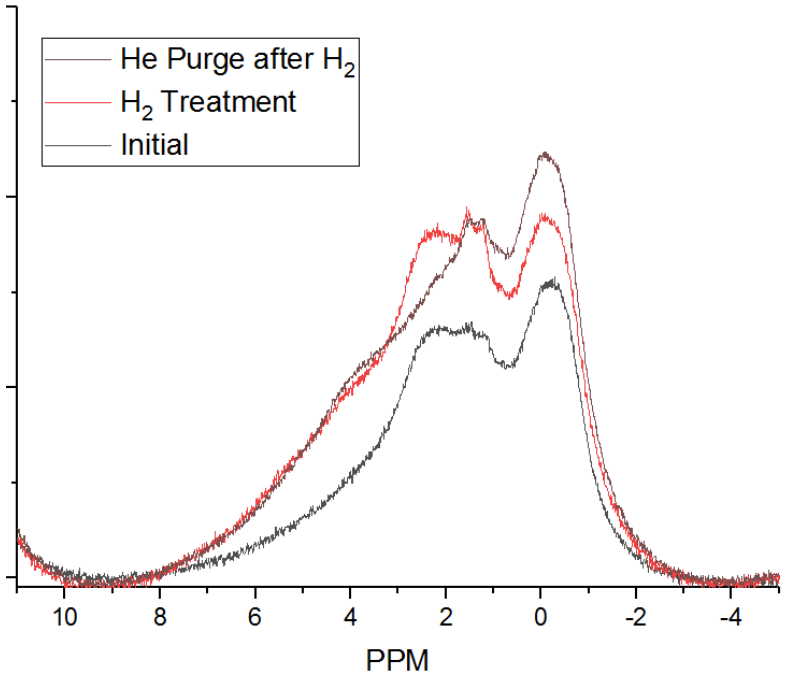

Figure S43.Spectra of 2% Pd/Al_2O_3 before, during, and after H_2 treatment.

Treatment of this sample with high pressures of hydrogen stimulate the appearance of PdH in the proton NMR spectra. As the temperature increases, the signal associated with the beta phase of PdH progressively narrows and migrates to the gaseous hydrogen signal. No alpha phase was observed throughout this process, likely due to broad lines and low intensity ad significantly shifted frequencies.

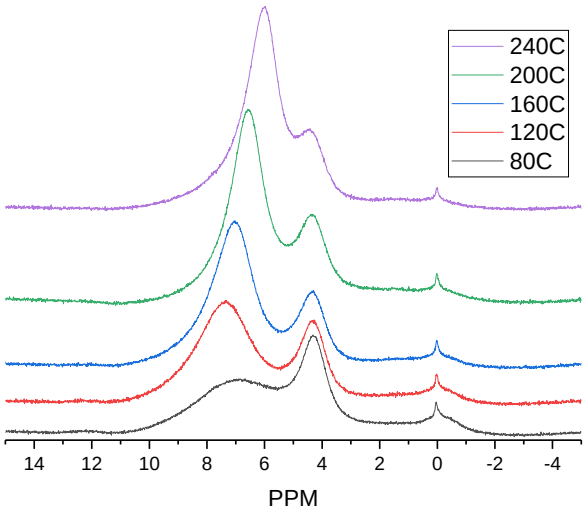

Figure S44. Spectra of 2% Pd/Al_2O_3 before, during a temperature ramp under 146 psig of hydrogen.

Ethanol Dehydration over Polyoxometalates

The dehydration of ethanol to olefins represents a potentially attractive method of deriving value-added products from renewable carbon sources. To offer a clear understanding of the mechanisms and rates for ethanol dehydration, well-defined polyoxometales have been studied to reveal the detailed kinetics of such a transition.[374] In an effort to explore the microkinetic model of such a system, *in situ* NMR was employed to assess the surface coverages of intermediate species during the process. Polyoxometalate materials with different heteroatoms (P, Si, Al, and Co) were synthesized and characterized. Two materials were selected due to their favorable observation by NMR (Al- and P-based Keggin strucgures). The synthesis of $H_5AlW_{12}O_{40}$ was monitored throughout the process. The results indicate that the Al species expected throughout the synthesis process were indeed present. Upon supporting the

polyoxometalate onto the support, the Keggin structures was retained. Similar observations were during the synthesis of $H_3PW_{12}O_{40}$.

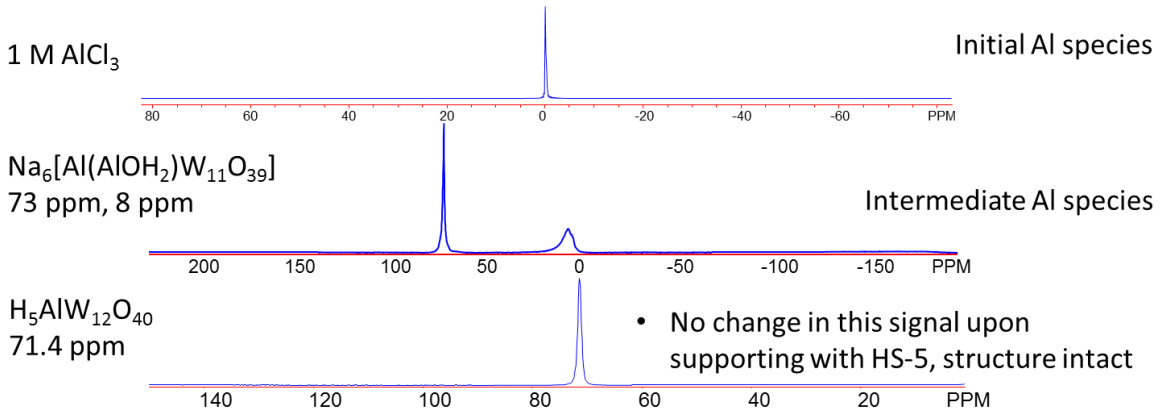

Figure S45. ^{27}Al NMR spectra of the synthesis of $H_5AlW_{12}O_{40}$.

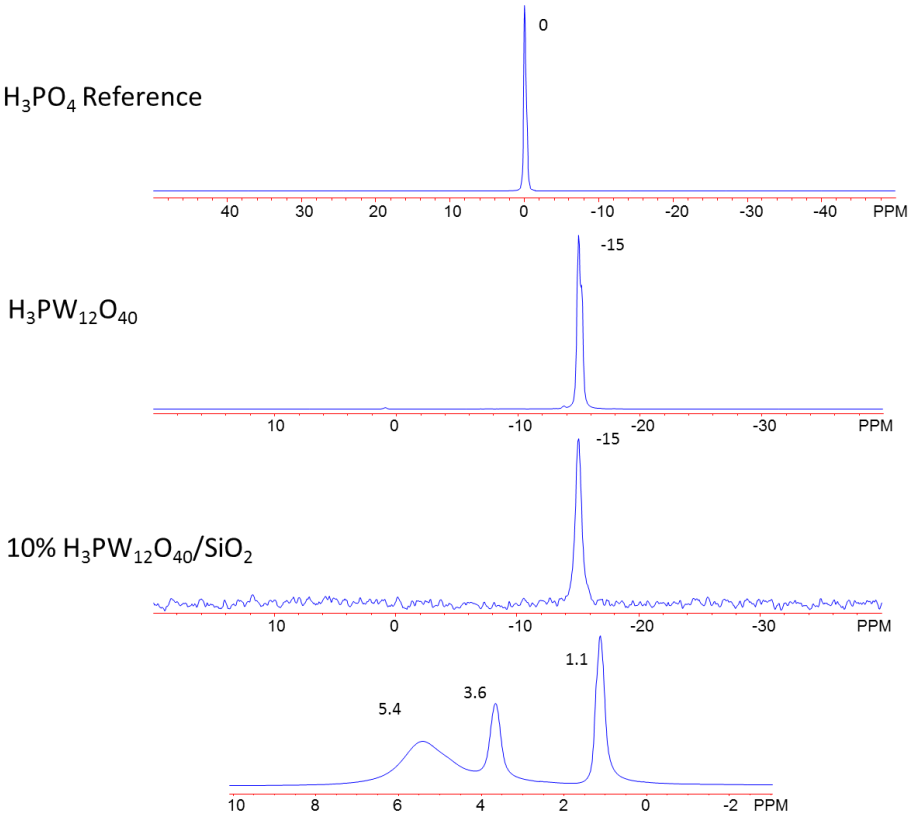

Figure S46. ^{31}P MAS NMR confirming the synthesis of supported $H_3PW_{12}O_{40}$.

Partial dehydration of the P-based polyoxometalate resulted in distinct ^{31}P and ^{1}H shifts from water interacting with some sites. Additionally, the relaxation rate was severely diminished due to the absence of nearby spins stimulating relaxation (17 minute recycle delay). The Al-polyoxometalate samples exhibits a number of signals depending on the state. The supported, hydrated sample shows a peak around 6 ppm from water interacting with acid sites. A peak at 3.9 ppm arises from water interacting with the silica surface. Dehydrated, only peaks around 3.7, 1.8, and 0.9 ppm are present. The peak at 1.8 ppm and downfield are ascribed to silanols. Unsupported, the $H_5AlW_{12}O_{40}$ features a single broad resonance at 10 ppm when dehydrated, corresponding to acid sites. These readily interact with water when hydrated and shift to 8.2 ppm. The progressive addition of water to the supported material reveals that water may solvate acid protons, which are initially invisible, potentially due to slow relaxation or dipolar interactions. This is evidenced by a high field water signal that migrates to the bulk water position with increased loading. Acid protons show preference to interacting with water, followed by silanols, which may migrate, in part, to 1.1 ppm. The 4 ppm peak is not an acid proton, or at least not exposed and available to interact with water. Modulation of the recycle delay demonstrates that the lack of proton observation is not due to relaxation effects, but may be related to strong dipolar interactions.

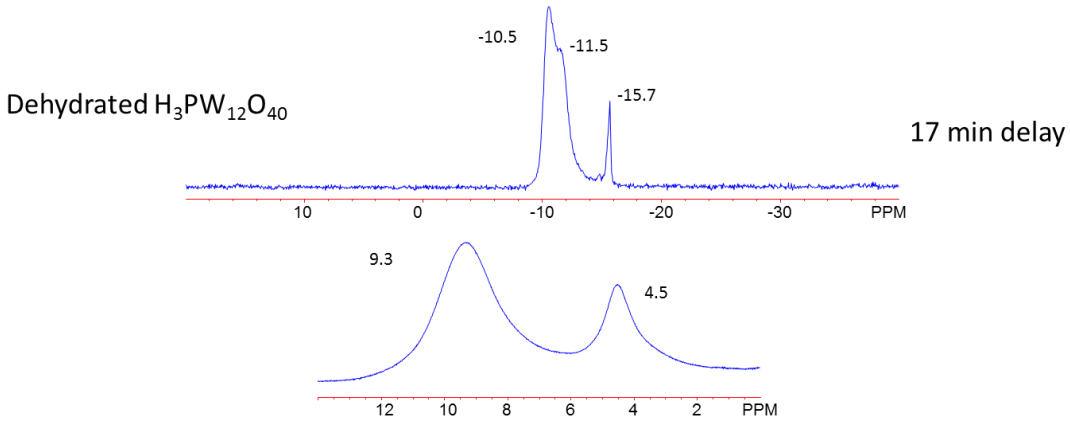

Figure S47. ^{31}P and ^{1}H MAS NMR of partially dehydrated $H_3PW_{12}O_{40}$.

.

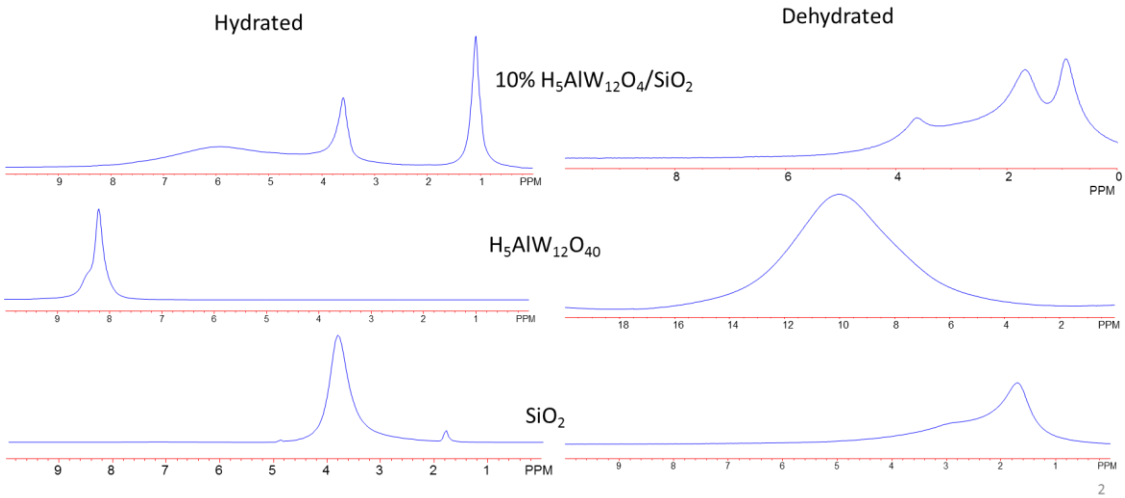

Figure S48. ^{1}H MAS NMR of hydrated and dehydrated $H_5AlW_{12}O_{40}$ and the support.

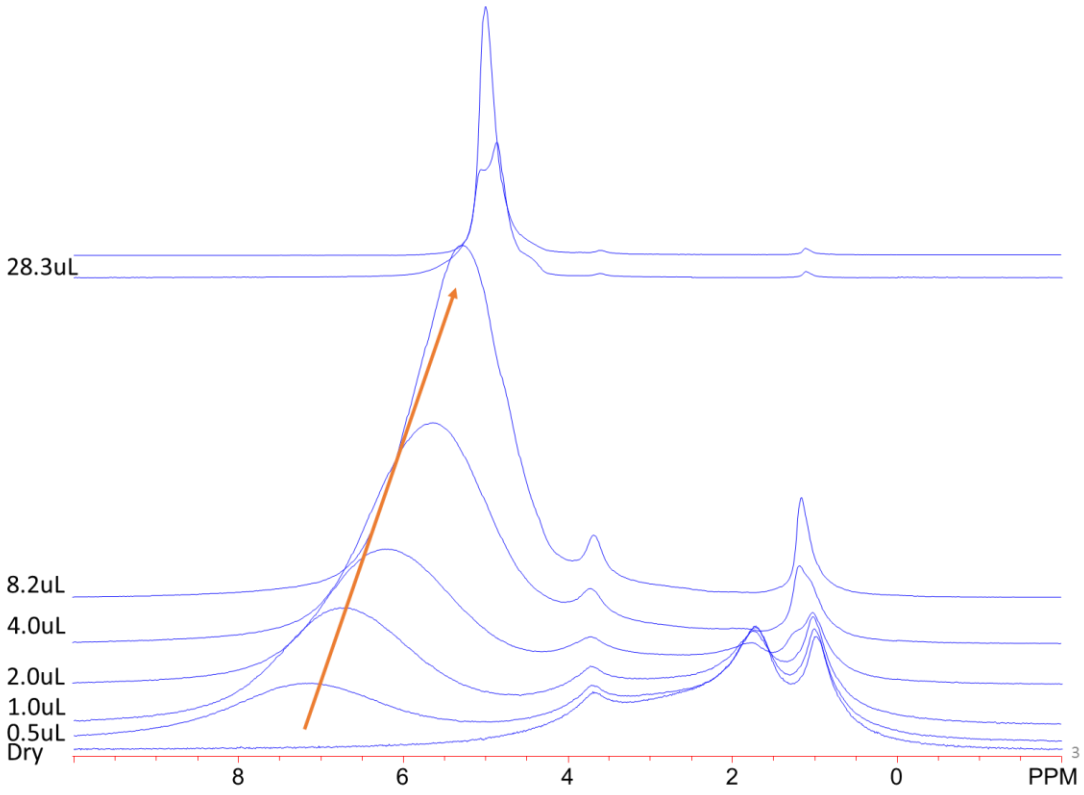

Figure S49. Progressive water addition to supported $H_5AlW_{12}O_{40}$ after equilibration at 100°C and returning to RT.

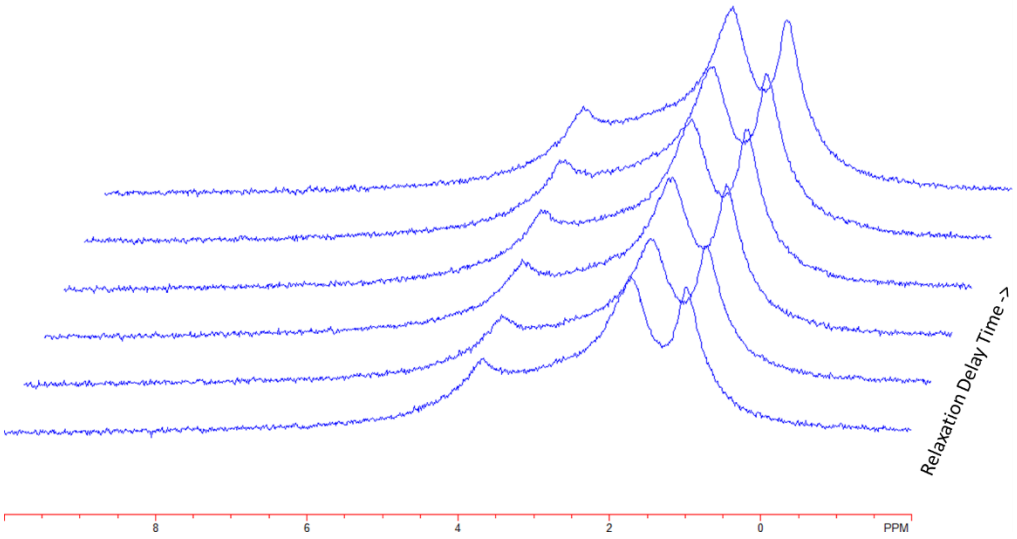

Figure S50. ^{1}H MAS NMR spectra of $H_5AlW_{12}O_{40}$ with extended relaxation delay times.

The impact of reactivity on the heteroatom of the kegging structures was also investigated. While slight modulations were observed for the process, especially with regards to broader features at elevated temperatures, no significant new peaks were observed. Such broadening may arise from reduced symmetry when the outer shell is coordinated to ethanol or a reactive intermediate.

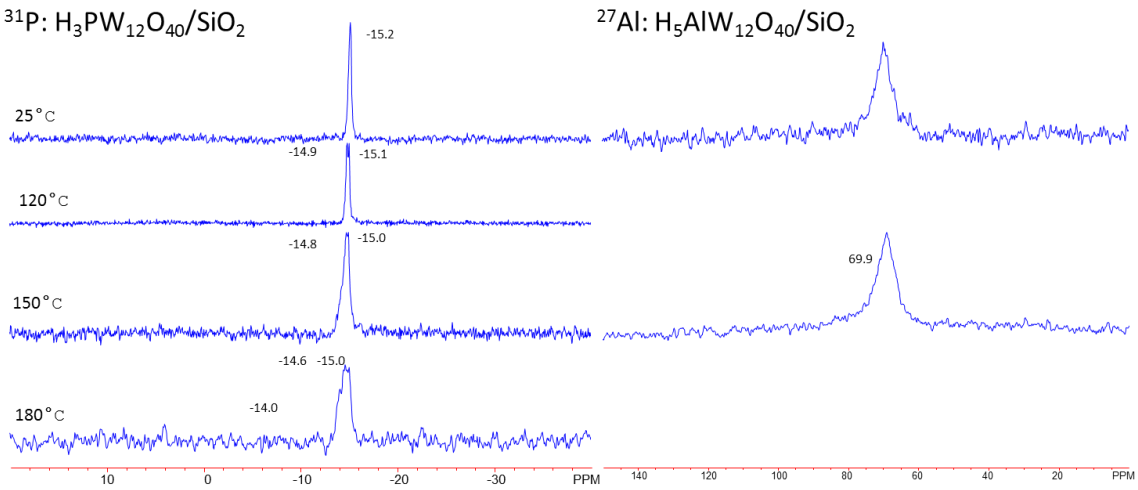

Figure S51. 10% $H_3PW_{12}O_{40}/SiO_2$ after in situ heating of 3.1 mg ethanol.

A key intermediate in the ethanol dehydration scheme is the ethoxy species. To understand the resonance position of this species on solid-acid catalyst, ethylene was applied to the rotor and allowed to take an equilibrium with surface ethoxy species. The resulting NMR revealed a broad 85 ppm resonance for $H_5AlW_{12}O_{40}$ and a 78 ppm signal for H-ZSM5, enabling a clear assignment of this species.

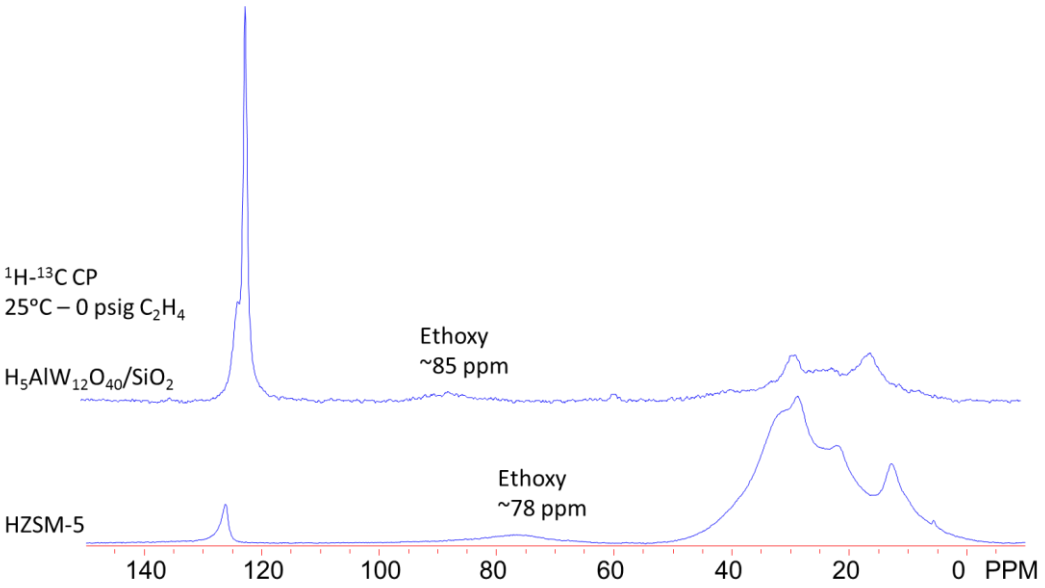

Figure S52. ^{1}H-^{13}C CP MAS NMR spectra of ethylene adsorbed on $H_5AlW_{12}O_{40}$ (top) and H-ZSM-5 (bottom).

Ethanol was introduced to the sealed rotor system and the temperature was increased to allow for the alcohol to react. At low temperatures, ethanol is observable at 58 ppm. Higher temperatures stimulate the development of ether at 66 ppm and ethylene at 120 ppm. Further oligomerization products are visible at ~15 ppm.

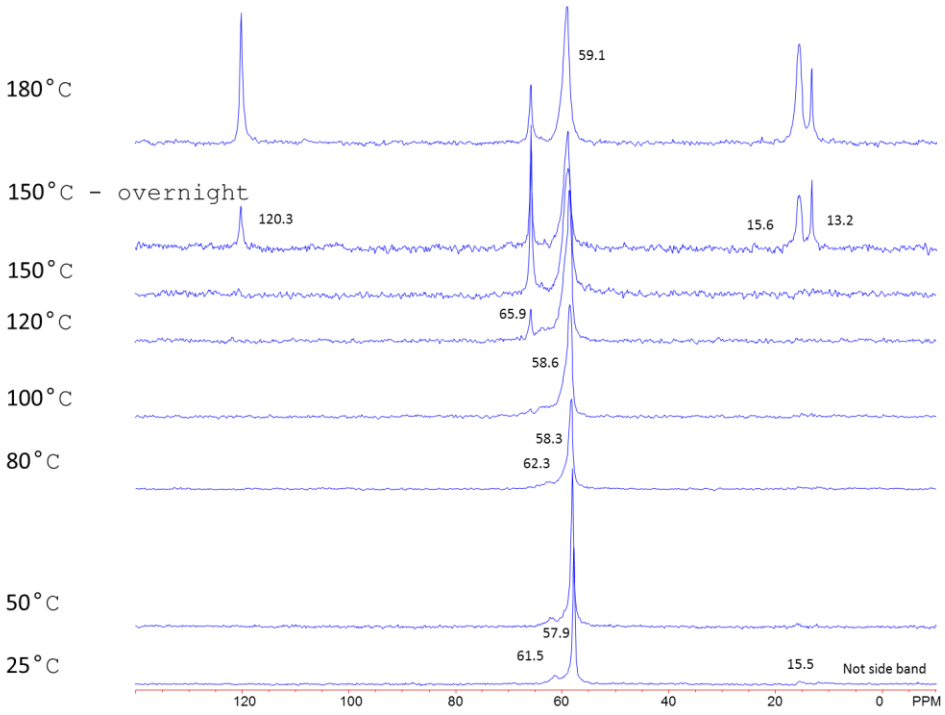

Figure S53. ^{13}C MAS NMR of supported $H_5AlW_{12}O_{40}$ with 2.2 mg ethanol as a function of temperature.

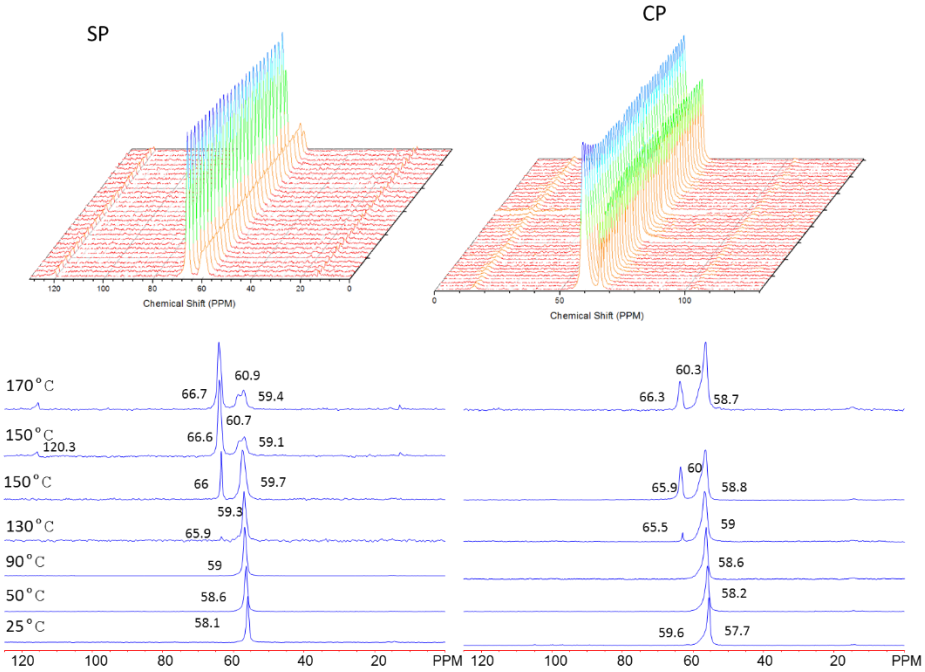

Figure S54 Comparison of. ^{13}C (left) and cross-polarization (right) MAS NMR of 97.7 mg of supported $H_3PW_{12}O_{40}$ with 2.3 mg ethanol as a function of temperature.

Due to the batch-like nature of the MAS rotor, limitations on EtOH pressure prevent EtOH pressures below 30 kPa with the original setup. 100-680 kPa probed in the first set of data. A follow up that employed the specially-design loading chamber extended these pressures to those relevant to the kinetic model. The ^{1}H-^{13}C CP experiment used to suppress mobile species and enhance signal of bound intermediates. Though not quantitative without extensive calibration, pulse parameters were retained to allow for semi-quantitative analysis. Based on the microkinetic model a decrease in monomer and ethoxy, and an increase in dimer and monomer-ethoxy is expected over this pressure range. The experiments were conducted by an initial increase of temperature to 71°C for 30 minutes to encourage equilibration. The sample was then quickly heated to 130°C and scan until products were just visible (~1 hour). Afterwards, the temperature was lowered to 25°C for enhanced resolution and to prevent further reaction during acquisition. The state of the sample at high temperature and low temperature were compared to illustrate the validity of this approach.

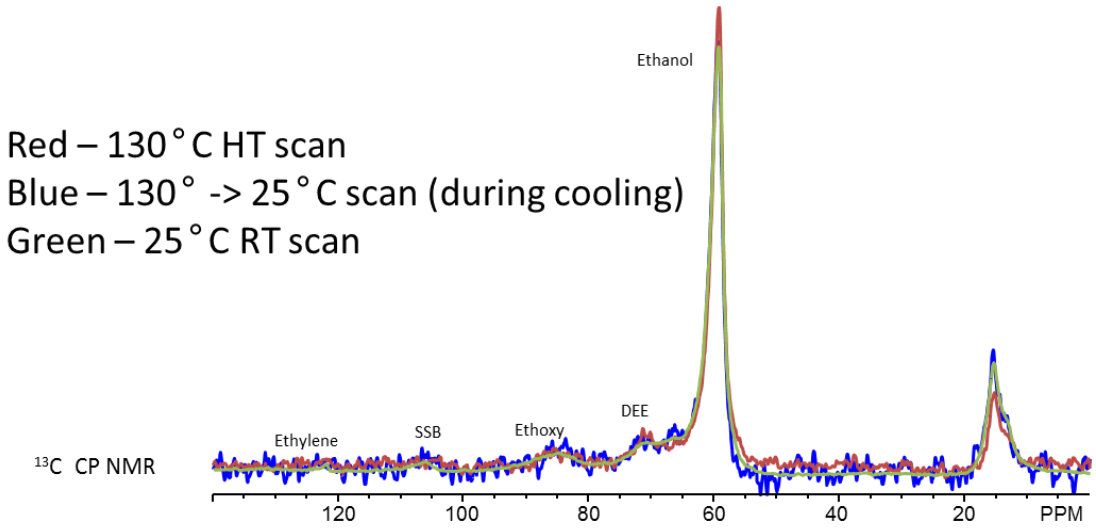

Figure S55. ^{1}H-^{13}C CP MAS NMR of ethanol dehydration on supported $H_5AlW_{12}O_{40}$ during high temperature treatment, during cooling, and at room temperature.

This experiment was conducted over a series of ethanol pressures (added by micro syringe). The results revealed a dynamic range of species signal intensities over the pressure range. Monomers, dimers, diethyl ether ethoxy, and ethylene were observed and quantified. The results show that the ethoxy and ethylene signals decrease with EtOH pressure from 100 to 700 kPa. DEE and dimer signals are invariant to pressure from 100 to 700 kPa, however, the monomer signal increases slightly with EtOH pressure from 100 to 700 kPa. These results are not fully consistent with what is expected, however, signal overlap between monomer-ethoxy and ethoxy, etc. makes this determination more challenging. Further the pressures far exceed those of the microkinetic model, making it highly desirable to examine this behavior under conditions relevant to the kinetic study. A further drawback to this analysis is the uncontrolled level of conversion and lack of insight provided for these species as a function of conversion. This will be rectified in a future iteration of the work.

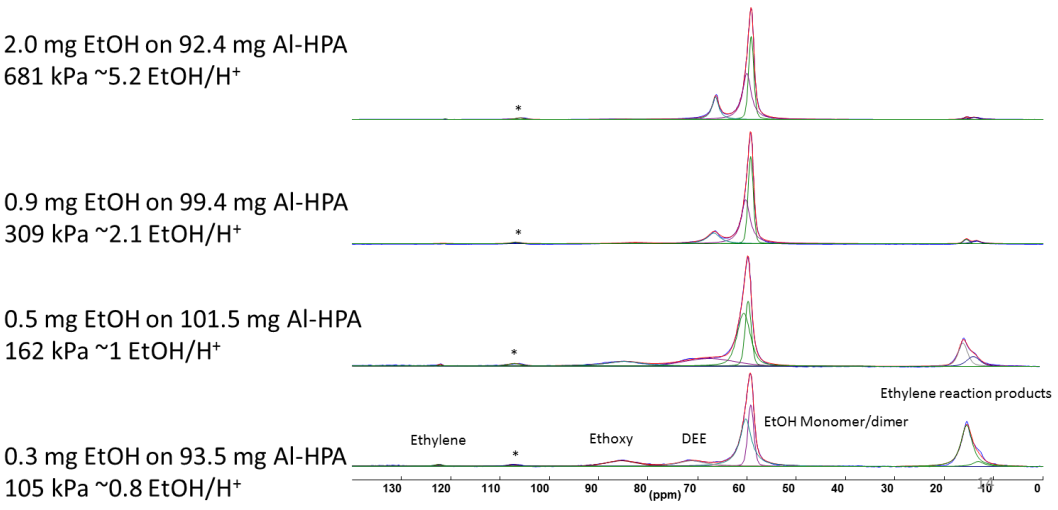

Figure S56. ^{1}H-^{13}C CP MAS NMR of ethanol dehydration on supported $H_5AlW_{12}O_{40}$ at different ethanol pressures.

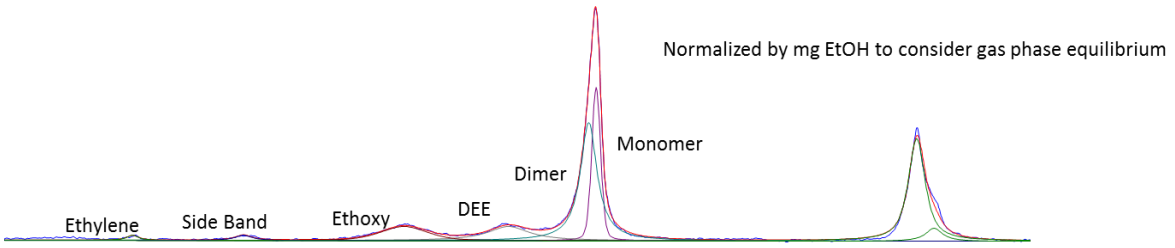

Figure S57. Representative ^{1}H-^{13}C CP MAS NMR of ethanol dehydration on supported $H_5AlW_{12}O_{40}$.

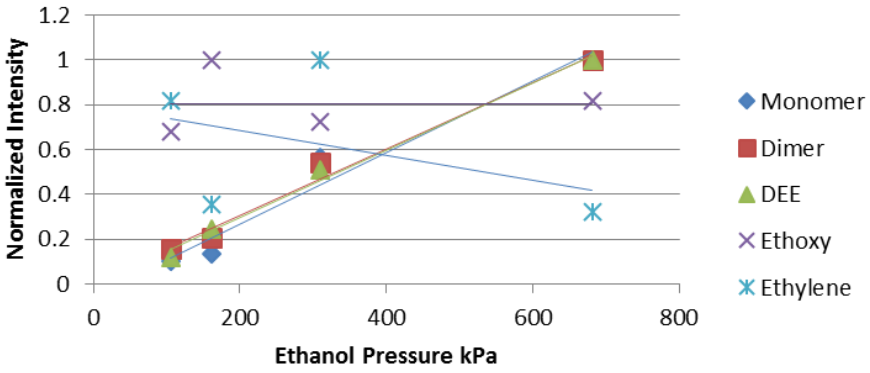

Figure S58. Normalized species intensities as a function of ethanol pressure in the rotor.

The assignment of these species are further supported by DFT-based calculations of the chemical shift. A model of $H_3PW_{12}O_{40}$ was constructed and the various surface species were introduced. Geometries were optimized with GGA: PW91 at the TZ2P, with Scalar ZORA relativistic effects considered.

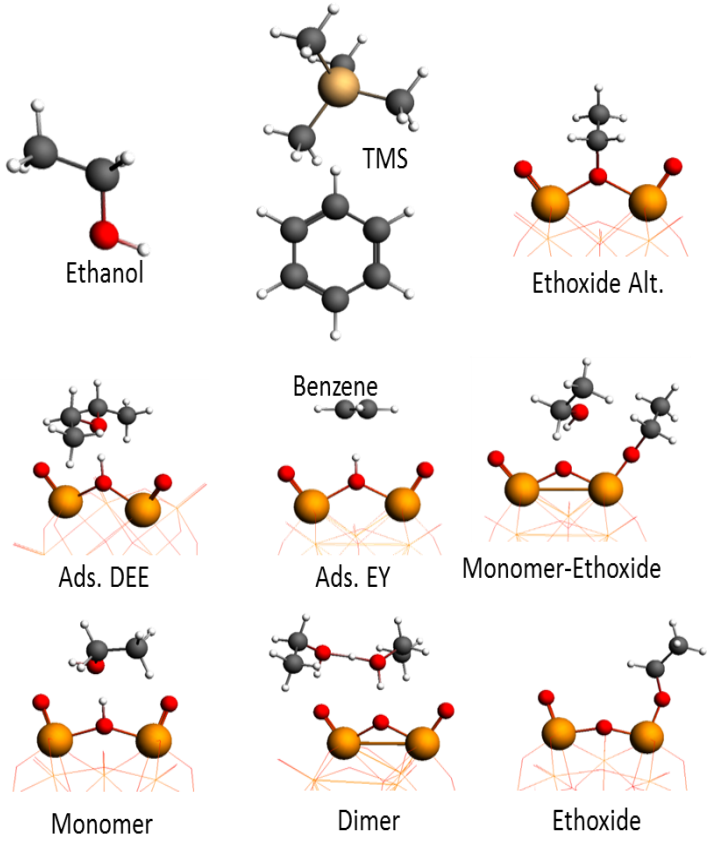

Figure S59.DFT-optimized structures of various proposed intermediates for ethanol dehydration on polyoxometalates.

To circumvent the aforementioned issues, the custom loading chamber was used to control the ethanol pressure at lower levels. Adsorption of the ethanol occurred until equilibrium was reached (monitored by NMR) at 60°C between the gas stream and adsorbed ethanol. The resulting sample was then reacted for periods of time and probed accordingly. Both single pulse and cross polarization were used, the CP to monitor the surface species and the SP to monitor the overall conversion. Though preliminary, there is an apparent increase in ethoxy signal at lower pressures, consistent with the predicted sum of ethoxy and monomer-ethoxy species from the microkinetic model. Further analysis of all collected spectra is ongoing.

Table S13. DFT-derived chemical shifts of various proposed intermediates for ethanol dehydration on polyoxometalates.

1-^{13}C Chemical Shifts	**Calculated**	**Experimental**
TMS	-4.30 ppm	0 ppm
Ethanol	62.42 ppm	64.4 ppm
Benzene	130.63 ppm	128.5 ppm
Ads. DEE	76.29 ppm	~66.2 ppm
Ads. EY	132.60 ppm	122.0 ppm
Monomer	66.91 ppm	59 ppm
Dimer	68.46 ppm	60 ppm
Ethoxide	88.99 ppm	84.5 ppm
Ethoxide Alt.	89.82 ppm	-
Ethoxide-Monomer	92.83, 63.95	-

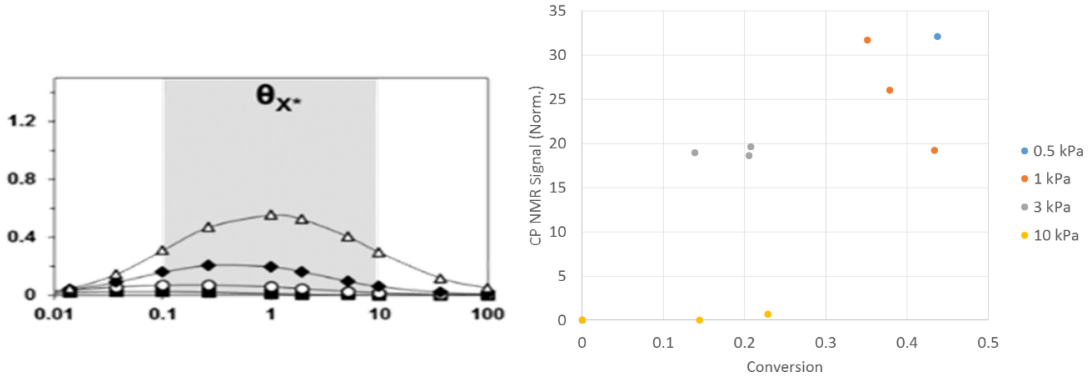

Figure S60. Comparison of ethoxy species CP MAS NMR signal as a function of conversion at different pressures compared to theoretically-derived trends of ethoxy coverage at different ethanol pressures.

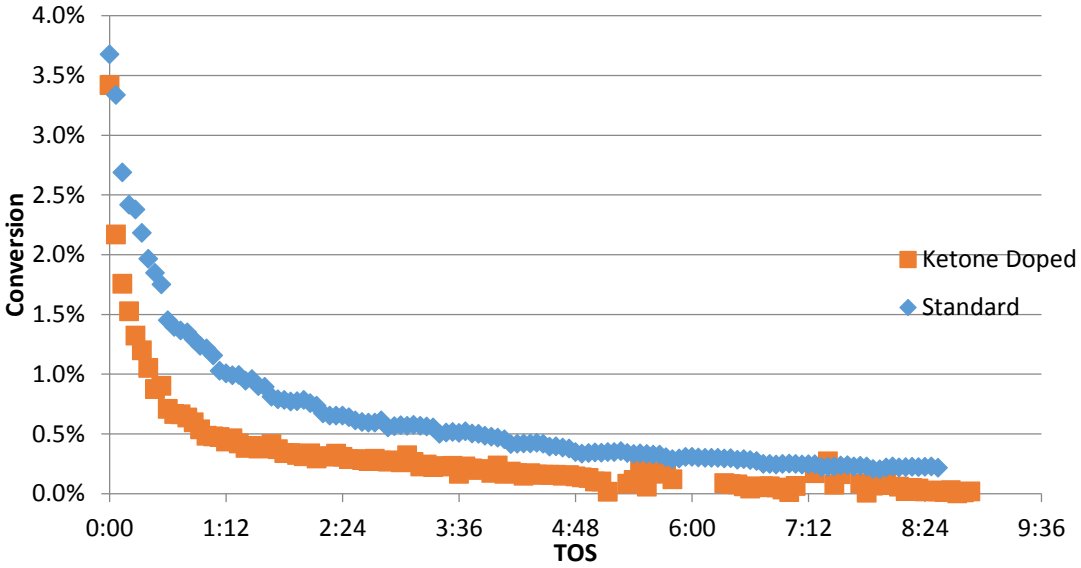

Figure S61. Ketone-driven deactivation of cyclohexanol dehydration on TiO_2 (001) using ketone doped feedgas (triple the cyclohexanone impurity quantity). First-order poisoning rate constant ~0.01/Pa/min, with an E_D of 20 kJ/mol).

Table S 14. 1,2-propanediol dehydration benchmarking on P25 titania.

SV ($hour^{-1}$)	X	$S_{aldehyde}$	C Balance	Rate (mol/mg/min x10^7)
3000	80%	95%	110%	1.721
7500	46%	98%	88%	3.045
20000	38%	95%	101%	6.002
30000	28%	96%	95%	7.429

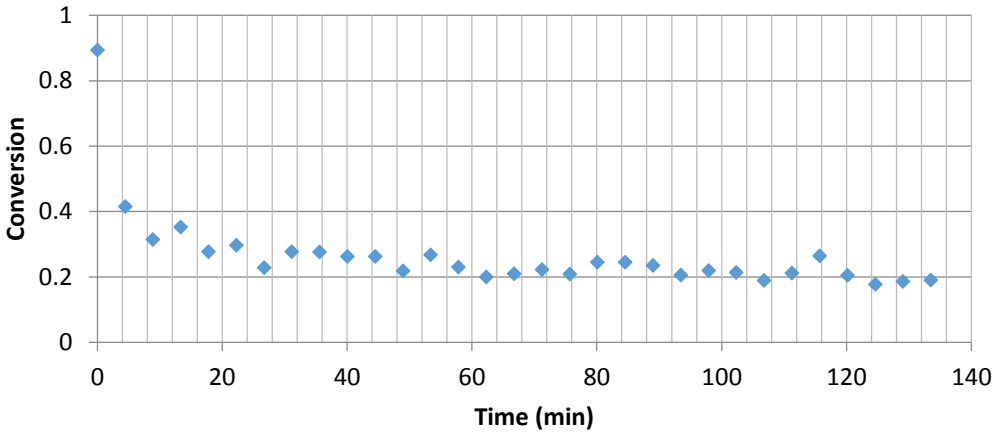

Figure S 62. 1,2-propanediol conversion over time profile illustrating quick deactivation and relatively steady performance after half an hour.

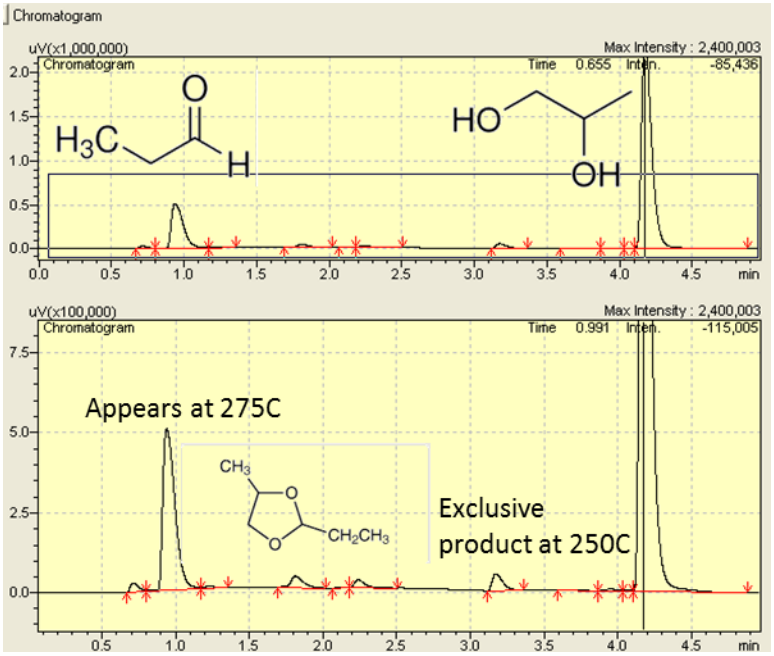

Figure S 63. Sample gas chromatogram of 1,2-propanediol dehydration over P25 titania.

Appendix F: The Mechanisms of Ethanol to Butenes over $Ag/ZrO_2/SiO_2$ by *In situ* ^1H MAS NMR

A drive for energy independence and carbon neutrality has resulted in the partial replacement of convention fossil fuels by transport biofuels, with bioethanol dominating the biofuels industry. Approximately 41 billion liters of bioethanol are manufactured per year with an estimated production increase on the order of 1-4% through 2026. This rapid growth, combined with transportation market saturation "blend wall", makes favorable the use of bioethanol as an economically attractive and renewable feedstock to produce bulk chemicals and fuels not derived from oil. A number of important bulk compounds such as hydrogen, ethylene, aldehydes, olefins, higher alcohols, ethers, ketones, and acetates can be generated from ethanol over mixed metal oxide catalysts.[375] C_4 olefins, in particular, are high-value products available from bioethanol upgrading: butadiene is one of the most important building blocks for the production of commercial polymers and polymer intermediates and butenes (1-butene, trans-2-butene, cis-2-butene, and isobutene) can be oligomerized to diesel/jet range hydrocarbons.

A 4% Ag/4% ZrO_2/SBA-16 catalyst has been formulated that exhibits the highest reported volumetric productivity in the ethanol to butadiene (ETB) reaction at 99% conversion of ethanol with a 70% butadiene yield and 90% yield of total valuable olefins.[376] Co-feeding hydrogen with ethanol over the same catalyst at elevated pressures (~100 psig) primarily converts ethanol to butenes. At 85.2% ethanol conversion, 51.1% selectivity to butenes and 0.4% selectivity to butadiene is observed. Butenes are important building blocks for high octane fuels, furthering the cause for a renewable fuel feedstock. As ethanol-derived products become

increasingly popular, clarification of the reaction pathways to butadiene and butenes will allow for the determination of structure-activity relationships necessary to produce industrially relevant and cost-efficient catalysts for renewable C_4 olefin production.

The production of butenes has been proposed to stem from a few pathways. It is desirable to elucidate which pathway dominates under the reaction conditions, driving further engineering of the catalyst for functionality that increases the selectivity to butenes. The first proposed pathway proceeds through the direct hydrogenation of crotonaldehyde to n-butanol, followed by a subsequent dehydration step to butenes. The second is crotyl alcohol isomerization to butanal and either the subsequent reduction to butanol or the deoxygenation of butanal to butenes. Finally, butenes may also be produced through the selective hydrogenation of 1,3 butadiene over transition metal sites. These three pathways are highlighted in the reaction network illustrated in Figure S64.

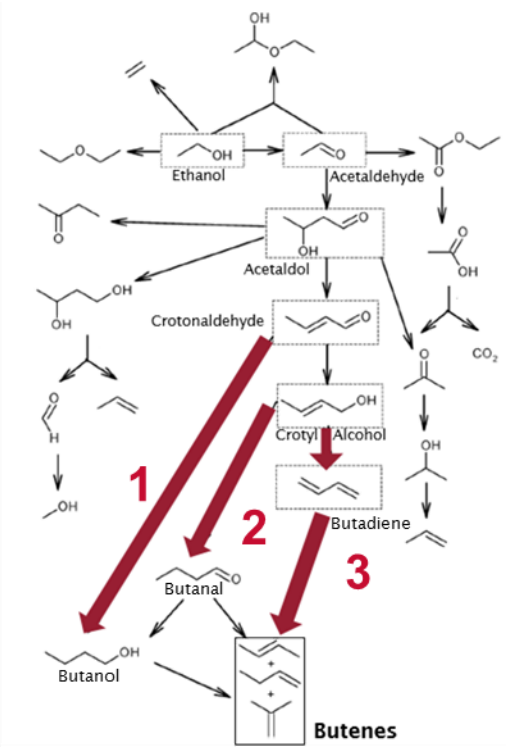

Figure S64. Reaction pathway proposed for ethanol to butenes.

Table S15. Selected reactivity data for ethanol to butenes

H_2 %, N_2 balance	Ethanol Conversion (%)	C2=	C4=	Butadiene	C2-C6 alkanes	Acetaldehyde	Olefins w/o BD
0	99	8.6	15.8	63.7	0.5	2.9	25.4
18.5	98	6.2	35.3	6.6	1.3	0.7	55.4
45	95.9	9.6	42.9	0	2	10.8	68.4
100	85.2	25.8	51.1	0.4	2.8	2.3	81.1

The effect of H_2 dilution on the catalytic performance of this catalyst is presented in Table S15. It can be seen that varying the degree of H_2 dilution (with N_2 balance) modulates the C4 olefin product distribution. Over the 4% Ag/4% ZrO_2/SBA-16 catalyst at the above reaction conditions a maximum selectivity to butenes of 51.1% is achieved at very low concentrations of

butadiene and 85.2% conversion of ethanol when 100% H_2 gas is co-fed with ethanol over the catalyst. The total selectivity to olefins (including ethylene and a small amount of propylene) observed without butadiene is 81.1%. Preliminary space velocity studies have suggested that butyraldehyde (i.e., butanal) is an intermediate in the reaction pathway to butenes from ethanol, but the extent to which this reaction pathway (and the other two possible routes described in the relevant literature section) participates in the total formation of product is not known. It is evident that furthering fundamental knowledge about active site participation in the ETB mechanism will provide insight into the activity of each site when catalyzing the formation of butenes. Additionally, it is also of substantial interest to determine the cause of selective hydrogenation over this system.

In situ NMR is a powerful technique that can be applied to investigate reactions pathways.[377-379] In particular, due to its high sensitivity natural abundance ^{1}H MAS NMR can be used to provide great temporal resolution (can be as short as seconds) in studying reaction networks as the chemical environment of the system components change. This summary details the investigation of the ethanol to butane reaction by *in situ* ^{1}H MAS NMR in an attempt to better clarify the key reaction pathways and site requirements for efficient conversion. It should be pointed out that the standard constant flow batch reactor cell involves passing fluid/gases over the catalyst bed, for our *in situ* MAS NMR rotor/reactor the reactants are sealed inside the rotor and the interaction between the reactants and the catalysts rely on translational diffusion. However, the low weight-hourly space velocity (0.23 hr^{-1}) is somewhat comparable to a sealed *in situ* MAS NMR rotor and our ability to tune the catalyst mass can provide some degree of control for this difference so that the results from *in situ* MAS NMR and batch reactor can be

compared/related. One further difference lies in the limitation of the 7.5 mm probe to a maximum temperature of 250°C. The flow reactor tests were all conducted at 325°C to overcome the barrier for the dehydrogenation of ethanol. To compensate, the most temperature demanding step in the dehydrogenation of ethanol is bypassed, instead a mixture of ethanol and crotonaldehyde (14 and 2.7 psi, respectively) were fed at a relatively mild 210°C, with the balance pressure of hydrogen by taking advantage of the lower temperature needed for converting crotonaldehyde. By studying a subset of the reaction pathway, the reaction mechanism can be successfully clarified.

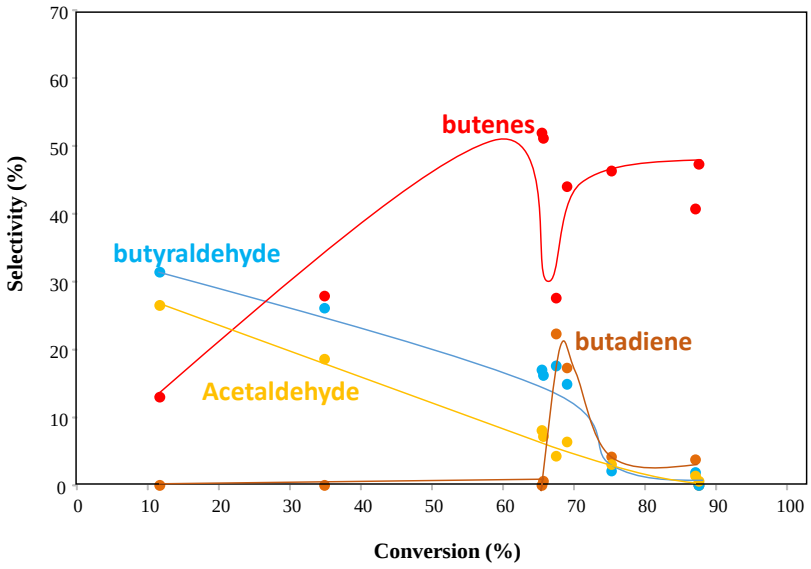

Figure S65. Primary product selectivities with conversion over 4Ag/4ZrO$_2$/SiO$_2$ (325C, 10psig, 24% EtOH in H$_2$).

Preliminary space velocity studies suggest that at low conversion of ethanol (higher space velocities), butenes are produced through the intermediate butyraldehyde from reduction of the C=C bond and subsequent deoxygenation to butane, potentially through butanol. At high ethanol conversion, butenes appear to be formed via both butyraldehyde and through butadiene hydrogenation.

All NMR spectra were collected with a 300 MHz Varian Inova NMR spectrometer operating at a ^{1}H Larmor frequency of 299.97 MHz. A sample spinning rate of 4540 Hz was employed at the magic angle for the experimental runs in a commercial 7.5 mm ceramic probe. A single-pulse sequence with a pulse width of 5 μs and a recycle delay time of 0.5 s were used. Each individual *in situ* MAS NMR spectrum was acquired using an accumulation number of 128, corresponding to a temporal resolution of 64 seconds. Temperatures were controlled using a commercial variable temperature heating stack. The sample temperature was measured across the relevant range with an external temperature ramp experiment with ethylene glycol as the thermometer.[377] All free indication decays were processed without line broadening and the Fourier transformed data were baseline subtracted to negate probe background.

To simulate the reactive environment of the catalyst as closely as possible within the magic angle spinning (MAS) NMR rotor, the 4% Ag/4% ZrO_2/SiO_2 catalyst was first activated at 450°C under nitrogen flow for 8 hours. The pretreated material was then sealed and transferred to a dry, N_2-purged glovebox where it was loaded into an all-ceramic, sealable, 7.5 mm outside diameter *in situ* MAS NMR rotor.[19, 235] A μl syringe was used to introduce the liquid reactants to the system prior to pressurizing. The *in situ* rotor is gas-tight and can withstand the high pressure environment the reaction produces. A specially designed loading chamber was used to introduce the hydrogen to match partial pressures of the reaction experiments (total pressure of 100 psi with 14 psi ethanol, 3.7 psi crotonaldehyde, and 82.3 psi hydrogen at 210°C). *In situ* ^{1}H MAS NMR spectra were collected as the temperature ramped from room temperature (25°C) to 210°C where the reaction was held until equilibrium was reached. Supporting experiments for identifying the chemical identities of the ^{1}H NMR peaks were conducted under similar

conditions with the temperature being ramped from 25°C to 210°C. The specific conditions for each run are reported in their respective sections as well as Table S16. All reported pressures are the constituent partial pressures at 210°C in the sealed NMR rotor.

Table S16. Experimental conditions of the in situ NMR experimental trials

Experiment	***$M_{catalyst}$ (mg)***	***$P_{substrate\ 1}$ (psi)***	***$P_{substratate\ 2}$ (psi)***	***P_{H2} (psi)***
1. Standard Condition	8.8	14.5 – Ethanol	3.9 – Crotonaldehyde	79
2. Enhanced Sensitivity	13.2	43.7 – Ethanol	11.4 – Crotonaldehyde	45
3. Isotopically-labeled	9.7	43.3 – D6 Ethanol	11.6 – Crotonaldehyde	47
4. Low Space Velocity	23.8	50.8 – Ethanol	13.7 – crotonaldehyde	45
5. Very Low Space Velocity	112.9	84.3 – Ethanol*	22.6 – crotonaldehyde	49
6. Inert Atmosphere	9.9	74.6 – Ethanol*	20.0 – crotonaldehyde	
7. Supporting Hydrogen	12.9			81
8. Supporting Butyraldehyde	10.8	17.2 – Butyraldehyde		122
9. Supporting Butanol	8.9	19.1 – Butanol		84
10. Supporting Crotyl Alcohol	10.6	29.9 – Crotyl Alcohol		78
11. Supporting Diethyl Ether	11.0	16.8 – Diethyl Ether		83
12. Supporting Butadiene	7.2	24.3 – Butadiene		146
13. Supporting Butene-1	15.3	40.5 – Butene-1		41

*A new syringe was employed for these two trials. Volumetrically, the pressures of ethanol should have been 43.3 and 11.6 psi.

To provide a basis for peak identification, ^{1}H chemical shifts were first estimated using the ChemNMR software. These predictions were directly compared to the experimental results of the NMR experiments and were a reasonable approximation to the experimentally observed signals. Many of the predicted values are predicted to overlap with another of other species, especially in the CH_3 region, but it is important to note that signature features are present at low field. For instance, formaldehyde, crotonaldehyde, acetaldehyde, and butyraldehyde are

predicted to have shifts of 9.6, 9.68, 9.79, and 9.72 ppm, respectively. These signature signals are distant from the vast expanse of signals between 1.5 and 3 ppm.

Table S17. Predicted ^{1}H NMR chemical shifts of compounds in the ETB pathway

Compound	**Structure**	**^{1}H Predicted**
Ethanol	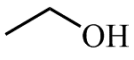	4.7, 3.59, 1.18
Acetaldehyde	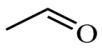	9.79, 2.2
3-hydroxybutanal	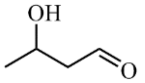	1.16, 6.77, 3.92, 2.65, 2.4, 9.72
Crotonaldehyde	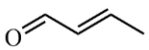	9.68, 6.05, 6.75, 1.88
Crotyl alcohol	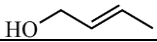	5.05, 4.18, 1.63, 5.67, 5.63
Butadiene	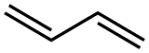	5.15, 6.31
Ethylene		5.25
Diethyl ether	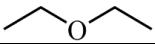	3.48, 1.21
1-ethoxyethano-1-ol	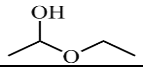	4.52, 5.5, 3.88, 1.39, 1.2
ethyl acetate	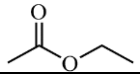	2.04, 4.12, 1.26
Acetic Acid	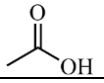	2.1, 11.0
Butan-2-one		2.12, 2.45, 1.06
Butyraldehyde	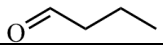	9.72, 2.38, 1.65, 0.98
Butanol	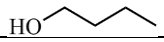	4.7, 3.64, 1.5, 1.39, 0.94
1,2-butanediol	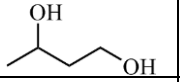	1.23, 4.03, 4.8, 1.68, 3.9, 4.7
Propene	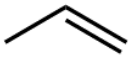	1.72, 5.83, 5.0
Formaldehyde	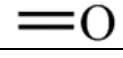	9.6
Methanol	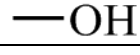	3.48, 4.3
Carbon dioxide	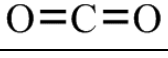	

Isopropanol		1.21, 4.02, 4.8
Butene-1	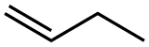	5.0, 5.8, 2.2, 0.78
Isobutene		1.72, 4.8
Butene-2		1.63, 5.42
Hydrogen	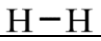	
Hydride	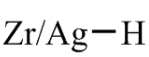	

1. Standard Condition *in situ* Experiment

The initial experiment used to explore the reaction network by *in situ* NMR was conducted to closely match the modified experimental conditions of the low velocity flow reactor. This experiment employed 8.8 mg of catalyst, an ethanol pressure of 14.5 psi, a crotonaldehyde pressure of 3.9 psi, and a hydrogen pressure of 79 psi. The time-resolved plot is visible in Figure S66 which shows the conversion of ethanol and crotonaldehyde to a variety of signals upfield of the broad hydrogen peak located at about 4 ppm.

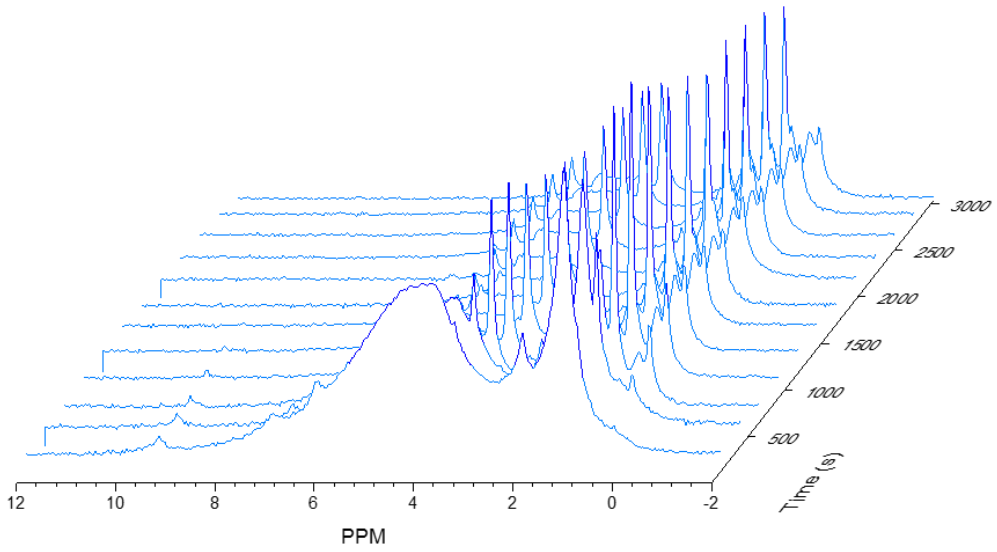

Figure S66 Time-resolved ^{1}H NMR of ethanol to butenes under the standard reaction condition.

The Stack plot visible in Figure S67 shows the evolution of proton signals during the temperature ramping step and after reaching the reaction temperature. The initial peaks associated with crotonaldehyde, hydrogen, and ethanol clearly demonstrate a decreased intensity in favor of new signals. In particular, a sharp peaks around 3.5 and 1.2 ppm are present which likely correspond to diethyl ether. A few prominent peaks emerged at the reaction temperature at 5.7 (and 5.0), 5.3, and 4.8 ppm. These peaks correspond well with the predicted chemical shifts for butane-1, butane-2, and isobutene. Upfield, signals are present near the predicted locations of their methyl groups (0.8, 1.7, and 2.2 ppm). Given the collected data that under these conditions, it is likely that butenes are formed. It should be noted that one reason for such generously resolved signals for butenes mid-field is the reduction in intensity from gas-phase hydrogen. Due to the overall dramatic decrease in spectral intensity (beyond what is expected from the Boltzmann effect) it is likely that the small, molecular hydrogen was leaking out of the rotor during this particular run of experiment. This problem is resolved in subsequent experimental

runs. However, due to low intensity H_2 peak butenes are clearly observed. Thus this experiment is still a useful experiment.

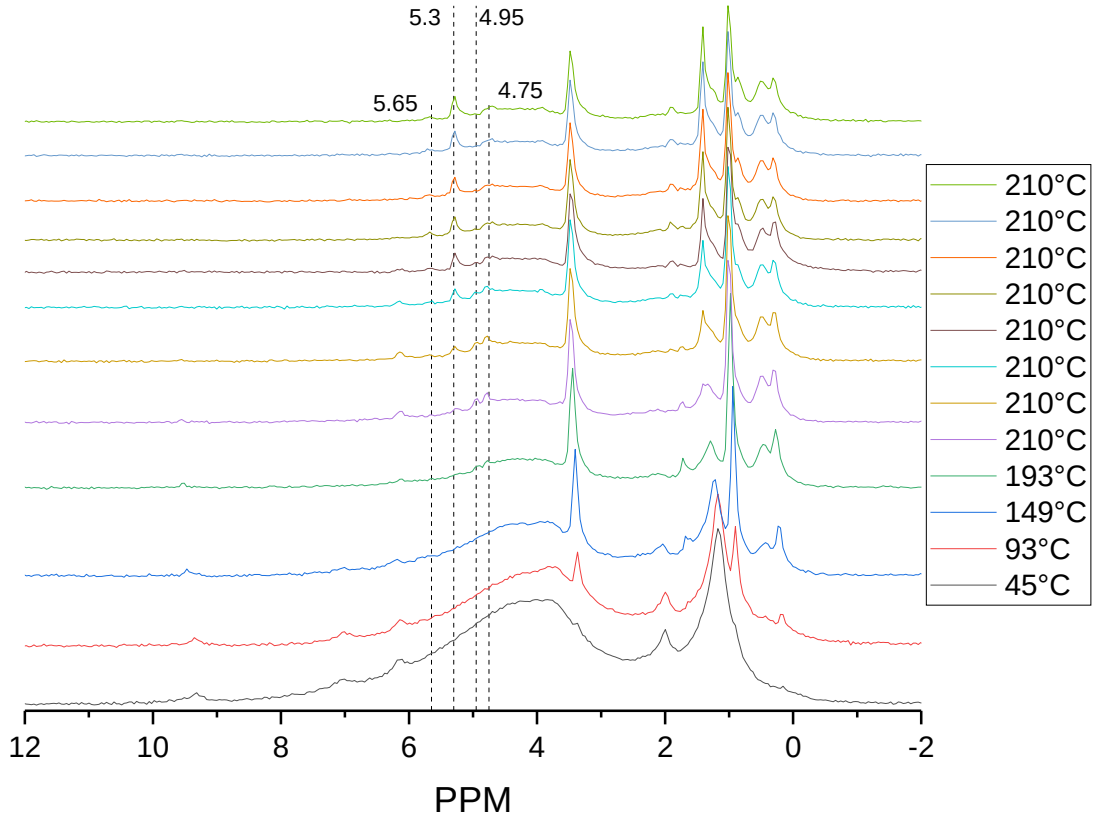

Figure S67. Stack-plot of spectra collected for ethanol to butenes under the standard reaction condition.

Unfortunately, transient information and well-resolved peaks were elusive in this experiment due to the low abundance of reacting species. Some features are apparently present, but obscured by poor signal to noise. The option to increase the repetitions would indeed improve signal to noise, but it would have the added side effect of significantly reducing temporal resolution. Based on the reactivity tests, enhancing the relative pressures of ethanol and crotonaldehyde, but keeping the total pressure constant, should still be representative of the reacting system. As such, the loading of these substrates were tripled to improve the intensity of the peaks above the noise level, a feat that would require nine times the number of scans.

2. Enhanced Sensitivity *in situ* Experiment

Due to the poor sensitivity, and thus low time resolution, of the low abundance of chemical species in the initial run, the experimental conditions were modified to enhance the signal by increasing the alcohol and aldehyde content. This experiment employed 13.2 mg of catalyst, an enhanced ethanol pressure of 43.7 psi, a crotonaldehyde pressure of 11.4 psi, and a hydrogen pressure of 45 psi, maintaining a total pressure near 100 psi at 210°C. The collected spectra as a function of both time and temperature are shown in Figure S68. These data show the clear evolution of peak signals over the course of the experiment with much greater resolution than collected under dilute conditions. Generally, the graphs show the gradual reduction of substrate crotonaldehyde and ethanol in favor of product species. Downfield of 9 ppm shows a particularly interesting evolution as cronaldehyde dissipates and at least two new species are generated. There are further dramatic and complex changes that occur between 0 and 3 ppm. At the end of this experiment, three primary peaks dominate the spectra that correspond to unreacted hydrogen, the methylene groups of diethyl ether, and the methyl groups of diethyl ether (Figure S69).

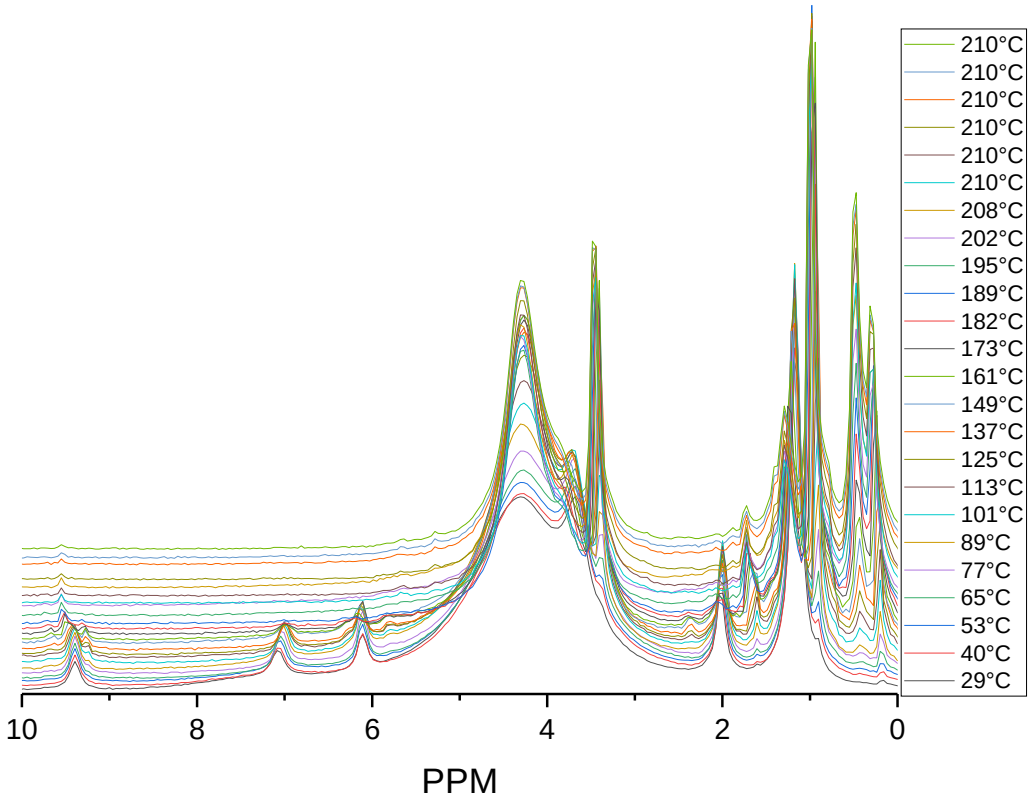

Figure S68. Stack-plot spectra of the enhanced sensitivity experiment.

Selected spectra of the thermal progression of the enhanced sensitivity run clearly shows the generation of new signals with time. Metal hydrides apparently dominate the high-field region around 0.4 ppm, numerous smaller peaks are revealed between 1 and 4 ppm, butenes are shown to arise midfield, diethyl ether (a dehydration product of ethanol) becomes prominent, and incremental transitions in the lowfield region near crotonaldehyde are revealed. To better understand these transitions, each region is considered separately.

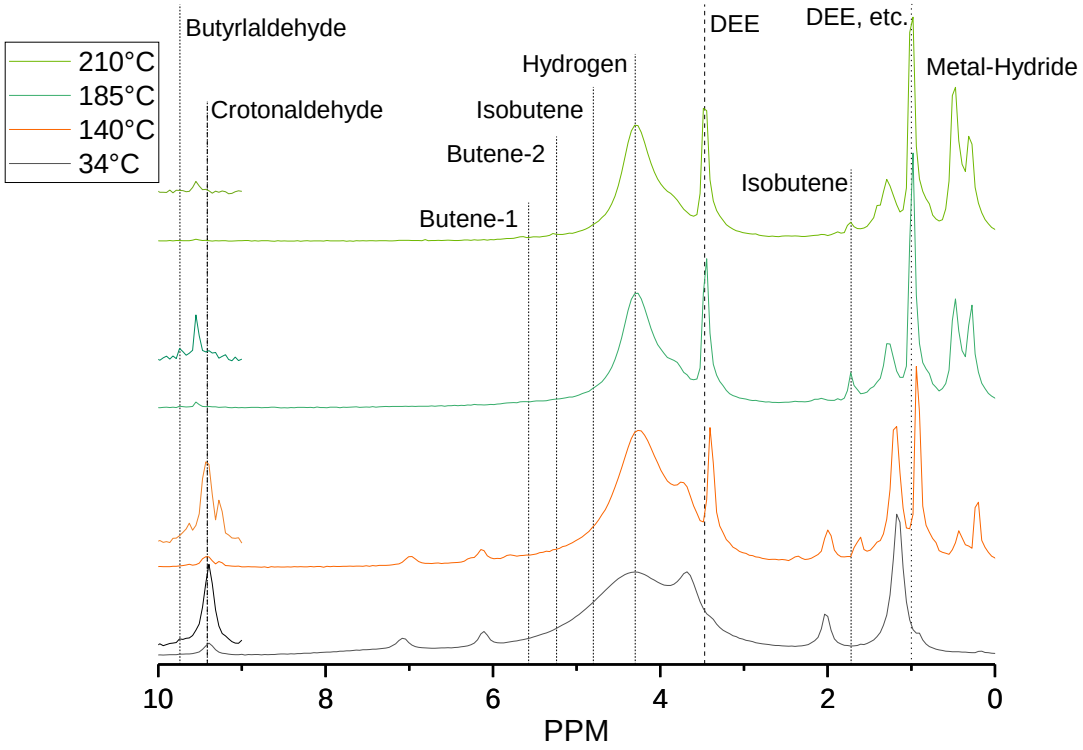

Figure S69. Selected spectra from the enhanced sensitivity experiment showing the evolution of product signals and highlighting the low-field changes occurring.

Focusing on the downfield region (Figure S70), three peaks corresponding to the protons of crotonaldehyde are apparent at 9.4, 7.05, and 6.12 ppm. With temperature, these features gradually diminish, generating a peak around 5.6 ppm. More interesting is the evolution of signals around 9 ppm. The 9.4 ppm peak corresponding to hydrogen bound to the primary carbon apparently shifts downfield with temperature as the chemical environment of these species are impacted and the intensity of the species decreases. It is worth mentioning that the secondary and tertiary carbon protons from crotonaldehyde, while migrating slightly themselves, are nearly dissipated by 189°C, yet the O=CH- carbon signal remains. Section 4. Low Space Velocity *in situ* Experiments demonstrates that this might suggest that this migration is actually a separate species at the same location that develops. At approximately 113°C, a side peak appears at 9.3

ppm. The features grows to a maximum at 137°C and then dissipates with continued reaction. Our reference experiments do not reveal a signal at this chemical shift for the fed compounds. As such, the dynamic nature of this constituent leads us to ascribe it to an adsorbed crotonaldehyde-like species that is apparently related to the further transformation to the feature at 9.7 ppm (assigned to butyraldehyde). A second peak at 5.9 follows a very similar evolution and so is speculated to also belong to this species. This may indicate the presence of an adsorbed species that is deshielded relative to crotonaldehyde and distinct from it.

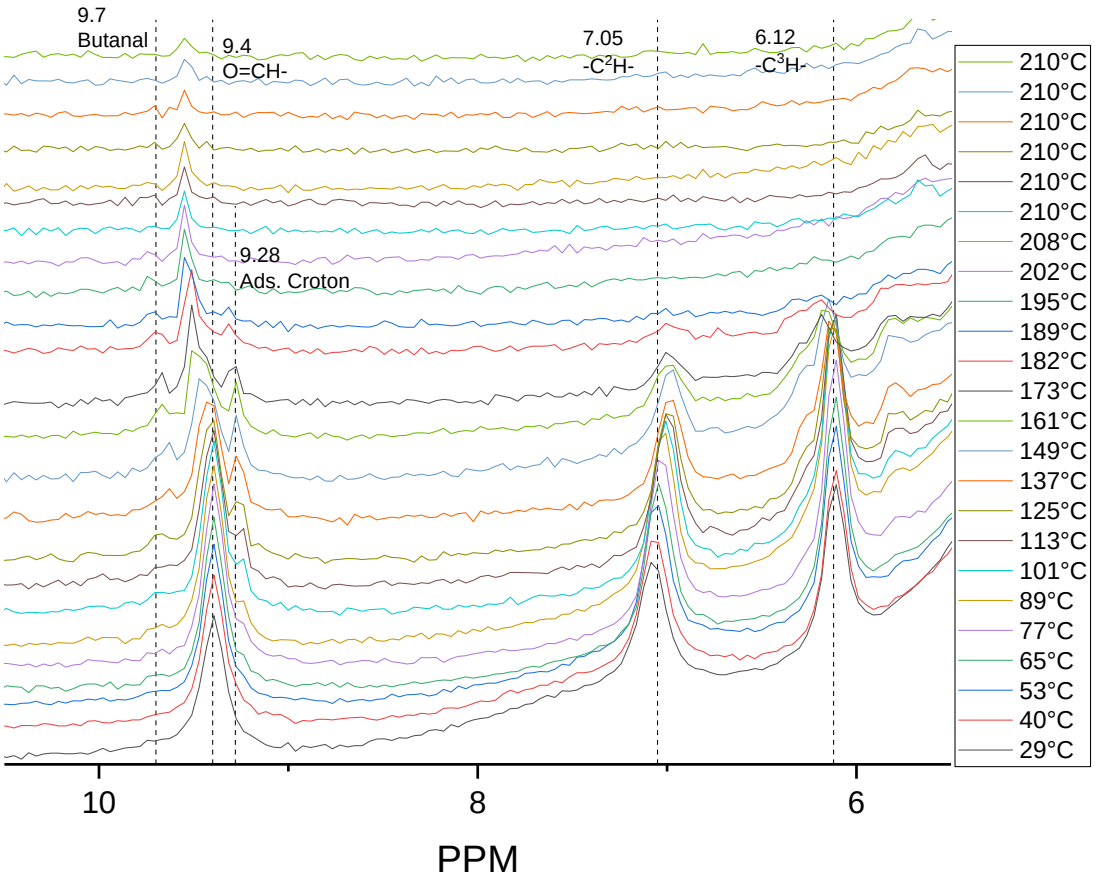

Figure S70. Expanded low field region of the enhanced signal reaction.

To solidify the assignment of butryladehyde, the spectra collected from co-feeding butyrlaldehyde with hydrogen were plotted along with a slice from the enhanced signal trial. The progressive increase in temperature is included in Figure S71 to justify the slightly differing peak position from that at room temperature. When the temperatures are comparable, the chemical environment, and thus the peak position of butyraldehyde, is comparable between the two trials. To better illustrate this, a single slice of the enhanced sensitivity *in situ* reaction experiment at 182°C was directly compared to a similar temperature slice (150°C) from an experiment where butyrlaldehyde was fed. It is clear from this graph that the identity of this species is clearly butyraldehyde, further evidenced by the secondary, tertiary, and quaternary carbons being present in addition to the primary carbon, though some signals overlap with resonances from other species in the enhanced sensitivity trial (top). Interestingly, the butyrlaldehyde trial also generates a signal around 9.6, strengthening the confidence in assigning this species to an adsorbed butrylaldehyde. From the predicted chemical shifts, both acetaldehyde and 3-hydroxybutanal could also generate peaks at this location. Other signatures from 3-hydroxybutanal are not observed and there is no evidence to suggest the concomitant evolution of other acetaldehyde features upfield. As such, we unambiguously assign this to butyraldehyde species.

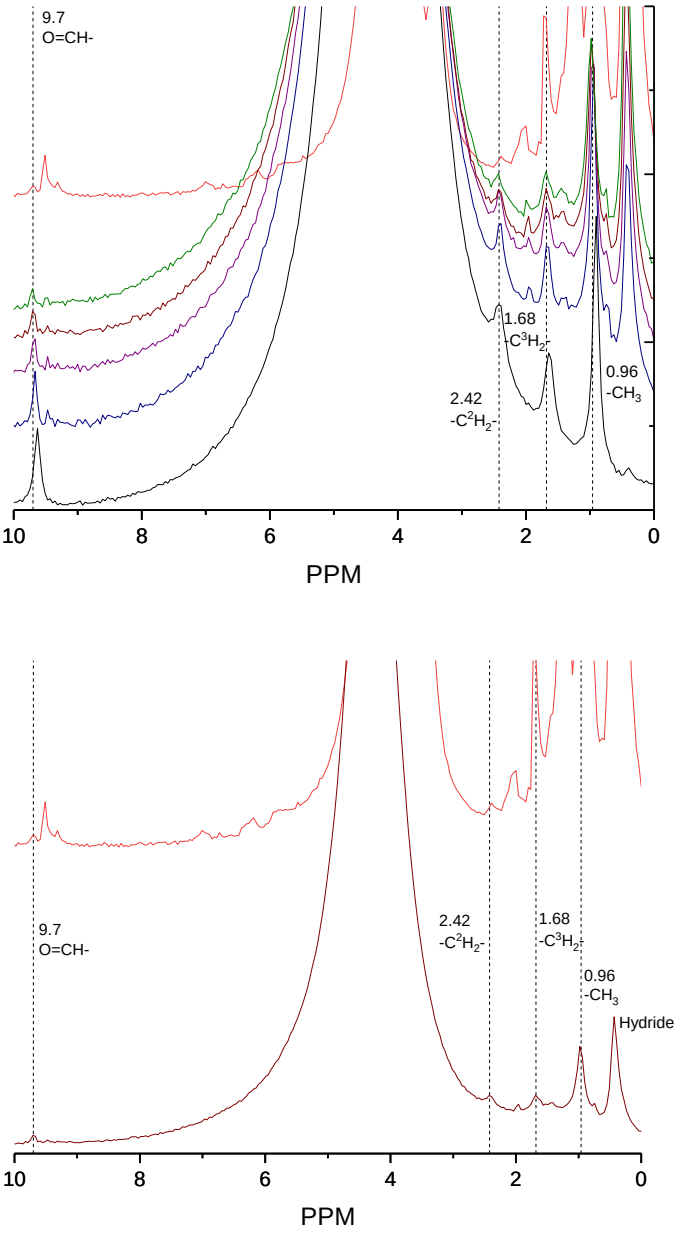

Figure S71. Enhanced signal spectrum (top) plotted with the butyraldehyde test clearly showing a change in the butyrlaldehyde environment with temperature. Bottom: Single spectrum of the enhanced signal trial plotted with butryaldehyde showing the presence of each peak.

At the late stages of the temperature ramping, distinct peaks previously observed at during the standard condition experiment revealed themselves at 5.7 (5.1), 5.3, and 4.75. These peaks were previously assigned to butenes and retain such an assignment here on the basis of

chemical shift and expected reaction products. The formation of these peaks is illustrated in Figure S72 and their specific identities and behaviors on the catalyst are revealed in the supporting trials.

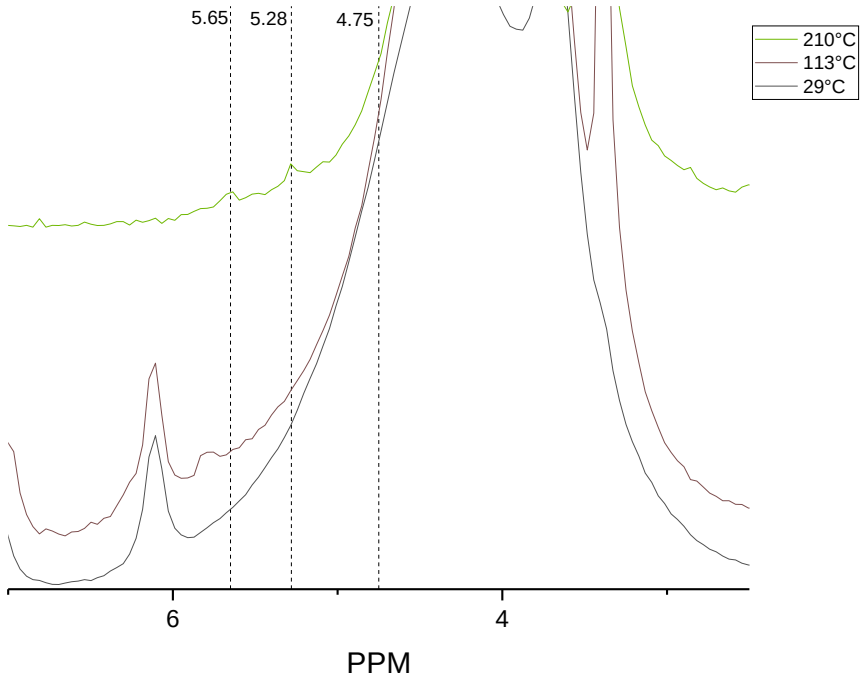

Figure S72. Mid-field region of the enhanced sensitivity experiment at the beginning, middle, and end of the reaction.

The high field region is much more complex due to the dramatic overlap of peaks (validated by the provided chemical shift predictions). While a full description of the dynamic behavior in this region would require intensive correlation and analysis, it should be pointed out that a number of peaks that may correspond to butane (2.1, 1.7, 1.6, 0.8 ppm) are present in the

final temperature scan, providing further evidence of butane formation. Selected spectra from across the trial are depicted in Figure S73.

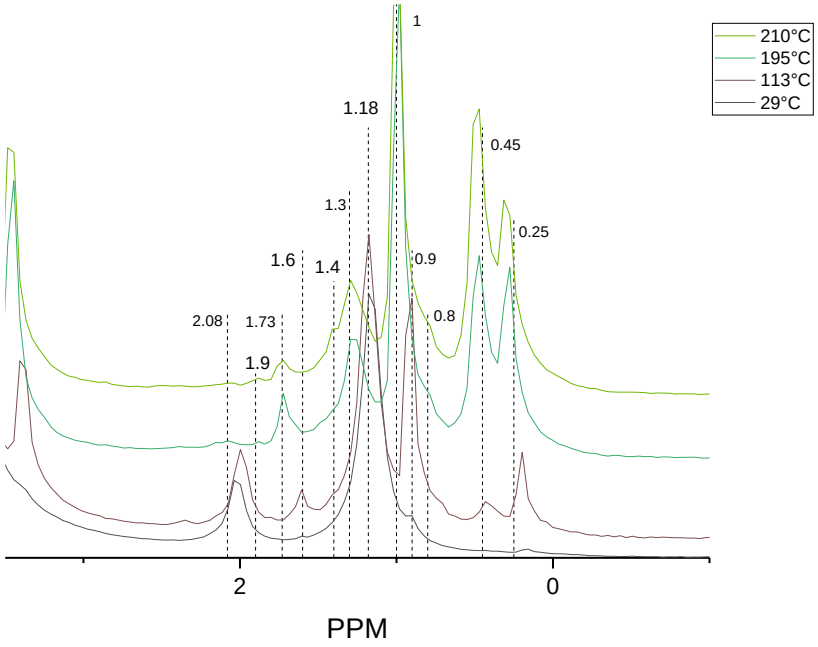

Figure S73. Up-field region of the enhanced signal in situ NMR trial.

3. Isotopically-labeled *in situ* Experiment

To gain fundamental insight on the pathways associated with ethanol to butane conversion that could not be observed under a standard condition, an experiment was conducted in which labeled ethanol was co-fed with natural abundance hydrogen and crotonaldehyde. This experiment employed 9.7 mg of catalyst, an enhanced D_6-ethanol pressure of 43.3 psi, a crotonaldehyde pressure of 11.6 psi, and a hydrogen pressure of 47 psi. The evolution of the crotonaldehyde signals is apparently similar to the enhanced loading trial. The most obvious difference is that diethyl ether, a dehydration product of ethanol, is not visible by proton NMR due to the ethanol being labeled. This is obvious from the stack plots presented in Figure S74.

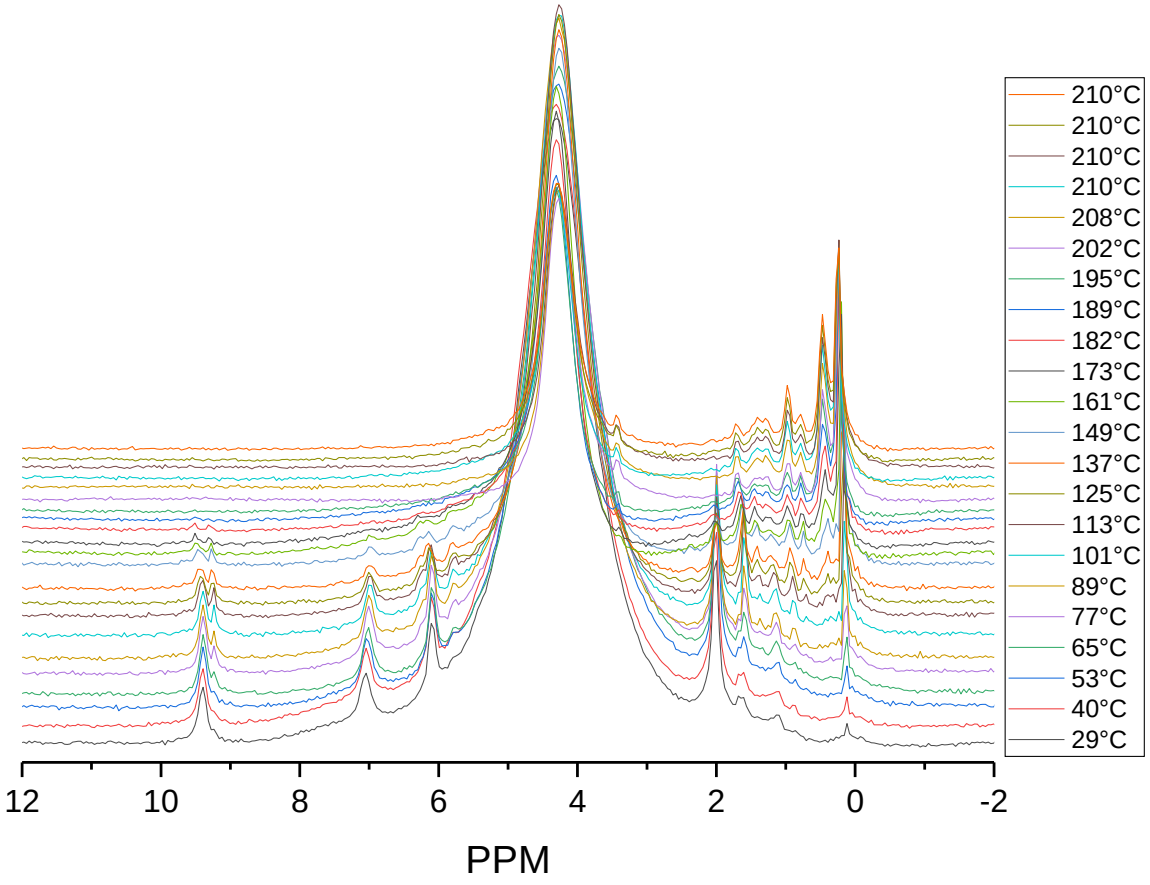

Figure S74. Isotopically labeled ethanol trial stack plot.

A major difference between the deuterated ethanol experiments and those conducted at the enhanced constituent pressure is the evolution of signals around 9 ppm. Though the signature peak from butyraldehyde was present in the trials employing natural abundance ethanol, this feature is apparently not present in the deuterated trial. This is highlighted in the temperature ramp spectra displayed in Figure S75. A side by side comparison of the two experiments is presented in Figure S76. This clearly illustrates the contrast between these two experiments and strongly suggests that the O=CH- proton on butyraldehyde is related to a proton from ethanol.

When considering the evolution of the crotonaldehyde signal in the enhanced sensitivity trial, the highest temperature region resulted in a peak deshielded from room temperature crotonaldehyde. This was speculatd to be related to an adsorbed species. This claim is further supported by Figure S77, which shows a very minor change in the crotonaldhyde signal and suggests and entirely new species at the maximum temperature. In looking at the 210°C temperature points from the two trials, it is possible that peaks ascribed to butenes are still present in the deuterated trial.

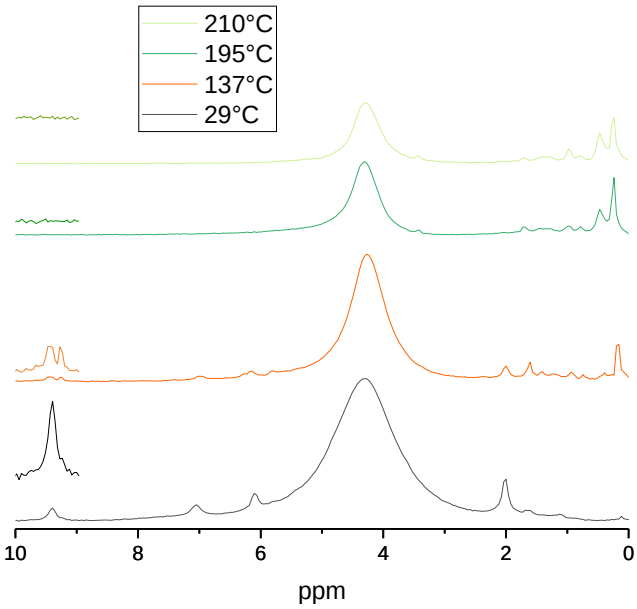

Figure S75. Representative spectra of deuterated ethanol used in the in situ NMR trials. The region near butyraldehyde is enhanced for clarity.

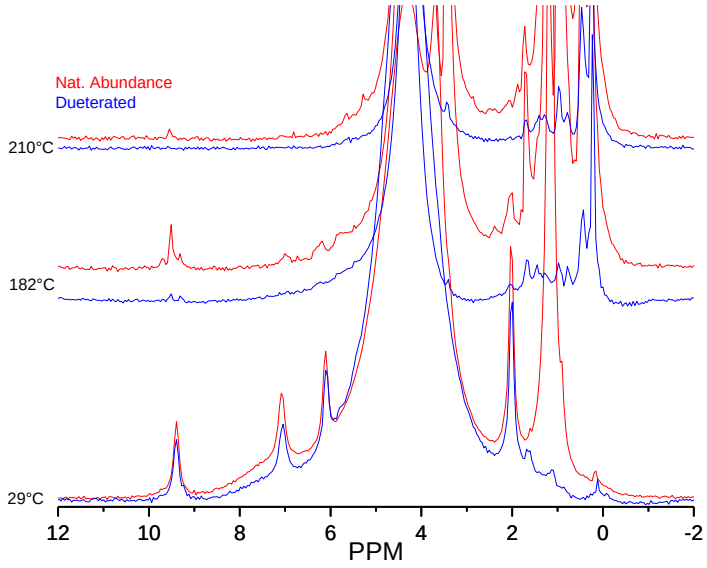

Figure S76. Comparative experiments with deuterated and natural abundance ethanol.

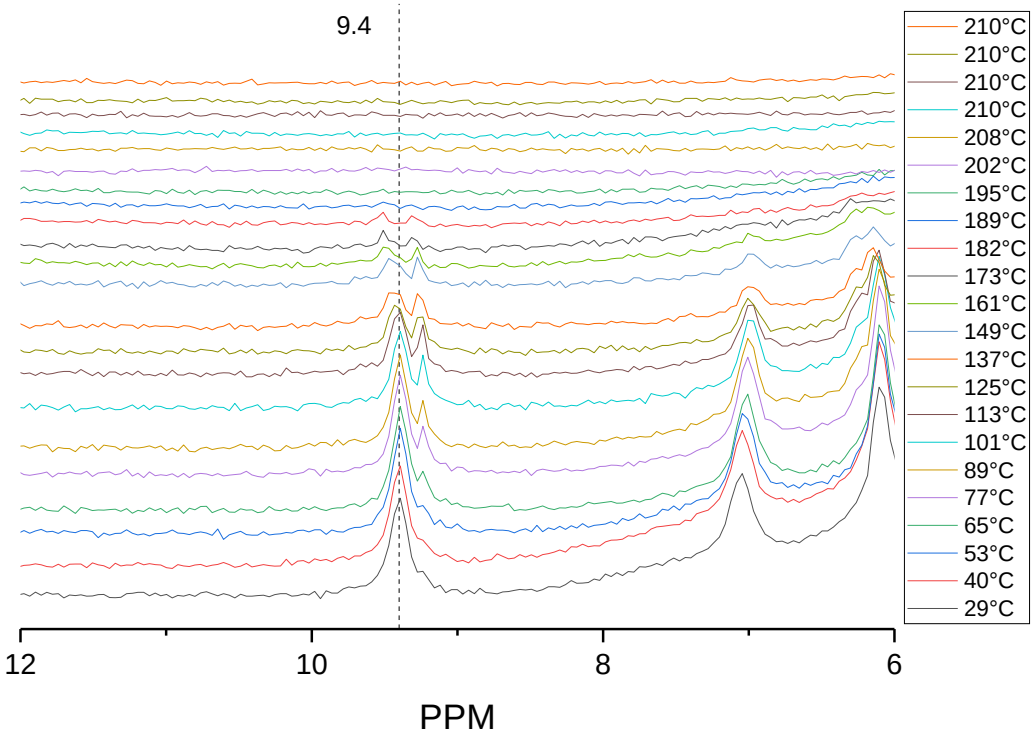

Figure S77. Expanded deuterated ethanol trial demonstrating the crotonaldehyde reaction evolution.

To compare the predictions to experimental observations and solidify confidence in peak assignments, supporting experiments were conducted by introducing key intermediates to the

catalyst under a hydrogen atmosphere and observing their interaction at room and reaction temperatures. Their conversions were monitored by *in situ* ^{1}H MAS NMR in case these could provide insight on the evolutions taking place in the ethanol to butenes reaction. Their results are presented farther below in the additional experiment sections.

4. Low Space Velocity *in situ* Experiment

Space velocity has been shown to have a notable effect on the conversion and product distribution. To simulate the impact of space velocity, the mass of the catalyst was altered to simulate a longer contact time. This experiment employed approximately double the mass at 23.8 mg of catalyst, an enhanced ethanol pressure of 50.8 psi, a crotonaldehyde pressure of 13.7 psi, and a hydrogen pressure of 47 psi, maintaining a total pressure near 110 psi at 210°C.

Upon initial observation, the evolution of signals when the catalyst quantity is doubled appears similar to the previous trial natural abundance trial. Crotonaldehyde and ethanol are consumed in preference of butane, diethyl ether, and many high field signals as shown in Figure S78. Some important and striking differences are observed, however. Namely, the features above 9 ppm shown a decrease in crotonaldehyde around 9.5 ppm as the adsorbed intermediate forms at 9.36 ppm around 100°C (with the accompanying peak at 5.9 ppm). However, as this peak narrows and shifts, possibly forming a separate species at the same position, low-field butyraldehyde signals are never observed, suggesting an alternate pathway may facilitate final product conversion. Notably, when examining signals in the mid-field region, a quintet and a doublet are observed at 6.2 and 5 ppm, respectively. These signals match exactly those observed for butadiene in the butadiene trial (see supporting experiments). When the space velocity is enhanced, this is apparently the preferred pathway to conversion to butane-1 (5.75, 4.85, 1.95,

and 0.92 ppm), butane-2 (5.35 and 1.48 ppm), and isobutene (4.75, and 1.48 ppm). Hydride species are also observed in this case.

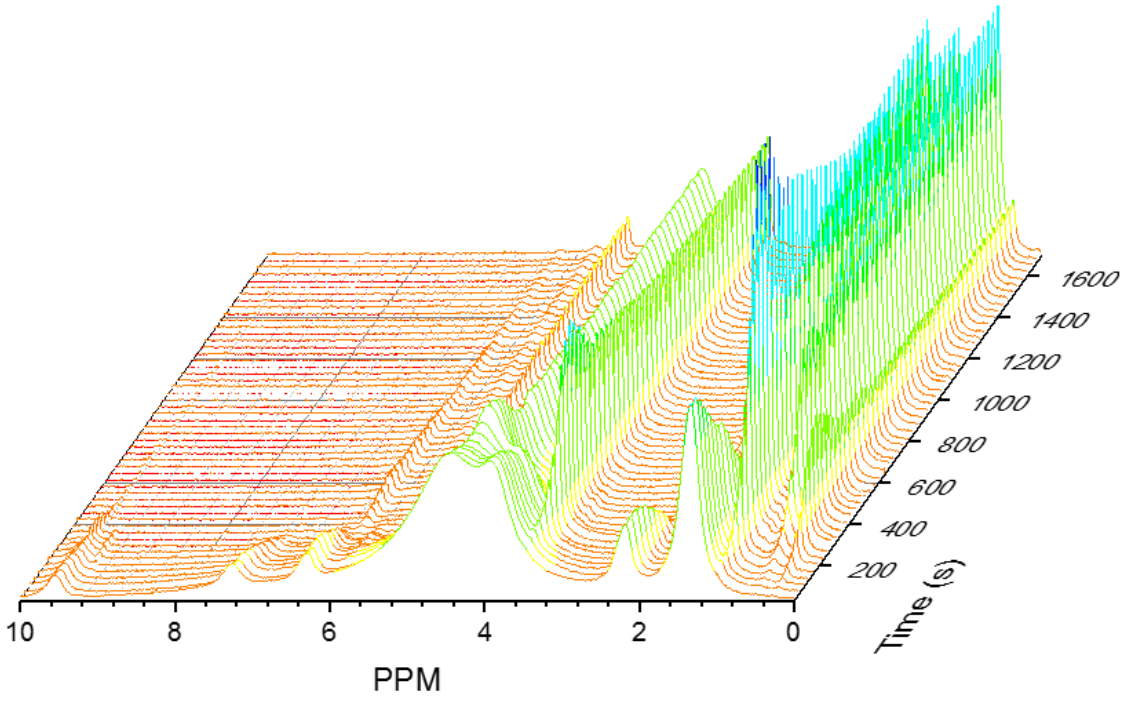

Figure S78. Waterfall time-lapsed plot of the double catalyst loading to simulate low space velocity.

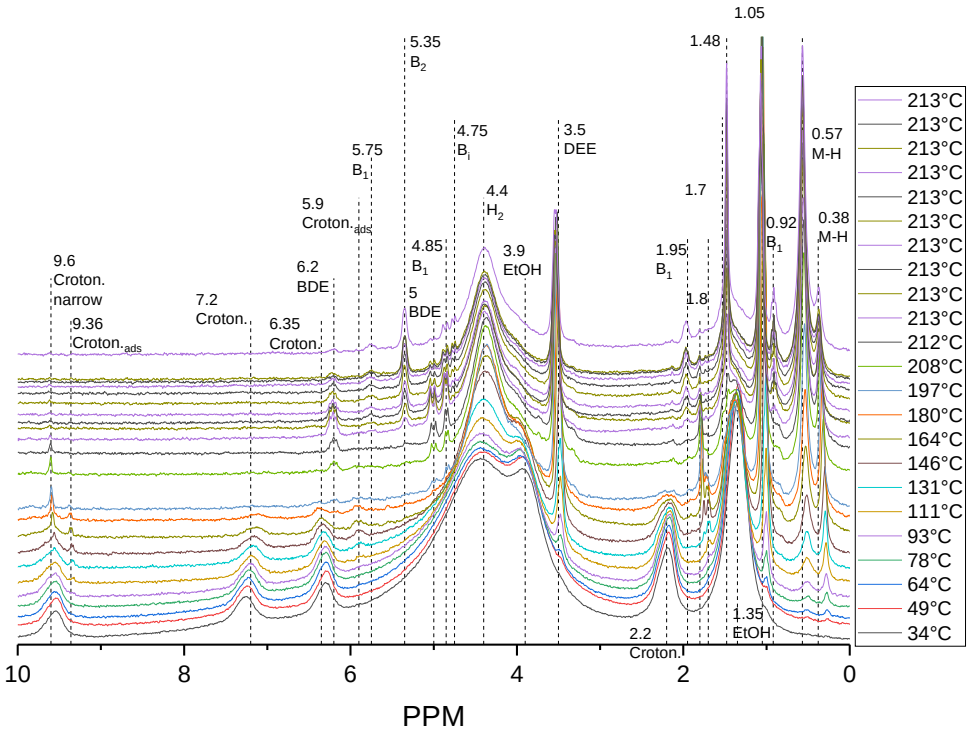

Figure S79. Stack plot of the double catalyst trial to simulate lower space velocity.

5. Very Low Space Velocity *in situ* Experiment

In an attempt to dramatically demonstrate the effect of space velocity, time times the catalyst amount was used. This experiment employed 112.9 mg of catalyst, an enhanced ethanol pressure of 84.3 psi, a crotonaldehyde pressure of 22.6 psi, and a hydrogen pressure of 49 psi, maintaining a total pressure near 156 psi at 210°C. It should be noted that the high ethanol and crotonaldehyde pressures were determined on a mass basis since there was a discrepancy between the amount added between volumetric and mass-determination methods.

Again, crotonaldehyde and ethanol convert in favor of what are likely butenes (5.5, 5.25 and 5 ppm), possibly butadiene (5 ppm), and diethyl ether (3.6 ppm). This trial shows the clear formation of butanal (9.75 ppm) at moderate temperatures, but many of the fine features are not

observed, such as the adsorbed crotonaldehyde-like intermediate. Furthermore, product peaks appear to be broader than in previous runs, obfuscating full confidence in the assignments. It is apparent that the pressures of ethanol and crotonaldehyde in this run were higher than in previous by looking at the peak intensities relative to that of hydrogen. Further, at the end of the experimental run, the selectivity to diethyl ether was much lower than in previous runs and much of the ethanol remained despite the favorability for bi-molecular dehydration. These spectral differences are due to the changing reactivity at the elevated pressure and catalyst quantity.

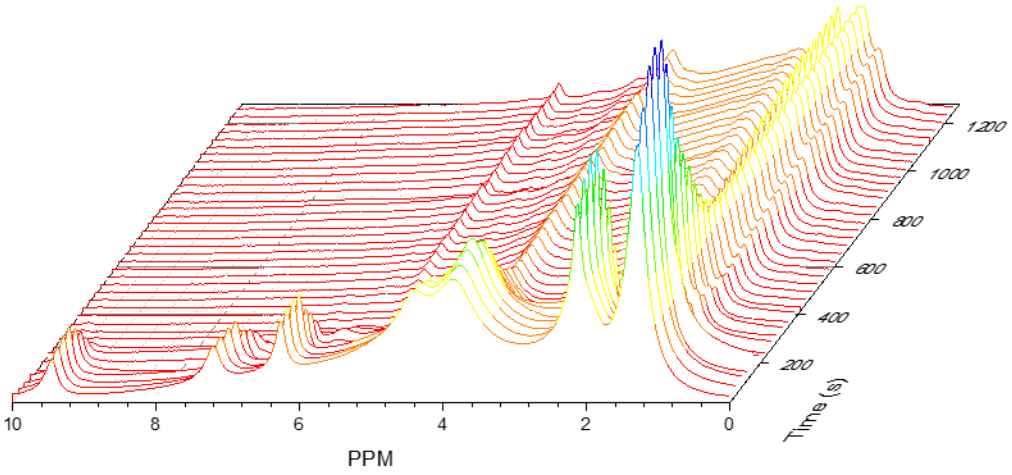

Figure S80. Waterfall plot of ETB over a very high quantity of catalyst (100 mg).

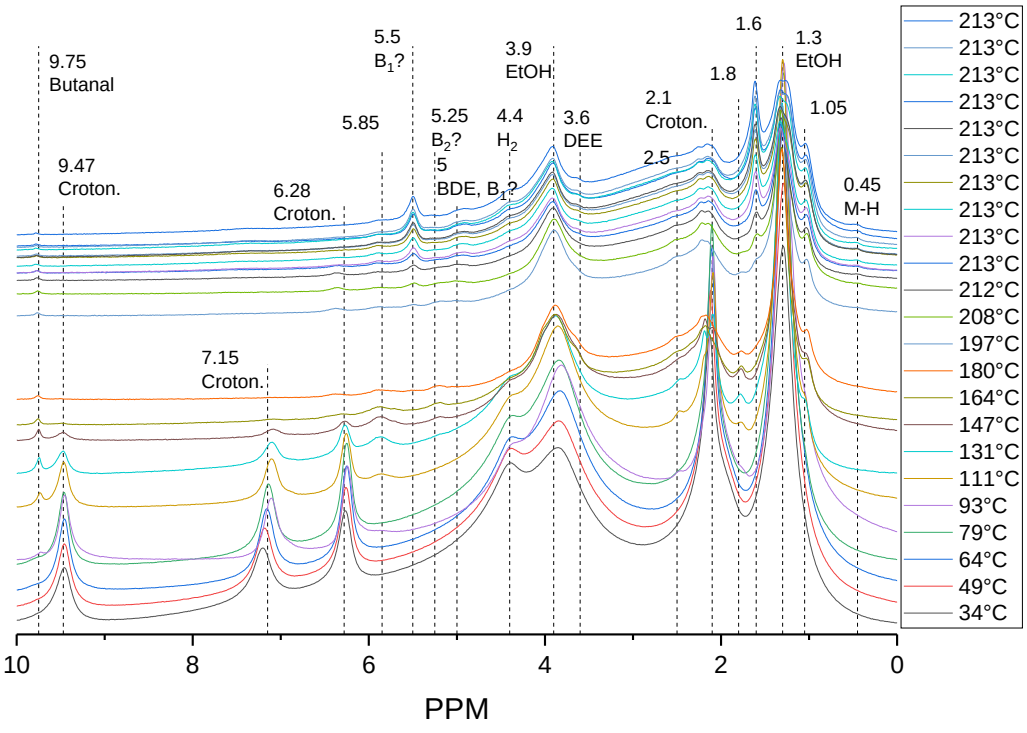

Figure S81. Stack-plot of ETB over a very high quantity of catalyst (100 mg).

6. Inert Atmosphere *in situ* Experiment

Hydrogen allows the reaction to proceed to butenes. In the absence of this reactant, the production of butadiene is favored. To confirm this spectroscopically, hydrogen was replaced with helium. This experiment employed 9.9 mg of catalyst, an enhanced ethanol pressure of 74.6 psi, a crotonaldehyde pressure of 20.0 psi, and a helium pressure of 45 psi, maintaining a total pressure near 140 psi at 210°C. It should be noted that the high ethanol and crotonaldehyde pressures were determined on a mass basis since there was a discrepancy between the amount added between volumetric and mass-determined methods.

This trial again showed nice conversion of crotonaldehyde and ethanol. Unlike previous trials where the broad hydrogen peak obscured the alcohol group in ethanol, C_2H_5-OH is clearly visible at 5 ppm and decreases as ethanol is converted. Similar to previous runs, diethyl ether is a major product during the initial temperature incline. The low field region shows the decline in signal from crotonaldehyde (9.62 ppm) while the species assigned to an adsorbed crotonaldehyde-like intermediate arises (9.35 and 5.9 ppm) before decreasing again. As the temperature increases, the narrow peak on top of crotonaldehyde (9.6 ppm) becomes apparent and decreases. Unlike the hydrogen-filled analog, the peak assigned butanal is not present, confirming that gaseous hydrogen is required to complete this step. Notably, there is no indication that butenes are formed, as expected due to the lack of hydrogenation substrate. Instead, butadiene appears to be the final C_4 product (6.2 and 4.85 ppm). A doublet peak also appears at 5 ppm that is left unassigned. Hydrides are apparently formed in this cases as well, suggesting that ethanol may play a role in their formation.

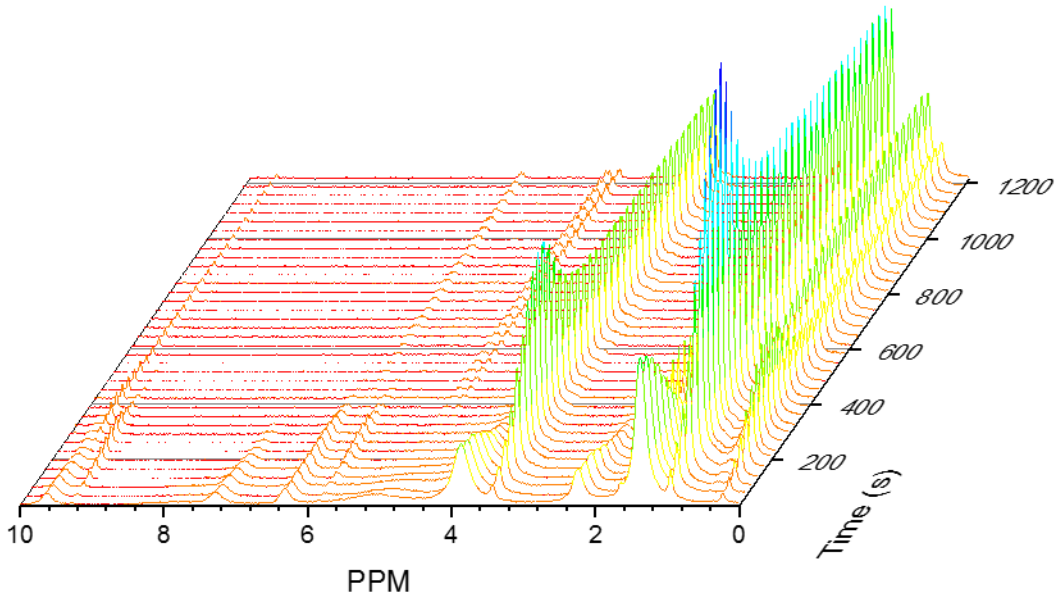

Figure S82. Time-lapsed waterfall plot of ethanol to butadiene in inert He.

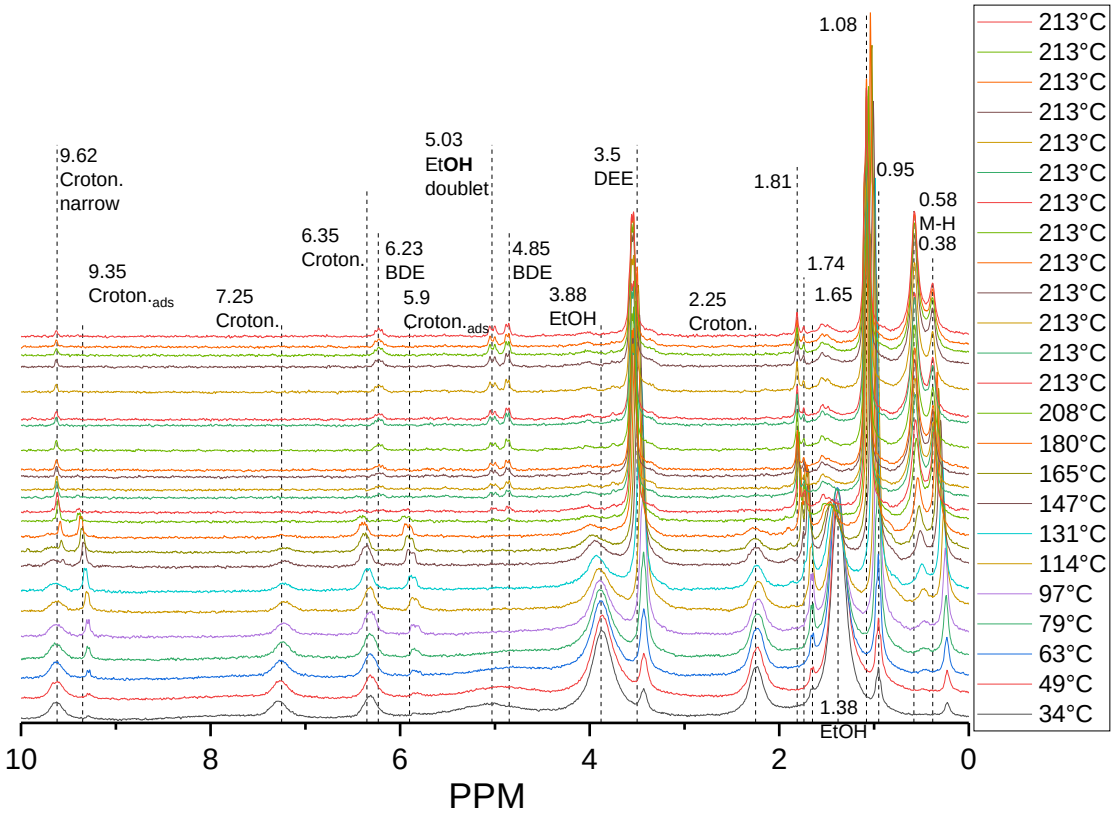

Figure S83. Stack-plot of ethanol to butadiene in inert He.

Conclusions and Direction

Based upon the analysis of this body of data, three primary conclusions can be reached regarding the pathway for butane formation. They are: 1) butyraldehyde represents an important pathway intermediate in the formation of butenes from ethanol. 2) The protonation step in the formation of butryladehyde requires the presence of ethanol and abstraction of the protons from ethanol in the formation of butyladehyde and subsequent formation of butane is a requirement of this pathway. 3) At lower space velocities (double the catalyst amount) the transient formation of butadiene is obvious, suggesting butadiene may be a dominant pathway to butenes. At ~10 times

the catalyst amount and higher pressures, this is not observed and butanal is apparently a dominant pathway. 4) In the absence of hydrogen, the crontaldehyde-like intermediate is still present, but butanal is never formed. Butadiene is an apparent product. 5) Two distinct types of hydride species can be observed during the experiments, likely associated with Zr or possibly Ag. Interestingly, hydrides are also apparently formed in the trial with He as the balance gas.

To enhance the understanding of this collected data as well as dig deeper into the requirements of thermochemical conversion, the following future studies are suggested:

a) Confirm the identity of each hydride species by analyzing their formation on Ag/SiO_2 and ZrO_2/SiO_2. It should be noted that Ag may be the active site responsible for H-H activation, but the stable hydride species rests on a Zr site. These experiments should help clarify that potential pathway as well.
b) ^{13}C labeling studies to confirm the dominant pathways to butadiene from ethanol

7. Supporting Trial with Hydrogen

The most rudimentary trail was to confirm any peaks associated with the catalyst material, hydrogen, and any interaction the two constituents might have. This experiment employed 12.9 mg of catalyst and a hydrogen pressure of 81 psi. At the initial time period depicted in Figure S84, two clear peaks were revealed; a broad resonance at 4.4 and a smaller one at 1.85 ppm. These two features are ascribed to hydrogen gas pressurized within the rotor and silanol groups, respectively. Over time, the silanol peak approximately maintains the original intensity, but apparently broadens slightly at increased temperatures. The hydrogen peak appears to decrease in intensity slightly, but this magnitude can be attributed to the Boltzmann effect. Additionally, new resonances develop upfield of these signals at approximately 0.4 ppm.

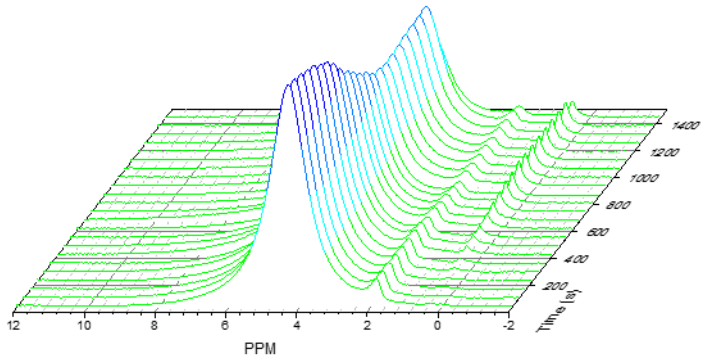

Figure S84. Time-resolved ^{1}H NMR of hydrogen interacting with the catalyst surface during temperature elevation.

Analyzing the stack plots of this experiment, the evolution of these high field signals is more apparent. Initially, the room temperature experiment offers a broad signal that gradually grows with temperature. The species becomes definitive around 70°C and continues to evolve at higher temperatures. Clear peak from this signal is visible at 0.43 ppm. A shoulder appears to be present around 0.18 ppm, approximately the same resonance as the narrow peak observed in previous experimental runs. Based on the limited available interactions that could be taking place, the thermally-instigated activation of the H-H bond on hydrogen is anticipated to result in the formation of metal hydride species that we observe at 0.43 and 0.18 ppm. The specific pathway of this activation and the identity are unknown, but these likely correlate to Ag-H or Zr-H species. Based on literature precedent, Zr-H is the anticipated identity, which may provide more than one type of stable hydride species. Contrasting to previous experiments, the upfield hydride peak is poorly defined for the hydrogen-only experiment.

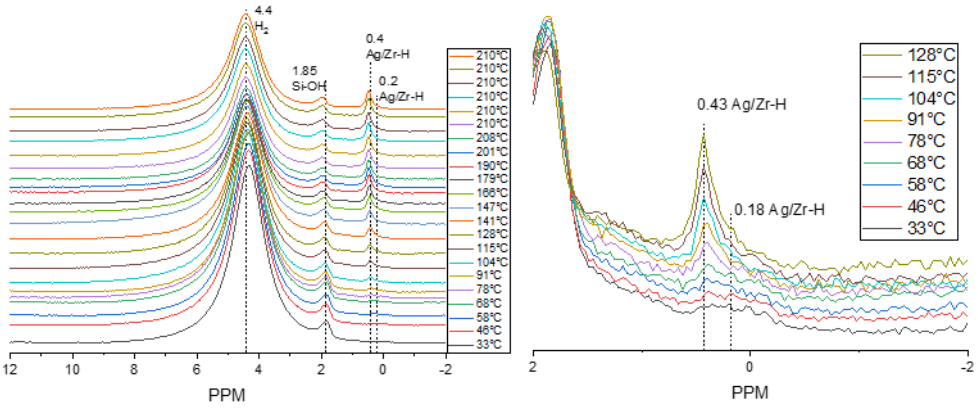

Figure S85. Stack plot ^{1}H NMR of hydrogen interacting with the catalyst surface during temperature elevation (left) and the expanded hydride region (right).

8. Supporting Trial with Butyraldehyde

An important trail was to confirm the experimental peak positions associated with butyraldehyde (butanal) and its thermochemical conversion. This experiment employed 10.8 mg of catalyst, a butyraldehyde pressure of 17.2 psi, and a hydrogen pressure of 122 psi. Based upon the depicted resonances in the following figures, the signatures of butyraldehyde are located at 9.67, 2.42, 1.65, and 0.93 ppm. The chemical environment of butyraldehyde is apparently disturbed as the temperature is increased, causing slight shifts in the NMR peaks. In analyzing the thermochemical transformation of this species co-fed with hydrogen, new peaks evolve, some of which correspond well with butanol such as the 1.52, 1.38 ppm dual peak feature (see the butanol trial). No peak at 3.64 ppm is clearly visible, but this week was also covered by hydrogen in the butanol experiment. The methyl group at 0.9 ppm is common between the two compounds. Careful analysis of the final scans of the butyraldehyde experiment may reveal small peaks associated with butenes, but the intensity is too low to provide confidence in this statement so it will be maintained as a possibility.

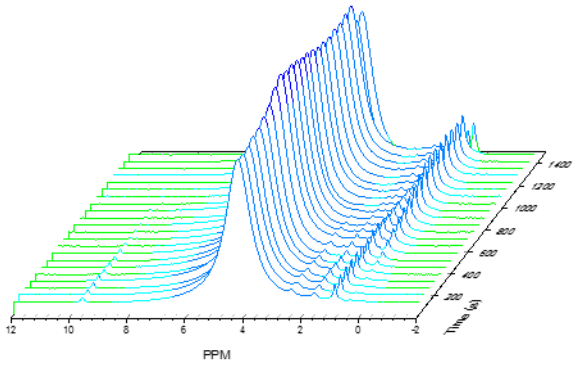

Figure S86. Time-resolved ^{1}H NMR of butyraldehyde and hydrogen interacting with the surface during temperature elevation.

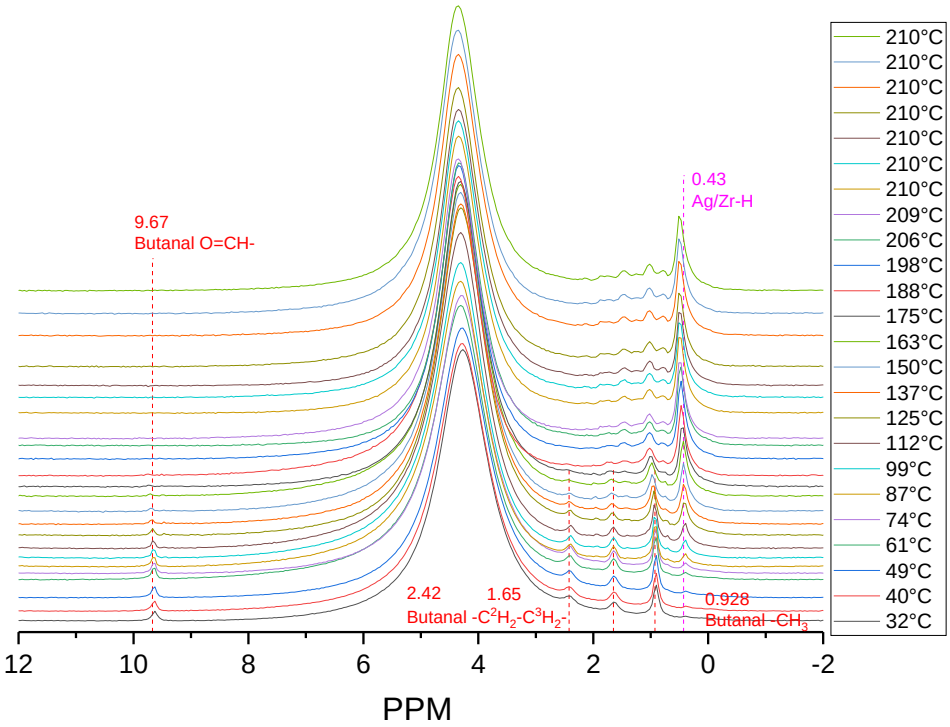

Figure S87. Stack-plot of butyraldehyde on Ag/Zr/SBA-16 during in situ NMR experiments.

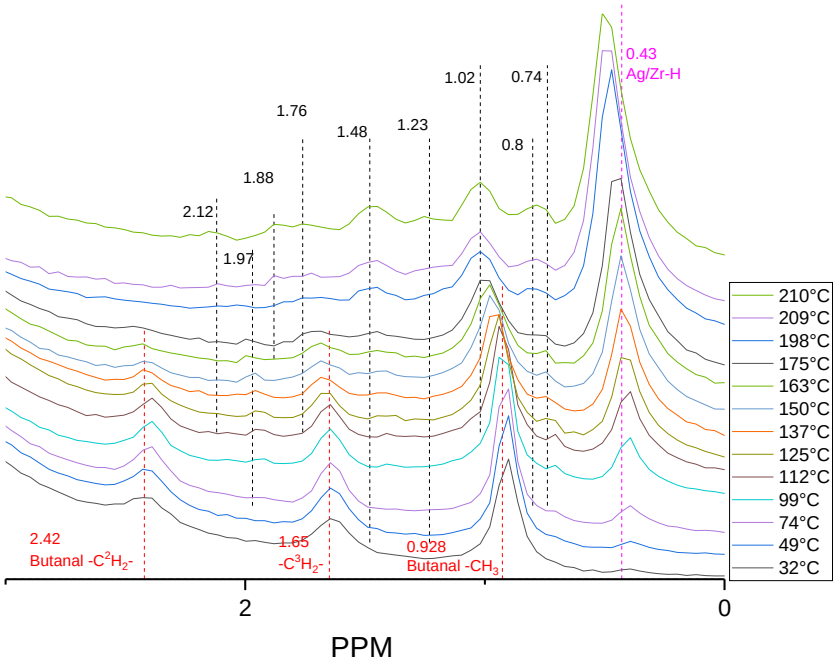

Figure S88. Selected spectra in the upfield region of the butyraldehyde in situ experiment.

9. Supporting Trial with Butanol

Butanol is another important intermediate for which the experimental peak positions and associated thermochemical conversion were monitored. This experiment employed 8.9 mg of catalyst, a butanol pressure of 19.1 psi, and a hydrogen pressure of 84 psi. Initially, peaks associated with hydrogen (4.35 ppm) and butanol (3.64, 1.52, 1.38, and 0.9 ppm) are the only observed resonances. As the temperature is increased, new species are formed at the expense of butanol intensity. As similar to the other experimental trials, hydride species arise near 0.4 ppm. However, new resonances (3.4, 1.7, 1.4, 1, and 0.8) are generated at elevated temperatures. No obvious features arise in the downfield of hydrogen that would solidify an assignment to the dehydrogenation to butyraldehyde or dehydration to butane.

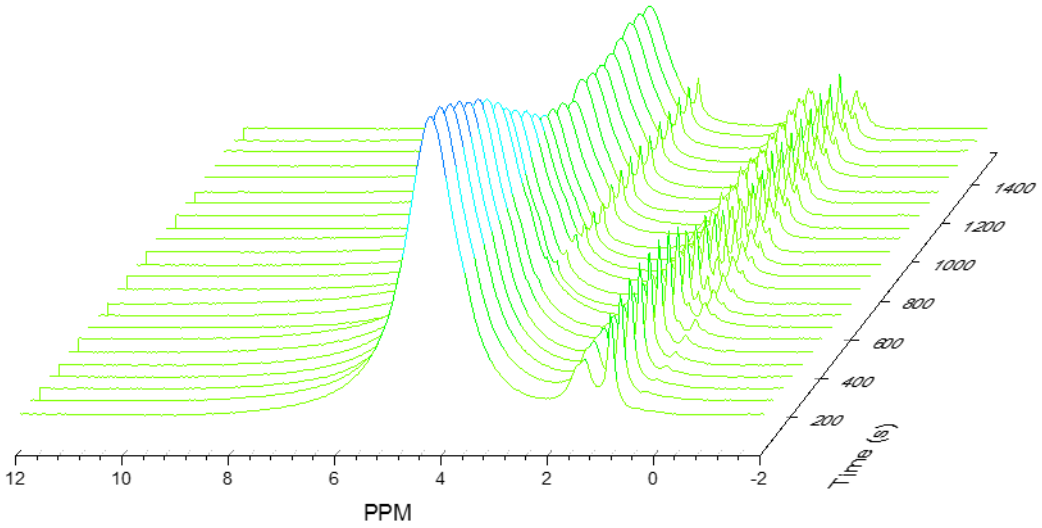

Figure S89. Time-resolved evolution of signals from the butanol trial.

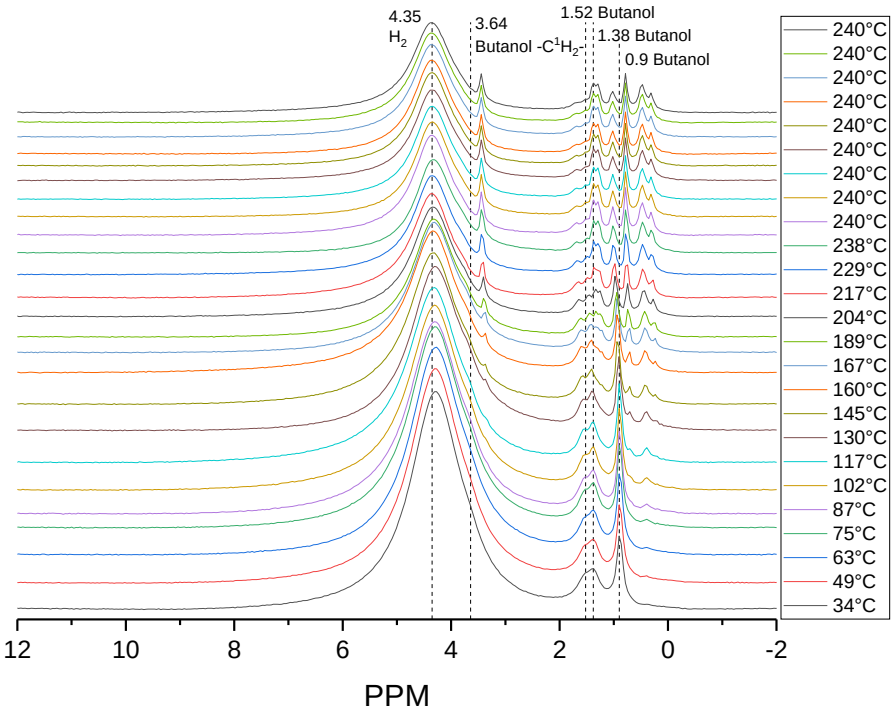

Figure S90. Stack-plot of the butanol in situ NMR trial.

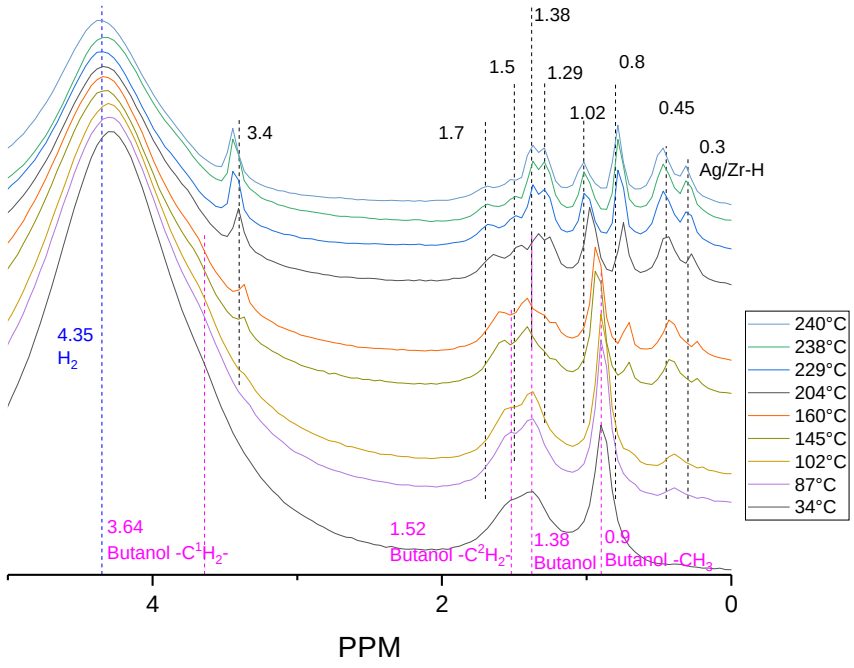

Figure S91. Selected spectral from the upfield region of the in situ NMR trial with butanol.

10. Supporting Trial with Crotyl Alcohol

Crotyl alcohol was also tested to determine the experimental peak positions and associated thermochemical conversion. This experiment employed 10.6 mg of catalyst, a crotyl alcohol pressure of 29.9 psi, and a hydrogen pressure of 78 psi. This experiment initiated with signals at 5.67, 4.9, and 1.7 ascribed to crotyl alcohol. Additional peaks from the compound are apparently obscured by the hydrogen resonance. As the temperature was increased, a wide array of new signals evolved. No signature peaks from either butadiene (6.3 ppm) or butyraldehyde (9.7 ppm) were observed, but peaks assigned to butenes are present (5.7, 1.9, 0.8 and 5.25, 1.6). Numerous additional peaks are also observed that are left unassigned. This trial confirms that crotyl alcohol alone can be converted to butane, but the pathway allowing this transformation is ambiguous under these conditions.

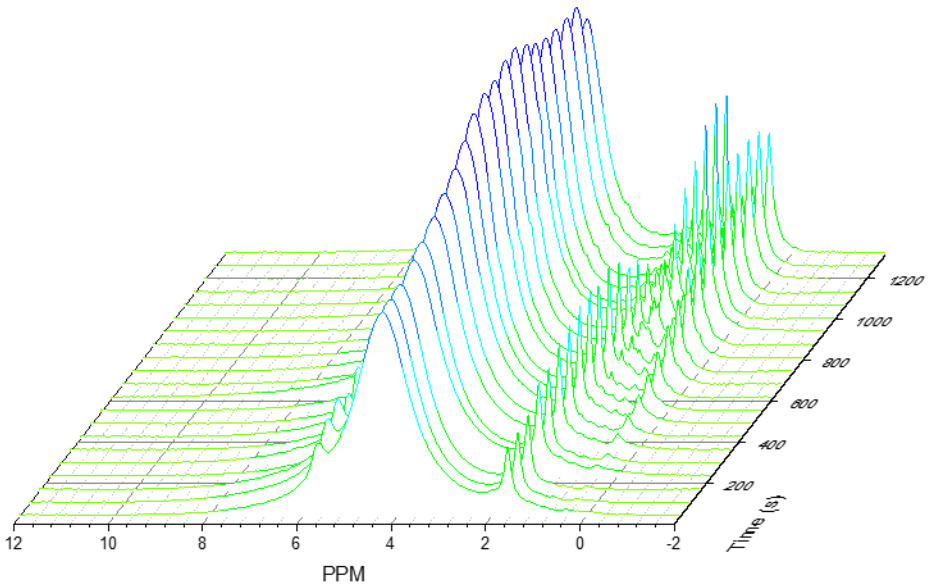

Figure S92. Time-resolved in situ NMR of crotyl alchol conversion.

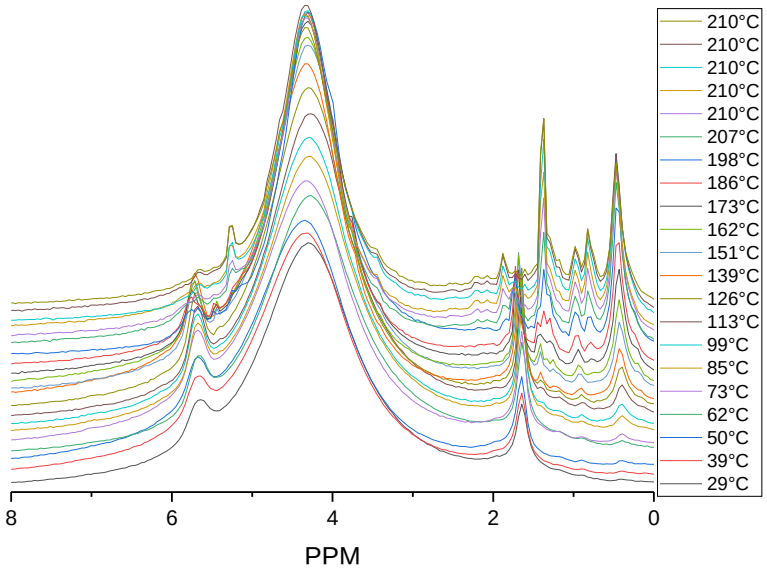

Figure S93. Stack-plot of the crotyl alcohol in situ NMR trial.

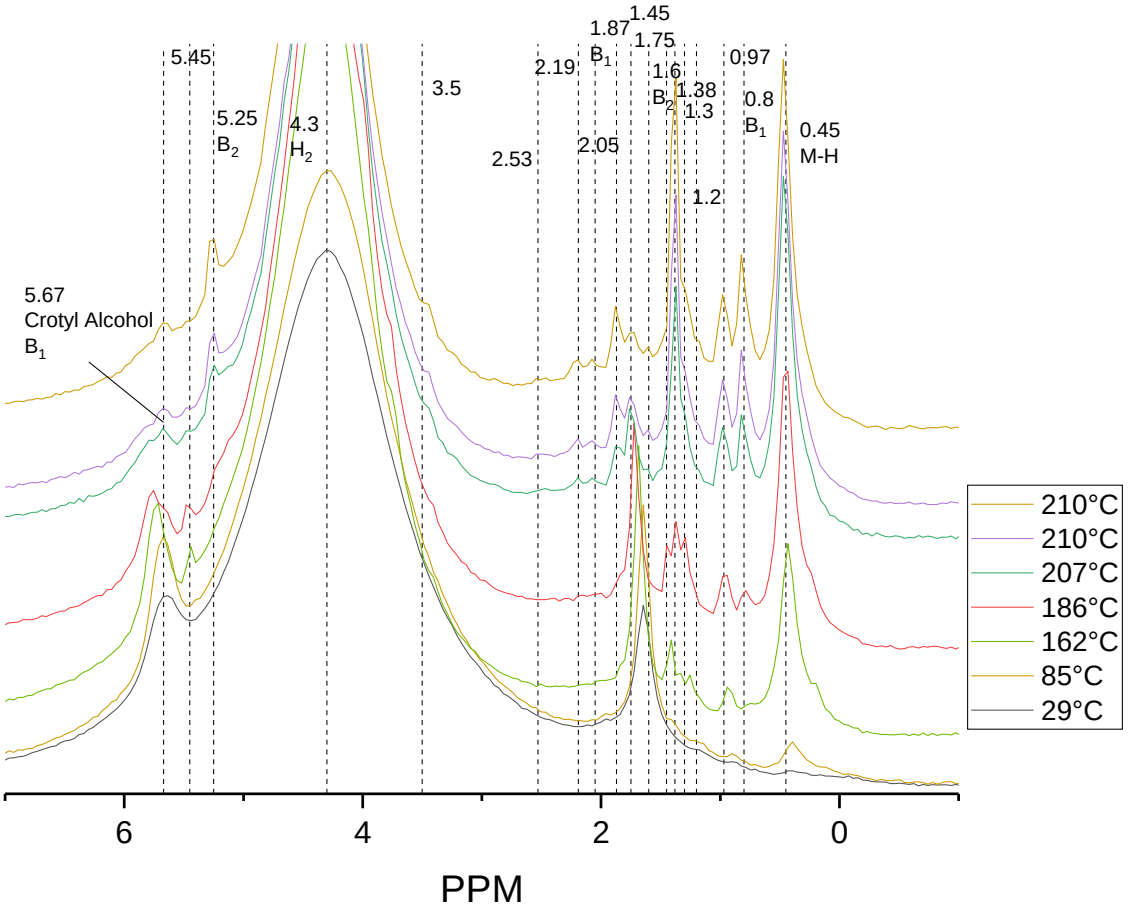

Figure S94. Zoomed in upfield region of the crotyl alcohol in situ ^{1}H NMR spectra.

11. Supporting Trial with Diethyl Ether

This experiment employed 11.0 mg of catalyst, a diethyl ether pressure of 16.8 psi and a hydrogen pressure of 83 psi, maintaining a total pressure near 100 psi at 210°C. The spectra provide confidence in the assignments of diethyl ether and highlight the distribution between adsorbed and gas phase species as a function of temperature for this catalyst.

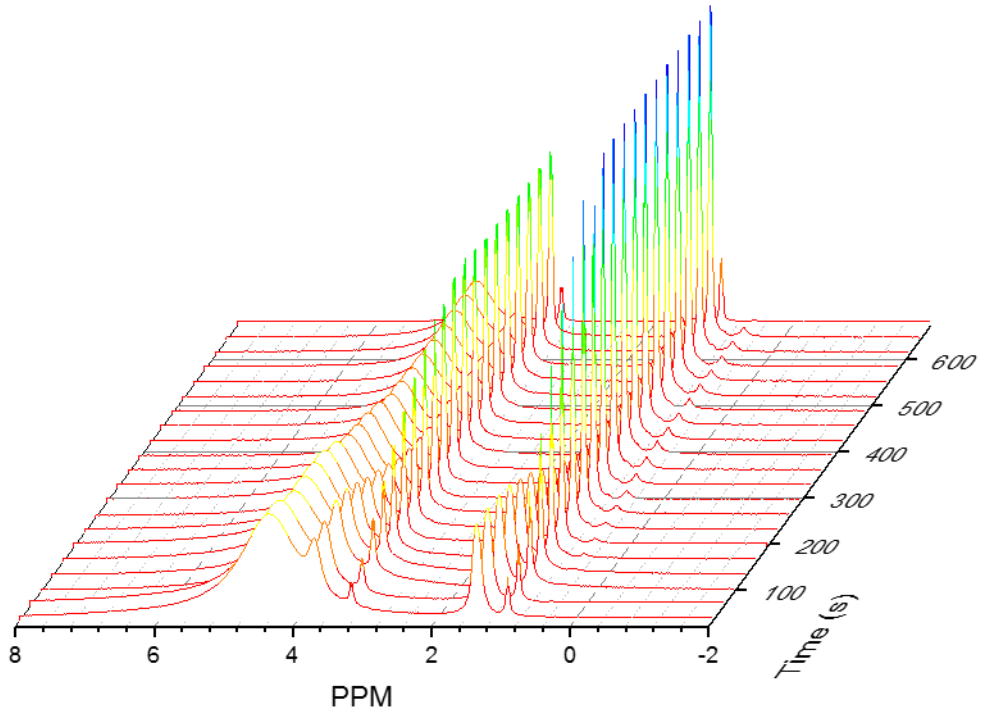

Figure S95. Stack-plot of the diethyl ether in situ NMR trial.

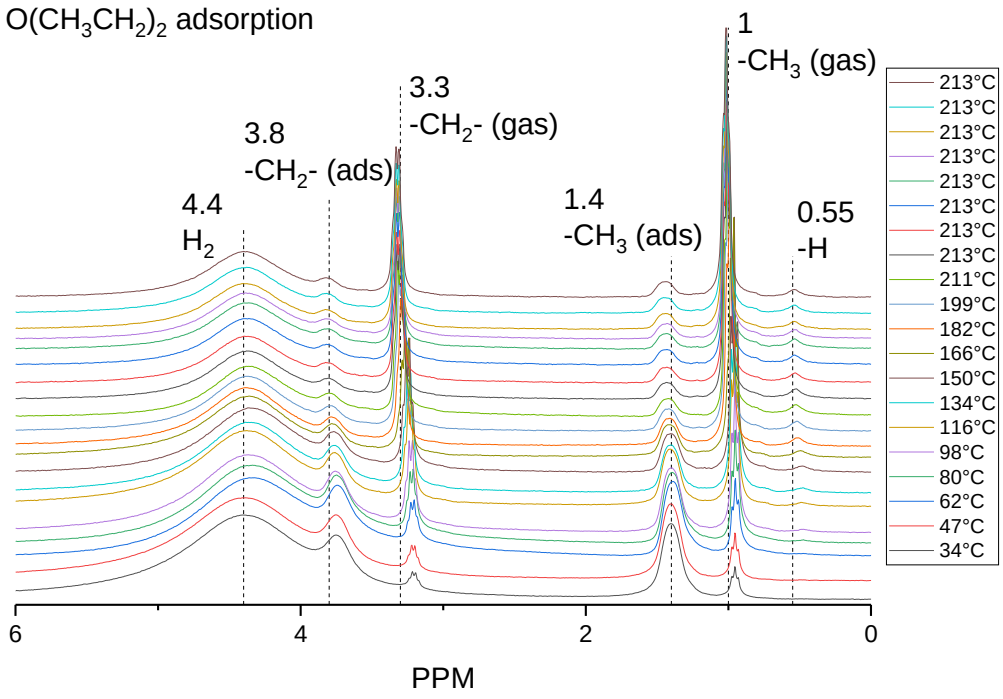

Figure S96. Zoomed in upfield region of the diethyl ether in situ ^{1}H NMR spectra.

12. Supporting Trial with Butadiene

This experiment employed 7.2 mg of catalyst, a butadiene pressure of 24.3 psi, and a hydrogen pressure of 146 psi, maintaining a total pressure near 170 psi at 210°C. These results provide a confident assignment of the locations of adsorbed and gas phase butadiene as well as the butenes that arise from hydrogenation of the butadiene.

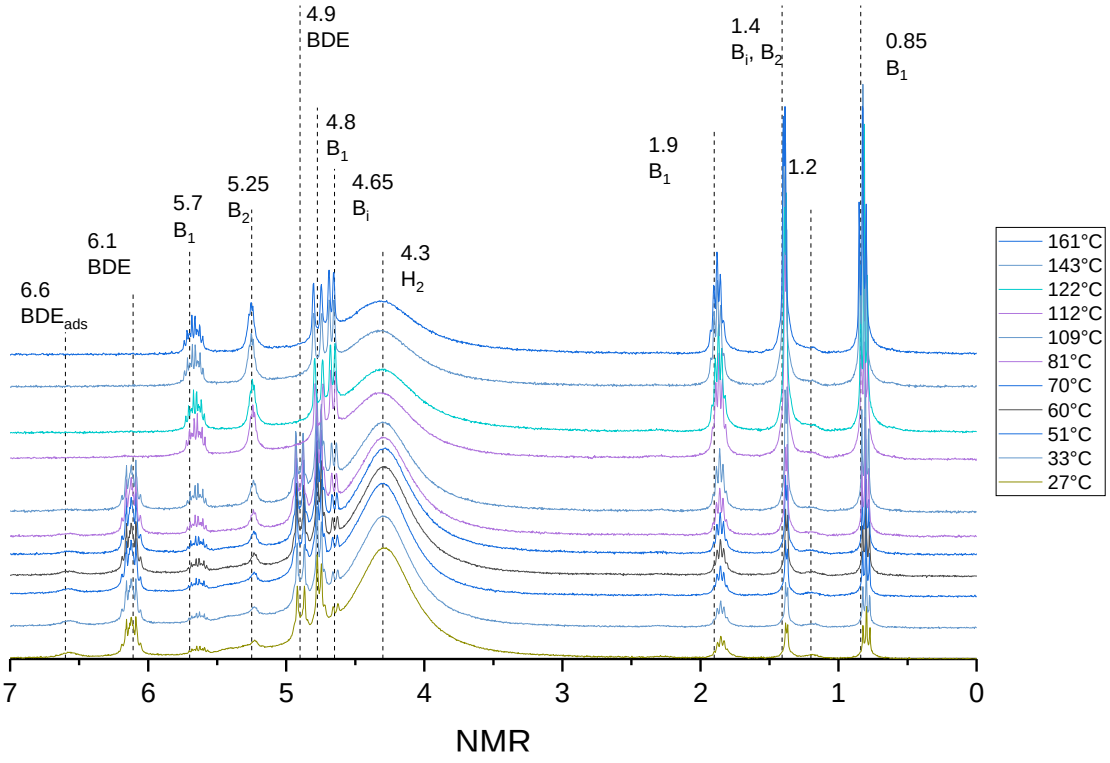

Figure S97. Stack plot of butadiene conversion with hydrogen.

13. Supporting Trial with 1-Butene

This experiment employed 15.3 mg of catalyst, a butene pressure of 40.5 psi and a hydrogen pressure of 41 psi, maintaining a total pressure near 80 psi at 210°C. The resulting spectra show the clear desorption of butene-1 and isomerization to the other butenes as the

temperature was elevated. The specific spectral assignments are detailed in the figure where the subscript refers to the isomer.

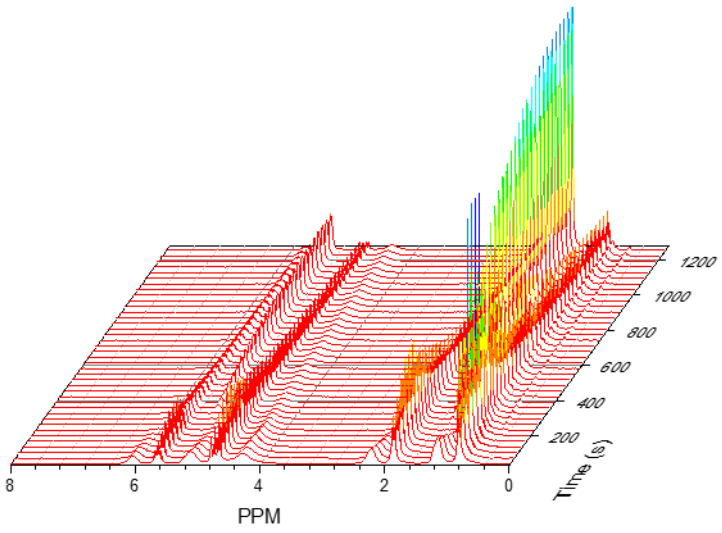

Figure S98. Time-lapsed waterfall plot of 1-butene isomerization.

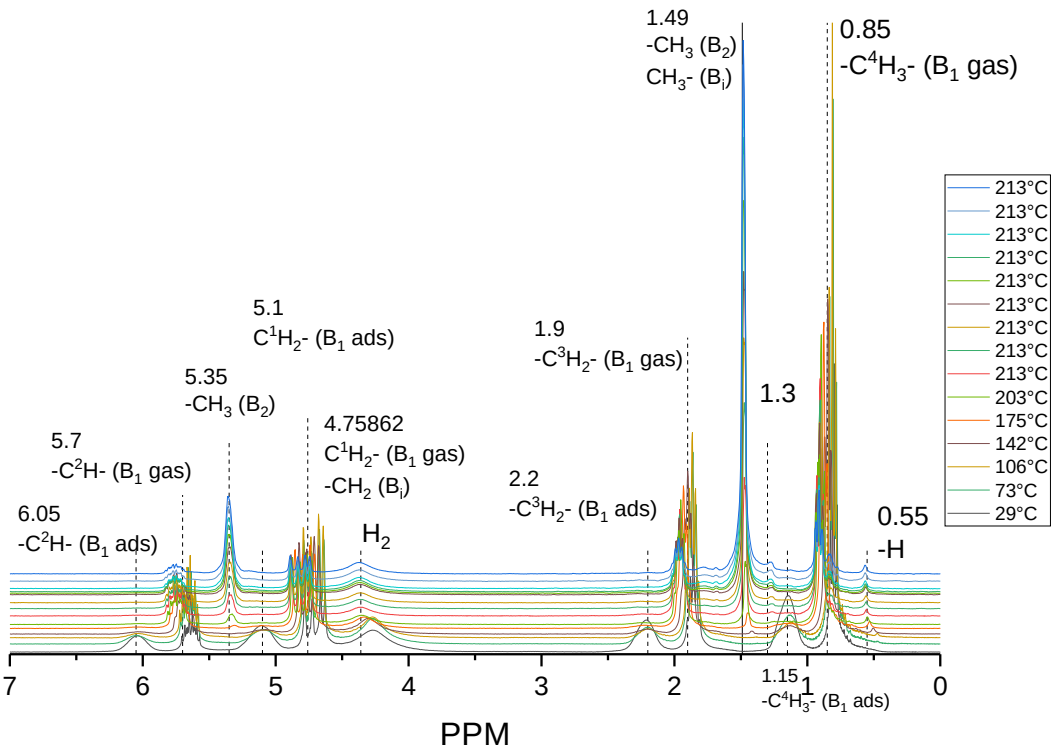

Figure S99. Stacked-plot of the 1-butene in situ ^{1}H NMR spectra.

Appendix G: Second-Order Quadrupolar Energy Perturbations

From the expanded energy term:

$$E^{(2)} = -\left(\frac{e^2qQ}{4I(2I-1)}\right)^2 \frac{m}{v_0}\Big[-\frac{1}{5}(I(I+1)-3m^2)(3+\eta^2)$$
$$+\frac{1}{28}(8I(I+1)-12m^2-3)\big((\eta^2-3)(3cos^2\theta-1)+6\eta^2 sin^2\theta cos2\varphi\big)$$
$$+\frac{1}{8}(18I(I+1)-34m^2-5)\Big(\frac{1}{140}(18+\eta^2)(35cos^4\theta-30cos^2\theta+3)$$
$$+\frac{3}{7}\eta sin^2\theta(7cos^2\theta-1)cos2\varphi+\frac{1}{4}\eta^2 sin^4\theta cos4\varphi\Big)\Big]$$

Assuming axial symmetry (η=0):

$$E^{(2)} = -\left(\frac{e^2qQ}{4I(2I-1)}\right)^2 \frac{m}{v_0}\Big[-\frac{3}{5}(I(I+1)-3m^2)-\frac{3}{28}(8I(I+1)-12m^2-3)(3cos^2\theta-1)$$
$$+\frac{1}{8}(18I(I+1)-34m^2-5)\left(\frac{18}{140}(35cos^4\theta-30cos^2\theta+3)\right)\Big]$$

Let:

$$P = -\left(\frac{e^2qQ}{4I(2I-1)}\right)^2 \frac{m}{\omega_0}$$

$$A = -\frac{3}{5}(I(I+1)-3m^2)$$

$$B = -\frac{3}{28}(8I(I+1)-12m^2-3)$$

$$C = \frac{1}{8}(18I(I+1)-34m^2-5) * \frac{18}{140}$$

Then:

$$E^{(2)} = P[A + B(3cos^2\theta - 1) + C(35cos^4\theta - 30cos^2\theta + 3)]$$

$$E^{(2)} = P\left[A + 3B\left(cos^2\theta - 1 + \frac{2}{3}\right) + C(35cos^4\theta - 30cos^2\theta + 3)\right]$$

Since:

$$cos^2\theta = 1 - sin^2\theta$$

$$cos^4\theta = \frac{3 + 4cos(2\theta) + cos(4\theta)}{8}$$

The energy becomes:

$$E^{(2)} = P\left[A - 3B\left(sin^2\theta + \frac{2}{3}\right) + C\left(35\left[\frac{3 - 4cos2\theta + cos4\theta}{8} + cos2\theta\right] - 30cos^2\theta + 3\right)\right]$$

Taking:

$$sin^4\theta = \frac{3 - 4cos2\theta + cos4\theta}{8}$$

$$E^{(2)} = P\left[A - 3B\left(sin^2\theta + \frac{2}{3}\right) + C(35sin^4\theta + 35cos^2\theta - 35sin^2\theta - 30cos^2\theta + 3)\right]$$

$$E^{(2)} = P\left[A - 3B\left(sin^2\theta + \frac{2}{3}\right) + C(35sin^4\theta + 5cos^2\theta - 35sin^2\theta + 3)\right]$$

Again, taking:

$$cos^2\theta = 1 - sin^2\theta$$

$$E^{(2)} = P\left[A - 3B\left(sin^2\theta + \frac{2}{3}\right) + C(35sin^4\theta + 5 - 5sin^2\theta - 35sin^2\theta + 3)\right]$$

$$E^{(2)} = P\left[A - 3B\left(sin^2\theta + \frac{2}{3}\right) + C(35sin^4\theta - 40sin^2\theta + 8)\right]$$

Collecting Terms, we arrive at:

$$E^{(2)} = P[A + 2B + 35Csin^4\theta + (-3B - 40C)sin^2\theta + 8C]$$

Collecting the orientation-independent terms as D:

$$D = A + 2B + 8C$$

Expanded, D is:

$$D = -\frac{3}{5}\big(I(I+1)\big) + \frac{9}{5}m^2 - \frac{3}{14}\big(8I(I+1)\big) + \frac{36}{14}m^2 + \frac{9}{14} + \frac{18}{140}\big(18I(I+1)\big) - \frac{612}{140}m^2 - \frac{90}{140}$$

Factoring the terms provides

$$D = -\frac{3}{5}\big(I(I+1)\big) - \frac{24}{14}\big(I(I+1)\big) + \frac{324}{140}\big(I(I+1)\big) + \frac{9}{5}m^2 + \frac{18}{7}m^2 - \frac{153}{35}m^2 - \frac{90}{140} + \frac{9}{14}$$

$$D = \left[\frac{-3}{5} - \frac{12}{7} + \frac{81}{35}\right]I(I+1) + \left[\frac{9}{5} + \frac{18}{7} - \frac{153}{35}\right]m^2 - \frac{9}{14} + \frac{9}{14}$$

$$D = 0 * I(I+1) + 0 * m^2 + 0 = 0$$

Therefore:

$$E^{(2)} = P[35Csin^4\theta - (3B + 40C)sin^2\theta]$$

Appendix H: Publication – Adsorption and Thermal Decomposition of Electrolytes on Nanometer Magnesium Oxide:An *in situ* ^{13}C MAS NMR Study

Reprinted with permission from Jian Zhi Hu,*‡ Nicholas R. Jaegers, ‡ Ying Chen, Kee Sung Han, Hui Wang, Vijayakumar Murugesan, and Karl Todd Mueller* *ACS Applied Materials and Interfaces* 2019.

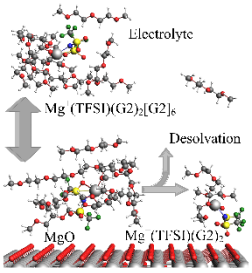

Abstract

Mg batteries have been proposed as potential alternatives to lithium ion batteries due to their lower cost, higher safety, and enhanced charge density. However, Mg metal readily oxidizes when exposed to an oxidizer to form a thin MgO passivation surface layer that blocks the transport of Mg^{2+} across the solid electrode-electrolyte interface (SEI). In this work, the adsorption and thermal decomposition of diglyme (G2) and electrolytes containing $Mg(TFSI)_2$ in G2 on 10 nm sized MgO particles are evaluated by a combination of *in situ* ^{13}C single pulse (SP), surface sensitive ^{1}H-^{13}C cross-polarization (CP) MAS NMR, and quantum chemistry calculations. At 180°C, neat G2 decomposes on MgO to form surface adsorbed $–OCH_3$ groups that are captured as a distinctive peak located at about 50 ppm in the CP/MAS spectrum. At low $Mg(TFSI)_2$ salt concentration, the main solvation structure in this electrolyte is solvent-separated ion pairs without extensive Mg-TFSI contact ion pairs. G2, likely including a small amount of G2 solvated Mg^{2+}, adsorbs onto the MgO surface. At high $Mg(TFSI)_2$ salt concentrations,

contact ion pairs between Mg and TFSI are formed extensively in the solution with the first solvation shell containing one pair of Mg-TFSI and two G2 molecules and the second solvation shell containing up to six G2 molecules, namely, $MgTFSI(G2)_2(G2)_6^+$. In the presence of MgO, $MgTFSI(G2)_2(G2)_6^+$ adsorbs onto the MgO surface. At 180°C, the MgO surface stimulates a desolvation process converting $MgTFSI(G2)_2(G2)_6^+$ to $MgTFSI(G2)_2^+$, and releasing G2 molecules from the second solvation shell of the $MgTFSI(G2)_2(G2)_6^+$ cluster into the solution. The $MgTFSI(G2)_2^+$ and $MgTFSI(G2)_2(G2)_6^+$ tightly adsorb onto the MgO surface and are observed by ^1H-^{13}C CP/MAS experiments. The results contained herein show that electrolyte composition has a directing role in the species present on the electrode surface, which has implications on the structures and constituents of the solid-electrolyte interface on working electrodes and can be used to better understand its formation and the failure modes of batteries.

Introduction

Energy storage represents an important technological field for continued global economic advancement. Batteries have long represented a convenient method for chemically storing energy, but rapidly increasing energy storage needs have driven extensive efforts to improve these materials in size, capacity, service life, and reusability. Rechargeable batteries such as Li-ion batteries have become a prominent power source for portable electronic device and electric vehicles.[380-381] However, the demand for improved performance has driven investigations into other multivalent cation systems. Mg metal batteries represent an attractive alternative to Li-ion technology due to Mg's marked potential energy density enhancement over Li-ion (3,833 vs 800 mA h/cc).[382] As such, extensive efforts have been made to better understand the interactions

between the electrode surfaces and electrolyte to drive the design of new materials with improved capacity and stability.[383] Repeated cycling introduces microstructure formation at the interface between the solid electrode and electrolyte due to migration of ionic species. This process often results in battery failure, highlighting the importance of identifying the interactions between the electrode surface and electrolyte to provide key understanding to the failure modes of Mg battery systems which may be used in the rational design of improved systems.

The true surface of Mg battery electrodes is complex in nature due to Mg-metal interaction with electrolytes and air, where reported evidence has shown that MgO is a major constitute in the SEI of the Mg-metal anode in a magnesium battery system containing $Mg(TFSI)_2$/glyme electrolytes.[384] This is because Mg metal readily oxidizes when exposed to an oxidizer, such as air,[385] to form a thin MgO surface layer. The presence of an MgO surface phase inevitably impacts the electrode surface-solvent/electrolyte interactions, thus affecting the performance of a Mg-battery. Further, the high molecular adsorption capacity of MgO enables molecules such as H_2O or CO_2 to readily adsorb on the MgO surface. These molecules may, in turn, block the adsorption sites, preventing electrolytes from interacting with the surface.[386-387] Indeed, it has been shown that the method of preparation affects the adsorption of molecules, which can modulate the reactivity for a variety of substrates.[388] This strongly suggests that even in battery applications the preparation of the cell may result in contrasting surface oxide layers, and thus, different performance.

Though the specific reactivity may differ, MgO surfaces exhibits dehydrogenation activity whereby alcohols have been shown to decompose into stable surface conjugate base species (methoxide, ethoxide, etc.) and carbonates, which may undergo further reactions with

extended-phase molecules or dehydrate in the absence of additional substrate interaction.[389-391] MgO is also effective at breaking C-O bonds such as those of methyl formate and dimethoxyethane (DME, glyme, or G1).[388, 392] The interactions of G1 with the MgO surface have been studied recently using computational modeling [392] due to its use as a solvent in Mg battery electrolytes, such as with Magnesium(II) bis(trifluoromethane sulfonyl) imide ($Mg(TFSI)_2$), an electrolyte that exhibits high resistivity towards oxidation, high conductivity, and compatibility with most cathode materials.[393] The most stable decomposition interaction of G1 with the MgO surface was predicted by density functional theory (DFT) to result in the cleavage of one C-O bond and the exchange of an H atom between two fragments to form methanol and methoxy ethane which proceed through a methoxy intermediate and remain adsorbed on the surface. The study found that G1 decomposition was kinetically hindered by the surface oxide overlayer.[392]

The thermochemical decomposition of solvent materials is an important consideration for battery performance. The electrochemical cycling of batteries results in elevated cell temperatures (potentially >60^{o}C during discharge, and even much greater locally at the electrode surface) [394-395] which may induce electrolyte and/solvent reactivity over the course of numerous charge-discharge cycles. Cycling at high external temperatures has been shown to reduce cell lifetime as well, providing further need to investigate such interactions under high thermal stress conditions.[396] *In situ* nuclear magnetic resonance (NMR) spectroscopy is a technique well-suited for probing the interactions between the solid surface and electrolyte materials.[8, 235] In this work, we employ NMR to study the solvent-surface interactions under *in situ* conditions of significantly elevated temperatures to simulate the adsorption and potential thermal decomposition of the solvent and electrolytes on the MgO surface. Specifically, we investigate

electrolytes containing $Mg(TFSI)_2$ in diglyme (G2) since G2 is another commonly used solvent in Mg-battery applications due to its improved stripping kinetics of Mg^0 over glyme (G1 or DME).[385]

Experimental Methods

Samples: Electrolytes of 0.1 M and 1.0 $Mg(TFSI)_2$ in G2 were prepared as follows in an argon-filled glove box: stoichiometric amount of $Mg(TFSI)_2$ (99.5 %, Solvionic, France) was added to G2 (99.5%, Sigma-Aldrich) in a 5 mL volumetric flask under stirring at room temperature. $Mg(TFSI)_2$ were dried for two days under vacuum at 180°C, and the G2 was dried over activated 3Å molecular sieves until its moisture content was determined to be below 30 ppm by a Karl-Fisher Titrator (Metrohm). Magnesium oxide nanopowder (MgO, 99.9%, 10 nm) was purchased from US Research Nanomaterials, Inc. with a size distribution of: 5% <5 nm, 90% ~10 nm, 5% >10 nm (with up to 1% as 30-40 nm) and a specific surface area of 85-120 m^2/g.

In situ natural abundance magic angle spinning (MAS) NMR spectroscopy. *In situ* ^1H and ^{13}C single pulse (SP) magic angle spinning (MAS) NMR experiments with high power proton decoupling were performed on a Varian-Agilent Inova wide-bore 300 MHz NMR spectrometer using a 7.5 mm ceramic pencil type MAS probe, operating at a ^{13}C and ^1H Larmor frequencies of 75.430 and 299.969 MHz, respectively. A customer made 7.5 mm outside diameter (OD) all zirconia MAS rotor that was capable of 100% fluid seal under the condition of a combined high temperature and high pressure operating environments [379] was employed for *in situ* MAS NMR

investigations. ^{13}C spectra were referenced to tetramethylsilane (TMS at 0 ppm) using adamantane as a secondary reference, i.e., with ^{13}C of CH_2 at 38.48 (downfield peak). All species, regardless of being adsorbed on the particle surface or in the bulk solution phase, are quantitatively detected by the SP experiment provided the recycle delay time (d1) is larger than five times the relaxation time when a $\pi/2$ pulse is used. By using a smaller tip pulse angle less than $\pi/2$, a reduced recycle delay time can be used for quantitative measurement. To determine the recycle delay time, an array of d1times was collected with $\pi/4$ pulses, and used to ensure d1 was sufficiently long for quantitative measurement (e.g. 5s).

^{1}H-^{13}C cross polarization (CP) MAS NMR was used to identify only those species that are adsorbed onto a solid surface since CP/MAS depends on static dipolar interaction between ^{1}H and ^{13}C spins. In bulk solutions, fast and random molecular motions reduce the time averaged ^{1}H and ^{13}C dipolar interaction to zero, so the species in bulk solution are not detected in the CP experiment. In contrast, the interaction of molecules with a solid surface limits the motion of the adsorbed molecules to yield a non-zero time averaged ^{1}H-^{13}C dipolar interaction that may be sufficiently strong for establishing an effective cross-polarization, making CP/MAS a surface sensitive method. Since the efficiency of a CP experiment depends on many factors such as the strength of ^{1}H-^{13}C dipolar interaction and the ^{1}H spin-lattice relaxation in the rotation frame, $T_{1\rho}$, a CP experiment at a fixed contact time is generally not quantitative, but is an excellent method for detecting surface species. A 0.5 s recycle delay time (d1), contact time (ct) time of 2.6 ms, and a ^{1}H decoupling field strength of 62.5 kHz were employed to collect these spectra.

Methods for loading samples into a sealed MAS NMR rotor. Prior to ^{13}C SP or ^{1}H-^{13}C CP/MAS NMR experiments, the 10 nm MgO powder samples were pretreated in a quartz tube connected to a vacuum (10^{-3} Torr with 20% O_2) manifold controlled to low O_2 partial pressure and heated to either 200 or 550°C for 10 hours. The valve on the quartz tube was closed and the samples were then allowed to cool prior to relocation to a dry nitrogen glove box for packing. The valve was opened and a controlled quantity of MgO powder was packed into a sealed NMR rotor. Subsequently, a controlled amount of either G_2 or G_2+ $Mg(TFSI)_2$ was added to the rotor in the glovebox, and quickly sealed. The seal of the rotor was confirmed by comparing the mass prior to and after the NMR measurements. In each case, identical masses were recorded, indicating a perfect seal of the MAS rotor during the measurements.

Quantum Chemistry Calculations: Computational modeling of the NMR chemical shifts was carried out using the Amsterdam Density Functional (ADF-2014) package.[397] Geometries were optimized using the generalized gradient approximation (GGA) with Grimme's third generation dispersion correction [398] applied to the Becke-Lee-Yang-Parr [328, 399] functional was employed for geometry optimization. All calculations were carried out by using the all-electron TZ2P basis set (Triple-ζ, 2-polarization function) with the Slater-type orbitals [400] implemented in the ADF program. ^{13}C NMR calculations were performed based on the geometry optimized structures at the same level of the theory and with the same basis set to evaluate the chemical shielding for each atom. The calculated ^{13}C chemical shielding for adamantane is 136.08 ppm. To convert the calculated shielding to the experimentally observed scale with reference to adamantane (38.48 ppm), the following equation is used, i.e., $\delta_{obs} = 136.08 - \delta_{calc} + 38.48$.

Results and Discussions

Reactivity of solvent G2 on MgO coated with carbonates: A single and relatively broad peak centered at about 167.6 ppm with a half linewidth of 484 Hz (or 6.42 ppm) is observed in the ^{1}H-^{13}C CP/MAS NMR spectrum of the 10 nm MgO powder pretreated at a temperature of 200°C (Figure 1a). This peak is attributed to surface carbonate (CO_3^{2-}), [234] including bicarbonate (HCO_3^-) and carbonate interacting with Mg, i.e., $MgCO_3$. [14-15] These carbonate species likely originate from CO_2's interaction with the MgO surface during the commercial MgO sample during manufacture (either from decomposition of surface formate species or from ambient air) [401] that cannot be removed at a pretreatment temperature of 200°C. The reactivity of this MgO sample with G2 at a reaction temperature of 180°C is shown in Figure 1b by the ^{1}H-^{13}C CP/MAS spectrum. In addition to the carbonate peak, there are at least five upfield peaks observed; c.a. 57.5, 67, 70.65, 72.12, and 78.63 ppm. All three ^{13}C peaks show a minor upfield shift of about 0.15 ppm when interacting with the material surface. Based on the pure G2 results, the peaks in Fig. 1b can be assigned as MgO surface adsorbed G2: CH_3(57.5ppm)-O-CH_2(72.12ppm)-CH_2(70.65ppm)-O-CH_2(70.65ppm)-CH_2(72.12ppm)-O-CH3 (57.5 ppm), and the MgO surface mediated decomposed products, or G2 interacting with surface carbonates, with peaks located at 78.63 and 67 ppm. Pure G2 inside the zirconia rotor shows no reactivity at 180°C (Figure 1c-1d), indicating that the stabilized bulk ZrO_2 crystal (rotor material) is inert to G2 under our reaction condition. This is evident by comparing the ^{13}C SP spectra prior to and after treating at 180°C for 1 h (Figure 1c and d). G2 does adsorb onto the inner surface of the rotor wall and the

adsorbed G2 can be captured by ^{13}C CP/MAS (Figure 1e) despite the rather low surface area of the rotor, i.e., $\pi \times 4.5$ mm$\times 15$ mm$=212$ mm^2.

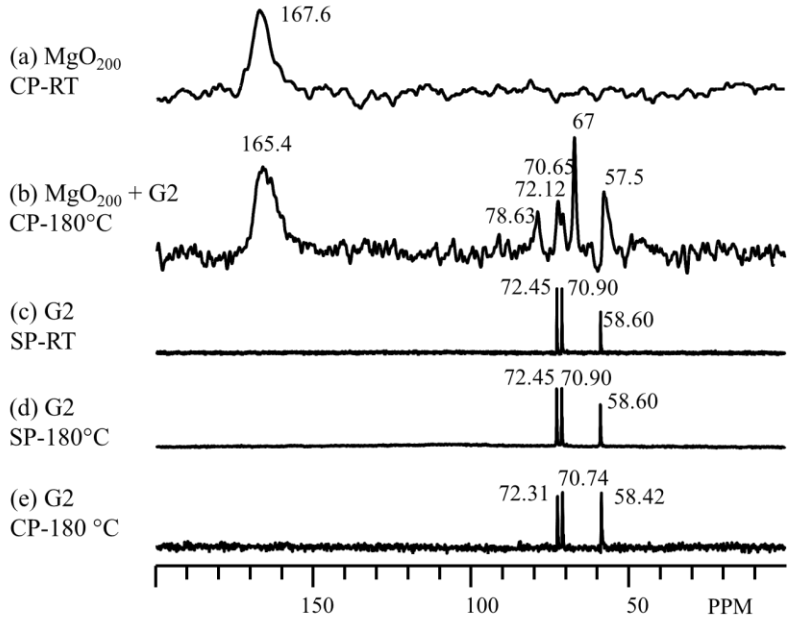

Figure 1. ^{13}C CP/MAS or SP/MAS spectra acquired at a sample spinning rate of about 3.5 kHz and at room temperature (RT). (a) CP/MAS of pure 10 nm MgO immediately after pretreatment at 200 ℃ (MgO_{200}); This spectrum was acquired after the mixture was heated to 180 ℃ for 1 hour; (a) was acquired with 97872 scans; (b) CP/MAS of 2 μl G2 + 66.1 mg MgO_{200}. This spectrum was acquired with 100k scans; (c-e) Are a sample comprised of 25 μl G2: (c) SP spectrum immediately taken after loading into the rotor, 128 scans were collected; (d) SP after heating to 180 ℃ for 1 hour with 1,748 scans; (e) CP spectrum with 99,052 scans.

Reactivity of solvent G2 on MgO with clean surface: Pretreatment of the 10 nm MgO powder at a temperature of 550°C and above effectively removes surface carbonates, generating a clean MgO surface, evidenced by the absence of the 167.7 ppm peak in Figure 2. To investigate the reactivity of G2 with a clean MgO surface (MgO_{550}), MgO_{550} was mixed with G2 in a sealed all-zirconia MAS rotor for NMR measurements. After *in situ* heating at 180°C for 1 hour, ^{13}C SP and ^{1}H-^{13}C CP/MAS were acquired and the results are presented in Figure 2. Surface methoxy

species (later validated by DFT) in the form of Mg-OCH_3, are clearly observed in the ^{1}H-^{13}C CP/MAS spectrum (Figure 2a) with its unique peak centered at ~50 ppm. This results from the cleavage of the –OCH_3 in G2 (CH_3O-CH_2CH_2-O-CH_2CH_2-OCH_3) by MgO at 180°C. The remaining G2 fragment interacts with the lattice oxygen of MgO surface to form a CH_3O-CH_2CH_2-O-CH_2CH_2-O-Mg structure. The decomposition process is depicted in Figure 3. Indeed, the ^{13}C CP/MAS spectrum between 55 and 75 ppm (Figure 2a1) cannot be fit by using only three peaks (58.53, 70.84 and 72.426 ppm) as those of SP spectrum (Figure 2b1). Three additional peaks assigned to CH_3O-CH_2CH_2-O-CH_2CH_2-O-Mg and located at approximately 56.96, 69 and 72.242 ppm are utilized to generate a good fit. The upfield shift relative to its corresponding SP –OCH_3 carbon spectral peak is justified by NMR computational modeling below. Note that the cleavage of –OCH_3 in DME (G1) has been previously suggested by computational modeling studies as a favorite mechanisms for DME decomposition on Mg-metal surface.[392]

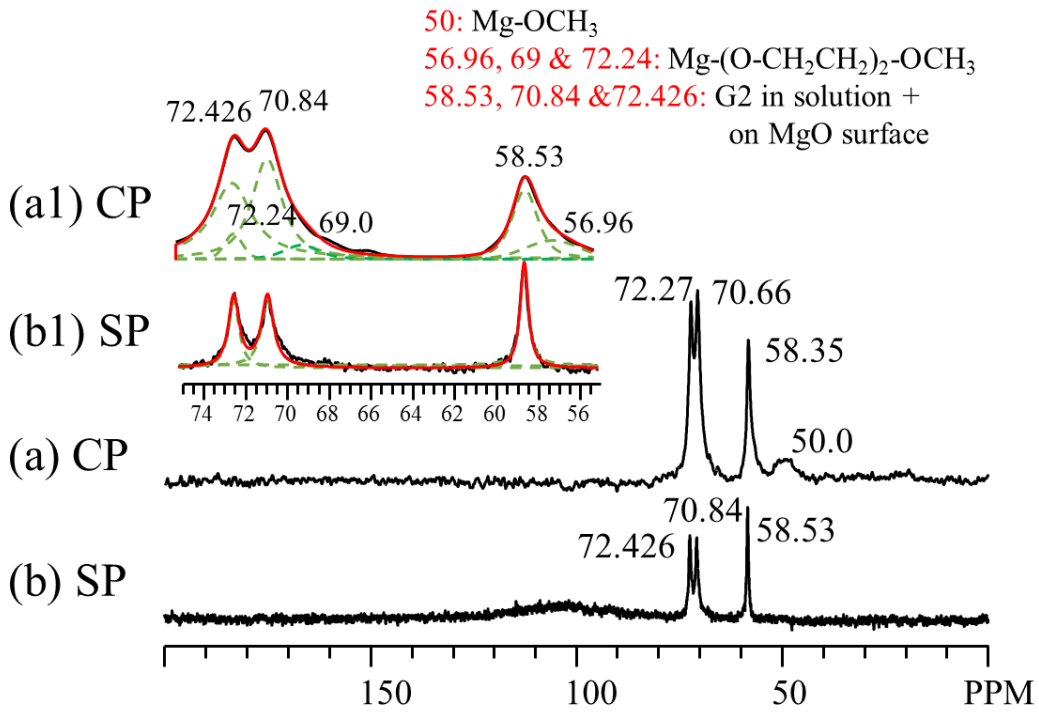

Figure 2. (a) ^{13}C CP/MAS and SP/MAS (b) spectra obtained on 115.7 mg MgO_{550} + 25 µl G2 after reacting at 180 ℃ for 1 hour. (a1) and (b1) are horizontally expanded regions of (a) and (b) between 55 and 75 ppm. (a) was acquired with 77,400 scans; (b) was acquired with 2,196 scans.

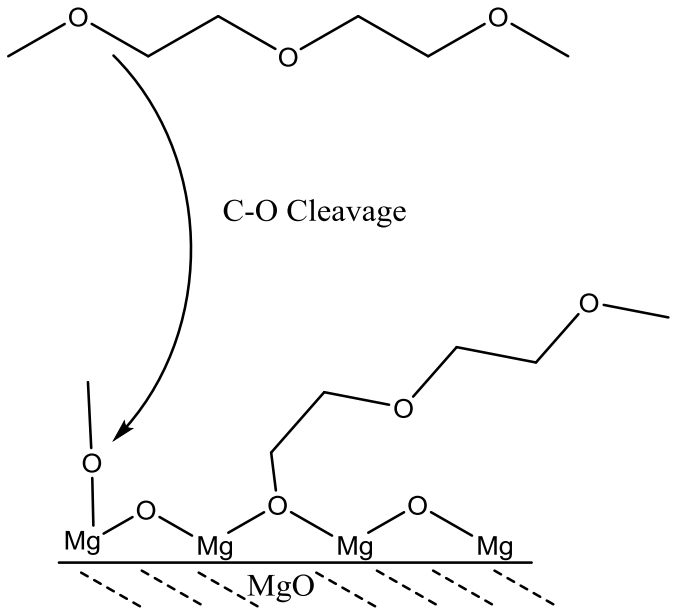

Figure 3. Schematic depiction of solvent G2 ($CH_3OCH_2CH_2OCH_2CH_2OCH_3$) decomposition on MgO to form CH_3OMg and $MgOCH_2CH_2OCH_2CH_2OCH_3$ via C-O cleavage of diglyme.

The adsorption of Electrolytes ($Mg(TFSI)_2$ + G2) on clean surface MgO: Two $Mg(TFSI)_2$ concentrations, i.e., 0.1 M and 1.0 M in G2, are examined for investigating electrolyte concentration-dependent adsorption and decomposition on a clean MgO surface. To investigate their reactivity with the inner wall of the zirconia rotor surface and the extent of Mg-TFSI contact ion formation, both ^{13}C SP and CP MAS NMR experiments were carried out first without using MgO_{550} for comparison to the spectra of neat G2. Clearly, no observable reaction between these two electrolytes and the rotor was observed based on the results presented in Figure 4, evident in the expanded spectral region from 55 to 75 ppm where only three ^{13}C peaks corresponding to G2 are observed. For the 0.1 M $Mg(TFSI)_2$ + G2 sample, the chemical shifts of the three ^{13}C peaks for G2, 58.568, 70.771 and 72.394 ppm prior to (Figure 4b) and post heat treatment at 180°C for 1 hour (Figure 4c) are essentially identical and slightly shifted upfield by 0.03 to 0.1 ppm when compared to neat G2 (Figure 4a). In contrast, 1.0 M $Mg(TFSI)_2$ + G2 reveals an $–OCH_3$ peak that is downfield shifted by about 1 ppm to 59.50 ppm while the two $–OCH_2CH_2O-$ peaks are upfield shifted by approximately 1 ppm to 69.77 and 71.46 ppm. It has been reported [383] that low salt concentrations (0.04 M) of $Mg(TFSI)_2$ in G2 result in nearly complete dissociation of Mg-TFSI while contact ion pairs are observed at higher concentrations (0.4 M) with one $TFSI^-$ anion in the first solvation shell around Mg^{2+}. Therefore in the 0.1 M $Mg(TFSI)_2$ + G2 sample, the majority of the Mg-TFSI are dissociated by G2 while for the 1.0 M $Mg(TFSI)_2$ + G2 sample, the majority of Mg-TFSI forms contact ion pairs. The difference in the shifts of ^{13}C peaks for the G2 in the 0.1 and 1M salt concentrations are, thus, a result of detailed solvation structural changes that is detailed by NMR computational modeling studies below.

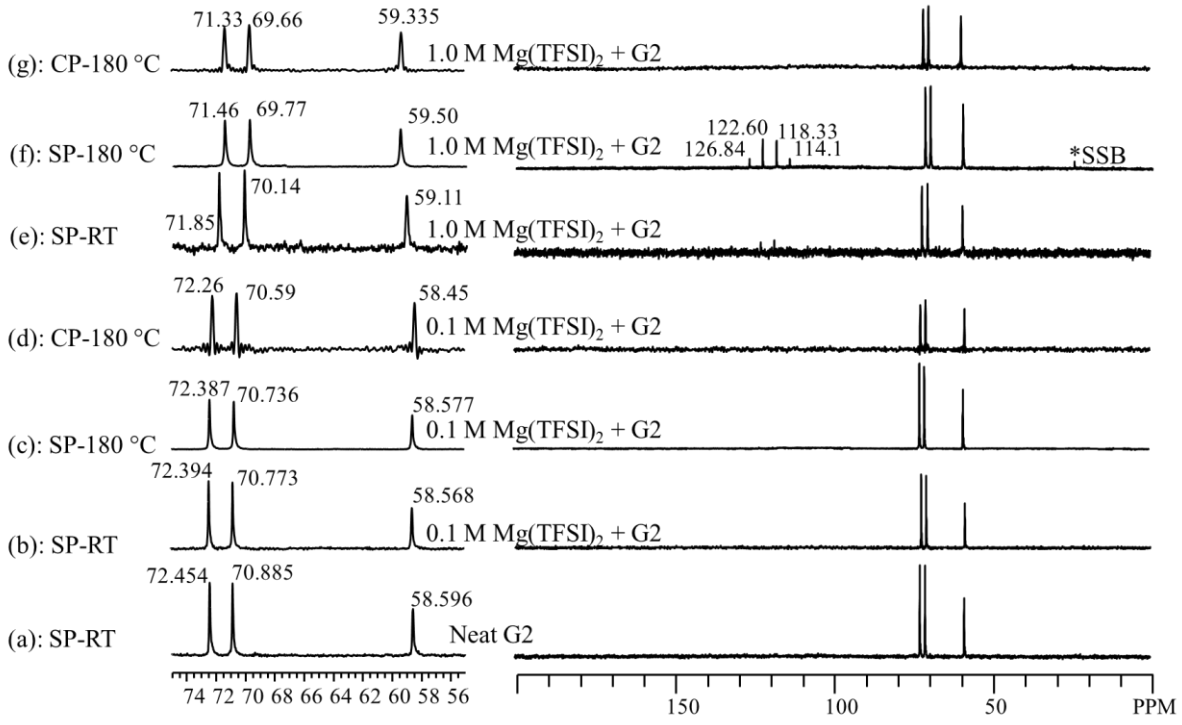

Figure 4. ^{13}C SP/MAS (a, b, c, e and f) and CP/MAS (d and g) spectra. (a) 25 μl pure G2; (b-d) 33.7 μl 0.1 M $Mg(TFSI)_2$ + G2; (e-g) 35 μl 1.0 M $Mg(TFSI)_2$ + G2. (a, b, e) prior to heat treatment; (c and f) after heat treatment. Number of scans are 128 (a), 70 (b), 4,000 (c), 160,000 (d), 24 (e), 4,000 (f), and 111,532 (g) scans, respectively. "" SSB indicates spinning sideband. The four peaks at 114.1, 118.33, 122.60 and 126.84 ppm are signals from TFSI-CF_3 carbon.*

Mixing MgO_{550} with 0.1 M $Mg(TFSI)_2$ in G2, reveals no evidence of electrolyte decomposition from the ^{13}C SP and CP/MAS spectra after thermal treatment at 180 °C for 1 hour (Figure 5). However, adsorption of G2 onto the MgO surface is captured in both the SP (Figure 5a and a1) and the CP (Figure 5b and b1) experiments with the corresponding peaks located at approximately 58.4, 70.65 and 72.23 ppm. The other three peaks in the SP/MAS spectrum, 58.69, 70.94, and 72.52 ppm, from the liquid phase G2 are not detected in the CP experiment due to fast random molecular motion. The relative abundance of these species may be quantified from SP spectral deconvolution (Supporting Information). The results indicate that about 63% of the G2 is present in the solution phase while the rest is surface constrained. The $–CF_3$ carbons of

TFSI are not detected in either the bulk solution phase or the MgO surface due to the low abundance and number of scans used. Nevertheless it is safe to say that the MgO surface contains a negligible amount of tightly bonded TFSI at the low salt concentration of 0.1 M.

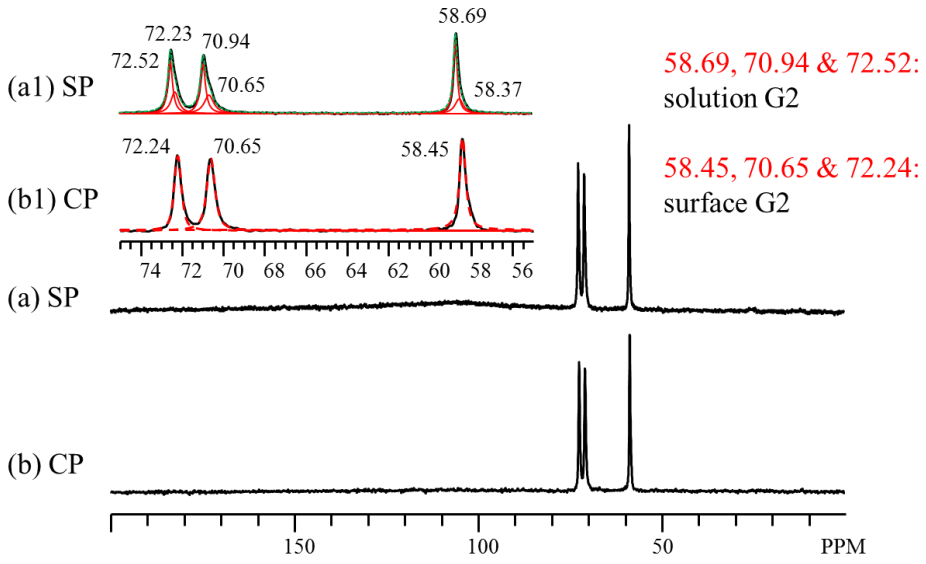

Figure 5. (a) ^{13}C SP/MAS (a) and CP/MAS (b) spectra obtained on 55.2 mg MgO_{550} (clean surface) + 34.5 mg 0.1 M $Mg(TFSI)_2$ in G2 after in situ heat treatment at 180 ℃ for 1 hour. (a1) and (b1) are horizontally expanded regions of (a) and (b), highlighting MgO surface adsorbed G2 with peaks located at approximately 58.4, 70.65 and 72.23 ppm. 4,000 (a) and 97,126 (b) scans were employed. No electrolytes decomposition is observed for this sample.

Significant changes are observed when the salt concentration is increased to 1.0 M. Figure 6 summarizes the ^{13}C SP/MAS and CP/MAS results obtained on a sample containing MgO_{550} and 1.0 M $Mg(TFSI)_2$ in G2 after *in situ* heat treatment at 180°C for 1 hour. SP/MAS detects all the species regardless they are in the bulk solution or adsorbed onto the MgO surface. Six major peaks are found in the SP/MAS spectra (Figure 6a and a1) that are related to G2 and/or surface adsorbed G2-Mg-TFSI complexes with peaks centered at about 59.5, 61.11, 69.0, 69.84, 70.81, and 71.6 ppm in addition to two minor shoulder peaks at 58.75 and 72.6 ppm. A set of relatively sharp solution $–CF_3$ carbons located at 113.89, 118.3, 122.58 and 127.1 ppm are also

observed. The two minor shoulder peaks have ^{13}C chemical shifts similar to the major solution ^{13}C SP/MAS peak in Figure 5a1 for the 0.1 M $Mg(TFSI)_2$ in G2, and are thus readily assigned to G2 molecules in solution. This free solution G2 species accounts for approximately 7% of the observed G2 signals (Supporting Information). The CP/MAS spectra, which detects only those species that are tightly adsorbed onto the MgO surface, (Figure 6b and b1) clearly show (i) TFSI anion is adsorbed onto the MgO surface, evidenced by the relatively broad peaks located at about 118.3 and 122.4 ppm for TFSI; and (ii) G2 molecules are adsorbed onto the MgO surface with peaks at 59.28, 69.74 and 71.49 ppm. Given the similarities of the ^{13}C chemical shifts for the adsorbed G2 (Figure 6b1) and those in bulk solution (Figure 4e and f), the surface adsorbed G2 and TFSI must also maintain contact ion pairs in the same way as pure electrolytes of 1.0 M $Mg(TFSI)_2$ in G2. Three new and symmetric peaks in the CP/MAS spectrum (Figure 6b1) are observed at 60.94, 68.85 and 70.63 ppm. Compared with their counterparts in the SP spectrum (Figure 6a1), these three peaks in the CP spectrum are sharper and upfield shifted by about 0.2 ppm, a trend that is consistent with surface adsorption discussed throughout this work. Furthermore, these three peaks have shift trends, i.e., with the $–OCH_3$ group shifted downfield and the two CH_2 groups shifted upfield, similar to 1.0 M electrolyte concentration vs neat G2 but with about 1.0 ppm more magnitude than the neat 1.0 M electrolytes. Given this trend, we hypothesize a different solvation structure of Mg-TFSI contact ion pair by G2 on MgO surface rather than G2 decomposed products on MgO surface. Quantum chemistry calculations are utilized to help identify the possible structures related to the 60.94, 68.85 and 70.63 ppm ^{13}C peaks.

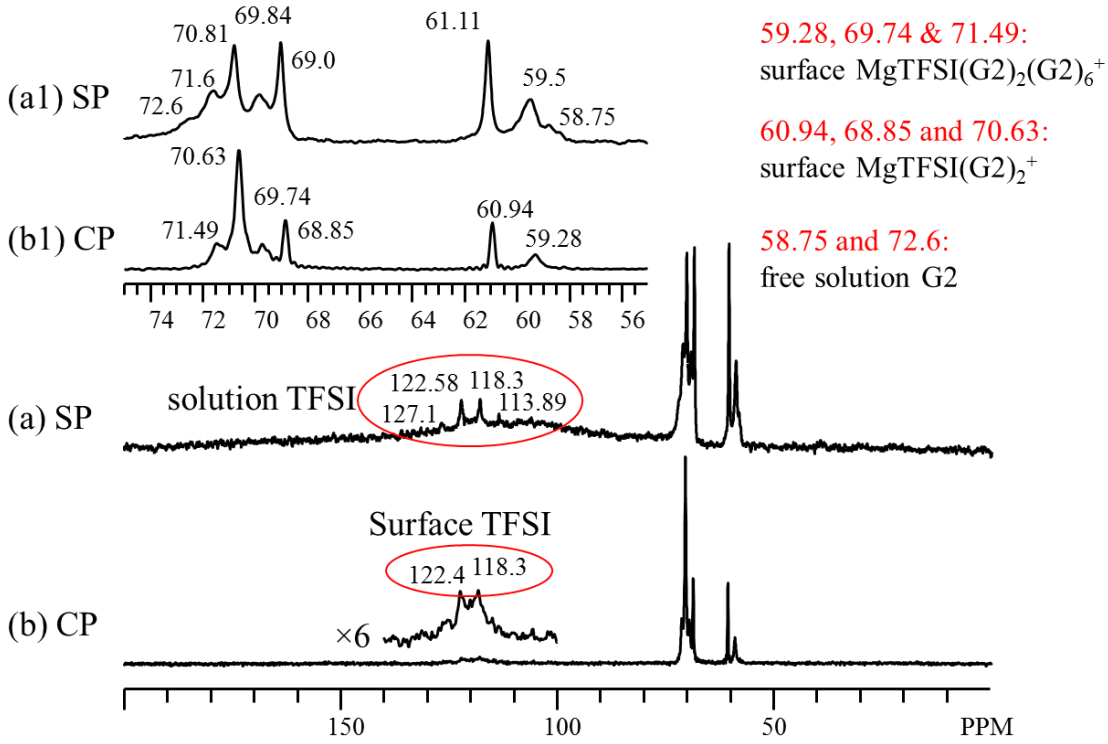

Figure 6. (a) ^{13}C SP/MAS (a) and CP/MAS (b) spectra obtained on 61.4 mg MgO_{550} (clean surface) + 36.5 mg 1.0 M $Mg(TFSI)_2$ in G2 after in situ heat treatment at 180 ℃ for 1 hour. (a1) and (b1) are horizontally expanded regions of (a) and (b), highlighting MgO surface mediated adsorption products with peaks at approximately 60.94, 68.85 and 70.63 ppm, surface adsorbed G2 with peaks located at approximately 59.28, 69.74 and 71.49 ppm, and surface adsorbed $TFSI^-$ at 118.3 and 122.4 ppm. Number of scans are 4,000 (a) and 70,500 (b) scans, respectively. No electrolytes decomposition is observed for this sample.

Quantum chemistry calculations

Validation of the methoxy groups on MgO surface: It is observed (Figure 2) that the decomposition of G2 over clean MgO surface produces a ^{13}C CP/MAS peak centered at about 50 ppm that is about 8.4 ppm upfield shifted relative to the $–OCH_3$ carbon in neat G2 (Figure 4). Quantum chemistry predicts a 7.7 ppm upfield shift relative to that of neat G2 (Figure 7a) using a small cluster model consisting of 8 Mg + 8 O and a $–CH_3$ group interacting with one of the interior O-atoms (Figure 7b). The excellent agreement between theory and the experimental

validates that the 50.0 ppm peak is indeed the $–OCH_3$ carbon from the decomposed G2. The decomposed $–OCH_3$ group occupying MgO surface lattice defect site would fit the model depicted in Figure 7. The remaining fragment of decomposed G2, i.e., CH_3-O-CH_2CH_2-OCH_2CH_2-, would interact with the MgO surface via the surface MgO lattice oxygen site, but the model in Figure 7 is too small for accurate prediction.

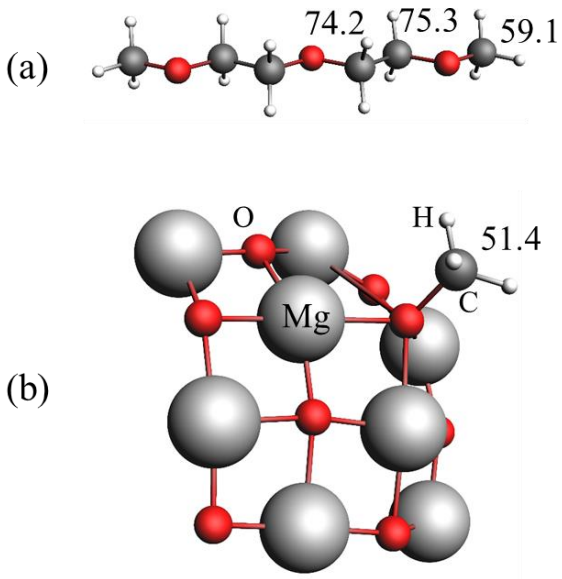

Figure 7. Models for quantum chemistry calculations of isotropic ^{13}C NMR chemical shielding. (a) Neat G2; (b) a $–OCH_3$ group on a model MgO surface carrying one positive charge simulating a surface defect site, i.e., an oxygen vacancy. The numbers labeled by the carbons are calculated absolute shielding.

Solvation structures in the electrolytes: For the 1.0 M $Mg(TFSI)_2$ in G2 sample there are, on average, 6.4 to 6.7 G2 molecules associated with one $Mg(TFSI)_2$. Contact ion pairs between Mg^{2+} and $TFSI^-$ form with the first solvation shell containing two G2 and the second solvation shell containing up to six G2 molecules are reported previously. [383] Given fast molecular exchange among the various G2 molecules, i.e., much faster than the NMR time scale of ms in

liquid, an average ^{13}C chemical shift of each chemically equivalent carbon is observed experimentally for each carbon position in G2 and TFSI. The calculated averaged ^{13}C chemical shifts for the models containing one pair of Mg-TFSI and two G2 in first shell, with 5 or 6 G2 in the second shell are listed in Table S18, where the calculated shifts on an isolated G2 molecule (i.e., neat G2) are also included for comparison. For the model of $(MgTFSI(G2)_2(G2)_6^+$, the results clearly show that the $–OCH_3$ carbon is downfield by about 0.83 ppm (higher ppm) relative to that of neat G2 while the two CH_2 carbons are upfield shifted by about 1.2 and 0.63 ppm (lower ppm) relative to those of neat G2, in excellent agreement with the experimental observations in Figure 4 (~1.0 ppm down field shift for $–OCH_3$ and about 1.0 ppm for each of the two CH_2 carbons experimentally). For the 0.1 M $Mg(TFSI)_2$ in G_2 sample, contact ion pairs (Mg-TFSI) should also form for part of the Mg^{2+} as the experimental ^{13}C chemical shift trends of the G2 (Figure 4) are similar to those of 1.0 M concentration albeit the amount of shifts are much smaller (i.e., with 0.03 ppm down field shift for $–OCH_3$ while about 0.11 and 0.06 ppm upfield shifted for the CH_2 carbons). The smaller shifts may be explained by the fast chemical exchange between the G2 in the solvation shells and those in the bulk solution since there are 90% of G2 are free. The existence of Mg^{2+} that are solvated only by G2 molecules for low $Mg(TFSI)_2$ concentration [383] is reported earlier that is validated by the calculated results on the model containing one Mg^{2+} solvated by 2 G2 in the 1st solvation shell and 5-6 G2 in the 2nd shells (Table S18). The calculated chemical shifts for the CH_2 carbons (averaged between the 1st and the 2nd shells) are almost the same to those of the neat G2 case while the $-OCH_3$ carbons is shifted downfield, a trend still consistent with experimental results on the 0.1 M Mg(TFSI)2 in G2 case. Given the large amount of free G2 in the 0.1 M sample, it is expected that most of the

Mg^{2+} are solvated only by G2 without forming contact Mg-TFSI ion pairs, consistent with the results obtained on the ^{25}Mg NMR and the related quantum chemistry studies earlier.[383]

*The nature of adsorbed species on MgO from ^{13}C CP/MAS for 1.0 M Mg(TFSI)2 in G2 (*Figure 6*b1)* Relative to the solvation structure of $MgTFSI(G2)_2(G2)_6^+$, the solvation structure of $MgTFSI(G2)_2^+$ predicted by quantum chemistry shows a downfield shift of 0.93 ppm for the –OCH_3 carbon of G2, and upfield shifts of 3.1 and 1.3 ppm for the two kinds of CH_2 carbons. These shift trends (i.e., up- or downfield) are in excellent agreement with experimental results of downfield shift of 1.7 for –OCH_3, upfield shifts of 0.89 and 0.86 ppm for the two CH_2 groups. Thus, we can assign the 60.94, 68.85 and 70.63 ppm ^{13}C peaks in the CP/MAS spectrum of the 1.0 M $Mg(TFSI)_2$ in G2 on MgO (Figure 6b1) to the solvated $MgTFSI(G2)_2^+$ clusters adsorbed on the MgO surface. It has been established above that the relatively broader peaks located at 59.28, 69.74, and 71.49 ppm in Figure 6b1 are from surface adsorbed $MgTFSI(G2)_2(G2)_6^+$ that is also the main solvation species in the 1.0 M sample. Based on the results obtained from this work, the physical picture of adsorption at high salt concentration of Mg(TFSI)2 in G2 (the 1M case) becomes clear. The solvation structure in the electrolytes ($MgTFSI(G2)_2(G2)_6^+$) interacts with the MgO surface and is thus captured in the CP spectrum. The MgO surface stimulates a desolvation process converting $MgTFSI(G2)_2(G2)_6^+$ to $MgTFSI(G2)_2^+$ and frees the G2 molecules in the second solvation shell of the $MgTFSI(G2)_2(G2)_6^+$ cluster back into the electrolyte solution. This lowers the concentration of the salt in the electrolytes, where the excessive G2 are observed in the ^{13}C SP spectrum with characteristic peaks at 58.75 and 72.6 ppm.

Conclusions

The adsorption and thermal decomposition of diglyme (G2) and electrolytes containing $Mg(TFSI)_2$ in G2 on 10 nm sized MgO particles are evaluated by a combination of *in situ* ^{13}C single pulse (SP), surface sensitive ^{1}H-^{13}C cross-polarization (CP) MAS NMR, and quantum chemistry calculations. The following results are obtained: At 180°C, neat G2 decomposes on MgO to form surface adsorbed $–OCH_3$ groups that are captured as a distinctive peak located at about 50 ppm in the CP/MAS spectrum. At low $Mg(TFSI)_2$ salt concentrations (i.e., 0.1 M $Mg(TFSI)_2$ in G2), the main solvation structure in this electrolytes is solvent-separated ion pairs, without extensive Mg-TFSI contact ion pairs. G2, likely including a small amount of G2 solvated Mg^{2+}, adsorbs onto the MgO surface. At high $Mg(TFSI)_2$ salt concentration (1.0 M $Mg(TFSI)_2$ in G2), contact ion pairs between Mg and TFSI are formed extensively in the solution with the first solvation shell containing one pair of Mg-TFSI and two G2 molecules and the second solvation shell containing up to six G2 molecules, namely, $MgTFSI(G2)_2(G2)_6^+$. In the presence of MgO, $MgTFSI(G2)_2(G2)_6^+$ adsorbs onto the MgO surface. Upon increasing the temperature to 180°C, the MgO surface stimulates a desolvation process converting $MgTFSI(G2)_2(G2)_6^+$ to $MgTFSI(G2)_2^+$, releasing G2 molecules from the second solvation shell of the $MgTFSI(G2)_2(G2)_6^+$ cluster into the solution. The $MgTFSI(G2)_2^+$ and $MgTFSI(G2)_2(G2)_6^+$ tightly adsorb onto the MgO surface and are observed by ^{1}H-^{13}C CP/MAS experiments. The results contained herein show that electrolyte composition has a directing role in the species present on the electrode surface, which has implications on the structures and

constituents of the solid-electrolyte interface on working electrodes and can be used to better understand its formation and the failure modes of batteries.

Table S18. Quantum chemistry predicted ^{13}C isotropic chemical shifts on various models of solvation structures of $Mg(TFSI)_2$ in G2. The chemical shifts are referenced to adamantane at 38.48 ppm: $\delta_{obs} = 136.08 - \delta_{calc} + 38.48$.

Structure	Label	CH_3 Avg. ppm (1^{st})[a] [2^{nd}][b]	CH_2 - Inner Avg. ppm (1^{st}) [2^{nd}]	CH_2 - Outer Avg. ppm (1^{st}) [2^{nd}]
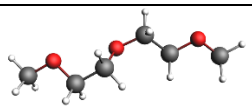	G2	59.07	74.15	75.27
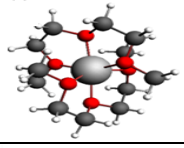	$Mg(G2)_2^{2+}$	61.71	73.14	74.11
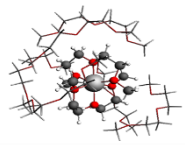	$Mg(G2)_2[G2]_6^{2+}$	61.12 (64.29) [60.07]	74.27 (72.88) [74.73]	75.21 (74.7) [75.38]
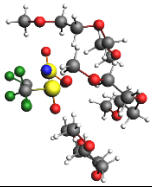	$TFSI(G2)_3^{-}$	58.9	75.2	76.8
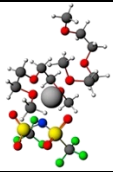	$MgTFSI(G2)_2^{+}$	60.83	69.83	73.30
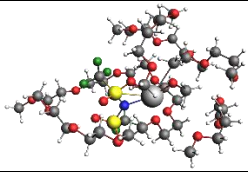	$MgTFSI(G2)_2[G2]_5^{+}$	60.8 (63.3) [59.8]	72.8 (70.9) [73.6]	75.1 (73.4) [75.7]
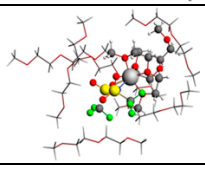	$MgTFSI(G2)_2[G2]_6^{+}$	59.9 (62.64) [58.99]	72.94 (71.31) [73.49]	74.64 (74.25) [74.77]

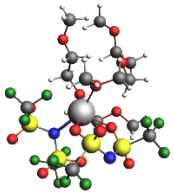	$MgTFSI_2(G2)_2$	59.1	76.4	75.7
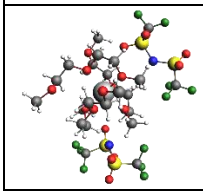	$MgTFSI_2(G2)_3$ From crystal	61.97	75.59	72.52

Note: [a] The average chemical shifts of each chemically equivalent carbon in the first solvation shell.

[b] The average chemical shifts of each chemically equivalent carbon in the second solvation shell.

Appendix I: Publication – Catalytic activation of ethylene C-H bonds on uniform d^8 Ir(I) and Ni(II) cations in zeolites: toward molecular level understanding of ethylene polymerization on heterogeneous catalysts

From Nicholas R. Jaegers,[&,*] Konstantin Khivantsev,[&,*] Libor Kovarik, Daniel W. Klas, Jian Zhi Hu, Yong Wang, and János Szanyi[&*] *Catalysis Science & Technology* 2019

ABSTRACT:

The homolytic activation of the strong C-H bonds in ethylene is demonstrated, for the first time, on d^8 Ir(I) and Ni(II) single atoms in the cationic positions of zeolites H-FAU and H-BEA under ambient conditions. The oxidative addition of C_2H_4 to the metal center occurs with the formation of a d^6 metal vinyl hydride, explaining the initiation of the olefin-polymerization cycle on d^8 M(I/II) sites in the absence of pre-existing M-H bonds. Under mild reaction conditions (80-220^{o}C, 1 bar), the catalytic dimerization to butenes and dehydrogenative coupling of ethylene to butadiene occurs over these catalysts. 1-Butene is not converted to butadiene under the reaction conditions applied. Post-reaction characterization of the two materials reveals that the active metal cations remain site-isolated whereas deactivation occurs due to the formation of carbonaceous deposits on the zeolites. Our findings have significant implications for the molecular level understanding of ethylene conversion and the development of new ways to functionalize C-H bonds under mild conditions.

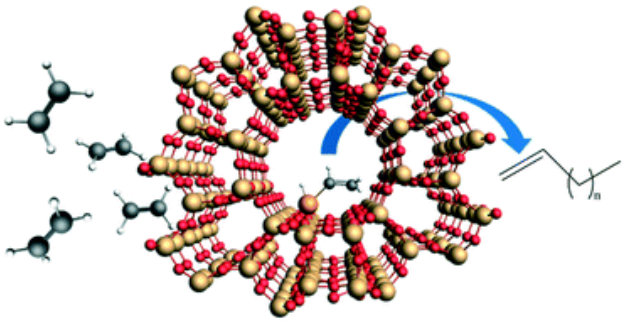

Zeolite-supported transition metals (single atoms, clusters, nanoparticles, etc.) represent an important class of materials with uses in the chemical industry, emissions controls, and as model systems to derive structure-function properties in catalysis.[83, 402-409] Among them, d^8 metals such as Ni(II), Rh(I), Ir(I), Pt(II), and Pd(II) have been the focus of many studies to better understand the genesis, speciation, and stability of such species for reactions such as hydrogenations, oxidations, as well as ethylene transformation (di- and oligomerization to butenes and higher oligomers).[410-413] For example, it was shown first in the 1950s that $Rh(I)(CO)_2$ and $Ir(I)(CO)_2$ species can be stabilized on oxide supports[414-415] and are active for ethylene conversion to butenes at room temperature, retaining their site-isolated nature after catalysis.[416-418]

The Rh ligand environment is tunable and hydrogen promotes butene formation despite not directly participating in the dimerization reaction (i.e., $2C_2H_4 \rightarrow C_4H_8$).[412, 417-418] This effect was explained in some studies by H_2 enhancing butene desorption on ($Rh(C_2H_4)_2$/HY).[16] Recently, however, the hydrogen partial pressure dependence of ethylene dimerization was systematically measured on $Rh(CO)_2$, $Rh(CO)(C_2H_4)$, Rh(CO)(H),[417] and $Rh(NO)_2$[412] complexes supported on HY zeolites. Positive reaction orders of ~0.7-1 confirmed that hydrogen indeed

promotes dimerization, where H_2 was shown to improve the rate of ethylene dimerization up to ~10 fold.[12,417] This was attributed to the formation of metal-hydride-supported species (observed and characterized experimentally[12,17,18]) which provide a low-energy pathway for dimerization via facile insertion of pi-coordinated ethylene into the M-H bond to form an M-Ethyl moiety which subsequently migrates into another pi-coordinated ethylene to form a Rh-Butyl species prior to facile β-H abstraction to produce butene-1.[412] This attribution was subsequently supported for ethylene dimerization on Ni/BEA, although Ni-H species were not observed directly.[419] Until now, it remained unclear how ethylene, in the absence of M-hydride species, can polymerize considering the importance of M-H intermediates in the Cossee-Arlman mechanism. Theoretical studies have identified potential mechanisms for ethylene dimerization on Ni/BEA where the metallocycle, proton-transfer, and Cossee-Arlman mechanisms were compared.[420] Also considered was the non-catalytic formation of a nickel vinyl intermediate via the heterolytic activation of a C-H bond over Ni(II)-O bond followed by the formation of an active Ni center.[20]

In this study, we demonstrate: 1). Preparation and characterization of highly uniform d^8 metal species. Ni(II) was selected because it has been a challenge to prepare well-defined uniform Ni-zeolite species. We have previously prepared d^8 Pt(II) and Pd(II) species[9] in zeolite uniformly and thus transferred this approach to a Ni/BEA system in order to unravel detailed structure catalytic-property relationships for the historically important system for ethylene polymerization. We also employ the well-defined square planar d^8 $Ir(I)(CO)_2$ complex anchored in zeolite FAU (like Ni(II)/FAU) because it grafts uniformly in zeolite and also has CO groups which, due to their high molar extinction coefficients and well-resolved nature, allow us to

observe ligand changes with enhanced resolution. 2). We obtain the reactivity for ethylene couplings on those materials, showing similar trends for both d^8 metals 3). We resolve a longstanding uncertainty in heterogeneous ethylene polymerization, one of the largest catalytic processes. Though supported metal ions (d^8 like Ni(II), Ir(I), Pd(II) or d^4 Cr(II) perform this reaction without the initiator/co-catalyst, the mechanism for ethylene polymerization initiation and the relevant intermediates involved have remained elusive for the last 50 years. We resolve these uncertainties using state-of-the-art infrared studies supported by microscopy and solid-state NMR measurements[58] for d^8 metal cations on solid supports. In short, ethylene polymerization starts with the homolytic activation of the C-H bonds of ethylene on extremely electrophilic d^8 M sites, resulting in the formation of d^6 metal vinyl hydride complexes which further react with ethylene to form a vinyl ethyl d^6 metal fragment. From this fragment, 1-butene can form either via direct reductive elimination or a Cossee-Arlman type step involving alkyl chain growth through alkyl migration and insertion into M-ethylene bonds.

Though reported for other d^8 metals, it is not straightforward to generate uniform Ni(II) species since they may graft to both silanol nests and various extra-framework zeolite positions, evidenced by IR spectroscopy of CO adsorption.[419] This brought into question the true active center for ethylene oligomerization activity.[421] To better understand the active centers for ethylene dimerization, well-defined supported complexes of Ir(I) and Ni(II) were generated, characterized, and tested in this study. These active centers not only demonstrate activity to butenes, but butadiene as well; a notable result since 1,3-butadiene is a high-value commodity chemical (~10 million tons per annum) that serves as a precursor to a wide range of plastics and

polymers. These reactions proceed via activation of C-H bonds of ethylene on a super electrophilic cationic metal center recently observed for a metal/zeolite system.[422]

A modified IWI method was previously used to produce atomically dispersed Pt and Pd in SSZ-13.[83] We slightly altered this procedure to synthesize 0.4 wt% Ni on BEA by reacting aqueous nickel nitrate with excess ammonia to produce a mononuclear Ni hexamine complex. This mitigates the formation of hydroxo-bridged Ni complexes, which are precursors to NiO nanoparticles, similar to the aqueous solution of $Pd(NO_3)_2$ that has the propensity to darken and form …-OH-Pd-OH-Pd-OH-… networks over time, even in acidic solutions.[83, 233, 423] The micropores of BEA zeolite (Si/Al ~ 12.5) were impregnated with this complex, dried in ambient air, and calcined at 550°C in static air. Infrared spectroscopy of adsorbed CO on this material substantiates the exclusive formation of 1 type of Ni(II)-CO in BEA zeolite. The C-O stretching vibrational band of this species is located at 2,211 cm^{-1} (Figure 8A).

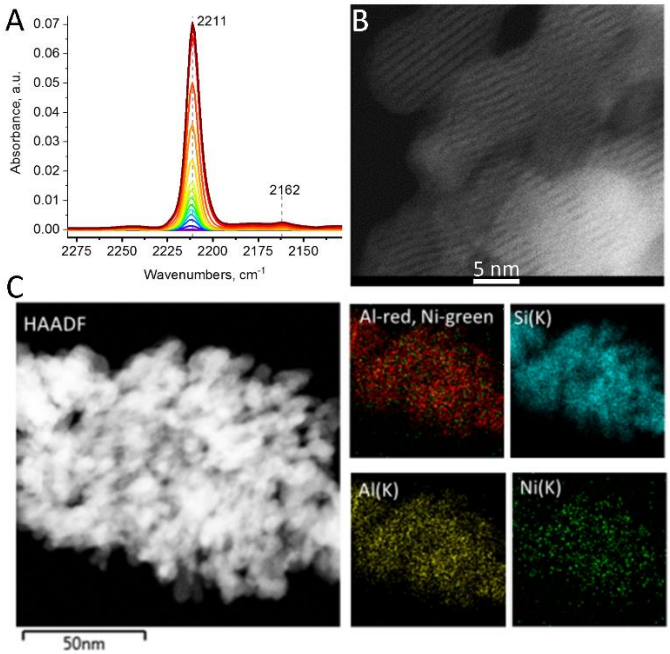

Figure 8. A). FTIR during CO adsorption on dry 0.4% Ni/BEA, P(CO)max=5 Torr (the band at 2162 cm-1 represents adsorbed 13CO molecules) B). High-resolution HAADF-STEM image of the 0.4% Ni/BEA material: straight channels in BEA nanocrystals are clearly imaged. No NiO clusters or particles observed (additional HAADF-STEM images provided in Figure S101) C). EDS mapping of Ni, Al, Si, and Ni/Al overlay in 0.4% Ni/BEA.

No NiO clusters or nanoparticles could be observed in the channels of BEA. EDS mapping confirmed the presence of Ni associated with BEA, corroborating the presence of uniform, isolated Ni sites in the sample (Fig. 1B and C, Figure S100-S3). Comprehensive interconversion maps of Ni(II)-CO, Ni(II)-NO, Ni(II)-C_2H_4, and Ni(II)(NO)(CO) complexes, never prepared through classical organometallic routes are discussed and available in the Supporting Information (Figure S103-S17). These provide new insight into the Ni/Zeolite chemistry complementary to the previous pioneering studies of Petkov et al.[424] In particular, a new phenomenon in solid supported systems is identified whereby low-temperature CO adsorption produces 2 peaks at 2,214 and 2,204 cm^{-1} (Figure S110), that do not belong to the Ni(II)$(CO)_2$ dicarbonyl complex (evidenced by their contrasting interactions with C_2H_4 and stability under vacuum, Figs. S12, S13). However, CO adsorption at room temperature produces only 1 band at 2,211 cm^{-1}. This indicates that at low temperatures, distinctive Al T-sites exist while at room temperature these sites become degenerate, possibly due to the flexibility of the zeolite framework or relativistic effects, revealing only the 2,211 cm^{-1} feature from CO adsorption on super electrophilic Ni(II)/2Al centers.

Unlike Rh(I)/FAU complexes, for which initial ligand environment impacts ethylene dimerization,[412, 417-418] both Ni(II)-CO and Ni(II)-NO undergo ligand replacement by ethylene to form Ni(II)-C_2H_4 complex under ambient conditions and lower temperatures (Figure S104, S9, S13-S15). This material was active for ethylene transformation to butenes, demonstrating that Ni(II) in the ion-exchange position is active for catalysis (Table S19). Remarkably, 80ºC was

sufficient to observe activity for both butadiene as well as butenes (1-butene as well as cis- and trans-2-butene) formation. Selectivity initially favored butadiene at 120ºC (~65%, TOF ~122 hr^{-1} with respect to butadiene formed and ~240 hr^{-1} with respect to ethylene molecules reacted, Table S1), however, selectivity quickly dropped to ~10% within the first 30 minutes (TOF ~ 10 hr^{-1}). Above 180ºC, activity for butadiene production is enhanced with selectivity around 20-30% on a molar basis at 200ºC and initial TOF ~200 hr^{-1}. Even at elevated temperatures, deactivation is observed both for butene and butadiene production with time on stream.

These results are noteworthy since C-H bond activation in ethylene (22 kJ/mol stronger than methane at 298K) is a challenging catalytic step. Accordingly, functionalization of ethylene typically involves reactions with its C=C bond and not the C-H bond directly. By activating the C-H bond in ethylene, the formal coupling of two vinyl C_2H_3 fragments enables the formation of butadiene.

Catalytically, butadiene can be produced by dehydrogenation of n-butane and 1-butene (Houdry process) or by ethanol conversion to butadiene, hydrogen, and water over a mixed metal oxide catalyst (Lebedev and Ostromyslenski process). These catalytic processes with unpromoted catalysts produce butadiene unselectively and are energy intensive (400-700°C).[425] The best current processes based on ethanol show excellent selectivity to butadiene for promoted materials (>90%) whereas the unpromoted, historically important Ta-containing material has a selectivity of ~15%. However, this process relies on a low ethanol feed rate (GHSV), features turnovers of ~ 1 hr^{-1} at 320°C, and suffers deactivation due to formation of polymeric carbonaceous deposits.[376, 426]

Though pathways from alcohol feedstocks exist, the catalytic conversion of ethylene to butadiene remains effectively unprecedented with just a few examples proposed. In 1983, $(C_5(CH_3)_5)_2Ti(C_2H_4)$ complexes in aromatic solvents were suggested to convert ethylene into 1,3-butadiene and ethane at 25°C and ~4 atm in a sealed batch reactor, though the reported TOF after one year was ~1-2 $year^{-1}$, rendering catalysis indeterminate.[427] Notably, in 2015 ethylene has been selectively converted to butadiene over FAU-supported $Rh(CO)_2$ and $Rh(CO)(C_2H_4)$ single-atom catalysts at 25ºC and 1 atm under continuous ethylene flow, yielding a TOF of ~2 hr^{-1},[417] marking the discovery of the dehydrogenative coupling of ethylene into butadiene ($2C_2H_4 \rightarrow C_4H_6 + H_2$). In 2018, an $Ir(C_2H_4)_2$(Phebox) organometallic complex was shown to convert ethylene catalytically via $3C_2H_4 \rightarrow C_4H_6 + C_2H_6$ with butene by-products [$S_{C4H6} < 45\%$; P: 2-12 atm; TOF: 0.25 hr^{-1} at 2 atm/100°C, 0.9 hr^{-1} at 12 atm/110ºC].[428] Despite this progress, the catalytic chemistry of butadiene formation from a cheap ethylene feedstock under mild conditions remains unattained, demonstrating the relevance of the observed butadiene activity at 120ºC for Ni/BEA. We note that fast deactivation at this temperature is not surprising considering that H-zeolites are often used as butadiene adsorbents.[429]

After catalysis, exposure of the sample to CO restores the original 2,211 cm^{-1} feature (Figure S115-S17), but to a lesser extent due to unsaturated carbonaceous deposits blocking the active sites, further confirmed by *in situ* ^{13}C NMR (Figure S123).[235] The absence of vibrational signatures for Ni(I) and Ni(0) carbonyl complexes further suggests that no reduction of Ni(II) occurred during ethylene dimerization and that Ni(II) in the ion-exchange positions of the zeolite is the active site in ethylene dimerization (Figure S116).

Moreover, post-reaction (200ºC in ethylene flow) CO adsorption reveals a peak around ~2,230 cm^{-1} (Figure S115-17) not present in the fresh sample. This corresponds to CO adsorbed on extraframework aluminium[430] formed under mild catalytic conditions in the presence of Ni(II) atoms and ethylene. Solid-state NMR further confirms this result via comparison of ^{27}Al MAS NMR spectra of fresh and spent samples (Figure S117) which show that dealumination indeed occurs under mild conditions, evidenced by a feature at ~30 ppm due to the presence of penta-coordinate extraframework Al sites as well as broadening of tetrahedral Al bands. Such mild conditions have been not previously reported to cause dealumination of the zeolite framework. This is likely due to polymerization of ethylene in the microporous channels and the subsequent breakage of pores.

In addition to the supported d^8 Ni(II) species, a 0.7 wt% $Ir(CO)_2$ species was prepared on H-FAU zeolite with Si/Al ~15 as for Ni/BEA. This formulation was previously characterized with EXAFS and FTIR,[431] where its interaction with ethylene was reported to produce $Ir(CO)(C_2H_4)$ complexes. Pulses of ethylene, followed by inert gas purging indeed produce only the $Ir(CO)(C_2H_4)$ complex in this study (Figure 9A,C).

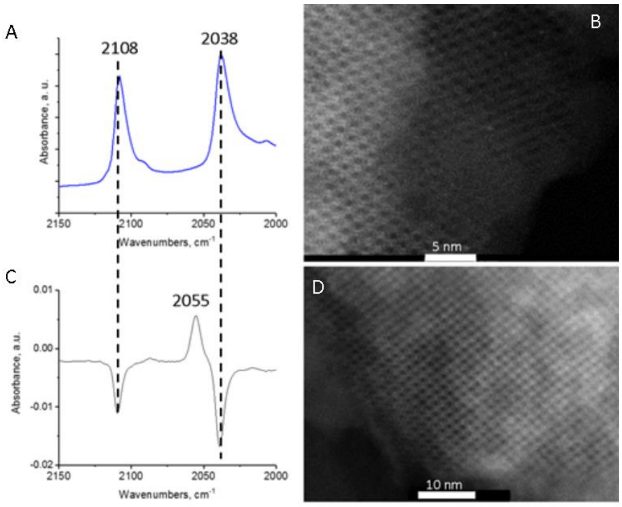

Figure 9. A). DRIFTS spectrum of the starting 0.7% Ir(CO)2/FAU Si/Al~15 material B). High-resolution HAADF-STEM image of the fresh Ir/FAU in [110] projection, individual Ir atoms can be seen in the supercages C). DRIFTS difference spectrum during reaction of Ir(CO)2/FAU with pulses of dilute ethylene, showing disappearance of 2,108 and 2,038 cm-1 bands of Ir(CO)2 and appearance of only 1 new band at 2,055 cm-1, belonging to Ir(CO)(C2H4)/FAU complex. D). High-resolution HAADF-STEM image of Ir(CO)2/FAU after ethylene catalysis at 225ºC for 1 hour, in the [110] projection, showing lack of Ir agglomeration.

DRIFTS confirms the successful grafting of the complex with the formation of symmetric and asymmetric CO stretches of the square-planar $Ir(CO)_2$ fragment at 2,108 and 2,038 cm^{-1}.[12,17,18] HAADF-STEM imaging (Figure S119, 2B) further confirms site-isolated nature of the complex in the zeolite micropores. Sample exposure to flowing pure C_2H_4 in the DRIFTS cell revealed transient behavior (Figure 10).

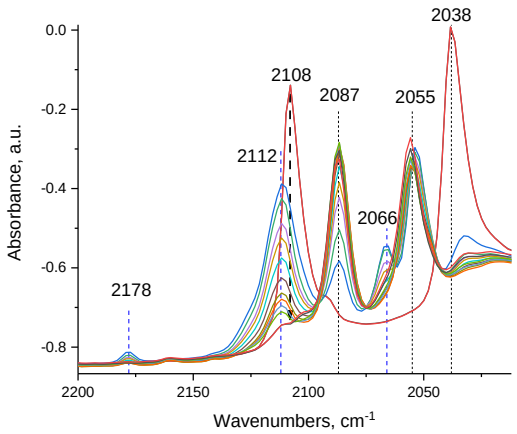

Figure 10. DRIFTS spectrum of 0.7% Ir(CO)2/FAU Si/Al~15 during exposure to flowing pure ethylene (the first 5 minutes).

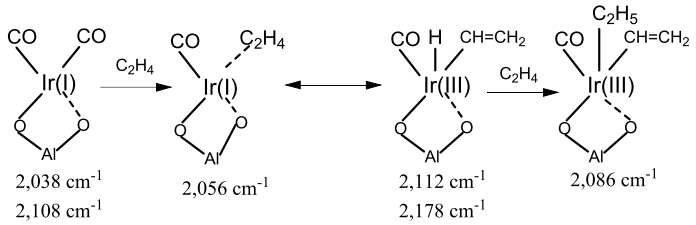

The peaks, belonging to the symmetric and asymmetric CO stretches of $Ir(CO)_2$, at 2,108 and 2,038 cm^{-1} declined while new features emerged. The 2,055 cm^{-1} feature has been previously assigned to the $Ir(CO)(C_2H_4)$ complex[12,17,18]; however, careful inspection of the spectra in the 2,060 – 2,030 cm^{-1} region reveals new features (Figure 11): the 2,066 and 2,053 cm^{-1} peaks decrease in concert as the 2,056 cm^{-1} feature of $Ir(CO)(C_2H_4)$ grows with clear isosbestic points (shaded).

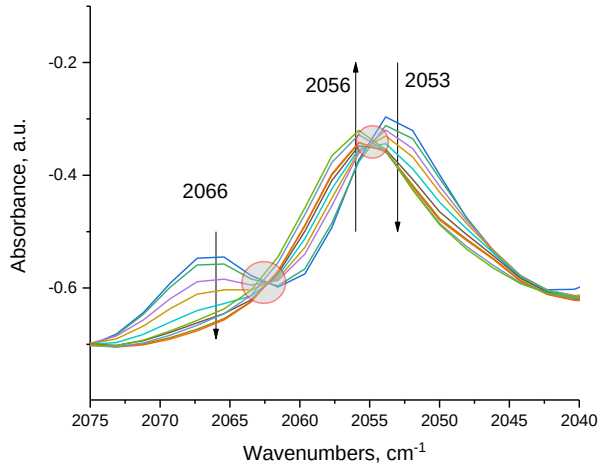

Figure 11. DRIFTS spectrum of 0.7% $Ir(CO)_2$/FAU Si/Al~15 during exposure to flowing ethylene (initial 5 minutes).

This indicates the stoichiometric transformation of $Ir(CO)_2$ into $Ir(CO)(C_2H_4)$, occurring via the following sequence:

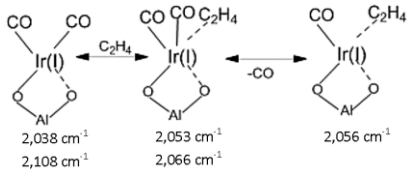

Initially, the square-planar $Ir(CO)_2$ accepts one C_2H_4 ligand to form a $Ir(CO)_2(C_2H_4)$ species which then expels one CO ligand, forming square-planar $Ir(CO)(C_2H_4)$. Concomitantly bands at 2,178 cm^{-1} (weak) and 2,112 cm^{-1} (intense) develop within the first 1 minute of ethylene exposure (Figure 12).

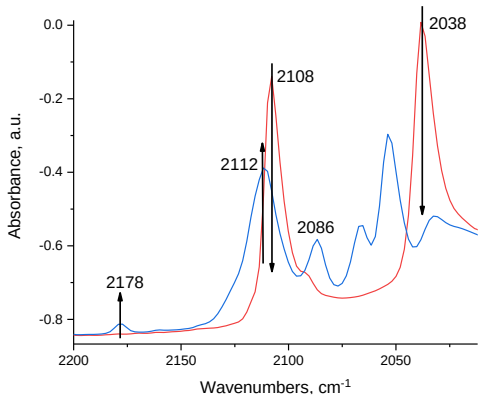

Figure 12. DRIFTS spectrum of 0.7% Ir(CO)2/FAU Si/Al~15 during exposure to ethylene (~1 minute). 2,178 and 2,112 cm-1 grow in concert.

The intense 2,112 cm^{-1} band belongs to the CO vibration of an oxidized Ir center (CO adsorbed on metal cations has high molar extinction coefficients) and the low intensity 2,178 cm^{-1} band corresponds to the Ir-H stretching vibration. Indeed, this fully agrees with the described synthesis of the first supported, transition metal carbonyl hydride complexes of $Rh(III)(H)_x(CO)$. and relatively low intensity of Rh-H stretching vibrations compared to CO vibrations. [17,18] We note that Rh(III) and Ir(III) have the same d^6 electronic configuration and provide the analogous (to Rh) synthesis of Ir(III) carbonyl hydride complex,[18] unambiguously identifying the Ir-H stretch at 2,150 cm^{-1}. Analogous to the selective synthesis of $Rh(III)(CO)H_2$ complexes from $Rh(CO)_2$,[18] the $Ir(CO)H_x$ species has been suggested from treatments of $Ir(CO)_2$/FAU with ethylene followed by hydrogen.[431] In that study, the authors failed to identify the Ir-H stretch, concluding that its signature is too weak to be observed. We treated our $Ir(CO)_2$

materials with C_2D_4, forming first Ir(I)(CO)(C_2D_4) which we then exposed to H_2 flow (Figs. S29, S30, S31). Both the actual spectra and difference spectra indicate selective conversion of Ir(CO)(C_2D_4) to the Ir(CO)$(H)_2$ complex with CO stretching observed at 2,065 cm^{-1} and the Ir-H stretch at 2,150 cm^{-1}. Isotopic shift experiments with D_2 (Fig. S31) confirm that the 2,150 cm^{-1} is indeed the Ir-H stretch.

As such, the simultaneous formation of new Ir-H and Ir-CO stretches arise from the generation of one species. The high-lying stretch of Ir-CO means that Ir is in the +3 oxidation state, signifying the unprecedented oxidative addition of the C-H bonds of ethylene to the Ir(CO) fragment with the formation of Ir(III)(CO)(H)(C_2H_3) carbonyl vynil hydrido-complex: C_2H_4-Ir(I)-CO ←→ C_2H_3-Ir(III)(H)(CO). These assignments and described behavior are further supported by observation of these species the *in situ* NMR data (Figure S23).

As the concentration of this complex reaches its maximum (~1 minute), the intensities of both the 2,112 and 2,178 cm^{-1} features reach their maxima and then decline in concert as a new CO stretching band develops at 2,086 cm^{-1} that has no corresponding Ir-H stretching band (Figure 13). This indicates the hydride is consumed during the reaction with ethylene. This suggests the consequent formation of an Ir(III)(CO)(C_2H_5)(C_2H_3) complex via ethylene insertion into the Ir-H bond.

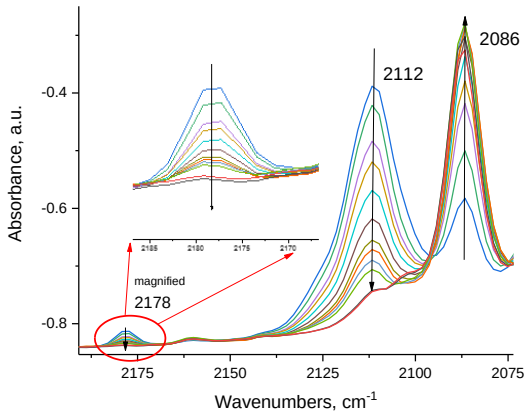

Figure 13. DRIFTS spectrum of 0.7% $Ir(CO)_2$/FAU during exposure to ethylene (~5 minutes). The 2,112 and 2,178 cm^{-1} bands decline simultaneously as the 2,087 cm^{-1} feature grows.

Furthermore, in order to unambiguously assign the 2,178 cm^{-1} band to the Ir-H stretch, we replicated the infrared experiment on $Ir(CO)_2$ and C_2H_4 with C_2D_4. We observed the absence of the 2,178 cm^{-1} band (Ir-H stretch), upon oxidative addition of C_2D_4 to the Ir(I) center. Instead, Ir(III)-D species forms (Fig. S32).

The observed room-temperature activation of C-H bonds with the formation of iridium carbonyl alkyl hydride complex is unprecedented. Such transformation have been only rarely described in organometallic literature[432] and never directly observed spectroscopically on any solid material. The bond is not split heterolytically on the M-O bond but instead it is activated homolytically via oxidative addition to an electrophilic d^8 metal center in the zeolite micropore. High coordinative unsaturation and superelectrophilicity of M cations in zeolite have been recently quantified for isoelectronic d^8 Pd(II) ions,[422] explaining why this reaction is favored over heterolytic activation of C-H bonds on covalent M-O bond. It is important to note that such a homolytic pathway of C-H bond activation has been previously overlooked in the metal/zeolite

and M/oxide literature. Indeed, heterolytic activation of strong X-H bonds (C-H of hydrocarbons and N-H of ammonia) normally require relatively high temperatures.[433-434]

Ethylene activity over $Ir(CO)_2$/FAU produces measurable amounts of butenes at temperatures above 80ºC and butadiene at temperatures above 180 ºC with the maximum rate of catalytic butadiene production at ~200-220ºC and selectivities to butadiene on the order 17-20% (Table S20). After catalysis, Ir remains site-isolated and does not agglomerate into Ir nanoparticles as evidenced by HAADF-STEM and FTIR data (Figure 9D). Formation of carbonaceous polymeric deposits, framework breakage, and dealumination similar to Ni/BEA is also observed. The ease with which oxidative addition of ethylene C-H bond to highly electrophilic Ir(I) center takes place at room temperature at 1 bar pressure of ethylene, suggests that C-H activation is not the rate-limiting step of the ethylene dimerization under these conditions: C-C coupling and/or beta-hydride elimination are expected to be rate-limiting steps in catalysis.

We construct two plausible catalytic pathways for butadiene (and butene) production. Two different steps of initial C-H bond activation are possible: 1) homolytic activation of C-H bond via oxidative addition to M d^8 center, which we observe experimentally (Figure S125) and 2) heterolytic activation of C-H bond on the M-Ozeolite pair (Figure S126), which we did not observe. Two ethylene molecules could also couple on single d^8 metal center with the formation of metallacyclopentane species (Figure S127), that were shown by Goldman and co-workers to form on $Ir(C_2H_4)_2$(Phebox) system by trapping via CO.[428] The stability of the species, as noted previously by Halpern,[435] does not mean that it is the true active state of the catalyst. Indeed,

most active species are formed transiently (as we observe experimentally for Ir(III)(H)(CO)(C_2H_3) species), hence mechanism in Fig. S26 is most likely operative.

Furthermore, deeper mechanistic insight into the pathway of butadiene production was achieved by refuting the direct dehydrogenation of butene into butadiene. When 1-butene was introduced to the catalyst at 150-200ºC, no butadiene was observed. Thus, the route to butadiene mechanistically differs from direct butene dehydrogenation. Indeed, such dehydrogenation does not take place on single Ir atoms under such mild conditions.

Notably, in the most probable reaction mechanism depicted in Fig. S26, we propose 1-butene formation directly from Ir(III)(CO)(C_2H_5)(C_2H_3) and Ni(IV)(C_2H_5)(C_2H_3) via reductive elimination of the ethyl and vinyl fragments with restoration of Ni(II) and Ir(I)-CO fragments which reform Ni(II)(C_2H_4) and Ir(I)(CO)(C_2H_4) in the presence of ethylene. It is also possible that beta-hydride elimination releases 1-butene from the M-(n-Butyl) intermediate, which forms when the ethyl group in M(C_2H_4)(C_2H_5) migrates. Butadiene may be formed analogous to this scheme but in this case the vinyl group of M(C_2H_3)(C_2H_4) fragment migrates, forming M-CH_2-CH_2-CH=CH_2, from which via beta-hydride elimination butadiene-1,3 is released.

These findings for supported Ni(II) and Ir(I) isolated sites may help reveal mechanistic uncertainties for the Cr/SiO_2 Phillips ethylene polymerization catalyst, extensively studied over 50 years. Though believed to follow a Cossee-Arlman Cr-alkyl mechanism, the low number of active sites (<10%), amorphous silica support, fast reaction rates, and the presence of multiple oxidation states of Cr prevented a thorough understanding of the initiation mechanism. Recent elegant studies[436] demonstrated that Cr(II) sites are required to start ethylene polymerization, and earlier kinetic studies suggested schemes consistent with activation of ethylene on Cr(II) sites to

form Cr(IV) vinyl hydride,[437-438] though this species has never been observed. Based on our current findings, we suggest that the active fraction of the catalyst could be the highly electrophilic Cr(II) species that can add ethylene via C-H oxidative addition to form a Cr(IV)-vinyl (C_2H_3)-hydride (H) species:

$$Cr(II) + C_2H_4 \leftrightarrow Cr(IV)(H)(CH=CH_2)$$

The formation of Cr-ethyl follows:

$$Cr(IV)(H)(CH=CH_2) + C_2H_4 \rightarrow Cr(IV)(C_2H_4)(H)(C_2H_3) \rightarrow Cr(IV)(C_2H_5)(C_2H_3).$$

$Cr(IV)(C_2H_5)(C_2H_3)$ sites may facilitate longer alkyl chain formation via alkyl migration:

$$Cr(C_2H_5)(C_2H_3) + C_2H_4 \rightarrow Cr(C_2H_4)(C_2H_5)(C_2H_3) \rightarrow Cr(C_4H_9)(C_2H_3)$$

$$Cr(IV)(C_4H_9)(C_2H_3) + nC_2H_4 \rightarrow Cr(IV)[(CH_2)_{3+2n}\,CH_3](C_2H_3)$$

Subsequently, direct reductive elimination of $CH_3(CH_2)_xCH=CH_2$ is possible which restores the Cr(II) site and re-starts the catalytic cycle:

$$Cr(IV)[(CH_2)_x\text{-}CH_3](C_2H_3) \rightarrow Cr(II)/SiO_2 + CH_3\text{-}(CH_2)_x\text{-}CH=CH_2$$

Beta-hydride elimination from $Cr(IV)[(CH_2)_x\text{-}CH_3](C_2H_3)$ could also restore $Cr(IV)(H)(C_2H_3)$ and re-start the polymerization cycle:

$$Cr(IV)[(CH_2)_x\text{-}CH_3](C_2H_3) \rightarrow Cr(IV)(H)(C_2H_3) + CH_3\text{-}(CH_2)_{x-2}\text{-}CH=CH_2$$

The proposed mechanism does not contradict experimental observations and provides a plausible explanation for the initiation uncertainties of the Phillips catalyst. Furthermore, support for this proposed mechanism is obtained from recent works, in which $\text{-}CH_2\text{-}CH_2\text{-}CH=CH_2$ sites

were suggested to form on the catalyst.[439] These sites can form from the vinyl migration in the following reaction sequence:

$Cr(IV)(C_2H_5)(C_2H_3) + C_2H_4 \rightarrow Cr(IV)(C_2H_4)(C_2H_5)(CH{=}CH_2) \rightarrow Cr(IV)(C_2H_5)(CH_2\text{-}CH_2\text{-}CH{=}CH_2)$

In conclusion, we provide the first experimental mechanistic evidence of how ethylene dimerization occurs and proceeds on d^8 M(I and II) cations in zeolites in the absence of an initial M-H species: the M-H bond is formed via the homolytic activation of ethylene's C-H bond (stronger than that of methane) on very electrophilic Ir(I) sites in the zeolite micropore. Further, the preparation of well-defined Ir(I) and Ni(II) d^8 in zeolites is demonstrated and accompanied by new chemistry and characterization for both systems before and after catalysis. Both Ni(II) and Ir(I) in zeolites produce butenes and, unprecedentedly, butadiene upon reaction with ethylene under mild conditions. Notably, Ni is more active at lower temperatures toward C-H bond activation than the expensive Ir.

Experimental Methods

Faujasite and Beta zeolites with Si/Al of ~15 and 12.5 respectively, were supplied by Zeolyst in the ammonium form. Transformation of faujasite to the H-form was conducted by calcination in flowing dry air at 400ºC followed by evacuation at 10^{-5} Torr and 400ºC. It was subsequently stored in a VAC moisture- and oxygen-free glovebox. Single iridium atoms were then anchored in the micropore supercages of the prepared H-FAU zeolite. To ensure suitable dispersion, a well-defined square planar $Ir(CO)_2(Acac)$ complex (strem, >98% purity) was delivered into the micropores via a non-polar solvent propagation method[12,17,18]. More

specifically, the precursor was dissolved in pentane (Sigma Aldrich, <10 ppm moisture) and introduced into the faujasite. Approximately 26 mg of the Ir complex was dissolved in ~10 ml dry pentane under intense stirring; then the solution was added through the needle into the Schlenk flask containing 2.00 grams of calcined dry H-FAU powder. $Ir(CO)_2$ fragments anchors to the zeolite through framework oxygen adjacent to Al T-atoms during this process. The pentane solution was subsequently evacuated for 5 hours under 10^{-5} Torr vacuum, leaving a dry powder of 0.7 wt% Ir/H-FAU.

Ni-BEA was synthesized by the modified IWI method we previously reported. In this, the NH_4-form of BEA with Si/Al~12.5 was used as the supporting zeolite. Nickel nitrate hexahydrate (Sigma Aldrich, 99.99%) was dissolved in a water/ammonia solution, producing a purple-coloured $[Ni(II)(NH_3)_6]$ complex with concentration 0.0757 M. The ammonia concentration was ~1.5 M. One pore volume equivalent (~0.9 cc/g BEA) of this solution was slowly introduced into zeolite powder with carefully mixing each aliquot. The resulting paste was dried at 80 ºC in flowing air and then calcined at 550ºC for 5 hours in a box furnace, yielding 0.4 wt% Ni/H-BEA.

The *in situ* static transmission IR experiments for Ni/BEA were conducted in a home-built cell housed in the sample compartment of a Bruker Vertex 80 spectrometer, equipped with an MCT detector and operated at 4 cm^{-1} resolution. The powder sample was pressed onto a tungsten mesh which, in turn, was mounted onto a copper heating assembly attached to a ceramic feedthrough. The sample could be resistively heated with temperature monitoring by a thermocouple spot welded onto the top center of the tungsten grid. Cold fingers on the CO-containing glass bulb were cooled with liquid nitrogen to prevent contamination by metal

carbonyls. NO was cleaned with multiple freeze–pump–thaw cycles. Special-grade ethylene (OxArc) with 99.995% purity was cleaned with liquid nitrogen prior to use to remove traces of moisture. The activated sample was employed as the spectrum background. Each spectrum reported is obtained from the average of 256 scans. Experiments at 77 K were performed with liquid nitrogen used as a coolant. Prior to FTIR measurements, the sample was activated by heating under vacuum at 200ºC to remove moisture. All dosed gases were undiluted.

DRIFTS spectra for Ir/FAU were recorded on a Nicolet iS50R FTIR spectrometer at 4 cm^{-1} resolution. The Ir/FAU powder was packed into the DRIFTS cell inside the dry glovebox, sealed and transferred to the FTIR where it was immediately connected to the gas manifold and exposed to flowing dry He. Special-grade ethylene (99.995% purity, OxArc) and UHP C_2D_4 was used for all experiments and UHP He flowing through oxygen and moisture traps was used as the inert gas. Spectra were referenced to an H-FAU background and 64 scans were averaged in each spectrum. Samples were loaded in a dry N_2 glovebox and transferred under N_2 to the infrared spectrometer. First the sample was purged with helium, and then experiments with pure ethylene or hydrogen flow were performed. Flow rates were ~10 cc/min.

HAADF-STEM analysis was performed with an FEI Titan 80-300 microscope operated at 300 kV. The instrument is equipped with a CEOS GmbH double-hexapole aberration corrector for the probe-forming lens which allows for imaging with 0.1 nm resolution in scanning transmission electron microscopy mode (STEM). The images were acquired with a high angle annular dark field (HAADF) detector with inner collection angle set to 52 mrad. The fresh Ir/FAU sample was loaded with no exposure to air. Spent Ir/FAU (220ºC under typical reaction conditions) was cooled down in the plug-flow reactor, purged with inert gas, and stored in the

glove box prior to loading into HAADF-STEM without exposure to air. The images were collected in various projection, tilted slightly off the zone axis (to better visualize the Ir atoms), and imaged immediately to minimize beam damage during the experiment. EDS maps of O, Si, Al, and Ni were obtained for Ni/BEA in order to better visualize presence of low-contrast Ni (compared to high-contrast Ir).

The reaction measurements were performed in a typical plug-flow quartz reactor. Samples were loaded into the reactor in the glove box and purged with dry (Restek O_2/H_2O traps) He before reaction. Ethylene (OxArc, 99.995% purity) was delivered into the system through a separate set of moisture and oxygen traps. Approximately ~30 mg of catalyst powder was loaded into the quartz reactor for each run. The ethylene flow rate was ~10 sccm/min in the undiluted stream to achieve a residence time of ~0.2 s. An Agilent 7890 Gas Chromatograph equipped with an FID was used to analyze the system effluent. An Agilent HP-PLOT/Q column (30 m, 0.53, 40 μm film) was used for separation. Hydrocarbons response factors were calibrated with hydrocarbon mixtures. Turn-over frequencies with respect to butadiene formation were calculated by the moles of butadiene produced divided by the moles of metal loaded into the zeolite sample per hour. Turn-over frequencies with respect to ethylene consumption towards butadiene formation were calculated by the moles of butadiene produced times two divided by the moles of metal loaded into the zeolite sample per hour. Turn-over frequencies with respect to butene formation were calculated by the total moles of all butenes produced divided by the moles of metal loaded into the zeolite sample per hour. Selectivities were calculated as the moles of the C_4 chemical of interest formed divided by the total C_4 chemicals simultaneously produced.

^{27}Al MAS NMR measurements were performed at room temperature on a Bruker 850 MHz NMR spectrometer operating at a magnetic field of 19.975 T. The corresponding ^{27}Al Larmor frequency was 221.413 MHz. All spectra were acquired at a sample spinning rate of 18.0 kHz (± 5 Hz) and externally referenced to 1.0 M aqueous $Al(NO_3)_3$ (0 ppm). ^{13}C and ^{1}H-^{13}C CP measurements were conducted on a Varian Inova 300 MHz spectrometers. The corresponding ^{13}C Larmor frequency was 75.43 MHz. Spectra were externally referenced to adamantae at 38.48 ppm and a sample spinning rate of 3.4 kHz at the magic angle was employed.

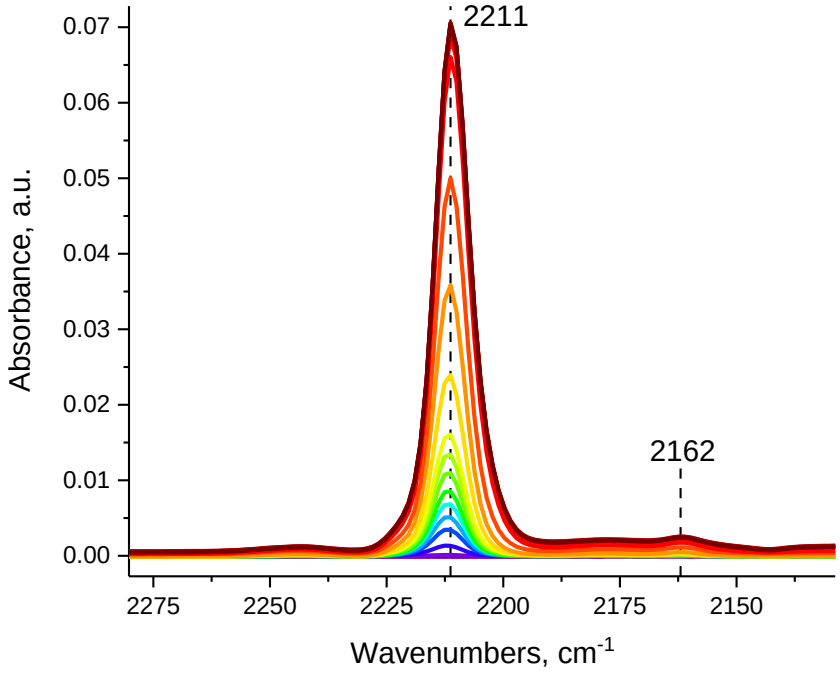

Figure S100. FTIR during CO adsorption on dry 0.4% Ni/BEA, $P(CO)_{max}$ =5 Torr.

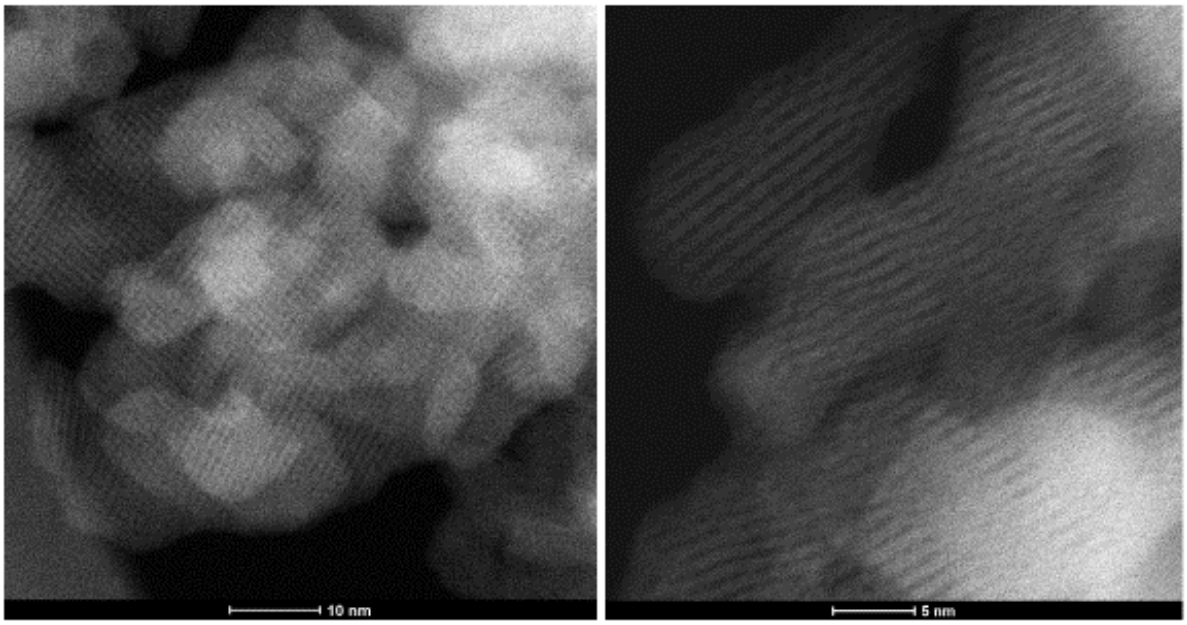

Figure S101. HAADF-STEM images of 0.4% Ni/BEA in different projections.

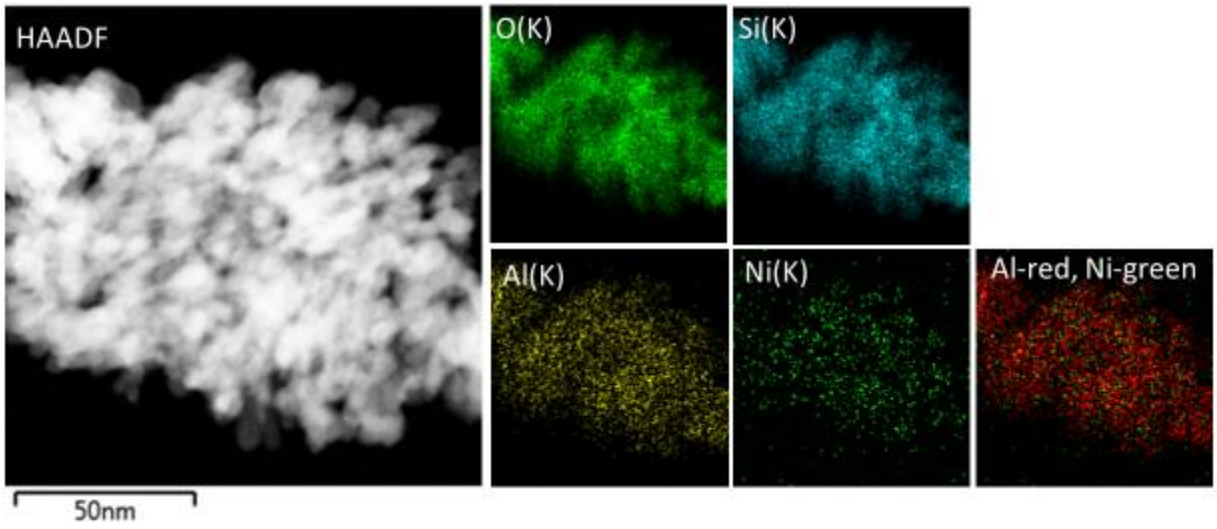

Figure S102. EDS maps of 0.4% Ni/BEA for O, Si, Al, Ni, overlay of Al and Ni maps, as well as the corresponding HAADF-STEM image for which EDS maps were collected.

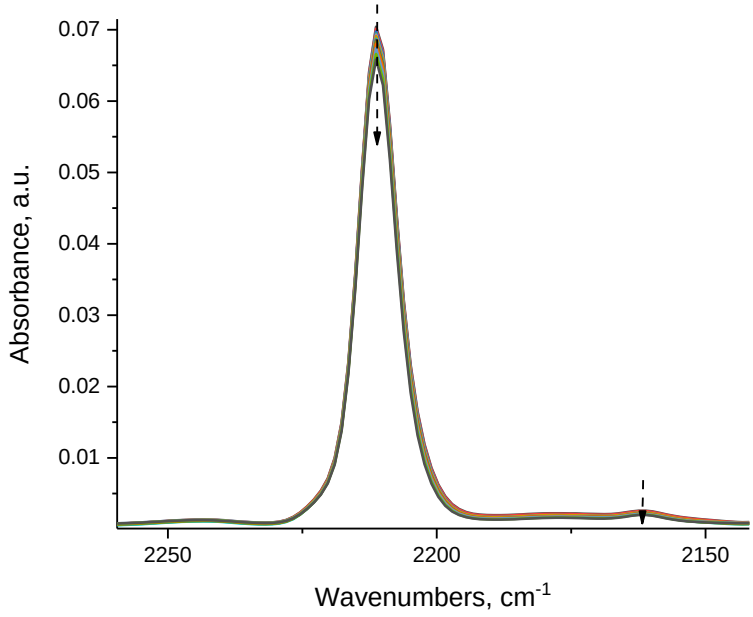

Figure S103. FTIR during vacuuming of Ni(II)-CO complex; Ni(II)-CO resists evacuation at RT. Final P=0.05 Torr.

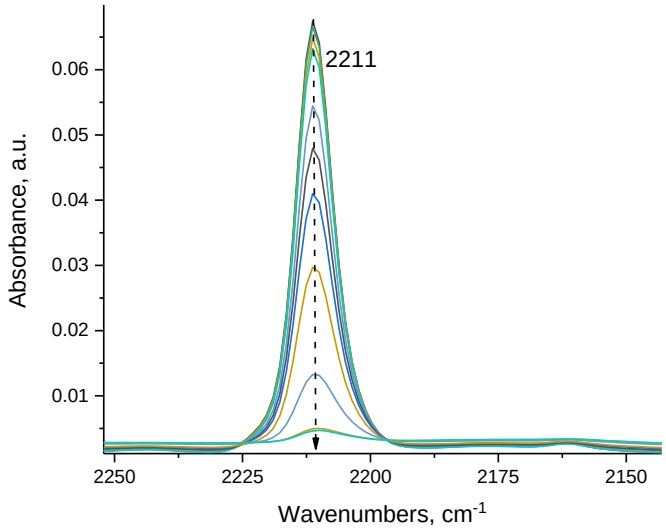

Figure S104. FTIR during ethylene adsorption (5 Torr) on Ni(II)-CO complex at RT. Ethylene completely displaces CO Ni(II)-CO + C_2H_4 → Ni-(C_2H_4) + CO

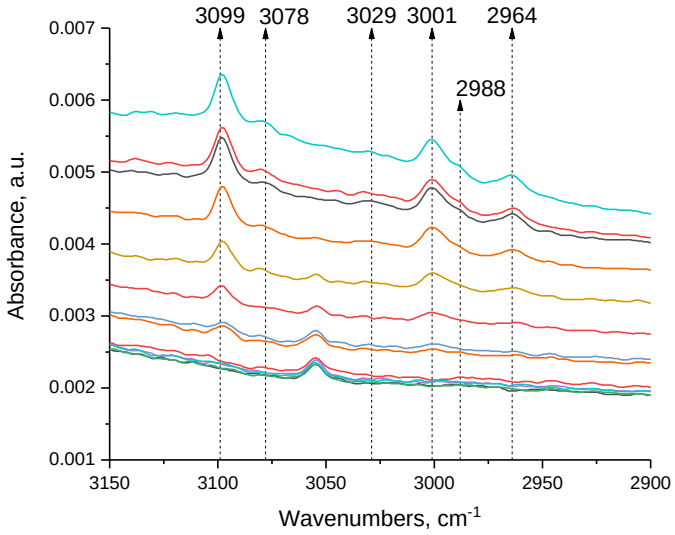

Figure S105. FTIR in the CH-stretching region during ethylene adsorption (5 Torr) on Ni(II)-CO complex at RT. The bands at 3,099, 3,078, 3,029 and 3,001 cm^{-1} are typical for pi-coordinated $H_2C=CH_2$ adsorbed on a d^8 metal center in organometallic compounds, such as in Rh(I) and Pd(II) in zeolite.

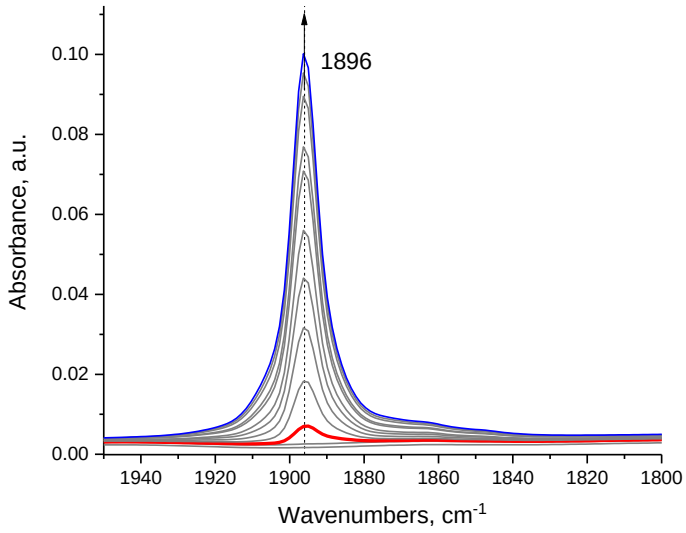

Figure S106. FTIR during NO adsorption on dry 0.4% Ni/BEA, P(NO)max=5 Torr; One type of Ni(II)-NO complex is formed. The FWHM of the NO band is ~12 cm^{-1}.

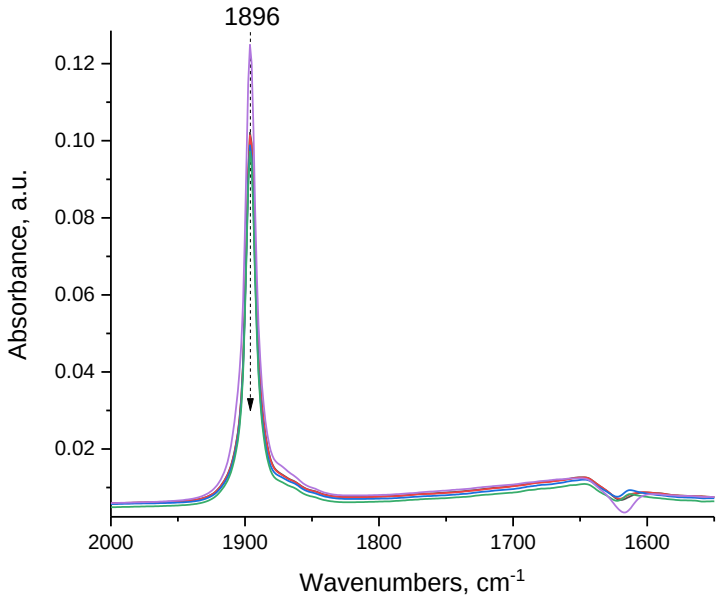

Figure S107. FTIR during vacuuming of Ni(II)-NO complex; Ni(II)-NO resists evacuation at RT. Final P=0.02 Torr.

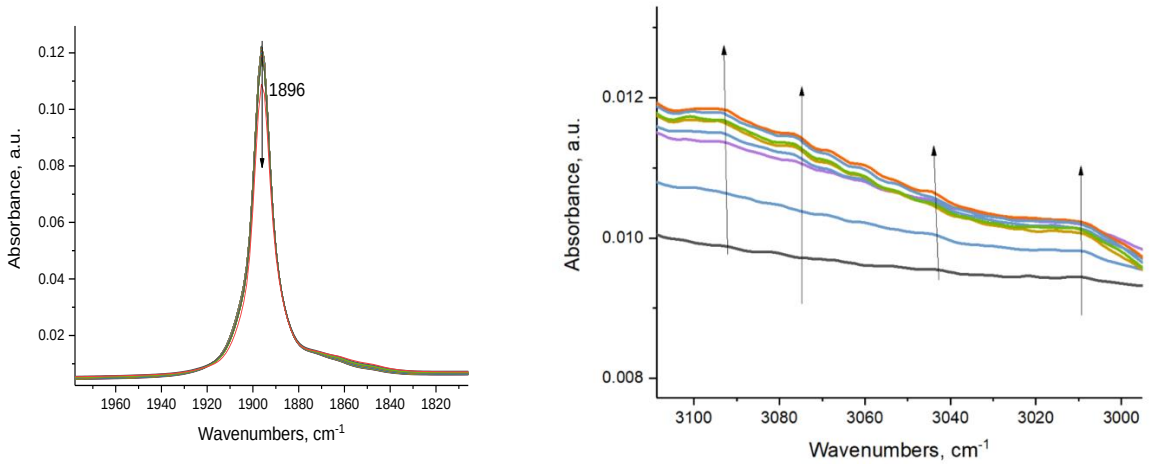

Figure S108. FTIR during ethylene adsorption (0.2 Torr) at RT on Ni(II)-NO. Ethylene displaces NO: Ni(II)-NO + C_2H_4 → Ni-(C_2H_4) + NO.

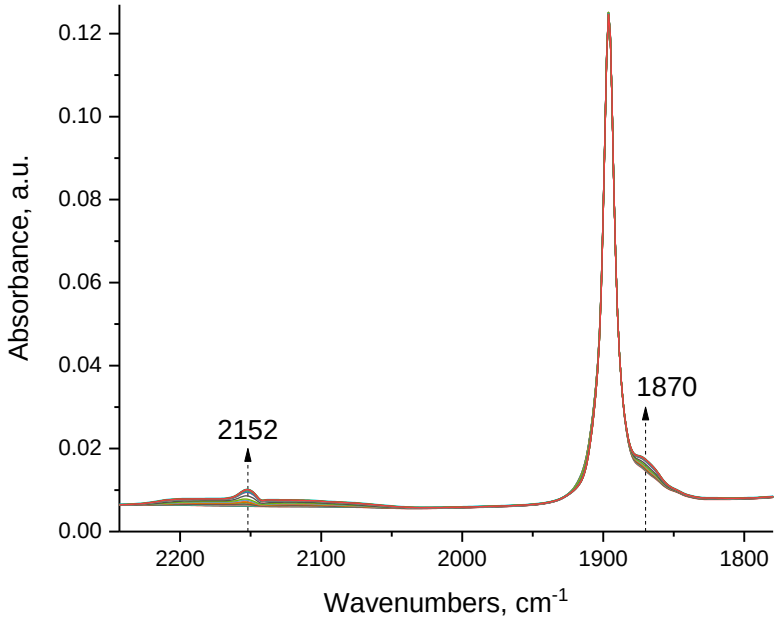

Figure S109. FTIR during CO adsorption (1 Torr) on the Ni(II)-NO complex. Ni(II)-NO is not displaced by CO, instead it forms Ni(II)(NO)(CO) complex with CO stretch at 2,152 cm^{-1} and NO stretch at 1,870 cm^{-1}.

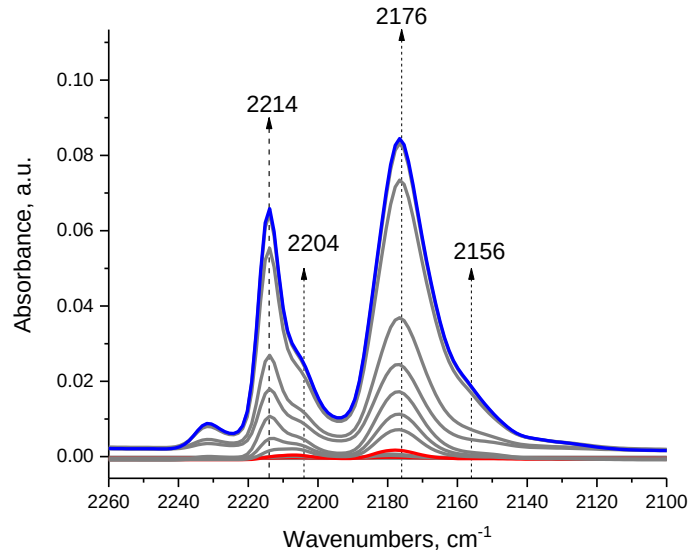

Figure S110. FTIR during CO adsorption (5 Torr) on 0.4% Ni(II)/BEA at liquid nitrogen (77 K) temperature. 2,214 and 2,204 cm^{-1} belong to CO adsorbed on Ni(II) ions. The 2,176 cm^{-1} band belong is CO adsorbed on Brönsted acid protons of H-BEA, the 2,156 cm^{-1} band is CO interacting with silanols.

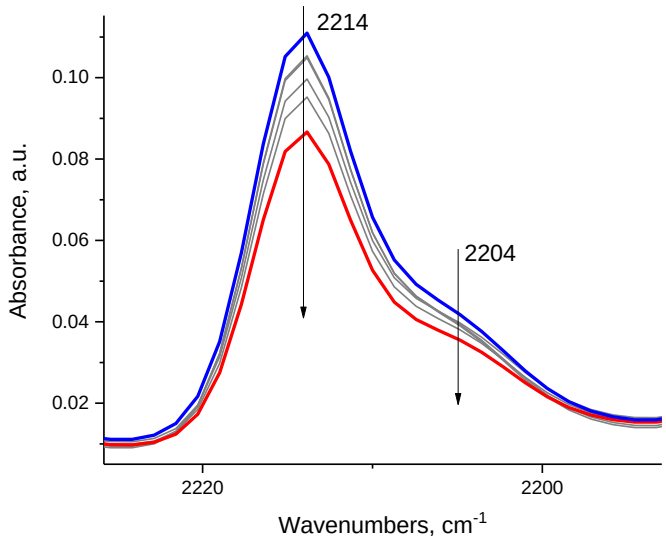

Figure S111. FTIR during vacuuming at liquid nitrogen temperature (77 K) of Ni(II)-CO complexes.

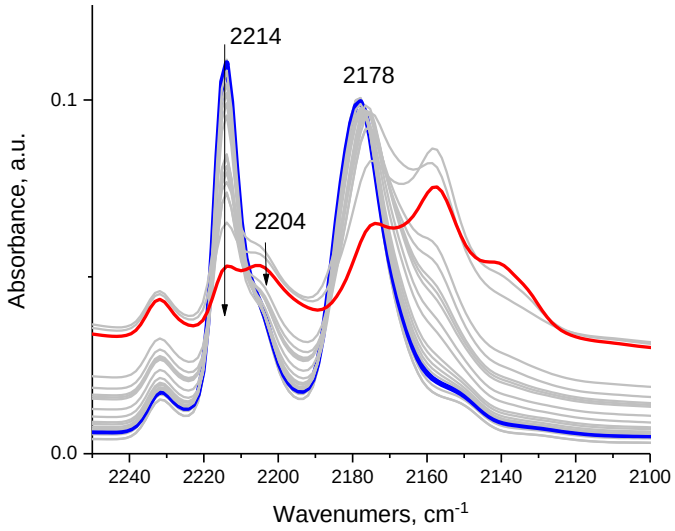

Figure S112. FTIR during C_2H_4 adsorption (2 Torr) at liquid nitrogen temperature (77 K) on Ni(II)-CO complexes. The 2,214 and 2,204 cm^{-1} CO bands of Ni(II)-CO complexes demonstrate markedly different behavior: the 2,214 cm^{-1} band decreases quickly but the 2,204 cm^{-1} band is relatively stable. This indicates that 2,214 and 2,204 cm^{-1} bands do not belong to a $Ni(II)(CO)_2$ dicarbonyl complex but to two different NI(II)-CO complexes, in which the 2,214 cm^{-1} [belonging to one Ni(II)-CO complex] is very susceptible to ligand replacement with ethylene even at 77K: Ni(II)-CO + C_2H_4 → Ni(II)-C_2H_4 + CO. Peculiarly, C_2H_4 easily displaces CO adsorbed on Brönsted acid protons of H-BEA (band at 2176 cm^{-1}).

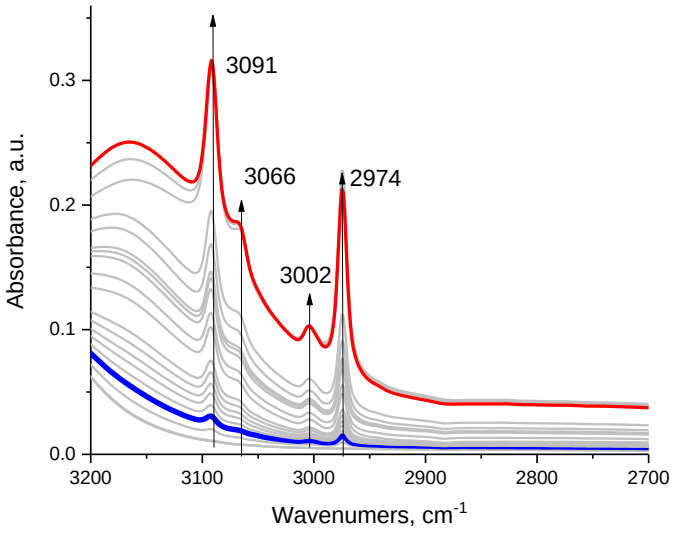

Figure S113. FTIR in the CH-stretching region during C_2H_4 adsorption (2 Torr) at liquid nitrogen temperature (77 K) on Ni(II)-CO complexes that were formed at 77 K (complimentary to Figure S112). The unusually intense bands at 3,091-2,074 cm^{-1} correspond to pi-coordinated $H_2C=CH_2$ interacting with –OH groups of zeolite: although this interaction is much weaker at RT, at liquid nitrogen such complexes are significantly more stable, thus the high intensity of these bands.

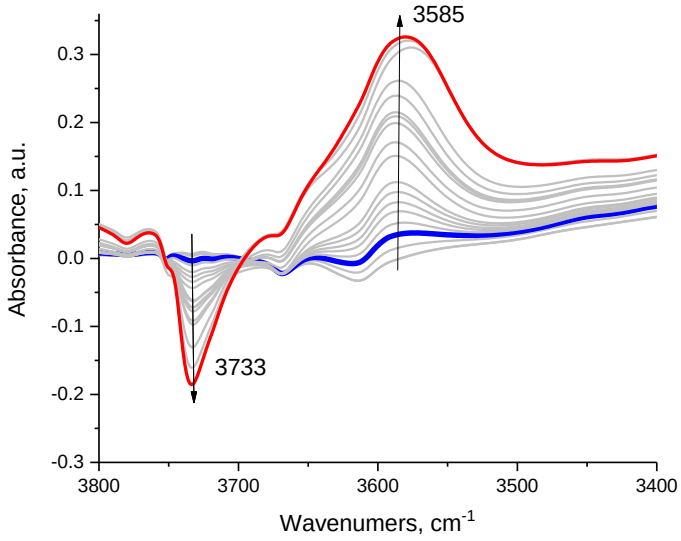

Figure S114. FTIR in the OH-stretching region during C_2H_4 adsorption (2 Torr) at liquid nitrogen temperature (77 K) on Ni(II)-CO complexes that were formed at 77 K (complimentary to Figure S112). OH bands of silanols at ~3,730 cm^{-1} decreases and forms a broad band at ~3,580 cm-1 due to formation of –OH--Ethylene adducts.

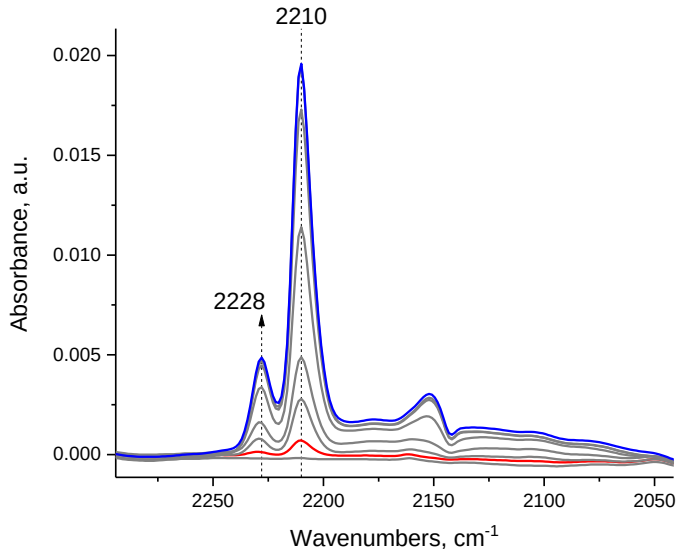

Figure S115. FTIR during CO adsorption (5 Torr) at RT on 0.4% Ni/BEA after C_2H_4 catalysis for 1 hr at 200ºC in the FTIR cell.

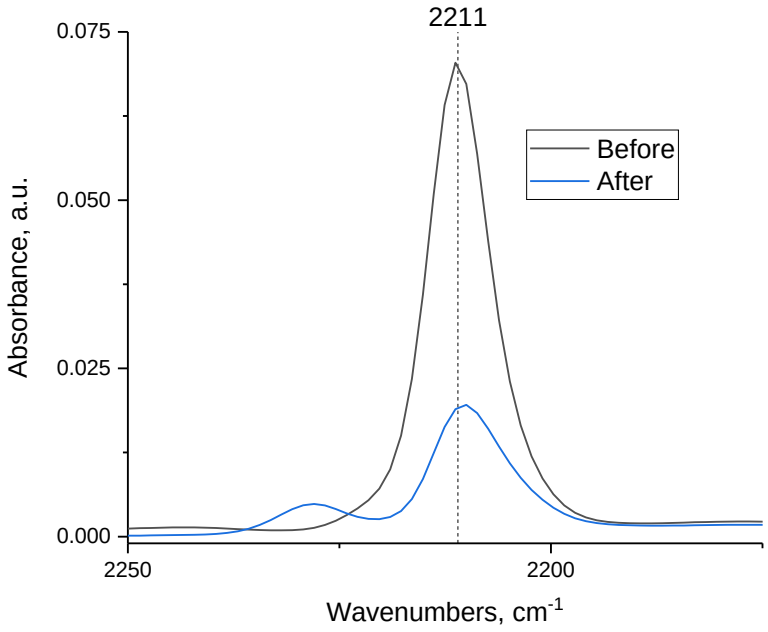

Figure S116. FTIR during adsorption of CO on dry 0.4% Ni/BEA P(CO)max=5 Torr, before and after exposed to C_2H_4 at 200ºC in the FTIR cell for 1 hr; Only one type of Ni(II)-CO complex forms. The ~2,228 cm^{-1} CO band is ascribed to CO adsorbed on extra-framework Al(III) sites. The FWHM of the CO band is ~ 9-10 cm^{-1}.

Table S19. Initial TOF (with respect to butadiene formation) and selectivity to butadiene for 0.4% Ni/BEA. Conditions: 30 mg, C_2H_4 flow rate 10 sccm/min, GHSV ~ 40,000 hr^{-1}

Temperature, ºC	Initial TOF, hr^{-1}	Initial Selectivity, %
80	6.7	35
120	122	65
200	203	29
250	180	31

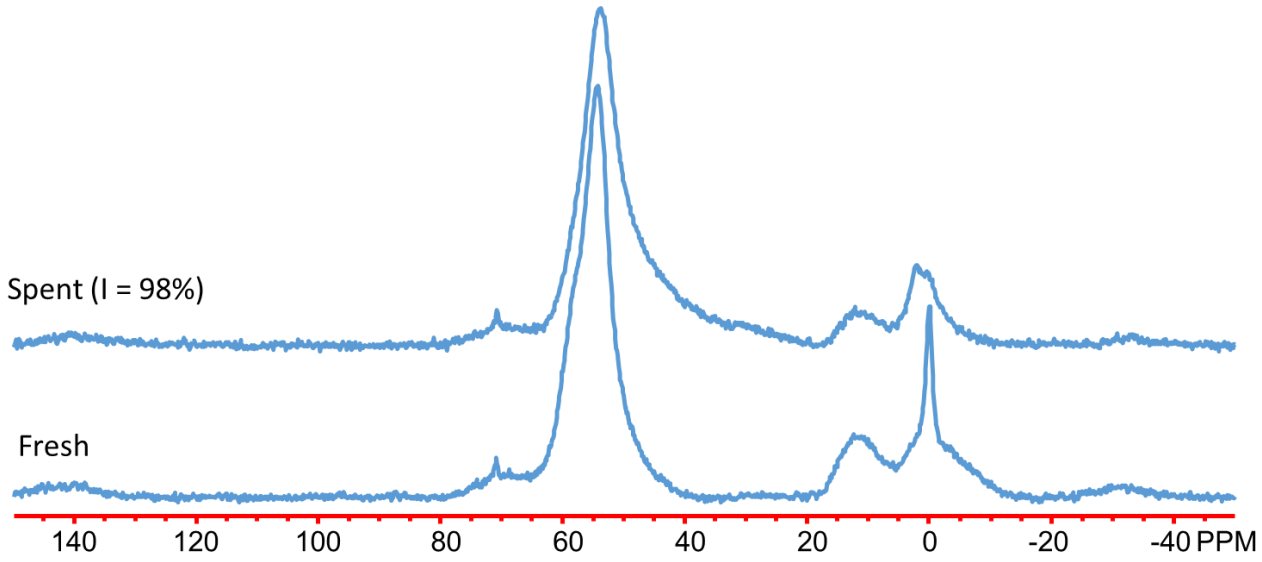

Figure S117. ^{27}Al MAS Solid-state NMR spectra for 0.4% Ni/BEA fresh (before catalysis) and spent (after C_2H_4 catalytic reaction at 220ºC for 1 hour).

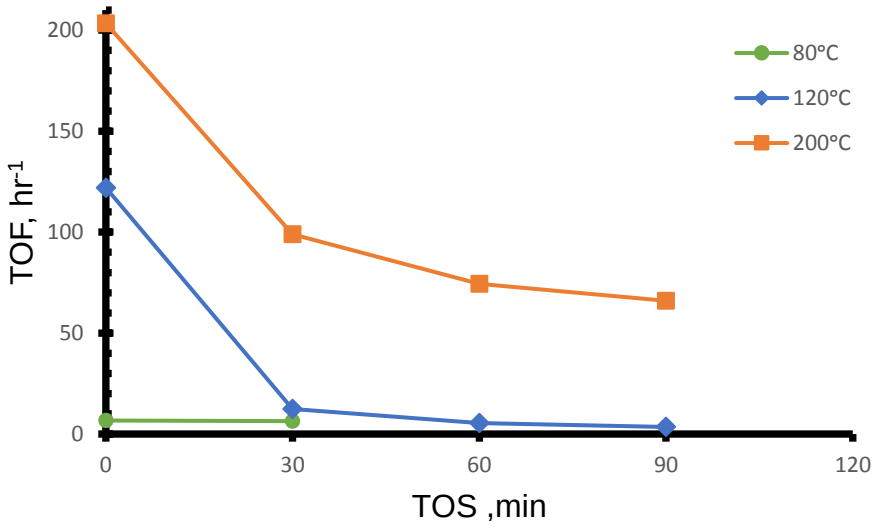

Figure S118. TOF (with respect to butadiene formation) trends as a function of time on stream for 0.4% Ni/BEA. Conditions: 30 mg, C_2H_4 flow rate 10 sccm/min, GHSV ~ 40,000 hr^{-1}

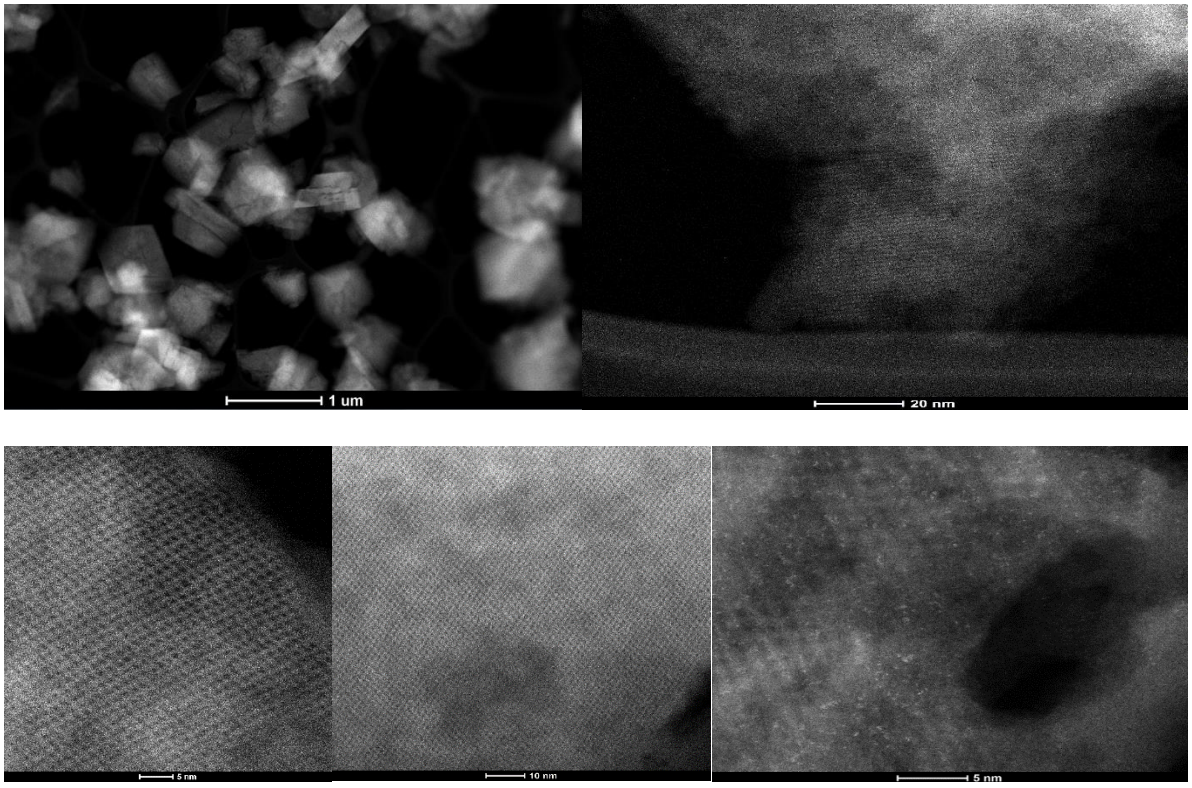

Figure S119. Additional HAADF-STEM images of 0.7% $Ir(CO)_2$/FAU in low magnification (showing absence of Ir nanoparticles) and high-magnification (showing presence of well-dispersed Ir atoms).

Table S20. Initial TOF (with respect to butadiene formation) and selectivity to butadiene for 0.7% $Ir(CO)_2$/FAU Conditions: 30 mg, C_2H_4 flow rate 10 sccm/min, GHSV ~ 40,000 hr^{-1}

Temperature, ºC	Initial TOF, hr^{-1}	Initial Selectivity, %
80	0	0 (100% selective to butenes, TOF ~1.5 hr^{-1})
180	0	0 (100% selective to butenes, TOF ~ 20 hr^{-1})
225	203	29
250	180	31

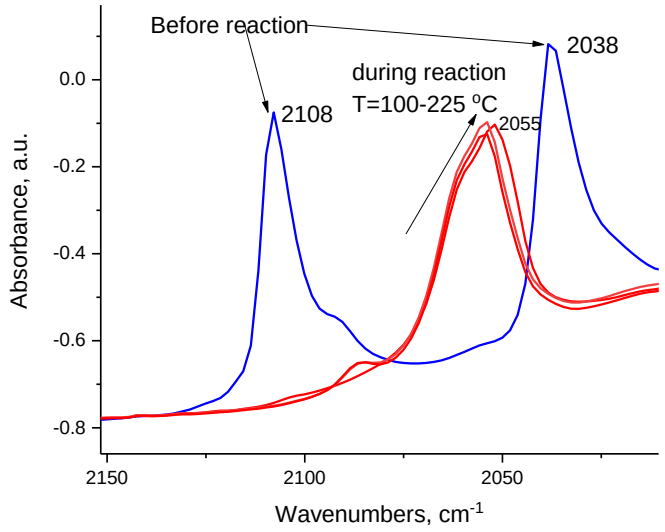

Figure S120. DRIFTS during $Ir(CO)_2$ reaction under pure C_2H_4 flow at 80-220ºC. $Ir(CO)(C_2H_4)$ is the only stable complex observed under these conditions.

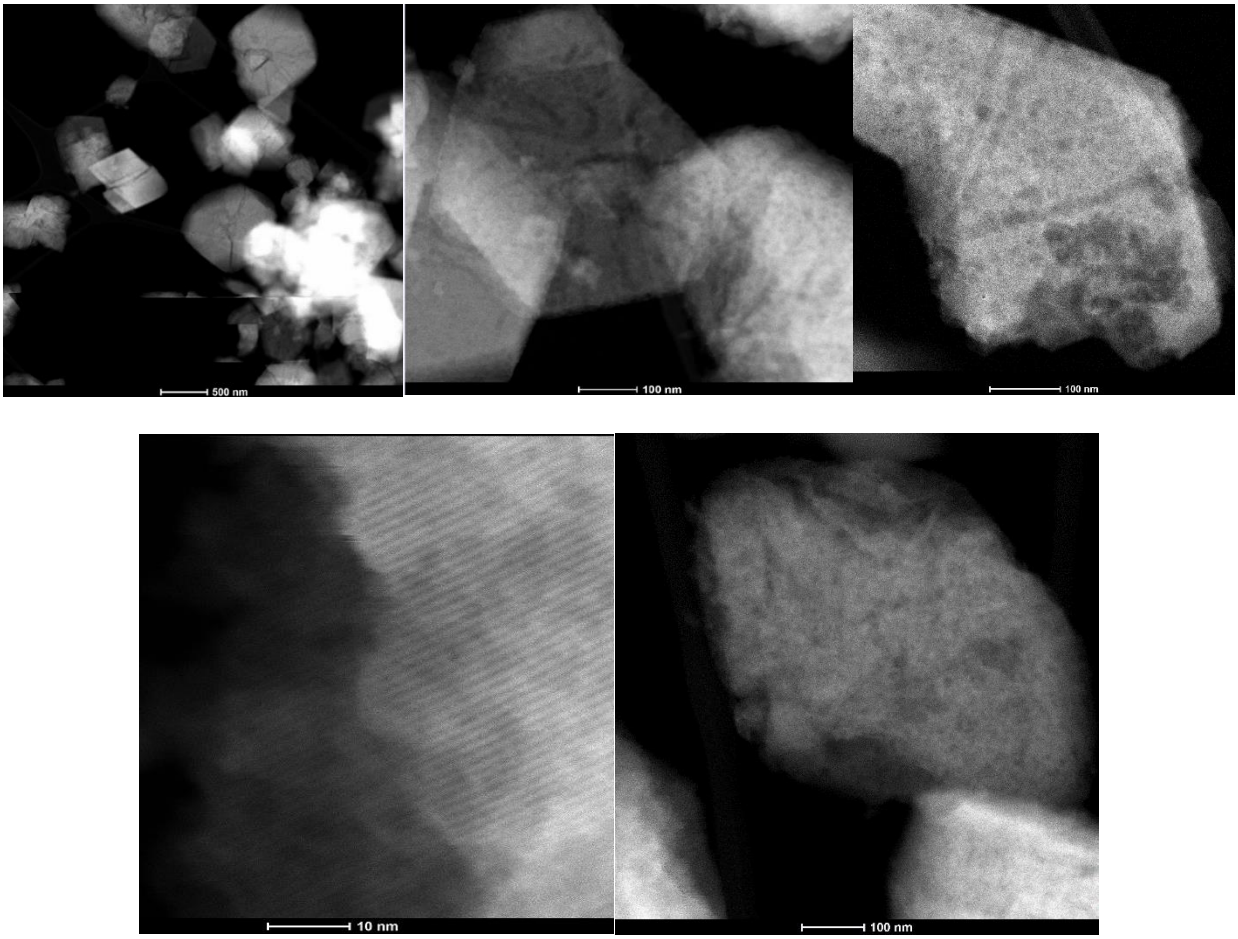

Figure S121. Additional HAADF-STEM images of 0.7% $Ir(CO)_2$/FAU, in low magnification and high-magnification after C_2H_4 catalysis at 200ºC. The sample was transferred from the reactor into the HAADF-STEM in a special sample holder void of oxygen and moisture.

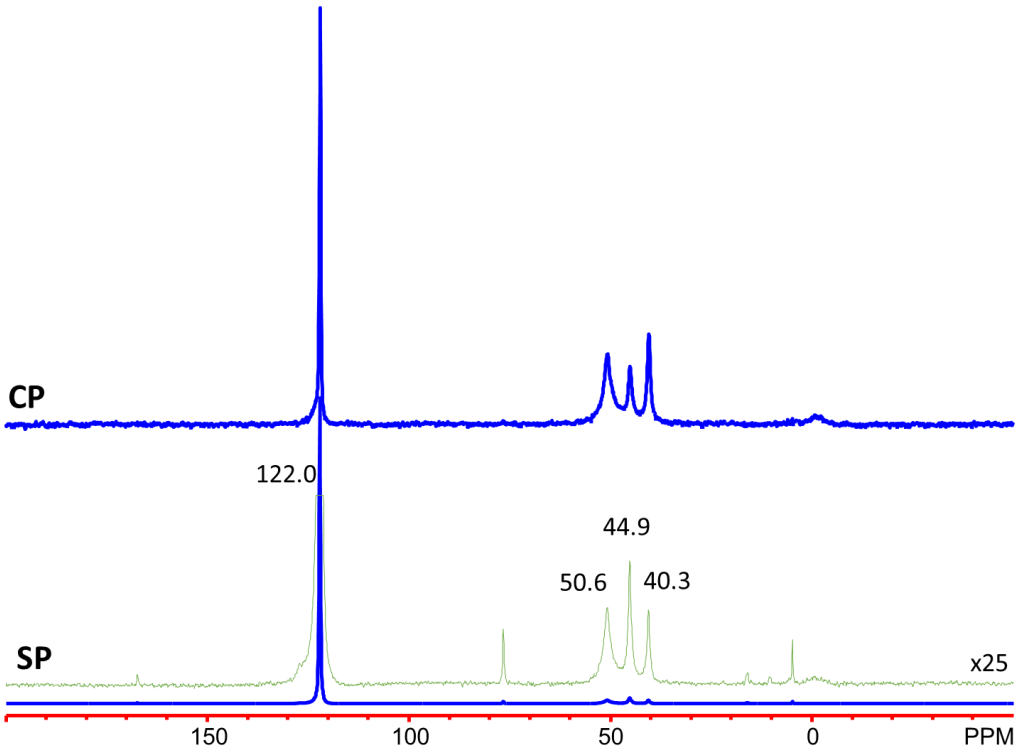

Figure S122. ^{13}C and ^{1}H-^{13}C CP MAS NMR spectra of 0.7% $Ir(CO)_2$/FAU after exposure of ~2" Hg $^{13}C_2H_4$ at room temperature. The MAS speed was 3,418 Hz. Peaks are assigned to ethylene (122 ppm, SSB: 167, 76.3 ppm), π - coordinated ethylene ligands (50.6 ppm, [J. Phys. Chem. B 2005, 109, 51, 24236-24243], and vinyl [Bulletin of the Academy of Sciences of the USSR, Division of chemical science, 1981, Volume 30, Issue 8, pp 1581, 13C NMR spectra and structure of iron carbonyl π complexes of vinylsilanes] (44.9 and 40.3 ppm), further supporting the infrared spectroscopy results. CP refers to cross-polarization. SP refers to single pulse.

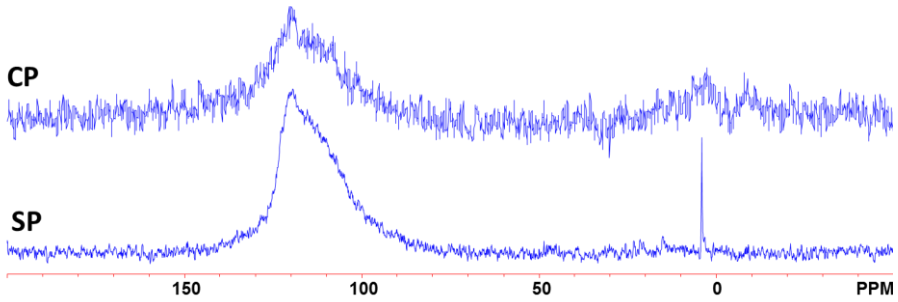

Figure S123. ^{13}C MAS Solid-state NMR spectra for 0.7% $Ir(CO)_2$/H-FAU after in situ reaction with $^{13}C_2H_4$ at 150ºC for 1 hr. Polymeric carbonaceous deposits are observed as a broad band in Cross-Polarization spectra between 80 and 150 ppm. Gas phase ethane is also present (4 ppm). [App. Cat. 1988, 45, 345-356] CP refers to cross-polarization. SP refers to single pulse.

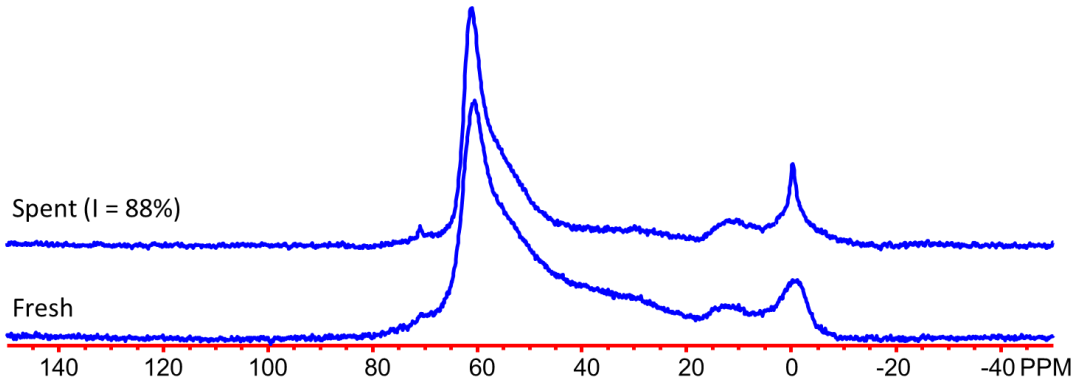

Figure S124. ^{27}Al MAS Solid-state NMR spectra for 0.7% $Ir(CO)_2$/FAU with Si/Al~15 fresh (before catalysis) and spent (after C_2H_4 catalytic reaction at 225ºC for 1 hour).

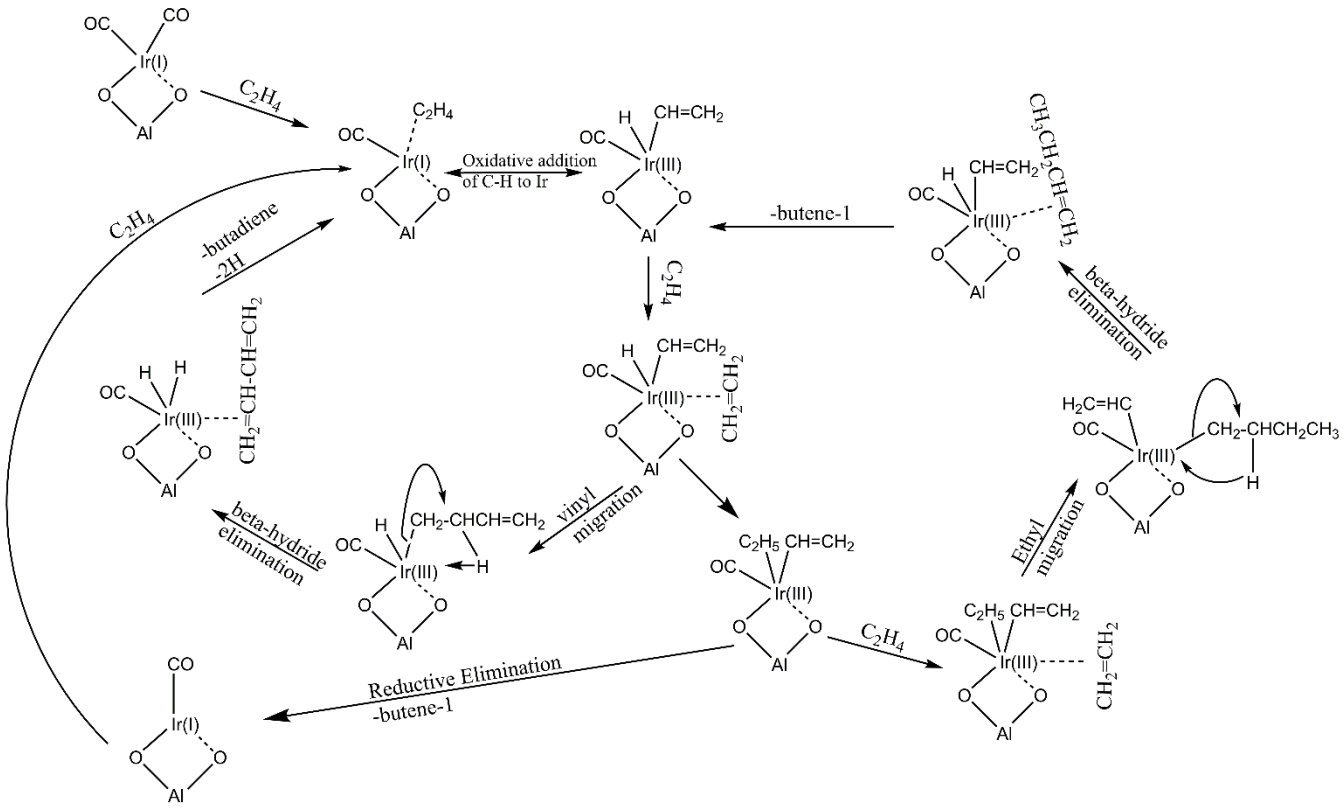

Figure S125. Probable mechanism for butene and butadiene formation from ethylene on $Ir(CO)_2$/FAU and Ni/BEA. In this mechanism C-H bond of ethylene is activated homolytically. Note, that completely analogous steps apply for Ni(II)/BEA system, except in that case no CO molecule is adsorbed on Ni. Oxidative addition of C-H bond of ethylene to Ni(II) produces Ni(IV)(H)(C_2H_3) nickel (IV) vinyl hydride species. Coordination of the metal atom to the zeolite framework is shown only as a representation and could be flexible.

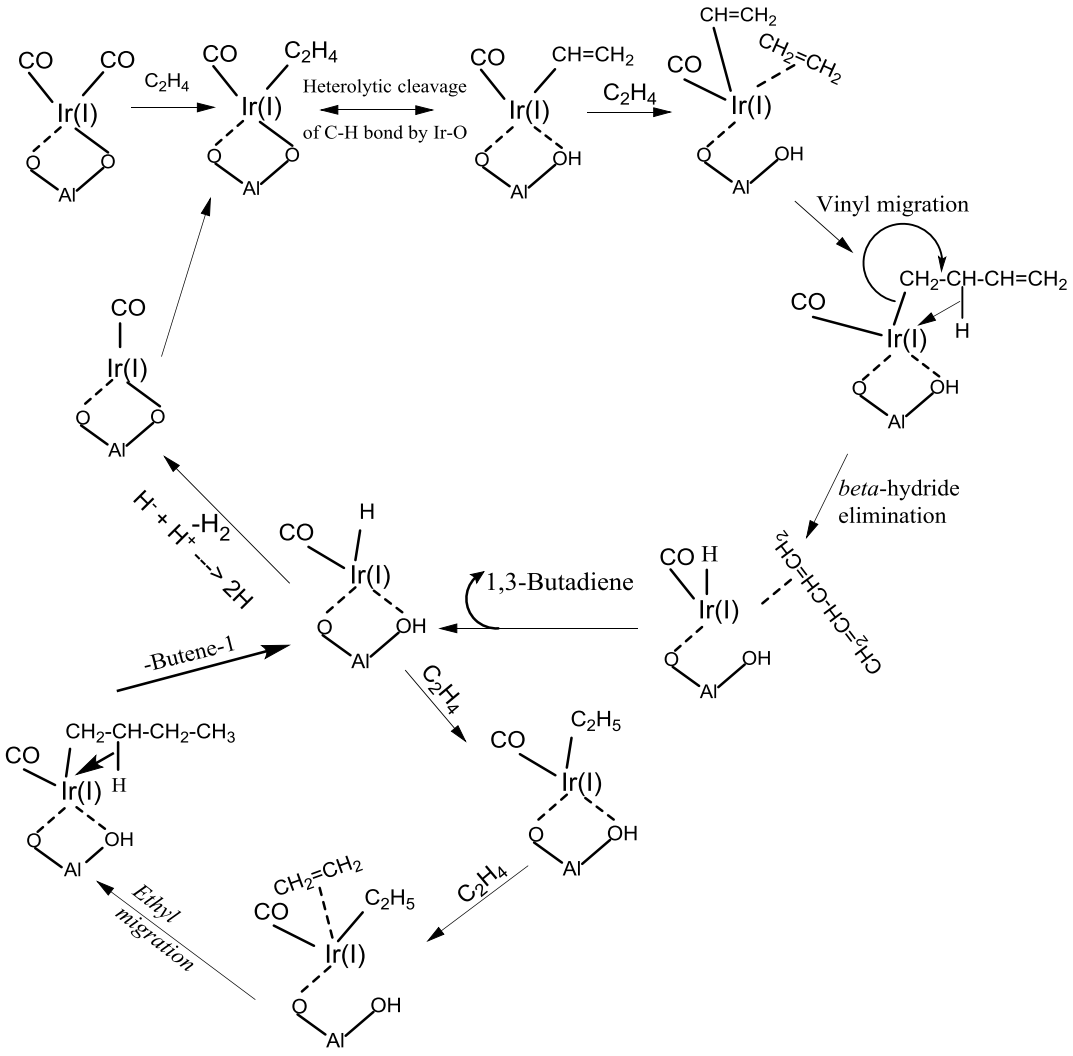

Figure S126. Probable mechanism for butene and butadiene formation from ethylene on Ir(CO)$_2$/FAU and Ni/BEA. In this mechanism, C-H bond of ethylene is activated heterolytically on Ir(I)-O and Ni(II)-O bonds. Note, that completely analogous steps apply for Ni(II)/BEA system, except in that case no CO molecule is adsorbed on Ni. Coordination of the metal atom to the zeolite framework is shown only as a representation and could be flexible.

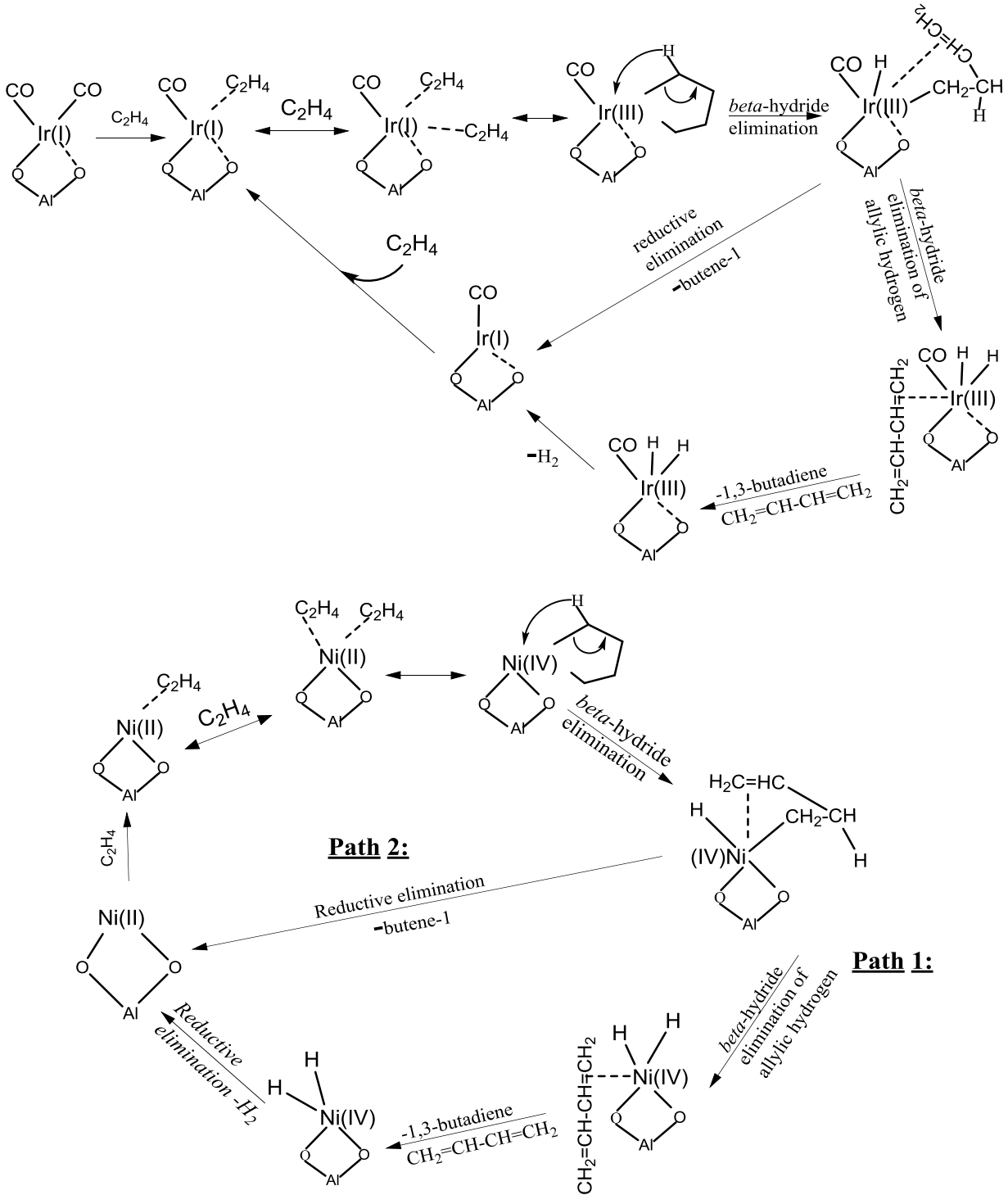

Figure S127. Mechanism for butene and butadiene formation from ethylene on Ir(CO)₂/H-FAU and Ni/BEA viametallocyclopentane intermediates. In this mechanism, two ethylene molecules couple on Ir(I) and Ni(II) sites with the formation or Ir(III) iridacyclopentane and Ni(IV) nickelcyclopentane intermediates initially. In the case of

Ni, no CO molecules are coordinated to Ni(II). Coordination of the metal atom to the zeolite framework is shown only as a representation and could be flexible.

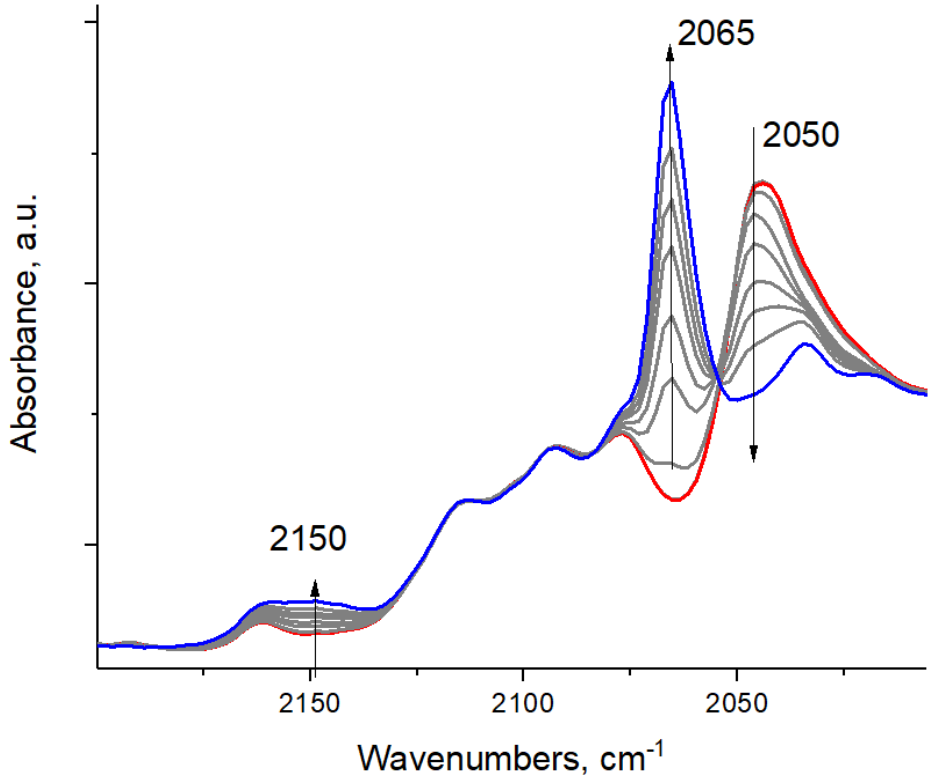

Figure S128. DRIFTS over time (1-5 minutes) of Ir(CO)(C_2D_4) during reaction with pure H_2 (H_2 flow ~10 cc/min). CO band of Ir(CO)(C_2D_4) at ~2,050 cm^{-1} selectively goes down and a new CO band grows at 2,065 cm^{-1}. Simultaneously, a weak band develops at 2,150 cm^{-1}, assigned to Ir-H stretch. The selective formation of Ir(III)(CO)H_2 complex takes place: Ir(I)(CO)(C_2H_4) + 2 H_2 → Ir(III)(CO)$(H)_2$ + C_2H_6

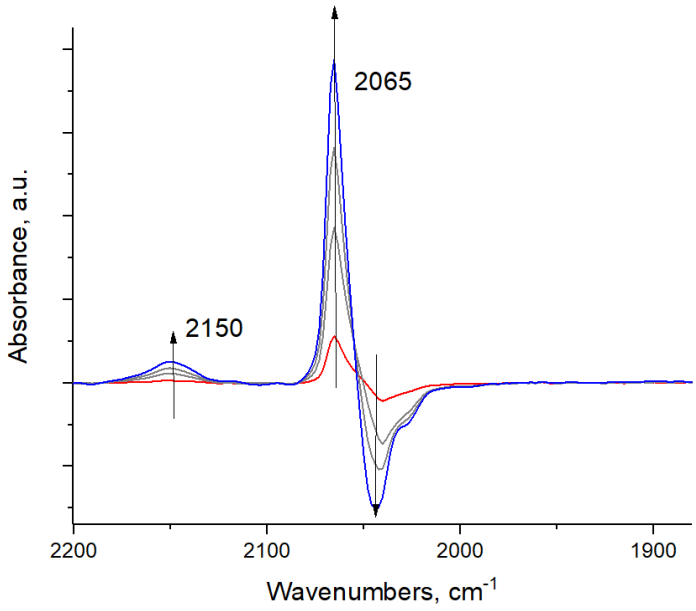

Figure S129. DRIFTS difference spectra (in time 1-5 minutes) during Ir(CO)(C_2D_4) during reaction with pure H_2 (H_2 flow ~10 cc/min). This shows clean selective conversion of Ir(I)(CO)(C_2D_4) to Ir(III)(CO)$(H)_2$. Unlike Rh(III)(CO)(H)x/FAU which has a complex Rh-H band structure due to the formation of families of rhodium carbonyl hydride complexes with undissociated and dissociated hydrogen ligands Rh(I)(CO)(H_2) and Rh(III)(CO)$(H)_2$ in FAU micropores (see references 17 and 18 in the main text), the Ir sample shows clean conversion to Ir(III)(CO)$(H)_2$

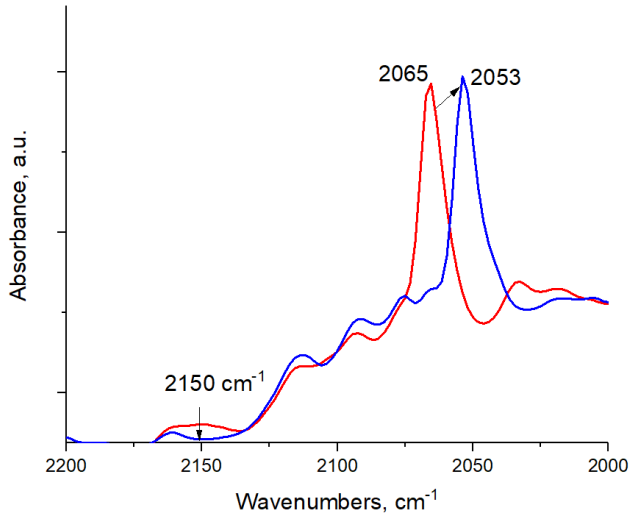

Figure S130. DRIFTS in time (2 minutes) during Ir(III)(CO)H_2 reaction with D_2. The following reaction takes place: Ir(III)(CO)$(H)_2$ + D_2 → Ir(III)(CO)$(D)_2$ + H_2; this fully confirms our assignment of 2150 cm^{-1} band to the Ir-H stretch, it disappears due to the formation of the Ir-D bond.

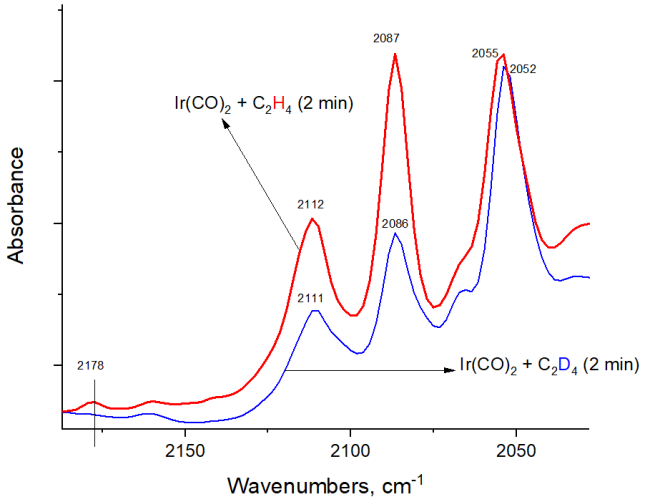

Figure S131. Comparison of DRIFTS spectra after the first 2 minutes of [Ir(CO)₂/FAU+C₂H₄] reaction (red spectrum) and [Ir(CO)₂/FAU + C₂D₄] reaction (blue spectrum). Note, that the 2,178 cm⁻¹ Ir-H band is absent in the C₂D₄ treated spectrum, confirming it is not a CO vibration but Ir-H vibration.

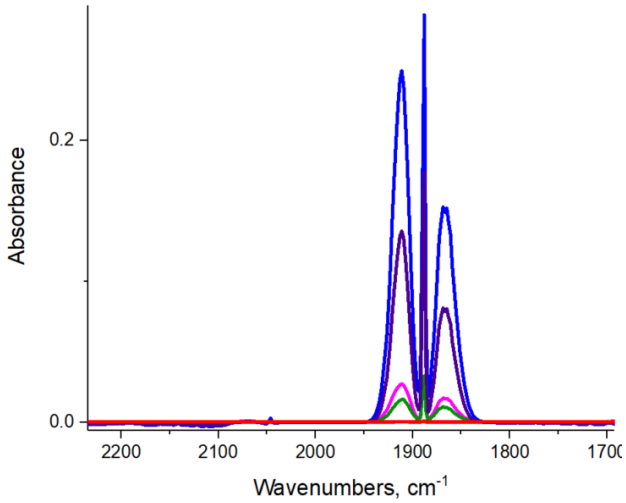

Figure S33. DRIFTS spectra during ethylene interaction Ni/BEA, showing no discernible features that could be attributed to Ni-H species. Dehydrated Ni/BEA sample was used as a background. Ethylene was flowed through the cell (blue spectrum in ethylene flow), we then purged ethylene with He continuously. The isoelectronic nature of Ni(IV), Rh(III), and Ir(III) hydrides, it is expected that the Ni(IV)-H stretch arise in the 2,100 cm-1 region. We note, however, that we were unable to observe the Ni(IV)-H intermediates either due to their small abundance and/or metastable nature. Furthermore, we believe that the Ni(IV)-H band stretching IR frequency would be difficult to identify is due to the low molar extinction coefficients of such species. Few such Ni-H IR frequencies are reported for well-defined organometallic nickel (I and II) hydride complexes for the same reason, and no to our knowledge no Ni(IV)-H complex has ever been reported. Only recently has Melanie Sanford's group produced these extremely metastable Ni(IV) complexes crystallographically under extreme conditions and with specialized ligands. More work is underway in our laboratory to identify the elusive intermediates.

Appendix J: Publication – Variable Temperature, Pressure Operando MAS NMR for Catalysis Science

From Nicholas R. Jaegers, Karl T. Mueller, Yong Wang, and Jian Zhi Hu* *Accounts of Chemical Research* (Under Review)

Abstract

The characterization of catalytic materials under working conditions is of paramount importance for a realistic depiction and comprehensive understanding of the system. Under such relevant environments, catalysts often exhibit properties or reactivity not observed under standard spectroscopic conditions. Fulfilling such harsh environments as high temperature and pressure is a particular challenge for solid-state NMR where samples spin several thousand times a second within a strong magnetic field. To address concerns of the disparities between spectroscopic environments and operando conditions, novel MAS NMR technology has been developed that enables the probing of catalytic systems over a wide range of pressures, temperatures, and chemical environments. In this account, new efforts to overcome the technical challenges in the development of operando MAS NMR will be briefly outlined. Emphasis will be placed on exploring the unique chemical regimes that take advantage of the new developments. With the progress achieved, it is possible to collect information on various nuclear constituents (^{1}H, ^{13}C, ^{23}Na, ^{27}Al, etc.) as well as assess time-resolved interactions and transformations.

Operando NMR enables the direct observation of chemical components and their interactions with active sites (such as Brønsted acid sites on zeolites) to reveal the nature of the

active center under catalytic conditions. Further, mixtures of such constituents can also be assessed to reveal the transformation of the active site when side products, such as water, are present. These interactions are observed across a range of temperatures (-10°C to 230°C) and pressures (vacuum to 100 bar) for both vapor and condensed phase analysis. When coupled with 2D NMR or computational modeling, specific binding modes are identified where the adsorbed state provides a distinct signature. In addition to vapor phase chemical environments, gaseous environments can be introduced and controlled over a wide range of pressures to support catalytic studies that require H_2, CO, CO_2, etc. Mixtures of three phases may also be employed. Such reactions can be monitored *in situ* to reveal the transformation of the substrates, active sites, intermediates, and products over the course of the study. Coupling operando NMR with isotopic labeling experiments reveals specific mechanistic insights otherwise unavailable. Examples of these strategies will be outlined to reveal important fundamental insights on working catalyst systems possible only under operando conditions. Extension of operando MAS NMR to study the solid-electrolyte interphase and solvation structures associated with energy storage systems and biomedical systems will also be presented to highlight the versatility of this powerful technique.

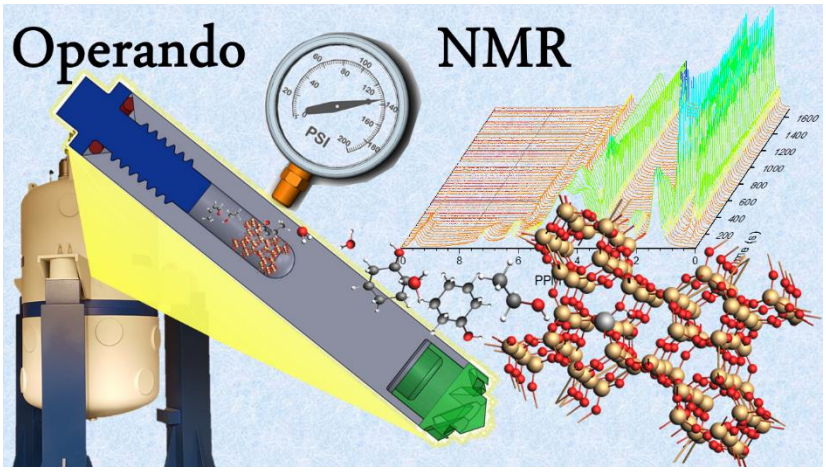

Modern chemical transformations extensively rely on catalytic chemistry to provide the desired product. Catalysts are involved in the production of an estimated 30% of all global products and 90% of chemicals[440], covering diverse industries as petrochemicals[441], emissions controls[58], and agriculture[442], to name a few. A solid understanding of how these systems function, either through structural characterization or mechanistic insight, is imperative for the thoughtful design of new materials or optimization of chemical processes. To address such questions, advanced characterization techniques have been developed to elucidate the underlying structures and reaction mechanisms of chemical systems. *In situ* and operando characterization is of particular interest due to the relevance of revealing the state of the catalyst under operating conditions, often at significantly elevated temperatures or pressures. Magic-angle spinning nuclear magnetic resonance spectroscopy (MAS NMR) is an excellent tool for such investigations on heterogeneous catalysts due to the non-destructive nature of the characterization and the sensitivity to small changes in the chemical environment of the nucleus. As such, the development of *in situ* and operando solid-state NMR technologies for high temperature and pressure has been a subject of great interest to catalysis and other fields.[8, 235]

Though a powerful technique used to probe chemical systems, overcoming the technical difficulties of a non-magnetic vessel capable of withstanding high temperatures and pressures while spinning several thousand times per second has been a challenging endeavor.

The early history of operando NMR has been extensively detailed elsewhere.[235] Briefly, early adaptations took the form of flame-sealed tubes[9-11] or polymer inserts[12-13] which exhibited undesirable operational limitations. Newer efforts for improved rotor performance have centered on rotor designs which can handle high temperatures and pressures under conditions of fast spinning rates, which were extensively used to reveal the nature of stored CO_2 for carbon sequestration.[14-15] Modern rotor schemes have suffered from limitations in the maximum operating temperature or sample volume due to the use of epoxy or ceramic inserts.[14-15, 443] The present state of the modern rotor design is depicted in Figure 14. The all-zirconia cavern-style rotor sleeve is milled with a threaded top to allow for a secure seal. Reverse threading prevents sample rotation from loosening the zirconia cap and an O-ring (or two) constitute the sealing surfaces, enabling a mechanical strength, chemical resistance, and temperature tolerance that is maximized for flexibility of performance. These designs are suitable for temperatures and pressures up to at least 250°C and 100 bar, limited by readily-available NMR probe technology. A complimentary technology was recently developed that substantially reduces unit production costs by employing simple snap-in features in a commercial rotor sleeve.[18] Termed WHiMS, this rotor avoids the need for specialize loading equipment by employing a check valve for gas loading. This design has been demonstrated to withstand 275 bar of pressure (20°C) or 325°C at significantly decreased pressure. Both of these rotor technologies are quite similar in sample volumes, ~400 µl for the 7.5 mm OD iterations. The preparation of solids and liquids in the

rotors is nearly identical and both are dependent on a force applied to an O-ring for sealing. The key differences in these designs stems from the required production and operation resources as well as the flexibility of gas atmosphere introduction. The WHiMS is more restrictive to a loading pressure higher than 5 bar and the rotor sized is limited to 5 mm and above due to the difficulties of engineering high mechanical strength plastic valves. The all-zirconia design is more scalable to smaller rotor sizes to accommodate limited sample applications and the requirement of faster sample spinning at high field for studying quardupolar nuclei (e.g., as small as <3.2 mm rotor size and spinning rate up to greater than 15kHz).

The WHiMS rotor takes advantage of a check valve to maintain internal pressure and offers the ease of gas introduction by simple exposure to a high-pressure external atmosphere. Gases may be sequentially added to the desired makeup, provided the external gas pressure exceeds both the internal pressure and the pressure required to open the check valve (>5 bar gauge for a 5 mm OD rotor). To charge the all-zirconia rotors with a gas atmosphere, a specially-designed rotor loading chamber must be utilized. The all-zirconia rotor would be fixed within the loading chamber, and gases of varying pressures (from vacuum up to >2,000 psi) and temperatures (<0 to >100°C) could be introduced to the chamber volume around the rotor by use of gas manifolds. When the conditions are satisfactory, the rotor cap is threaded closed using a bit piece that matches the cap style (exploded hex or socket of the appropriate size) that is magnetically coupled to a rotating rod on the exterior of the chamber, enabling tight environmental control and eliminating the need for a rotating high pressure sealing surface. Viewing windows on the chamber enable the observation of the cap seating while maintaining the desired environment. The modular nature of the interior enables rotors from 9.5 mm to 2.5

mm to be used in the same system with a small change in the rotor stage components. As such, the complementary technologies offer options for either preparation convenience and fewer resource requirements or a more expansive range of control of the internal environment of the rotor. Due to the range of convenience and control options, these two technologies have been used for an array of applications to strengthen scientific understanding of catalytic systems.

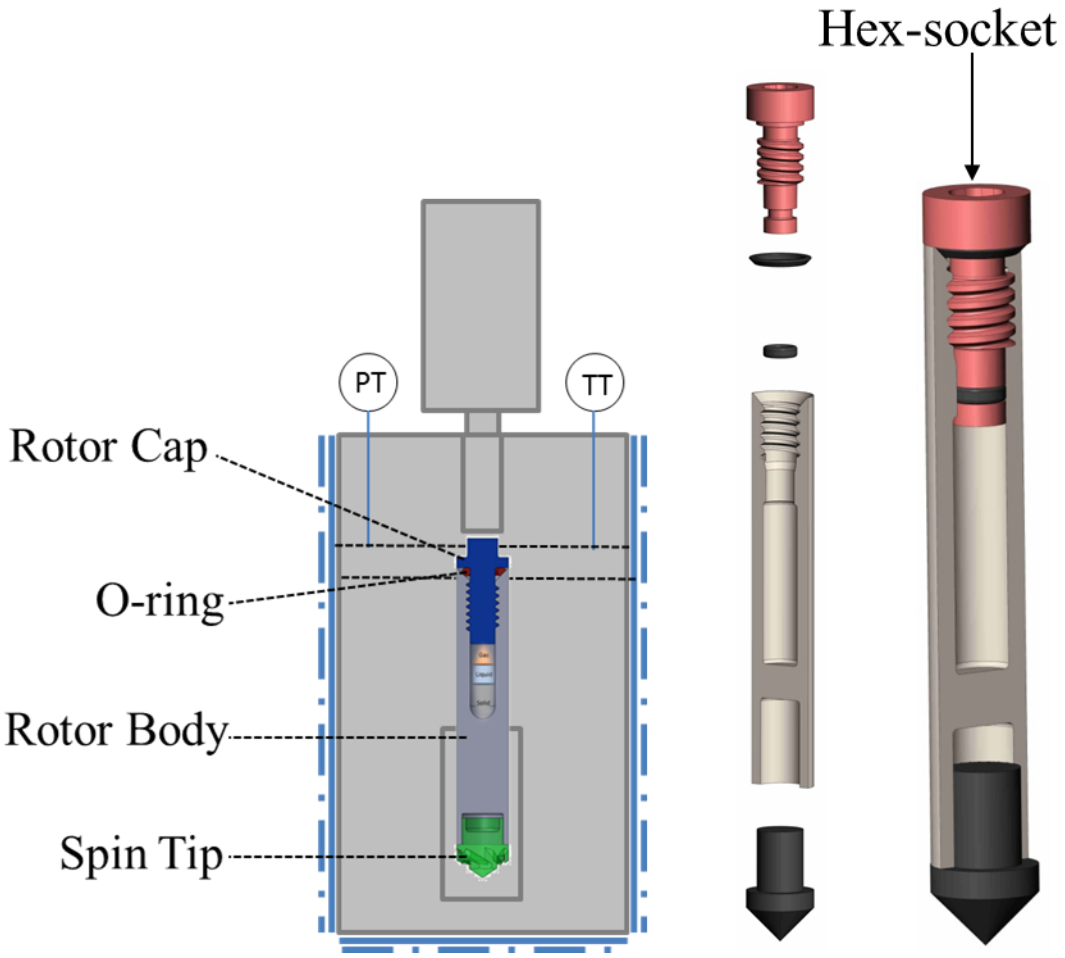

Figure 14. Schematic of high-temperature, high-pressure operando NMR rotors loaded within the specially-designed loading chamber and an internal component view. Adapted with permission from J. Z. Hu et al, Chem. Comm. 2015, 51, 13458-13461. Copyright 2015 Royal Society of Chemistry.

In addition to batch-style *in situ* NMR investigations, continuous flow NMR probes have been employed to better mimic the conditions of a fixed-bed reactor while taking advantage of the benefits afforded by MAS.[22-26] In these designs, an axial tube delivers gases to the bottom of the catalyst bed which were then allowed to flow up and leave through the top of the rotor. Alternatively, the gas profile entered the top and exited the bottom with the aid of a slight vacuum on the exit channel to encourage flow.[444] While such efforts certainly have brought unique insight and represent advancement in technical capabilities, the technique suffers from channeling of the catalyst bed and other issues of flow induced by backpressure and/or mixing of gases with the bearing and drive gas of the MAS technique.[444] Nevertheless, such technologies continue to provide unique insight and offer new opportunities to couple characterization techniques. The inclusion of quartz window on the bottom of the NMR rotor, for example, has been shown to be an effective method for coupling NMR measurements with UV-vis spectroscopy.[445]

The scalable nature of rotor design and modular loading chamber components makes it an excellent tool for multinuclear investigations on the structure of catalyst materials since an array of probes, and thus spinning rates, and magnetic fields may be employed to provide a thorough illustration of the material. A recent publication has reviewed the characterization of active metal sites in zeolites by NMR,[446] but the evolution of the materials synthesis process which generates an active catalyst structure is uniquely possible with specialized NMR capabilities that enable high pressure and temperature resilience. Such transformations have been reported for the crystallization of $AlPO_4$-5 where operando ^{1}H, ^{13}C, ^{27}Al, and ^{31}P MAS NMR were combined to reveal a semi-crystalline phase that served as an intermediate during the

hydrolysis and condensation reactions which constitute the crystallization mechanism.[19, 447-448] In this example, NMR was able to clearly show the expulsion of excess water, phosphate, and aluminum to yield a crystalline catalytic solid. Similar principles can be applied to understand the formation of catalytic materials in zeolites.

^{23}Na and ^{27}Al are attractive nuclei to observe such operando transitions due to their sensitivity and presence in a variety of synthesis gels.[449] For example, the formation of the faujasite (FAU) zeolite crystal structure was previously described by operando ^{23}Na and ^{27}Al MAS NMR, revealing the kinetics of crystallization of the material structure at elevated temperature and pressure.[450] The time-resolved spectroscopic data presented in Figure 15 illustrate not only the importance of temporal resolution for observing the evolution of centerband features, but how spinning sidebands can also offer unique insight into the evolution of the structure. Figure 15A-C reveal the presence and evolution of two ^{27}Al species: solid tetrahedral aluminum from the framework (Al_{Ft} at 62 ppm) which shifted from 60 ppm as the extended framework formed and a narrow, liquid ^{27}Al species ($Al(OH)_X^-$ at ~76 ppm) which would shift slightly depending on hydroxyl replacement with siloxy groups. The intensity of Al_{Ft} increased and the linewidth decreased during the crystallization process, indicating the improved crystallinity over the course of the experiment. The $Al(OH)_X^-$ species decreased in intensity as it was incorporated into the framework, while the linewidth was relatively invariant.

The ^{23}Na species were also monitored during framework formation. While the asymmetric centerband feature narrowed and slightly moved downfield, this was shown to actually constitute both the solid and aqueous sodium that were superimposed and complicated a detailed analysis of the formation of FAU. Second-order quadrupolar interactions were

sufficiently suppressed under these conditions, however, to gain insight from the spinning sidebands (Figure 15D-E) which exhibited two distinct framework cationic sites at -20 ppm (sodalite positions) and -22 ppm (supercage positions). Both species grow as the crystallization process completes and the sodalite population reaches saturation prior to that of the supercage. Further, it is shown that cationic sites populate supercage and sodalite sites at a ratio of 70:30, which provides direct evidence to the types of confined environments to which substrate molecules and their reactive intermediate states are subject.

Not only is the formation of an extended crystal structure of a material of great importance, but so is the behavior of the catalytically active site. Identification of the active center of a catalyst is appropriately regarded as an integral step in evaluating the performance of a catalyst material and discerning the underlying reaction mechanisms. Material surfaces have dynamic structures that are significantly impacted by the local environments around the active centers.[109, 230] As such, it is necessary to conduct spectroscopic measurements under conditions relevant to the reaction of interest to gain a firm understanding of the true nature of the active centers. Acidic zeolite sites, for example, are well known to catalyze an abundance of reactions. Their acid sites are highly sensitive to the chemical environment and readily adapt to changes in the surrounding atmosphere.

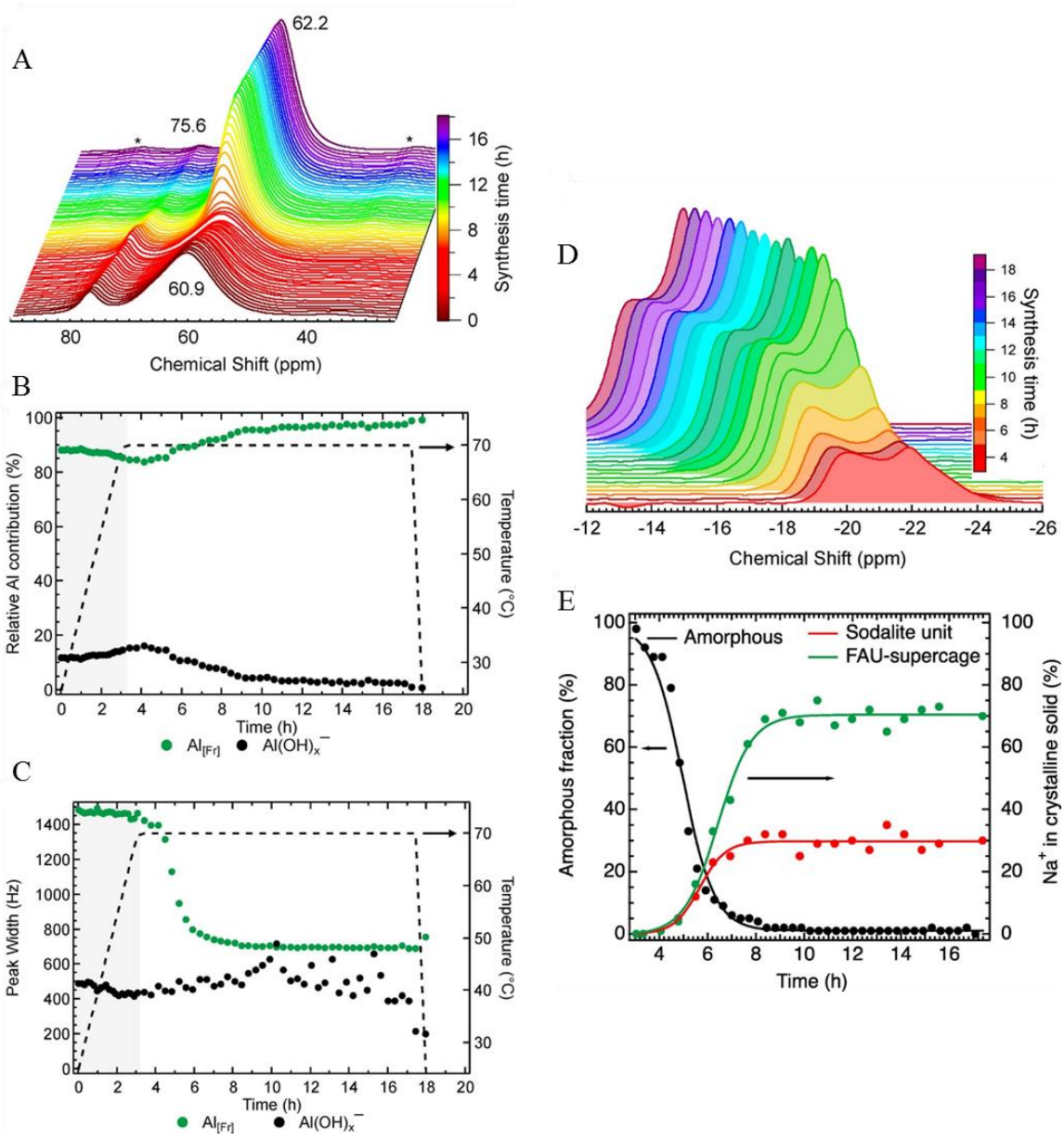

Figure 15. (A) In situ ^{27}Al MAS NMR spectra showing the changes during the synthesis of FAU. Deconvolution of the spectra (3-hour heating period shaded in gray) led to modulation of the peak area (B) and line width (C) observed for liquid $Al(OH)_x^-$ and solid tetrahedral Al ($Al_{[Fr]}$). Changes in the spinning side band associated with solid Na^+ material as a function of synthesis time (D). A high-field peak and a low-field peak were identified at −22 and −20 ppm, respectively. Panel E shows the kinetic transformation of amorphous material into crystalline FAU as directed by the speciation of Na^+ ions [plotted as formed fraction of the final concentration of sodalite (− 20 ppm) and the supercage (− 22 ppm)]. Reprinted with permission from S. Prodinger et al. Chem. Mater. 2018, 30, 888-897. Copyright 2018 American Chemical Society.

Recently, the impact of water on zeolite HZSM-5 was detailed by employing a combination of *in situ* ^{1}H single-pulse and ^{1}H-^{29}Si cross-polarization NMR, depicted in Figure 16.[230] It was shown that under conditions of hydration, the Brønsted acid proton would progressively detach from the framework oxygen atom. At low water loadings, the detachment took the form of an elongated H_{BA}-O_F bond due to hydrogen bonding of the acid proton with one adsorbed water molecule. Under this regime, the ^{1}H-^{29}Si CP NMR illustrated an increase in silicon species due to the more efficient polarization of silicon atoms from the additional proximal protons. With the subsequent addition of water at hydration levels exceeding two water molecules per BAS, the *in situ* ^{1}H-^{29}Si CP NMR signals were suppressed. Concurrently, selective excitation spin-echo experiments revealed a ^{1}H peak at 9 ppm which represents a hydronium ion (H_3O^+) that is difficult to observe otherwise. Experimental and computation evidence confirmed the presence and assignment of hydrated hydronium ions which solvate the acid proton from the framework sites and undergo extensive molecular motion and exchange with surrounding water molecules. Both the longer ^{1}H-^{29}Si distances and the increased mobility led to a smaller CP signals. This exchange was found to extensive at elevated temperatures, even at low water concentrations. The employment of Hahn-echo and cross-polarization pulse sequences have also been used to discriminate between molecules reacting in the pore and at the pore mouth of zeolites to identify the active centers. It was found that the etherification of citronellene with ethanol primarily occurs on the pore mouth instead of the zeolite pore due to ethanol's preferential adsorption in the pore and the easily accessible acid sites at the pore opening.[451]

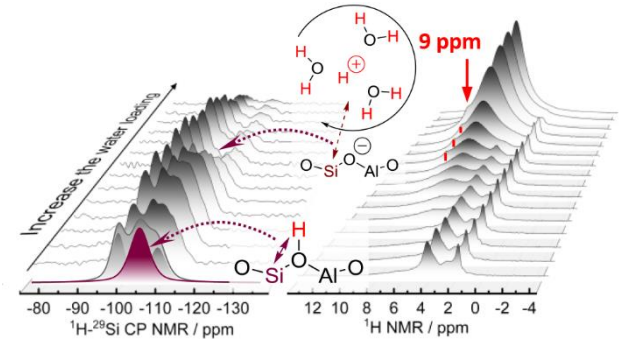

Figure 16. Schematic representation of the genesis and stability of hydronium ions in HZSM-5 as a function of water content in the framework. Reprinted with permission from M. Wang et al. J. Am. Chem. Soc. 2019, 141, 3444-3455. Copyright 2019 American Chemical Society.

A firm mechanistic description is also of great interest for understanding the chemistry operating during a reaction on the defined active centers. *In situ* NMR offers extensive opportunities to highlight the underlying chemical pathways of reactivity for heterogeneous catalysts. This may come from isotopic labeling to trace out a pathway, or identification of the presence and dynamics of surface intermediates.[452-454] In particular, extensive work has been conducted to trace out the mechanisms of reactions within zeolite frameworks, owning to the relatively well-defined structures they offer.[455-457] Propane activation over Zn/H-MFI, for example, was explored by *in situ* NMR to highlight the formation of a zinc-propyl species in concert with Zn-OH groups prior to propane conversion This dissociative adsorption initiates reactivity on the zinc center and contrasts the protonation mechanism observed on the Brønsted acid sites of unmodified zeolites.[458-460] Zinc modification was also studied for the carbonylation of ethane which reveals zinc-ethyl and methoxy species as the key intermediates.[461]

Due to the elevated temperatures and pressures required for condensed phase reactions, sealed rotors are uniquely suited for an *in situ* analysis of the evolution of species during the process. The dehydration of cyclohexanol, for example, has also been of interest and explored in

detail by *in situ* NMR in conjunction with kinetic studies.[443] It was demonstrated that the aqueous-phase dehydration of 1-^{13}C-cyclohexanol on H-BEA zeolite occurs through a cyclohexyl cation which undergoes a 1,2-hydride shift via an E1 mechanism. Such insights were extended to more complex reaction networks involving cyclohexanol and water. For example, phenol alkylation in H-BEA zeolite has been the focus of multiple studies due to the strong interest in catalytic conversion of lignin-derived phenolic compounds to improve the value of the chemicals and identify the key reaction pathways for the transformation thereof.[265, 377]

Such processes include alkylation and dealkylation transitions which adjust the carbon number of substrate species and pose interesting mechanistic questions which can be addressed by *in situ* NMR.[462] The alkylation of phenol is an electrophilic aromatic substitution which can take place with either alcohols (protonated alcohol) or alkenes (carbenium) as alkylation agents. The alkylation of phenol with cyclohexanol and cyclohexene in decalin was previously studied by *in situ* ^{13}C MAS NMR. The results revealed a detailed pathway whereby alkylation products were minimal until a majority of the cyclohexanol co-reactant was dehydrated to cyclohexene on the acid sites.[377] This was shown to be caused by the absence of reactive electrophile, which was present as a cyclohexyl carbenium when the cyclohexanol concentration was suppressed. This carbenium is directly formed by the protonation of cyclohexene by the Brønsted acid site and not during the dehydration of cyclohexanol. Subsequent work greatly expanded upon these observations in high detail only possible with *in situ* NMR to show a thorough view of how alkylating reagents and solvents alter the reaction pathways of H-BEA-catalyzed phenol alkylation.[265]

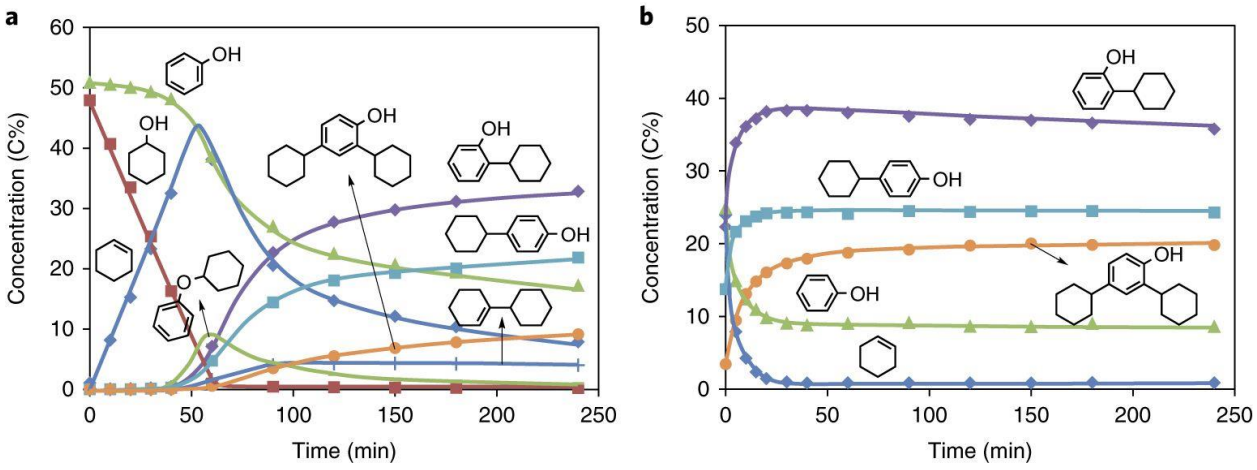

Figure 17. Reaction with cyclohexanol (a). Reaction with cyclohexene (b). Green triangles, phenol; red squares, cyclohexanol; blue diamonds, cyclohexene; purple diamonds, 2-cyclohexylphenol (2-CHP); blue squares, 4-cyclohexylphenol (4-CHP); orange circles, 2,4-dicyclohexylphenol (2,4-DCHP); green line, cyclohexyl phenyl ether (CHPE); blue crosses, 1-cyclohexylcyclohexene (1-CC). Reaction conditions: 5.0 g phenol, 5.0 g cyclohexanol (a) or cyclohexene (b), 0.2 g (a) or 1.0 g (b) H-BEA-150, 100 ml decalin, 5 MPa (ambient temperature) H_2, stirred at 700 r.p.m., 160°C. Reprinted with permission from Y. Lui et al. Nat. Cat., 2018, 1, 141-147. Copyright 2018 Springer.

Figure 17 reveals the time-resolved development of phenol alkylation with cyclohexanol (a) and cyclohexene (b), in solvent decalin. As previously reported, dehydration of cyclohexanol (red squares) to cyclohexene (blue diamonds) and dicyclohexyl ether was the primary transformation during the first period of time in the reaction at 160°C. Phenol (green triangles) remained relatively unperturbed during this induction period. Not until ~70% of the cyclohexanol was dehydrated did C-C and C-O bond coupling alkylated phenol products form. The C-C alkylation products steadily increased with time, while the C-O alkylation products exhibited a transient behavior characterized by an enhancement in signal intensity after the induction period, followed by a decrease in concertation at higher reactions times. In contrast, when cyclohexene was used as an alkylation agent, the reaction initiated immediately. The concentration of cyclohexanol in the aqueous phases did not play a role in the observed reation rate, but this was an influencing factor when decalin was used as a solvent. Based upon this

observation and the detailed results of the reaction with cyclohexanol as the alkylating agent, a scheme was proposed on the basis of monomer and dimer pathways (Figure 18).

^{13}C scrambling in decalin was shown to occur between 3- and 4-^{13}C-cyclohexenes after an induction period, in direct contrast to aqueous phase observations where 1-, 3- and 4-^{13}C-cyclohexenes scramble from the initial phase of the reaction. It was suggested that cyclohexanol does not form a lower-activity alcohol-alcohol dimer in water-filled pores, which is prevalent in aprotic solvents such as decalin. The monomer-dimer distribution is also suggested to not increase dramatically as cyclohexanol was consumed, resulting in a lower concentration of carbenium ions compared to the aqueous phase. Instead, the scrambling is a direct result of the readsorption of cyclohexene onto the active center. It was also revealed that hydrated hydronium ions exhibited less-favorable carbenium ion formation than the non-hydrated acid sites present in apolar solvents, despite the necessity of cyclohexanol to dehydrate prior to carbenium ion formation from cyclohexene. Such insights were made possible by the contributions of *in situ* NMR observing the fine dynamic development of chemical species.

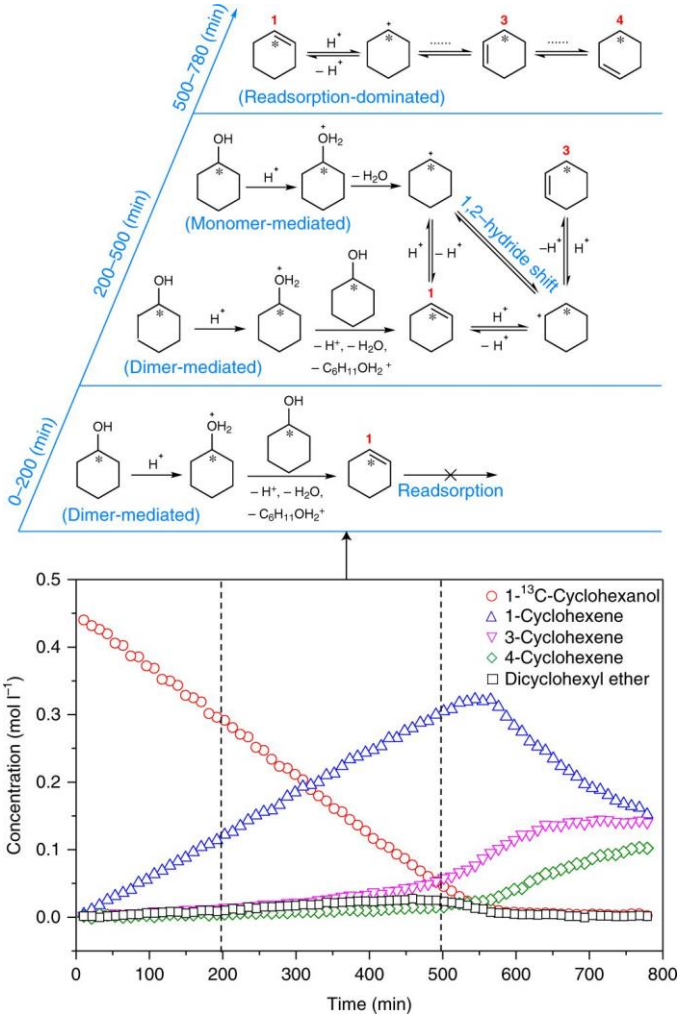

Figure 18. Reaction pathways proposed on the basis of in situ ^{13}C NMR measurements of 1-^{13}C-cyclohexanol dehydration on HBEA in decalin at 126 °C. Within 0–200 min, a significant fraction of the reaction occurs via elimination from alcohol dimer species (the monomer path not shown), while cyclohexene re-adsorption is severely hindered; within 200–500 min, olefin formation occurs via monomeric (increased contribution) and dimeric cyclohexanol (reduced contribution), and cyclohexene re-adsorption becomes less hindered with decreasing surface abundance of dimer species; within 500–780 min, cyclohexene re-adsorption becomes more pronounced after more than 70% of cyclohexanol is converted, and the distribution of labels becomes fully randomized at the end. Reprinted with permission from Y. Lui et al. Nat. Cat., 2018, 1, 141-147. Copyright 2018 Springer.

In addition to the consumption of phenol, its generation from the hydrogenolysis of benzyl phenyl ether, catalyzed by Ni/γ-Al_2O_3 has been investigated by MAS NMR employing the WHiMS rotor system.[463] This systems reveals the unique role a co-reactant can play in the chemical transformation of interest. The key finding enabled by the use of *in situ* NMR showed

that 2-propanol, the solvent employed in the study, served as the source of H_2 during the reaction, dehydrogenating to acetone.

In addition to monitoring reactions for heterogeneous catalysis, sealed MAS rotors offer distinct advantages in monitoring the transformations occurring in biological systems as well as the interphase and solvation structures in electrochemical energy storage systems. This rotor technology has demonstrated suitability for use in biological tissue examination, as shown in Figure 19.[19] *In situ* MAS NRM analysis of an in-tact tissue from a mouse liver enabled the observation of a variety of chemical constituents such as glucose, glycogen, and an array of functional groups. Modulation of the temperature without a loss in signal indicates that such sealing capabilities will eliminate the concern for biofluid leaking, advantageous for both safety and experimental accuracy. Since the rotor may easily accommodate low temperatures, it enables extended analysis at conditions which prevent biological tissue degradation. Such a sealing rotor

simplifies the metabolic profiling of intact tissues by MAS NMR.

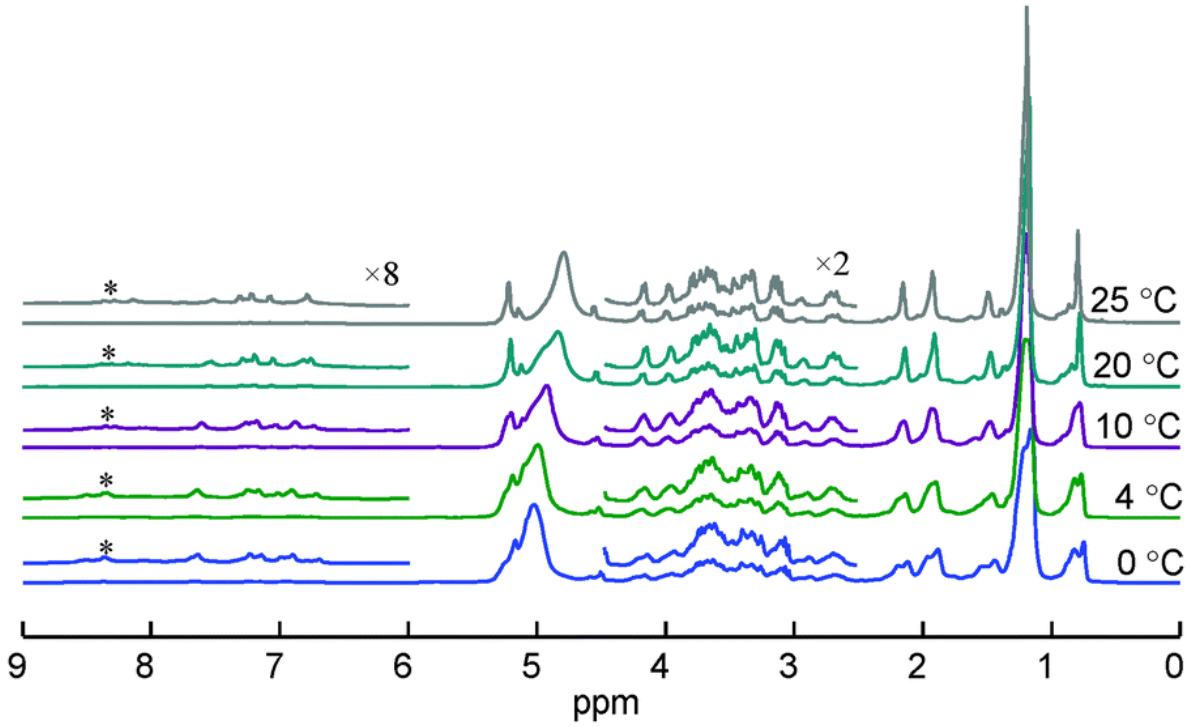

Figure 19. Stacked plot of the variable-temperature ^{1}H MAS NMR spectrum of 280 mg mouse-liver from 0 ℃ to 25 ℃. Reprinted with permission from J. Z. Hu et al, Chem. Comm. 2015, 51, 13458-13461. Copyright 2015 Royal Society of Chemistry.

Another related subject includes that of understanding the interfacial interactions and solvation structures of materials for energy storage. Similar to catalysis applications, much of the critical chemistry for electrochemical cells occurs at the surface. Figure 20 highlights this concept for electrolyte 1.0M $Mg(TFSI)_2$ in diglyme (G2) interacting with a simulated MgO passivation layer of a Mg electrode.[464] Employing sealed rotors enabled the investigation of the thermal adsorption and decomposition of the electrolytes without a loss of solution. At elevated temperatures, diglyme solvent was shown to decompose on the MgO layer to form surface methoxy species. With low $Mg(TFSI)_2$ concentrations, solvent-separated ion pairs were the dominating feature of the spectrum. G2 also adsorbs onto the MgO surface. At high salt

concentrations, however, contact ion pairs form between Mg and TFSI in the solution and the $MgTFSI(G2)_2(G2)_6^+$ cation adsorbs onto the MgO surface. Elevated temperatures stimulate desolvation converting the surface-interacting solvation structure to $MgTFSI(G2)_2^+$ and releasing G2 molecules from the second solvation shell of the original cluster into the solution. Employing such a technique for battery applications demonstrates that the composition of the electrolyte has a directing role in the species present on the electrode surface, which may impact the structures and constituents of the solid–electrolyte interface on working electrodes. Such detailed observations of surface-interacting and solutions species at elevated temperatures are greatly benefitted by sealed *in situ* rotors.

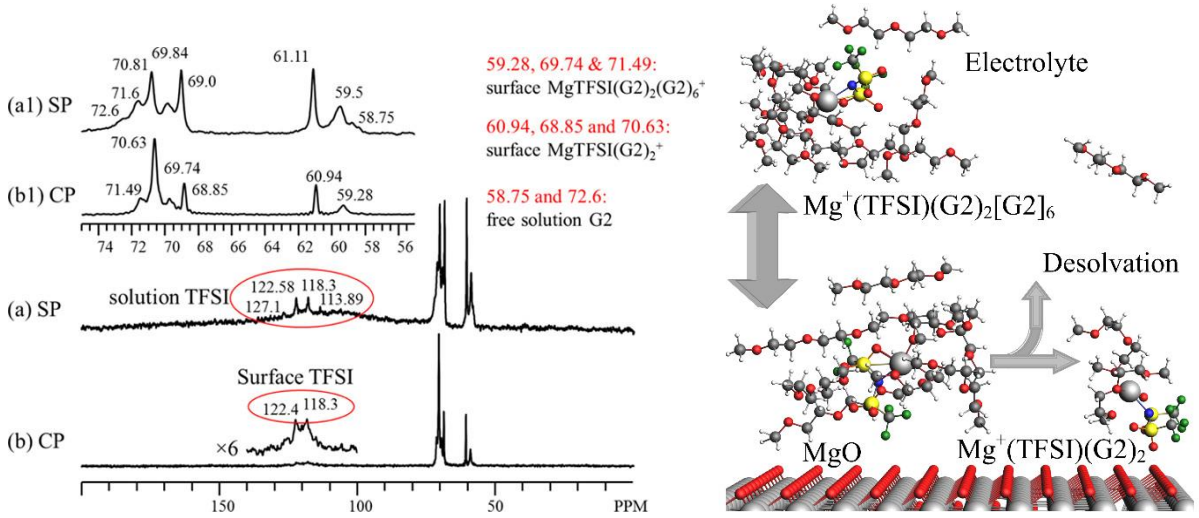

Figure 20. ^{13}C SP/MAS (a) and CP/MAS (b) spectra obtained on MgO and 1.0 M $Mg(TFSI)_2$ in G2 after in situ heat treatment at 180 °C for 1 h. (a1,b1) are horizontally expanded regions of (a,b), highlighting MgO surface-mediated adsorption products with peaks at approximately 60.94, 68.85, and 70.63 ppm, surface adsorbed G2 with peaks located at approximately 59.28, 69.74, and 71.49 ppm, and surface adsorbed $TFSI^-$ at 118.3 and 122.4 ppm. No electrolyte decomposition is observed for this sample. The right side depicts the desolvation process. Reprinted with permission from J.Z. Hu et al. ACS App. Mater. Inter. 2019. Copyright 2019 American Chemical Society.

The described studies represent the capabilities of the current state of *in situ* NMR technology whereby the formation and identification of the nature of the catalytic active sites can be described in detail and a robust analysis of reaction mechanisms at relevant conditions is

possible. Reactions occurring in vacuum atmospheres up to several hundred bar and from low temperatures (well below 0 °C) to 250°C are realizable in systems containing mixtures of solids, liquids, and gases. Such a diverse and inclusive operating range sets broad limits for the types of systems that can be analyzed by *in situ*/operand NMR methods. The future work will be strongly based on employing the current methods to explore the challenging mixed-phase systems at finely-controlled pressures, not previously possible, while addressing key molecular-level questions posed in the field of catalysis. Such efforts will involve extending operations to smaller rotor sizes for faster spinning at higher magnetic fields, such as to enable well-resolved *in situ* quadrupolar nuclei NMR like that of ^{27}Al MAS NMR at 850 MHz. Such efforts are already underway and represent a dramatic improvement over the current precedent. The adaptability of such methods make *in situ* NMR an attractive option for a variety of applications. In fact, not only is it relevant to catalysis, but *in situ*/operando NMR is gaining popularity among fields such as geochemistry,[465-467] energy storage,[8, 464] and biology.[19, 468]

Appendix K: Publication – *In situ* and Ex Situ NMR for Battery Research

From Jian Zhi Hu,*‡ Nicholas R. Jaegers,‡ Mary Y. Hu, and Karl Todd Mueller* *Journal of Physics: Condensed Matter* 2018, 30, 463001.

Abstract

A rechargeable battery stores readily convertible chemical energy to operate a variety of devices such as mobile phones, laptop computers, electric automobiles, etc. A battery generally consists of four components: a cathode, an anode, a separator and electrolytes. The properties of these components jointly determine the safety, the lifetime, and the electrochemical performance. They also include, but are not limited to, the power density and the charge as well as the recharge time/rate associated with a battery system. An extensive amount of research is dedicated to understanding the physical and chemical properties associated with each of the four components aimed at developing new generations of battery systems with greatly enhanced safety and electrochemical performance at a significantly reduced cost for large scale applications. Advanced characterization tools are a prerequisite to fundamentally understanding battery materials. Considering that some of the key electrochemical processes can only exist under *in situ* conditions, which can only be captured under working battery conditions when electric wires are attached and current and voltage are applied, make *in situ* detection critical. Nuclear magnetic resonance (NMR), a non-invasive and atomic specific tool, is capable of detecting all phases, including crystalline, amorphous, liquid and gaseous phases simultaneously and is ideal for *in situ* detection on a working battery system. Ex situ NMR on the other hand can provide more detailed molecular or structural information on stable species with better spectral resolution

and sensitivity. The combination of *in situ* and ex situ NMR, thus, offers a powerful tool for investigating the detailed electrochemistry in batteries.

1. Introduction

The efficient storage of energy has seen a remarkable escalation in importance as an increasingly mobile and energy-demanding global population arises. Since the first voltaic piles were produced over 200 years ago, progressive improvements to this technology have been made to decrease the size, increase the capacity, lengthen the service life, and even allow for the reuse of the cell. Due to the convenience of recharging, batteries, in particular Li-ion batteries, have become the dominant power source for portable electronic devices and mobile electrically-powered vehicles.[380-381] Consumer demand for devices with enhanced power cycle lifetimes has driven the development of rechargeable batteries with continually increasing energy density. As these improvements are realized, a given battery class may reach the theoretical maximum energy density limit, requiring the use of different internal materials for continued progress. As such, extensive research efforts have focused on improving the performance of these energy storage devices by utilizing alternative materials within the battery. Judicious electrochemical improvements require a thorough understanding of the chemical interactions taking place within the battery, prompting a need for thorough scientific research into these technologies.

The chemistry of batteries occurs with four basic components: two electrodes (cathode and anode), a separator, and an electrolyte. The anode (negative terminal) serves as the source of electrons in the electric circuit. The cathode (positive terminal) accepts these electrons. The

electrons are transferred through the electrolyte as ions, allowing for the flow of current. Each of the electrolyte constituents (i.e. solvent, salts and other additives) has a dramatic impact on the performance of the battery and can impact the chemistry of the other materials. The operation of a battery is reliant upon electron and ion transfer across solid-solid and solid-liquid interfaces. Within a given phase, changes in one component can impact the response of electron and ion transfer as well as the reversibility. For rechargeable battery systems, the repeated cycling induces the formation of microstructures at the solid-electrolyte interface (SEI) as well as in the electrode itself due to the migration of ionic species, which is often responsible for battery failure. Thus, it is necessary to have a deep understanding of each component and how they will impact the battery's performance.

The physical and chemical properties of electrolytes are directly derived from the composition of the electrolyte. Maximizing the conductivity, ionic fluidity, non-reactivity with electrodes, and stable operating temperature range are important attributes of an electrolyte. Anodes should be efficient reducing agents that exhibit good conductivity, high coulombic output, and stability. Cathodes, on the other hand, should be efficient oxidizing agents over the desired voltage and stable when in contact with the electrolyte. The separator is a porous membrane that prevents the direct contact of the two electrodes. It must be stable under the reactive conditions and uniformly permeable to the ions or electrolytes carrying the ions.

There exist a number of important considerations regarding the electrode design beyond electrochemical potential. On one hand, the formation of soluble intermediate species is critical to harnessing the power of the cell, but dissolved species can also be an indicator of failure, requiring the use of carefully designed materials to limit the diffusion of soluble species, as in

the case of utilizing sulfur-impregnated carbon nanotubes as a cathode to mitigate diffusion and improve cycle stability.[469] Refinements to the design of electrodes can also be made to prevent significant volumetric expansion of the cell, which is highly undesirable in commercial applications. In one such example, a sulfur-titania yolk-shell architecture was used to preemptively provide void space for volumetric expansion.[470] Other architectures can be envisioned to improve the conductivity of the electrodes.[471]

Despite these efforts, there is still much to learn about the species generated on electrodes and in the SEI during operation. Their nature and the mechanisms by which these microstructures arise are difficult to ascertain. Further, the specific reasons for a given electrolyte showing promising performance over another are not always intuitive, requiring careful molecular level experimental observations to understand the fundamental principles at work. The SEI is often poorly understood as well, despite being a key component in advanced electrochemical devices. This interface forms as solvent and electrolyte salts are reduced to oligomers and crystals on the electrode surface. These electrolytes are stabilized at potentials beyond their thermodynamic limits, enabling the reversibility of the reaction. However, the chemistry, formation mechanism, and cycle-induced evolution of these are largely unknown, promoting a strong desire for detailed investigations.[472]

A variety of techniques have been employed to evaluate the performance and chemistry of batteries to better understand their operation and failure mechanisms for continued enhancements to performance. Techniques unrelated to NMR have provided excellent insight for battery technology. Many of these methods will be briefly discussed to provide an overview of the insight they provide. Cyclic voltammetry, for instance, is extensively used to characterize the

general electrochemical performance of a battery, such as the stability and reversibility of the reaction at a given potential.[473] More detailed analysis allows for a measurement of the electrode reaction kinetics.[474] This technique, however, fails to provide a clear and detailed picture of the molecular changes that occur throughout the repetitive cycling process. In particular, this technique lacks a decisive description of the chemical evolution of the various battery components and how this dynamic process impacts the properties of the cell.

Beyond the standard electrochemical performance evaluations, characterization of the materials encourages a deeper understanding of system limitations and potential enhancement routes. One such avenue for characterization is the direct imaging of the battery with microscopy techniques.[475-476] The advent of highly-developed aberration-corrected scanning and transmission electron microscopy (TEM) has propelled the capability to atomic-scale imaging.[477-482] Ex situ beam imaging has been widely applied to analyze the structural features of battery constituents, but failed to capture information related to the dynamics of the charge/discharge cycles.[483-485] *In situ* investigation of batteries with TEM is challenging owning to the high-vacuum operation of the equipment and subsequent incompatibility with liquid electrolytes. To mitigate this, three strategies have been explored to provide an *in situ* analysis of these materials. The first, an open-cell configuration utilizing ionic liquid-based electrolytes, takes advantage of nanowire anodes that are wetted by the ionic liquid to mimic an electrolyte system.[486-487] It has been used to study a number of anode materials, including Si, Ge, Al_2O_3, SnO_2, ZnO, graphene, Sn, and carbon nanotubes.[488-494] This concept, however, suffers from ionic liquid polymerization in the presence of the electron beam, significantly shortening the number of charge/discharge cycles allowable by the system. The next, another open-cell configuration but using metal and metal oxide

electrolytes, has been used for Li metal and silicon electrodes with a lithium oxide electrolyte.[495] Variations exist, but this design can be used with Na-, Mg-, and Ca-ion battery systems as well.[496-497] Again, this configuration is not representative of a truly rechargeable battery due to limitations on the charging cycles and beam-induced effects, but these open cell configurations offer significant advantages in spatial resolution imaging and chemical analysis by electron energy loss spectroscopy.[497] Finally, a closed liquid cell battery design has been employed to better mimic the electrolyte diffusion and electrode interaction characteristics exhibited in a typical cell. Initiated by studies on copper nanoparticle growth from an electrolyte solution, electrochemical cells for *in situ* TEM were developed to push the technology forward.[498-499] Working battery cells soon followed that allowed for the direct observation of the lithiation, ion transport, and SEI layer formation.[500-503] However, replicating a realistic number of charge/discharge cycles is still a concern with this technology. In addition to these, liquid observation is also possible to monitor changes in electrolytes, but further development in the field is required to match the performance of analyzing the solid components.[476]

Raman spectroscopy can also be used to characterize changes in battery components. Ex situ Raman spectroscopy and ellipsometry have been employed to characterize the carbon films used as electrodes in Li-ion cells.[504] For example, they have shown that the structure of different carbon samples is degraded slightly through progressive discharge cycles. In addition to observing changes to the carbon anodes, cathodic $LiCoO_2$ rock-salts have been shown to deintercalate lithium species and result in seemingly random Li^+ occupations of the available sites on the lattice.[505] In addition to the information ex situ Raman can offer, *in situ* Raman sampling cells have also been employed to observe the specific cycling stages in which

intercalation of electrolyte ions into graphitic electrodes occurs.[506-507] For instance, similar technologies have been used to show the specific redox steps proceeding at given voltage transitions for Li-ion and Li-S batteries, for example.[508-509] Surface reaction mechanisms at the electrolyte-electrode interface can be probed as well, as was performed for Li-ion and Li-V_2O_5 systems.[510-512] It has even been used to show the complex and oscillatory distribution of ions in various regions of the separator and other fragments of the battery.[513-514] UV-vis spectroscopy has also been shown to provide quantitative evidence on the polysulfide chain growth during Li-S battery operation.[515] Similarly, infrared methods have played a role in better understanding the nature of the SEI.[516-517] These real-time capabilities have notably contributed to a deeper understanding of the changes that occur within the battery.

A number of X-ray methods have contributed to the scientific understanding of battery systems by analyzing samples both *in situ* and ex situ.[518] X-ray diffraction (XRD), for instance, can be used to understand the phase and layer spacing of electrodes.[519] An early demonstration of *in situ* XRD measurements for electrochemical applications focused on understanding the phases generated during the intercalation of lithium into graphite during electrochemical cycling.[520] This work studied various Li:C_6 ratios and found a random distribution of Li at low Li content with more distinct phases arising with the intensification of metal content, accompanied by an increasing carbon layer spacing as the lithium content increased. Utilizing synchrotron radiation and a specially designed cell, Walus *et al.* were able to separate the diffraction pattern contributions from individual electrodes in a Li-S battery from the signal of the entire cell.[521] This demonstrated the formation of Li_2S on the anode at the early stages of the discharge cycle and complete consumption during the subsequent charge. Additionally, XRD was used to

demonstrate the formation of a different sulphur allotrope after recrystallization. Numerous additional *in situ* XRD studies have focused on the crystalline phases present for a variety of battery systems; Li-Si, Li-MO_x, Li-air, Li-ion, Na-ion, etc.[522-529] An *in situ* XANES cell has also been used, though less commonly due to the necessity of a synchrotron, to investigate electrodes and electrolytes for sulfur speciation on the sulfur K-edge, showing the impact of sulfur species on capacity.[530-531]

X-ray photoelectron spectroscopy (XPS) and Auger electron Spectroscopy (AES) have been used both *in situ* and ex situ to understand the bonding and oxidation state of the electrodes throughout the cycling process, but these techniques suffer from drawbacks related to the need to operate under ultra-high vacuum (UHV) conditions and difficulties with mitigating the relevance of closed cell designs with open cell detection sensibility.[532-533] To address the concern about operating under UHV conditions, recent XPS efforts on Li-air battery research take advantage of a special *in situ* "ambient pressure" cell that allows for reaction monitoring up to 500 mtorr (0.0007 bar), which demonstrated notable differences in the Li species present upon discharge as compared to UHV studies.[534] Though an impressive improvement, this pressure falls significantly short of ambient (1 bar). Despite these shortfalls in realistic condition representation, key insights have been gained from employing the technique with complementary experiments.[535-537] Additionally, XPS benefits from the ability to detect the presence of organic impurities on the electrode surface that arise from power cycling.[538]

In situ and ex situ nuclear magnetic resonance (NMR) spectroscopies have contributed significantly to the field. NMR allows detailed molecular level information related to electrolyte, separator, and electrodes all to be observed if contained within the detection RF

(radio frequency) coil. Although not without its own limitations in sensitivity, it holds many unique advantages and has been thoughtfully developed over the last two decades. For one, NMR is (generally) a quantitative technique that allows for tracking the concentration of species regardless if they are liquid, solid, gaseous phases or a mixture of these phases from sample to sample or over time as the electrochemical reaction proceeds. For solid phases, both the amorphous and the crystalline phase can be captured at the same time. It should be noted that quantitative measurements are limited to skin depth when applied to metals and thus the thickness of the microstructure and bulk surface area must be considered.[539] Another significant advantage to NMR is that it is non-destructive, allowing non-invasive detection of the process under true *in situ* conditions where unique species may only exist. The true *in situ* conditions include, but are not limited to, operating at a wide temperature range, e.g., from well below 0°C to well over 100°C, and operating at pressures ranging from well below ambient to 100 bars and above.[235, 377, 379, 447] Furthermore, the layout of the battery components and the size of the battery can be made the same as commercially available mini-sized batteries. The only exception here is that the outmost stainless container is replaced by a plastic holder to allow the RF field to penetrate into the battery electrodes, separator and electrolytes. In combining the *in situ* NMR with the detailed molecular information of stable species obtained by ex situ methods, NMR can be an invaluable addition to the experimental arsenal of a battery investigation.[540-542]

Two additional differences between characterization by NMR and other techniques are the intrinsic length and time scales of the measurements performed. Herein, we seek to provide an overview of these scales for NMR, but would refer the reader to other literature on the spatial and temporal limits of other methods.[543] The time scale associated with NMR is not a straight-

forward, singular concept. In fact, it should be regarded as a collection of scales due to the abundance of phenomena that this spectroscopy technique may probe. While changes to specific chemical signals can be monitored during a process, the mobility of these species and their interactions with surrounding media reveal unique transient information. These phenomena will be discussed to give the reader a sense of the capabilities NMR processes that can be employed to better understand battery systems.

The local chemical environment of the nucleus being analyzed directly impacts observed chemical shifts. Such a measure for the local environment relinquishes insight on the bonding structure and lengths, torsion angles, hydrogen bonding networks, secondary structures, and electric charges.[544] Due to the multiple factors determining the observed frequency, theoretical calculations that simulate bonding structure and secondary structures are often necessary for a deeper interpretation of the observed signals. Such calculations have shown the important impact of a second solvation shell on the observed solute chemical shifts, suggesting a length scale on the order of nm.[545] Nucleus-electron coupling has also been shown to impact NMR signals, suggesting a range of a few angstroms.[546] Further lengths scales could arise from the molecular motion of the nucleus itself as it is exposed to different environments. Environment-specific information is commonly used to provide dynamic speciation of observed signals. Though it has relatively low temporal resolution, chemical species transformation during a time-lapsed *in situ* experiment is one direct measure of the time scale for NMR spectroscopy. This type of experiment monitors changes in the chemical structure over a period of time. For example, in 5.3. In-situ NMR on Li-ion battery research we recount the evolution of ^{7}Li species on the electrode over time during electrochemical cycling and highlight the changes in species

identity over time. The time scale to analyze such transformations is heavily dependent upon the system. Factors such as the nucleus, relaxation environment, spin abundance, and experiment type all play an important role in determining the minimum time for analysis. This type of experiment can be conducted on a wide range of time scales, typically on the order of seconds (or fractions of a second) for an abundant ^{1}H system to hours or even days on a less favorable nucleus. Similar time resolutions (though often extended) can be applied to observe the change (or derivative) of other transient behaviors described, such as a change in the chemical exchange rate during a reaction.

In addition to the chemical shift value describing length-based information, the linewidth of a given signal provides the dynamic properties of a molecule, such as the rotational and translational behaviors. Though related to the relaxation mechanisms (see below), this motion is also related to the interchanging of species environment. This phenomenon is termed chemical exchange and is readily elucidated by NMR.[547] In this, a given nucleus may sample a range of magnetic environments, such as an interchanging ligand state, during the exchange process and the resulting NMR spectrum will provide kinetic data on the exchange rate. The concept is analogous to the uncertainty principle whereby the uncertainty in the resonance frequency is inversely proportional to the lifetime in a given state. For instance, when the exchange rate is relatively high, the lifetime in a given state is low and the resonant frequency is apparent. The temporal limitations of chemical exchange are determined by the frequency difference between two species, and thus the nucleus and magnetic field, according to Equation 14.

$$\tau_{coalescense} = \left(\sqrt{2}\pi\Delta\nu\right)^{-1} \quad \text{Eq. 18}$$

$$= k^{-1}$$

Where $\Delta\nu$ represents the frequency difference between the magnetic environments. For a slowly exchanging process, each resonance is well-resolved. Exchange Spectroscopy (EXSY) has been used in this regime to quantify dynamics on the ms time scale.[548] As the exchange rate increases, the lines broaden and migrate towards the weighted average signal location. When the exchange rate reaches about an order of magnitude higher than the frequency difference, the resonances are averaged to a single broad line. On this time scale, fractions of ms, the Carr-Purcell Meiboom-Gill Relaxation Dispersion (CPMG RD) approach can be applied to refocus the exchange broadening with the spin-echo pulse sequence to elucidate the relationship between this observed broadening and the exchange rate.[549] This single line narrows to reveal a sharper resonance up until about three orders of magnitude faster exchange than the frequency difference.[550] To visualize the range of time scales for the exchange process, the reader can imagine the case of two resonances at the extremes of a given nucleus' chemical shift range. The time scale involved in the averaging of these two species can be approximated by Equation 1, bearing in mind the effect of magnetic field on the frequency difference. As shown in Table 28, the NMR time scale for ^{1}H exchange at 7T varies from 0.2 s (given 1 Hz resolution) down to 58 μs for the full range of 3.9 Hz. Since the frequency range (columns 3 and 5) vary based on the field strength, so too does the NMR time scale for exchange, where a proportional reduction is observed between columns 4 and 6.

Table 28. Representative chemical shift ranges and times scales for nuclei at two magnetic fields.

Nucleus	Approx. Shift Range, ppm	Shifts at 7T, kHz	7T Time scale	Shifts at 19.9T, kHz	19.9T Time Scale
^{1}H	13	0 - 3.9	0.2s - 57.7µs	0 - 11.1	0.2s - 20.4µs
^{2}H	13	0 - 0.6	0.2s - 0.4ms	0 - 1.7	0.2s - 0.1ms
^{6}Li	28	0 - 1.2	0.2s - 0.2ms	0 - 3.5	0.2s - 64.2µs
^{7}Li	28	0 - 3.3	0.2s - 68.9µs	0 - 9.3	0.2s - 24.3µs
^{13}C	200	0 - 15.1	0.2s - 14.9µs	0 - 42.8	0.2s - 5.3µs
^{15}N	900	0 - 27.4	0.2s - 8.2µs	0 - 77.6	0.2s - 2.9µs
^{17}O	1160	0 - 47.2	0.2s - 4.8µs	0 - 133.7	0.2s - 1.7µs
^{19}F	300	0 - 84.7	0.2s - 2.7µs	0 - 240	0.2s - 0.9µs
^{25}Mg	70	0 - 5.6	0.2s - 40.5µs	0 - 15.7	0.2s - 14.3µs
^{29}Si	519	0 - 30.9	0.2s - 7.3µs	0 - 87.7	0.2s - 2.6µs
^{31}P	700	0 - 85	0.2s - 2.6µs	0 - 241	0.2s - 0.9µs
^{51}V	1900	0 - 150	0.2s - 1.5µs	0 - 425	0.2s - 0.5µs
^{133}Cs	160	0 - 6.3	0.2s - 35.7µs	0 - 17.8	0.2s - 12.6µs

The observation of dipole-dipole coupling by NMR can also indicate the time scale of molecular motion. The scalar coupling constant can be applied to Equation 1 to provide the threshold for the exchange rate. If the lifetime of the species in a given environment is short compared to the inverse of the coupling constant, no coupling will be observed in favor of a single resonance. Typical coupling constants for ^{1}H-^{1}H, ^{13}C-^{1}H, and ^{15}N-^{1}H may be around 10, 150, and 50 Hz. These correspond to about 22, 1.5, and 4.5 ms, respectively, though this can be reduced to the ps time scale in specialized applications.[551] Since J-coupling is not impacted by field, these time scales are field independent and directly impacted by the chemical bonding.

In addition to gaining insight on the time scales involved with dynamic chemical environments, NMR is widely used to study the relaxation time scales of chemical species. T_1,

for instance, is a measure of the longitudinal NMR relaxation that describes the rate in which excited nuclear states relax to equilibrium magnetization in the direction of the applied field. This relaxation is governed by modulation of the nuclear spin energy levels from fluctuations in magnetic interactions with components that match the Larmor frequency of the nucleus. This could arise from such physical processes as vibrations, torsion angle rotations, and looping motions.[550] The spin-lattice dipolar relaxation rate (reciprocal time) is described by Equation 2 and shows a maximum rate at $\omega\tau_C = 0.6158$, where ω is the resonant frequency and τ_C is the correlation time.[552] Though an indirect measure of the time scale, it is important to note that it is dependent upon the Larmor frequency, and thus the magnetic field, where the time scale of molecular motion associated with this relaxation is on the order of $(2\pi\Upsilon)^{-1}$. Though spin-lattice relaxation times are typically on the order of seconds, the corresponding time scale for molecular motion (translation, rotation, or vibration) is on the order of 0.1 to 10 ns. In considering the relaxation initiated by paramagnetic centers, such as a rotating metal complex, the time scale for this motion can extend down to tens of picoseconds.[553] On a similar time order, but often smaller in magnitude to the spin-lattice relaxation time, transverse relaxation via spin-spin interactions can similarly be detected. The characteristic dipolar equation describing T_2 can be found in Equation 3. Further system insight can be obtained through measurements of the two relaxation rates. Through this, time scale uncertainties can be drastically reduced to reveal the correlation time between species, τ_C.

$$\frac{1}{T_1} = \frac{3}{160}\frac{\mu_0\gamma^4\hbar^2}{r^6}\left[\frac{\tau_C}{1+\omega^2\tau_C^2} + \frac{4\tau_C}{1+4\omega^2\tau_C^2}\right] \quad (19)$$

$$\frac{1}{T_2} = \frac{3}{320}\frac{\mu_0 \gamma^4 \hbar^2}{r^6}\left[3\tau_C + \frac{5\tau_C}{1+\omega^2\tau_C^2} + \frac{2\tau_C}{1+4\omega^2\tau_C^2}\right] \quad (20)$$

Where γ is the gyromagnetic ratio (rad/s/T), ħ is the reduced Plank's constant (1.05456 x 10^{-34} m^2 kg/s), ω is the Larmor frequeny (s^{-1}), and μ_0 is the magnetic permeability of free space (1.2566x10^{-6} H/m). Transverse relaxation in the rotating from can also be employed to elucidate the time scale for fast exchange rates that are challenging to determine by other methods (such as CPMG) due to the maximum pulsing rate.[554] For these high exchange rates, a technique exists that enables the determination of $T_{1\rho}$. This approach is further advantaged by the enhanced sensitivity of minor species in an exchange process and by the requirement of only one static field strength. This method provides the potential to identify exchange rates on the order of ms to μs.[555] The interested reader is directed to other sources for details on the pulsing schemes for $T_{1\rho}$ determination.[556]

Given the variety of mechanisms by which NMR can provide insight into the time scales of the chemical interactions, it can certainly be considered an attractive option to probe chemical systems. Though this review and many published works primarily analyze the time scales associated with changes to the species identity (chemical shift), the framework for additional insight exists, demonstrating the power for NMR to supply a wealth of information about chemical systems *in situ*. Figure 21 provides a summary of the applicable time scales for NMR.

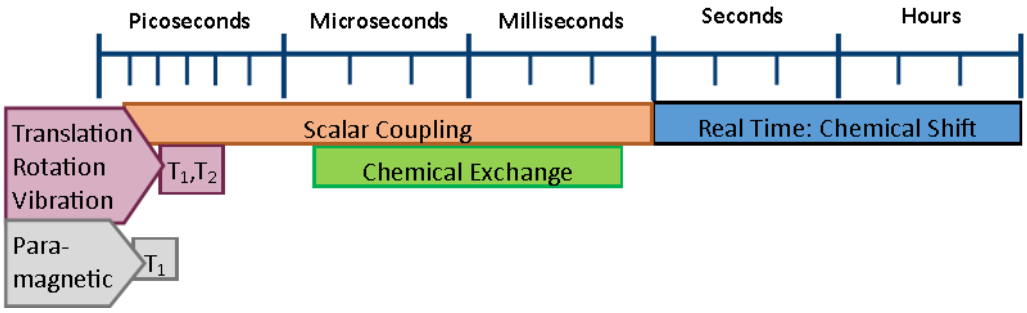

Figure 21. Sketch of time scale summary

A recent review by the Grey group has described their own thorough endeavors related to NMR spectroscopy applied to batteries.[557] The article outlines the purpose for utilizing NMR spectroscopy to understand battery systems as well as specific instructions for sample and experimental preparation and design. Other, battery-class specific reviews are described in the relevant sections. Herein, we describe the development of *in situ* and ex situ solid-state NMR for battery research and discuss key examples that highlight the power of NMR in battery research. The included examples are specifically centered on chemical shift-structure relationships to identify the types of species present in batteries and electrolytes. These methods are complimented with computational chemistry to make accurate assignments of the observed spectral featured. An understanding of the temporal resolution on the time scale of several seconds and higher is described to monitor the chemical transformations during cycling.

2. In-situ NMR technologies

Distinct advantages present themselves in conducting *in situ* observation. Apart from the advantage of observing the state of the material during the entire process instead of only discrete stages of a transformation, *in situ* investigation does not require numerous samples to be prepared for a full understanding of an entire process, saving time and promoting sample

consistency. Instead, one representative sample can be scanned throughout the entire process. Importantly, some transient species can only exist when the electric wires are attached to the battery systems with current constantly applied.[558-559] There are, however, technical challenges in successfully devising an apparatus suitable for *in situ* investigation. A number of iterations have taken place to promote *in situ* capabilities that have better reliability, sensitivity, and longevity.

The first demonstration of *in situ* NMR for batteries came from technology developed by Rathke et al. at Argonne National Laboratory.[560] Their design employed a toroid cavity in their custom built probe similar to that developed for magnetic resonance imaging.[561-562] The first battery experiments used Li-ion coin and cylindrical cell containers that integrated operation with the RF coil.[563-564] This was an exciting advancement that allowed for ^{7}Li NMR observations on a live battery system where charge-discharge cycling took place directly in the magnet. The drawback on employing the toroid coil was that the same copper disc (or central wire) was simultaneously used as both the current collector and radio frequency conductor for NMR signal excitation and detection. This means that for *in situ* measurement to begin, the battery operation had to stop periodically or non-periodically. Still, the battery was charged and discharged within the probe and magnet and measurements were taken shortly after the cycling was stopped, but this was a severe limitation in terms of truly *in situ* measurement.

Though the toroid design for in-situ experiments provided a new frontier for the investigation of a functioning battery, it suffered from challenges in conformity with standard (Lithium ion) battery designs in addition to severely limited signal-to-noise ratios. In the mid-nineties, small, flexible, plastic Li-ion batteries with the capability of being recharged were

demonstrated by Bellcore, offering improved application flexibility.[565] To address the aforementioned disadvantages of the toroid design, this plastic cell design was sized for utilization as an *in situ* NMR cell by Chevallier et. al. in Orléans, France in 2003.[566] This allowed for direct use inside an NMR probe for truly *in situ* electrochemical cycling since recording in open-circuit mode was no longer a limitation.[567] A schematic of the plastic bag cell and the accompanying detection and cycling system is shown in Figure 22. In this design, each electrode was supported on a copper current collector before being treated in a 1% solution of poly(vinylidene fluoride-hexaflouropropylene (PVDF-HFP) in acetone and laminated (130°C, 20 psi) to opposite sides of a separator membrane composite composed of PVDF-HFP and dibutyl phthalate. With the stack activated with electrolyte prior to the second electrode being laminated to the separator, the two electrodes, separated by a membrane and resting between current collectors, were then packaged into an ultra-thin aluminum blue bag measuring 4 cm by 8 mm. These plastic bag cells provided a low cost and flexible option for *in situ* measurement, but experienced relatively short lifetimes (five days has been reported) due to cell breakage and permeability. The cells can also experience large electrical resistance.[568] Al-coated bags have been used to extend the cell lifetime, but these decrease the sensitivity of the experiment.[567] Early demonstrations of ^{7}Li *in situ* NMR for battery technology with these plastic cells allowed for up to 2 mg of Li and 16.7 mg of graphite to be involved in the intercalation process.[569] This design allowed for the successful observation of reversible lithium intercalation into the carbon layer, where a direct charge transfer from lithium is realized. After the formation of these intercalated species, lithium is capable of penetrating the graphitic nanopores to form quasi-metallic species that registered downfield.[566] It has also allowed for the firm identification of the

dense interstitial LiC_6 and LiC_{12} as well as clarified the true identity of the dilute LiC_9 stage, demonstrating the importance of careful sample preparation (washing stage) for the ex situ NMR data collected in the decades prior.[570-572]

While the flat plastic cell propelled *in situ* NMR for battery applications and reduced the metallic components contained within, it suffered from key drawbacks such as the restriction to plastic electrodes and fragility that leads to solvent leakage and a loss of electrical contact. To address this, an improved design made especially for Li-ion batteries was constructed from a cylindrical plastic housing with a threaded seal, reducing the sealing area and metallic components while providing good cycling characteristics, as demonstrated with ^{31}P NMR for on Cu_3P electrode in the Li-ion battery.[573] Another design is based on a cylindrical micro-battery developed for a telemetry system for salmon tracking.[574] This jelly roll structure was subsequently used to study Li-S batteries where the Kel-F holder containing the battery cell sat directly inside the RF coil and a charge cycler, could be connected to the apparatus outside of the magnet.[575] Similar versions of the cell have been used for lithium alloy and graphene oxide battery studies.[576-577] Briefly, the battery was comprised of cells symmetrically fabricated by two flat Li metal foils (7 mm x 7 mm x 0.75 mm) separated by a flat glass fiber and inserted into the Kel-F holder. An electrolyte, such as propylene carbonate, was incorporated and the entire system was glued/epoxy sealed with a Kel-F cap containing a 1 mm hole in the center for the copper wires carrying the current..[578] The cell and glass spacers fit tightly inside the plastic holder, which is capped and glued shut prior to placement inside the probe and magnet. The design can be subsequently improved by removing the need to rely on glue to form the seal by utilizing O-rings. Further improvements come from stacking, but separating, electrodes and

connecting them electrically in parallel to enhance the sensitivity of the spectroscopy. The use of O-rings will improve operating conditions and quality of the seal.

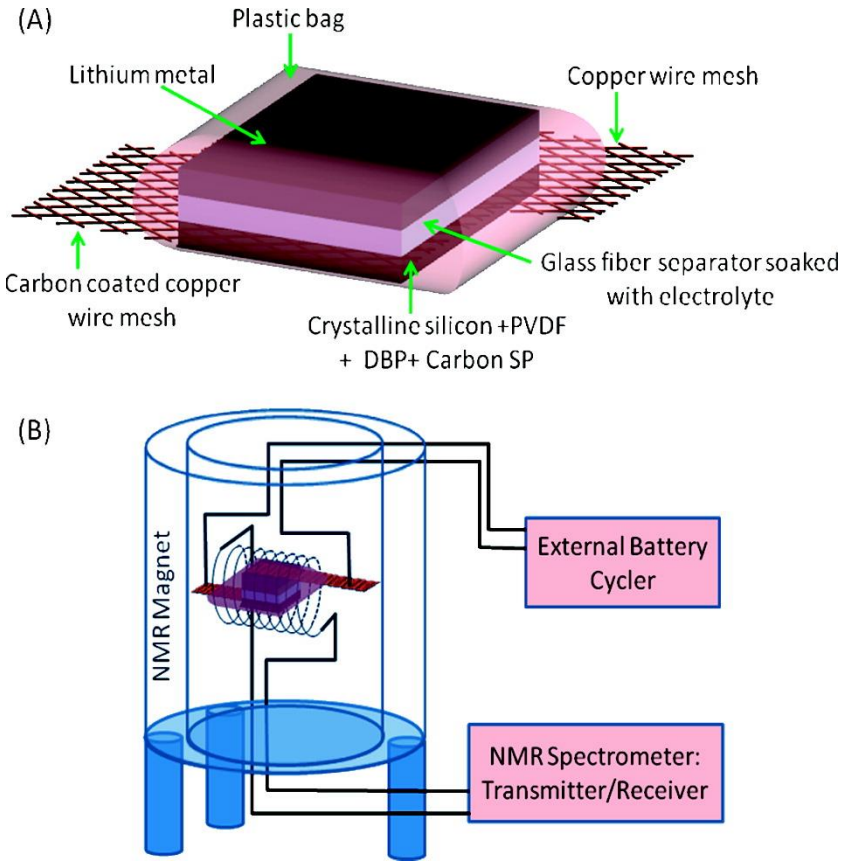

Figure 22. (A) Schematics of the flexible plastic battery used for the in situ static NMR experiment and (B) the in situ static NMR setup. A similar, but more detailed schematic with photographs has been published by O. Pecher et. al. [568] Reprinted with permission from Key et al. J. Am. Chem. Soc. 2009. Copyright Elsevier 2009.[579]

The most recent design of an *in situ* NMR battery cell was developed in Germany by Kayser et al.[580] The design incorporated carefully 3-D printed components that enabled a rigid seal, reproducible cell compression, and long-run capabilities (tested up to 2400 hours). The battery cell is placed on the bottom of a hollow plastic cell body. The body has a smaller hole which the battery covers wherein a contacting stick will consistently apply the same pressure to the bottom of the cell due to a change in diameter of the shaft and hole. A top piece slides into

the bore of the cell body to contact the top of the cell. This also has a hole for a second contacting stick to similarly apply a consistent contact to the battery cell. The entire apparatus is sealed tight with nuts that compress bellowed cutting rings. This method has shown good sealing with a loss of just 1 bar of 15 after 1 day. Based on the material components used, the cell should be able to tolerate up to 120°C and exhibit good chemical resistance over many years. The entire cell fits into a homemade saddle coil positioned with careful attention to the alignment within the magnetic field to ensure consistent and reproducible measurements.[568, 581-582] Though still a new development, this cell paves the way in understanding the degradation pathways for batteries across hundreds of cycles due to its reliability and robustness.

Nowak et al. have developed an *in situ* battery cell for liquid electrolyte measurements.[583] This device employs a cylindrical battery that rests atop the electrolyte measurement area, i.e., an extended compartment containing only liquid electrolytes intentionally placed inside the NMR detection coil. The authors report ^{1}H and ^{19}F measurements to monitor signals associated with fluoroethylene carbonate and fluoromethyl methyl carbonate during electrochemical cycling. Through these initial demonstrations, a detection limit of 200 μmol/L was determined for ^{1}H and ^{19}F in this cell.

3. Ex-situ NMR techniques

While *in situ* techniques are certainly the pinnacle of representing a battery's operational condition, difficulties can arise in capturing the species of nuclei that are relatively more challenging to probe in terms of both sensitivity and linewidth. While ^{1}H, ^{7}Li, and in some cases ^{13}C are great candidates for time-resolved NMR spectroscopy, low sensitivity, low abundance, and quadrupolar nuclei strongly rely on magic angle spinning (MAS) and longer spectral

acquisitions for a detailed and highly resolved picture of the sample's chemical state, especially when in the solid state. Battery applications employ an array of atoms that can be probed with NMR, including ^{1}H, ^{2}H, ^{6}Li, ^{7}Li, ^{13}C, ^{15}N, ^{17}O, ^{19}F, ^{25}Mg, ^{29}Si, ^{31}P, ^{51}V, ^{133}Cs, and others.[505, 584-591] Many of these are either quadrupolar or low abundance nuclei.

While informative, the highly abundant and spin ½ nuclei do not always provide the clearest understanding of the chemical system. To compensate, less abundant or quadrupolar nuclei are often probed to investigate the detailed molecular environments in battery materials. Low abundance nuclei are a particular challenge for this relatively insensitive spectroscopic technique. ^{17}O, for example, is a nucleus with natural abundance of only 0.038%. Moving to a high field can help promote a stronger oxygen signal through a more pronounced Zeeman interaction. However, more distinct advantages can come from employing a probe that allows for a larger sample volume since the detected signal is directly proportional to the number of spins in the coil. If isotopic enrichment is not practical, an increase in sample volume is generally the simplest way of boosting a signal to acquire detailed information about a chemical system. ^{17}O is also a quadrupolar nucleus, resulting in relatively broader lines. A number of interactions contribute to the resulting spectrum, as indicated by this summation of Hamiltonians:

$$H_{Int} = H_Z + H_D + H_{CS} + H_K + H_J + H_P + H_Q^1 + H_Q^2 + H_Q^n + \cdots$$

where the Zeeman (Z), dipolar (D), chemical shielding (CS), Knight shielding (K), spin-spin coupling (J), paramagnetic (P), and nth-order quadrupolar (Q) interactions can all play a role in

the resulting NMR signal. Quadrupolar nuclei generally suffer from low symmetry and wider lines due to the quadrupolar interactions that arise from the anisotropyof the nucleus charge distribution with the electron field gradient. This quadrupolar effect can be partially reduced by employing more powerful magnetic fields. In cases where the quadrupolar nucleus also resides in a solid, which may be in the case of extracted SEI, more advanced techniques are required for high resolution spectroscopy. The advent of MAS has also had a dramatic impact on the interpretation of NMR spectra.[592] This technique allowed for solid samples to approach resolutions obtained with liquid samples by averaging out many of the interactions that impact line-width. Odd-ordered Quadrupolar Hamiltonians converge to zero when the sample is rotated at 54.74º with respect to the external magnetic field, leaving behind only the even-ordered quadrupolar terms and dramatically improving the signal to noise ratio of a spectrum. As outlined later, the strategies of employing larger sample volumes, higher magnetic field, and MAS have all been used to make experimental observations on natural abundance, quadrupolar and solid samples.

While highly abundant nuclei are relatively more studied due to the ease of acquisition, in some cases they are not the best suited for an application. Lithium-based batteries, in particular, have a large body of research where ^{7}Li and ^{6}Li NMR have been both utilized to gain insight on the system.[577, 585, 593-596] ^{7}Li is a spin 3/2 nucleus of 92.5% natural abundance, making its acquisition easy relative to ^{6}Li (I=1, 7.5% nat. abundance). Further ^{6}Li also suffers from low sensitivity due to its generally longer relaxation times; however, the quadrupole moment is smaller than that of ^{7}Li (~$2.4\cdot10^{-30}$ vs ~$4\cdot10^{-30}$ e m^2) and dipole-dipole interactions are also much weaker, allowing for higher spectral resolution and significantly enhanced structural

information.[597-599] This can provide a direct benefit *in situ*ations in which 2 Li are near each other, a closer approximation of the isotropic chemical shift is desired, or the source of relaxation is not well-understood. For batteries, the relatively more challenging ^{6}Li might be a preferred technique if a variety of Li species are present and high spectral resolution is required to distinguish the signals. An additional advanced method for ex situ analysis of Li-based batteries includes pulsed field gradient (PFG) NMR, which has been employed to secure a firmer understanding of the role of temperature in the solvation structure of Li, Cs, and H species.[600]

While significant strides have been made to push traditional battery system investigations towards *in situ* conditions, redox flow technology is primarily probed ex situ due to the difficulty of pumping steady streams of electrolytes along an interface while simultaneously detecting NMR-active species. These studies typically involve detailing the solubility and solvation structures of electrolytes in a given system to better understand solvent and ion interactions at different solute concentration levels to show the concomitant fluctuations of contact-ion pair presence and solvent-solvent or solvent-ion interactions.[601] Ex situ NMR has been shown to reveal the key insights on the impact of functionalizing electrolyte components, such as ferrocene, towards enhancing the solubility to overcome performance barriers of non-aqueous electrolytes.[602-603] Similarly, the rational design of electrolytes has been demonstrated for the vanadium redox system where the effects of chlorine have been discerned.[604-607] Indeed, NMR has become an important technique for characterizing the chemistry of electrolytes in redox flow battery systems.[608-613] This same strategy can be broadly applied to electrolyte systems of an array of battery classes. An example for understanding the solvation structure of electrolytes for Mg-based batteries will be detailed in Section 5.5. It is important to mention that the NMR

interpretation for many of these electrolyte systems is aided by computational modeling, which will be discussed in the subsequent section.

4. The role of computational modeling

While direct experimental observations are essential to a deep scientific understanding of a given battery process, computational approaches are gaining both popularity and importance for their predictive capabilities in chemical systems. Computational approaches become further important for relatively complicated spectroscopic studies where a given chemical system does not have a well-defined library of reference compounds that represent the chemical environments being probed. This might arise from unique environments only observed during a reactive process, or an entirely new material that has never before been probed. In these cases, it is often beneficial to complement NMR studies with computational simulations. As it applies to interpreting the NMR spectra related to batteries, two techniques serve as the primary aides in elucidating the signals observed; density functional theory (DFT) and molecular dynamics (MD).

DFT modeling is a computer-based method that uses quantum mechanics to describe the electronic structure of a many-body system. Functionals of the electron density are used to compute system properties. This method relies on exchange-correlation functional approximations that account for expectation differences when wave functions overlap and the influence of other electrons on a translating particle. This method allows for one to calculate the geometry and electron density of a system that can be used to compare to experimental observations. As it applies to battery systems, DFT can be used to better understand which structures show preferential formation during lithiation or model the effects of defects on cathodes.[614] It can also be used to calculate NMR parameters for comparison to collected spectra.

A variety of methods can be used to accomplish this task.[615] A common method includes using the Gauge-Including Atomic Orbital (GIAO) approach.[331-332, 616] In this, the shielding of a nucleus can be expressed as a second derivative of the total electronic energy referenced to an external magnetic field and magnetic moment of the nucleus. This method overcomes the unphysical "gauge" complication of coordinate origin selection in the calculation and has been shown to deliver accurate results in comparing calculations to experimental results. Though many codes lack the ability to accommodate periodic NMR chemical shift calculations, the gauge-including projector augmented wave (GIPAW) method has enabled such computations.[617] This has reduced barriers to computations on systems that would typically require very large clusters to accurately model. Along with Quantum Espresso, PARATEC, and others, the CASTEP package, in particular, has been extensively used to apply this periodic method to battery research.[618] Much like experimental methods, the computational shielding calculations require the use of a reference compound, a library of which are available across the literature. All electron Slater basis sets tend to be used for these types of calculations since they describe core electrons more accurately than pseudo-potentials or Gaussians. Core electrons are generally free but the importance of accounting for these is not absolute given that sufficient shell electrons are accounted for.[619] This approach has been widely used to compare computational and experimental spectra ^{17}O or ^{25}Mg NMR in Li and Mg batteries.[589, 620] The DFT approach has also been used to understand electrolyte systems for which solvent effect codes, such as the Conductor-like Screening Model (COSMO), or the inclusion of sufficient solvent shells are required.[621] This has been applied to better understand the solvent effects in a system.[622-623]

An additional challenge can present itself in applying DFT to heavier elements in batteries, such as for vanadium- or cesium-containing battery components, where the electrons of the *4d* orbitals begin to exhibit strong relativistic effects, requiring the use of the more computationally expensive (relative to the Schrödinger equation) Dirac equation. DFT-based total shielding calculations can be regarded as a sum of paramagnetic, diamagnetic, and spin-orbit coupling contributions. While relativistic effects may be accounted for without considering spin-orbit coupling, their applicability to accurate NMR calculations can be limited.[624] As such, NMR calculations considering relativistic effects often take advantage of the Zeroth-Order Regular Approximation (ZORA).[335-336] This method accounts for special relativity in heavier elements as electron speeds become more significant. ZORA is an excellent approximation to the fully relativistic Dirac equation, especially near the valance region. This improves the identification of species continuing heavier elements and secures greater confidence in the computational results. This computational method can be used to predict the NMR chemical shifts of structures that are likely to be present in the system. It should be noted that pure DFT calculations will not natively account for thermal effects on chemical shift since the calculations are based on 0 K. Effects such as chemical exchange between two species will require more robust methods to elucidate the structures present in the sample.

Still today, it can be difficult for DFT to accurately describe intermolecular interactions, especially dispersion forces where further perturbation terms may be necessary.[625] It is also challenging to model very large systems with hundreds of atoms to account for extended-order solvation schemes. To help determine the structure of a many-molecule system, MD simulations can be employed as a useful tool in understanding the nature of a battery system. Molecular

Dynamics is a computational tool for understanding the motion of a many-bodied system based on Newton's equations of motions. *Ab initio* Molecular Dynamics simulations take this concept a step further and compute forces using Shrödinger's equations.[626] This powerful technique has been widely applied to study the SEI formation on Li-ion batteries.[627-630] It has also been used to understand the properties of electrolytes in batteries.[631-632] Diffusion coefficients, for instance, can be approximated and compared to MRI values as well to better predict the state of the electrolyte during battery operation. MD can be also be used for NMR calculations by taking the structures most likely to be present based on MD simulations and calculating the chemical shielding with DFT.

What may be a more robust approach would be to directly combine the strengths of the two methods to generate an aiMD-DFT, time-averaged picture of the chemical system. In this method, the MD simulation generates a series of snapshots from the trajectory for the molecules in the system. These configurations are used in DFT calculations to determine the NMR shielding tensors, which can be used to generate a weighted-average chemical shift of the configurations present for a given system. This combinatorial approach has been used extensively in solvated ionic platinum species, but can be useful in understanding complex electrolyte systems for battery applications.[633-635]

5. Selections from recent research

The extraordinary importance of understanding the fundamental interactions in a given electrochemical cell has driven extensive research in the area with powerful *in situ* NMR investigations. Though numerous studies have been conducted that take advantage of this tool,

the following important works demonstrate well the capabilities of these methods across a number of battery systems.

5.1. In-situ NMR on Li-composite ion battery research

Composite anodes consisting of lithium and other metals (such as group IV Sn, Ge, Si) are attractive alternatives for traditional lithium anodes in Li-ion batteries. For instance, the use of Li-Sn composites have been investigated with NMR to demonstrate a 50% enhancement of lithium adsorption over carbon.[636] A brief review of *in situ* ^{7}Li NMR efforts in this area is available elsewhere that highlights the use of silicon, of interest due to its relatively high theoretical capacity.[541] Despite the interest in such materials, the precise structure of the lithiated species can be elusive to diffraction efforts due to the amorphous nature of the species. Lithium silicides, for example, have four reported stable crystalline phases, but electrochemical lithiation at room temperature favors an amorphous silicide. NMR has been applied to bridge the gap for these species by monitoring the transformation of lithium species during electrochemical cycling.[579]

Silicon presents a popular material for composite anodes that has been investigated to better understand delithiation.[596] One prominent example of Li-Si composites is reproduced in Figure 23. This illustrates the evolution of ^{7}Li species with time, whose signals strongly depend on their coordination environment with Si. Initially, four peaks are present between 0 and 8 ppm which relate to Li in the electrolyte, SEI on the positive and negative electrodes, and Li_XC. A broad peak ascribed to small silicon clusters begins to form around 18 ppm during the discharge process, which migrates to 14 ppm (A2). Additionally a resonance at 4.5 ppm (magenta) related to silicon clusters forms with discharging, indicating further breakage of the silicon linkages. The

peak that forms in the later stages of discharge at -10 ppm arises from overlithiated, crystalline $Li_{15}Si_4$, which was not observed ex situ. The use of NMR helped solidify the understanding of Li-Si systems, explaining the nature of species present under reaction conditions and showing the reactivity o amorphous lithium silicides. Additionally, the authors discovered that excess-Li could facilitate self-discharge at low voltages, resulting in a loss of capacity for Si batteries.

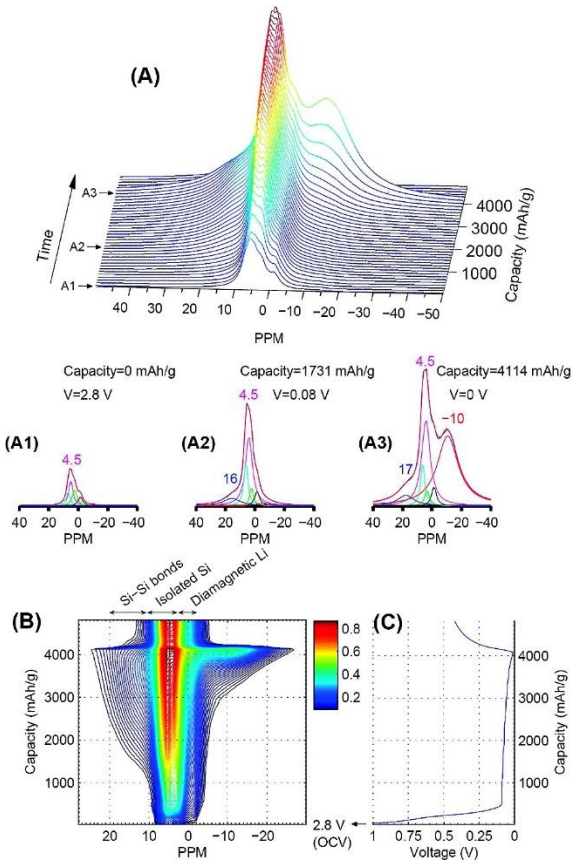

Figure 23. Stacked (a) and contour (b) plots of ^{7}Li in situ NMR spectra of a Li/Si battery during the first discharge and beginning of the first charge with corresponding electrochemical curve (c). a1-a3 show deconvoluted spectra at particular voltages. Reprinted with permission from J. Am. Chem. Soc., 2009, 131, 9239-9249. Copyright 2009, American Chemical Society. [637]

Balancing the anode's high energy densities (992, 1,623, and 4,200 mAh g^{-1} for Sn, Ge and Si respectively) with excellent substrate lithium diffusivity and electrical conductivity places Li-Ge as an attractive option.[638-640] NMR has also been used to better understand strategies for

stabilizing the structure of this composite. For instance, conventional methods of incorporating the group IV metals result in poor capacity retention across cycling. This effect stems from the drastic volume changes during the lithiation and delithiation process coupled with unstable formation of the SEI film. However, embedding Ge on a conductive scaffold can assist in the minimization of the detrimental volume fluctuations; however, inhomogeneity of metal deposition still negatively impacts the retention of energy storage capacity.[641-642] To mitigate the effect, core-shell structures have been employed that show enhanced resistivity towards storage degradation.[643-644] Despite these enhancements, the mechanisms by which Ge core-shells impact Li cycling were unclear, complicating performance optimization. Tang et al. employed Ge nanorodes encapsulated by bamboo-type multiwall carbon nanotubes (Ge@CNT) for a Ge-Li planar half-cell battery and *in situ* NMR to better describe the roles of Ge in the Li-Ge battery.[576]

Figure 24 shows the *in situ* ^{7}Li NMR results obtained during the first two charging cycles of a Ge@CNT Li-Ge battery half-cell, plotted as a function of cell capacity. They observed four ^{7}Li resonance lines centered at 24, 13, 10, and -24 ppm which were monitored together with the ^{7}Li signals of the electrolyte and SEI (0 ppm). From a detailed analysis of the collected data, supplemented with XRD, TEM, and STEM, it was concluded that the significantly shielded signal at -24 ppm could be attributed to an overlithiated $Li_{15+\Theta}Ge_4$ phase that was only present during the electrical contact. This phase was uniquely identifiable by NMR (not XRD or TEM) under reaction conditions. The absence of this overlithiated phase promoted the formation of a broad signal downfield that was attributed to a more amorphous Ge phase that may enhance the lithiation/delithiation rate. The remaining peaks could be assigned likewise by the properties

exhibited during the various experiments (see Table 29). They showed much greater stability towards a lack of electrical contact.

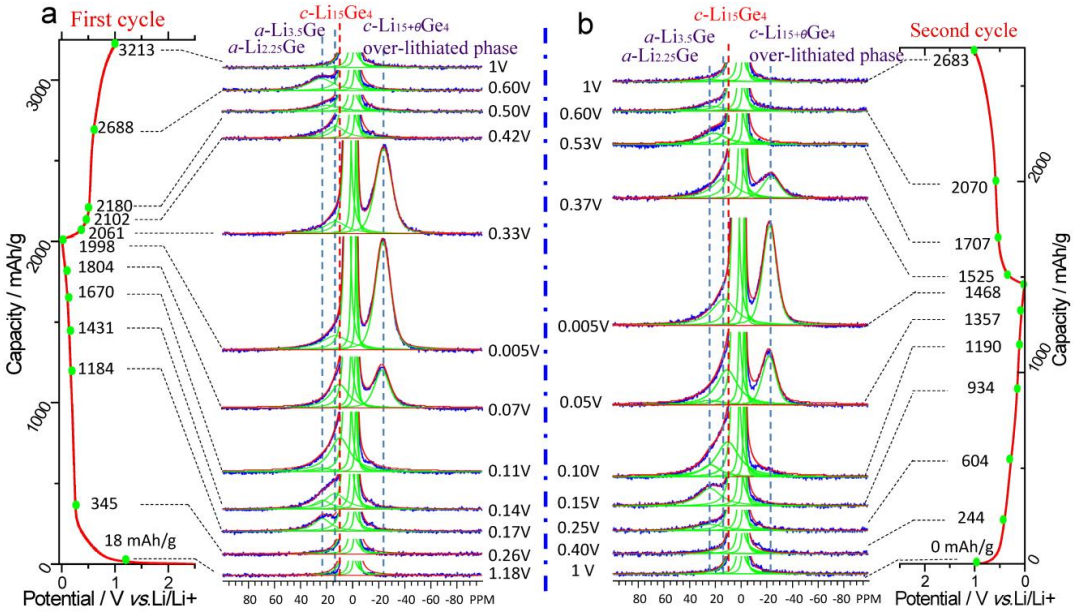

Figure 24. Selected in situ [7]Li NMR spectra of the Ge@CNT composite during the first (a) and second (b) charge/discharge cycles. Reprinted with permissions from J. Am. Chem. Soc. 137, 7, 2600-2607. Copyright 2015 American Chemical Society. [576]

Table 29. Summary of in situ [7]Li NMR Observations. Reprinted with permissions from J. Am. Chem. Soc. 137, 7, 2600-2607. Copyright 2015 American Chemical Society.

Resonance index	**Assigned Phase**	**Chemical shift/ppm**	**Potential / Capacity***	**Crystal property**	**Observed by**
R1	$Li_{2.25}Ge$	24	0.17/839	Amorphous	NMR (In-situ ^7Li)
R2	$Li_{3.5}Ge$	13	0.14/1086	(In-situ XRD[645] and TEM)	NMR (In-situ ^7Li)
R3	$Li_{15}Ge_4$	10	0.11/1325	Crystalline phase (In-situ XRD[645] and TEM)	NMR (In-situ ^7Li), In-situ XRD[645]
R4	$Li_{15+\theta}Ge_4$	-24	0.005/1653	Over-lithiated	NMR (In-situ ^7Li)

This study enabled key understandings surrounding the Li-Ge battery system, in particular, the reaction pathway during electrochemical cycling. The *in situ* ^{7}Li NMR studies revealed that the reversibility of lithiation in Ge@CNT is mediated by coexisting amorphous and crystalline phases present in the battery. It also enabled a deep understanding of the system's electrically-driven metastable $Li_{15+\Theta}Ge_4$ phase that was only possible during electrical contact on the carbon walls that encapsulated the Ge. Using a combination of the techniques, the authors were able to propose a reaction pathway that accounts for all spectroscopic and microscopic observations as well as phase transitions available during cycling:

$$Ge(c) \rightarrow Li_{2.26}Ge(a) \rightarrow Li_{15}Ge_4(c) + Li_{3.5}Ge(a)$$
$$\rightarrow Li_{15+\theta}Ge_{4,metastable}(c) + Li_{3.5}Ge_{metastable}(a)$$

where (c) indicates a crystalline phase and (a) is the designation for amorphous. This model well-reflects the progression of phases identified with the *in situ* NMR to describe the lithiation process during electrochemical cycling. It was speculated that the enhanced capacity from such carbon-encapsulated Ge was related to the formation of these metastable states during electrical contact. Such observations are unique to *in situ* NMR and promote a deeper understanding of composite battery systems. A number of additional *in situ* NMR studies have focused on composite anode and cathode materials using ^{6}Li and ^{7}Li, to provide a detailed understanding of the microstructure formation of Li dendrites, ion hopping, and phase transitions with a variety of electrode materials.[579, 646-648]

5.2. In-situ NMR on Li-S battery research

Lithium-sulfur electrochemical cells are battery systems that hold great potential advantages over conventional Li-ion batteries due to improvements in specific energy (~2,500 Wh kg^{-1}) and low-cost production options.[649-651] In these systems, soluble lithium polysulfide species are formed as intermediates important to the energy transfer chemistry; however, dissolved species may also lead to poor electrochemical performance and failure. Though a number of *in situ* methods have highlighted the importance of the reaction in system understanding, they failed to provide a quantitative look at the evolution of the present species, instead focusing on identification of discrete sulfur or lithium polysulfide compounds.[519, 652] *In situ* NMR has the distinct advantage of simultaneously identifying and quantifying all NMR-active species during the charge, discharge, and standby periods of battery cycling. This concept was applied to the Li-S system using the cylindrical microbattery *in situ* NMR cell pictured in Figure 25A.[653] A lithium metal anode (100 μm thick in blue) was separated from the cathode with Celgard 2500 of thickness 25 μm (red). The sulfur-based cathode film (ca. 175 μm thick) was laminated onto an aluminum mesh (green) where binding utilized polytetrafluoroethylene. In this system, the transient nature of Li species was monitored over several charge/discharge cycles to capture the microstructural evolution of the species in the various components of the battery.

The resulting ^{7}Li spectra were plotted as a function of time, where each spectrum was collected in just 4 minutes (see Figure 25B). Representative spectra were selected and deconvoluted (Figure 25C) to identify eight unique lithium species that could be identified with high confidence due to a more solid understanding of the evolution of these during the charge/discharge process (Figure 25D) not available during ex situ measurement.[530] Though ex

situ measurement of each the separator, cathode, and anode could be compared, a more clear assignment of these peaks arose based on the observed chemical shift, known species previously identified at a given voltage, and the line intensity change as the experiment progressed. This first *in situ* study using the cylindrical micro Li-S battery demonstrated that the reaction pathways were composed of mixed species in a complex environment instead of discrete step-by-step reactions.

For example, peak 1 at -128 ppm was identified as a soluble long-chain polysulfide since S_8 is expected to reduce to this species at around 2.3 V. This was confirmed by the maximum intensity arising during the 2.1 V charge plateau, a minimum during the end of the discharge when insoluble Li_2S_2/Li_2S dominate, and on the basis of chemical shift value. This species was shown to directly and rapidly convert to long-chain polysulfides instead of relying on the accumulation of additional LiS_4 species. Further, this peak and its analog at -100 ppm were not visible except under *in situ* conditions and is attributed to Li^+ interacting with long-chain polysulfides as well as sulfide radicals. The second peak (-71 ppm) was similarly associated with soluble long-chain polysulfides such as Li_2S_8 or Li_2S_6. The remaining peaks, high field peaks 3 (-34 ppm) and 4 (-7 ppm), were described as insoluble Li_2S_2 or Li_2S on the lithium electrode.

Peaks 5, 6, and 7 were challenging to clearly identify, but on the basis of Li metal shifts near 250 ppm (Knight Shift from electrons in the conduction band) these are tentatively assigned as quasi-metallic, porous lithium species. These species also follow the opposite trend as the polysulfide signals. Peak 5 reaches a maximum intensity as the cell is fully charged whereas peaks 6-8 reached their maximum at 50% charge and declined to a local minimum at full charge. This suggests the growth of the porous lithium species in the deposition process and the

concomitant reduction of the signals for peaks 6-8. These peaks were further found to relate to Li involved in creating the SEI. In particular, signal 8 (254 ppm) is assigned as a dendritic or thin mossy Li environments on the anode material.

In situ NMR also supports the hypothesis that the reaction pathways during charge and discharge differ due to the evolution of species observed and the differing lengths of the two plateaus of the charge-discharge curve.

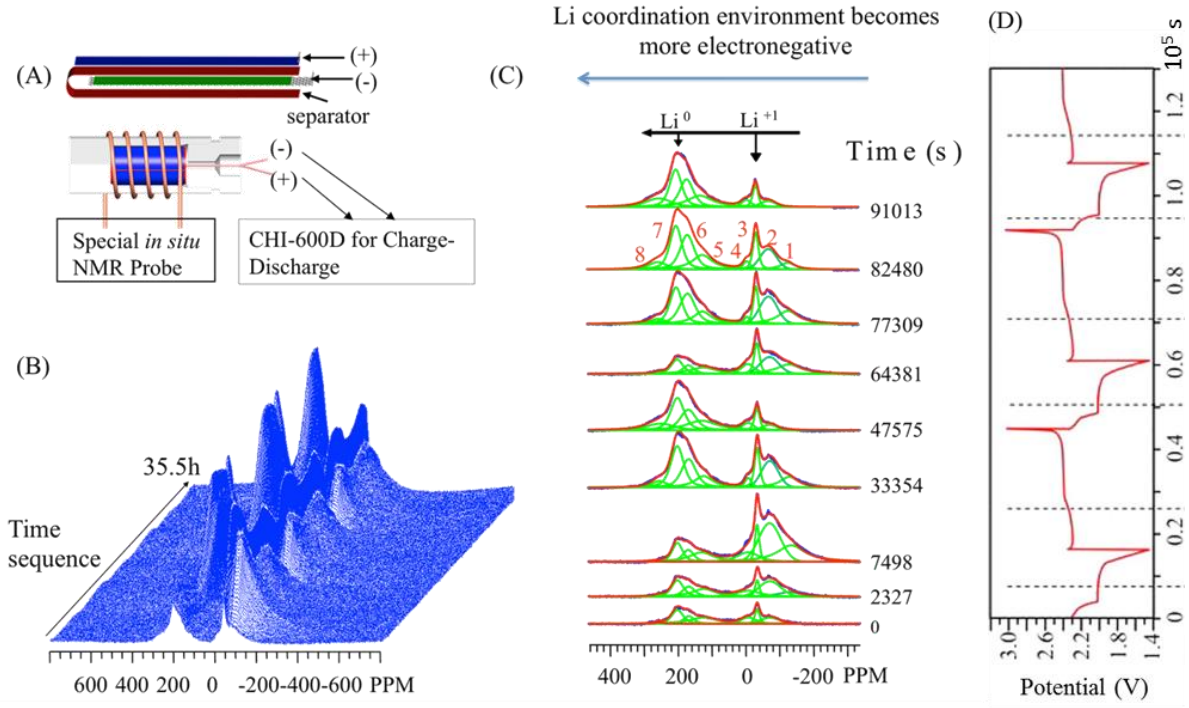

Figure 25. In situ NMR data collected for a Li-S battery system showing A) schematic of the cylindrical microbattery, fitted into the in situ NMR probe, B) stacked-plot data of 500 in situ ^{7}Li NMR spectra in the functioning Li-S battery cell during the charge/discharge cycle, C) major peaks of interest extracted at selected times by fitting the spectra, and D) the voltage profile of the Li-S cell used in the NMR measurements. Peaks are labeled as (1,2) soluble long-chain polysulfides, (3,4) insoluble Li_2S_X on the electrodes, (5-7) quasi-metallic, porous lithium, and (8) dendritic Li. Adapted with permissions from Nano Lett. 15, 5, 3309-3316. Copyright 2015 American Chemical Society. [653]

This important *in situ* work was able to clarify the evolution of species involved in SEI layer formation as well as anode surface roughening and dendritic nucleation. Unique

polysulfide environments became apparent during the charge and discharge process that cannot be captured by ex situ investigation. Confirmation of transient free radical presence offers key insights into the degradation of battery performance. Observations like those collected for this Li-S battery study offer molecular-level insights that are crucial to the accelerated development of the technology. A number of ex situ NMR studies employing ^{7}Li and ^{1}H NMR have continued to investigate the key uncertainties surrounding this technology to compliment *in situ* studies such as See et al.'s attempts to better describe the Li-S phase diagram.[530, 654-656]

5.3. In-situ NMR on Li-ion battery research

Numerous highly respectable efforts have employed *in situ* NMR to detail the chemical transformations occurring, such as extraction, insertion, and dendritic growth.[543, 573, 582, 657] For instance, the effect of carbon coating graphite for use as an anode was shown to have two sites for lithium; the graphite core and soft-carbon shell for intercalation and storage, respectively. The 7Li NMR showed the the relative abundance of the two sites was well correlated to the extent of coating, explaining the decrease in irreversible capacity and increase in coulombic efficiency.[658] Recently, lithium-ion battery technology utilizing reduced graphene oxide (rGO) has attracted great interest as a high capacity alternative to graphite anodes due to its high surface area and conductivity.[659-664] However, the lithiation mechanism for rGO was poorly understood relative to that of graphite-based cells, where differences in the mechanisms are evidenced by its increased capacity over graphite (600-1000 mA h g^{-1} vs 372 mA h g^{-1}). To better understand the evolution of the SEI layer on rGO, *in situ* studies employing Raman spectroscopy and an NMR battery cell were conducted to monitor the temporal evolution of the G-band and ^{7}Li signal during the charge and discharge cycle.[577]

For both the graphite and rGO anodes, the *in situ* Raman shows a decrease in the G-band at ~1582 cm^{-1} as the battery was discharged. This was ascribed to a resonance loss by the intercalation of Li, increasing the homogeneity of the sample. In the case of graphite, a 9 cm^{-1} upshift is observed during cathodic polarization due to the donated electrons to the carbon. Contrasting the graphite's loss of G-band below 0.2 V, the rGO sees this disappearance around 0.3 V. To provide additional insight, Tang et al. used *in situ* ^{7}Li NMR to monitor the specific chemical environments of lithium species. A number of distinct lithium species were detected in the *in situ* experiments. Upfield, a broad peak at -3 ppm and a few small, sharp peaks around 0 ppm were present. The sharp peaks at 0 are indicative of solvated lithium species while the broad signal is attributed to a combination of lithium intercalated into the rGO lattice and adsorbed on the surface functional groups present on rGO.[665-666] Downfield, three peaks at 244, 250, and 265 ppm are present that relate to the Li-metal electrode. The peaks at 244 and 250 were attributed to a 10 µm skin layer on the Li-metal surface while the 265 ppm peak was assigned to the Li-metal fibers perpendicular to the metal surface.[539] Notable changes were observed for the broad peak at -3 ppm and the peak at 265 ppm that provided insight on the electrochemical process. As seen in Figure 26, the evolution of the various chemical species present could be tracked along the charge/discharge cycles.

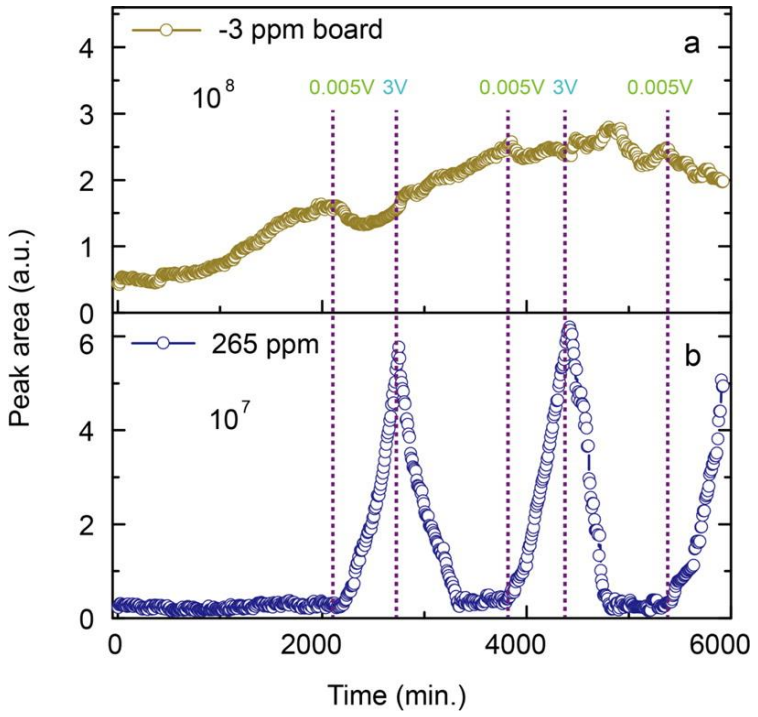

Figure 26. In situ NMR peak area evolution of the (a) -3 ppm broad and (b) 265 ppm peaks during the charge and discharge cycles. Reprinted with permission from J. Phys. Chem. C 120, 5, 2600-2608. Copyright 2016 American Chemical Society. [577]

The -3 ppm peak intensity evolution shows the clear enhancement of signal over the course of the experiment, approximately quadrupling in intensity by the end of the third charge cycle. The intensity of the intercalated/adsorbed lithium species is shown to increase over the discharge periods and reduce in abundance as the cell is charged. Conversely, the Li-metal fibers (256 ppm) remain nearly absent until charging initiates, reaching a maximum at the end of the first charging cycle. As discharging is initiated, the peak intensity falls as lithium ions are peeled from the surface of the metal. The concurrent and opposite behaviors during cycling demonstrate well the fate of Li species in electrochemical cycling. Tang et al. made the interesting observation that only a small portion of the -3 ppm species is participating in the cycling, suggesting that a majority of the lithium that had moved to rGO were inactive and participating in the formation of the SEI with the surface functional groups (-H, -OH, -COOH, -C=O, etc.).

The second charge/discharge cycle demonstrated an increased Li-metal species compared to the first cycle, showing a relative stabilization of the SEI after the first cycle. This observation was confirmed by the third cycle, which may serve to explain the high capacity of rGO during the first cycle and reliability during subsequent cycles, quantified by the area of the Li-metal peak.

Combined with the CV and additional NMR experiments, it was concluded that the primary difference between rGO and graphite was the preference of rGO to intercalate Li via surface adsorption instead of the conventional graphite mechanism. The passive SEI in rGO was formed during the first electrochemical cycle and was stabilized afterward. Approximately 36% of the intercalated Li^+ was recycled during the first cycle. While the detailed structure of Li in the SEI could not be resolved, the differentiation between Li^+ in the SEI and the counterpart on the rGO is directly visible as a function of time and electrochemical cycling. This study highlights the power of NMR to observe quantitative, real-time descriptions of battery constituents under unique chemical environments. Additional NMR studies related to this topic have made a variety of contributions to our understanding of Li-ion batteries.[541, 573, 582] Important and decisive observations, such as the mass transport limitations present in high-power Li-ion powered vehicle applications, are greatly assisted by these *in situ* NMR methods.[667]

5.4. In-situ and ex situ high-field NMR studies of Li-metal batteries

Li-metal batteries offer a high energy density option relative to Li-ion battery technology, but also pose a number of challenges in the safe recharging of the cell. The origin of the rechargeable Li-metal battery research finds itself in the 1970s.[668] Of interest as an anode due to its low electrochemical potential (-3.04 V with respect to hydrogen electrode), low material density (0.534 g cm^{-3}), and high theoretical capacity (3860 mA h g^{-1}), limited success was

realized due to poor columbic efficiency and dendritic growth of Li during charging cycles.[669-670] The cycling stability of Li strongly depends on the interactions with the electrolyte, in particular where organic solvents render Li unstable and promote the formation of these microstructures. It has been identified that addition of certain species to the electrolyte forms a uniform, solid SEI or alloy with Li during deposition that can suppress dendrite formation and thus increase the cycling life.[671-675] For example, one approach to suppress dendritic growth is based on a self-healing electrostatic shield where low concentrations of Cs^+ or Rb^- in the base electrolyte form a positively charged electrostatic shield around the nucleation points (Li tips). This forces deposition to adjacent regions to reduce dendrite formation.[676] Microscopy even identified a dendrite-free Li film, suggesting the presence of synergistic effects between the Cs^+ and SEI.[677] Previous *in situ* NMR investigations on Li batteries have quantitatively tracked the real time dynamics under working conditions.[542, 563, 567] One study even highlighted the deposition of dendritic Li on the Li electrode during cycling.[539] This study, however, found a wide range of possible shifts (242 to 272 ppm) for a given species depending on its orientation with respect to the magnetic field. To amplify potential important signals in this region, the bulk magnetic susceptibility effect was clarified by employing planar symmetric Li metal cells measured as a function of the normal direction relative to the magnetic field for the study of the Li-metal battery system with and without the Cs^+ additive.[585]

The study highlighted the importance of Cs^+ in the formation of well-aligned Li nanorods and reversibility of the Li electrode. Though a number of studies readily utilize ^{7}Li NMR, this one also incorporated ^{133}Cs NMR technics to probe the dynamics of Cs^+ in the battery. The *in situ* ^{133}Cs NMR clearly showed the migration of Cs^+ to the Li electrode to form a positively

charged electrostatic shield during the charging process, evidenced by a significantly broadened signal compared to the narrow signal of a solvated Cs species. It was found that the Cs intensity was retained and reversibly solvated at the other end of the electrochemical cycle. The results also indicated a much larger fraction of the Li taking part in the cycling process when the additive was present. The rods generated in the absence of Cs tended to be much thicker and lead to a large fraction of inactive lithium species.

In addition to *in situ* Li-metal investigation, NMR has provided unique insights with ex situ techniques, particularly for low-sensitivity nuclei. The formation of new SEI layers as the battery was cycled that trap metallic lithium in the passivation film poses a potential safety hazard, making the SEI a target for detailed investigation.[678-679] One notable example of ex situ NMR took advantage of ^{1}H, ^{6}Li, ^{13}C, and ^{19}F NMR to study the SEI formed on the copper electrode. Wan et al. employed the unique advantages of ^{6}Li NMR over ^{7}Li NMR to obtain a higher spectral resolution in the recovered SEI of a number of Cu|Li cells.[680]

This work analyzed the SEI extracted from Cu|Li cells using two different concentrations of lithium bis(fluorosulfonyl)imide (LiFSI) in 1,2-dimethoxyethane (DME) as electrolytes (LiFSI-DME samples), including one lithium bis(trifluoromethanesulfonyl)imide (LiTFSI)-DME sample. The cells were cycled such that a 1 h deposition time was utilized to a capacity of 1.0 mA h cm^{-2} and the stripping was controlled to an upper cutoff voltage of 0.5 V vs Li/Li^{+}. These cells were cycled 200 times prior to SEI extraction, preparation, and loading into a sealed 3.2 mm MAS rotor for ex situ ^{6}Li MAS NMR measurement. The authors were able to identify a number of lithium species using high-field ^{6}Li NMR spectroscopy. Across all samples investigated, metallic Li (264 ppm) was present that can stem from dead Li and broken dendrites

that failed to cycle during the final delithiation stage. Relatively more metallic lithium is present in the least concentrated electrolyte (i.e., the 1 M LiFSI-DME), but fewer lithiated species can be observed compared to the other two concentrations, showing the clear impact of solution concentration on lithium species. By employing reference compounds and taking advantage of the higher spectral resolution afforded by ^{6}Li NMR over ^{7}Li NMR, six additional Li species were identified in the SEI of these cells: LiFSI, LiF, Li_2O_2, Li_2S, and Li_2O. Fluorine-containing compounds were verified by ^{19}F MAS NMR due to the highly sensitive nature of these signals to the chemical environment of F. ^{1}H and ^{13}C MAS NMR were also used to rule out potential Li species.

The spectra from the 15 to -15 ppm region can be viewed in Figure 27. The 4M LiFSI-DME sample (Figure 27a) contained Li_2O (2.8 ppm), Li_2S (2.4 ppm), LiOH (1.3 ppm), Li_2O_2 (-0.1 ppm), LiF (-0.9 ppm), and LiFSI (-1.8 ppm). The 1M LiFSI-DME sample (Figure 27b) could be deconvoluted with peak that aligned well to those of the 4M LiFSI-DME sample, except that no ^{19}F peak was present, suggesting that the -1.1 ppm peak is a different species from LiF; a number of options were proposed in the full text. Figure 27c shows the spectrum for the 3M LiTFSI-DME sample, which showed similar features as the 4M LiFSI-DME sample, but without Li_2O and the presence of LiTFSI instead of LiFSI. Higher concentrations of LiFSI/DME resulted in an overall thicker SEI with fewer dead Li-metal species. This trend was observable across the three samples and explained the enhanced electrochemical performance at high LiFSI concentrations in DME. While this is one example of ex situ NMR assisting in the characterization of how Li-metal battery formulation impacts the SEI, numerous others are available in the literature.[597, 681]

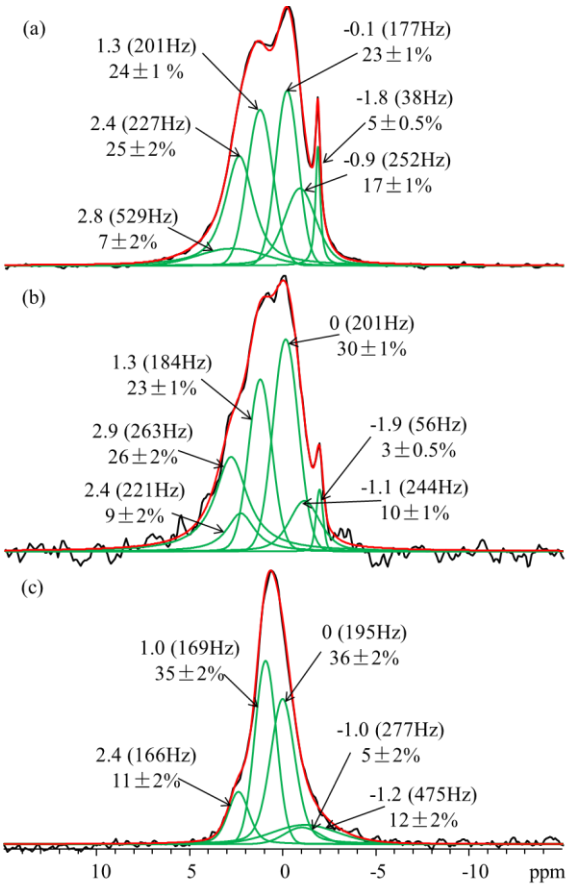

Figure 27. The expanded spectral region plots between -15 and 15 ppm and the deconvolutions of the ^{6}Li MAS NMR spectra obtained at high field of 850 MHz spectrometer for the SEIs harvested from Cu|Li batteries with (a) 4 M LiFSI-DME, (b) 1 M LiFSI-DME, and (c) 3 M LiTFSI-DME as electrolyte. Peaks are assigned to Li_2O (2.8 ppm), Li_2S (2.4 ppm), LiOH (1.3 ppm), Li_2O_2 (-0.1 ppm), LiF (-0.9 ppm), and LiFSI (-1.8 ppm). Reprinted with permissions from ACS Appl. Mater. Interfaces 9, 17, 14741-14748. Copyright 2017American Chemical Society.[680]

5.5. Ex-situ NMR studies of solvation structures

A key component to battery systems are the electrolytes responsible for energy transfer. Their observation by NMR can lead to a detailed understanding of the electronic environment and thus their molecular arrangements. While a number of electrolyte components have been mentioned previously, less abundant and recorded nuclei can provide valuable insight. The challenge associated with this, however, is the low concentration and abundance of species, such as ^{17}O in nonaqueous carbonate electrolytes.[682] In this, Bogle et al. were the first to employ

natural abundance ^{17}O NMR measurements to such electrolyte systems, demonstrating a maximum of six ethylene carbonate molecules in the Li^+ solvation sheath accompanied by dimethyl carbonate.

Often, a confident assignment of signals for such electrolyte systems is hindered by the structural interpretation of the lines observed. Without supporting experimental data for similar structures and trends, it can be very challenging to describe the exact coordination of molecules in the electrolyte, necessitating the application of theoretical calculations. Our group's recent work highlights the power of combining NMR spectroscopy with high-level theoretical calculations for a deeper understanding of battery-related electrolyte systems.[683] For such applications, our group utilizes often a specialized large sample volume probe established for ultra-high field (850-900 MHz) was employed.[387, 684-685] The probe permitted up to 2 ml in sample volume, allowing for natural abundance detection of Mg at concentrations as low as 10 mM within just a couple hours of sampling (S/N ~ 60). The first reported application of the probe with respect to battery technology employed the technology for analyzing the natural abundance ^{17}O signals in lithium-based electrolytes.[684] In this work, Deng *et al.* collected natural abundance ^{17}O spectra of Li-bis(trifluoromethane sulfonyl) imide (LiTFSI) at concentrations around 20 mM to elucidate the solvation structures of LiTFSI in various solvents and mixtures of the solvents. Accompanying the high-sensitivity NMR studies, DFT-based models of the solvation structures helped determine the coordination and exchange structures of Li^+ in the solvents at various concentrations in an attempt to understand the barriers a given electrolyte might encounter during battery operation. A more recent study highlights this principle by combining electrochemical evaluation, high-field natural abundance ^{25}Mg NMR, classical

molecular dynamics simulations, and DFT-based chemical shift calculations to understand the solvation structure for Mg-based battery technology.[686]

Due to a rise in evidence suggesting that the solvation structure of a liquid electrolyte has a dramatic impact on the electrochemical performance of batteries, a detailed investigation of Mg-battery electrolytes was conducted by dissolving magnesium borohydride [$Mg(BH_4)_2$] and $Mg(TFSI)_2$ in diglyme (DGM).[623, 687-688] The rational development of improved electrolytes requires an understanding of how the components interact with each other, and as such, how the solvation structure plays an important role in the resulting properties. Mg batteries offer an attractive alternative to Li-ion designs due to the potential to triple the volumetric energy density.[382] However, a number of challenges exist in utilizing Mg as an energy carrier. One prominent drawback is the employment of an electrolyte capable of operating across a wide electrochemical window while simultaneously allowing reversible plating/stripping of Mg. [30] Since Mg forms an ionically blocking layer when exposed to oxygen, inhibition of deposition is a difficult challenge for Mg-based battery systems to overcome, driving the need for a designer electrolyte system to either prevent or reduce this interaction of the SEI.[689-690] Halo, organo, and organo-halo salts are known to allow reversible Mg deposition, but they have limited anodic stability and conductivity.[691] A more conductive salt such as $Mg(TFSI)_2$ suffers from difficulties in the reversible stripping process. To better understand how continued improvements to these electrolytes can be realized, a detailed assessment of the structural aspects is required to understand the solvation environments.

Our team has investigated the solvation structures of Mg^{2+} with varying concentrations and combinations of $TFSI^-$ and BH_4^- mixtures using a combined experimental and theoretical

approach, chiefly employing the large sample volume probe for natural abundance ^{25}Mg NMR measurements combined with quantum chemistry calculations and molecular dynamics simulations to relate the electrolyte structures to their electrochemical performance.[686] The experimental results as well as the predicted shift accounting for molecular exchange are presented in Figure 28. Figure 28a shows the experimental results of the natural abundance ^{25}Mg experiments from pure 0.01 M $Mg(BH_4)_2$ (a), mixed $Mg(BH_4)_2$ and $Mg(TFSI)_2$ electrolytes (b-f) to pure 0.4 M $Mg(TFSI)_2$ (g). The observed experimental shifts of the various counter-ion concentration ratios agree well with those predicted based on the molecular exchange principle:

$$\delta_m = \frac{c_1}{c_1 + c_2}\delta_1 + \frac{c_2}{c_1 + c_2}\delta_2$$

where c_i is the concentration of a given species and δ_i is the chemical shift of the pure, dilute Mg salt.

To interpret the results, molecular dynamics simulations were employed to predict likely structures of the salts at various concentrations. Analyzing the residence time and radial distribution of the molecules in the simulation provided a clearer picture of which structures were most likely and to which electrolyte components Mg shared coordination. The resulting structures were then used as models for DFT-based chemical shift calculations. This approach assisted in interpreting the NMR data to provide clear evidence on the solvation structures of the electrolytes due to the agreement between experimental and computational data.

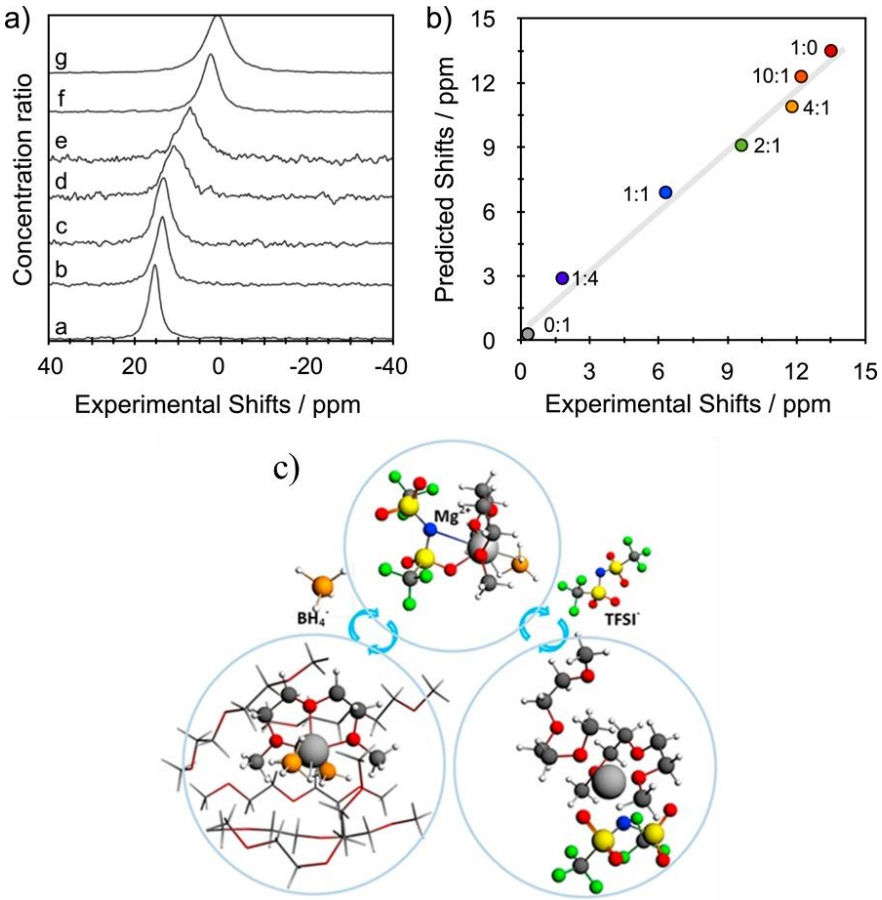

Figure 28. a) ^{25}Mg NMR spectra of $Mg(BH_4)_2$ and $Mg(TFSI)_2$ dissolved in DGM with different concentrations of ($Mg(BH_4)_2$: $Mg(TFSI)_2$). (a) 0.01 M : 0 M; (b) 0.01 M : 0.001 M; (c) 0.01 M : 0.0025 M; (d) 0.01 M: 0.005 M; (e) 0.01 M : 0.01 M; (f) 0.01 M: 0.04 M; (g) 0 M : 0.4 M. b) correlation between the predicted chemical shifts and experimental results. c) proposed solvation structure rearrangement mechanism. The labels on the points are the molar ratios of $Mg(BH_4)_2$: $Mg(TFSI)_2$. Adapted with permissions from Nano Energy 46, 436-446. Copyright 2018 Elsevier.[686]

For the pure $Mg(BH_4)_2$ salt dissolved in DGM, the 1st solvation shell contains two BH_4^- anions and one DGM as a tridentate chelating the Mg^{2+}, the second shell has 5-6 DGMs. The $Mg(TFSI)_2$ dissolved in DGM appears to take a first solvation shell containing one DGM as a tridentate ligand and a second as a monodentate ligand. A single $TFSI^-$ donates an oxygen and nitrogen atom to the Mg^{2+} cation. The second solvation shell contains ~4 DGM molecules. When the two salts are mixed, a fast exchange between the two pure component structures was discovered that proceeds through a third, intermediate structure containing one of each $BH4^-$,

$TFSI^-$, and DGM in the first solvation shell and 5 DGMs in the second shell. This intermediate structure was classified by molecular dynamics and accurately explains the observed shifts at high salt concentrations. The efficiency of the electrochemical performance was maximized at a $BH4^-$:$TFSI^-$ ratio of 1:4 and was attributed to the enhanced molecular dynamics and improved stability of the TFSI identified by the combined NMR and computational approaches. This work provides a clear demonstration of the power of NMR in characterizing the effect of the electrolyte solvation structure on electrochemical performance.

Combined computational and NMR efforts have also improved scientific understanding of electrolyte mixtures in redox-flow batteries. Investigations of electrolyte stability led to the development of a mixed-acid system with a dramatic increase in energy density and stability over conventional vanadium redox-flow batteries, for which NMR and theoretical evidence were combined to suggest the effect could be attributed to improved anion selection for the ligand exchange process.[604-605] Similar concepts were applied to lithium-based redox-flow systems. Comprehensive NMR and DFT analysis was used to design and characterize an ionic-derivatized ferrocene to be the active redox species in the electrolyte. The enhanced dynamic interactions between solvent and electrolyte led to increased solubility that improved battery performance. Characterization identified that the Li-graphite anode prevented dendritic growth and SEI instability to promote stability over many charge-discharge cycles.[692] Indeed, the combination of NMR with DFT calculations of the chemical shift has deepened the pool of knowledge relating to electrolyte structures, but the dynamics of these processes are important too. Briefly, the role of NMR and MD calculations in elucidating battery science will be mentioned.

Since solvation structures are in constant motion and chemical species in electrolytes are diffusing, pulse-field gradient (PFG) approaches have also been employed to elucidate the solvation structure and dynamics.[693-694] This technique has been used to show the strong relationship between cationic transference number and diffusivity.[695] Robust efforts to predict specific diffusion constants have also been proposed based on extensive NMR efforts.[696] Due to the empirical nature of these models, a more theoretical approach could provide a deeper understanding of diffusion in electrolyte systems. To support measurements of structure and diffusion, computational MD predictions the diffusion constants can be well-matched with experimental values.[697] In this way, computational efforts that are not DFT-based have also played an important role in characterizing electrolyte systems.

5.6. Magnetic Resonance Imaging

Worth mentioning, magnetic resonance imaging (MRI) is a technology closely related to NMR that has also been used in battery science to visualize the growth patterns of dendrites.[698-699] This magnetic resonance technique has provided insight on the unique structures present on electrodes, including dendritic formation mechanisms, the impact of cycling, and important concepts in improving the design of battery materials.[699-700] A number of atoms that are commonly found in the cathodes, anodes, and electrolytes of batteries, such as Li, O, C, H, N. Na, Mg, etc., are suitable for detection with MRI, making it a highly relevant tool for discovery of the transformations taking place during the charge/discharge cycles of a variety of electrochemical cells. One such example is the concentration gradient of ions in electrolyte that form when current is applied. *In situ* ^{7}Li imaging was applied to demonstrate this in Li-ion systems, showing directly local differences during *in situ* operation.[701] Combining this with

diffusion measurements has also provided a time and specially resolved picture of the diffusive behavior of electrolytes in a battery. [702] MRI has also been applied to show changes in the magnetic field around a battery, circumventing the need for RF penetration into the cell. In this way, changes in susceptibility related to lithiation can be observed and the potential for MRI to detect defects in a cell has been suggested, offering a powerful, non-invasive tool for battery assessment.[703] Already it has been demonstrated to aid in the understanding of the irreversible nature of degraded battery performance resulting from Li microstructures and non-uniform lithium distribution on graphite. Given the ability to visualize distributions of species (electrolytes, charges, etc.) MRI provides a unique spacial description of battery cells during operation. Doubtless, with the advantages magnetic resonance imaging can provide, it will continue to be an essential asset to *in situ* battery research.

6. Concluding remarks & outlook

Given the importance of batteries in modern society, a deep understanding of these chemical systems at the molecular level is of paramount importance for continued technological advancement. Understanding the failure mechanisms and properties of different batteries will direct future research efforts to solving the key challenges in capacity, longevity, and efficiency. Herein, we have outlined the technological advances and techniques that make such discoveries possible. *In situ* NMR is truly a powerful tool for battery research and has been used as such for about two decades to better understand these electrochemical systems. We have shown the unique advantages NMR processes over other techniques and the importance of *in situ* measurement where some species can only be observed when current is applied to the real, functioning battery. Additionally, we have shown the unique advantages of conducing ^{6}Li, ^{17}O

and ^{25}Mg NMR at the ultra-high field of 850 MHz for obtaining the detailed chemical compositions in the cycled electrodes and the solvation structures of ions in electrolytes by coupling with molecular dynamics studies and DFT NMR calculations. Continued progress will be made in the area where further research will be focused on applying the newest cell designs with O-ring sealing for handling elevated temperature and pressure and 3-D printed bodies for long-run studies of battery cycling. Future efforts to enhance the signal for detection of less abundant nuclei in these batteries is also an area of interest and may be realized by applying additional cells in parallel. Other sensitivity enhancement techniques, notably, the technique of dynamic nuclear polarization (DNP) that can potentially increase an NMR signal by up to 2-4 orders of magnitude via transferring paramagnetic electron polarization from a polarization agent by taking advantage of the much larger electron Zeeman interaction, [704], [705],[706] may further help to advance the application of NMR in energy storage research. One final area that lacks extensive literature is the detailed time scale information on various processes that NMR can probe.[697] Such information will provide unprecedented insight into the interaction mechanisms and molecular motion at play within these systems. Regardless of the focus of these next developments, NMR will clearly maintain importance in understanding the electrochemical process as new battery systems are developed that progressively improve our current technology as the iterative approach dictates.